



University of HUDDERSFIELD

University of Huddersfield Repository

Clemett, Christopher John

SYNTHESIS, CO-ORDINATION CHEMISTRY AND CHEMOSENSITIVITY STUDIES OF SELF-ASSEMBLED ANION RECEPTORS

Original Citation

Clemett, Christopher John (2022) SYNTHESIS, CO-ORDINATION CHEMISTRY AND CHEMOSENSITIVITY STUDIES OF SELF-ASSEMBLED ANION RECEPTORS. Doctoral thesis, University of Huddersfield.

This version is available at <http://eprints.hud.ac.uk/id/eprint/35699/>

The University Repository is a digital collection of the research output of the University, available on Open Access. Copyright and Moral Rights for the items on this site are retained by the individual author and/or other copyright owners. Users may access full items free of charge; copies of full text items generally can be reproduced, displayed or performed and given to third parties in any format or medium for personal research or study, educational or not-for-profit purposes without prior permission or charge, provided:

- The authors, title and full bibliographic details is credited in any copy;
- A hyperlink and/or URL is included for the original metadata page; and
- The content is not changed in any way.

For more information, including our policy and submission procedure, please contact the Repository Team at: E.mailbox@hud.ac.uk.

<http://eprints.hud.ac.uk/>

University of
HUDDERSFIELD

SYNTHESIS, CO-ORDINATION CHEMISTRY AND CHEMOSENSITIVITY

STUDIES OF SELF-ASSEMBLED ANION RECEPTORS

CHRISTOPHER JOHN CLEMETT

A thesis submitted to the University of Huddersfield in partial fulfilment of the requirements for the
degree of Doctor of Philosophy

The University of Huddersfield

January 2022

Declarations

i. The author of this thesis (including any appendices and/ or schedules to this thesis) owns any copyright in it (the “Copyright”) and s/he has given The University of Huddersfield the right to use such Copyright for any administrative, promotional, educational and/or teaching.

ii. Copies of this thesis, either in full or in extracts, may be made only in accordance with the regulations of the University Details of these regulations may be obtained from the Librarian. Details of these regulations may be obtained from the Librarian. This page must form part of any such copies made.

iii. The ownership of any patents, designs, trademarks and any and all other intellectual property rights except for the Copyright (the “Intellectual Property Rights”) and any reproductions of copyright works, for example graphs and tables (“Reproductions”), which may be described in this thesis, may not be owned by the author and may be owned by third Such Intellectual Property Rights and Reproductions cannot and must not be made available for use without permission of the owner(s) of the relevant Intellectual Property Rights and/or Reproductions.

Abstract

Anions are an essential component of all life. In particular, the phosphate anion is used extensively in the agricultural industry to improve crop yield and ultimately feed the population. However, phosphate reserves are rapidly depleting and overuse causes eutrophication through phosphate runoff which remains a critical environmental issue. One solution to these problems is the sequestering of aqueous phosphate through the use of self-assembled supramolecular anion receptors. Supramolecular chemistry concerns itself with the interactions between discrete molecular species, and in particular, self-assembly is an attractive field to develop anion receptors as complex, selective, efficient, and tuneable anion binding compounds can be constructed from smaller pre-programmed subunits. The essential biological need for phosphates is due to their presence in numerous cellular regulatory processes and, as a consequence, the ability to reliably bind this anion in aqueous and physiological media may have important implications in biological systems.

With these goals in mind, research continued on a previously synthesised ligand (L^1). After improving the synthesis of one of the precursors, co-ordination with zinc(II) and manganese(II) in the presence of sulfate and phosphate led to trinuclear species (i.e. $[(L^1)_2M_3(EO_4)]^{n+}$ where $M = Zn^{2+}$ or Mn^{2+} and $E = S$ ($n = 4$) or P ($n = 3$)) being obtained, but in the absence of a strongly-binding anion, a mononuclear complex was instead observed (i.e. $[(L^1)M]^{2+}$ where $M = Zn^{2+}$ or Mn^{2+}). Complexes obtained using these two metals led to the observed hydrolysis of phosphate monoesters; conversely, the copper-based complex instead bound to these anions, leading to investigation of the activity of the complex when reacted with various phosphorylated amino acids, and subsequently, the potential activity of all three complexes toward cancer cells in vitro. Upon investigation, all complexes demonstrated toxicity to a variety of cancer cell lines. Whilst the manganese-based complex showed only modest selectivity compared to non-cancerous cells, the copper- and zinc-based complexes not only showed unprecedented potency even at the sub-micromolar level they also demonstrated selectivity indices of up to approximately 2,000-fold, indicating some potential application for these complexes in chemotherapy.

To further the research into anion receptor self-assembly and investigate the effects of ligand alteration on capsule anion-extraction selectivity, three new ligands were designed and synthesised. These new ligands all contained the same pyridyl-thiazole N-donor binding domains and the amine group capable of interaction with anions but the spacer unit was varied; from the central triethylamine unit that L^1 is constructed from to a tris(aminomethyl)ethane unit in L^2 , to a triamino-cyclohexane unit in L^3 , to a tris(aminoethyl)methane unit in L^4 . Co-ordination of these ligands to various copper(II) salts

led to the formation of trinuclear cages encapsulating anions in two of the three ligands in both the solid-state and in mass spectrometry studies. Whilst the final ligand showed colour changes indicative of capsule formation, no complexes were isolated in the solid-state, possibly due to the lack of flexibility of the spacer and a decrease in the host volume due to the shortened length of the spacer unit.

In an effort to improve the practicality of anion extraction, two other ligands were designed and synthesised which incorporated hydrophobic aliphatic ester chains in order to increase the solubility of the final complex in organic solvents. To investigate the ability of these complexes to sequester hydrophilic anions from aqueous media, biphasic extraction experiments were performed where anion-containing water samples were treated using immiscible organic solutions containing each complex; ion chromatography measurements of the aqueous layers before and after treatment indicated that phosphates were preferentially extracted by one of these ligands, and that a mere twenty-percent excess of complex to phosphate was sufficient to remove ninety-four percent of total phosphate concentration.

In this work three main important facets in the design and reactivity of self-assembled anion-binding cryptand have been demonstrated: 1) the ability to bind and hydrolyse phosphate can have very important biological implications, 2) the spacer unit can be varied significantly and as long as they are sufficiently flexible then a large variety of bridging units can be employed and these have the same desirable anion binding properties and 3) modification of the ligand chain will allow the formation of complexes that abstract anions into organic solvents – which may be useful for the removal of pollutant anion on an industrial scale. These results indicate a very promising future for supramolecular chemistry, with potential applications in both the pharmaceutical and industrial sectors being realised from experiments using very small changes to an already existing ligand.

Acknowledgements

Personal

First and foremost, I would like to thank my supervisor Professor Craig R. Rice. Not only for taking a chance and accepting me as a PhD student in the first place, but for his subsequent unwavering and round-the-clock support which has made this PhD possible. I will be forever indebted to you for the past four years.

Secondly, I would like to thank all of my friends, especially Robert Faulkner, Hannah Lynch and Georgina Armitage for their endless support and mirth in the lab which have made this period enjoyable. Thank you for being patient, endlessly forgiving and always willing to go the extra mile.

Finally, I would like to express my deepest gratitude to my family. My parents, Roderick and Julie, for both their emotional and financial support – none of this could have been possible without you providing a roof over my head and food on my table. Also, to my beloved other half Fiona Williams, thank you for managing to stay cheerful in spite of my endless grumbling.

Scientific

Thank-you to Professor Craig Rice for both the analysis of crystals by X-ray crystallography and for his guidance on these projects, as well as his proofreading of this thesis. Also to Dr. Robert Faulkner for his ESI-MS analysis of complexes. A special thank-you must be extended to Professor Roger Phillips, Dr. Simon Alison, and Emma Pinder; between them, they performed the biological testing reported within this thesis, and more besides. Simon and Roger also deserve an extra thank-you for proofreading the biological aspect of this report.

Contents

Declarations	i
Abstract	ii
Acknowledgements	iv
Personal	iv
Scientific	iv
Contents	v
List of Figures	vii
List of Schemes	xxxvii
List of Tables	xxxviii
1. Introduction.....	1
1.1. Supramolecular chemistry and self-assembly	1
1.1.1. Supramolecular and metallosupramolecular chemistry	1
1.1.2. Supramolecular self-assembly	2
1.2. Anions	2
1.2.1. Anions in biological systems	5
1.2.2. Anion receptors	6
1.2.3. Anion-directed self-assembly	16
1.2.4. Self-assembled anion receptors	24
Aims	53
2. Co-ordination Chemistry and Chemosensitivity Studies of Complexes of L¹	55
2.1. Continuing the co-ordination chemistry of ligand L¹	55
2.1.1. Synthesis	55
2.1.2. Co-ordination chemistry	56
2.2. Chemosensitivity studies	69
2.3. Mechanistic studies	74
3. Spacer Effects on Anion Selectivity.....	78
3.1. Ligand L²	78
3.1.1. Synthesis	78
3.1.2. Co-ordination chemistry	81
3.2. Ligand L³	83
3.2.1. Synthesis	83
3.2.2. Co-ordination chemistry	87
3.3. Ligand L⁴	92

3.3.1. Synthesis	92
3.3.2. Co-ordination chemistry	108
3.3.3. Selectivity experiments	120
4. Lipophilic Receptors to Extract Aqueous Anions into Organic Media....	128
4.1.1. Synthesis	128
4.2. Co-ordination chemistry	136
5. Conclusions.....	144
6. Experimental	146
6.1. Chapter 2	147
6.1.1. Synthesis of ligand L^1	147
6.1.2. Complex synthesis	148
6.1.3. Crystallography of L^1 complexes	154
6.1.4. Mass spectrometry studies	159
6.1.5. NMR studies	171
6.1.6. UV-Vis-NIR studies	176
6.1.7. Cell studies	179
6.2. Chapter 3	190
6.2.1. Synthesis of ligand L^2	190
6.2.2. Synthesis of ligand L^3	198
6.2.3. Crystallography of L^3 complexes	204
6.2.4. Mass spectrometry studies of L^3 complexes	206
6.2.5. Synthesis of ligand L^4	208
6.2.6. Crystallography data of L^4 complexes	236
6.2.7. Mass spectrometry studies of L^4 complexes	238
6.2.8. UV-Vis-NIR studies of L^4 complexes	242
6.2.9. Ion chromatography studies of L^4 complexes	248
6.3. Chapter 4	253
6.3.1. Synthesis of intermediary 5.3	253
6.3.2. Synthesis of ligand L^5	261
6.3.3. Synthesis of ligand L^6	264
6.3.4. Mass spectrometry studies of L^5 and L^6 complexes	267
6.3.5. UV-Vis-NIR studies of L^5 and L^6 complexes	269
6.3.6. Ion chromatography studies of L^5 and L^6 complexes	271
7. References.....	291

List of Figures

Figure 1.1. Algal blooms in Lake Taihu directly affected more than 2 million people.^{22,23}

Figure 1.2. a) structure of ATP;²⁹ b) spacefill crystal structure of DNA. Phosphates are shaded.³⁰

Figure 1.3. a) structure of macrocycle **1**; b) crystal structure of receptor showing the binding of two perchlorate anions.⁴⁰ Colour code: grey, C; blue, N; red, O; white, H; green, Cl.

Figure 1.4. Bis-indole urea anion receptors **2a** and **2b**.⁴² a) crystal structure of [**2a**·C₆H₅COO]⁻; b) DFT calculated structure of [**2b**·H₂PO₄]⁻. Colour code: black, C; blue, N; red, O; white, H; orange, P. Non-acidic hydrogen atoms omitted for clarity in a).

Figure 1.5. Polyindole-based anion receptor **3**.⁴³ Crystal structures of a) [**3**·3AcO]⁻, b) [**3**·SO₄]²⁻, c) [**3**·HPO₄]²⁻, d) dimer formed from the phosphate species, i.e. ([**3**·HPO₄]²⁻)₂. Colour code: black, C; blue, N; red, O; white, H; yellow, S; violet, P. Non-acidic hydrogen atoms have been omitted for clarity.

Figure 1.6. a) structure of indole-containing receptor **4**.⁴⁴ Solid-state structures of b) [**4**·Cl]⁻; c) ([**4**·CH₃CO₂]⁻)₂·H₂O. Thermal ellipsoids shown at 30% probability level.

Figure 1.7. Mechanically-locked rotaxane receptors **5a** and **5b**.⁴⁵ a) assembly of receptors from component parts; crystal structures of b) [**5a**·Cl] and c) [**5b**·Cl]. Disorder and non-acidic hydrogen atoms omitted for clarity.

Figure 1.8. a) Receptors **6a** – **6k**;⁴⁶ b) crystal structure of [**6g**₂·CO₃]²⁻; c) viability of various cancer cell lines after exposure to receptors **6a** – **6h**. Cell lines: GLC-4 = human small cell lung carcinoma; A549 = human alveolar adenocarcinoma, SW480 = human colon adenocarcinoma, A375 = human melanoma and CAL27 = tongue squamous cell carcinoma. Colour code for crystal structure: grey, C; blue, N; red, O; white, H.

Figure 1.9. Receptors **7a** and **7b**.⁵¹ Solid-state structures of a) **7a**·Cl⁻; b) **7b**·2MeOH. Colour code: grey, C; blue, N; red, O; white, H; green, Cl. Counterions and non-acidic hydrogen atoms have been omitted for clarity.

Figure 1.10. Receptors a) **8a** and b) **8b**.⁷³ X-ray crystal structures of c) **8a**₂·PF₆⁻; d) **8b**₂·2F⁻ with receptors coloured for clarity. Colour code: green, C; blue, N; red, O; white, H; chartreuse, F; purple, P (except d). Non-acidic hydrogen atoms omitted for clarity.

Figure 1.11. Receptor **9**.⁷⁴ a) structure of receptor **9**. Solid-state structures of a) **9**₂·2F⁻·6H₂O; b) **9**₂·2Cl⁻·2H₂O; c) **9**₂·2NO₃⁻; d) **9**₂·2CH₃CO₂⁻. Colour code: grey, C; blue, N; red, O; white, H; chartreuse, F; green, Cl. The receptor skeletons are coloured and non-acidic hydrogen atoms omitted for clarity.

Figure 1.12. Receptor **10**.⁷⁵ Solid-state structures of a) **10**·(SO₄)₂⁴⁻; b) **10**₃·(PO₄)₂⁶⁻. Colour code: grey, C; blue, N; red, O; white, H; yellow, S; orange, P except in b) where the receptor skeletons are coloured for clarity. Non-acidic hydrogen atoms and counterions omitted for clarity.

Figure 1.13. a) receptor **11**.⁷⁶ Solid-state structures of b) **11**₂·2F⁻·3MeOH; c) [**11**Cu(phen)]·BF₄. Colour code: grey, C; blue, N; red, O; white, H; lime, F; pink, B; dark orange, Cu; light orange, P. Non-acidic hydrogen atoms and counterions omitted for clarity. Thermal ellipsoids shown at 50% probability level.

Figure 1.14. a) structure of receptors **12a-c**.⁷⁷ Solid-state structures of b) [H**12a**-I], showing hydrogen-bonding from three receptors in the crystal lattice; c) [H**12a**·ClO₄]·DMF; d) [H**12a**·SiF₆]. Colour code: b) grey, C; blue, N; red, O; white, H; purple, I; c) green, Cl; d) beige, Si; chartreuse, F. Receptors in c) and d) coloured for clarity. Non-acidic hydrogen atoms and counterions omitted for clarity.

Figure 1.15. Receptor **13**.⁷⁸ a) structure of receptor **13**; b) crystal structure of $([\mathbf{13}\cdot\text{H}_2\text{PO}_4])_2^{2-}$ with half omitted to show hydrogen-bonding interactions; c) spacefill diagram of dimerised $([\mathbf{13}\cdot\text{H}_2\text{PO}_4])_2^{2-}$. Colour code: grey, C; blue, N; red, O; white, H; chartreuse, F; orange, P. Counterions and non-acidic hydrogen atoms omitted for clarity.

Figure 1.16. Receptor **14**.⁷⁹ a) schematic of formation of the complex **14** from the tren-based cage ligand and copper(II) perchlorate; b) removal efficiency of cyanide anions with increasing amount of solid receptor added. Initial concentration = 80 ppm.

Figure 1.17. Receptor **15**.⁸⁰ a) structure of ligand used in receptor **15**; b) solid-state crystal structure of $[\mathbf{15}\cdot\text{SO}_4]$ with ligands coloured for clarity; c) solid-state crystal structure of $[\mathbf{15}\cdot\text{Cl}_2]$ with ligands coloured for clarity. Colour code: red, O; yellow, S; green, Cl; white, H; blue, Pt. Non-acidic hydrogen atoms omitted for clarity.

Figure 1.18. Receptor **16**.⁸¹ a) Structure of ligand as its bromide salt; b) conformers adopted by receptor **16**; c) solid-state crystal structure of $[\mathbf{16a}\cdot\text{SO}_4]^{5+}$, illustrating hydrogen-bonding through the aromatic Py-CH donor units marked C10; d) solid-state crystal structure of $[\mathbf{16b}\cdot\text{NO}_3]^{6+}$ with hydrogen-bonding instead occurring from acidic imidazole hydrogen atom marked at C14. Colour code: grey, C; white, H; red, O; blue, N; yellow, S; teal, Cu; fuchsia, Fe; green, F; pink, B. Counterions and non-acidic hydrogen atoms omitted for clarity.

Figure 1.19. Cage receptor **17**.⁸² a) structure of ligand used in receptor **17**; b) solid-state structure of $[\mathbf{17}\cdot\text{NO}_3]^{3+}$, with ligands coloured for clarity; c) hydrogen-bonding interactions between acidic imidazole hydrogen atoms and oxo-anion. Colour code: grey, c; blue, N; white, H; red, O; dark teal, Pd. Non-acidic hydrogen atoms and counterions omitted for clarity.

Figure 1.20. bptz-based receptor **18**.⁸³ a) structure of bptz; b) crystal structure of $[\text{L}_5\text{Fe}_5\cdot 10\text{MeCN}\cdot\text{SbF}_6]^{9+}$ (anion disordered, 50% equivalence); c) crystal structure of $[\text{L}_4\text{Fe}_4\cdot 8\text{MeCN}\cdot\text{BF}_4]^{7+}$ (anion disordered, 50% equivalence); d) hydrogen-bonding interactions

in $[L_4Fe_4 \cdot 8MeCN \cdot BF_4]^{7+}$, each colour interaction representing one position of disorder. Colour code: grey, C; blue, N; lime, F; fuchsia, Fe; yellow, Sb; purple, B. Thermal ellipsoids shown at 50% probability level. Hydrogen atoms and counterions omitted for clarity.

Figure 1.21. Tetrahedral receptors **19a** and **19b**.⁸⁴ a) route of assembly of **19a** (green) and **19b** (purple); b) anion selectivity between the two complexes; c) (left to right) (top row) crystal structure of $[19a \cdot BF_4]^{7+}$, $[19a \cdot OTf]^{7+}$, $[19a \cdot ReO_4]^{7+}$, (bottom row) crystal structure of $[19a \cdot PF_6]^{7+}$, $[19a \cdot SbF_6]^{7+}$, $[19b \cdot SbF_6]^{7+}$; d) anion exchange between complexes facilitated by strong acid. Colour code for c): grey, C; dark blue, N; green, F; white, H; yellow, Zn; blue, Re; pink, B; orange, P; purple, Sb.

Figure 1.22. Receptor **20**.^{85,86} a) structure of ligand used to assemble receptor **20**; b) crystal structure of $[20 \cdot FeCl_4]^{7+}$ showing py-CH \cdots A⁻ hydrogen-bonding interactions. Colour code: dark blue, Fe; green, Cl; white, H. Thermal ellipsoids shown at 50% probability level. Ligands coloured and non-acidic hydrogen atoms and counterions omitted for clarity.

Figure 1.23. Structure of ligands used in receptors a) **21a** and b) **21b**.^{87,88} c) crystal structure of $[21a \cdot BF_4]^{7+}$; d) crystal structure of $[21a \cdot BF_4]^{7+}$ with non-hydrogen-bonding motifs omitted for clarity; e) crystal structure of $[21b \cdot ClO_4]^{7+}$; f) crystal structure of dinuclear complex observed when assembled using nickel instead of cobalt (i.e. $[L_3Ni_2]^{4+}$). Colour code: dark blue, Co; dark green, Ni; light green, Cl; chartreuse, F; pink, B; white, H. Ligands are coloured and non-acidic hydrogen atoms and counterions omitted for clarity.

Figure 1.24. Receptors **22a** and **22b**.^{91,92} a) structure of bis-(bipyridyl)urea ligands used in **22a** and **22b**; b) crystal structure of $[22a \cdot PO_4]^{5+}$ with ligands coloured for clarity; c) hydrogen-bonding interactions involved in $[22a \cdot PO_4]^{5+}$; d) crystal structure of $[22b \cdot SO_4]^{6+}$ with ligands coloured for clarity; e) hydrogen-bonding interactions in the crystal structure of $[22b \cdot SO_4]^{6+}$, which are

analogous to those present in $[22a \cdot PO_4]^{5+}$. Colour code: grey, C; blue, N; red, O; green, P; yellow, S; white, H. Non-acidic hydrogen atoms and counterions omitted for clarity.

Figure 1.25. Receptor **23**.⁹³ a) Ligand used in receptor **23**. Crystal structures of a) $[23 \cdot BF_4]^{5+}$; b) $[23 \cdot SbF_6]^{5+}$; c) $[L_2Ag_2]^{2+}$. Colour code: grey, C; blue, N; chartreuse, F; pale grey, Ag; pink, B; purple, Sb. Hydrogen atoms and counterions omitted for clarity.

Figure 1.26. atu-based receptor **24**.⁹⁴ a) structure of atu displaying tautomeric co-ordination products; b) truncated co-ordination structure of $[24 \cdot X]^{3+}$ showing the encapsulation of a single halide; c) co-ordination structure of $[24 \cdot Cl]^{3+}$ and hydrogen-bonding present in the capsule. Colour code: dark green, Ni; yellow, S; green, Cl; white, H. Ligands coloured, non-acidic hydrogen atoms and counterions omitted for clarity.

Figure 1.27. Receptor **25**.⁹⁵ a) structure of ligand used in the assembly; b) crystal structure of $[L_2Cu_2 \cdot H_2PO_4]^{3+}$ showing both copper-phosphate co-ordinate and ligand-phosphate hydrogen-bonding interactions. Thermal ellipsoids shown at 50% probability level. Colour code: grey, C; blue, N; white, H; yellow, S; red, O; orange, Cu; light orange, P. Counterions and non-acidic hydrogen atoms omitted for clarity.

Figure 1.28. a) crystal structure of the triple helicate $[L_3Cu_3 \cdot (H_2PO_4)_3]^{3+}$; b) crystal structure of the dimerised hexameric cluster $[(L_3Cu_3 \cdot (H_2PO_4)_3)_2]^{6+}$; c) spacefill representation of cluster $[(L_3Cu_3 \cdot (H_2PO_4)_3)_2]^{6+}$ showing encapsulation of the phosphate anions; d) inter- and intramolecular phosphate hydrogen-bonding interactions present in the trinuclear (left) and hexameric (right) clusters. Thermal ellipsoids shown at 50% probability level. Colour code: grey, C; blue, N; white, H; yellow, S; red, O; orange, Cu; light orange, P except in d) and e) where ligands are coloured and non-acidic hydrogen atoms omitted for clarity. Counterions also omitted for clarity.

Figure 1.29. Receptors **26a** and **26b**.⁹⁶ a) structure of ligands used in **26a** (left) and **26b** (right); b) crystal structure of **26a** when assembled using copper(II) triflate, encapsulating phosphate anion (i.e. $[\text{Cu}_2\text{L}_2(\text{H}_2\text{PO}_4)]^{3+}$); c) crystal structure of the trinuclear assembly incorporating the trifluoroboro-phosphate unit (i.e. $[\text{Cu}_3\text{L}_3(\text{F}_3\text{BOPO}_3)]^{3+}$); d) crystal structure of **26b** when assembled using copper(II) triflate; e) crystal structure of dinuclear assembly of **26b** having reacted with two tetrafluoroborate anions (i.e. $[\text{Cu}_2\text{L}_2((\text{F}_3\text{BO})_2\text{PO}_2)]^{3+}$). Thermal ellipsoids shown at 30% probability level. Colour code: grey, C; blue, N; white, H; yellow, S; red, O; orange, Cu; light orange, P; pink, B; chartreuse, F except in c) and e) where ligands are coloured and non-acidic hydrogen atoms omitted for clarity. Counterions also omitted for clarity.

Figure 1.30. Receptors formed from ligand L^1 .⁹⁷ a) structure of L^1 ; b) crystal structure of $[\text{L}^1_2\text{Cu}_3(\text{BF}_4)]^{5+}$; c) crystal structure of $[\text{L}^1_2\text{Cu}_3(\text{Br})]^{5+}$; d) crystal structure of $[\text{L}^1_2\text{Cu}_3(\text{SiF}_6)]^{4+}$; e) crystal structure of $[\text{L}^1_2\text{Cu}_3(\text{PO}_4)]^{3+}$; f) hydrogen-bonding interactions in $[\text{L}^1_2\text{Cu}_3(\text{PO}_4)]^{3+}$. Colour code: orange, Cu; lime, F; pink, B; brown, Br; mint, Si; orange, P; red, O; blue, N; white, H; light orange, Se. Ligands are coloured and non-acidic hydrogen atoms and counterions omitted for clarity. Thermal ellipsoids shown at 30% probability level.

Figure 1.31. Structures of $[\text{L}^1_2\text{Cu}_3\text{SeO}_4]^{4+}$ and $[\text{L}^1_4\text{Cu}_8(\text{SeO}_3)_4]^{8+}$.⁹⁸ a) crystal structure of $[\text{L}^1_2\text{Cu}_3\text{SeO}_4]^{4+}$; b) crystal structure of $[\text{L}^1_4\text{Cu}_8(\text{SeO}_3)_4]^{8+}$; c) spacefill structure of $[\text{L}^1_4\text{Cu}_8(\text{SeO}_3)_4]^{8+}$ showing encapsulation of anions. Colour code: orange, Cu; lime, F; pink, B; brown, Br; mint, Si; orange, P; red, O; blue, N; white, H; light orange, Se. Ligands are coloured and non-acidic hydrogen atoms and counterions omitted for clarity. Thermal ellipsoids shown at 30% probability level.

Figure 2.1. Mononuclear complexes of L^1 . Structures of a) $[\text{L}^1\text{Zn}]^{2+}$; b) $[\text{L}^1\text{Mn}(\text{H}_2\text{O})_2]^{2+}$. Colour code: blue-grey, Zn^{2+} ; violet, Mn^{2+} ; red, O; blue, N; yellow, S; grey, C; white, H. Perchlorate anions and non-acidic hydrogen atoms omitted for clarity. Thermal ellipsoids shown at 50% probability level.

Figure 2.2. a) crystal structure of $[\text{L}^1_2\text{Zn}_3(\text{SO}_4)]^{4+}$; b) crystal structure with ligands coloured for clarity; c) co-ordination and hydrogen-bonding of the metals and ligand to the SO_4^{2-} anion. Colour code: blue-grey, Zn^{2+} ; red, O; blue, N; yellow, S; grey, C; white, H (apart from (b) where the ligands have been coloured for clarity). Non-acidic hydrogen atoms and tetrafluoroborate anions are omitted for clarity. Thermal ellipsoids shown at the 50% probability level.

Figure 2.3. a) crystal structure of $[\text{L}^1_2\text{Mn}_3(\text{SO}_4)(\text{H}_2\text{O})_2]^{4+}$; b) crystal structure with ligands coloured for clarity; c) co-ordination and hydrogen-bonding of the metals and ligand to the SO_4^{2-} anion. Colour code: lilac, Mn^{2+} ; red, O; blue, N; yellow, S; grey, C; white, H (apart from (b) where the ligands have been coloured for clarity). Non-acidic hydrogen atoms and perchlorate anions are omitted for clarity. Thermal ellipsoids shown at the 50% probability level.

Figure 2.4. a) crystal structure of $[\text{L}^1_2\text{Cu}_3(\text{PhOPO}_3)]^{4+}$; b) crystal structure with ligands coloured for clarity; c) co-ordination and hydrogen-bonding of the metals and ligand to the PhOPO_3^{2-} anion. Colour code: dark orange, Cu^{2+} ; orange, P; red, O; blue, N; yellow, S; grey, C; white, H (apart from (b) where the ligands have been coloured for clarity). Non-acidic hydrogen atoms and tetrafluoroborate anions are omitted for clarity. Thermal ellipsoids shown at the 50% probability level.

Figure 2.5. a) crystal structure of $[\text{L}^1_2\text{Zn}_3(\text{PO}_4)]^{3+}$; b) crystal structure with ligands coloured for clarity; c) co-ordination and hydrogen-bonding of the metals and ligand to the PO_4^{3-} anion. Colour code: blue-grey, Zn^{2+} ; orange, P; red, O; blue, N; yellow, S; grey, C; white, H (apart from (b) where the ligands have been coloured for clarity). Non-acidic hydrogen atoms and perchlorate anions are omitted for clarity. Thermal ellipsoids shown at the 50% probability level.

Figure 2.6. a) crystal structure of $[\text{L}^1_2\text{Mn}_3(\text{PO}_4)(\text{H}_2\text{O})_2]^{3+}$; b) crystal structure with ligands coloured for clarity; c) co-ordination and hydrogen-bonding of the metals and ligand to the PO_4^{3-} anion. Colour code: lilac, Mn^{2+} ; orange, P; red, O; blue, N; yellow, S; grey, C; white, H (apart from (b)

where the ligands have been coloured for clarity). Non-acidic hydrogen atoms and perchlorate anions are omitted for clarity. Thermal ellipsoids shown at the 50% probability level.

Figure 2.7. ^1H NMR (10% D_2O in CD_3CN) analysis of phenylphosphate hydrolysis by $[\text{L}^1_2\text{Zn}_3]^{6+}$. Aromatic regions of spectra of a) $[\text{L}^1_2\text{Zn}_3]^{6+} + \text{Bu}_4\text{NH}_2\text{PO}_4$, b) $[\text{L}^1_2\text{Zn}_3]^{6+} + \text{PhOPO}_3\text{Na}_2$, $T = 0$, c) $[\text{L}^1_2\text{Zn}_3]^{6+} + \text{PhOPO}_3\text{Na}_2$, $T = 1$ hr incubated at 80°C , d) phenol. The NMR solutions were prepared by dissolving L^1 and $\text{Zn}(\text{C}_2\text{H}_3\text{O}_2)_2$ (in a ratio of 1:1.5) in CD_3CN (600 μL). The relevant anion (0.5 equiv w.r.t ligand) was dissolved in D_2O (60 μL) and these solutions were then combined. Heating of the sample was carried out at 80°C in a water bath for a specified amount of time.

Figure 2.8. Phosphatase activity of $[\text{L}^1_2\text{Zn}_3]^{6+}$. Proton coupled ^{31}P NMR spectra using different substrates including PhOPO_3 (spectra A to D), serine phosphate (spectra E to H), threonine phosphate (spectra I to L) and tyrosine phosphate (spectra M to P). Specific details for each ^{31}P NMR spectra are as follows: Spectra A, E, I and M represent substrate alone (44 hrs incubated at 37°C); Spectra B, F, J and N represent $[\text{L}^1_2\text{Zn}_3]^{6+}$ plus substrate ($t = 0$ min); Spectra C, G, K and O represent $[\text{L}^1_2\text{Zn}_3]^{6+}$ plus substrate incubated at 37°C for 19 hours; Spectra D, H, L and P represent $[\text{L}^1_2\text{Zn}_3]^{6+}$ plus substrate incubated at 37°C for 44 hours. The ^{31}P NMR of $[\text{L}^1_2\text{Zn}_3(\text{PO}_4)]^{3+}$ gives a signal at 8.6 ppm. The doubling up of some of the ^{31}P signals in $[\text{L}^1_2\text{Zn}_3(\text{PO}_4)]^{3+}$ (H, P and L) is attributed to formation of a mixture of diastereoisomers between the racemic cryptand and the resolved chiral amino acids which will form an ion-pair ($[\text{L}^1_2\text{Zn}_3(\text{PO}_4)](\text{RCH}(\text{NH}_2)\text{CO}_2)^{2+}$) and does not occur with the achiral phenyl phosphate.

Figure 2.9. Chemosensitivity response of a panel of human cancer and non-cancer cell lines to 96 hours continuous exposure to self-assembling test compounds. a) the potency of compounds tested against cancer cell lines versus non-cancer cell lines*; b) Selectivity index (SI)** for $[\text{L}^1_2\text{Cu}_3]^{6+}$; c) Selectivity index (SI)** for $[\text{L}^1_2\text{Zn}_3]^{6+}$; d) IC_{50} values for the clinically approved platinates (cisplatin, oxaliplatin and carboplatin) and $[\text{L}^1_2\text{Mn}_3]^{6+}$; e) corresponding SI** results (e).

Figure 2.10. Effect of the complex anion on potency and selectivity. a) The effect of various anions on the relative potency* of the Zn^{2+} complex; b) Effects of the anion on selectivity; these results are expressed as relative SI**.

Figure 2.11. Effects of $[\text{L}^1_2\text{Zn}_3]^{6+}$ (a and c) and $[\text{L}^1_2\text{Cu}_3]^{6+}$ (b and d) on the activity of purified human kinases. a) percentage inhibition of kinases by $[\text{L}^1_2\text{Zn}_3]^{6+}$; b) percentage inhibition of kinases by $[\text{L}^1_2\text{Cu}_3]^{6+}$; c) Kinases whose activity is stimulated by $[\text{L}^1_2\text{Zn}_3]^{6+}$; (d) Kinases whose activity is stimulated by $[\text{L}^1_2\text{Cu}_3]^{6+}$. Kinases were exposed to complexes at a concentration of $10\ \mu\text{M}$; full results are presented in the Experimental section.

Figure 2.12. Western blot analysis of purified recombinant a) AMPK and b) Src following exposure to $[\text{L}^1_2\text{Zn}_3]^{6+}$ and $[\text{L}^1_2\text{Cu}_3]^{6+}$. Purified enzymes were incubated with complexes ($50\ \mu\text{M}$) for 4 hours in the presence of ATP prior to analysis.

Figure 3.1. ^1H NMR (CDCl_3) spectrum of **2.1**. N.B. the signals at 11.1 and 9.1 ppm corresponding to the two amide environments. * CHCl_3 impurity. ** H_2O impurity.

Figure 3.2. ^1H NMR ($(\text{CD}_3)_2\text{SO}$) spectrum of **2.2**. N.B. the signals at 7.7 and 7.1 ppm corresponding to the thiourea proton environments. * $(\text{CD}_3)(\text{CD}_2\text{H})\text{SO}$ impurity. ** H_2O impurity, coincident with the signal corresponding to the CH_2NH environment, as evidenced by the slight “shoulders” on the signal.

Figure 3.3. ^1H NMR ($(\text{CD}_3)_2\text{SO}$) spectrum of **L²**. N.B. the aromatic signals indicative of the pyridyl- (8.60, 7.94, 7.82, 7.29 ppm), thiazole- (7.31 ppm) and amine- (8.04 ppm) groups. * $(\text{CD}_3)(\text{CD}_2\text{H})\text{SO}$ impurity. ** H_2O impurity.

Figure 3.4. Comparison of the two bridging groups in **L¹** and **L²**. N.B. the much shorter chain between the three -NH domains in **L²** ($\text{RN-CH}_2\text{CCH}_2\text{-NR}$) vs **L¹** ($\text{RN-CH}_2\text{CH}_2\text{NCH}_2\text{CH}_2\text{-NR}$).

Figure 3.5. ^1H NMR ($(\text{CD}_3)_2\text{SO}$) spectrum of **3.1**. N.B. Three aromatic signals corresponding to the three mono-substituted phenyl groups. One aliphatic signal is coincident with one of the solvent signals. $^*(\text{CD}_3)(\text{CD}_2\text{H})\text{SO}$ impurity. $^{**}\text{H}_2\text{O}$ impurity.

Figure 3.6. ^1H NMR ($(\text{CD}_3)_2\text{SO}$) spectrum of **3.2**. N.B. Very broad signals as a result of intra- and intermolecular hydrogen-bonding. $^*(\text{CD}_3)(\text{CD}_2\text{H})\text{SO}$ impurity. $^{**}\text{H}_2\text{O}$ impurity.

Figure 3.7. ^1H NMR ($(\text{CD}_3)_2\text{SO}$) spectrum of **L³**. N.B. Three aliphatic and six aromatic proton environments. $^*(\text{CD}_3)(\text{CD}_2\text{H})\text{SO}$ impurity. $^{**}\text{H}_2\text{O}$ impurity. $^{***}\text{NH}_4^+$ impurity.

Figure 3.8. ^{13}C NMR ($(\text{CD}_3)_2\text{SO}$) spectrum of **L³**.

Figure 3.9. a) crystal structure of $[\text{L}^3_2\text{Cu}_3(\text{SO}_4)]^{4+}$; b) crystal structure with ligands coloured for clarity; c) co-ordination and hydrogen-bonding of the metals and ligand to the SO_4^{2-} anion. Colour code: dark orange, Cu^{2+} ; red, O; blue, N; yellow, S; grey, C; white, H (apart from (b) where the ligands have been coloured for clarity). Non-acidic hydrogen atoms and perchlorate anions are omitted for clarity. Thermal ellipsoids shown at the 50% probability level.

Figure 3.10. ESI-MS of $[\text{L}^3_2\text{Cu}_3(\text{SO}_4)](\text{trif})_4$ showing ions at m/z 1954 and 901 corresponding to $\{[\text{L}^3_2\text{Cu}_3(\text{SO}_4)](\text{trif})_3\}^+$ and $\{[\text{L}^3_2\text{Cu}_3(\text{SO}_4)](\text{trif})_2\}^{2+}$.

Figure 3.11. a) crystal structure of $[\text{L}^3_2\text{Cu}_3(\text{Br})]^{5+}$; b) crystal structure with ligands coloured for clarity; c) co-ordination and hydrogen-bonding of the metals and ligand to the Br^- anion. Colour code: dark orange, Cu^{2+} ; brown, Br; red, O; blue, N; yellow, S; grey, C; white, H (apart from (b) where the ligands have been coloured for clarity). Non-acidic hydrogen atoms and tetrafluoroborate anions are omitted for clarity. Thermal ellipsoids shown at the 50% probability level.

Figure 3.12. ESI-MS of $[\text{L}^3_2\text{Cu}_3(\text{Br})](\text{trif})_5$ showing ions at m/z 2085 and 968 corresponding to $\{[\text{L}^3_2\text{Cu}_3(\text{Br})](\text{trif})_4\}^+$ and $\{[\text{L}^3_2\text{Cu}_3(\text{Br})](\text{trif})_3\}^{2+}$ respectively.

Figure 3.13. Aliphatic region of the ^1H NMR (CDCl_3) spectrum of **4.1**. N.B. the signal at 5.98 ppm corresponding to the alkene proton.

Figure 3.14. Aliphatic region of the ^1H NMR (CDCl_3) spectrum of **4.2** N.B. the septet at 2.79 and doublet at 2.49 ppm indicative of the $\text{HC}(\text{CH}_2\text{R})_3$ group.

Figure 3.15. Aliphatic region of the ^1H NMR (CDCl_3) spectrum of **4.4** N.B. the triplets at 4.13 and 1.69 ppm corresponding to the $\text{HC}(\text{CH}_2\text{CH}_2\text{R})_3$ group; the $\text{HC}(\text{CH}_2\text{CH}_2\text{R})_3$ signal coincides with the $\text{HC}(\text{CH}_2\text{CH}_2\text{R})_3$ signal.

Figure 3.16. Aliphatic region of the ^1H NMR (CDCl_3) spectrum of **4.4**. N.B. the broad singlet at 4.89 ppm indicative of the three -OH protons.

Figure 3.17. Aliphatic regions of the ^1H NMR (CDCl_3) spectrum of **4.5**. N.B. the strong singlet peak at 2.96 ppm indicative of three identical methanesulfonate groups.

Figure 3.18. ^1H NMR ($(\text{CD}_3)_2\text{SO}$) spectrum of **4.5a**. N.B. pair of doublets of doublets in the aromatic region indicative of a phthalimide group. *(CD_3)(CD_2H)SO impurity. ** H_2O impurity. *** DMF impurity.

Figure 3.19. Aliphatic region of the ^1H NMR ($(\text{CD}_3)_2\text{SO}$) spectrum of **4.5b**. N.B. comparatively lower shifts for all three aliphatic signals. *(CD_3)(CD_2H)SO impurity. ** H_2O impurity.

Figure 3.20. ^1H NMR spectrum of **4.6**. * CHCl_3 impurity.

Figure 3.21. ^1H NMR spectrum of **4.7** with broad amine peaks due to hydrogen-bonding interactions.

Figure 3.22. ^1H NMR spectrum of **4.8** showing aromatic and aliphatic protons expected. Also present is the singlet corresponding to the -NH proton at 5.44 ppm. * CHCl_3 impurity.

Figure 3.23. ^1H NMR spectrum of **4.9**, showing neither the mesylate CH_3 signal from **4.5** nor the amine singlet from **4.8**, indicative of complete reaction. * CHCl_3 impurity, ** CH_2Cl_2 impurity.

Figure 3.24. ^1H NMR spectrum of L^4 . The presence of the peak at 5.88 ppm corresponding to the three -NH groups, as well as the absence of the peaks corresponding to the three MeO-, -CH₂-Ph, and the four aromatic protons indicates that the protecting group has been successfully removed. *CHCl₃ impurity.

Figure 3.25. ^{13}C NMR spectrum of L^4 with eight aromatic signals and three aliphatic signals, indicating that the para-methoxybenzyl protecting group is no longer present.

Figure 3.26. a) crystal structure of $[\text{L}^4_2\text{Cu}_3(\text{SO}_4)]^{4+}$; b) crystal structure with ligands coloured for clarity; c) co-ordination and hydrogen-bonding of the metals and ligand to the SO_4^{2-} anion. Colour code: dark orange, Cu²⁺; red, O; blue, N; yellow, S; grey, C; white, H (apart from (b) where the ligands have been coloured for clarity). Non-acidic hydrogen atoms and perchlorate anions are omitted for clarity. Thermal ellipsoids shown at the 50% probability level.

Figure 3.27. ESI-MS spectrum of $[\text{L}^4_2\text{Cu}_3](\text{ClO}_4)_6$.

Figure 3.28. ESI-MS spectrum of $[\text{L}^4_2\text{Cu}_3(\text{SO}_4)](\text{ClO}_4)_4$.

Figure 3.29. UV-Vis-NIR absorption spectra of solutions of a) $[\text{L}^4_2\text{Cu}_3](\text{trif})_6$; b) $[\text{L}^4_2\text{Cu}_3](\text{trif})_6$ plus the addition of one equivalent of tetra-*N*-butylammonium sulfate. Concentration of $[\text{L}^4_2\text{Cu}_3](\text{trif})_6$ = 0.8 mM (1:1 acetonitrile in water).

Figure 3.30. a) crystal structure of $[\text{L}^4_2\text{Cu}_3(\text{SiF}_6)]^{4+}$; b) crystal structure with ligands coloured for clarity; c) co-ordination and hydrogen-bonding of the metals and ligand to the SiF_6^{2-} anion. Colour code: dark orange, Cu²⁺; beige, Si; lime, F; red, O; blue, N; yellow, S; grey, C; white, H (apart from (b) where the ligands have been coloured for clarity). Non-acidic hydrogen atoms and perchlorate anions are omitted for clarity. Thermal ellipsoids shown at the 50% probability level.

Figure 3.31. UV-Vis-NIR absorption spectra of solutions of a) $[\text{L}^4_2\text{Cu}_3](\text{trif})_6$; b) $[\text{L}^4_2\text{Cu}_3](\text{trif})_6$ plus the addition of one equivalent of ammonium hexafluorosilicate. Concentration of $[\text{L}^4_2\text{Cu}_3](\text{trif})_6 = 0.8 \text{ mM}$ (1:1 acetonitrile in water).

Figure 3.32. a) crystal structure of $[\text{L}^4_2\text{Cu}_3(\text{PO}_4)]^{3+}$; b) crystal structure with ligands coloured for clarity; c) co-ordination and hydrogen-bonding of the metals and ligand to the PO_4^{3-} anion. Colour code: dark orange, Cu^{2+} ; orange, P; red, O; blue, N; yellow, S; grey, C; white, H (apart from (b) where the ligands have been coloured for clarity). Non-acidic hydrogen atoms and perchlorate anions are omitted for clarity. Thermal ellipsoids shown at the 50% probability level.

Figure 3.33. ESI-MS spectrum of $[\text{L}^4_2\text{Cu}_3(\text{PO}_4)](\text{ClO}_4)_3$.

Figure 3.34. UV-Vis-NIR absorption spectra of solutions of a) $[\text{L}^4_2\text{Cu}_3](\text{trif})_6$; b) $[\text{L}^4_2\text{Cu}_3](\text{trif})_6$ plus the addition of one equivalent of tetra-*N*-butylammonium dihydrogen phosphate. Concentration of $[\text{L}^4_2\text{Cu}_3](\text{trif})_6 = 0.8 \text{ mM}$ (1:1 acetonitrile in water).

Figure 3.35. a) crystal structure of $[\text{L}^4_2\text{Cu}_3(\text{AsO}_4)]^{3+}$; b) crystal structure with ligands coloured for clarity; c) co-ordination and hydrogen-bonding of the metals and ligand to the AsO_4^{3-} anion. Colour code: dark orange, Cu^{2+} ; violet, As; red, O; blue, N; yellow, S; grey, C; white, H (apart from (b) where the ligands have been coloured for clarity). Non-acidic hydrogen atoms and perchlorate anions are omitted for clarity. Thermal ellipsoids shown at the 50% probability level.

Figure 3.36. ESI-MS spectrum of $[\text{L}^4_2\text{Cu}_3(\text{AsO}_4)](\text{ClO}_4)_3$.

Figure 3.37. UV-Vis-NIR absorption spectra of solutions of a) $[\text{L}^4_2\text{Cu}_3](\text{trif})_6$; b) $[\text{L}^4_2\text{Cu}_3](\text{trif})_6$ plus the addition of one equivalent of disodium arsenate. Concentration of $[\text{L}^4_2\text{Cu}_3](\text{trif})_6 = 0.8 \text{ mM}$ (1:1 acetonitrile in water).

Figure 3.38. Range of colours observed with complexes of L^4 and $\text{Cu}(\text{trif})_2$: a) $[\text{L}^4_2\text{Cu}_3]^{6+}$; b) $[\text{L}^4_2\text{Cu}_3]^{6+} + \text{AsO}_4^{3-}$; c) $[\text{L}^4_2\text{Cu}_3]^{6+} + \text{PO}_4^{3-}$; d) $[\text{L}^4_2\text{Cu}_3]^{6+} + \text{CO}_3^{2-}$; e) $[\text{L}^4_2\text{Cu}_3]^{6+} + \text{NO}_3^-$; f) $[\text{L}^4_2\text{Cu}_3]^{6+} + \text{Cl}^-$; g)

$[\text{L}^4_2\text{Cu}_3]^{6+} + \text{SO}_4^{2-}$; h) $[\text{L}^4_2\text{Cu}_3]^{6+} + \text{SiF}_6^{2-}$; i) $[\text{L}^4_2\text{Cu}_3]^{6+} + \text{SeO}_4^{2-}$. Complexes assembled in a 1:1 MeCN/H₂O solution with one equivalent of the corresponding anion as either their sodium, ammonium or tetra-*N*-alkylammonium salts at a concentration of 0.88 mM.

Figure 3.39. UV-Vis-NIR absorption spectra of solutions of a) $[\text{L}^4_2\text{Cu}_3](\text{trif})_6$; b) $[\text{L}^4_2\text{Cu}_3](\text{trif})_6 + \text{AsO}_4^{3-}$; c) $[\text{L}^4_2\text{Cu}_3](\text{trif})_6 + \text{H}_2\text{PO}_4^-$; d) $[\text{L}^4_2\text{Cu}_3](\text{trif})_6 + \text{CO}_3^{2-}$. Anions added as either their sodium, ammonium or tetra-*N*-alkylammonium salts as one equivalent with respect to complex. Concentration of $[\text{L}^4_2\text{Cu}_3](\text{trif})_6 = 0.8$ mM (1:1 acetonitrile in water).

Figure 3.40. UV-Vis-NIR absorption spectra of solutions of a) $[\text{L}^4_2\text{Cu}_3](\text{trif})_6$; e) $[\text{L}^4_2\text{Cu}_3](\text{trif})_6 + \text{HSO}_4^-$; f) $[\text{L}^4_2\text{Cu}_3](\text{trif})_6 + \text{SeO}_4^{2-}$; g) $[\text{L}^4_2\text{Cu}_3](\text{trif})_6 + \text{SiF}_6^{2-}$. Anions added as either their sodium, ammonium or tetra-*N*-alkylammonium salts as one equivalent with respect to complex. Concentration of $[\text{L}^4_2\text{Cu}_3](\text{trif})_6 = 0.8$ mM (1:1 acetonitrile in water).

Figure 3.41. UV-Vis-NIR absorption spectra of solutions of a) $[\text{L}^4_2\text{Cu}_3](\text{trif})_6$; h) $[\text{L}^4_2\text{Cu}_3](\text{trif})_6 + \text{NO}_3^-$; i) $[\text{L}^4_2\text{Cu}_3](\text{trif})_6 + \text{Cl}^-$. Anions added as either their sodium, ammonium or tetra-*N*-alkylammonium salts as one equivalent with respect to complex. Concentration of $[\text{L}^4_2\text{Cu}_3](\text{trif})_6 = 0.8$ mM (1:1 acetonitrile in water).

Figure 3.42. UV-Vis-NIR absorption spectra of solutions of a) $[\text{L}^4_2\text{Cu}_3](\text{trif})_6$; b) $[\text{L}^4_2\text{Cu}_3](\text{trif})_6 + \text{NaH}_2\text{PO}_4$ followed by NaHSO_4 ; c) $[\text{L}^4_2\text{Cu}_3](\text{trif})_6 + \text{NaHSO}_4$ followed by NaH_2PO_4 ; d) $[\text{L}^4_2\text{Cu}_3(\text{SO}_4)](\text{trif})_4$; e) $[\text{L}^4_2\text{Cu}_3(\text{PO}_4)](\text{trif})_3$ in 1:1 acetonitrile in water. Anions added as one equivalent with respect to complex. Concentration of $[\text{L}^4_2\text{Cu}_3](\text{trif})_6 = 0.8$ mM.

Figure 3.43. UV-Vis-NIR absorption spectra of solutions of a) $[\text{L}^4_2\text{Cu}_3](\text{trif})_6$; b) $[\text{L}^4_2\text{Cu}_3](\text{trif})_6 + \text{Na}_2\text{HPO}_4$ followed by Na_2SO_4 ; c) $[\text{L}^4_2\text{Cu}_3](\text{trif})_6 + \text{Na}_2\text{SO}_4$ followed by Na_2HPO_4 ; d) $[\text{L}^4_2\text{Cu}_3(\text{PO}_4)](\text{trif})_3$ in 1:1 acetonitrile in water. Anions added as one equivalent with respect to complex. Concentration of $[\text{L}^4_2\text{Cu}_3](\text{trif})_6 = 0.8$ mM.

Figure 3.44. Percentage removal of NaCl, NaNO₃, NaH₂PO₄ and NaHSO₄ anions upon precipitation with [L⁴₂Cu₃](trif)₆. The contribution from the background concentration of the anions (~10%) has been removed.

Figure 3.45. Percentage removal of NaCl, NaNO₃, Na₂HPO₄ and Na₂SO₄ anions upon precipitation with [L⁴₂Cu₃](trif)₆. The contribution from the background concentration of the anions (~10%) has been removed.

Figure 4.1. ¹H NMR (CDCl₃) spectrum of **5.1**. N.B. aromatic signals indicative of a disubstituted pyridyl-ring. Aliphatic doublet at 4.84 ppm shifted highly due to its proximity to a hydroxyl group. *CHCl₃ impurity.

Figure 4.2. ¹H NMR (CDCl₃) spectrum of **5.2**. N.B. four new aliphatic signals corresponding to the hexanoyl linkage; two -CH₂- groups are coincident at 1.34 ppm. *CHCl₃ impurity.

Figure 4.3. ¹H NMR (CDCl₃) spectrum of **5.3**. N.B. shifted ketone singlet signal (4.87 ppm) which integrates to two hydrogen atoms indicative of a -COCH₂Br unit. *CHCl₃ impurity.

Figure 4.4. ¹H NMR (CDCl₃) spectrum of ligand L⁵. N.B. eight aliphatic signals, four aromatic signals and one -NH triplet signal at 6.02 ppm indicative of successful ligand synthesis. *CHCl₃ impurity. **CH₂Cl₂ impurity.

Figure 4.5. ¹H NMR (CDCl₃) spectrum of ligand L⁶. N.B. three aliphatic signals at 3.65, 2.64 and 1.00 ppm indicative of the trisubstituted cyclohexane ring. *CHCl₃ impurity.

Figure 4.6. Extraction experiments of a DCM solution of a) - e) [L⁵₂Cu₃]⁶⁺, f) - j) [L⁶₂Cu₃]⁶⁺. Organic solutions partitioned with: a) and f) ultrapure water; aqueous solutions containing b) and g) one equivalent of Na₂HPO₄, c) and h) one equivalent of each of NaCl, NaNO₃, NaHSO₄ and NaH₂PO₄, d) and i) one equivalent of each of NaCl, NaNO₃, Na₂SO₄ and Na₂HPO₄ and e) and j) one equivalent of each of NaF, NaCl, NaBr and NaI.

Figure 4.7. UV-Vis-NIR absorption spectra of a) $[\text{L}^5_2\text{Cu}_3]^{6+}$; b) $[\text{L}^5_2\text{Cu}_3]^{6+}$ plus half an equivalent of tetra-*N*-butylammonium dihydrogen phosphate. Concentration of complex = 0.8 mM (3% MeOH in DCM).

Figure 4.8. UV-Vis-NIR absorption spectra of a) $[\text{L}^5_2\text{Cu}_3]^{6+}$; b) $[\text{L}^5_2\text{Cu}_3]^{6+}$ plus half an equivalent of tetra-*N*-butylammonium hydrogen sulfate. Concentration of complex = 0.8 mM (3% MeOH in DCM).

Figure 4.9. UV-Vis-NIR absorption spectra of a) $[\text{L}^6_2\text{Cu}_3]^{6+}$; b) $[\text{L}^6_2\text{Cu}_3]^{6+}$ plus half an equivalent of tetra-*N*-butylammonium dihydrogen phosphate. Concentration of complex = 0.8 mM (3% MeOH in DCM).

Figure 4.10. UV-Vis-NIR absorption spectra of a) $[\text{L}^6_2\text{Cu}_3]^{6+}$; b) $[\text{L}^6_2\text{Cu}_3]^{6+}$ plus half an equivalent of tetra-*N*-butylammonium hydrogen sulfate. Concentration of complex = 0.8 mM (3% MeOH in DCM).

Figure 6.1. ^1H NMR (10% CD_3OD in CD_3CN) spectra of the aromatic region for $[\text{L}^1_2\text{Zn}_3(\text{PO}_4)](\text{OTf})_3$.

Figure 6.2. ^{13}C NMR (10% CD_3OD in CD_3CN) spectra of $[\text{L}^1_2\text{Zn}_3(\text{PO}_4)](\text{OTf})_3$.

Figure 6.3. ^1H NMR (10% CD_3OD in CD_3CN) spectra of the aromatic region for $[\text{L}^1_2\text{Zn}_3(\text{SO}_4)](\text{OTf})_4$.

Figure 6.4. ^{13}C NMR (10% CD_3OD in CD_3CN) spectra for $[\text{L}^1_2\text{Zn}_3(\text{SO}_4)](\text{OTf})_4$.

Figure 6.5. ESI-MS of $[\text{L}^1\text{Zn}](\text{ClO}_4)_2$.

Figure 6.6. ESI-MS of $[\text{L}^1\text{Mn}](\text{ClO}_4)_2$.

Figure 6.7. ESI-MS of $[\text{L}^1_2\text{Zn}_3(\text{SO}_4)](\text{ClO}_4)_4$.

Figure 6.8. ESI-MS of $[\text{L}^1_2\text{Mn}_3(\text{SO}_4)](\text{ClO}_4)_4$.

Figure 6.9. ESI-MS of $[\text{L}^1_2\text{Cu}_3(\text{PhOPO}_3)](\text{ClO}_4)_4$.

Figure 6.10. ESI-MS of $[\text{L}^1_2\text{Zn}_3(\text{PhOPO}_3)](\text{ClO}_4)_4$.

Figure 6.11. ESI-MS of $[\text{L}^1_2\text{Mn}_3(\text{PhOPO}_3)](\text{ClO}_4)_4$.

Figure 6.12. ESI-MS of $[\text{L}^1_2\text{Cu}_3(\text{PhOPO}_3)](\text{ClO}_4)_4$ after being heated at 80°C for 1 hour.

Figure 6.13. ESI-MS of $[\text{L}^1_2\text{Zn}_3(\text{PhOPO}_3)](\text{ClO}_4)_4$ after being heated at 80°C for 1 hour.

Figure 6.14. ESI-MS of $[\text{L}^1_2\text{Mn}_3(\text{PhOPO}_3)](\text{ClO}_4)_4$ after being heated at 80°C for 1 hour.

Figure 6.15. ESI-MS of $[\text{L}^1_2\text{Zn}_3(\text{ATP})(\text{CH}_3\text{CO}_2)_2]$.

Figure 6.16. ESI-MS of $[\text{L}^1_2\text{Zn}_3(\text{ATP})(\text{CH}_3\text{CO}_2)_2]$ after heating at 37°C for 60 hours.

Figure 6.17. ^{31}P NMR spectrum (600 μL HEPES 60 mmol (@ pH 7.4) and 200 μL d_6 -DMSO) of a) $\text{PhOPO}_3\text{Na}_2$, 44hrs incubated @ 37 °C, b) $[\text{L}^1_2\text{Zn}_3]^{6+} + \text{PhOPO}_3\text{Na}_2$, T = 0, c) $[\text{L}^1_2\text{Zn}_3]^{6+} + \text{PhOPO}_3\text{Na}_2$, T = 19 hrs incubated @ 37 °C, d) $[\text{L}^1_2\text{Zn}_3]^{6+} + \text{PhOPO}_3\text{Na}_2$, T = 44 hrs incubated @ 37 °C, e) $[\text{L}^1_2\text{Zn}_3]^{6+} + \text{Bu}_4\text{NH}_2\text{PO}_4$. The NMR solutions were prepared by dissolving L^1 and $\text{Zn}(\text{C}_2\text{H}_3\text{O}_2)_2$ (in a ratio of 1:1.5) in d_6 -DMSO (200 μL). The relevant anion (0.5 equiv w.r.t ligand) was dissolved in HEPES (600 μL , @ pH 7.4) and these solutions were then combined. Heating of the sample was carried out by incubating the sample @ 37 °C.

Figure 6.18. ^{31}P NMR spectrum (10% D_2O in CD_3CN) of a) $[\text{L}^1_2\text{Zn}_3]^{6+} + \text{Bu}_4\text{NH}_2\text{PO}_4$, b) $[\text{L}^1_2\text{Zn}_3]^{6+} + \text{PhOPO}_3\text{Na}_2$, T = 0, c) $[\text{L}^1_2\text{Zn}_3]^{6+} + \text{PhOPO}_3\text{Na}_2$, T = 1 hr incubated @ 80 °C, d) phenol. The NMR solutions were prepared by dissolving L^1 and $\text{Zn}(\text{C}_2\text{H}_3\text{O}_2)_2$ (in a ratio of 1:1.5) in CD_3CN (600 μL). The relevant anion (0.5 equiv w.r.t ligand) was dissolved in D_2O (60 μL) and these solutions were then combined. Heating of the sample was carried out @ 80 °C in a water bath for the specified amount of time.

Figure 6.19. ^1H NMR spectra (600 μL HEPES (@ pH 7.4) and 200 μL d_6 -DMSO) of a) $[\text{L}^1_2\text{Zn}_3]^{6+} + \text{peptide-OPO}_3^{2-}$ (HMRSAMS*GLHLVKRR) t = 0, b) $[\text{L}^1_2\text{Zn}_3]^{6+} + \text{peptide-OPO}_3^{2-}$ t = 48 hrs @ 37 °C, c) $[\text{L}^1_2\text{Zn}_3]^{6+} + \text{peptide-OPO}_3^{2-}$ t = 48 hrs @ 37 °C and then 2 hrs 80°C, d) $[\text{L}^1_2\text{Zn}_3]^{6+} + \text{peptide-OPO}_3^{2-}$

OPO₃²⁻ + Bu₄NH₂PO₄ with the shift at ~9 ppm corresponding to [L¹₂Zn₃(PO₄)]³⁺. The NMR solutions were prepared by dissolving L¹ and Zn(C₂H₃O₂)₂ (in a ratio of 1:1.5) in d₆-DMSO (200 μL). The peptide-OPO₃²⁻ (0.5 equiv w.r.t ligand) was dissolved in HEPES (600 μL, 60 mmol @ pH 7.4) and these solutions were then combined. Heating of the sample was carried out by incubating the sample @ 37 °C and a further 2 hrs @ 80 °C in a water bath.

Figure 6.20. ³¹P NMR spectra (600 μL HEPES (60 mmol @ pH 7.4) and 200 μL d₆-DMSO) of [L¹₂Zn₃]⁶⁺ showing the signal at ~ 9 ppm corresponding to [L¹₂Zn₃(PO₄)]³⁺ demonstrating no competition from HEPES as no observed signal at ~ 0 ppm corresponding to free phosphate. Solution contains an approximately 10-fold excess of HEPES.

Figure 6.21. ³¹P NMR spectra (600 μL HEPES (60 mmol @ pH 7.4) and 200 μL d₆-DMSO) of [L¹₂Zn₃(PO₄)]³⁺ plus one equivalent of Na₂O₂POPh showing the signal at ~ 9 ppm corresponding to [L¹₂Zn₃(PO₄)]³⁺ and -2.5 ppm corresponding to Na₂O₂POPh. No change in either the ratio of [L¹₂Zn₃(PO₄)]³⁺ to Na₂O₂POPh and no signal at ~ 0 ppm (corresponding to free PO₄³⁻) was observed, indicating lack of catalytic activity.

Figure 6.22. ³¹P NMR spectra (600 μL HEPES (60 mmol @ pH 7.4) and 200 μL d₆-DMSO) of [L¹₂Zn₃(SO₄)]⁴⁺ plus one equivalent of NaH₂PO₄ showing the signal at ~ 9 ppm corresponding to [L¹₂Zn₃(PO₄)]³⁺ and ~ 0 ppm corresponding to unbound NaH₂PO₄. This indicates that a proportion, but not all, of the sulfate has been displaced but the presence of “free” NaH₂PO₄ demonstrates that [L¹₂Zn₃(SO₄)]⁴⁺ still persists as the major species (~ 66%).

Figure 6.23. Concentration of 4-nitrophenol (mM) verses time in the presence of different complexes.

Figure 6.24. Calibration curve of 4-nitrophenol (10% DMSO in 60 mM HEPES-buffered H₂O).

Figure 6.25. The effect of anions of the potency of [L¹₂Cu₃]⁶⁺ and [L¹₂Zn₃]⁶⁺. The results represent the mean IC₅₀ values ± standard deviation for at least three independent experiments.

Figure 6.26. The effect of anions on the selectivity of $[\text{L}^1_2\text{Cu}_3]^{6+}$ and $[\text{L}_2\text{Zn}_3]^{6+}$. All values presented here were determined from the mean IC_{50} values in Figure 6.25 for each of the non-cancer cell lines (ARPE-19, MCF10A and NP1) used in this study. As mean IC_{50} values are used to calculate SI, no error bars are presented. The experimental error is accounted for in Figure 6.25.

Figure 6.27. The effect of anions on the potency and selectivity relative to $[\text{L}^1_2\text{Cu}_3]^{6+}$ and $[\text{L}^1_2\text{Zn}_3]^{6+}$. Relative potency was determined by dividing the IC_{50} of test compounds plus respective anions divided by IC_{50} values for $[\text{L}^1_2\text{Cu}_3]^{6+}$ and $[\text{L}^1_2\text{Zn}_3]^{6+}$. Values > 1 represent an increase in potency and conversely, values < 1 represent a reduction in potency. Relative selectivity index (SI) values were determined by dividing the SI value for test compounds plus respective anions divided by SI values for $[\text{L}^1_2\text{Cu}_3]^{6+}$ and $[\text{L}^1_2\text{Zn}_3]^{6+}$. Values > 1 represent an increase in selectivity and conversely, values < 1 represent a reduction in selectivity.

Figure 6.28. Comparative selectivity of $[\text{L}^1_2\text{M}_3]^{6+}$ to $[\text{L}^1\text{M}]^{2+}$ and L^1 . The selectivity index (SI) values were determined by dividing the mean IC_{50} of each test compound against ARPE-19 cells by the mean IC_{50} for HCT116 p53^{+/+} and p53^{-/-} cells. The results demonstrate that whilst $[\text{L}^1\text{M}]^{2+}$ and L^1 are cytotoxic to cells, selectivity for cancer cells is property confined primarily to the $[\text{L}^1_2\text{M}_3]^{6+}$ complexes. $[\text{L}^1\text{M}]^{2+}$ refers to an experiment where stoichiometric amounts of ligand and metal ions are used (as opposed to 2L^1 plus 3M^{2+}) thereby forcing the formation of $[\text{L}^1\text{M}]^{2+}$. In all likelihood, in the presence of tetrahedral oxoanions, this would result in forming $[\text{L}^1_2\text{M}_3(\text{EO}_4)]^{3/4+}$ (where E = P or S) and free ligand.

Figure 6.29. The effect of $[\text{L}^1_2\text{Zn}_3]^{6+}$ and $[\text{L}^1_2\text{Cu}_3]^{6+}$ on the activity of recombinant human kinases. The compounds were submitted to the MRC Protein Phosphorylation and Ubiquitination Unit International Centre for Kinase Profiling (University of Dundee) and tested at a concentration of 10 μM against 140 human kinases (Premier Screen).

Figure 6.30. Effects of $[L^1_2Zn_3]^{6+}$ on phospho-T172 levels of recombinant AMPK α 1 and phospho-S108 levels of recombinant AMPK β 1. a) and b) time course of 50 μ M $[L^1_2Zn_3]^{6+}$ co-incubation with recombinant AMPK enzyme (α 1 β 2 γ 1 for (a) and α 2 β 1 γ 1 for (b)) and effects on phosphorylation levels of T172 of AMPK α 1 (a) and S108 of AMPK β 1 (b). Densitometric quantification of levels of phosphorylated AMPK subunit and relative to total levels of the subunit are indicated; all quantification relative to t = 0; c) effect of increasing concentrations of $[L^1_2Zn_3]^{6+}$ (0-50 μ M, 2-fold dilution series) on phospho-S108 AMPK β 1 relative to total AMPK β 1. Similar results were obtained in a minimum of n = 2 independent experiments.

Figure 6.31. Influence of AMP and ATP on the effects of $[L^1_2Zn_3]^{6+}$ on phosphorylation levels of recombinant AMPK and on AMPK kinase activity. a) and b) Effects of no ATP, 50 μ M ATP or 50 μ M AMP on the effects of 50 μ M $[L^1_2Zn_3]^{6+}$ on phospho-T172 AMPK α 1 of α 1 β 2 γ 1 AMPK kinase (a) and phospho-S108 of AMPK β 1 of α 2 β 1 γ 1 AMPK kinase (b). Densitometric quantification of levels of phosphorylated AMPK subunit and relative to total levels of the subunit are indicated; all quantification relative to solvent control. For a) and b), similar results were obtained in a minimum of n=2 independent experiments. c) effect of increasing concentrations of AMP (0, 80, 160 μ M) on AMPK kinase inhibition by $[L^1_2Zn_3]^{6+}$. % AMPK activity is relative to activity in the vehicle control \pm AMP (0, 80 or 160 μ M AMP). N = 2 independent experiments, with corresponding data points as indicated.

Figure 6.32. 1H NMR Spectrum of **2.1** [300 MHz, $CDCl_3$]. * $CHCl_3$ impurity. ** H_2O impurity.

Figure 6.33. ^{13}C NMR Spectrum of **2.1** [100 MHz, $CDCl_3$].

Figure 6.34. ^{13}C NMR Spectrum of **2.1** (blue) with the corresponding DEPT-135 (red) and DEPT-90 (green) NMR spectra [100 MHz, $CDCl_3$].

Figure 6.35. 1H NMR Spectrum of **2.2** [400 MHz, $(CD_3)_2SO$]. * $(CD_3)(CD_2H)SO$ impurity. ** H_2O impurity.

Figure 6.36. ^{13}C NMR Spectrum of **2.2** [100 MHz, $(\text{CD}_3)_2\text{SO}$].

Figure 6.37. ^{13}C NMR Spectrum of **2.2** (blue) with the corresponding DEPT-135 (red) and DEPT-90 (green)

Figure 6.38. ^1H NMR Spectrum of **L²** [400 MHz, $(\text{CD}_3)_2\text{SO}$]. *(CD_3)(CD_2H)SO impurity. ** H_2O impurity.

Figure 6.39. ^{13}C NMR Spectrum of **L²** [100 MHz, $(\text{CD}_3)_2\text{SO}$].

Figure 6.40. ^{13}C NMR Spectrum of **L²** (blue) with the corresponding DEPT-135 (red) and DEPT-90 (green) NMR spectra [100 MHz, $(\text{CD}_3)_2\text{SO}$].

Figure 6.41. ^1H NMR Spectrum of **3.1** [400 MHz, $(\text{CD}_3)_2\text{SO}$]. *(CD_3)(CD_2H)SO impurity. ** H_2O impurity.

Figure 6.42. ^{13}C NMR Spectrum of **3.1** [100 MHz, $(\text{CD}_3)_2\text{SO}$].

Figure 6.43. ^{13}C NMR Spectrum of **3.1** (blue) with the corresponding DEPT-135 (red) and DEPT-90 (green) NMR spectra [100 MHz, $(\text{CD}_3)_2\text{SO}$].

Figure 6.44. ^1H NMR Spectrum of **3.2** [600 MHz, $(\text{CD}_3)_2\text{SO}$]. *(CD_3)(CD_2H)SO impurity. ** H_2O impurity.

Figure 6.45. ^1H NMR Spectrum of **L³** [600 MHz, $(\text{CD}_3)_2\text{SO}$]. *(CD_3)(CD_2H)SO impurity. ** H_2O impurity. *** NH_4^+ impurity.

Figure 6.46. ^{13}C NMR Spectrum of **L³** [150 MHz, $(\text{CD}_3)_2\text{SO}$].

Figure 6.47. ^{13}C NMR Spectrum of **L³** (blue) with the corresponding DEPT-135 (red) and DEPT-90 (green) NMR spectra [150 MHz, $(\text{CD}_3)_2\text{SO}$].

Figure 6.48. ESI-MS of $[\text{L}^3_2\text{Cu}_3(\text{Br})](\text{trif})_5$ showing ions at m/z 2085 and 968 corresponding to $\{[\text{L}^3_2\text{Cu}_3(\text{Br})](\text{trif})_4\}^+$ and $\{[\text{L}^3_2\text{Cu}_3(\text{Br})](\text{trif})_3\}^{2+}$ for each ligand respectively. The isotope pattern for the ion at m/z 2085 is shown inset (top observed and bottom calculated).

Figure 6.49. ESI-MS of $[\text{L}^3\text{Cu}_3(\text{SO}_4)](\text{trif})_4$ showing ions at m/z 1954 and 901 corresponding to $\{[\text{L}^3]_2\text{Cu}_3(\text{SO}_4)](\text{trif})_3\}^+$ and $\{[\text{L}^3]_2\text{Cu}_3(\text{SO}_4)](\text{trif})_2\}^{2+}$ for each ligand respectively. The isotope pattern for the ion at m/z 901 is shown inset (top observed and bottom calculated).

Figure 6.50. ^1H NMR Spectrum of **4.1** [400 MHz, CDCl_3].

Figure 6.51. ^{13}C NMR Spectrum of **4.1** [100 MHz, CDCl_3].

Figure 6.52. ^{13}C NMR Spectrum of **4.1** (blue) with the corresponding DEPT-135 (red) and DEPT-90 (green) NMR spectra [100 MHz, CDCl_3].

Figure 6.53. Aliphatic region of the ^1H NMR Spectrum of **4.2** [400 MHz, CDCl_3].

Figure 6.54. ^{13}C NMR Spectrum of **4.2** [100 MHz, CDCl_3].

Figure 6.55. ^{13}C NMR Spectrum of **4.2** (blue) with the corresponding DEPT-135 (red) and DEPT-90 (green) NMR spectra [100 MHz, CDCl_3].

Figure 6.56. Aliphatic region of the ^1H NMR Spectrum of **4.3** [400 MHz, CDCl_3].

Figure 6.57. ^{13}C NMR Spectrum of **4.3** [400 MHz, CDCl_3].

Figure 6.58. ^{13}C NMR Spectrum of **4.3** (blue) with the corresponding DEPT-135 (red) and DEPT-90 (green) NMR spectra [100 MHz, CDCl_3].

Figure 6.59. Aliphatic region of the ^1H NMR Spectrum of **4.4** [300 MHz, CDCl_3].

Figure 6.60. Aliphatic region of the ^{13}C NMR Spectrum of **4.4** [100 MHz, CDCl_3].

Figure 6.61. Aliphatic region of the ^{13}C NMR Spectrum of **4.4** (blue) with the corresponding DEPT-135 (red) and DEPT-90 (green) NMR spectra [100 MHz, CDCl_3].

Figure 6.62. Aliphatic region of the ^1H NMR Spectrum of **4.5** [400 MHz, CDCl_3].

Figure 6.63. Aliphatic region of the ^{13}C NMR Spectrum of **4.5** [100 MHz, CDCl_3].

Figure 6.64. Aliphatic region of the ^{13}C NMR Spectrum of **4.5** (blue) with the corresponding DEPT-135 (red) and DEPT-90 (green) NMR spectra [100 MHz, CDCl_3].

Figure 6.65. ^1H NMR Spectrum of **4.6** [400 MHz, CDCl_3]. * CHCl_3 impurity.

Figure 6.66. ^{13}C NMR Spectrum of **4.6** [100 MHz, CDCl_3].

Figure 6.67. ^{13}C NMR Spectrum of **4.6** (blue) with the corresponding DEPT-135 (red) and DEPT-90 (green) NMR spectra [100 MHz, CDCl_3].

Figure 6.68. ^1H NMR Spectrum of **4.7** [400 MHz, $(\text{CD}_3)_2\text{SO}$].

Figure 6.69. ^{13}C NMR Spectrum of **4.7** [100 MHz, $(\text{CD}_3)_2\text{SO}$].

Figure 6.70. ^{13}C NMR Spectrum of **4.7** (blue) with the corresponding DEPT-135 (red) and DEPT-90 (green) NMR spectra [100 MHz, $(\text{CD}_3)_2\text{SO}$].

Figure 6.71. ^1H NMR Spectrum of **4.8** [400 MHz, CDCl_3]. * CHCl_3 impurity.

Figure 6.72. ^{13}C NMR Spectrum of **4.8** [100 MHz, CDCl_3].

Figure 6.73. ^{13}C NMR Spectrum of **4.8** (blue) with the corresponding DEPT-135 (red) and DEPT-90 (green) NMR spectra [100 MHz, CDCl_3].

Figure 6.74. ^1H NMR Spectrum of **4.9** [400 MHz, CDCl_3]. * CHCl_3 impurity. ** CH_2Cl_2 impurity.

Figure 6.75. ^{13}C NMR Spectrum of **4.9** [100 MHz, CDCl_3].

Figure 6.76. ^{13}C NMR Spectrum of **4.9** (blue) with the corresponding DEPT-135 (red) and DEPT-90 (green) NMR spectra [100 MHz, CDCl_3].

Figure 6.77. ^1H NMR Spectrum of **L⁴** [400 MHz, CDCl_3]. * CHCl_3 impurity.

Figure 6.78. ^{13}C NMR Spectrum of L^4 [100 MHz, CDCl_3].

Figure 6.79. ^{13}C NMR Spectrum of L^4 (blue) with the corresponding DEPT-135 (red) and DEPT-90 (green) NMR spectra [100 MHz, CDCl_3].

Figure 6.80. ESI-MS spectrum of $[\text{L}^4_2\text{Cu}_3](\text{ClO}_4)_6$.

Figure 6.81. ESI-MS spectrum of $[(\text{L}^4)_2\text{Cu}_3(\text{SO}_4)](\text{ClO}_4)_4$.

Figure 6.82. ESI-MS spectrum of $[(\text{L}^4)_2\text{Cu}_3(\text{PO}_4)](\text{ClO}_4)_3$.

Figure 6.83. ESI-MS spectrum of $[(\text{L}^4)_2\text{Cu}_3(\text{AsO}_4)](\text{ClO}_4)_3$.

Figure 6.84. UV-Vis-NIR absorption spectra of a solution of $[(\text{L}^4)_2\text{Cu}_3](\text{trif})_6$ in 1:1 MeCN in H_2O plus the addition of one equivalent of various anions (as either their ammonium, sodium, tetra-*N*-ethyl- or tetra-*N*-butyl-ammonium salts). $[(\text{L}^4)_2\text{Cu}_3](\text{trif})_6 = 0.8 \text{ mM}$.

Figure 6.85. UV-Vis-NIR absorption spectra of a solution of $[(\text{L}^4)_2\text{Cu}_3](\text{trif})_6$ in 1:1 MeCN in H_2O plus the addition of one equivalent of tetra-*N*-butyl-ammonium dihydrogen phosphate. $[(\text{L}^4)_2\text{Cu}_3](\text{trif})_6 = 0.8 \text{ mM}$.

Figure 6.86. UV-Vis-NIR absorption spectra of a solution of $[(\text{L}^4)_2\text{Cu}_3](\text{trif})_6$ in 1:1 MeCN in H_2O plus the addition of one equivalent of disodium arsenate. $[(\text{L}^4)_2\text{Cu}_3](\text{trif})_6 = 0.8 \text{ mM}$.

Figure 6.87. UV-Vis-NIR absorption spectra of a solution of $[(\text{L}^4)_2\text{Cu}_3](\text{trif})_6$ in 1:1 MeCN in H_2O plus the addition of one equivalent of tetra-*N*-butylammonium nitrate. $[(\text{L}^4)_2\text{Cu}_3](\text{trif})_6 = 0.8 \text{ mM}$.

Figure 6.88. UV-Vis-NIR absorption spectra of a solution of $[(\text{L}^4)_2\text{Cu}_3](\text{trif})_6$ in 1:1 MeCN in H_2O plus the addition of one equivalent of tetra-*N*-butylammonium hydrogen sulfate. $[(\text{L}^4)_2\text{Cu}_3](\text{trif})_6 = 0.8 \text{ mM}$.

Figure 6.89. UV-Vis-NIR absorption spectra of a solution of $[(L^4)_2Cu_3](trif)_6$ in 1:1 MeCN in H₂O plus the addition of one equivalent of tetra-*N*-ethylammonium chloride. $[(L^4)_2Cu_3](trif)_6 = 0.8$ mM.

Figure 6.90. UV-Vis-NIR absorption spectra of a solution of $[(L^4)_2Cu_3](trif)_6$ in 1:1 MeCN in H₂O plus the addition of one equivalent of disodium carbonate. $[(L^4)_2Cu_3](trif)_6 = 0.8$ mM.

Figure 6.91. UV-Vis-NIR absorption spectra of a solution of $[(L^4)_2Cu_3](trif)_6$ in 1:1 MeCN in H₂O plus the addition of one equivalent of ammonium hexafluorosilicate. $[(L^4)_2Cu_3](trif)_6 = 0.8$ mM.

Figure 6.92. UV-Vis-NIR absorption spectra of a solution of $[(L^4)_2Cu_3](trif)_6$ and $[(L^4)_2Cu_3(SO_4)](trif)_4$ in 1:3 MeCN in H₂O. To $[(L^4)_2Cu_3](trif)_6$ was added one equivalent of monosodium sulfate and monosodium dihydrogenphosphate, in the order shown, and then the addition reversed. $[(L^4)_2Cu_3](trif)_6 = 0.8$ mM.

Figure 6.93. UV-Vis-NIR absorption spectra of a solution of $[(L^4)_2Cu_3](trif)_6$ and $[(L^4)_2Cu_3(PO_4)](trif)_3$ in 1:3 MeCN in H₂O. To $[(L^4)_2Cu_3](trif)_6$ was added one equivalent of disodium sulfate and disodium hydrogenphosphate, in the order shown, and then the addition reversed. $[(L^4)_2Cu_3](trif)_6 = 0.8$ mM.

Figure 6.94. Calibration curve (ppm) for chloride, nitrate, phosphate and sulphate anions.

Figure 6.95. Ion Chromatography chromatograms: 0.5 mM standard.

Figure 6.96. Experiment IC-1 Ion Chromatography chromatograms: NaCl, NaNO₃, NaH₂PO₄ and NaHSO₄ (0.0208 mmols of each) after exposure to $[(L^4)_2Cu_3](trif)_6$ (0.0208 mols). The response at ~15 mins is due to CF₃SO₃⁻ anions.

Figure 6.97. Experiment IC-2 Ion Chromatography chromatograms: NaCl, NaNO₃, Na₂HPO₄ and Na₂SO₄ (0.0208 mmols of each) after exposure to $[(L^4)_2Cu_3](trif)_6$ (0.0208 mols). The response at ~15 mins is due to CF₃SO₃⁻ anions.

Figure 6.98. ^1H NMR Spectrum of **5.1** [400 MHz, CDCl_3]. * CHCl_3 impurity.

Figure 6.99. ^{13}C NMR Spectrum of **5.1** [100 MHz, CDCl_3].

Figure 6.100. ^{13}C NMR Spectrum of **5.1** (blue) with the corresponding DEPT-135 (red) and DEPT-90 (green) NMR spectra [100 MHz, CDCl_3]. * CH_2Cl_2 impurity.

Figure 6.101. ^1H NMR Spectrum of **5.2** [300 MHz, CDCl_3]. * CHCl_3 impurity.

Figure 6.102. ^{13}C NMR Spectrum of **5.2** [100 MHz, CDCl_3].

Figure 6.103. ^{13}C NMR Spectrum of **5.2** (blue) with the corresponding DEPT-135 (red) and DEPT-90 (green) NMR spectra [100 MHz, CDCl_3].

Figure 6.104. ^1H NMR Spectrum of **5.3** [400 MHz, CDCl_3]. * CHCl_3 impurity.

Figure 6.105. ^{13}C NMR Spectrum of **5.3** [100 MHz, CDCl_3]. * CH_2Cl_2 impurity.

Figure 6.106. ^{13}C NMR Spectrum of **5.3** (blue) with the corresponding DEPT-135 (red) and DEPT-90 (green) NMR spectra [100 MHz, CDCl_3]. * CH_2Cl_2 impurity.

Figure 6.107. ^1H NMR Spectrum of **L⁵** [300 MHz, CDCl_3]. * CHCl_3 impurity. ** CH_2Cl_2 impurity.

Figure 6.108. ^{13}C NMR Spectrum of **L⁵** [100 MHz, CDCl_3].

Figure 6.109. ^{13}C NMR Spectrum of **L⁵** (blue) with the corresponding DEPT-135 (red) and DEPT-90 (green) NMR spectra [100 MHz, CDCl_3].

Figure 6.110. ^1H NMR Spectrum of **L⁶** [400 MHz, CDCl_3]. * CHCl_3 impurity.

Figure 6.111. ^{13}C NMR Spectrum of **L⁶** [100 MHz, CDCl_3].

Figure 6.112. ^{13}C NMR Spectrum of **L⁶** (blue) with the corresponding DEPT-135 (red) and DEPT-90 (green) NMR spectra [100 MHz, CDCl_3].

Figure 6.113. ESI-MS of $[(L^5)_2Cu_3(PO_4)](trif)_3$ showing ions at m/z 2606 and 1228 corresponding to $\{[(L^5)_2Cu_3(PO_4)](trif)_2\}^+$ and $\{[(L^5)_2Cu_3(PO_4)](trif)\}^{2+}$ respectively. The isotope pattern for the ion at m/z 1228 is shown inset (top observed and bottom calculated). The ion at m/z 2606 is small but reproducible.

Figure 6.114. ESI-MS of $[(L^6)_2Cu_3(PO_4)](trif)_3$ showing ions at m/z 2572 and 1221 corresponding to $\{[(L^6)_2Cu_3(PO_4)](trif)_2\}^+$ and $\{[(L^6)_2Cu_3(PO_4)](trif)\}^{2+}$ respectively. The isotope pattern for the ion at m/z 1222 is shown inset (top observed and bottom calculated). The ion at m/z 2572 is small but reproducible.

Figure 6.115. UV-Vis-NIR absorption spectra of a solution of $[(L^5)_2Cu_3](trif)_6$ in 3% MeOH in DCM plus the addition of one equivalent of various anions (as either their tetra-*N*-ethyl- or tetra-*N*-butyl-ammonium salts). Concentration of $[(L^5)_2Cu_3](trif)_6 = 0.8$ mM.

Figure 6.116. UV-Vis-NIR absorption spectra of a solution of $[(L^6)_2Cu_3](trif)_6$ in 3% MeOH in DCM plus the addition of one equivalent of various anions (as either their tetra-*N*-ethyl- or tetra-*N*-butyl-ammonium salts). Concentration of $[(L^6)_2Cu_3](trif)_6 = 0.8$ mM.

Figure 6.117. IC calibration curve of 0.2 – 1.0 mM solutions of NaCl for experiment IC-3.

Figure 6.118. IC calibration curve of 0.2 – 1.0 mM solutions of NaNO₃ for experiment IC-3.

Figure 6.119. IC calibration curve of 0.2 – 1.0 mM solutions of NaH₂PO₄ for experiment IC-3.

Figure 6.120. IC calibration curve of 0.2 – 1.0 mM solutions of NaHSO₄·H₂O for experiment IC-3.

Figure 6.121. IC calibration curve of 0.2 – 1.0 mM solutions of NaCl for experiment IC-4.

Figure 6.122. IC calibration curve of 0.2 – 1.0 mM solutions of NaNO₃ for experiment IC-4.

Figure 6.123. IC calibration curve of 0.2 – 1.0 mM solutions of Na₂HPO₄·2H₂O for experiment IC-4.

Figure 6.124. IC calibration curve of 0.2 – 1.0 mM solutions of $\text{Na}_2\text{SO}_4 \cdot 10\text{H}_2\text{O}$ for experiment **IC-4**.

Figure 6.125. IC calibration curve of 0.2 – 1.0 mM solutions of $\text{Na}_2\text{HPO}_4 \cdot 2\text{H}_2\text{O}$ for experiment **IC-5 – IC-8**.

Figure 6.126. An IC plot of the background signals present in the ultrapure water used for experiments **IC-3 – IC-10**.

Figure 6.127. An IC plot showing the individual peak for Cl^- ions at 0.6 mM concentration at 5.47 minutes.

Figure 6.128. An IC plot showing the individual peak for NO_3^- ions at 0.6 mM concentration at 8.64 minutes.

Figure 6.129. An IC plot showing the individual peak for PO_4^{3-} ions at 0.6 mM concentration at 12.36 minutes.

Figure 6.130. An IC plot showing the individual peak for SO_4^{2-} ions at 0.6 mM concentration at 14.09 minutes.

Figure 6.131. An IC plot showing the individual peak for triflate ions at 0.6 mM concentration at 16.51 minutes.

Figure 6.132. The IC chromatogram showing the four individual peaks of the mono-sodium salts at 0.6 mM concentration with the peaks at 5.43, 8.56, 12.20 and 13.85 minutes corresponding to Cl^- , NO_3^- , PO_4^{3-} and SO_4^{2-} ions respectively.

Figure 6.133. The IC chromatogram of experiment **IC-3** after treatment with the $[(\text{L}^5)_2\text{Cu}_3](\text{trif})_6$ complex showing the amounts of Cl^- , NO_3^- , PO_4^{3-} and SO_4^{2-} ions present. The peak at 16.20 minutes corresponds to triflate anions.

Figure 6.134. The IC chromatogram of experiment **IC-3** after treatment with the $[(L^6)_2Cu_3](trif)_6$ complex showing the amounts of Cl^- , NO_3^- , PO_4^{3-} and SO_4^{2-} ions present. The peak at 16.15 minutes corresponds to the triflate anions.

Figure 6.135. The IC chromatogram plot showing the four individual peaks of the di-sodium salts at 0.6 mM concentration with the peaks at 5.42, 8.53, 12.16 and 13.82 minutes corresponding to Cl^- , NO_3^- , PO_4^{3-} and SO_4^{2-} ions respectively.

Figure 6.136. The IC chromatogram of experiment **IC-4** after treatment with the $[(L^5)_2Cu_3](trif)_6$ complex showing the decrease in amounts of Cl^- , NO_3^- , PO_4^{3-} and SO_4^{2-} ions present. The peak at 16.15 minutes corresponds to triflate anions.

Figure 6.137. The IC chromatogram of experiment **IC-4** after treatment with the $[(L^6)_2Cu_3](trif)_6$ complex showing the decrease in amounts of Cl^- , NO_3^- , PO_4^{3-} and SO_4^{2-} ions present. The peak at 16.12 minutes corresponds to triflate anions.

Figure 6.138. An IC plot showing the individual peak for PO_4^{3-} ions at 0.66 mM concentration at 12.17 minutes.

Figure 6.139. The IC chromatogram for experiment **IC-5** showing the total amount of PO_4^{3-} ions left in the aqueous solution after treatment with the $[(L^5)_2Cu_3](trif)_6$ complex. The peak at 16.09 minutes corresponds to triflate anions.

Figure 6.140. The IC chromatogram for experiment **IC-6** showing the total amount of PO_4^{3-} ions left in the aqueous solution after treatment with the $[(L^5)_2Cu_3](trif)_6$ complex where the complex was formed from the corresponding masses of ligand and $Cu(trif)_2$ in Table 3. The peak at 16.04 minutes corresponds to triflate anions.

Figure 6.141. The IC chromatogram for experiment **IC-7** showing the total amount of PO_4^{3-} ions left in the aqueous solution after treatment with the $[(L^5)_2Cu_3](trif)_6$ complex where the complex was

formed from the corresponding masses of ligand and $\text{Cu}(\text{trif})_2$ in Table 3. The peak at 16.00 minutes corresponds to triflate anions.

Figure 6.142. The IC chromatogram for experiment **IC-8** showing the total amount of PO_4^{3-} ions left in the aqueous solution after treatment with the $[(\text{L}^6)_2\text{Cu}_3](\text{trif})_6$ complex where the complex was formed from the corresponding masses of ligand and $\text{Cu}(\text{trif})_2$ in Table 3. The peak at 16.11 minutes corresponds to triflate anions.

Figure 6.143. The IC chromatogram for experiment **IC-9** showing the total amount of PO_4^{3-} ions left in the aqueous solution after treatment with the $[(\text{L}^6)_2\text{Cu}_3](\text{trif})_6$ complex where the complex was formed from the corresponding masses of ligand and $\text{Cu}(\text{trif})_2$ in Table 3. The peak at 16.08 minutes corresponds to triflate anions.

Figure 6.144. The IC chromatogram for experiment **IC-10** showing the total amount of PO_4^{3-} ions left in the aqueous solution after treatment with the $[(\text{L}^6)_2\text{Cu}_3](\text{trif})_6$ complex where the complex was formed from the corresponding masses of ligand and $\text{Cu}(\text{trif})_2$ in Table 3. The peak at 16.05 minutes corresponds to triflate anions.

List of Schemes

Scheme 2.1. Improved synthesis of ligand **L¹** from tris-(2-aminoethyl)amine.

Scheme 3.1. Synthesis of ligand **L²** from 1,1,1-tris(aminomethyl)ethane trihydrochloride.¹⁰⁶

Scheme 3.2. Synthesis of ligand **L³** from cis,cis-1,3,5-cyclohexanetriamine trihydrobromide.^{109,110}

Scheme 3.3. Synthesis of **HC(CH₂CH₂OMs)₃ 4.5** from dimethyl-1,3-acetonedicarboxylate.¹¹¹

Scheme 3.4. Synthesis of ligand **L⁴** from trimesylate **4.5** via the phthalimide **4.5a** and triamine **4.5b**.

Scheme 3.5. Synthesis of ligand **L⁴** from trimesylate **4.5** via the protected species **4.9**.

Scheme 3.6. Failed attempts to remove the benzyl- protecting group.¹¹²⁻¹¹⁷

Scheme 4.1. Synthesis of brominated 2-acetylpyridine derivative **5.3** from (2-(2-methyl-1,3-dioxolan-2-yl)pyridin-4-yl)methanol.^{118,119}

Scheme 4.2. Synthesis of ligands **L⁵** and **L⁶** from brominated acetylpyridine- species **5.3** and respective thioureas.

Scheme 6.1. Synthesis of ligand **L¹**.

Scheme 6.2. Synthesis of ligand **L²**.

Scheme 6.3. Synthesis of ligand **L³**.

Scheme 6.4. Synthesis of ligand **L⁴**.

Scheme 6.5. Synthesis of brominated 2-acetylpyridine derivative **5.3**.

Scheme 6.6. Synthesis of ligand **L⁵**.

Scheme 6.7. Synthesis of ligand **L⁶**.

List of Tables

Table 4.1. Percentage of phosphate anion extracted from aqueous solutions of Na_2HPO_4 after exposure to organic media containing each complex for 18 hours. Complexes assembled using copper(II) trifluoromethanesulfonate. Initial concentration of $\text{Na}_2\text{HPO}_4 = 0.66 \text{ mM}$.

Table 4.2. Percentage of each anion extracted in aqueous solutions of NaCl , NaNO_3 , NaHSO_4 and NaH_2PO_4 after exposure to organic media containing each complex for 18 hours. Initial concentration of each anion = 0.66 mM . $\text{pH} = 2.79$.

Table 4.3. Percentage of each anion extracted in aqueous solutions of NaCl , NaNO_3 , Na_2SO_4 and Na_2HPO_4 after exposure to organic media containing each complex for 18 hours. Initial concentration of each anion = 0.66 mM . $\text{pH} = 8.85$.

Table 6.1. X-ray crystallographic data for $[\text{L}^1_2\text{Cu}_3(\text{PhOPO}_3)]^{4+}$, $[\text{L}^1\text{Zn}]^{2+}$, $[\text{L}^1_2\text{Zn}_3(\text{PO}_4)]^{3+}$ and $[\text{L}^1_2\text{Zn}_3(\text{SO}_4)]^{4+}$.

Table 6.2. X-ray crystallographic data for $[\text{L}^1\text{Mn}]^{2+}$, $[\text{L}^1_2\text{Mn}_3(\text{PO}_4)]^{3+}$ and $[\text{L}^1_2\text{Mn}_3(\text{SO}_4)]^{4+}$.

Table 6.3. Concentration of 4-nitrophenol (mM) at 24 hr at $37 \text{ }^\circ\text{C}$.

Table 6.4. X-ray crystallographic data for $[\text{L}^3_2\text{Cu}_3(\text{SO}_4)]^{4+}$ and $[\text{L}^3_2\text{Cu}_3(\text{Br})]^{5+}$.

Table 6.5. X-ray crystallographic data for $[\text{L}^4\text{Mn}]^{2+}$, $[\text{L}^4_2\text{Mn}_3(\text{PO}_4)]^{3+}$ and $[\text{L}^4_2\text{Mn}_3(\text{SO}_4)]^{4+}$.

Table 6.6. Conditions for ion chromatography analysis of L^4 complexes.

Table 6.7. Monosodium experiment **IC-1** Ion Chromatography results.

Table 6.8. Disodium experiment **IC-2** Ion Chromatography results.

Table 6.9. The masses of ligand and stoichiometric amounts of $\text{Cu}(\text{trif})_2$ used in experiments **IC-6** – **IC-**

Table 6.10. Conditions for ion chromatography analysis of L^5 and L^6 complexes.

Table 6.11. Amount of Cl^- , NO_3^- , PO_4^{3-} and SO_4^{2-} ions present in the aqueous solution after treatment with the $[(L^5)_2Cu_3](trif)_6$ and the $[(L^6)_2Cu_3](trif)_6$ complexes. Initial theoretical maximum concentration of each anion = 0.66 mM.

Table 6.12. Amount of Cl^- , NO_3^- , PO_4^{3-} and SO_4^{2-} ions present in the aqueous solution after treatment with the $[(L^5)_2Cu_3](trif)_6$ and the $[(L^6)_2Cu_3](trif)_6$ complexes. Initial theoretical maximum concentration of each anion = 0.66 mM.

Table 6.13. Decrease in the amount of PO_4^{3-} ions present in the aqueous solution as the ratio of the $[(L^5)_2Cu_3](trif)_6$ complex present increases (initial concentration of PO_4^{3-} = 0.66 mM).

Table 6.14. Decrease in the amount of PO_4^{3-} ions present in the aqueous solution as the amount of the $[(L^6)_2Cu_3](trif)_6$ complex present increases (initial concentration of PO_4^{3-} = 0.66 mM).

Abbreviations

A	Anion
Ac	Acetyl
ATP	Adenosine triphosphate
atu	Amidinothiourea
bptz	3,6- <i>bis</i> (2-pyridyl)-1,2,4,5-tetrazine
br	Broad
Bu	Butyl (<i>n</i> -, unless otherwise specified)
Cy	Cyclohexyl
d	Doublet
DCM	Dichloromethane
DIPEA	<i>N,N</i> -diisopropylethylamine
DMSO	Dimethylsulfoxide
DNA	Deoxyribonucleic acid
ESI-MS	Electrospray ionisation mass spectrometry
Et	Ethyl
HEPES	4-(2-hydroxyethyl)-1-piperazineethane sulfonic acid
IC	Ion chromatography
IC ₅₀	Half maximal inhibitory concentration
L	Ligand
M	Metal
m	Multiplet
<i>m</i> -	<i>Meta</i> -
m/z	Mass-to-charge ratio
Me	Methyl-
MeCN	Acetonitrile

MeOH	Methanol
Ms	Mesyl
NMR	Nuclear magnetic resonance
<i>o</i> -	<i>Ortho</i> -
<i>p</i> -	<i>Para</i> -
Ph	Phenyl
phen	1,10-phenanthraline
Py	Pyridyl
q	Quartet
quint	Quintet
RNA	Ribonucleic acid
s	Singlet
sept	Septet
SI	Selective index
t	Triplet
Tf	Triflyl
THF	Tetrahydrofuran
TLC	Thin layer chromatography
tren	Tris(2-aminoethyl)amine
trif	Trifluoromethanesulfonate
Tz	Thiazolyl
w.r.t	With respect to
X	Halide

1. Introduction

1.1. Supramolecular chemistry and self-assembly

1.1.1. Supramolecular and metallosupramolecular chemistry

Supramolecular chemistry has been coined as “chemistry beyond the molecule” – that is, the formation of systems consisting of multiple discrete molecular species.¹⁻⁴ Whereas “traditional” chemistry is built around *intra*-molecular covalent and ionic bonding interactions, supramolecular species are based on *inter*-molecular non-covalent interactions including hydrogen bonds, van der Waals forces, and polar attraction interactions.⁵ These forces are utilised extensively within the field in order to assemble complex multimolecular architectures.

Within supramolecular architectures, metal cations are frequently used as nuclei to bind discrete parts together. This is achieved through forming metal-ligand co-ordination bonds through interactions between lone pairs on organic donor species and positively charged ionic metal centres. Metallosupramolecular chemistry concerns itself with this field; whilst the non-metallic species are typically large, neutral organic scaffolds, metal-directed architectures typically make use of an ionic metal salt resulting in a charged complex.

1.1.2. Supramolecular self-assembly

One subset of supramolecular chemistry, “self-assembly” concerns itself with the design of pre-programmed molecular species which form specific systems using intermolecular non-covalent interactions, a process which is reversible and therefore self-correcting. This is a process where a disordered system of pre-existing compounds forms an organized structure as a consequence of specific pre-programmed interactions among the components themselves and does so without external direction. This allows the formation of large complex molecules to be constructed by expressing the information present within the smaller subunits and negates the need for a chemist to conventionally synthesise the target molecule; only the syntheses of simpler, smaller, pre-programmed sub-units are required.

Self-assembly is ubiquitous in both chemical and biological systems; indeed, the process is used extensively throughout nature and is the manner in which many biologically essential species are made, including phospholipid barriers, amino acid-based polymers such as proteins, enzymes and nucleic acids.^{6,7} This process has also been suggested by some as a potential source of the origin of life.⁸ As a result of the far-reaching natural applications of the self-assembly process, a great deal of research effort has been expended to develop new self-assembled systems.

1.2. Anions

In chemistry, ionic compounds are formed from two species – one of which carries a net positive charge (the cation) and the other carrying a net negative charge (the anion). Cations are usually metal

ions or protonated amines and are found dispersed widely throughout the environment and biological systems and the chemistry behind these species has been widely studied and is now well understood.

The negatively-charged counterpart of the cation is the anion which, whilst also being essential to all living organisms, has not been studied nearly as much despite their widespread chemical, environmental and biological applications.⁹⁻¹² For example, the major anions dissolved in seawater are chlorides, carbonates, sulfates and bromides, all of which are essential chemical compounds and found throughout the rich and diverse marine life that reside there.¹³ Whilst they are rarely naturally present in biological systems, fluorides are added to drinking water to reinforce tooth enamel, reacting with the terminal calcium hydroxide bonds on the surface of the enamel making them chemically inert.¹⁴ Due to its importance in biological processes, iodide salts are commonly added to table salt to help prevent iodine deficiency and thyroid issues.¹⁵ Sulfates, nitrates and phosphates are all essential as fertilisers and are, along with potassium salts, commonly employed in the agricultural industry to boost crop growth and yield.¹⁶

In particular, the phosphate anion is a vitally important fertiliser with modern agriculture requiring 1 ton of phosphate fertiliser to produce 130 tons of grain and annual demand is growing twice as fast as the growth in human population.^{17,18} Despite this dependency, the entire production of this vital compound is sourced from a finite supply which is becoming more scarce, expensive and concentrated in only a few countries. Indeed, the “peak phosphate problem” is of ever-growing concern and some scientists believe that demand will outstrip supply in 20-30 years and reserves will be depleted in the next 50 to 100 years.^{19,20} To combat this issue some mechanism in which the use of phosphate can be made sustainable has to be urgently developed, if a dramatic decrease in food production is to be avoided.²¹

Somewhat ironically, the inefficient use of phosphorus throughout food systems has significant environmental ramifications. Runoff from fertilised cropland enters rivers, lakes and oceans and this massive artificial increase in nutrient content causes toxic algal blooms (Figure 1.1).^{22,23} These blooms are not only unsightly but decrease biodiversity in the affected area by reducing the transmissible light that aquatic plant life relies on, and frequently render the water unusable by humans. This process is termed eutrophication, and can be observed when phosphate concentrations exceed as little as 0.02 mg L⁻¹.²⁴ One such event happened in Lake Taihu; one of the largest lakes in China, a cyanobacterial bloom in 2007 caused the water to become toxic, green and foul-smelling, leaving over 2 million people without drinking water for over a week (Figure 1.1).^{22,23}



Figure 1.1. Algal blooms in Lake Taihu directly affected more than 2 million people.^{22,23}

Examples of affected areas are numerous and increasing, with pollution causing substantial health issues with massive financial implications and humanitarian cost in both developed and emerging countries. For example, Lake Erie in the US, Lake Winnipeg in Canada and Lake Nieuwe Meer in the Netherlands have all experienced similar levels of eutrophication and subsequent algal blooms.²⁵⁻²⁷ Invariably, these are caused by the leaching of phosphate-rich fertilisers from the surrounding arable land and are exacerbated by rising global temperatures.

Obviously, this is a substantial challenge for modern science as the ability to remove and recycle phosphate from aquatic systems would have considerable implications solving two major problems: both mitigating eutrophication and enabling the sustainable production of phosphate fertilisers. The ability to reduce phosphate pollution of aquatic systems and the importance of phosphate sustainability are two of the most challenging goals for the chemical, agricultural and environmental sciences.

Environmental issues are not limited to those caused by phosphate pollution, as other anions such as arsenate and chromate are inherently toxic and possibly carcinogenic and a mechanism to remove these from aquatic systems would also be highly advantageous.

1.2.1. Anions in biological systems

The huge demand for phosphates as fertilisers is driven largely by the vital role of the anion in biological systems. Indeed, phosphate-based molecules are crucial for most (if not all) living matter to function due to their ability to form phospho-esters which are stable at physiological pH but are easily and reversibly hydrolysed to free phosphate by enzyme catalysts.²⁸ Phosphate esters permeate the whole biological infrastructure, from the backbone of DNA and RNA (Figure 1.2b) to the storage and transfer of chemical energy by ATP (Figure 1.2a).^{29–31}

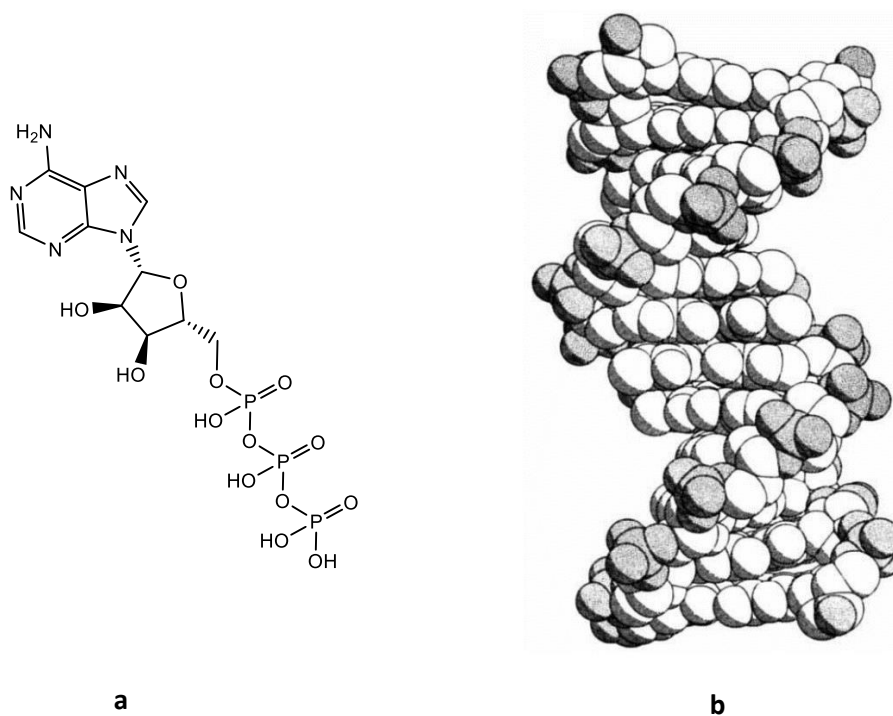


Figure 1.2. a) structure of ATP;²⁹ b) spacefill crystal structure of DNA. Phosphates are shaded.³⁰

One important role of phosphate-based molecules in biological chemistry is facilitated by the kinases, which are a class of enzyme that catalyses the transfer of phosphate ester groups from high-energy, phosphate-donating molecules (e.g. ATP) to specific substrates. Kinases are critical in metabolism, cell signalling, protein regulation, cellular transport, secretory processes and many other cellular pathways, which makes them particularly important to cell biology.³²

1.2.2. Anion receptors

Whilst there have been large research efforts in investigating, detecting and sequestering cations, until recently anion receptor chemistry has been largely neglected. Recently however, attention is being drawn to these due to their increasingly widespread industrial, environmental and medical applications. Modern anion receptors usually consist of organic molecules containing functional

groups capable of binding to anions through hydrogen-bonding interactions (mainly alcohols, amines and amides). Hydrogen-bonding occurs when a hydrogen atom is electrostatically attracted to a more electronegative element.

However, anions are particularly difficult to detect and sequester – far more so than their positively charged counterparts. Not only are anions typically much larger than cations, resulting to weak electrostatic interactions with a receptor, but solvation effects result in anions being stable in aqueous solution, complicating their extraction – an issue compounded by the fact that many anions are very hydrophilic. Species with multiple protonation stages will also have variable charges and shape depending on pH (e.g. H_2PO_4^- , HPO_4^{2-} , PO_4^{3-}) and typically the greater the extent of deprotonation, the more heavily the anion will be solvated in water. The primary measure of this difficulty is the hydration energy of anions, which is related to the size of anion and relative charge, as well as whether the anion is protic or aprotic.^{33–35}

The structure and properties of an anion receptor determines the type, size, and charge of anions it can typically bind to. However, “traditional” organic anion receptors are organic compounds which have poor solubility in aqueous media which is suboptimal as anion extraction is most useful when applied in water. Anion receptors in general are continually being researched with more and more attention being turned to potential applications for them, which include organocatalysis, processing radioactive waste and carbon dioxide scrubbing – as well as many potential applications within the biological field which are only recently being investigated.^{36–39}

Hossain and co-workers were able to synthesise a simple perchlorate binder **1** using a 30-membered ring assembly consisting of two *para*-bis(aminomethyl)benzene rings connected by two

dipropylmethylamine linkages; the resulting ring is capable of binding one perchlorate at either end using hydrogen-bonding interactions from its secondary, now protonated, benzyl-amine groups in the solid-state (Figure 1.3).⁴⁰ Additional research by this group has demonstrated that the substitution of the central *p*-xylyl- for thiophene- groups adjusts the ability of this macrocycle to bind to sulfate anions.⁴¹

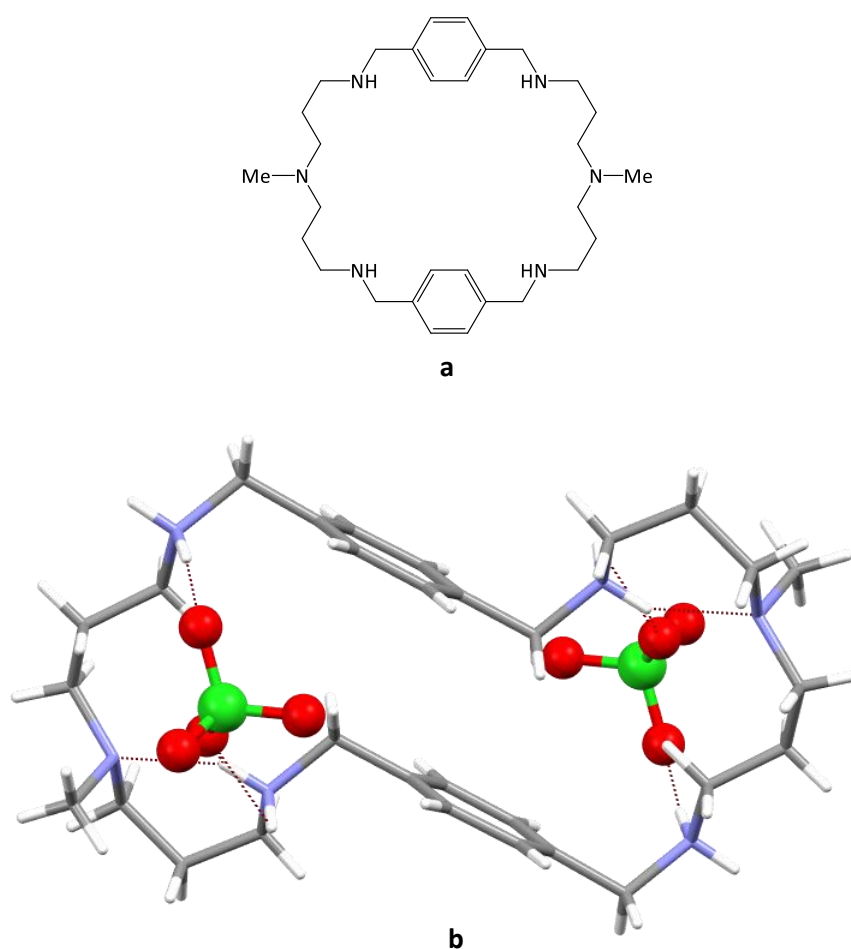


Figure 1.3. a) structure of macrocycle **1**; b) crystal structure of receptor showing the binding of two perchlorate anions.⁴⁰ Colour code: grey, C; blue, N; red, O; white, H; green, Cl.

Gale has demonstrated that indole-containing species can be designed as anion co-ordinators due to their -NH hydrogen-bond donors. Organic receptors **2a** and **2b** demonstrate how these molecules can

interact with the benzoate and dihydrogen phosphate anions respectively.⁴² This is achieved using multiple indole groups conjoined by a urea linkage (Figure 1.4), binding anions through a total of four hydrogen-bonding interactions; one from each of two indole -NH donors and two from the central urea amide -NH donors.

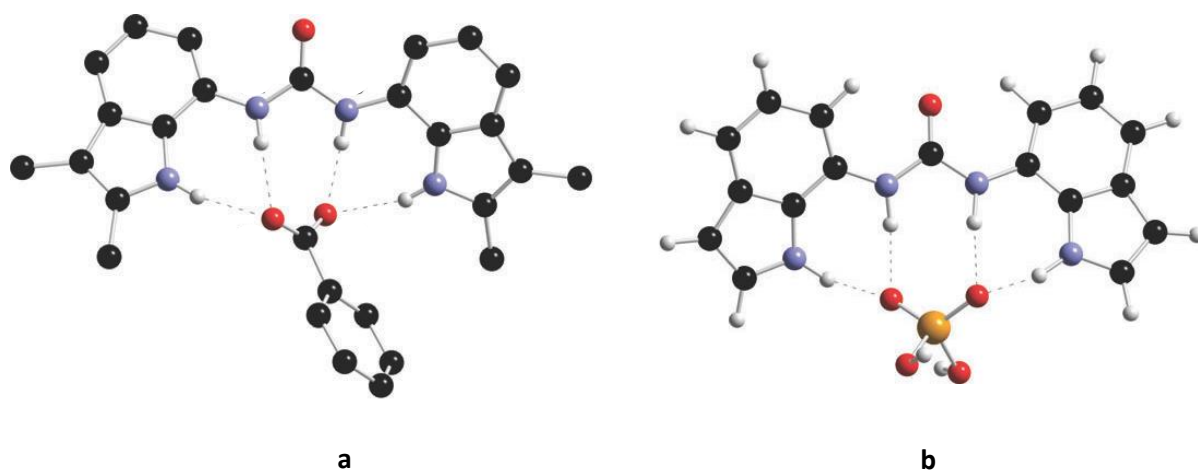


Figure 1.4. Bis-indole urea anion receptors **2a** and **2b**.⁴² a) crystal structure of [**2a**·C₆H₅COO⁻]; b) DFT calculated structure of [**2b**·H₂PO₄⁻]. Colour code: black, C; blue, N; red, O; white, H; orange, P. Non-acidic hydrogen atoms omitted for clarity in a).

Additional research carried out by Gale concerns indole-containing anion sensors. Receptor **3** was developed which contains a similar diindolyl-urea central group as **2a** and **2b** but adjacent to each indole -NH unit is an amide-indole group which contributes an additional two hydrogen-bond donor sites each (Figure 1.5a).⁴³ This “upgrades” the receptor to not only bind three benzoate anions rather than only one, but also enabling the detection of either hydrogen phosphate or dibasic sulfate (Figure 1.5b and c). Upon binding to the anion, the phosphate-containing species is able to dimerise through two -POH...OP- hydrogen-bonding interactions (Figure 1.5d).

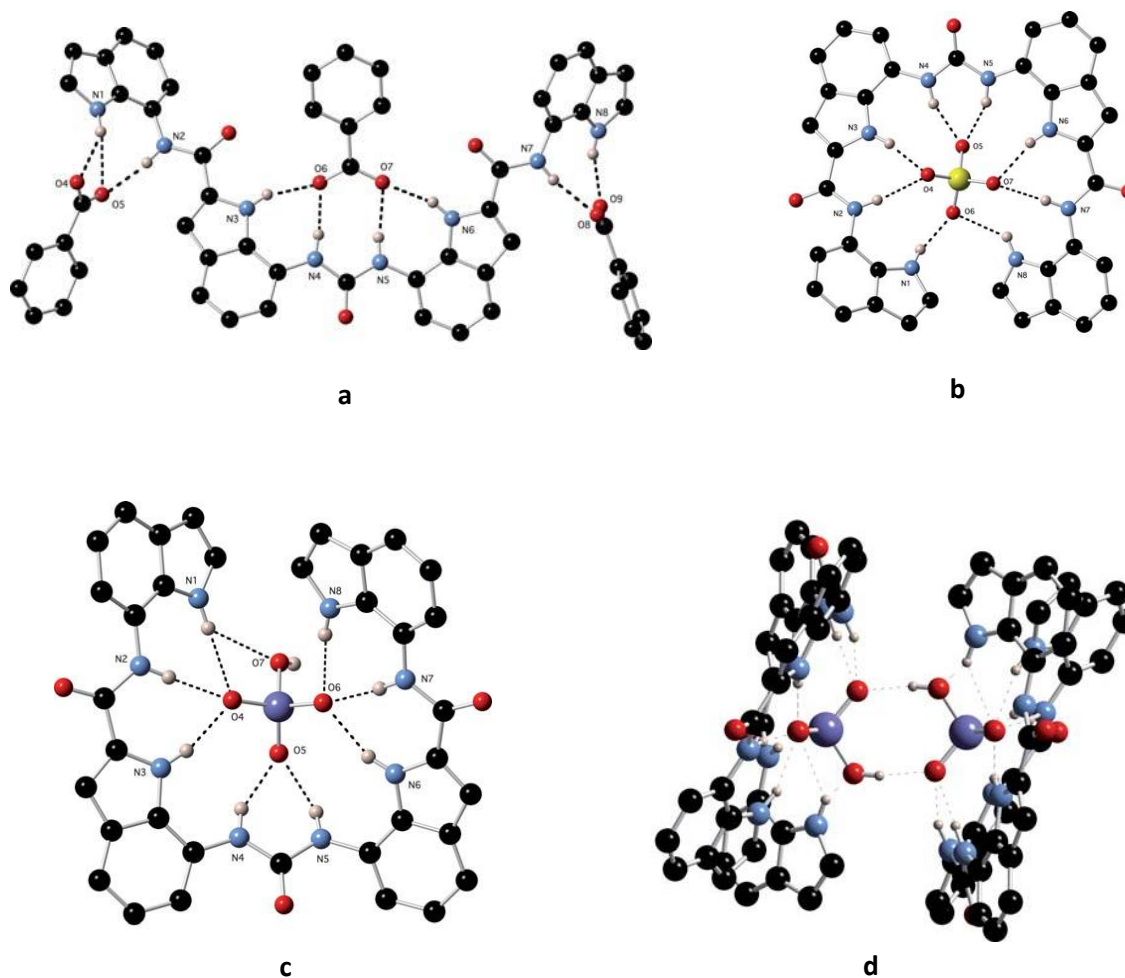


Figure 1.5. Polyindole-based anion receptor **3**.⁴³ Crystal structures of a) $[3 \cdot 3\text{AcO}]^-$, b) $[3 \cdot \text{SO}_4]^{2-}$, c) $[3 \cdot \text{HPO}_4]^{2-}$, d) dimer formed from the phosphate species, i.e. $([3 \cdot \text{HPO}_4]^{2-})_2$. Colour code: black, C; blue, N; red, O; white, H; yellow, S; violet, P. Non-acidic hydrogen atoms have been omitted for clarity.

Indole -NH donor units have also been used by Yan *et al.* in the diindolylquinoxaline-based receptor **4**.⁴⁴ Either chloride or acetate anions can be bound in the solid-state, with dihydrogen phosphate and fluoride also having evidence of being bound in solution through UV-Vis-NIR or fluorescence titration studies. Anions are held in place through hydrogen-bonding interactions from the indole -NH donor units on either side of the receptor (Figure 1.6).

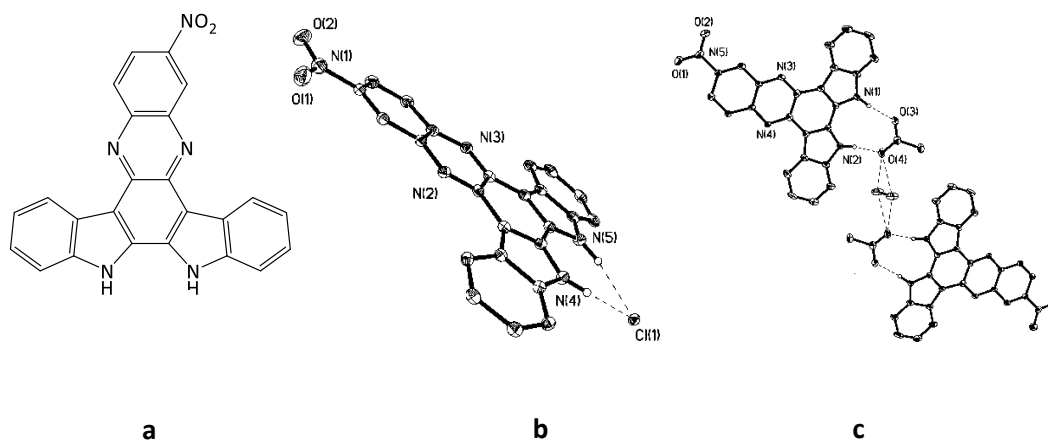


Figure 1.6. a) structure of indole-containing receptor **4**.⁴⁴ Solid-state structures of b) $[4 \cdot \text{Cl}]$; c) $([4 \cdot \text{CH}_3\text{CO}_2]^-)_2 \cdot \text{H}_2\text{O}$. Thermal ellipsoids shown at 30% probability level.

Beer and co-workers have shown that binding between two different receptors is also feasible, through the use of rotaxane species such as **5a** and **5b**.⁴⁵ By introducing sterically bulky groups onto either side of a 3,5-diamidopyridine linking group, chloride anions can be bound between the central amide -NH groups (Figure 1.7a). A polyether chain with terminal amines is then co-ordinated to the “free” side of the anion and ring-closed to form a mechanically interlocked ring, binding the chloride through two -NH \cdots Cl⁻ hydrogen-bonding interactions (Figure 1.7b and c).

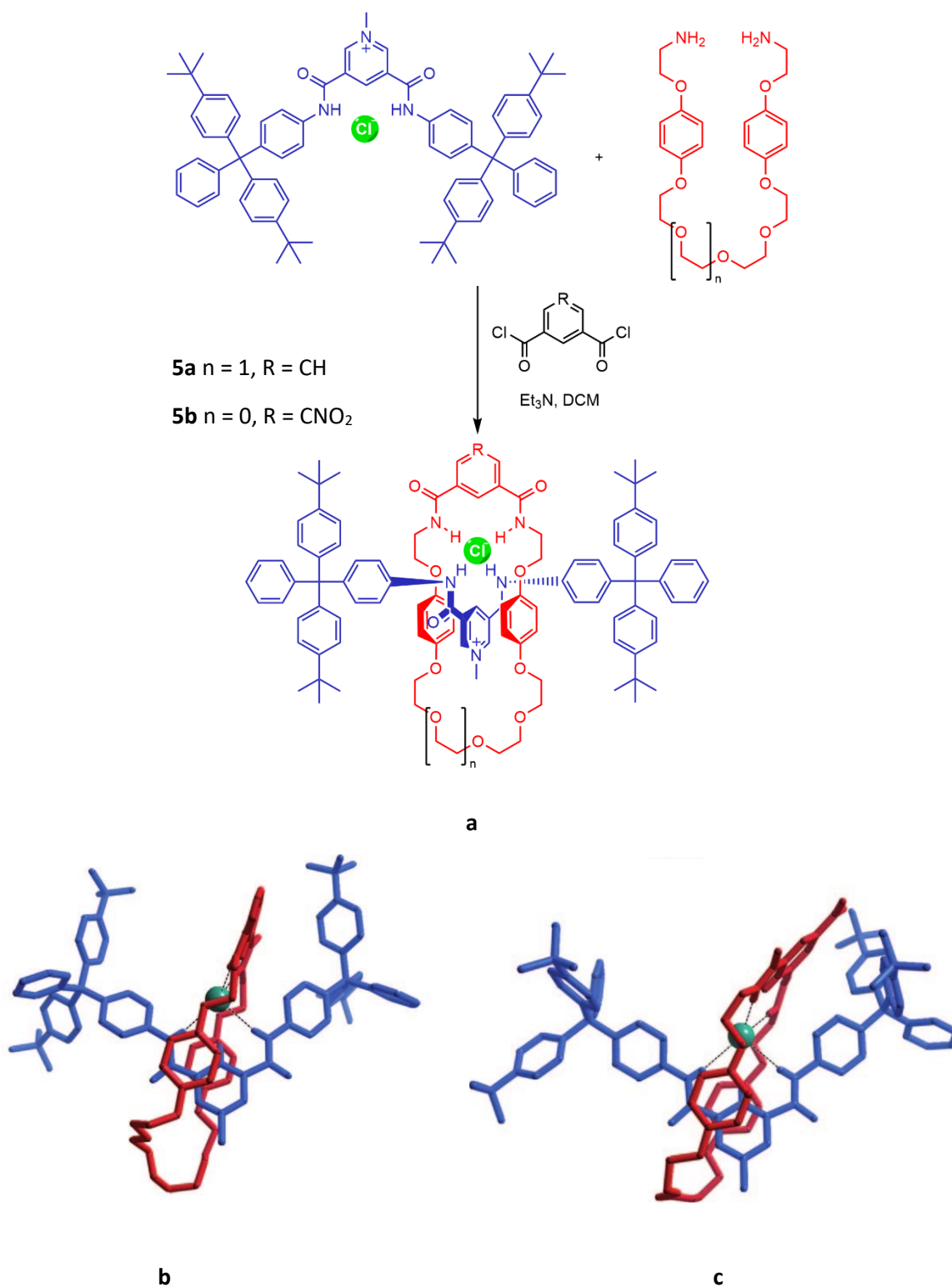


Figure 1.7. Mechanically-locked rotaxane receptors **5a** and **5b**.⁴⁵ a) assembly of receptors from component parts; crystal structures of b) [5a-Cl] and c) [5b-Cl]. Disorder and non-acidic hydrogen atoms omitted for clarity.

Further research has been done by Gale into the potential biological applications of organic-based anion receptors. Receptors **6a** – **6k** were designed to act as anion transporters across phospholipid bilayers; the potency of these receptors prompted investigation of their *in vitro* cytotoxic properties.⁴⁶ Anion transport is achieved through hydrogen-bonding interactions between four -NH bond donor sites on the central *ortho*-phenyl-*bis*-urea group which allows these species to bind chloride and carbonate, as well as carboxylate anions such as fumarate and maleate. Issues in the transport of carboxylates such as these has been linked to Alzheimer's and Huntington's disease, as well as kidney conditions.⁴⁷⁻⁵⁰ Additionally, the receptors show varying degrees of cytotoxicity towards a variety of human cancer cells *in vitro* (Figure 1.8c).

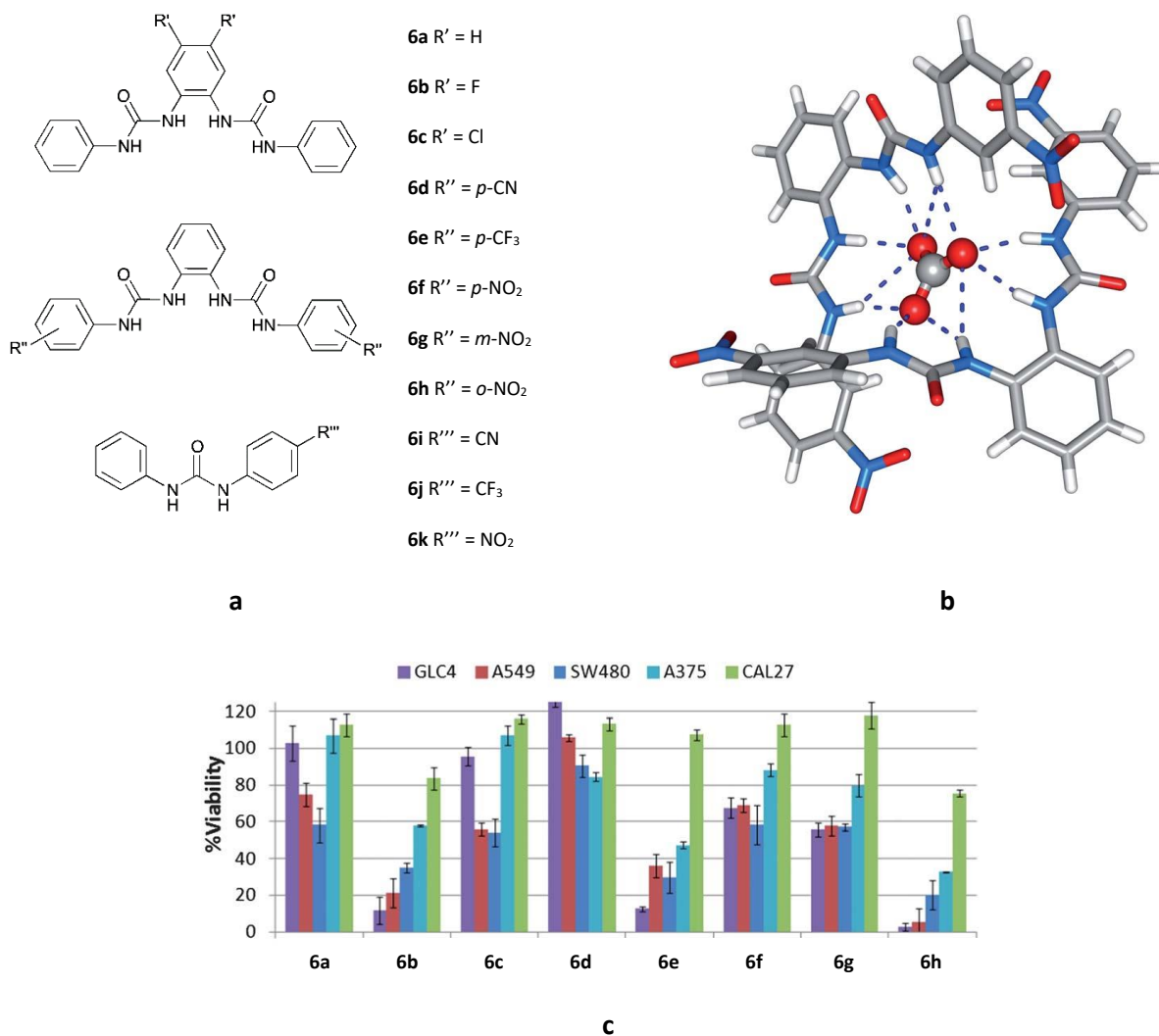


Figure 1.8. a) Receptors **6a** – **6k**;⁴⁶ b) crystal structure of $[6g_2-CO_3]^{2-}$; c) viability of various cancer cell lines after exposure to receptors **6a** – **6h**. Cell lines: GLC-4 = human small cell lung carcinoma; A549 = human alveolar adenocarcinoma, SW480 = human colon adenocarcinoma, A375 = human melanoma and CAL27 = tongue squamous cell carcinoma. Colour code for crystal structure: grey, C; blue, N; red, O; white, H.

Lee, Hay and Sessler have together developed several calixpyrrole receptors; specifically, receptors **7a** and **7b** consist of a “pyrrole-strapped” and “furan-strapped” receptor respectively.⁵¹ These comprise of a central calix pyrrole ring (in this case, four pyrrole rings connected via aliphatic bridges) which has been linked at opposite ends by an arching “strap”, at the top of which lies either a disubstituted pyrrole or a furan ring (**7a** and **7b** respectively). The former of these is shown to bind to chloride anions

in the solid-state through four $\text{-CH}\cdots\text{Cl}^-$ interactions and five $\text{-NH}\cdots\text{Cl}^-$ interactions – four from the calix-[4]-pyrrole ring and one from the pyrrole on the linking “strap” (Figure 1.9a). It is reported that receptor **7b** is less suited to the chloride anion due to the loss of one hydrogen-bond donor unit. Indeed, at present no structural information for the chloride complex of this species has been obtained, but rather the system adopts a structure incorporating two methanol molecules, indicating that the capsule may have either incorrect size or geometry of binding domains to accommodate the chloride anion (Figure 1.9b).

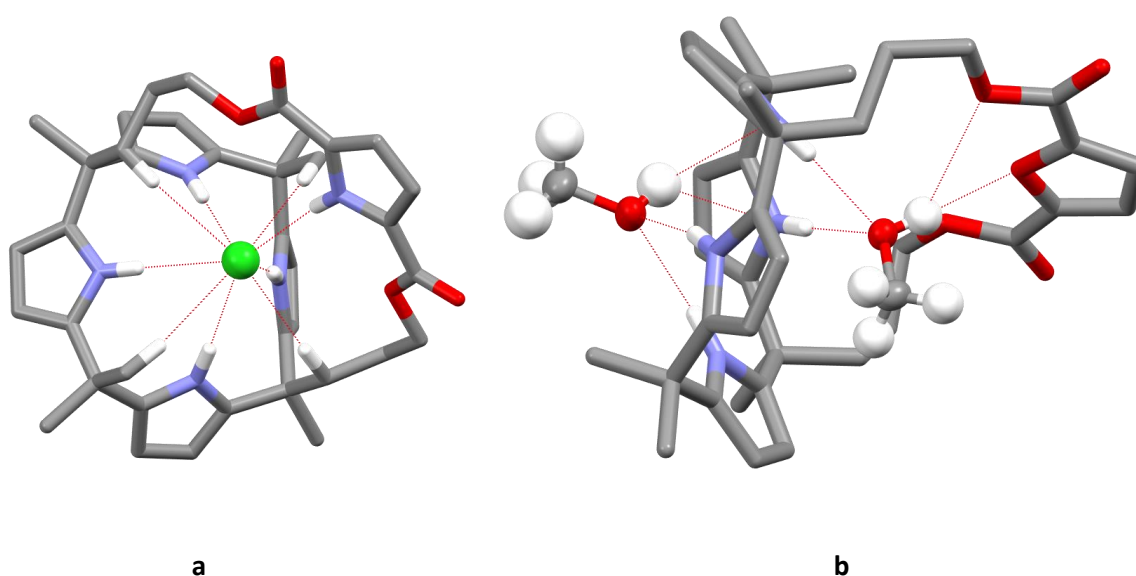


Figure 1.9. Receptors **7a** and **7b**.⁵¹ Solid-state structures of a) **7a**·Cl⁻; b) **7b**·2MeOH. Colour code: grey, C; blue, N; red, O; white, H; green, Cl. Counterions and non-acidic hydrogen atoms have been omitted for clarity.

Other organic-based receptors are continually being developed.^{52–72} However, whilst the organic scaffolded anion receptors have advanced the field significantly, they are often difficult to prepare with their synthesis consisting of multiple steps. Additionally, these may not be suitable for anion extraction in aqueous media as their organic frameworks are generally insoluble in water.

1.2.3. Anion-directed self-assembly

Anion receptors can undergo intermolecular self-assembly when exposed to anions. For example, receptors **8a** and **8b** synthesised by the Gale group exhibit anion-directed self-assembly when bound to the hexafluorophosphate and fluoride anions respectively.⁷³ These receptors incorporate two mono- (**8a**) or dinitrophenyl-amide (**8b**) units on either side of a *meta*-disubstituted phenyl group. In the case of receptor **8a**, when binding the hexafluorophosphate anion, two receptors bind to a single anion through three hydrogen-bonding interactions from the amide -NH donor units for a total of six interactions – one to each of the fluorine atoms of the hexafluorosilicate anion (Figure 1.10c). Similarly, **8b** binds fluoride by forming a helicate structure incorporating two receptor units bound to two fluoride anions (Figure 1.10d). The bound fluorides are held in place above and below the assembly through two -NH \cdots F⁻ hydrogen-bonding interactions each, one from both receptors, leaving one -NH donor unit free on the opposing side of each strand to bind another fluoride anion.

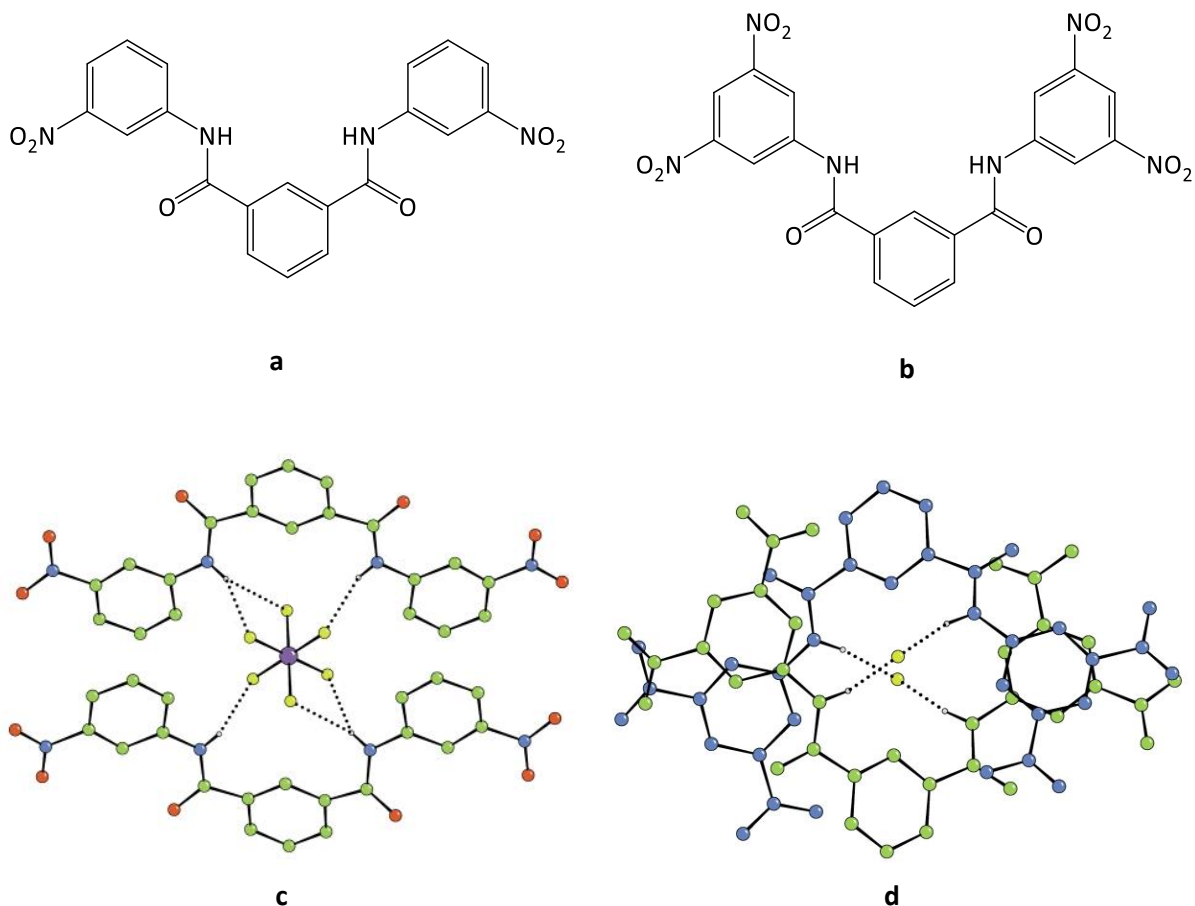


Figure 1.10. Receptors a) **8a** and b) **8b**.⁷³ X-ray crystal structures of c) **8a**₂·PF₆⁻; d) **8b**₂·2F⁻ with receptors coloured for clarity. Colour code: green, C; blue, N; red, O; white, H; chartreuse, F; purple, P (except d). Non-acidic hydrogen atoms omitted for clarity.

Tripodal receptor **9**, developed by Ghosh and co-workers, is capable of binding a variety of anions.⁷⁴ Similar to Gale's receptors **8a** and **8b**, this uses a central phenyl group to connect nitrophenylamide units; however, three of these units are incorporated to form a tripodal receptor which can self-assemble to form complexes when reacted with fluoride, chloride, acetate and nitrate anions. In the case of fluoride, two fluoride anions are encapsulated in the resulting assembly, in addition to 6 water molecules (Figure 1.11b). These are bound through hydrogen-bonding interactions between the anion and the amide -NH units and supplemented by a network of interactions between the encapsulated water molecules. Only two of the six total amide units bind to fluoride anions, while the other four are

bound to the lattice water molecules. The same receptor is also able to bind chloride, acetate and nitrate anions, whereupon the anion is not entirely encapsulated, rather the receptor forms discrete dimerised species with two anions and two receptors (Figure 1.11b - d). These are all held in place through interactions between amide -NH and several phenyl -CH hydrogen-bond donor units and each anion.

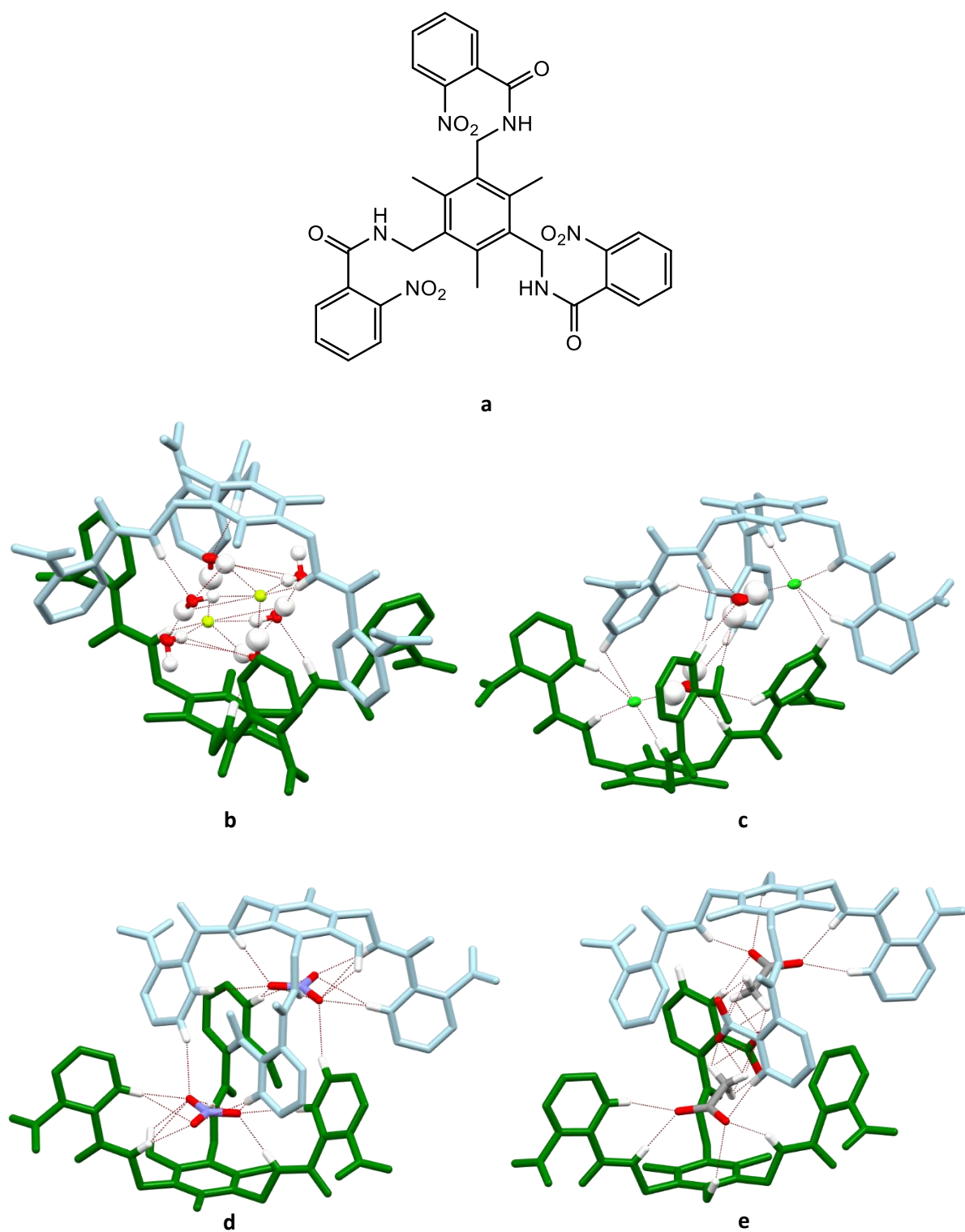


Figure 1.11. Receptor **9**.⁷⁴ a) structure of receptor **9**. Solid-state structures of a) $9_2 \cdot 2F \cdot 6H_2O$; b) $9_2 \cdot 2Cl \cdot 2H_2O$; c) $9_2 \cdot 2NO_3$; d) $9_2 \cdot 2CH_3CO_2^-$. Colour code: grey, C; blue, N; red, O; white, H; chartreuse, F; green, Cl. The receptor skeletons are coloured and non-acidic hydrogen atoms omitted for clarity.

The Wu group has synthesised a receptor which changes its co-ordination motif when interacting with phosphate and sulfate anions.⁷⁵ Receptor **10** has a symmetrical skeleton of two phenyl-diurea units connected by an ethylenediamine bridge, allowing it to bind anions through urea -NH...A⁻ hydrogen-bonds. When bound to sulfate, two anions are bound by one receptor through four hydrogen-bonding interactions between the oxygen atoms of the anion and four of the urea -NH donor units (Figure 1.12a). However, upon co-ordination of phosphate, three receptor strands and two phosphate anions are incorporated in a self-assembled helicate structure (i.e. [10₃(PO₄)₂]⁶⁻). Hydrogen-bonding interactions form between each of the oxygen atoms on the phosphate and three urea -NH donor units, such that each phosphate is held in place through 12 interactions (Figure 1.12b).

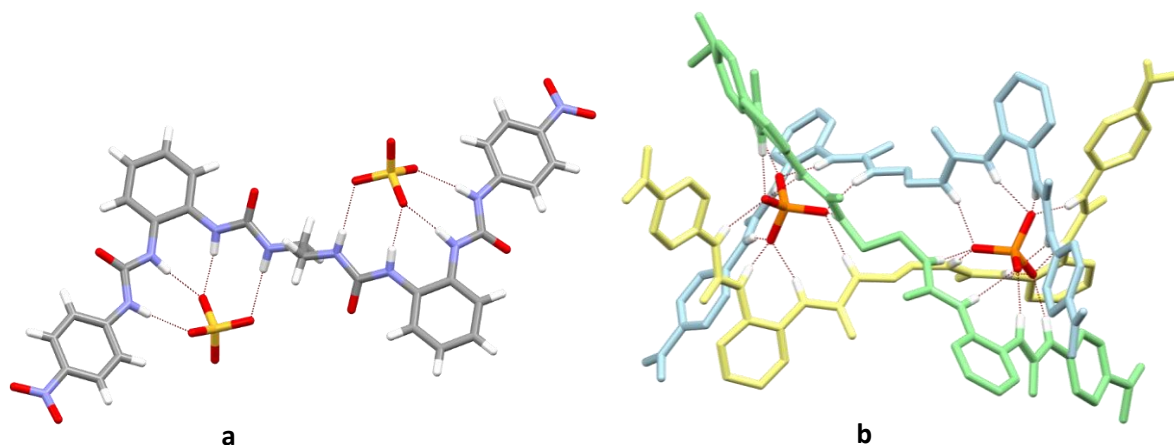


Figure 1.12. Receptor **10**.⁷⁵ Solid-state structures of a) **10**·(SO₄)₂⁴⁻; b) **10**₃·(PO₄)₂⁶⁻. Colour code: grey, C; blue, N; red, O; white, H; yellow, S; orange, P except in b) where the receptor skeletons are coloured for clarity. Non-acidic hydrogen atoms and counterions omitted for clarity.

Browning *et al.* developed a *tris*-indolyl substituted phosphine ligand, **11**, which was capable of forming both independent assemblies with anions as well as metal-containing assemblies with copper(I).⁷⁶ Reaction with one equivalent of halide, acetate, hydrogensulfate, nitrate or tetrafluoroborate anions in organic media resulted in a downfield shift of the indolyl -NH signal in the ¹H NMR spectrum, corresponding to the binding of the anion through -NH...A⁻ hydrogen-bonding

interactions. This was corroborated by the solid-state structure of **11**·F⁻ which showed three hydrogen-bonds between the fluoride anion and the three indole -NH donor groups (Figure 1.13b). The coordination chemistry of this receptor was also measured using copper(I) tetrafluoroborate, in which case the receptor bound the copper(I) cation through the central phosphorus linkage whilst simultaneously binding the tetrafluoroborate anion through three indole -NH···F interactions (Figure 1.13c). 1,10-Phenanthroline was also added to co-ordinate the free sites on the copper(I) cation.

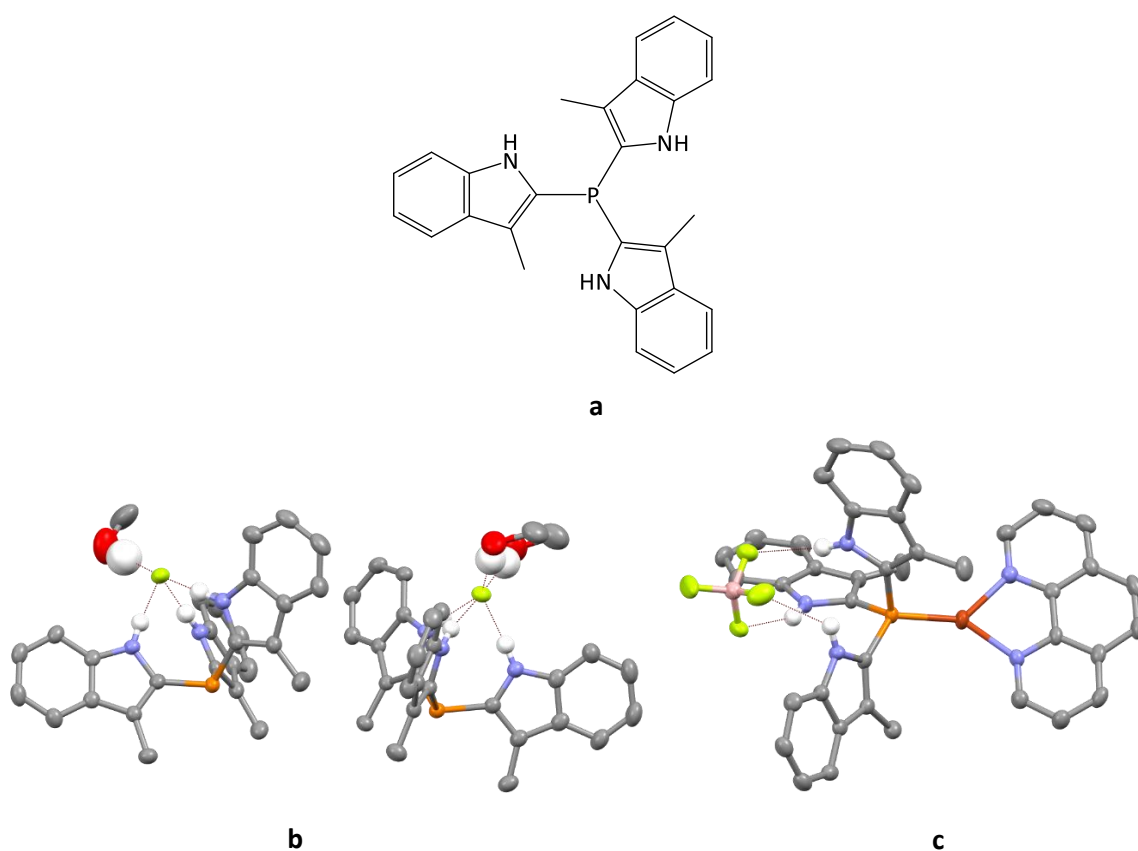


Figure 1.13. a) receptor **11**.⁷⁶ Solid-state structures of b) **11**₂·2F⁻·3MeOH; c) [**11**Cu(phen)]·BF₄. Colour code: grey, C; blue, N; red, O; white, H; lime, F; pink, B; dark orange, Cu; light orange, P. Non-acidic hydrogen atoms and counterions omitted for clarity. Thermal ellipsoids shown at 50% probability level.

Several receptors are built using tris(2-aminoethyl)amine (tren) as a backbone. This is a particularly useful building block for tripodal receptors due to its three -NH_2 donor sites in a tripodal arrangement. One such example has been made by Ghosh, who added a nitrobenzoyl- group onto each of tren's three primary amine groups to form receptors **12a** (4-nitro-), **12b** (2-nitro-) and **12c** (3-nitro-substituted respectively, Figure 1.14a).⁷⁷ NMR studies suggest that whilst all three are capable of binding fluoride in solution (DMSO-d_6), the 2-nitro- variant exclusively binds fluorides in these conditions whereas the 3- and 4-nitro- receptors are capable of binding chlorides. Additionally, receptor **12c** shows weak -NH peak shift indicative of bromide binding, which is exclusive amongst the three. None of these show iodide or oxoanion (NO_3^- , ClO_4^- , HSO_4^-) binding in DMSO-d_6 . In the solid-state however, receptor **12a** is capable of binding iodide, perchlorate and hexafluorosilicate – analysis of these complexes by X-ray crystallography indicates that anions are bound through aromatic $\text{-CH}\cdots\text{A}^-$, aliphatic $\text{-CH}\cdots\text{A}^-$ and $\text{-NH}\cdots\text{A}^-$ hydrogen-bonding interactions (Figure 1.14b - d).

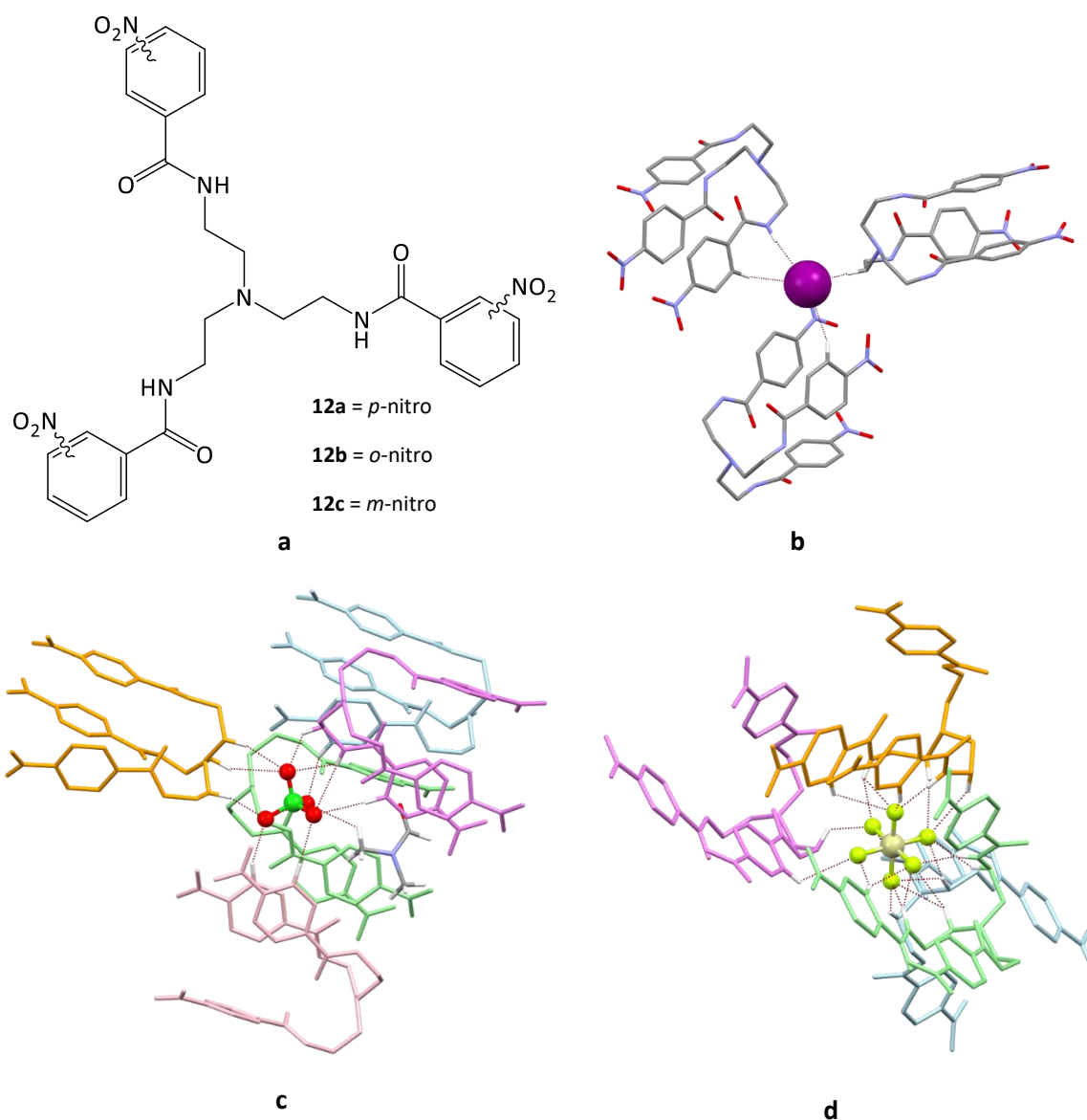


Figure 1.14. a) structure of receptors **12a-c**.⁷⁷ Solid-state structures of b) [**H12a**·I], showing hydrogen-bonding from three receptors in the crystal lattice; c) [**H12a**·ClO₄]·DMF; d) [**H12a**·SiF₆]. Colour code: b) grey, C; blue, N; red, O; white, H; purple, I; c) green, Cl; d) beige, Si; chartreuse, F. Receptors in c) and d) coloured for clarity. Non-acidic hydrogen atoms and counterions omitted for clarity.

Ghosh and co-workers have also used the tren unit through reaction with pentafluorophenyl isocyanate to form the *tris*-pentafluorophenylurea substituted tren receptor **13**.⁷⁸ This is able to bind phosphates through hydrogen-bonding interactions by dimerising through self-assembly into a cage-

like structure and binding through its urea -NH donor units (Figure 1.15a). Using these, dimeric phosphates are held within the cage (Figure 1.15b and c).

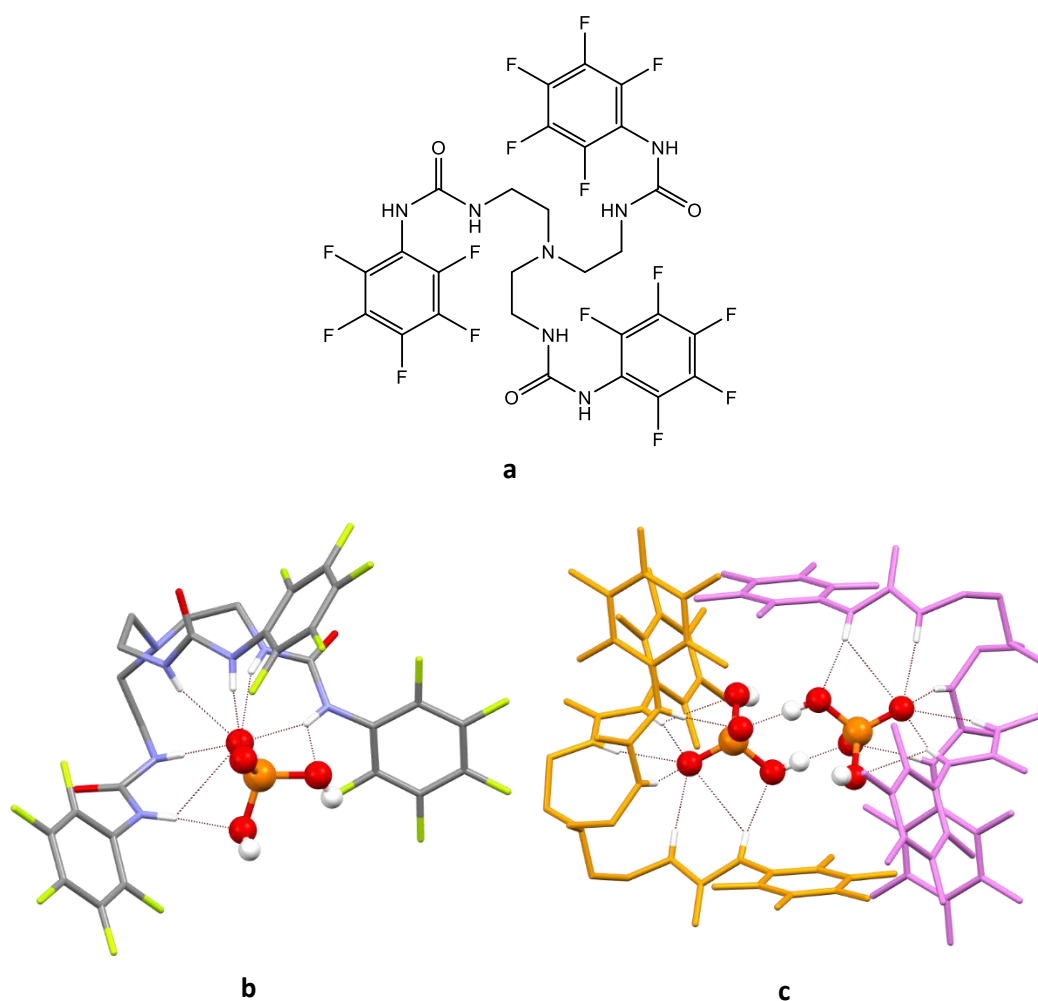


Figure 1.15. Receptor **13**.⁷⁸ a) structure of receptor **13**; b) crystal structure of $([13 \cdot H_2PO_4])_2^{2-}$ with half omitted to show hydrogen-bonding interactions; c) spacefill diagram of dimerised $([13 \cdot H_2PO_4])_2^{2-}$. Colour code: grey, C; blue, N; red, O; white, H; chartreuse, F; orange, P. Counterions and non-acidic hydrogen atoms omitted for clarity.

1.2.4. Self-assembled anion receptors

Self-assembled architectures can be designed and pre-programmed in such a way that upon co-ordination they function as anion receptors; this is particularly advantageous as large and complex

receptors can be formed from simple “sub-units” and the design of these allows control of the form and function of the receptor. These are specifically distinct from the examples of self-assembly *within* anion receptors above, as individual components are generally not capable of strongly binding anions; only when self-assembled are these able to bind anions. Typically, these receptors are constructed from ligands (organic species with the ability to co-ordinate a positively charged metal species) and one or more metal cations, forming an assembly with the motif $[M_xL_x]^{n+}$. The ligands can be pre-programmed to contain binding sites to sequester and encapsulate anions, with the metal anion interaction usually accompanied by either $-OH\cdots A^-$, $-NH\cdots A^-$ or $-CH\cdots A^-$ hydrogen-bonding interactions.

Usage of metals in these supramolecular self-assembled receptors allows the construction of a variety of intricate complexes. The Ghosh group recently developed the self-assembled receptor **14** using a tren-based tripodal cage ligand, which when co-ordinated to two copper(II) ions (i.e. $[LCu_2]^{4+}$) is capable of selectively extracting cyanide anions from aqueous media.⁷⁹ The copper(II) centres are bound through four $NH\cdots Cu$ co-ordination interactions comprising of three from the secondary amines of the tren moieties and one $N\cdots Cu$ interaction from the central tertiary amine (Figure 1.16a). The receptor initially binds to four perchlorate anions which are displaced upon treatment of an aqueous solution of cyanide, where the cyanide anion is bound by bridging the two metal ions. As a result, cyanide anions are preferentially sequestered and bound by the receptor and, by using an excess of the receptor, up to 94.8% of the cyanide anions in a 80 ppm solution were extracted within 30 minutes (Figure 1.16b).

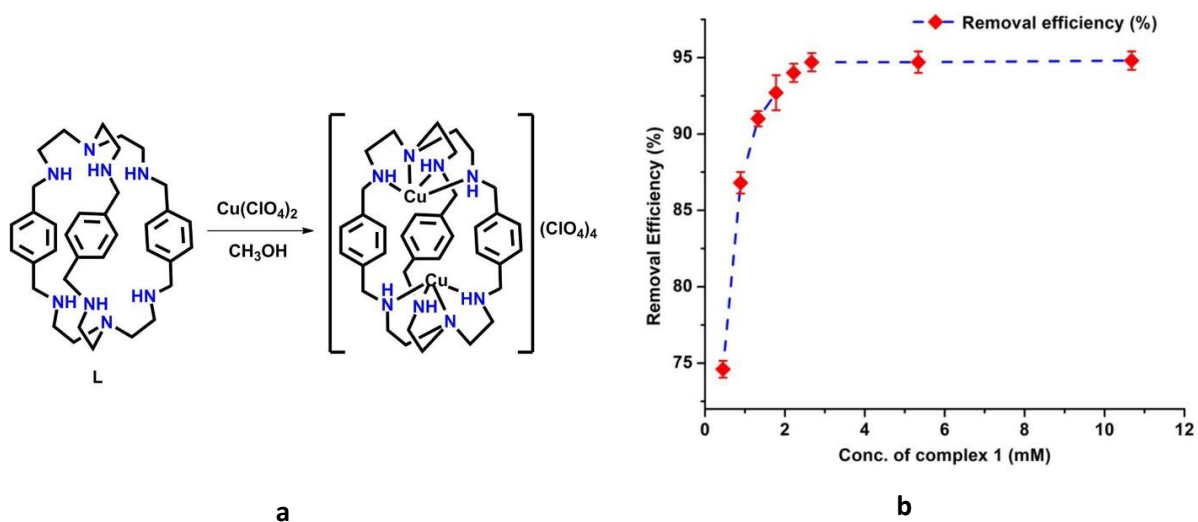


Figure 1.16. Receptor **14**.⁷⁹ a) schematic of formation of the complex **14** from the tren-based cage ligand and copper(II) perchlorate; b) removal efficiency of cyanide anions with increasing amount of solid receptor added. Initial concentration = 80 ppm.

Loeb and co-workers synthesised an isoquinolin-8-ylurea-based ligand, which contains a quinoline N-donor unit and a urea hydrogen-bond donor.⁸⁰ Reaction of this with platinum(II) results in a mononuclear complex with four ligands coordinating the metal ion, which adopts a square planar geometry forming receptor **15** which contains a total of eight -NH hydrogen-bond donor units. Chloride, bromide, iodide, dibasic sulfate and dihydrogen phosphates are all capable of being bound by the complex through two main methods. When binding tetrahedral anions, all four ligand strands bind a single anion giving the receptor a “cone” shape (Figure 1.17b); the anion is bound to the four ligand strands through all eight urea -NH domains and all four of the -CH binding domains on the closest positions of each isoquinoline moiety. In the case of the halides however, two distinct binding domains are formed with two of the four ligand strands separated into pairs and adopting a *transoid* conformation to each other, enabling each domain to bind a separate halide anion via four -NH \cdots X⁻ and two -CH \cdots X⁻ hydrogen-bonds (Figure 1.17c).

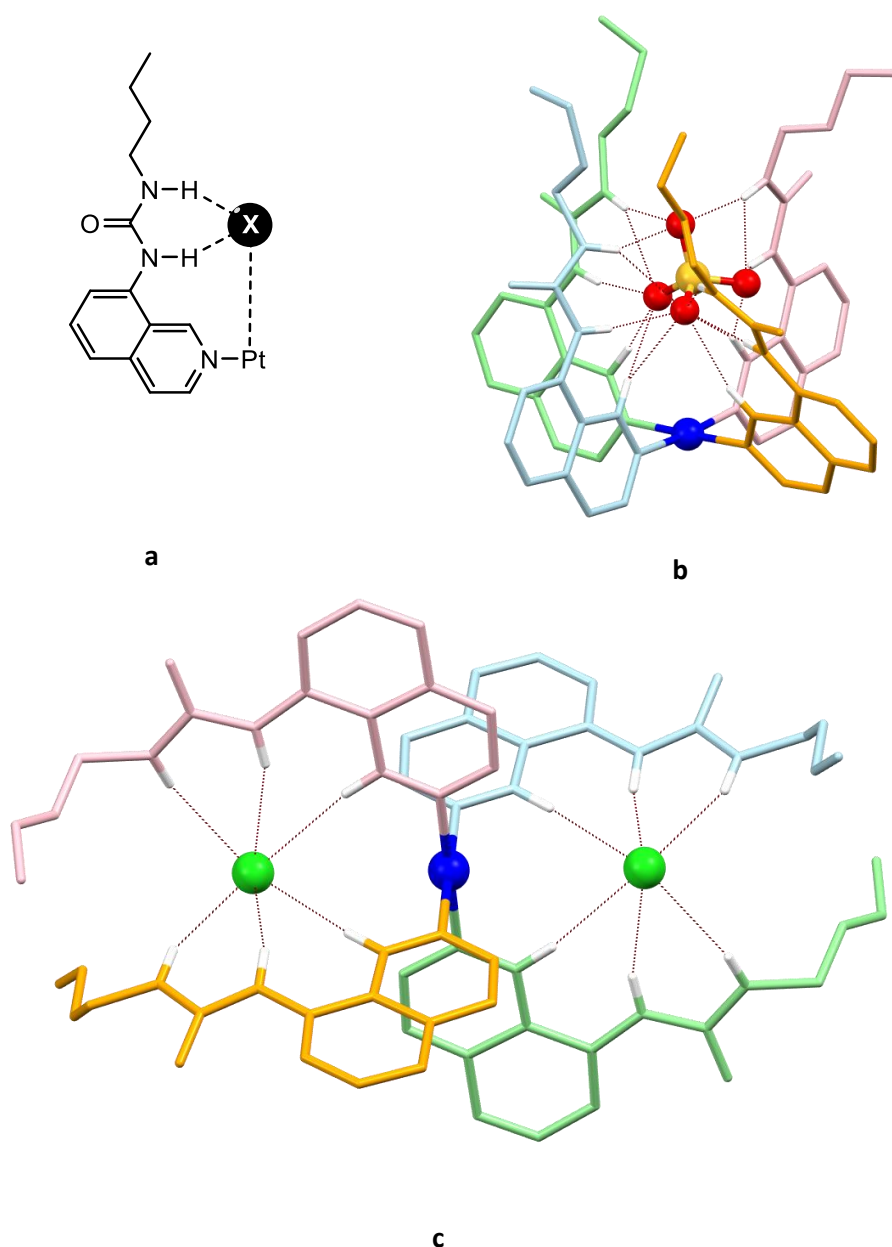


Figure 1.17. Receptor **15**.⁸⁰ a) structure of ligand used in receptor **15**; b) solid-state crystal structure of [**15**·SO₄] with ligands coloured for clarity; c) solid-state crystal structure of [**15**·Cl₂] with ligands coloured for clarity. Colour code: red, O; yellow, S; green, Cl; white, H; blue, Pt. Non-acidic hydrogen atoms omitted for clarity.

Wu's research group have used a tetradentate *bis*-bipyridinyl-imidazole ligand to form complex **16** which actively changes configuration depending on the shape of the anion it encapsulates (Figure

1.18).⁸¹ The singly-cationic ligand co-ordinates iron(II) and copper(II) nuclei forming a cage using three ligands and two metal cationic centres (i.e. $[L_3M_2]^{7+}$, M = Fe (**16a**), Cu (**16b**)) which sequesters various anions through hydrogen-bonding interactions; in the case of the tetrahedral anions tetrafluoroborate, perchlorate and sulfate, interactions arise between the anion atoms and the *N*-adjacent aromatic -CH donor unit of the disubstituted pyridyl- groups and a mesocate structure is formed as a result (Figure 1.18c). However, upon encapsulation of a spherical or trigonal planar anion, a helical structure is instead obtained, as bonding occurs instead between the acidic imidazole -CH donor unit and the anion (Figure 1.18d).

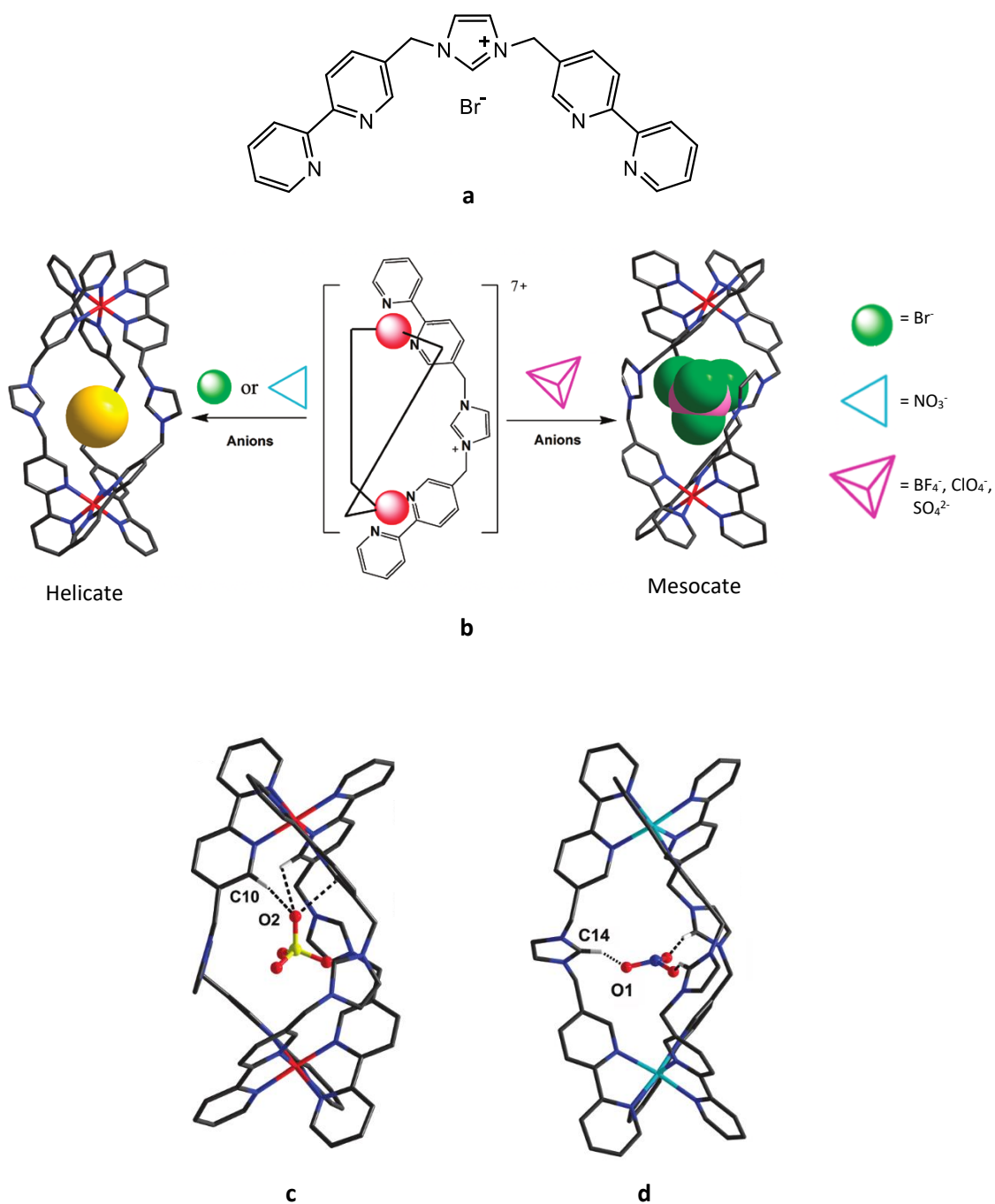


Figure 1.18. Receptor **16**.⁸¹ a) Structure of ligand as its bromide salt; b) conformers adopted by receptor **16**; c) solid-state crystal structure of $[\mathbf{16a}\cdot\text{SO}_4]^{5+}$, illustrating hydrogen-bonding through the aromatic Py-CH donor units marked C10; d) solid-state crystal structure of $[\mathbf{16b}\cdot\text{NO}_3]^{6+}$ with hydrogen-bonding instead occurring from acidic imidazole hydrogen atom marked at C14. Colour code: grey, C; white, H; red, O; blue, N; yellow, S; teal, Cu; fuchsia, Fe; green, F; pink, B. Counterions and non-acidic hydrogen atoms omitted for clarity.

A palladium-based nitrate encapsulating cage **17** was developed by Sun.⁸² Two *N*-methylbenzimidazole domains are bridged by an anthracene spacer forming a ligand that contains two remote *N*-donor units which, when reacted with half an equivalent of palladium(II), self-assembles into a dinuclear cage from two metal centres and four ligand strands, i.e. [L₄Pd₂]⁴⁺. This cage can selectively encapsulate nitrate through hydrogen-bonding interactions between the oxygen atoms of the anion and six of the eight tertiary -NCH donor units present in the imidazole ring of each ligand (Figure 1.19c), leaving two domains un-co-ordinated. Binding studies *versus* the chloride encapsulated host suggest that larger anions such as hydrogensulfate, dihydrogenphosphate and triflate are not bound within this complex, whilst bromide, iodide, tetrafluoroborate and nitrites have binding affinities weaker than that of chloride. The nitrate anion shows an encapsulation equilibrium constant two orders of magnitude higher than that for chloride demonstrating its affinity for the nitrate anion.

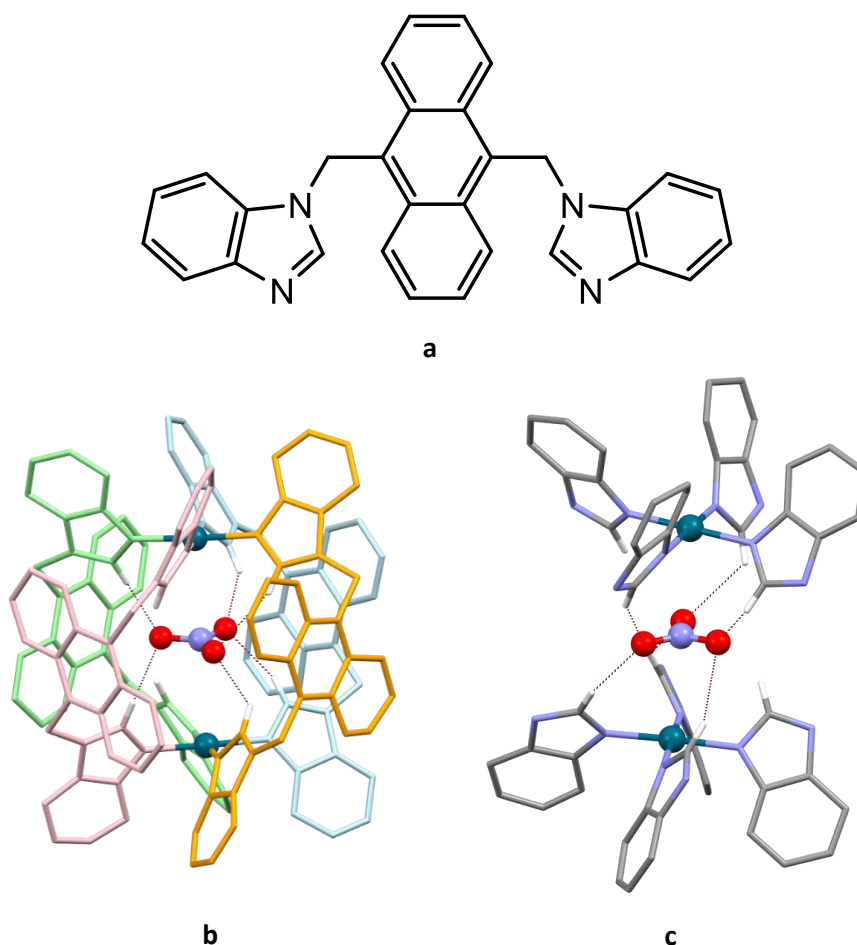


Figure 1.19. Cage receptor **17**.⁸² a) structure of ligand used in receptor **17**; b) solid-state structure of $[\mathbf{17}\cdot\text{NO}_3]^{3+}$, with ligands coloured for clarity; c) hydrogen-bonding interactions between acidic imidazole hydrogen atoms and oxo-anion. Colour code: grey, C; blue, N; white, H; red, O; dark teal, Pd. Non-acidic hydrogen atoms and counterions omitted for clarity.

Chifotides and co-workers have self-assembled receptor **18** which changes motif based on the anion present.⁸³ The capsule was synthesised from 3,6-bis(2-pyridyl)-1,2,4,5-tetrazine (bptz, Figure 1.20a) and co-ordinated with a variety of iron(II) salts. The resulting self-assembled species is anion dependent as either a pentanuclear cage when hexafluoroantimonate anion is present (i.e. $[\text{Fe}_5\text{L}_5\text{SbF}_6]^{9+}$, Figure 1.20b), or a tetranuclear cube when the tetrafluoroborate anion is used (i.e. $[\text{Fe}_4\text{L}_4\text{BF}_4]^{7+}$, Figure 1.20c and d). Both of these assemblies bind anions through four anion $\cdots\pi$ interactions to the tetrazine rings of each ligand (Figure 1.20d). Solutions of these assemblies can be

reverted to an equal mixture of the two through heating in a solution of an excess of the opposing anion, highlighting the reversible nature of self-assembly.

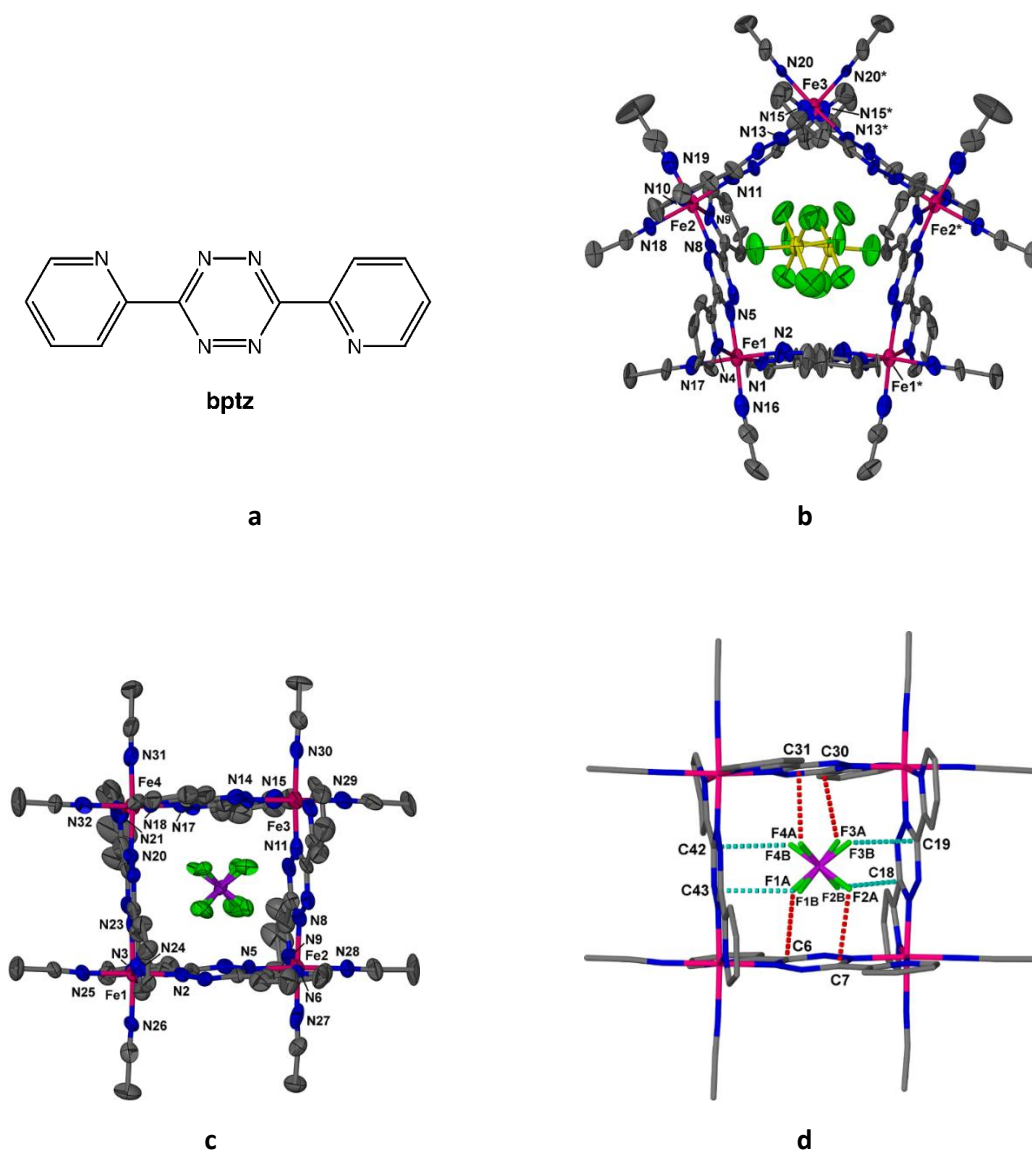


Figure 1.20. bptz-based receptor **18**.⁸³ a) structure of bptz; b) crystal structure of $[L_5Fe_5 \cdot 10MeCN \cdot SbF_6]^{9+}$ (anion disordered, 50% equivalence); c) crystal structure of $[L_4Fe_4 \cdot 8MeCN \cdot BF_4]^{7+}$ (anion disordered, 50% equivalence); d) hydrogen-bonding interactions in $[L_4Fe_4 \cdot 8MeCN \cdot BF_4]^{7+}$, each colour interaction representing one position of disorder. Colour code: grey, C; blue, N; lime, F; fuchsia, Fe; yellow, Sb; purple, B. Thermal ellipsoids shown at 50% probability level. Hydrogen atoms and counterions omitted for clarity.

Tetranuclear cages have been employed extensively by the Nitschke group, with recent results demonstrating host-guest behaviour with self-assembled tetrahedral receptors. One example of these consists of a tetranuclear assembly formed by Schiff base condensation of a trigonal tritopic amine spacer and pyridyl aldehydes and ketones in the presence of zinc(II) salts and these form capsules, **19a** (when reacted with di(2-pyridyl)ketone) and **19b** (when reacted with 2-formylpyridine, Figure 1.21a).⁸⁴ Upon co-ordination, four ligands co-ordinate to four zinc(II) centres (i.e. $[L_4Zn_4]^{8+}$); the metal cation centres are each bound by three ligand strands through their bidentate domains, consisting of one pyridyl-*N* donor and one imine-*N* co-ordination site each, creating a tetrahedral capsule. These capsules are capable of encapsulating both anions (including triflate, hexafluoroantimonate, hexafluorophosphate and perrhenate, Figure 1.21c) and neutral compounds (Figure 1.21b). In a solution of both complexes, guests can be exchanged between the two hosts through the addition and subsequent neutralisation of triflimidic acid (Figure 1.21d).

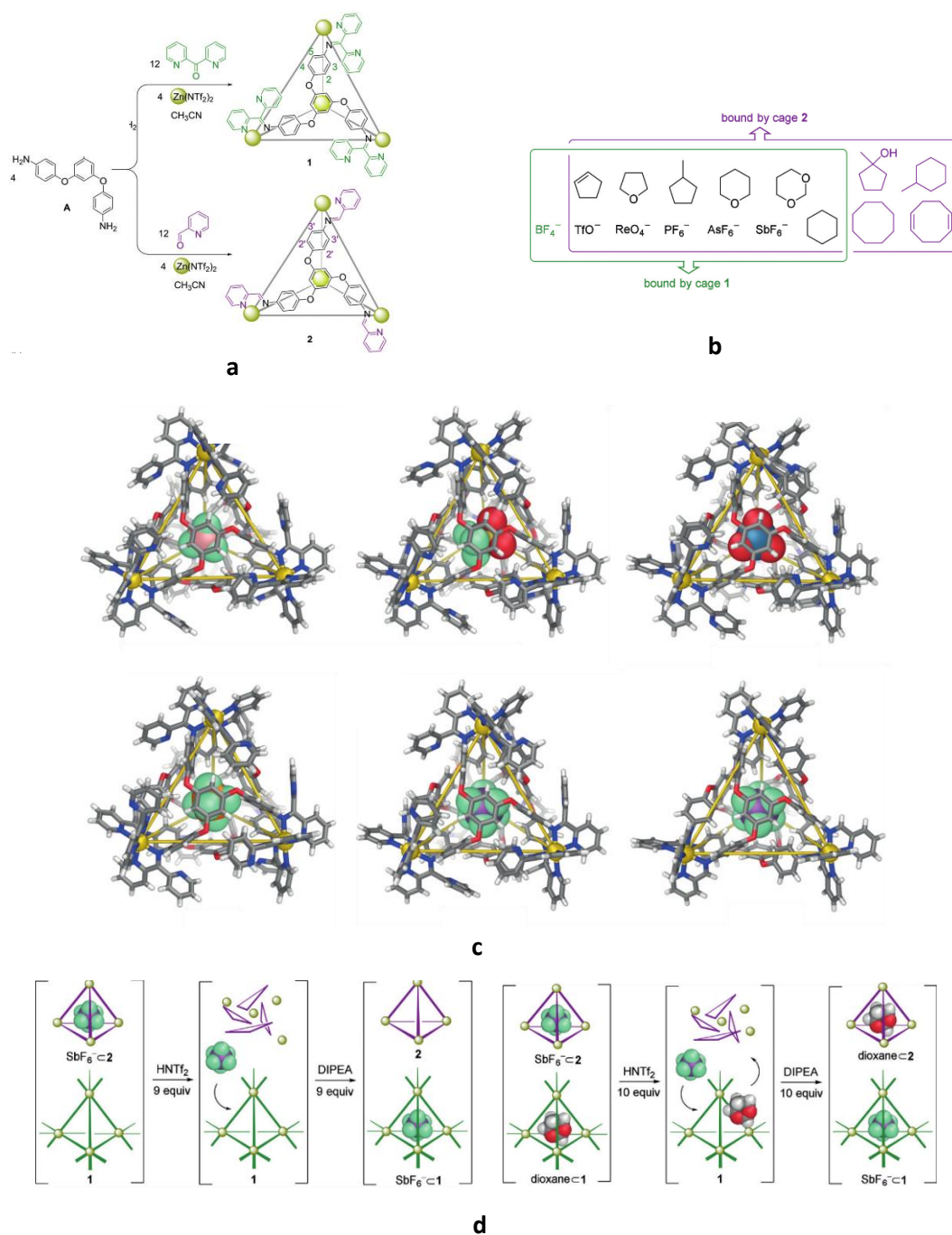


Figure 1.21. Tetrahedral receptors **19a** and **19b**.⁸⁴ a) route of assembly of **19a** (green) and **19b** (purple); b) anion selectivity between the two complexes; c) (left to right) (top row) crystal structure of $[\mathbf{19a}\cdot\text{BF}_4]^{7+}$, $[\mathbf{19a}\cdot\text{OTf}]^{7+}$, $[\mathbf{19a}\cdot\text{ReO}_4]^{7+}$, (bottom row) crystal structure of $[\mathbf{19a}\cdot\text{PF}_6]^{7+}$, $[\mathbf{19a}\cdot\text{SbF}_6]^{7+}$, $[\mathbf{19b}\cdot\text{SbF}_6]^{7+}$; d) anion exchange between complexes facilitated by strong acid. Colour code for c): grey, C; dark blue, N; green, F; white, H; yellow, Zn; blue, Re; pink, B; orange, P; purple, Sb.

Lindoy's group have developed receptor **20** using a *bis*-(methylbipyridine) ligand which, being tetradentate, is capable of forming a cage when co-ordinated to iron(II) nuclei.⁸⁵ The capsule is assembled from six ligand strands co-ordinating four metal centres (i.e. Fe₄L₆); each ligand binds two metal centres through each of the two bidentate binding domains, and in turn each metal centre is co-ordinated to three ligand strands in an octahedral geometry (Figure 1.22b). The receptor is capable of encapsulation of a tetrachloroferrate anion (Fe^{III}Cl₄⁻), which is achieved through three pyridyl -CH...Cl-Fe hydrogen-bonding interactions per chlorine atom for a total of 12 (Figure 1.22b). Previous work in this area has also shown that this capsule binds tetrafluoroborate and hexafluorophosphate, indicating a range of anion size and geometries are also possible.⁸⁶

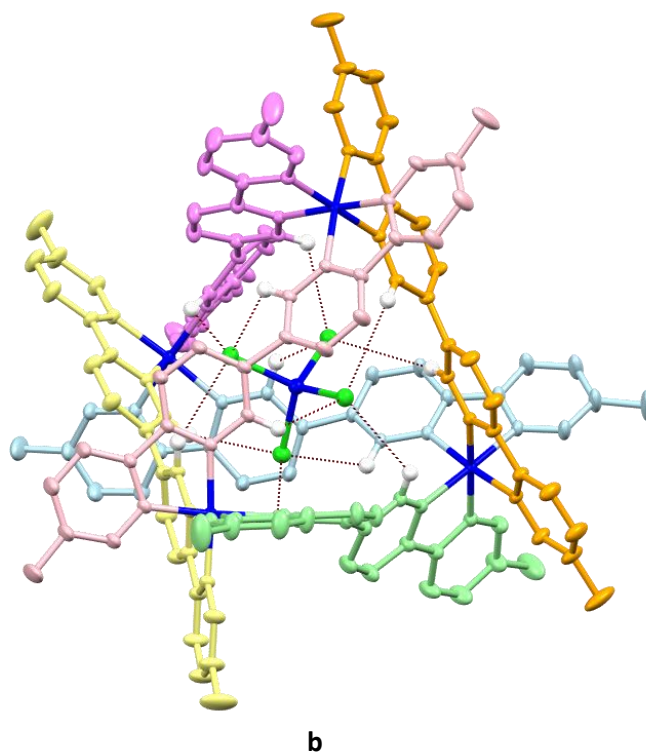
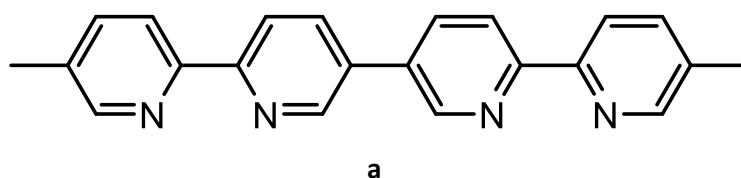


Figure 1.22. Receptor **20**.^{85,86} a) structure of ligand used to assemble receptor **20**; b) crystal structure of $[20 \cdot \text{FeCl}_4]^{7+}$ showing $\text{py-CH} \cdots \text{A}^-$ hydrogen-bonding interactions. Colour code: dark blue, Fe; green, Cl; white, H. Thermal ellipsoids shown at 50% probability level. Ligands coloured and non-acidic hydrogen atoms and counterions omitted for clarity.

The usage of pyridyl- group *N*-co-ordination domains has also been used extensively by the Ward group. The ligands used in assemblies **21a** and **21b** have similar skeletons, consisting of two pyridyl-pyrazole groups connected by an *ortho*-disubstituted phenyl (**21a**) or a 2,3-disubstituted-naphthyl (**21b**) group.^{87,88} As a result, their anion binding methods are similar in that their two pyridyl-pyrazole domains co-ordinate to cobalt(II) cationic nuclei and form a tetrahedral complex (i.e. $[\text{L}_6\text{Co}_4]^{8+}$) which encapsulates anions. The four cobalt(II) nuclei are six co-ordinate, bound to three pyridyl-pyrazole

domains for a total of six Co...N co-ordination interactions each; conversely, each ligand is bound to two metal centres. The resultant cage binds the tetrafluoroborate and perchlorate anions, through hydrogen-bonding interactions between the exterior atoms of the tetrahedral anion (i.e. O and F for ClO₄⁻ and BF₄⁻ respectively) and one of the aliphatic -CH₂- hydrogen atoms on the three closest ligand strands – resulting in a total of twelve -CH...F or -CH...O interactions (Figure 1.23d). The assembly of these complexes was also attempted with nickel(II) nuclei, but on co-ordination, a dinuclear complex was instead observed (i.e. [L₃Ni₂]⁴⁺), both in mass spectrometry studies and in the solid-state (Figure 1.23d).

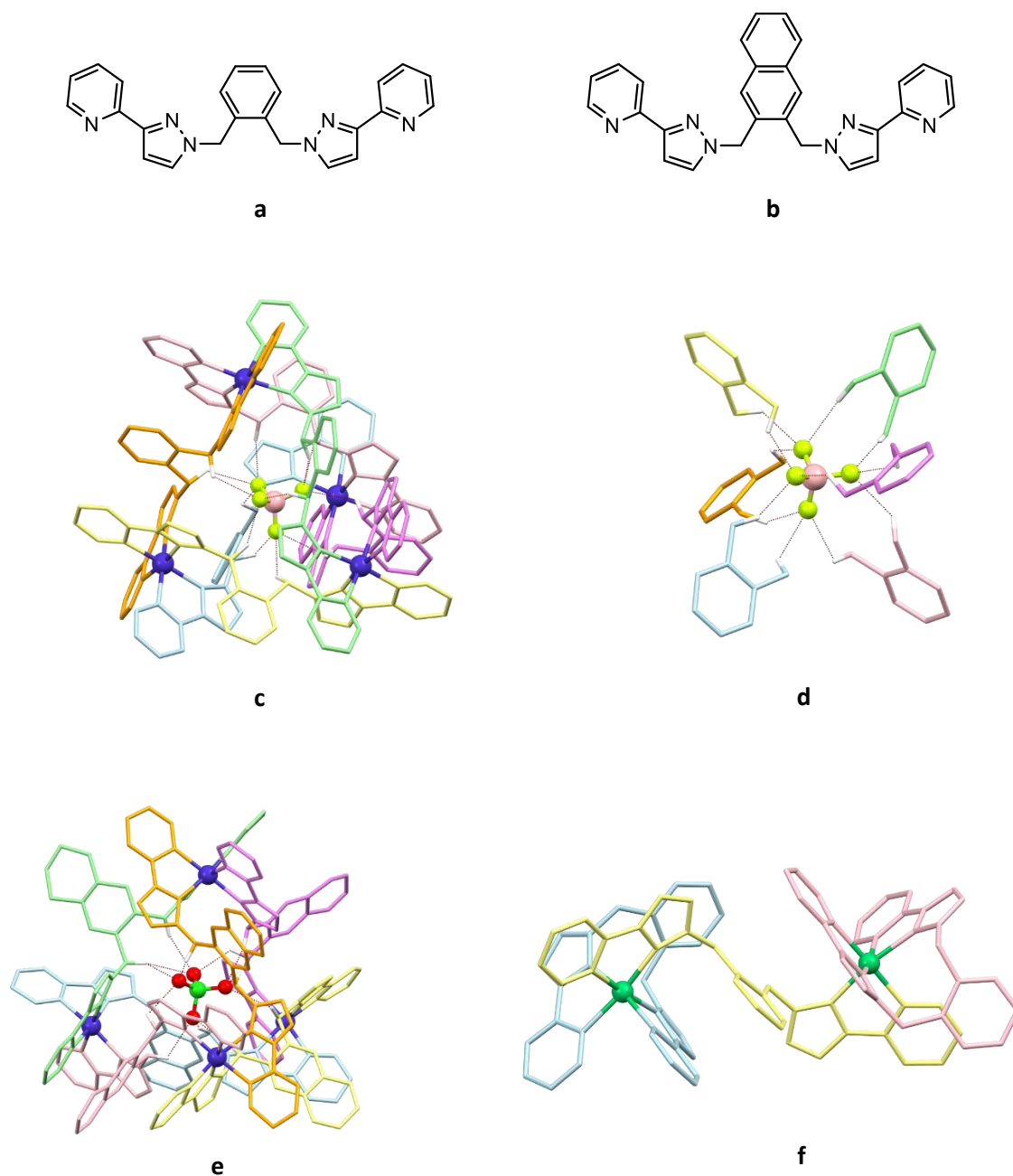


Figure 1.23. Structure of ligands used in receptors a) **21a** and b) **21b**.^{87,88} c) crystal structure of $[21\mathbf{a}\cdot\text{BF}_4]^{7+}$; d) crystal structure of $[21\mathbf{a}\cdot\text{BF}_4]^{7+}$ with non-hydrogen-bonding motifs omitted for clarity; e) crystal structure of $[21\mathbf{b}\cdot\text{ClO}_4]^{7+}$; f) crystal structure of dinuclear complex observed when assembled using nickel instead of cobalt (i.e. $[\text{L}_3\text{Ni}_2]^{4+}$). Colour code: dark blue, Co; dark green, Ni; light green, Cl; chartreuse, F; pink, B; white, H. Ligands are coloured and non-acidic hydrogen atoms and counterions omitted for clarity.

Custelcean also used the M_4L_6 motif in receptor **22a** and **22b**, designed through the use of computer-aided design software *HostDesigner*.^{89–91} *Bis*-(bipyridyl) urea ligands were co-ordinated to nickel(II) (**22a**, R = H) or zinc(II) (**22b**, R = *t*-Bu) centres forming a capsule which are capable of binding a variety of tetrahedral oxo-anions through twelve hydrogen-bonding interactions between the urea -NH donor units and the oxygen atoms of the anion (Figure 1.24b and e).⁹² Selectivity studies *versus* the selenate anion suggest that phosphate, chromate and sulfate are more strongly bound than selenate, which itself is more strongly bound than the larger molybdate and tungstate anions, found to be caused by both the complementarity and flexibility of the receptor and the properties of the anions.

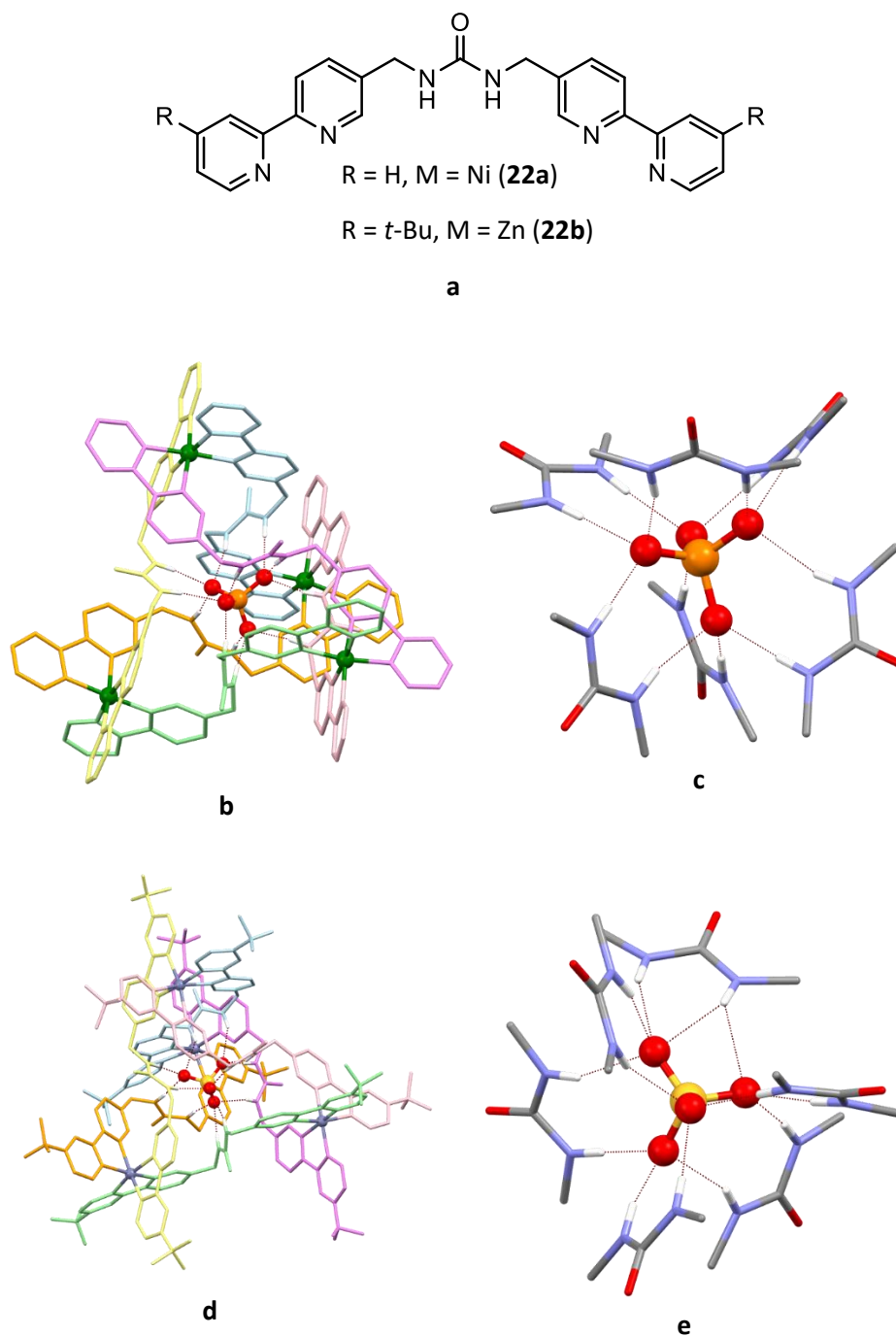


Figure 1.24. Receptors **22a** and **22b**.^{91,92} a) structure of bis-(bipyridyl)urea ligands used in **22a** and **22b**; b) crystal structure of $[\mathbf{22a} \cdot \text{PO}_4]^{5+}$ with ligands coloured for clarity; c) hydrogen-bonding interactions involved in $[\mathbf{22a} \cdot \text{PO}_4]^{5+}$; d) crystal structure of $[\mathbf{22b} \cdot \text{SO}_4]^{6+}$ with ligands coloured for clarity; e) hydrogen-bonding interactions in the crystal structure of $[\mathbf{22b} \cdot \text{SO}_4]^{6+}$, which are analogous to those present in $[\mathbf{22a} \cdot \text{PO}_4]^{5+}$. Colour code: grey, C; blue, N; red, O; green, P; yellow, S; white, H.

Non-acidic hydrogen atoms and counterions omitted for clarity.

Champness and co-workers have used a ligand strand consisting of two 4-ethynylpyridine groups connected by a 2,2'-bipyridyl bridge.⁹³ This self-assembles into a metallocupramolecular cage **23** when co-ordinated to either silver(I) or copper(I) which is capable of encapsulating both the tetrahedral tetrafluoroborate and octahedral hexafluoroantimonate anions (i.e. $[L_6M_6A]^{5+}$, Figure 1.25b and c). Six ligand strands form this cage co-ordination structure through a total of four Ag...N interactions each. Each cation is bound by three ligand strands with two co-ordination bonds from the central bipyridyl- bidentate donor of one ligand strand and two from the "terminal" pyridyl- N-donor group of two distinct ligand strands. This forms a cavity which can host one anionic species (in this case, tetrafluoroborate (Figure 1.25b) or hexafluoroantimonate (Figure 1.25c). Interestingly, in the presence of a much larger anion (in this case, $[Co(C_2H_{11}B_9)]^-$), the complex still favours the much smaller tetrafluoroborate anion; when this is not present however, two ligands assemble into a dinuclear assembly with two metal centres (Figure 1.25d), likely due to the inability of the host to expand to the extent that the much larger anion is accommodated.

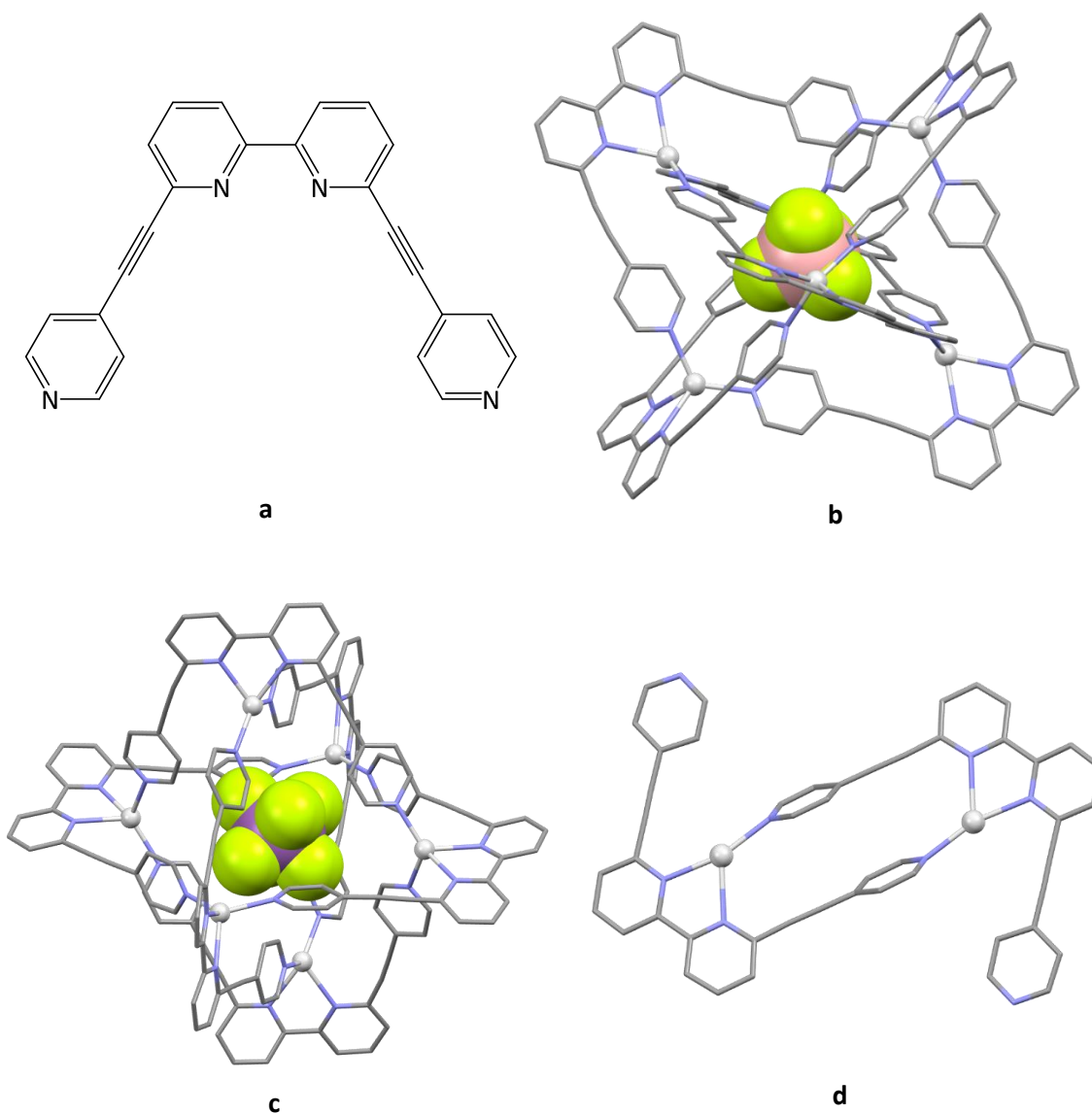


Figure 1.25. Receptor **23**.⁹³ a) Ligand used in receptor **23**. Crystal structures of a) $[23 \cdot \text{BF}_4]^{5+}$; b) $[23 \cdot \text{SbF}_6]^{5+}$; c) $[\text{L}_2\text{Ag}_2]^{2+}$. Colour code: grey, C; blue, N; chartreuse, F; pale grey, Ag; pink, B; purple, Sb.

Hydrogen atoms and counterions omitted for clarity.

Mingos and co-workers have used a self-assembled cage to encapsulate chloride and bromide.⁹⁴ This was achieved through the usage of eight units of amidinothiourea (atu) which forms co-ordinate bonds with six nickel(II) centres (i.e. $[(\text{atu})_8\text{Ni}_6]^{4+}$) through both $\text{Ni} \cdots \text{S}$ and $\text{Ni} \cdots \text{N}$ interactions. Both of these form approximately square planar arrangements about the nickel centres, forming receptor **24** as a cage with four “edges” (Figure 1.26b and c). The halide is encapsulated within this species through

hydrogen-bonding interactions between the nickel-bound amine units and the central halide, resulting in a total of eight $\text{-NH}\cdots\text{X}^-$ interactions (Figure 1.26c). Distortion of the four square planar $\text{Ni}\cdots\text{S}$ groups also indicate some interaction between the top and bottom “facial” nickel moieties and the halide.

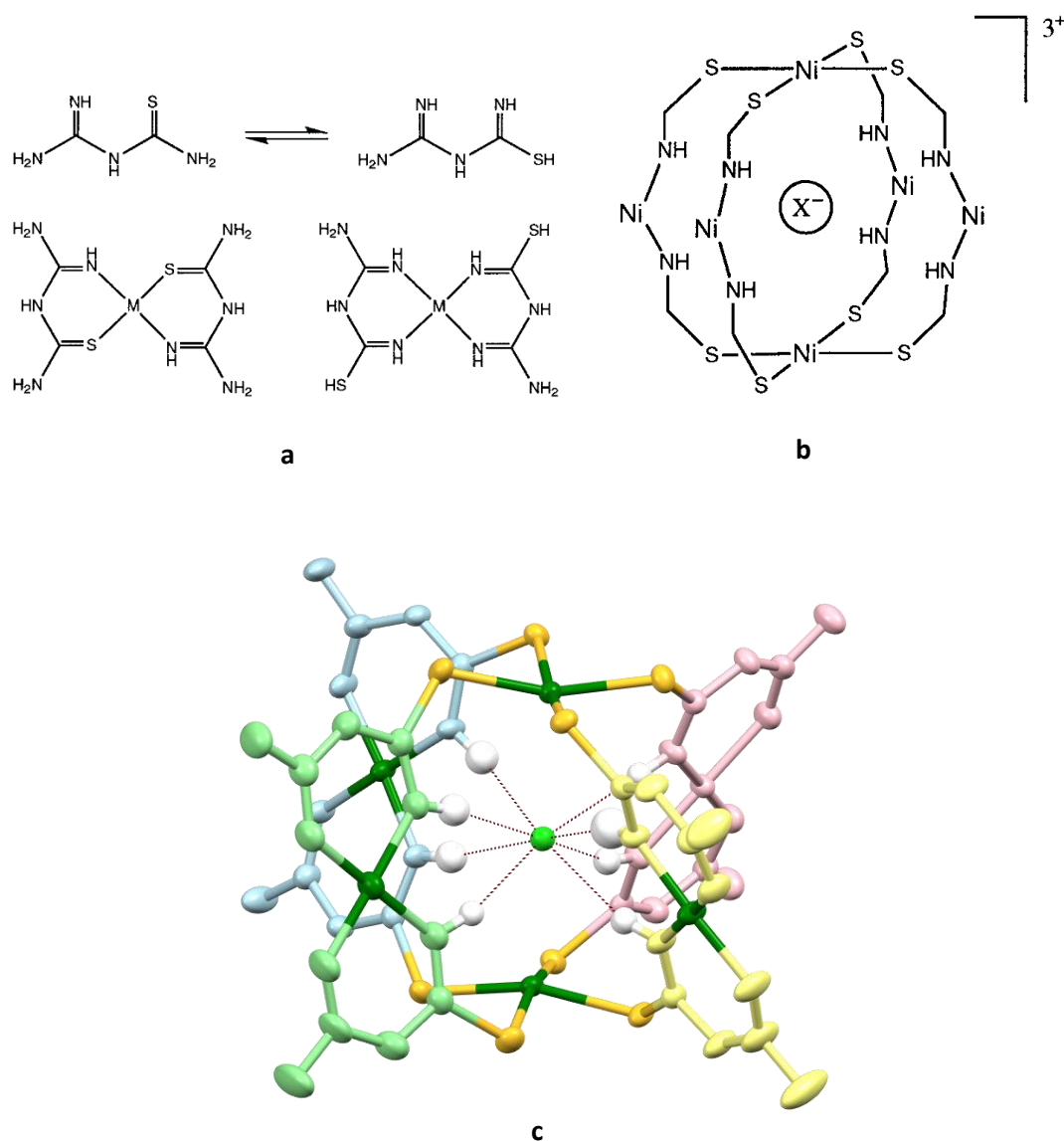


Figure 1.26. atu-based receptor **24**.⁹⁴ a) structure of atu displaying tautomeric co-ordination products; b) truncated co-ordination structure of $[\mathbf{24}\cdot\text{X}]^{3+}$ showing the encapsulation of a single halide; c) co-ordination structure of $[\mathbf{24}\cdot\text{Cl}]^{3+}$ and hydrogen-bonding present in the capsule. Colour code: dark green, Ni; yellow, S; green, Cl; white, H. Ligands coloured, non-acidic hydrogen atoms and counterions omitted for clarity.

Work in the Rice group has focused on the self-assembly of anion receptors from pyridyl-thiazole ligands and transition metal ions. Largely, receptors consist of metallosupramolecular self-assembled macromolecules, featuring ligands with two or more pyridyl-thiazole-amine bidentate domains connected by a linking group which can bind to both cationic metal centres through pyridyl- and thiazole- N-donor units, and form hydrogen-bonding interactions to anions through the secondary amine -NH units. These are employed not only due to the relative reliability of the synthesis of each ligand, but also due to the pre-programmable nature of each ligand allowing the targeting of specific anions by the subsequent receptor.

For example, receptor **25** is assembled from a ligand featuring two of these pyridyl-thiazole-amine moieties connected using a *meta*-disubstituted phenyl- group.⁹⁵ When reacted with copper(II), a dinuclear double helicate is formed (i.e. $[L_2Cu_2]^{4+}$). In this, each ligand co-ordinates both copper nuclei through each of its pyridyl- and thiazole- N-donor domains (Figure 1.27b). Upon reaction of this complex with half an equivalent of dihydrogen phosphate, the assembly binds the anion through two “bridging” $Cu \cdots OP$ co-ordination interactions and two ligand $-NH \cdots O$ hydrogen-bond interactions (Figure 1.27b).

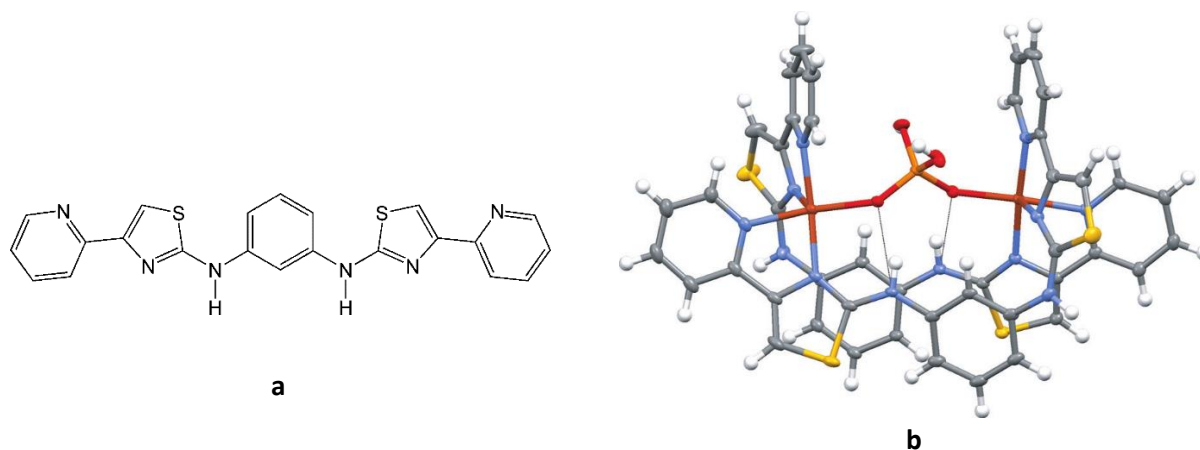


Figure 1.27. Receptor **25**.⁹⁵ a) structure of ligand used in the assembly; b) crystal structure of $[L_2Cu_2 \cdot H_2PO_4]^{3+}$ showing both copper-phosphate co-ordinate and ligand-phosphate hydrogen-bonding interactions. Thermal ellipsoids shown at 50% probability level. Colour code: grey, C; blue, N; white, H; yellow, S; red, O; orange, Cu; light orange, P. Counterions and non-acidic hydrogen atoms omitted for clarity.

Reaction of this complex with a further half equivalent of dihydrogen phosphate causes the complex to form a trinuclear helicate (i.e. $[L_3Cu_3(H_2PO_4)_3]^{3+}$, Figure 1.28a). In this conformation, each ligand again binds two copper nuclei through the same pyridyl-thiazole bidentate moieties, but the complex instead adopts a trinuclear assembly. Three phosphate anions are instead held within this helicate, through one $Cu \cdots OP$ co-ordination bond and two $-NH \cdots O$ hydrogen-bond interactions. Furthermore, “inter-guest” $POH \cdots OP$ interactions also hold the anions together in a cluster (Figure 1.28d) and the complex subsequently dimerises into a hexameric assembly whereby two trinuclear subunits bind through six phosphate $POH \cdots OP$ hydrogen-bonds (i.e. $[L_3Cu_3(H_2PO_4)_3]_2^{6+}$, Figure 1.28b - d).

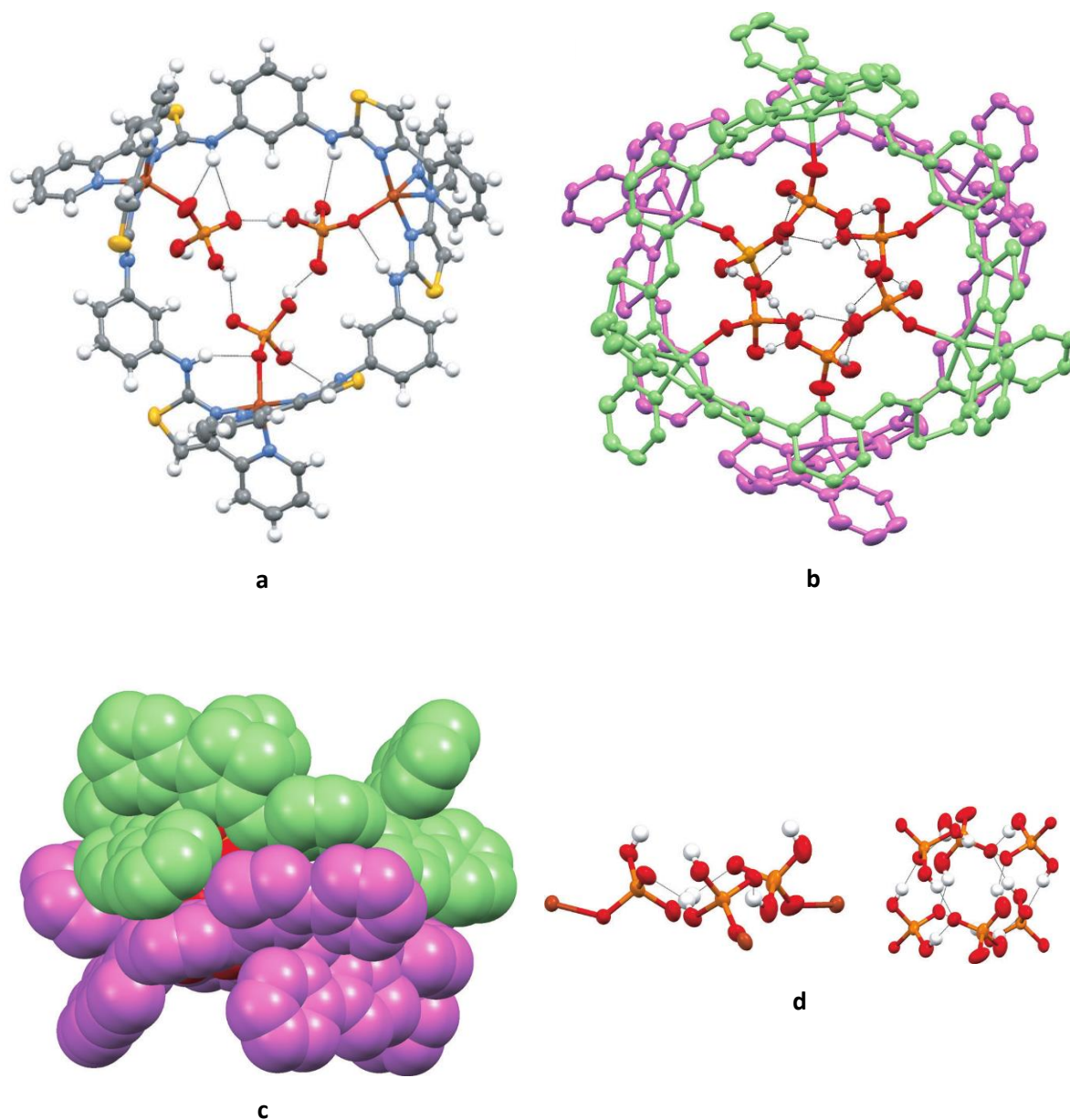


Figure 1.28. a) crystal structure of the triple helicate $[L_3Cu_3 \cdot (H_2PO_4)_3]^{3+}$; b) crystal structure of the dimerised hexameric cluster $[(L_3Cu_3 \cdot (H_2PO_4)_3)_2]^{6+}$; c) spacefill representation of cluster $[(L_3Cu_3 \cdot (H_2PO_4)_3)_2]^{6+}$ showing encapsulation of the phosphate anions; d) inter- and intra-molecular phosphate hydrogen-bonding interactions present in the trinuclear (left) and hexameric (right) clusters. Thermal ellipsoids shown at 50% probability level. Colour code: grey, C; blue, N; white, H; yellow, S; red, O; orange, Cu; light orange, P except in d) and e) where ligands are coloured and non-acidic hydrogen atoms omitted for clarity. Counterions also omitted for clarity.

Two related ligands were used in receptors **26a** and **26b**, in which two pyridyl-thiazole moieties are connected by an ethylenediamine (**26a**) or a 1,4-diaminobutane (**26b**) bridge (Figure 1.27a).⁹⁶ Both of these receptors are analogous in their binding mechanisms; two ligands bind two copper(II) nuclei through pyridyl- N- and thiazole- N-donor moieties to form receptors which bind to dihydrogenphosphate, with general formula $[L_2Cu_2]^{4+}$ upon reaction with copper(II) triflate (Figure 1.29b). The phosphate is held in place through a series of hydrogen-bonding interactions between the oxygen atoms of the ligand, but also $Cu \cdots O=P$ co-ordinate interactions. However, when complex **26a** is assembled using the tetrafluoroborate anion rather than triflate, a trinuclear assembly is instead formed (i.e. $[Cu_3L_3]^{6+}$), which shows phosphate reactivity to the tetrafluoroborate anion (Figure 1.29c). In this assembly, three copper(II) nuclei are bound by three ligand strands through each pyridyl-thiazole bidentate domain forming a trinuclear cage assembly. The tetrahedral phosphate anion is now held in the centre of this assembly through three $Cu \cdots OP$ co-ordinate interactions and several ligand $-NH \cdots OP$ hydrogen-bonding interactions. The unbound phosphate oxygen atom points “upward” from the assembly and binds to a trifluoroborate subunit which is presumed to arise from reaction with a tetrafluoroborate anion, which sits atop the assemblies (Figure 1.29c). Similarly, the tetrafluoroborate-incorporating structure with receptor **26b** also displays phosphate-tetrafluoroborate reaction; however, in this assembly the trinuclear complex is not observed. Instead, analogous to the triflate structure, a dinuclear assembly is observed which incorporates a deprotonated phosphate anion which is bound through only two $Cu \cdots OP$ co-ordinate interactions, leaving two oxygen atoms unbound which both react and bind one trifluoroborate each (Figure 1.29e).

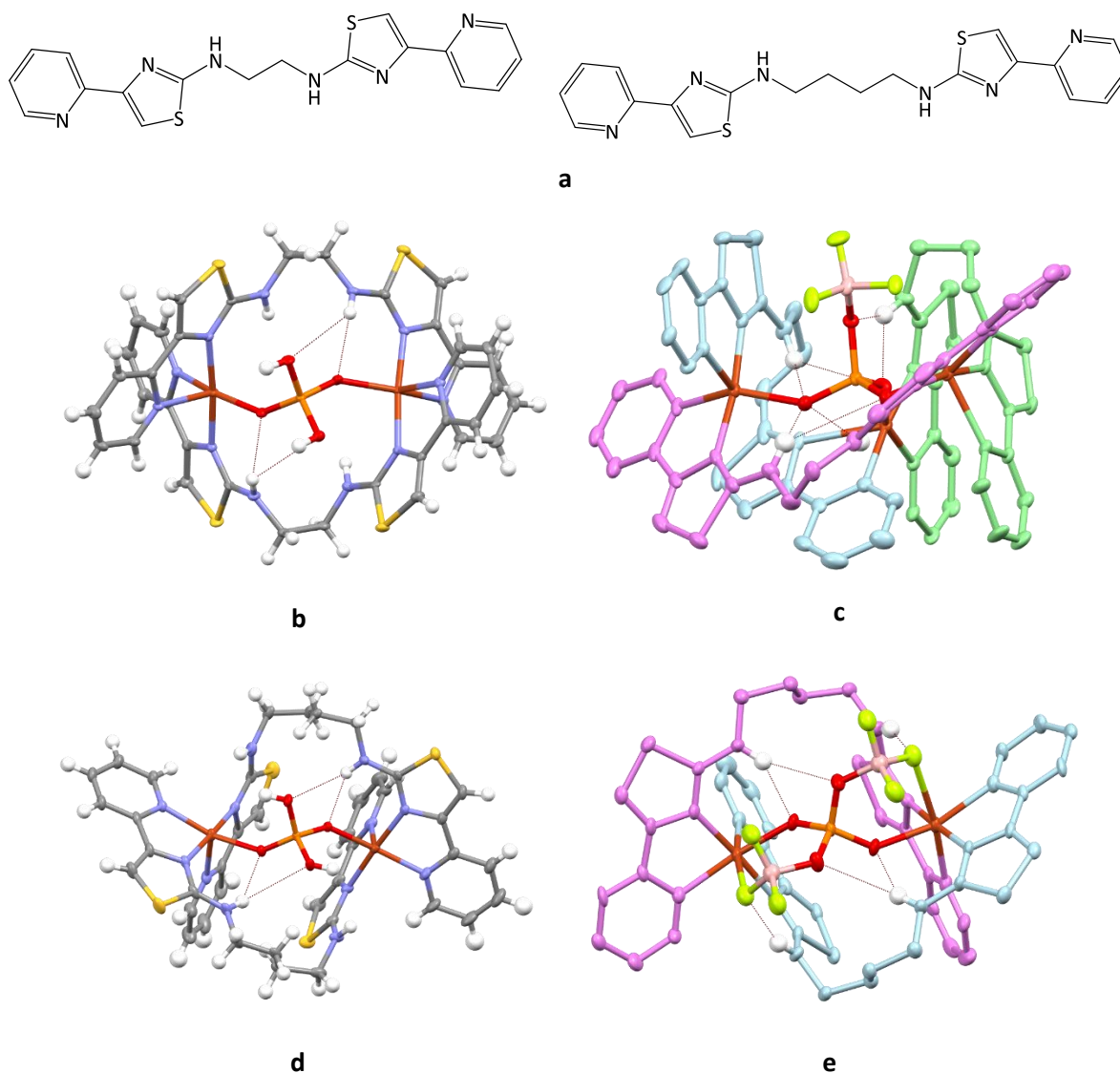


Figure 1.29. Receptors **26a** and **26b**.⁹⁶ a) structure of ligands used in **26a** (left) and **26b** (right); b) crystal structure of **26a** when assembled using copper(II) triflate, encapsulating phosphate anion (i.e. $[\text{Cu}_2\text{L}_2(\text{H}_2\text{PO}_4)]^{3+}$); c) crystal structure of the trinuclear assembly incorporating the trifluoroborophosphate unit (i.e. $[\text{Cu}_3\text{L}_3(\text{F}_3\text{BOPO}_3)]^{3+}$); d) crystal structure of **26b** when assembled using copper(II) triflate; e) crystal structure of dinuclear assembly of **26b** having reacted with two tetrafluoroborate anions (i.e. $[\text{Cu}_2\text{L}_2((\text{F}_3\text{BO})_2\text{PO}_2)]^{3+}$). Thermal ellipsoids shown at 30% probability level. Colour code: grey, C; blue, N; white, H; yellow, S; red, O; orange, Cu; light orange, P; pink, B; chartreuse, F except in c) and e) where ligands are coloured and non-acidic hydrogen atoms omitted for clarity. Counterions also omitted for clarity.

Recently, a new ligand was developed by the Rice group which incorporates three pyridyl-thiazole bidentate moieties on each end of a *tris*-(2-aminoethyl)amine linking unit giving a potentially hexadentate ligand **L**¹ (Figure 1.30a).⁹⁷ This ligand is capable of co-ordination to a variety of copper(II) salts, which gives a cage assembly of motif [**L**₂Cu₃]⁶⁺. In this, each ligand binds three copper(II) nuclei through each of its pyridyl-thiazole bidentate domains for a total of four N...Cu interactions on each cation, and in turn, each copper is bound by both ligands. The resultant capsule is capable of binding a variety of shapes and sizes of anion (e.g. phosphate, sulfate, carbonate, bromide, iodide, chromate and tungstate, Figure 1.30b - e) through both Cu...A⁻ co-ordination bonds as well as several ligand - NH...A⁻ hydrogen-bonding interactions. The receptor is particularly selective in its activity in that phosphates are preferentially bound over other anions; indeed, upon reaction with one equivalent of phosphate, UV-Vis-NIR studies indicate that tetrafluoroborate, perchlorate, bromide, iodide and sulfate are all ejected from the capsule and replaced with phosphate. Ion chromatography studies also indicate that the receptor is capable of removing up to 80% of phosphate in a solution containing other anions.

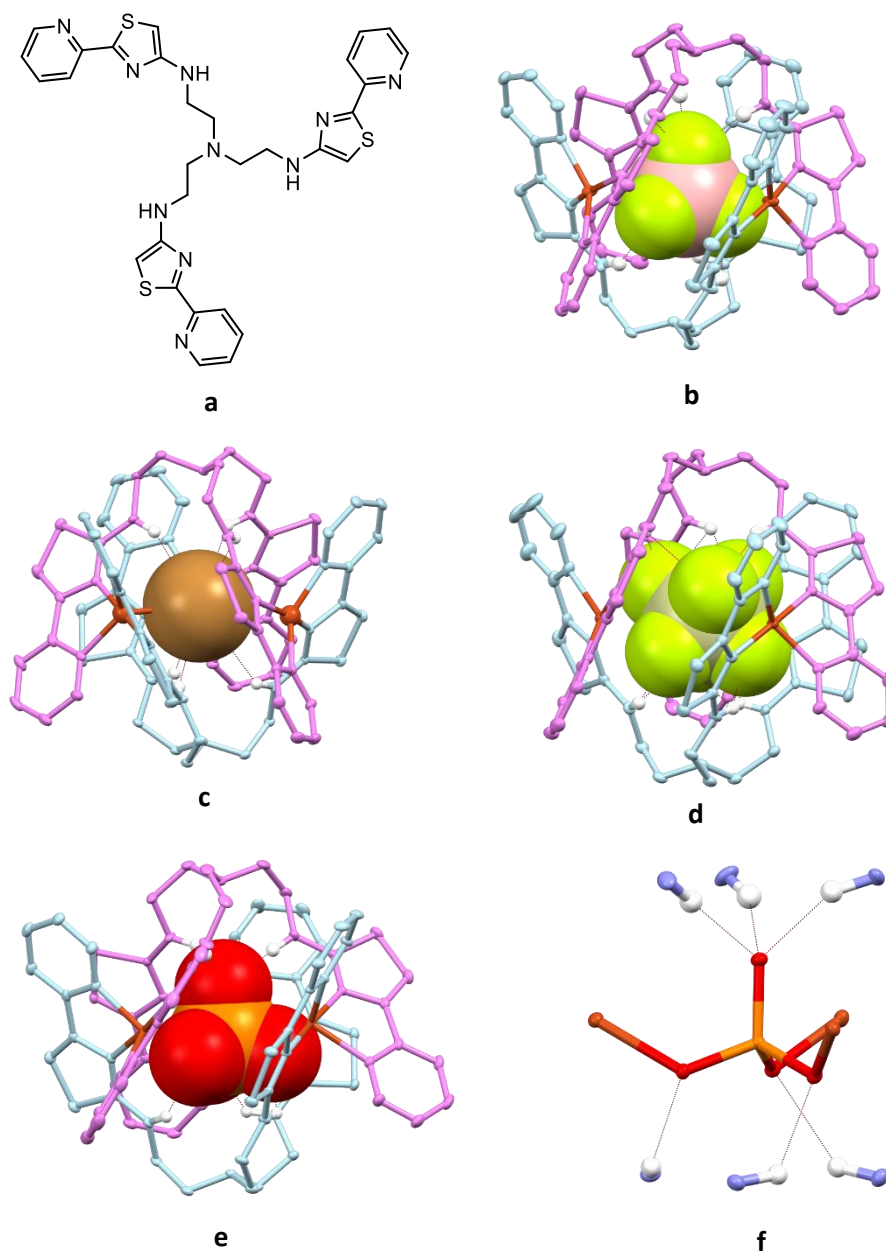


Figure 1.30. Receptors formed from ligand L^1 .⁹⁷ a) structure of L^1 ; b) crystal structure of $[L^1_2Cu_3(BF_4)]^{5+}$; c) crystal structure of $[L^1_2Cu_3(Br)]^{5+}$; d) crystal structure of $[L^1_2Cu_3(SiF_6)]^{4+}$; e) crystal structure of $[L^1_2Cu_3(PO_4)]^{3+}$; f) hydrogen-bonding interactions in $[L^1_2Cu_3(PO_4)]^{3+}$. Colour code: orange, Cu; lime, F; pink, B; brown, Br; mint, Si; orange, P; red, O; blue, N; white, H; light orange, Se. Ligands are coloured and non-acidic hydrogen atoms and counterions omitted for clarity. Thermal ellipsoids shown at 30% probability level.

Research has also shown that the receptor is capable of adopting different conformers when exposed to the selenite anion *versus* the expected species with the selenate anion ($[\text{L}^1_2\text{Cu}_3\text{SeO}_4]^{4+}$, Figure 1.31a).⁹⁸ Instead, an octanuclear assembly is observed (i.e. $[\text{L}^1_4\text{Cu}_8(\text{SeO}_3)_4]^{8+}$, Figure 1.31b and c).⁹⁸ The expected assembly of $[\text{L}^1_2\text{Cu}_3\text{SeO}_3]^{4+}$ was also observed as a minor component, but is theorised to only form in systems where the amounts of each component (ligand, metal, anion) are stoichiometrically incorrect to form the octanuclear assembly.

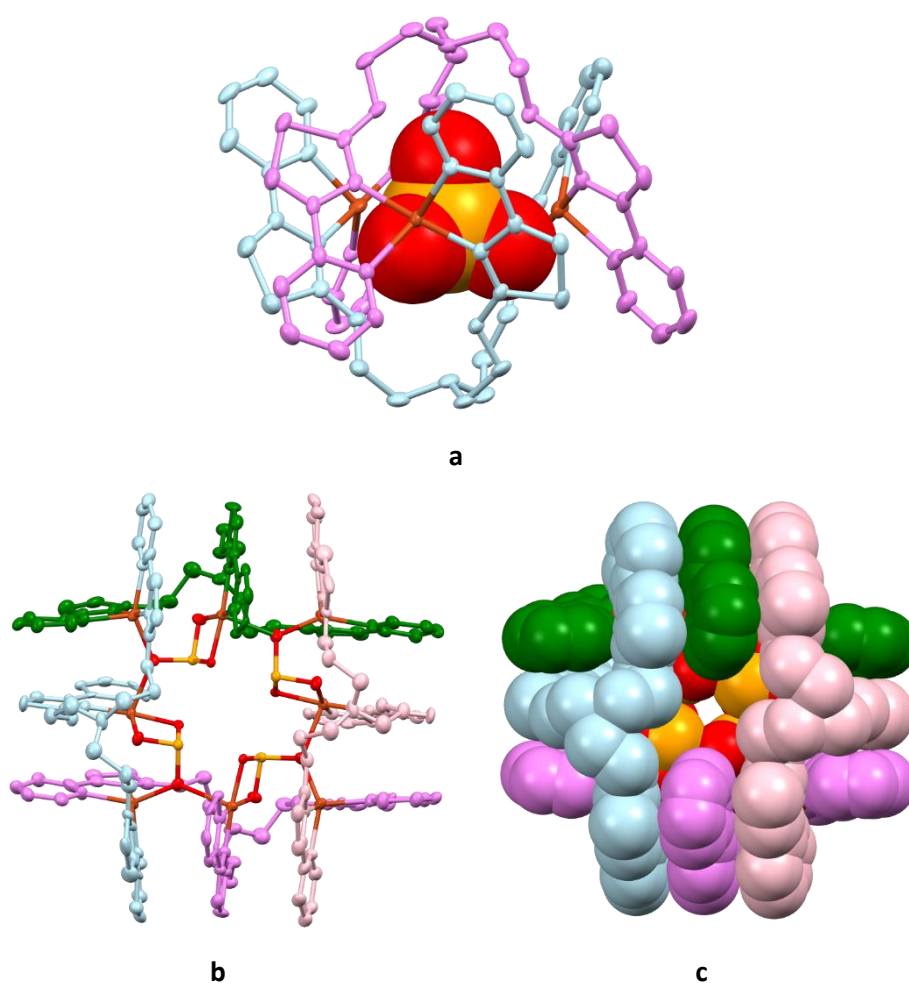


Figure 1.31. Structures of $[\text{L}^1_2\text{Cu}_3\text{SeO}_4]^{4+}$ and $[\text{L}^1_4\text{Cu}_8(\text{SeO}_3)_4]^{8+}$.⁹⁸ a) crystal structure of $[\text{L}^1_2\text{Cu}_3\text{SeO}_4]^{4+}$; b) crystal structure of $[\text{L}^1_4\text{Cu}_8(\text{SeO}_3)_4]^{8+}$; c) spacefill structure of $[\text{L}^1_4\text{Cu}_8(\text{SeO}_3)_4]^{8+}$ showing encapsulation of anions. Colour code: orange, Cu; lime, F; pink, B; brown, Br; mint, Si; orange, P; red, O; blue, N; white, H; light orange, Se. Ligands are coloured and non-acidic hydrogen atoms and counterions omitted for clarity. Thermal ellipsoids shown at 30% probability level.

As has been demonstrated by this work, reaction of suitable ligands with metal ions can lead, if properly instructed, to supramolecular species interacting strongly and specifically with anions. The latter part of this work involving the formation of the trinuclear cryptate (e.g. $[\text{L}^1_2\text{Cu}_3]^{6+}$) shows particular promise as it selectively and strongly binds phosphate in aqueous media. It is both this ligand (e.g. L^1) and derivatives of tripodal ligands, containing three amine-substituted pyridyl-thiazole domains capable of forming cryptates that bind anions, that have formed the basis of the subsequent investigation contained in this thesis.

Aims

The first aim of the project demonstrated within this thesis was primarily to expand on the previous research done using ligand L^1 by investigating its ability to bind to other first-row transition metals (namely zinc and manganese cations). The anion binding affinities of these new complexes would be examined when co-ordinated to both phosphate and sulfate. These (along with the copper-based complex) would then be reacted with various phosphate-based esters to investigate the properties of these complexes in both the solid-state and solution. From these, the biological effects (specifically the *in vitro* cytotoxicity) of both the “empty” cryptand (i.e. $[L^1_2M_3]^{6+}$) and anion-containing complexes (i.e. $[L^1_2M_3PO_4]^{3+}$ and $[L^1_2M_3SO_4]^{4+}$) would be investigated and compared to traditional platinum-based chemotherapy agents.

The second aim of the project was to investigate the effects of changing the central spacer of ligand L^1 . Since this would almost certainly affect the anion selectivity of the resultant complexes, these would then be analysed using similar experiments to those used to measure the L^1 complexes, in order to evaluate anion compatibility and compare their selectivities. To do this, new ligands were proposed, all incorporating the same amine-thiazole-pyridine binding motifs as ligand L^1 but adjusting the central spacer. Whilst L^1 incorporates a central tris(2-aminoethyl)amine moiety to link its binding domains, the first new ligand (L^2) uses 1,1,1-tris(aminomethyl)ethane unit to provide a smaller cavity on coordination; the second (L^3) uses 1,3,5-triaminocyclohexane as a central group; the third uses tris(2-aminoethyl)methane to link its co-ordination sites, as it was theorised that the central tertiary methine group would act as a $-CH\cdots A^-$ hydrogen-bond donor, improving binding strength. Once these ligands had been synthesised, their binding abilities would be investigated primarily using copper(II) salts and an array of anions with a range of both shape and charges. To do this, their solid-state structures would be examined using X-ray crystallography and solutions of complexes would be analysed using

mass spectrometry and UV-Vis-NIR spectroscopy. Ion chromatography would also be used on aqueous solutions of these in order to investigate the selectivity of each complex at various *pH* levels.

Finally, the receptors assembled from ligand **L¹** and **L³** would be adapted to include aliphatic ester groups in order to increase the solubility of the complexes in organic media and decrease their solubility in aqueous solutions. This was theorised to allow the extraction of ordinarily hydrophilic anions (i.e. PO_4^{3-} , SO_4^{2-}) into organic media. These ligands would be co-ordinated to copper(II) salts and their properties would be analysed by mass spectrometry. To investigate the selectivity and extraction efficiency of the complexes made from these new ligands, aqueous solutions of various salts would be treated with immiscible, organic solutions of each complex to analyse their binding properties *via* ion chromatography.

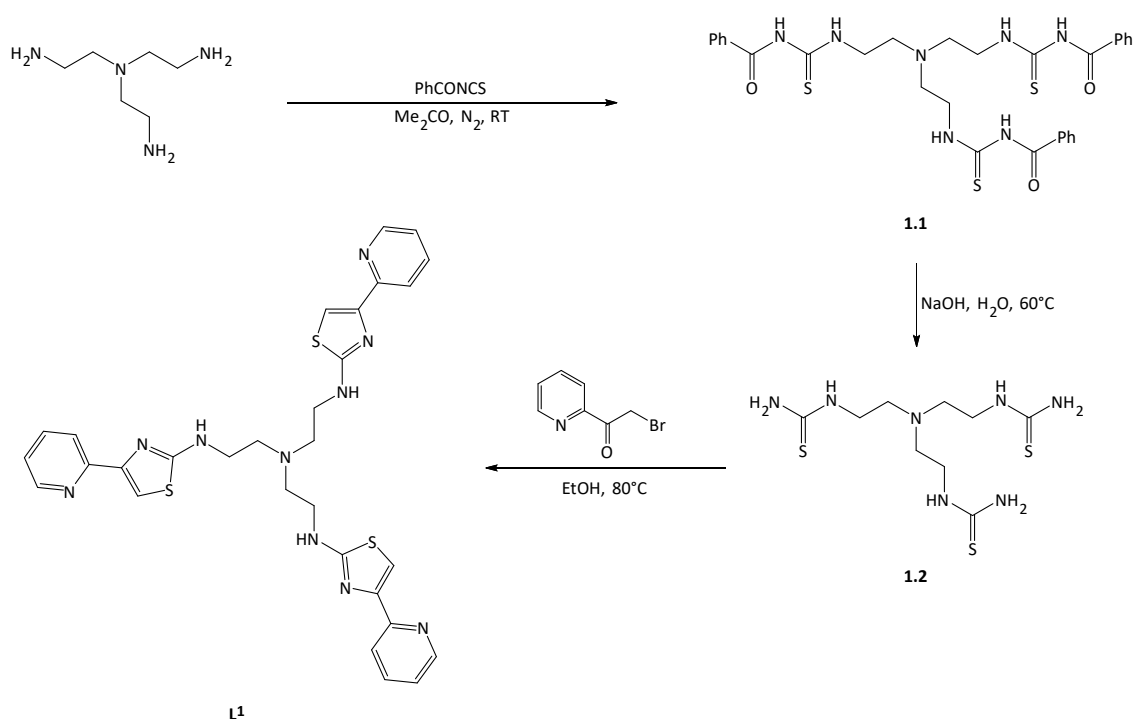
2. Co-ordination Chemistry and Chemosensitivity Studies of Complexes of L¹

All of the biological work for this chapter has been performed by Prof. Roger Phillips, Dr. Simon Alison and Emma Pinder.

2.1. Continuing the co-ordination chemistry of ligand L¹

2.1.1. Synthesis

Ligand L¹ was prepared as previously reported, but minor adjustments were made to improve one intermediate step of the synthesis to improve yield, purity of the product and the replicability of the process (Scheme 2.1).^{97,99}



Scheme 2.1. Improved synthesis of ligand L¹ from tris-(2-aminoethyl)amine.

Firstly, the benzoyl-protected thiourea **1.1** was produced from *tris*-(2-aminoethyl)amine via reaction with benzoyl isothiocyanate as previously reported, but it was found that when using acetone as the reaction solvent rather than acetonitrile the *tris*-benzoylated product precipitated directly from solution, which was simply be filtered and washed with acetone. This was more desirable than the methods used previously which involved a forced precipitation using water, decanting and triturating with acetone to obtain the product. This was then converted to the *tris*-thiourea **1.2** by stirring in hot sodium hydroxide solution, cooling and filtration, followed by reaction with 2-(α -bromoacetyl)pyridine in ethanol to give the final ligand **L¹** as previously reported.⁹⁷

2.1.2. Co-ordination chemistry

All the previous co-ordination chemistry using this ligand, while extensive, focused on the complexes formed with copper(II) cations and various anions. The logical extension of this work was to investigate the co-ordination chemistry of this ligand with different metal ions.

[L¹Zn]²⁺ and [L¹Mn(H₂O)₂]²⁺

Reaction of 1.5 equivalents of **L¹** with either zinc(II) perchlorate (in acetone and water solution) or manganese(II) perchlorate (in acetonitrile and water solution) results in pale-yellow coloured solutions in both cases. On slow evaporation, yellow crystals are deposited; analysis of these shows that the ligand forms a mononuclear complex [L¹M]²⁺ as demonstrated by X-ray crystallography and ESI-MS. In the solid-state the zinc complex contains a 6-co-ordinate Zn²⁺ cation co-ordinated by six nitrogen atoms from three pyridyl-thiazole bidentate units from the same ligand (Figure 2.1a). In the Mn²⁺ analogue the metal ion is again 6-co-ordinate, but this arises from co-ordination by four *N*-donor atoms from two bidentate pyridyl-thiazole units and two *O*-donor atoms from two water molecules (Figure 2.1b). Both complexes differ from the Cu²⁺ complex which can form the trimetallic capsule (e.g.

$[\text{L}^1_2\text{Cu}_3]^{6+}$) even in the presence of weakly interacting anions. The difference is attributed to the ability of Cu^{2+} to form 4-co-ordinate complexes (at least with pyridyl-thiazole donors) whereas both Zn^{2+} and Mn^{2+} prefer higher-co-ordinate geometry and, without a strongly coordinating anion present, a simple mononuclear species is formed (despite the reactant stoichiometry of two ligands and three metal ions used). The co-ordination of water in the Mn^{2+} complex (e.g. $[\text{L}^1\text{Mn}(\text{H}_2\text{O})_2]^{2+}$) is a consequence of the oxophilic nature of this hard cation, and this behaviour is mirrored in all the structures with this metal.

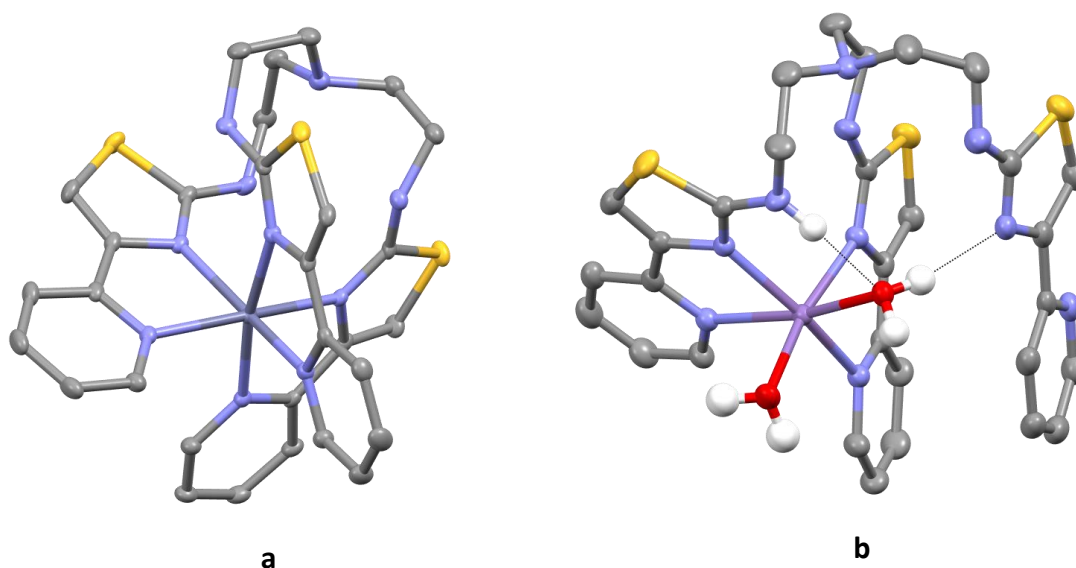
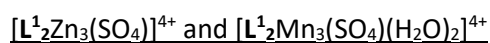


Figure 2.1. Mononuclear complexes of L^1 . Structures of a) $[\text{L}^1\text{Zn}]^{2+}$; b) $[\text{L}^1\text{Mn}(\text{H}_2\text{O})_2]^{2+}$. Colour code: blue-grey, Zn^{2+} ; violet, Mn^{2+} ; red, O; blue, N; yellow, S; grey, C; white, H. Perchlorate anions and non-acidic hydrogen atoms omitted for clarity. Thermal ellipsoids shown at 50% probability level.



Reaction of L^1 with either Mn^{2+} or Zn^{2+} with tetra-*N*-butylammonium hydrogensulfate (in the correct stoichiometric proportions) results in colourless and yellow solutions respectively. X-ray diffraction analysis of the crystals deposited from these solutions show the formation of a trimetallic capsule in which sulfate anions are encapsulated (e.g. $[\text{L}^1_2\text{M}_3(\text{SO}_4)]^{4+}$) (Figure 2.2 and Figure 2.3). In the solid-

state, the Zn^{2+} is isostructural to the Cu^{2+} complex with a trinuclear $[L^1_2Zn_3]^{6+}$ assembly and within it is an encapsulated sulfate anion (e.g. $[L^1_2Zn_3(SO_4)]^{4+}$). Each of the three Zn^{2+} atoms are 5-co-ordinate arising from four *N*-donor atoms from two bidentate pyridyl-thiazole units and one *O*-donor from the sulfate anion. The sulfate is held within the capsule through three metal-oxygen co-ordination bonds to the lower three of the four tetrahedral oxygen atoms. These are supplemented by six $-NH\cdots O$ hydrogen bonding interactions – one to each of the metal-co-ordinated oxygen atoms and three to the remaining oxygen atom in the upper portion of the cavity (Figure 2.2c).

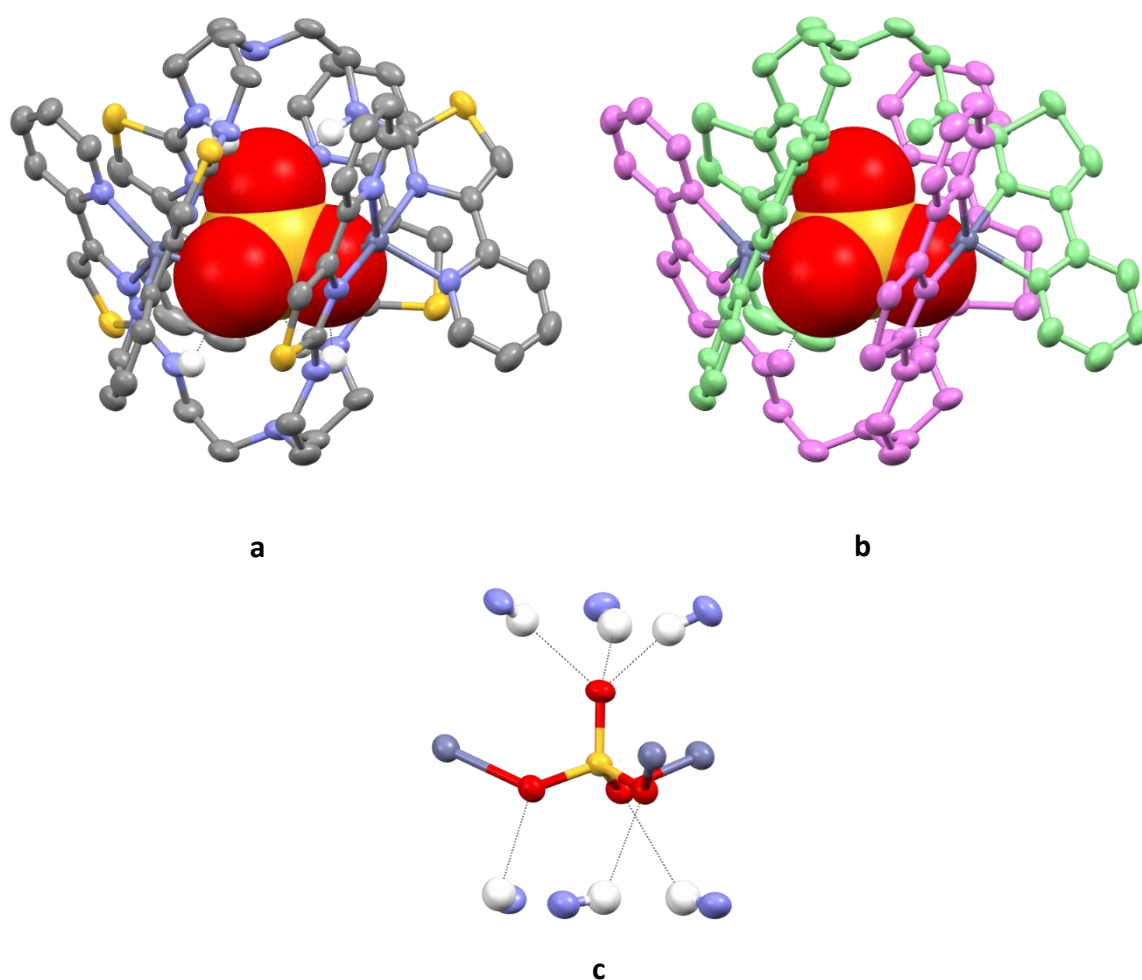


Figure 2.2. a) crystal structure of $[L^1_2Zn_3(SO_4)]^{4+}$; b) crystal structure with ligands coloured for clarity; c) co-ordination and hydrogen-bonding of the metals and ligand to the SO_4^{2-} anion. Colour code: blue-grey, Zn^{2+} ; red, O; blue, N; yellow, S; grey, C; white, H (apart from (b) where the ligands have

been coloured for clarity). Non-acidic hydrogen atoms and tetrafluoroborate anions are omitted for clarity. Thermal ellipsoids shown at the 50% probability level.

The Mn^{2+} forms a very similar type of assembly but each of the Mn^{2+} metal ions are 6-co-ordinate, which for one of the metal ions arises from four *N*-donor atoms from two bidentate pyridyl-thiazole units and two oxygen donors from the sulfate anion (Figure 2.3). The remaining two ions are also 6-co-ordinate and are co-ordinated by two bidentate *N*-donor ligands but are co-ordinated by one oxygen atom from the sulfate anion and one water molecule (e.g. $[\text{L}^1_2\text{Mn}_3(\text{SO}_4)(\text{H}_2\text{O})_2]^{4+}$). This demonstrates that whilst with weakly interacting anions (e.g. halides, perchlorate, and tetrafluoroborate) both Zn^{2+} and Mn^{2+} form mononuclear complexes, whereas tetrahedral oxoanions template the formation of the trimetallic capsule.

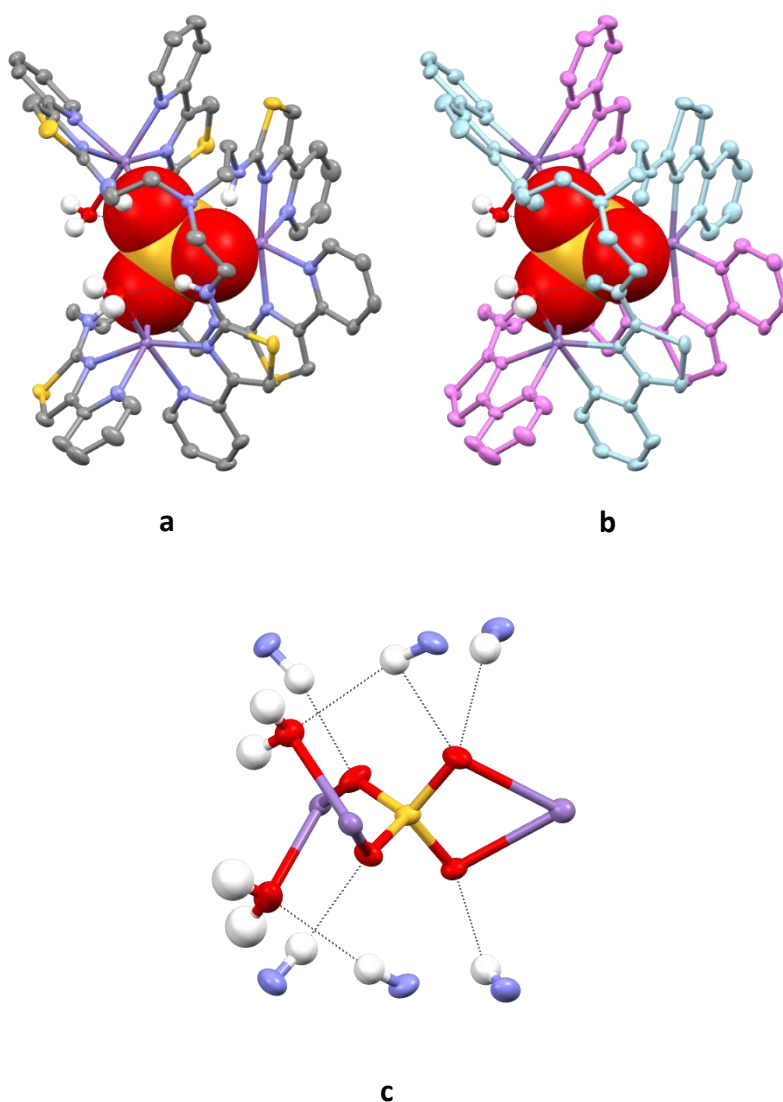


Figure 2.3. a) crystal structure of $[\text{L}^1_2\text{Mn}_3(\text{SO}_4)(\text{H}_2\text{O})_2]^{4+}$; b) crystal structure with ligands coloured for clarity; c) co-ordination and hydrogen-bonding of the metals and ligand to the SO_4^{2-} anion. Colour code: lilac, Mn^{2+} ; red, O; blue, N; yellow, S; grey, C; white, H (apart from (b) where the ligands have been coloured for clarity). Non-acidic hydrogen atoms and perchlorate anions are omitted for clarity.

Thermal ellipsoids shown at the 50% probability level.

$[\text{L}^1_2\text{Cu}_3(\text{PhOPO}_3)]^{3+}$

Addition of disodium phenylphosphate to a solution of $[\text{L}^1_2\text{Cu}_3]^{6+}$ in 1:1 an acetonitrile-water solution results in a colour change from light blue to green. Crystals were then deposited after several days and analysis by X-ray crystallography shows that the trimetallic capsule is still formed but held inside

the host is a PhOPO_3^{2-} anion. In a very similar fashion to the other oxoanions, PhOPO_3^{2-} is co-ordinated to the three Cu^{2+} metal ions supplemented by a series of $-\text{NH}\cdots\text{A}^-$ interactions. However, due to the phenyl substituent the ligands adopt a slightly different conformation allowing the phenyl unit to occupy a cleft formed by two pyridyl-thiazole units (Figure 2.4).

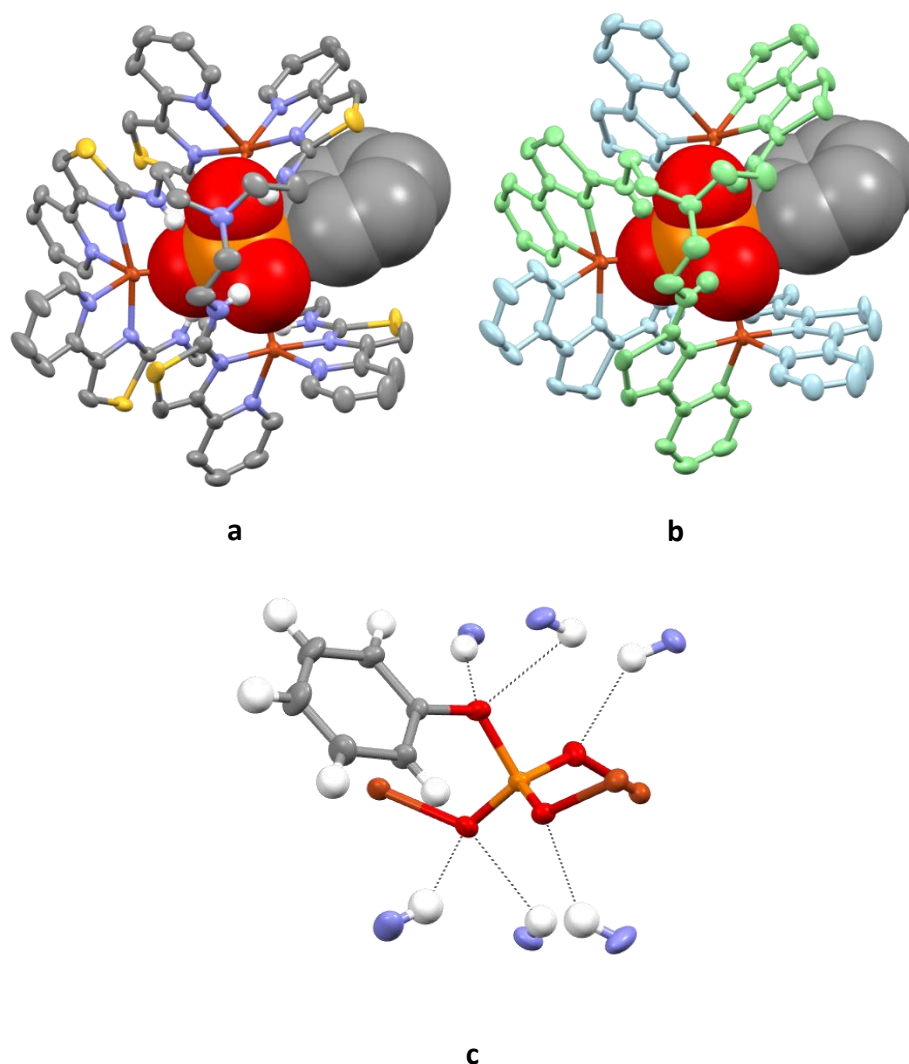


Figure 2.4. a) crystal structure of $[\text{L}^1_2\text{Cu}_3(\text{PhOPO}_3)]^{4+}$; b) crystal structure with ligands coloured for clarity; c) co-ordination and hydrogen-bonding of the metals and ligand to the PhOPO_3^{2-} anion. Colour code: dark orange, Cu^{2+} ; orange, P; red, O; blue, N; yellow, S; grey, C; white, H (apart from (b) where the ligands have been coloured for clarity). Non-acidic hydrogen atoms and tetrafluoroborate anions are omitted for clarity. Thermal ellipsoids shown at the 50% probability level.

$[\text{L}^1_2\text{Zn}_3(\text{PO}_4)]^{3+}$ and $[\text{L}^1_2\text{Mn}_3(\text{PO}_4)]^{3+}$

Reaction of two equivalents of L^1 , three equivalents of either $\text{M}(\text{ClO}_4)_2$ (where $\text{M} = \text{Zn}^{2+}$ or Mn^{2+}) and $\text{PhOPO}_3\text{Na}_2$ results in a very different species. In the solid-state both structures contain a central PO_4^{3-} anion held within the molecule by a series of interactions between the metal ions and amine hydrogen atoms (Figure 2.5 and Figure 2.6). The $[\text{L}^1_2\text{Mn}_3(\text{PO}_4)]^{3+}$ complex is similar to the sulfate analogue and the three 6-co-ordinate Mn^{2+} metal ions are co-ordinated by two bidentate N-donor ligand domains but one metal ion is co-ordinated by two oxygen atoms from the anion and the remaining two metal ions are co-ordinated by one anion oxygen atom and a water molecule. The $[\text{L}^1_2\text{Zn}_3(\text{PO}_4)]^{3+}$ is slightly different from the sulfate analogue and one metal ion is 6-co-ordinate arising from co-ordination of two bidentate N-donor ligand units and two oxygen atoms of the anion. The remaining two metal ions are 5-co-ordinate as only one oxygen atom from the anion interacts with the metal.

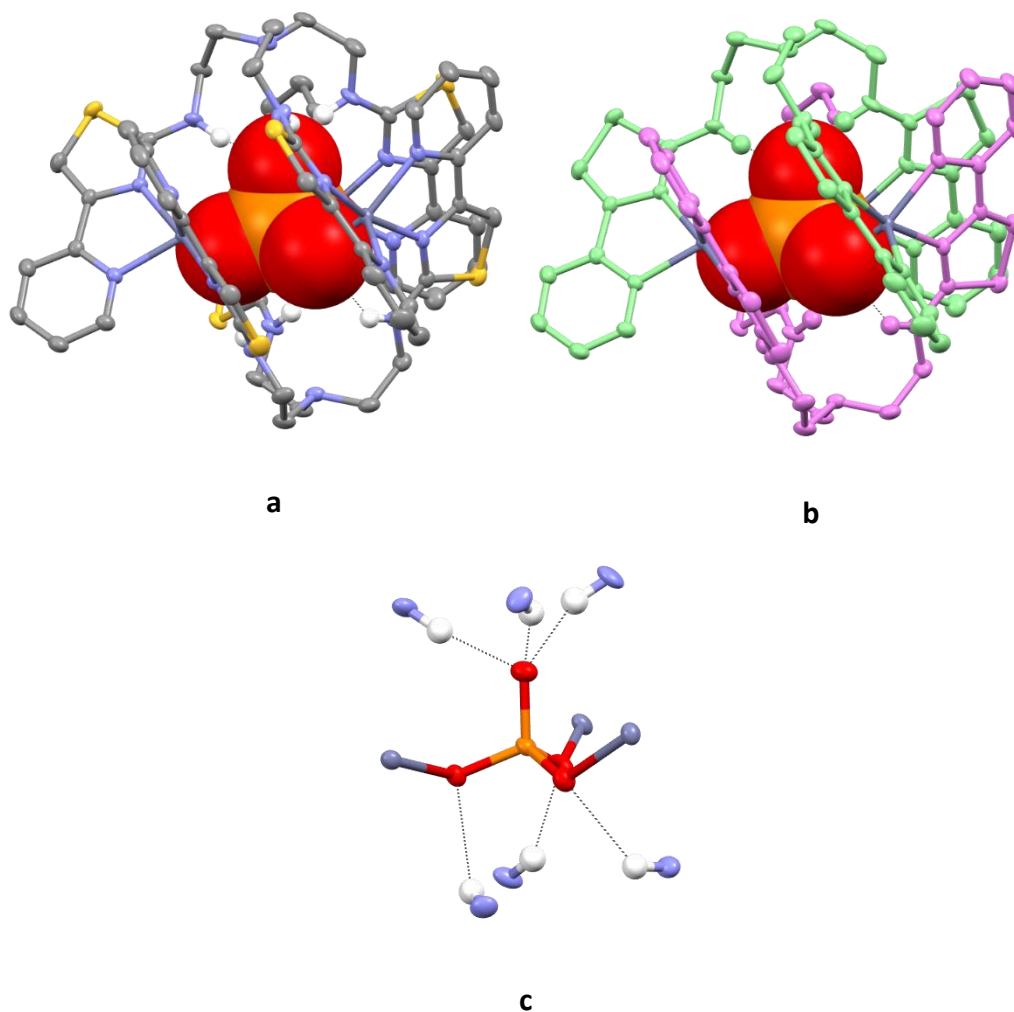


Figure 2.5. a) crystal structure of $[L^1_2Zn_3(PO_4)]^{3+}$; b) crystal structure with ligands coloured for clarity; c) co-ordination and hydrogen-bonding of the metals and ligand to the PO_4^{3-} anion. Colour code: blue-grey, Zn^{2+} ; orange, P; red, O; blue, N; yellow, S; grey, C; white, H (apart from (b) where the ligands have been coloured for clarity). Non-acidic hydrogen atoms and perchlorate anions are omitted for clarity. Thermal ellipsoids shown at the 50% probability level.

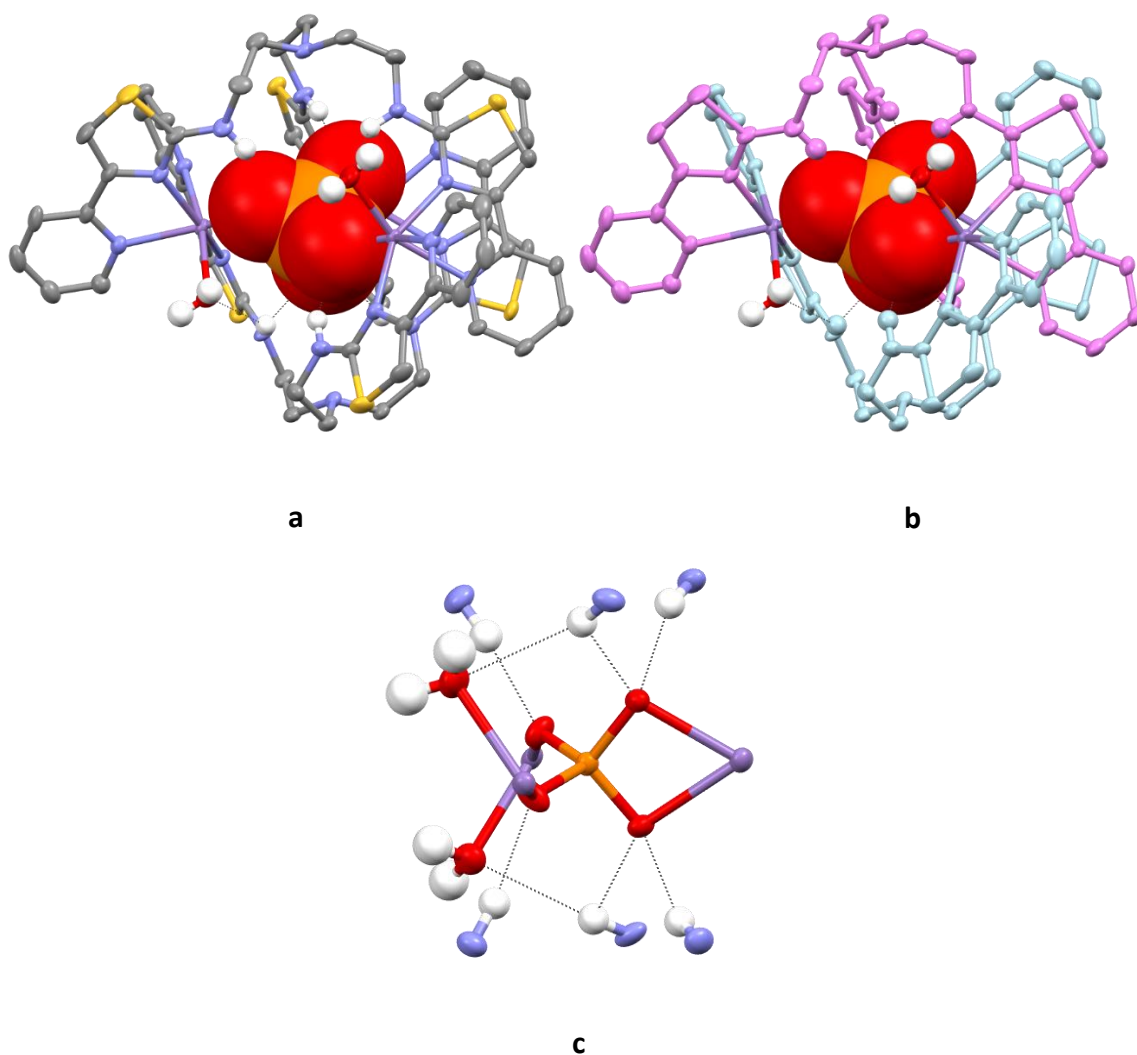


Figure 2.6. a) crystal structure of $[L^1_2Mn_3(PO_4)(H_2O)_2]^{3+}$; b) crystal structure with ligands coloured for clarity; c) co-ordination and hydrogen-bonding of the metals and ligand to the PO_4^{3-} anion. Colour code: lilac, Mn^{2+} ; orange, P; red, O; blue, N; yellow, S; grey, C; white, H (apart from (b) where the ligands have been coloured for clarity). Non-acidic hydrogen atoms and perchlorate anions are omitted for clarity. Thermal ellipsoids shown at the 50% probability level.

This metal-dependent reactivity is also observed in the ESI-MS. Reaction of $[L^1_2Cu_3](ClO_4)_6$ with $PhOPO_3Na_2$ in water and acetonitrile gives ions at m/z 1914, 1024, 788 and 463 corresponding to $\{[L^1_2Cu_3(PhOPO_3)](ClO_4)_3\}^+$, $\{[L^1Cu_2(PhOPO_3)](ClO_4)\}^+$, $\{[L^1Cu](ClO_4)\}^+$ and $\{[L^1Cu_2(PhOPO_3)]\}^{2+}$ respectively (Figure 6.9); heating this sample at $80^\circ C$ shows no change in the ESI-MS spectrum

indicating that the phenylphosphate dianion remains intact (Figure 6.12). A similar reaction of $\text{PhOPO}_3\text{Na}_2$ with zinc(II) perchlorate and L^1 gave an ESI-MS with ions at m/z 1920 and 910 corresponding to $\{[\text{L}^1_2\text{Zn}_3(\text{PhOPO}_3)](\text{ClO}_4)_3\}^+$ and $\{[\text{L}^1_2\text{Zn}_3(\text{PhOPO}_3)](\text{ClO}_4)_2\}^{2+}$ respectively (Figure 6.10). Lower molecular weight ions at m/z 1029, 791 and 464 corresponding to $\{[\text{L}^1\text{Zn}_2(\text{PhOPO}_3)](\text{ClO}_4)\}^+$, $\{[\text{L}^1\text{Zn}](\text{ClO}_4)\}^+$ and $\{[\text{L}^1\text{Zn}_2(\text{PhOPO}_3)]\}^{2+}$ were also observed. However, heating this sample at 80°C results in a dramatic change in the ESI-MS with the spectrum now much simplified with ions at m/z 1743 and 822 corresponding to $\{[\text{L}^1_2\text{Zn}_3(\text{PO}_4)](\text{ClO}_4)_2\}^+$ and $\{[\text{L}^1_2\text{Zn}_3(\text{PO}_4)](\text{ClO}_4)\}^{2+}$ (Figure 6.13). This demonstrates that initially the Zn^{2+} containing complex reacts with phenyl phosphate dianion and in a similar fashion to the Cu^{2+} analogue and forms the trinuclear complex incorporating this anion (e.g. $[\text{L}^1_2\text{Zn}_3(\text{PhOPO}_3)]^{4+}$). However, after either a few days at room temperature or heating at 80°C for one hour the anion is hydrolysed and phosphate is encapsulated within the complex. This hydrolysis is also confirmed by ^1H NMR spectroscopy as reaction of two equivalents of L^1 , three equivalents of $\text{Zn}(\text{ClO}_4)_2$ and $\text{PhOPO}_3\text{Na}_2$ initially gives a broad complex spectrum but after one hour at 80°C gave a spectrum that contains signals corresponding to $[\text{L}^1_2\text{Zn}_3(\text{PO}_4)]^{3+}$ accompanied with signals corresponding to the phenol hydrolysis product (Figure 2.7). Reaction with manganese(II) perchlorate is similar to the Zn^{2+} analogue with ions in the ESI-MS corresponding to binding of phenyl phosphate initially observed (e.g. $\{[\text{L}^1\text{Mn}_2(\text{PhOPO}_3)](\text{ClO}_4)\}^+$, Figure 6.11) but ions corresponding to hydrolysis (e.g. $\{[\text{L}^1_2\text{Mn}_3(\text{PO}_4)](\text{ClO}_4)_2\}^+$ and $\{[\text{L}^1_2\text{Mn}_3(\text{PO}_4)](\text{ClO}_4)\}^{2+}$) observed after heating for one hour (Figure 6.14).

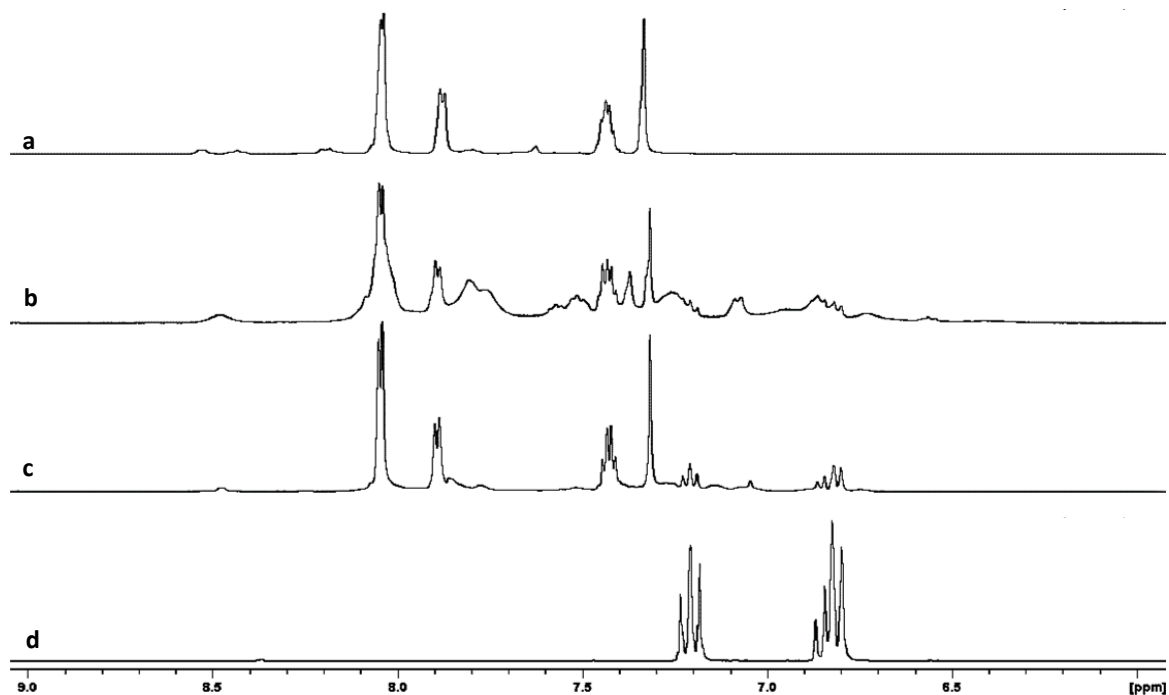


Figure 2.7. ^1H NMR (10% D_2O in CD_3CN) analysis of phenylphosphate hydrolysis by $[\text{L}^1_2\text{Zn}_3]^{6+}$. Aromatic regions of spectra of a) $[\text{L}^1_2\text{Zn}_3]^{6+} + \text{Bu}_4\text{NH}_2\text{PO}_4$, b) $[\text{L}^1_2\text{Zn}_3]^{6+} + \text{PhOPO}_3\text{Na}_2$, $T = 0$, c) $[\text{L}^1_2\text{Zn}_3]^{6+} + \text{PhOPO}_3\text{Na}_2$, $T = 1$ hr incubated at 80°C , d) phenol. The NMR solutions were prepared by dissolving L^1 and $\text{Zn}(\text{C}_2\text{H}_3\text{O}_2)_2$ (in a ratio of 1:1.5) in CD_3CN ($600\ \mu\text{L}$). The relevant anion (0.5 equiv w.r.t ligand) was dissolved in D_2O ($60\ \mu\text{L}$) and these solutions were then combined. Heating of the sample was carried out at 80°C in a water bath for a specified amount of time.

The Zn^{2+} complex shows substrate specific differences in the rates of hydrolysis and its phosphatase activity. Analysis of the hydrolysis of phenyl phosphate dianion by the Zn^{2+} complex (in a 30%:70% mixture of DMSO and buffered H_2O solution (HEPES pH 7.5)) by ^{31}P NMR shows a signal at -1.5 ppm corresponding to unhydrolysed PhOPO_3^{2-} at $t = 0$ (Figure 2.8, trace B). After 19 hours at 37°C the major signal present is now observed at 8.6 ppm which is at an identical chemical shift to $[\text{L}^1_2\text{Zn}_3(\text{PO}_4)]^{3+}$ and after 44 hours no signal corresponding to PhOPO_3^{2-} is observed (Figure 2.8, trace C, D). In a similar experiment using 4-nitrophenyl phosphate no ^{31}P signals could be detected that corresponded to the starting material following mixing with the Zn^{2+} complex indicating almost immediate hydrolysis. Only

$[\text{L}^1_2\text{Zn}_3(\text{PO}_4)]^{3+}$ was observed, coupled with a rapid yellowing of the solution due to the formation of 4-nitrophenolate.

Given the importance of protein phosphorylation in inter- and intra- cellular signalling and to cell function, and its common dysregulation in cancers, it was next analysed whether the zinc complex could dephosphorylate phosphorylated amino acids serine, threonine and tyrosine.^{100,101} Indeed, the zinc complex resulted in dephosphorylation of phosphorylated amino acids serine- PO_3^{2-} and tyrosine- OPO_3^{2-} at similar hydrolysis rates to PhOPO_3^{2-} with substantial hydrolysis occurring over 24 hours and completion after 48 hours (Figure 2.8, spectra E-H; M-P). Dephosphorylation of the amino acid threonine- OPO_3^{2-} by the zinc complex was much slower however and after 48 hours threonine- OPO_3^{2-} was still the major species (Figure 2.8, spectra I-L). Differences in reactivity towards different substrates can be attributed to both steric and electronic effects. The difference in reactivity towards phenyl phosphate compared to the 4-nitro derivative is likely a consequence of the electron-withdrawing nitro group, which will enhance the hydrolysis. Serine- PO_3^{2-} , tyrosine- OPO_3^{2-} and threonine- OPO_3^{2-} all have similar electronic properties but threonine has a methyl substituent close to the phosphorylated site and it would seem likely this would result in unfavourable steric interactions upon binding of $[\text{L}^1_2\text{Zn}_3]^{6+}$ as the $-\text{CHCH}_3$ unit would be housed deep in the cleft of the self-assembled species (Figure 2.5). It seems probable that this interaction would reduce the ability of the cryptand to bind the anion and hence reduce the hydrolysis rate. Both serine and tyrosine are less sterically demanding (tyrosine- OPO_3^{2-} is very similar to PhOPO_3^{2-} and serine- PO_3^{2-} has a less sterically demanding $-\text{CH}_2-$ unit in this position) and consequently are hydrolysed more rapidly.

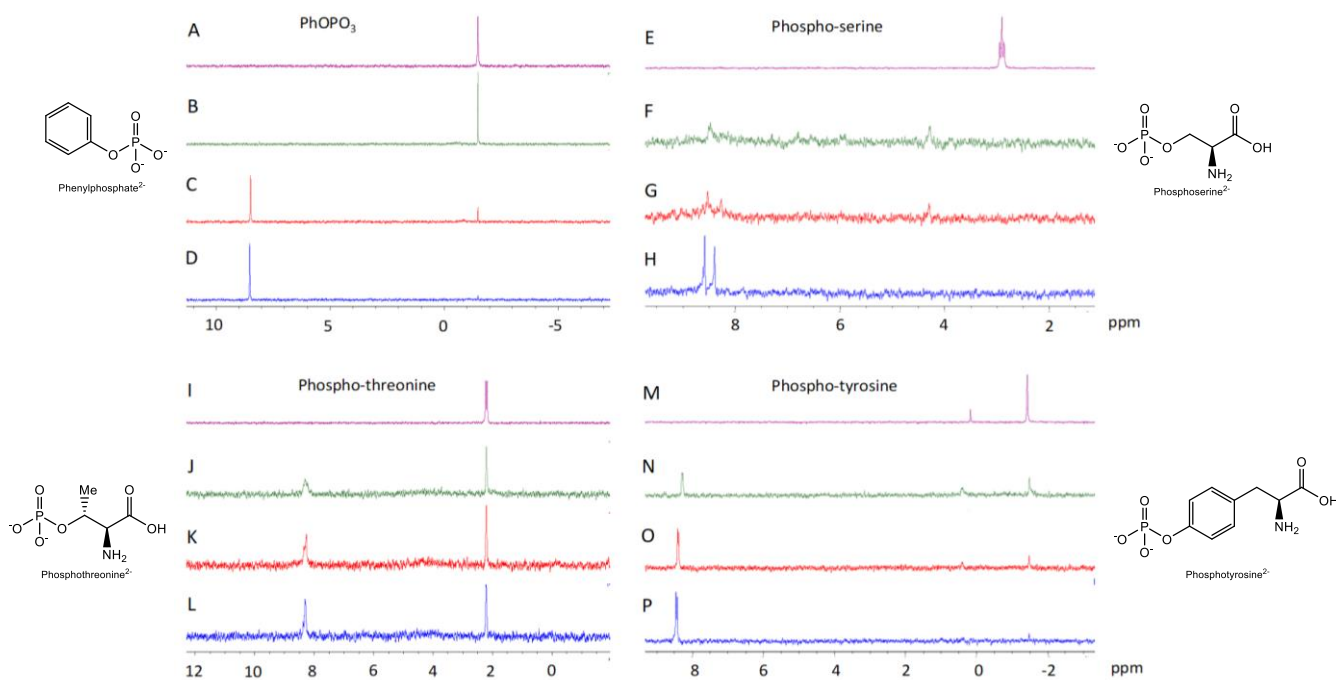


Figure 2.8. Phosphatase activity of $[\text{L}^1_2\text{Zn}_3]^{6+}$. Proton coupled ^{31}P NMR spectra using different substrates including PhOPO_3 (spectra A to D), serine phosphate (spectra E to H), threonine phosphate (spectra I to L) and tyrosine phosphate (spectra M to P). Specific details for each ^{31}P NMR spectra are as follows: Spectra A, E, I and M represent substrate alone (44 hrs incubated at 37 °C); Spectra B, F, J and N represent $[\text{L}^1_2\text{Zn}_3]^{6+}$ plus substrate ($t = 0$ min); Spectra C, G, K and O represent $[\text{L}^1_2\text{Zn}_3]^{6+}$ plus substrate incubated at 37 °C for 19 hours; Spectra D, H, L and P represent $[\text{L}^1_2\text{Zn}_3]^{6+}$ plus substrate incubated at 37 °C for 44 hours. The ^{31}P NMR of $[\text{L}^1_2\text{Zn}_3(\text{PO}_4)]^{3+}$ gives a signal at 8.6 ppm. The doubling up of some of the ^{31}P signals in $[\text{L}^1_2\text{Zn}_3(\text{PO}_4)]^{3+}$ (H, P and L) is attributed to formation of a mixture of diastereoisomers between the racemic cryptand and the resolved chiral amino acids which will form an ion-pair ($[\text{L}^1_2\text{Zn}_3(\text{PO}_4)](\text{RCH}(\text{NH}_2)\text{CO}_2)^{2-}$) and does not occur with the achiral phenyl phosphate.

The rate of substrate hydrolysis is also dependent upon the metal used in the self-assembly process. It is clear from the solid-state and ESI-MS data that $[\text{L}^1_2\text{Cu}_3]^{6+}$ does not hydrolyse phenyl phosphate but incorporates this anion within the assembly e.g. $[\text{L}^1_2\text{Cu}_3(\text{PhOPO}_3)]^{4+}$. Comparison of the reactivity

of the Zn^{2+} species versus the Mn^{2+} by monitoring the hydrolysis of 4-nitrophenyl phosphate by UV-Vis-NIR spectroscopy shows that after 24 hours the Mn^{2+} has hydrolysed with three times more phosphate, indicating that the manganese-based complex is more active than the zinc-based species.

2.2. Chemosensitivity studies

The ability of the complexes to hydrolyse the phosphorylated amino acids prompted biological studies. These studies focused on (a) determining the potency of complexes against cancer and non-cancer cells; (b) by comparing the responses of cancer and non-cancer cells, an *in vitro* selectivity index can be determined (expressed as the ratio of the IC_{50} values for non-cancer cells to cancer cells); and (c), assessing the activity of potent and selective complexes against a panel of purified kinases in cell-free assays.

Various cancer cell lines were exposed to $[L^1_2Cu_3]^{6+}$, $[L^1_2Zn_3]^{6+}$ and $[L^1_2Mn_3]^{6+}$; both the zinc- and copper-based complexes displayed IC_{50} (i.e. the concentration needed to inhibit half of the maximum biological response) values at the sub-micromolar level – the zinc-based complex in particular had typical IC_{50} values between 0.07 and 0.5 μM , with the notable exceptions being the pancreatic cancer cell lines PSN1 and MiaPaCa2, and the glioblastoma cancer stem cell model GBM1 (Figure 2.9). Despite the inherent chemoresistance of cancer stem cells,¹⁰² both complexes showed preferential activity toward the GBM1 cell line compared to all three tested non-cancerous cell models which included human brain progenitor cells (NP1). MiaPaCa2 was inherently resistant to both complexes, having an IC_{50} value of $>10 \mu M$; however, this was still 2.5 – 3 orders of magnitude lower than those for the ARPE-19 and MCF10A non-cancerous cells (IC_{50} values of $>150 \mu M$ ARPE-19 and MCF10A cell lines when exposed to $[L^1_2Zn_3]^{6+}$).

The impressive selectivity of the complexes is indicated by both the copper- and zinc-based complexes displaying selectivity indices (SIs) of over 10-fold for most cancer cell lines when tested against all three non-cancerous cell models. The copper complex displayed selectivity indices of over 100, approaching ~600 in the case of HCT116 p53^{-/-} cancer cells when tested against the non-cancerous MCF10A model; the zinc complex displayed extraordinarily high values which were over 2000 in the case of the HCT116 p53^{-/-} cancer cells when compared to the non-cancerous cell lines ARPE-19 and MCF10A. Whilst these results are substantially better than comparable values for the clinically-approved platinate chemotherapy drugs commonly used (Figure 2.9a – c, cf. d and e), the manganese-based complex displayed comparable potency and selectivity indices compared to the platinate compounds (Figure 2.9d and e).

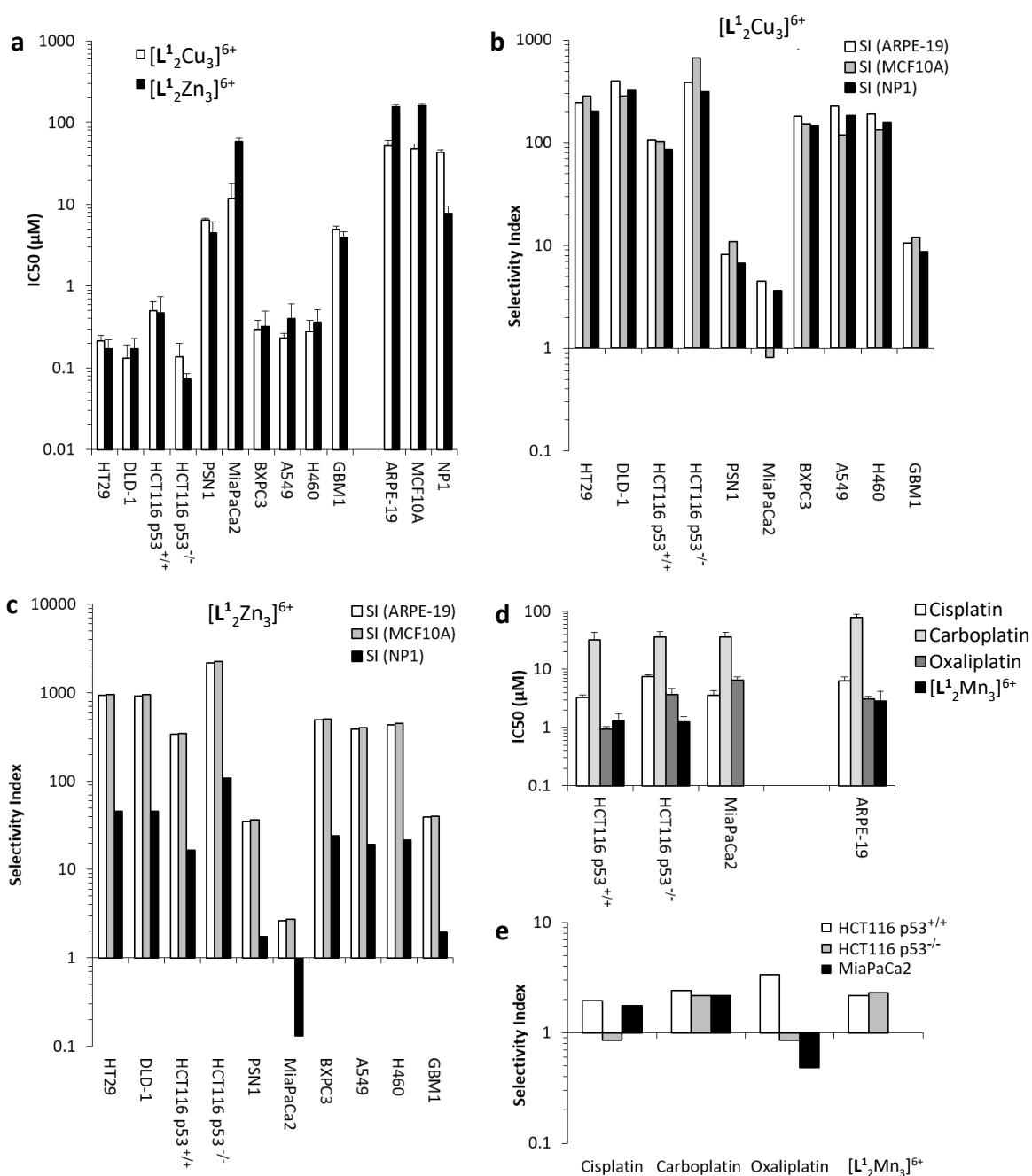


Figure 2.9. Chemosensitivity response of a panel of human cancer and non-cancer cell lines to 96 hours continuous exposure to self-assembling test compounds. a) the potency of compounds tested against cancer cell lines versus non-cancer cell lines*; b) Selectivity index (SI)** for $[L^1_2Cu_3]^{6+}$; c) Selectivity index (SI)** for $[L^1_2Zn_3]^{6+}$; d) IC_{50} values for the clinically approved platinates (cisplatin, oxaliplatin and carboplatin) and $[L^1_2Mn_3]^{6+}$; e) corresponding SI** results (e).

*cancer cells tested: HT-29, DLD-1, HCT116 p53^{+/+} and p53^{-/-}, PSN1, MiaPaCa2, BxPC3, A549, H460 and GBM1; non-cancer cells tested: ARPE-19, MCF10A and NP1. Each value represents the mean $IC_{50} \pm$ standard deviation from a minimum of three independent experiments.

**SI is defined as the mean IC_{50} against the particular non-cancer cell line model divided by the mean IC_{50} against the particular cancer cell line. SI values > 1 indicate that the test compound is more active against the particular cancer cell line than the corresponding non-cancer cells. As the SI value is calculated using the mean IC_{50} values, experimental error is not included in these figures.

These highly promising results prompted further investigation. Pre-loading the capsule with various anions at the point of assembly (prior to cell exposure) affects both the potency and selectivity of the complexes. This is variable both between each complex and dependent on anion. The zinc complex in particular displayed distinct results from those using the unloaded capsule – for example, the capsule was around 10% as potent against several of the cancer cell lines when doped with sulfate and phenylphosphate but resulted in over 30 times increased selectivity against the PSN1 cancer cell line in comparison to the ARPE-19 non-cancerous cell model (Figure 2.10). However, the HT-29, DLD-1, BxPC3 and A549 lines all displayed increased resistance to the zinc complex when pre-assembled with anion, demonstrating some potential for the tunability of the complex by altering the metal and/or anion.

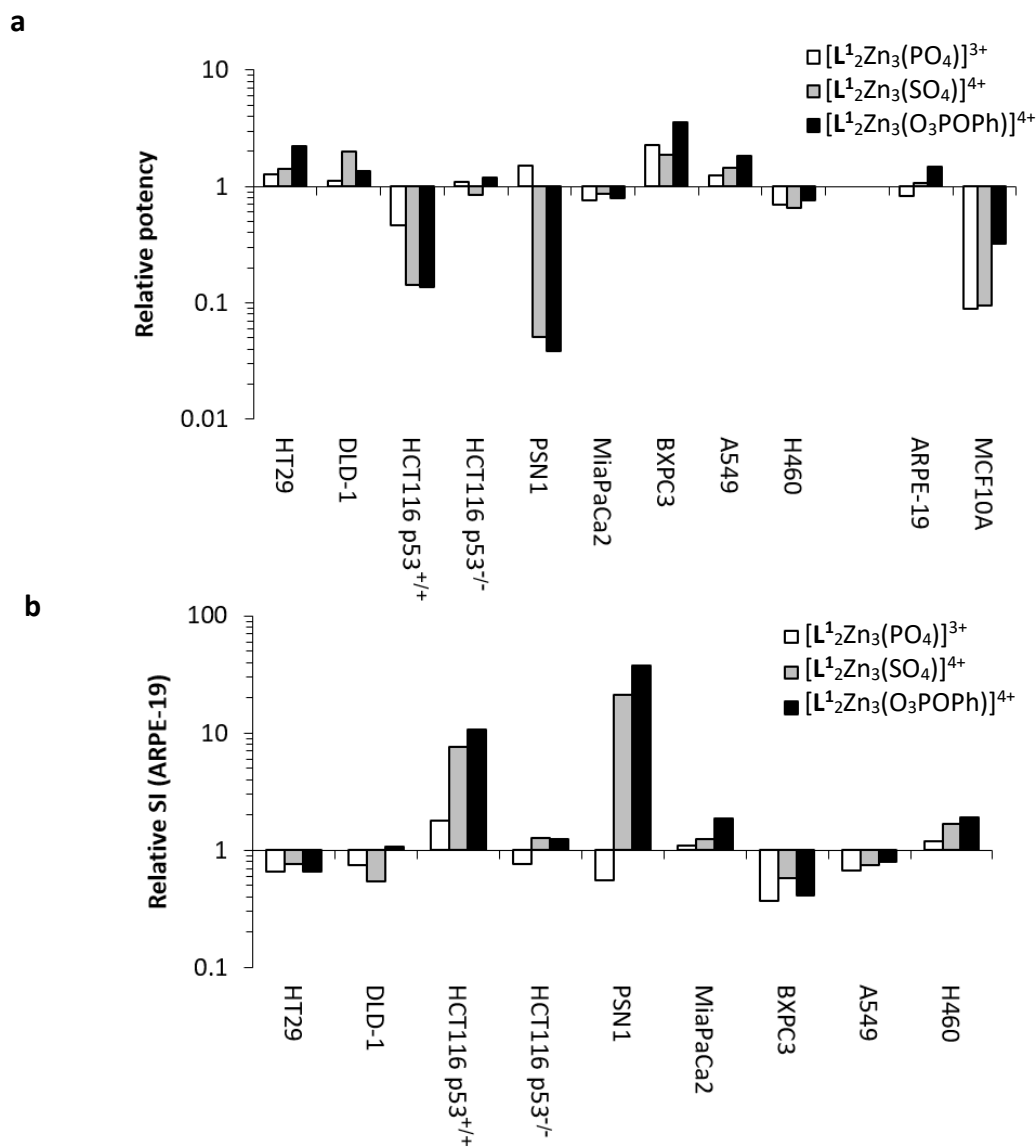


Figure 2.10. Effect of the complex anion on potency and selectivity. a) The effect of various anions on the relative potency* of the Zn^{2+} complex; b) Effects of the anion on selectivity; these results are expressed as relative SI**.

*Relative potency is defined as the IC_{50} of $[L^1_2Zn_3(PO_4)]^{3+}$, $[L^1_2Zn_3(SO_4)]^{4+}$ or $[L^1_2Zn_3(O_3POPh)]^{4+}$ divided by the IC_{50} of $[L^1_2Zn_3]^{6+}$ (values < 1 and > 1 indicate increased and decreased potency respectively).

**Relative SI is defined as the SI of $[L^1_2Zn_3(PO_4)]^{3+}$, $[L^1_2Zn_3(SO_4)]^{4+}$ or $[L^1_2Zn_3(O_3POPh)]^{4+}$ divided by the SI of $[L^1_2Zn_3]^{6+}$ (values > 1 and < 1 indicate increased and decreased selectivity respectively).

2.3. Mechanistic studies

Given the ability of the zinc-based complex to dephosphorylate the amino acids phosphothreonine, phosphoserine and phosphotyrosine (Figure 2.8) and the copper-based complex to bind phenylphosphate (Figure 2.4), further investigation led to examination of the effects of the complexes on kinases (a class of enzyme which catalyse addition of phosphate groups to biological substrates). Both of these complexes displayed inhibitory activity against a variety of protein kinases with many cases approaching 100% inhibition at the tested complex concentration (Figure 2.11a and b). The copper-based complex displayed inhibition of a greater number of kinases than the zinc-based complex, which may reflect the lower selectivity index of the copper-based complex. One hypothesised mechanism of inhibition, the direct dephosphorylation of ATP by the complexes, was disproved by mass spectroscopy; very little or no hydrolysis was observed when ATP was incubated with either complex alone (Figure 6.15 and Figure 6.16), nor was a phosphorylated AMPK peptide despite the fact that AMPK was one of the most heavily inhibited kinases (Figure 2.11a and b).

Conversely, several kinases were stimulated by the complexes (Figure 2.11c and d), possibly through activity on the kinases themselves; dephosphorylation (through the zinc complex) or binding (through the copper complex) of the phosphorylated regulatory amino acids may lead to kinase inhibition or stimulation.

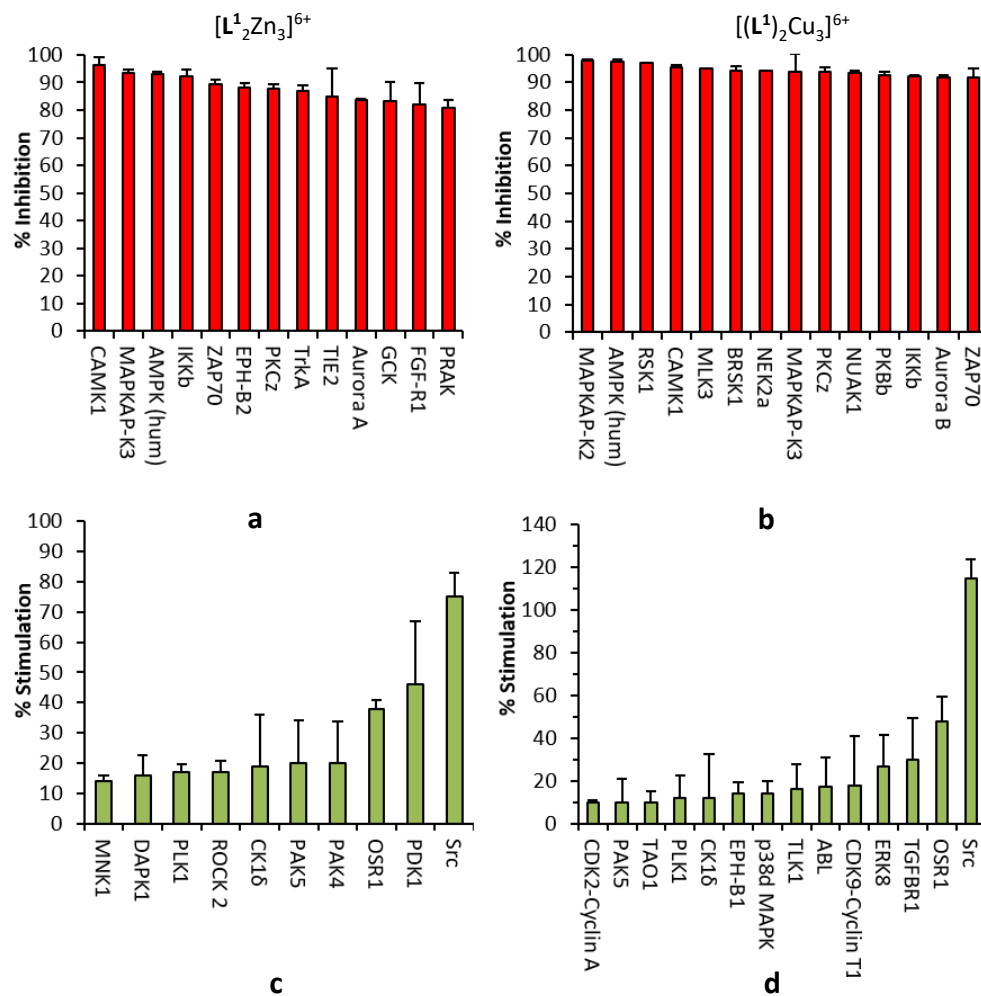


Figure 2.11. Effects of [L¹₂Zn₃]⁶⁺ (a and c) and [L¹₂Cu₃]⁶⁺ (b and d) on the activity of purified human kinases. a) percentage inhibition of kinases by [L¹₂Zn₃]⁶⁺; b) percentage inhibition of kinases by [L¹₂Cu₃]⁶⁺; c) Kinases whose activity is stimulated by [L¹₂Zn₃]⁶⁺; (d) Kinases whose activity is stimulated by [L¹₂Cu₃]⁶⁺. Kinases were exposed to complexes at a concentration of 10 μM; full results are presented in the Experimental section.

To further investigate the mechanisms of this activity, various phosphorylated amino acids of two key kinases (AMPK and Src) were analysed following incubation of the kinases with the two complexes. Phosphorylation of AMPK at threonine-172 (p-T172) stimulates AMPK activity;¹⁰³ however, the two complexes significantly reduced the p-T172 levels in the AMPK kinase, detected by immunoblotting at a molecular weight of ~63 kDa (Figure 2.12). For the Src kinase, effects on the Y527 and Y416

regulatory phosphorylated amino acids were examined. Phosphorylation of the Y527 and Y416 domains is known to inhibit and promote the kinase activity of the Src kinase respectively.^{104,105} Incubation of the Src with the zinc-based complex resulted in a decrease in p-Y527 of around 30% and an increase in p-Y416 of around 5-fold (Figure 2.12), both of which would be expected to promote kinase activity in Src.

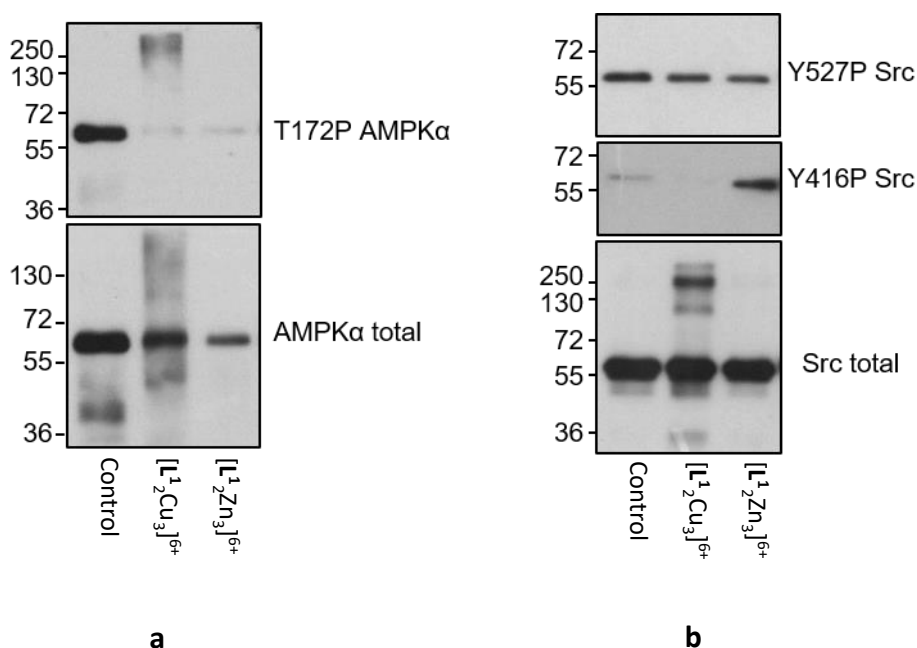


Figure 2.12. Western blot analysis of purified recombinant a) AMPK and b) Src following exposure to [L¹₂Zn₃]⁶⁺ and [L¹₂Cu₃]⁶⁺. Purified enzymes were incubated with complexes (50 μM) for 4 hours in the presence of ATP prior to analysis.

Evidently, these complexes are toxic to cancer cells *in vitro* but are substantially less toxic to non-cancerous cells. Furthermore, the toxicity and possible mode of action changes with different metal ions and the selectivity can be further modulated by the addition of different anions encapsulated within the cryptand. It is possible that a large variety of complexes can be generated by varying the ligand strand, metal ion and encapsulated anion easily generating a large library of compounds – and these could (and looking at the data described - would) generate different pharmaceutical compounds

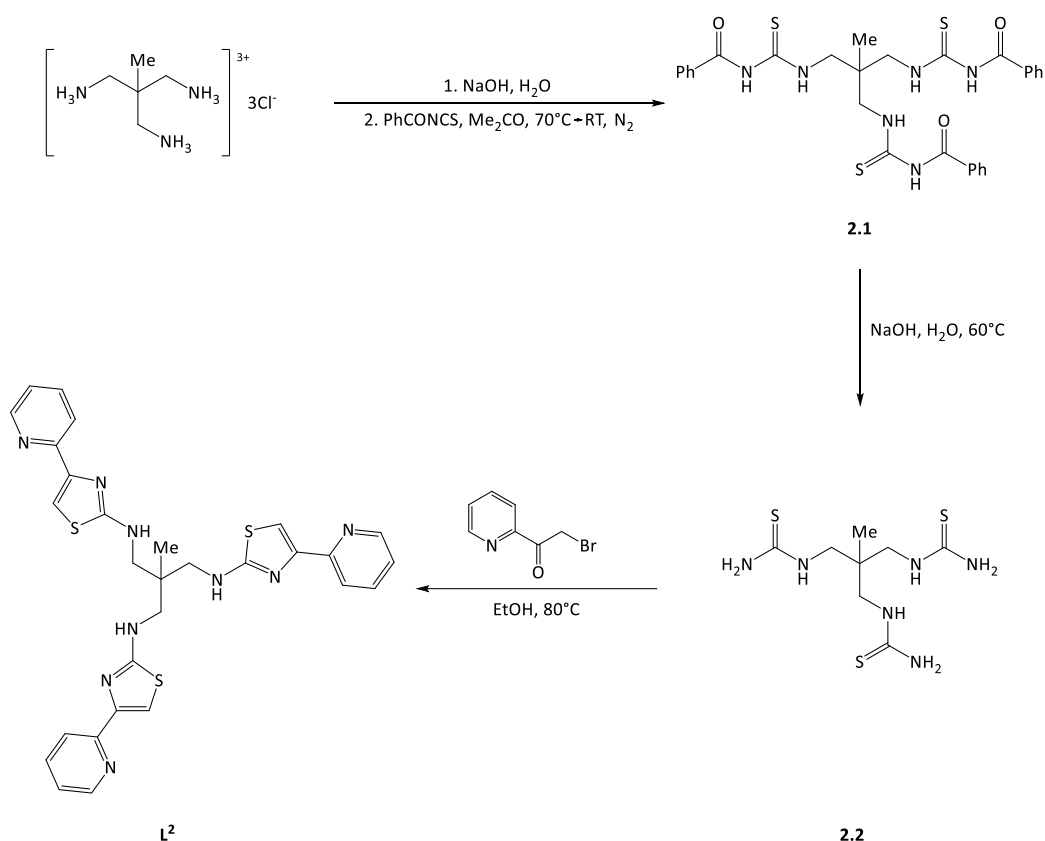
which would all have different effects on a variety of cancer cell lines. The ability of using supramolecular chemistry to self-assemble bioactive compounds in such a manner would have obvious and far-reaching implications.

3. Spacer Effects on Anion Selectivity

3.1. Ligand L^2

3.1.1. Synthesis

Ligand L^2 is similar to both ligand L^1 in that the ligand contains three pyridyl-thiazole-amine domains connected by a central aliphatic bridging unit but in the case of L^2 this bridge consists of a *tris-N*-substituted 1,1,1-*tris*(aminomethyl)ethane group. It was envisaged that this smaller spacer would form a smaller cavity on co-ordination, resulting in a capsule more selective to smaller anions. This ligand was produced from 1,1,1-*tris*(aminomethyl)ethane trihydrochloride by following a similar scheme to the synthesis of ligand L^1 (Scheme 3.1).¹⁰⁶



Scheme 3.1. Synthesis of ligand L^2 from 1,1,1-*tris*(aminomethyl)ethane trihydrochloride.¹⁰⁶

Following deprotonation of the starting material, the overnight reaction of the triamine with benzoyl isothiocyanate produced a yellow-orange solution with a white ammonium chloride precipitate, formed during the initial in-situ preparation of benzoyl isothiocyanate.¹⁰⁷ The pure product **2.1** was extracted from this mixture by precipitation of the crude product by pouring the solution onto water, extraction the subsequent orange oil into dichloromethane and product purified by recrystallisation from hot ethanol. This was confirmed to be the product by the addition of the signature thioamide and amide peaks at 11.1 and 9.1 ppm respectively, as well as the presence of aromatic signals indicative of *mono*-substituted phenyl- groups (Figure 3.1).

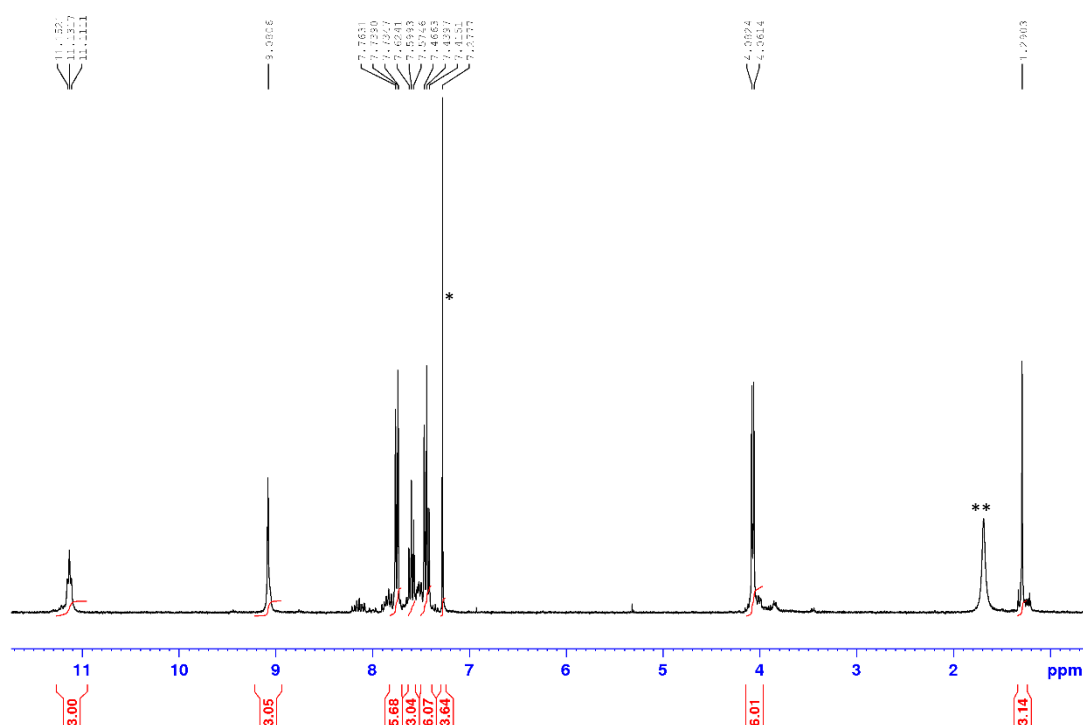


Figure 3.1. ^1H NMR (CDCl_3) spectrum of **2.1**. N.B. the signals at 11.1 and 9.1 ppm corresponding to the two amide environments. * CHCl_3 impurity. ** H_2O impurity.

From this, the intermediate was debenzoylated using hot sodium hydroxide solution to hydrolyse this to the thiourea product **2.2**. The product was confirmed to be debenzoylated by ^1H NMR spectroscopy,

due to the absence of the three sharp aromatic signals corresponding to the phenyl- groups (Figure 3.2).

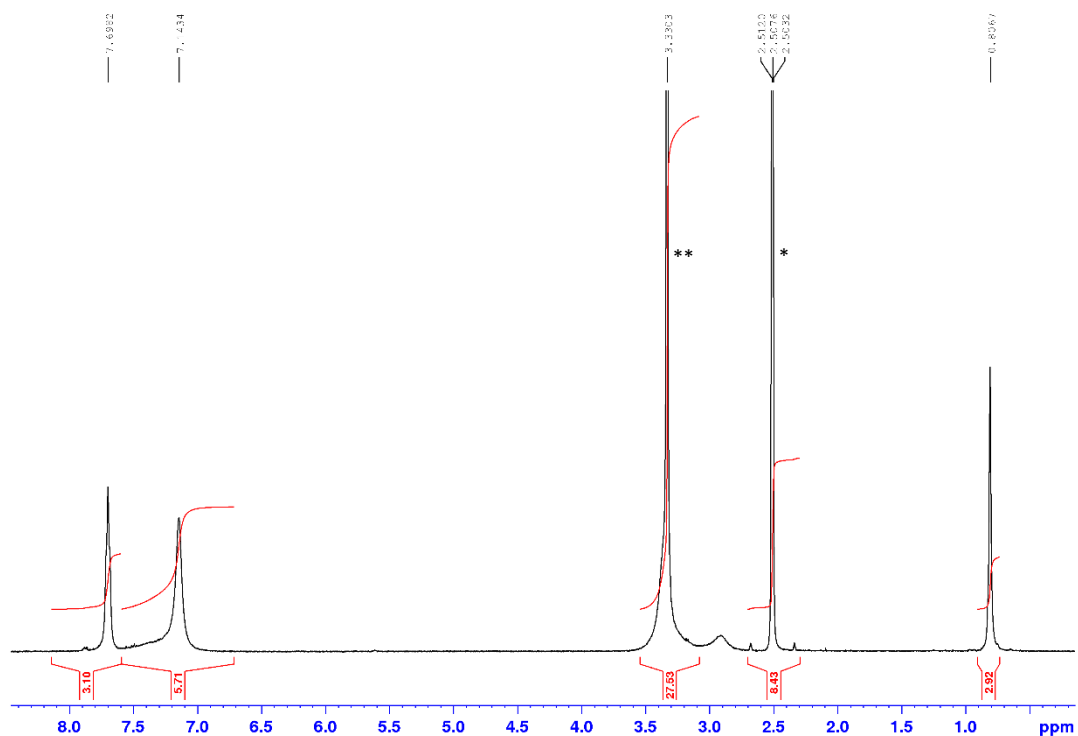


Figure 3.2. ^1H NMR ($(\text{CD}_3)_2\text{SO}$) spectrum of **2.2**. N.B. the signals at 7.7 and 7.1 ppm corresponding to the thiourea proton environments. $*$ $(\text{CD}_3)(\text{CD}_2\text{H})\text{SO}$ impurity. $**$ H_2O impurity, coincident with the signal corresponding to the CH_2NH environment, as evidenced by the slight “shoulders” on the signal.

Finally, the *tris*-thiourea **2.2** was converted to the final ligand by reaction with 2-(α -bromoacetyl)pyridine in ethanol, leaving the crude product as its hydrobromide salt. This was deprotonated in ammonia and filtered to isolate pure ligand **L²**. This was confirmed by ^1H NMR, as evidenced by the presence of the five aromatic signals corresponding to the pyridyl-thiazole domain, and the absence of the broad singlet characteristic of the $-\text{NH}_2$ groups in the *tris*-thiourea **2.2** starting material (Figure 3.3).

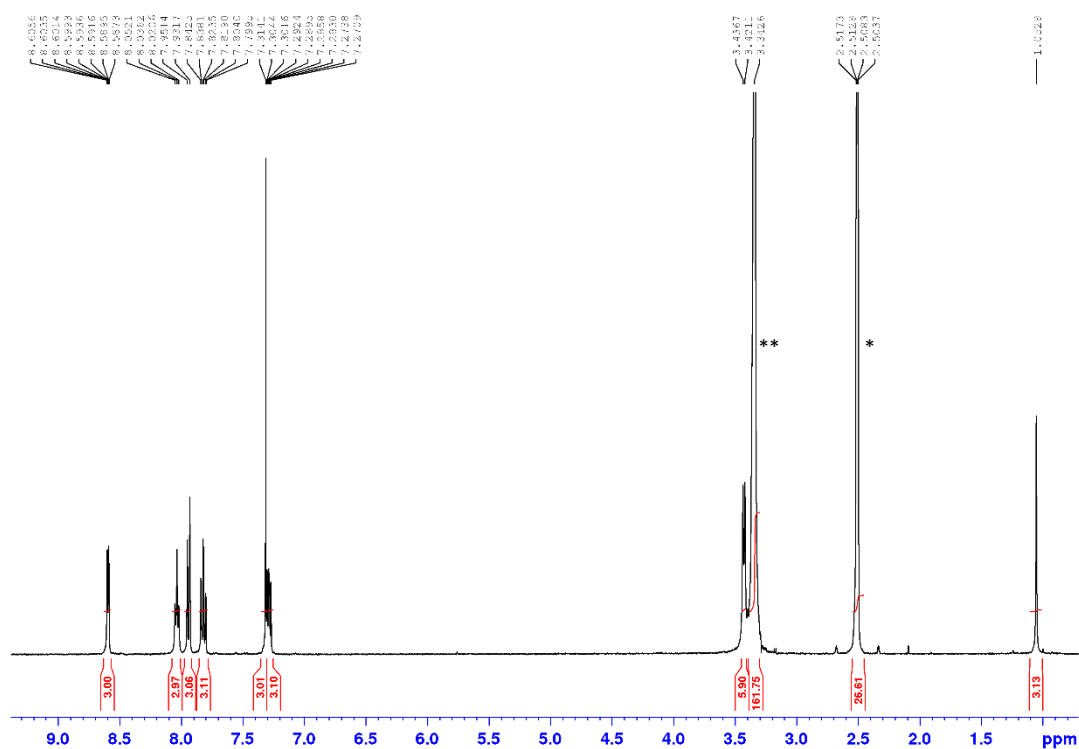


Figure 3.3. ^1H NMR ($(\text{CD}_3)_2\text{SO}$) spectrum of L^2 . N.B. the aromatic signals indicative of the pyridyl- (8.60, 7.94, 7.82, 7.29 ppm), thiazole- (7.31 ppm) and amine- (8.04 ppm) groups. * $(\text{CD}_3)(\text{CD}_2\text{H})\text{SO}$ impurity. ** H_2O impurity.

3.1.2. Co-ordination chemistry

When ligand L^2 is reacted with various metal salts and anions, colour changes indicative of complex formation are observed. However, despite over 100 attempts to produce crystalline material with various solvents, metal salts, anions, techniques and conditions, no crystals of sufficient analytical quality could be obtained. Whilst the absence of crystalline material does not mean that the ligand does not co-ordinate the metal cations (indeed the colour change is indicative of co-ordination complexes forming), it is possible that lack of crystals suitable for X-ray diffraction is due to the lack of a single molecular entity and perhaps oligomeric compounds are formed. This may be due in part to

the smaller size of the ligand bridge resulting in the complex to be too small to properly encapsulate anions, in comparison with ligand L^1 (e.g. four bonds separating the amine units in L^2 as opposed to six for L^1 , Figure 3.4). Analysis by ESI-MS would be relatively uninformative; whilst it would undoubtedly give ions corresponding to complex formation, the actual species in solution would be unclear.

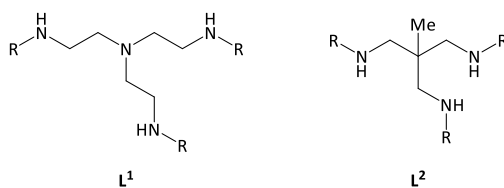
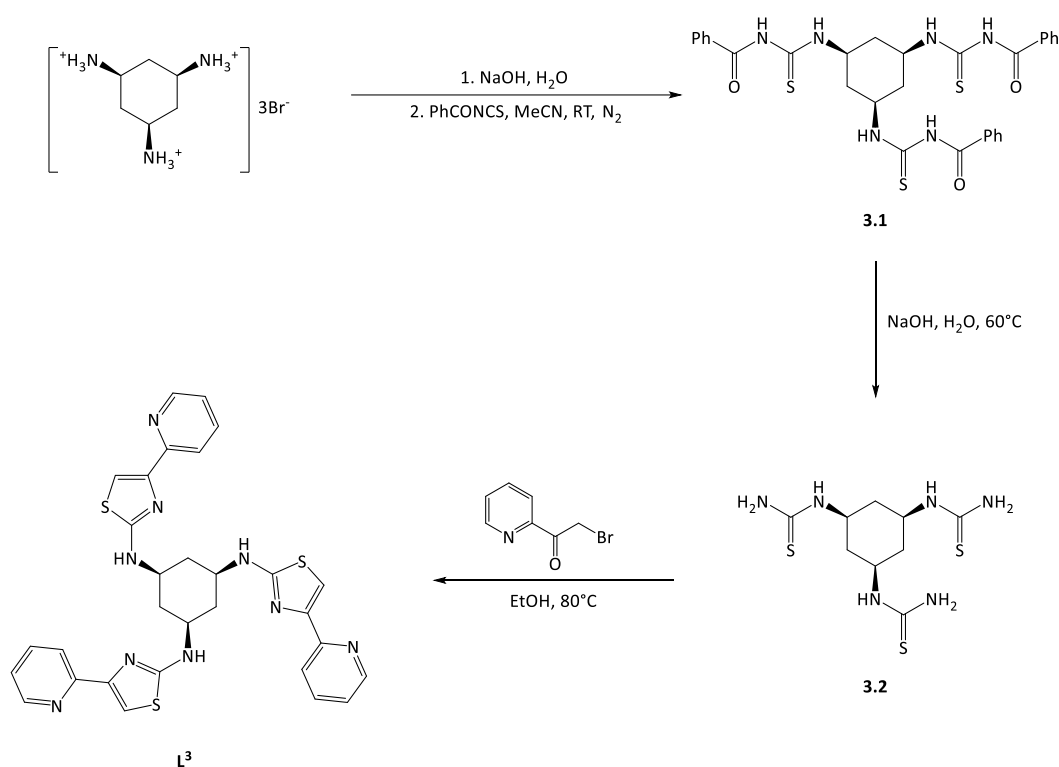


Figure 3.4. Comparison of the two bridging groups in L^1 and L^2 . N.B. the much shorter chain between the three -NH domains in L^2 ($RN-CH_2CCH_2-NR$) vs L^1 ($RN-CH_2CH_2NCH_2CH_2-NR$).

3.2. Ligand L³

3.2.1. Synthesis

Ligand L³ was designed to be similar to L¹, incorporating three bidentate domains joined by a central bridging group.¹⁰⁸ However, in this case it would employ a *cis,cis*-1,3,5-triaminosubstituted cyclohexane bridging unit. This was synthesised from *cis,cis*-1,3,5-cyclohexanetriamine as a starting material (Scheme 3.2).^{109,110}



Scheme 3.2. Synthesis of ligand L³ from *cis,cis*-1,3,5-cyclohexanetriamine trihydrobromide.^{109,110}

Following deprotonation of the starting material with concentrated sodium hydroxide solution, *cis,cis*-1,3,5-cyclohexanetriamine was reacted with benzoyl isothiocyanate in acetonitrile under an atmosphere of nitrogen. The resultant pale-yellow precipitate was isolated by vacuum filtration and washed with minimal acetonitrile. The product was confirmed pure by the presence of three signals in the aromatic region of the ¹H NMR spectrum, in addition to the two amine signals corresponding to the thiourea group (Figure 3.5).

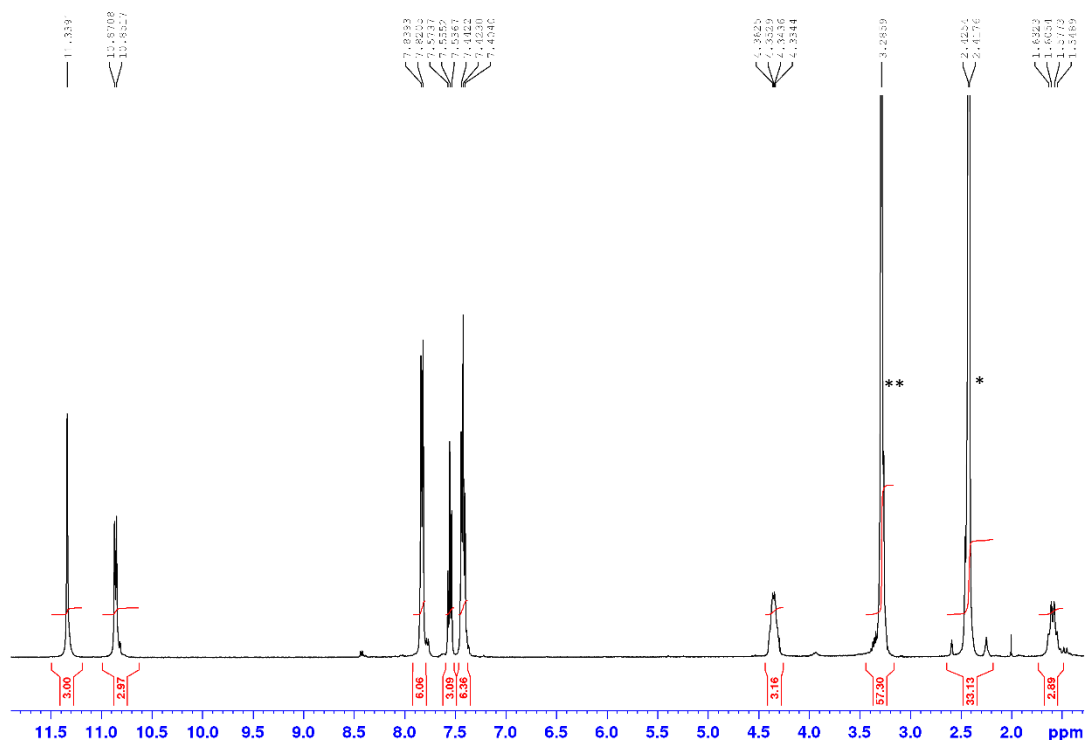


Figure 3.5. ^1H NMR ($(\text{CD}_3)_2\text{SO}$) spectrum of **3.1**. N.B. Three aromatic signals corresponding to the three mono-substituted phenyl groups. One aliphatic signal is coincident with one of the solvent signals. * $(\text{CD}_3)(\text{CD}_2\text{H})\text{SO}$ impurity. ** H_2O impurity.

This was then hydrolysed to the *tris*-thiourea **3.2** by stirring in hot sodium hydroxide solution overnight, leaving the product as a white precipitate which was isolated by vacuum filtration and washed with minimal water. The ^1H NMR spectrum for this compound has very broad signals (which is common for compounds containing multiple thiourea units) due to strong inter- and intra-molecular hydrogen-bonding interactions (Figure 3.6). Nevertheless, no starting material remained and only a small amount of benzoic acid was present, so this product was used without further purification.

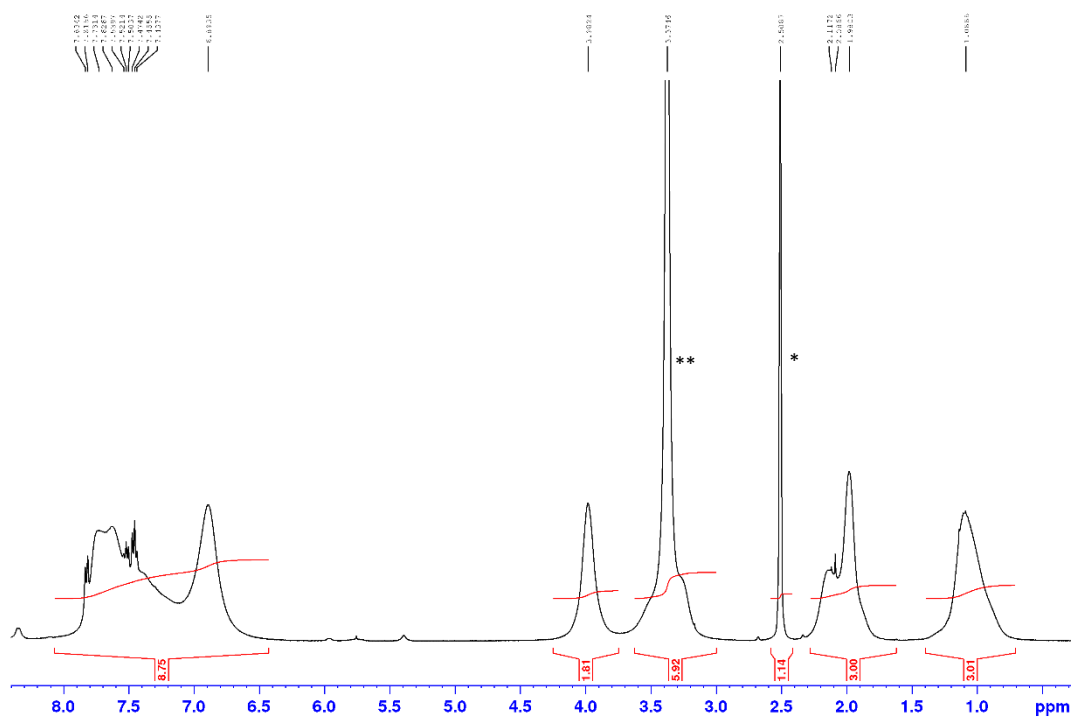


Figure 3.6. ^1H NMR ($(\text{CD}_3)_2\text{SO}$) spectrum of **3.2**. N.B. Very broad signals as a result of intra- and intermolecular hydrogen-bonding. * $(\text{CD}_3)(\text{CD}_2\text{H})\text{SO}$ impurity. ** H_2O impurity.

The *tris*-thiourea **3.2** was then reacted with 2-(α -bromoacetyl)pyridine in ethanol to produce the product as its insoluble, yellow hydrobromide salt. This was isolated by vacuum filtration, stirred in concentrated ammonia, filtered once again and washed with cold water to leave the pure ligand **L³**. This was confirmed by ^1H NMR spectroscopy, as signals corresponding to both thiazole and pyridyl-groups are present (Figure 3.7). The ^{13}C spectrum also contains the correct group of signals for this compound; two aliphatic carbon environments and eight aromatic environments (Figure 3.8).

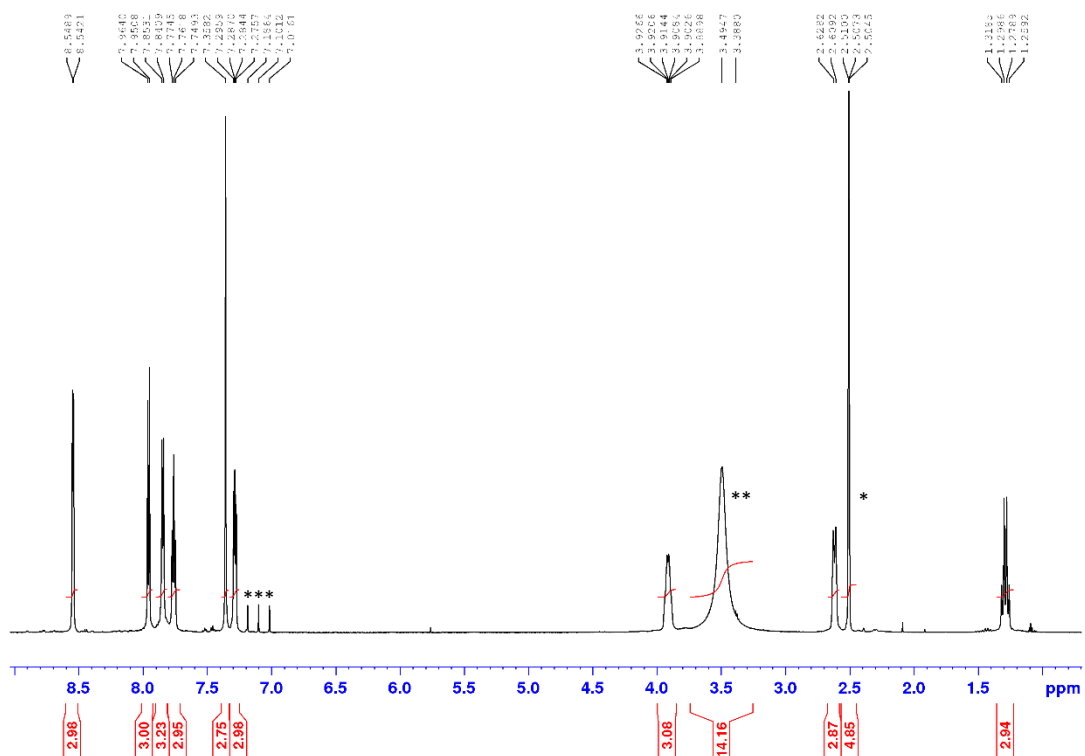


Figure 3.7. ^1H NMR ($(\text{CD}_3)_2\text{SO}$) spectrum of L^3 . N.B. Three aliphatic and six aromatic proton environments. $*$ $(\text{CD}_3)(\text{CD}_2\text{H})\text{SO}$ impurity. $**$ H_2O impurity. $***$ NH_4^+ impurity.

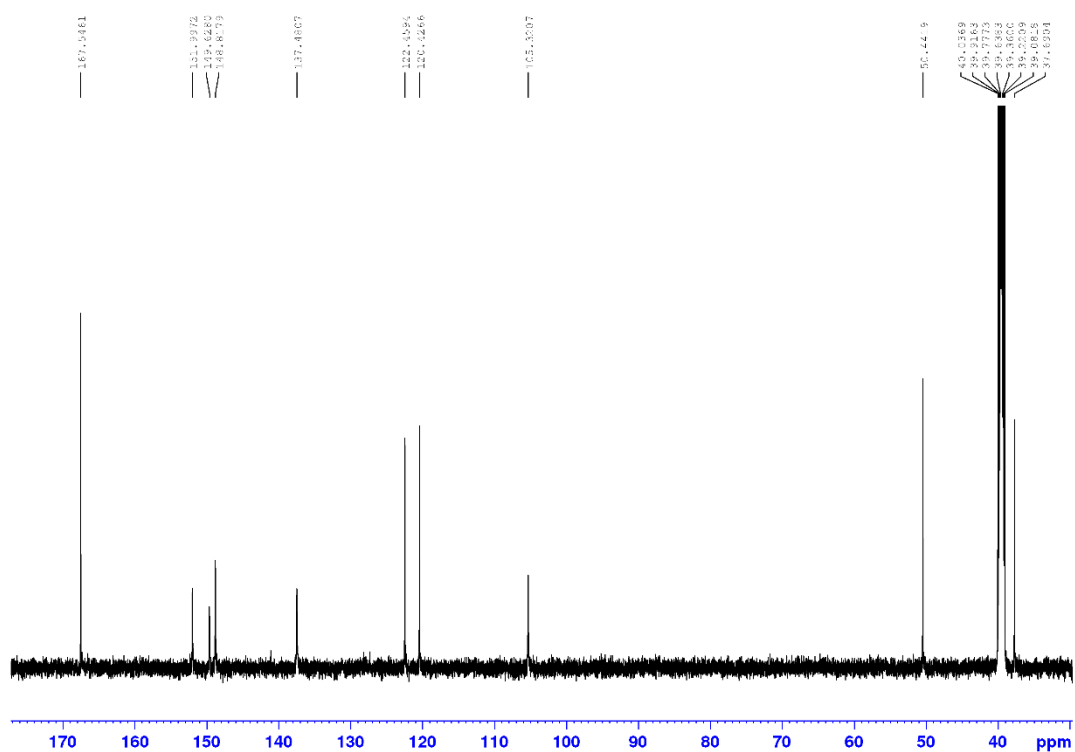


Figure 3.8. ^{13}C NMR ($(\text{CD}_3)_2\text{SO}$) spectrum of L^3 .

3.2.2. Co-ordination chemistry

$[\text{L}^3_2\text{Cu}_3(\text{SO}_4)]^{4+}$

Reaction of ligand L^3 with 1.5 equivalents of copper(II) perchlorate in acetonitrile gave a tan-coloured solution, which turned yellow on addition of half an equivalent of tetra-*N*-butylammonium sulfate. Slow diffusion of diethyl ether into this solution deposited yellow crystals which were analysed by single-crystal X-ray diffraction. In the solid-state, two ligand strands co-ordinate three copper atoms through three thiazole- $\text{N}\cdots\text{Cu}$ and three pyridyl- $\text{N}\cdots\text{Cu}$ interactions (i.e. $[\text{L}^3_2\text{Cu}_3]^{6+}$). In turn, the three copper cations are each co-ordinated to the two ligand strands by four $\text{Cu}\cdots\text{N}$ interactions. In a similar manner to complexes observed with L^1 , this forms a complex which features a cavity and encapsulates a sulfate anion (i.e. $[\text{L}^3_2\text{Cu}_3(\text{SO}_4)]^{4+}$, Figure 3.9). This anion is held in place through three $\text{Cu}\cdots\text{O}$ co-

ordination interactions, formed between three of the oxygen atoms on the sulfate anion and the three copper centres (average Cu...O bond length 2.14 Å); this is supplemented by -NH...O hydrogen-bonding interactions formed between the three metal-bound oxygen atoms of the sulfate anion and the three -NH hydrogen-bond donor sites on one of the ligand strands (average -NH...O bond length 2.02 Å). The remaining oxygen atom on the sulfate anion binds to all three -NH donor sites on the opposing ligand strand (average -NH...O bond length 2.12 Å; Figure 3.9c).

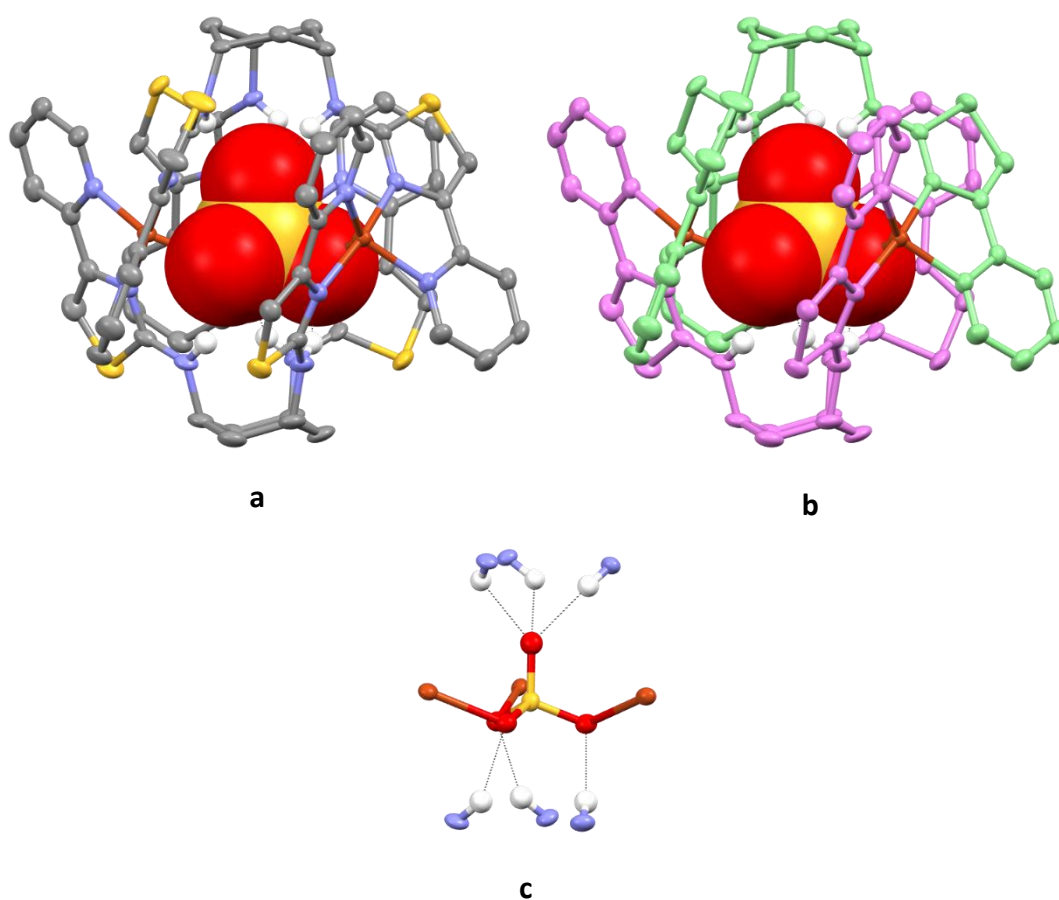


Figure 3.9. a) crystal structure of $[\text{L}^3_2\text{Cu}_3(\text{SO}_4)]^{4+}$; b) crystal structure with ligands coloured for clarity; c) co-ordination and hydrogen-bonding of the metals and ligand to the SO_4^{2-} anion. Colour code: dark orange, Cu^{2+} ; red, O; blue, N; yellow, S; grey, C; white, H (apart from (b) where the ligands have been coloured for clarity). Non-acidic hydrogen atoms and perchlorate anions are omitted for clarity.

Thermal ellipsoids shown at the 50% probability level.

Reaction of the ligand with 1.5 equivalents of copper(II) trifluoromethanesulfonate, followed by half an equivalent of tetra-*N*-butylammonium hydrogen sulfate gave ESI-MS ions at m/z 1954 and 901 corresponding to $\{[\text{L}^3_2\text{Cu}_3(\text{SO}_4)](\text{trif})_3\}^+$ and $\{[\text{L}^3_2\text{Cu}_3(\text{SO}_4)](\text{trif})_2\}^{2+}$ (Figure 3.10).

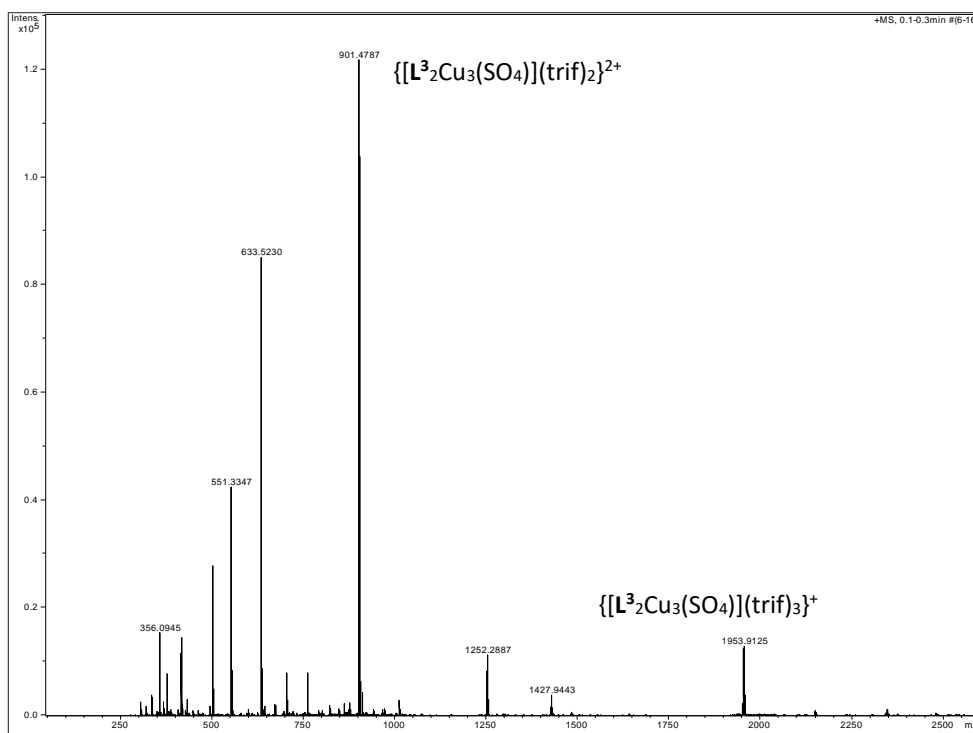


Figure 3.10. ESI-MS of $[\text{L}^3_2\text{Cu}_3(\text{SO}_4)](\text{trif})_4$ showing ions at m/z 1954 and 901 corresponding to $\{[\text{L}^3_2\text{Cu}_3(\text{SO}_4)](\text{trif})_3\}^+$ and $\{[\text{L}^3_2\text{Cu}_3(\text{SO}_4)](\text{trif})_2\}^{2+}$.

$[\text{L}^3_2\text{Cu}_3(\text{Br})]^{5+}$

Reaction of ligand L^3 with 1.5 equivalents of copper(II) tetrafluoroborate in acetonitrile gave a tan-coloured solution, but on addition of aqueous tetra-*N*-butylammonium bromide gave a blue solution. Slow evaporation of this solution deposited dark-blue crystals which were analysed by single-crystal X-ray diffraction. In the solid-state, this complex followed the same structure as that of the sulfate-containing complex whereby two ligand strands co-ordinated three metal centres to form a capsule (i.e. $[\text{L}^3_2\text{Cu}_3]^{6+}$), however instead a bromide anion is encapsulated (i.e. $[\text{L}^3_2\text{Cu}_3(\text{Br})]^{5+}$, Figure 3.11). Due

to the spherical shape and large size of this guest, it is able to interact with all three metal centres simultaneously through Cu⋯Br interactions (average Cu⋯Br bond length 2.93 Å), whilst also forming six hydrogen-bonding interactions with the -NH donor sites on each opposing ligand strand (average -NH⋯Br bond length 2.91 Å; Figure 3.11c).

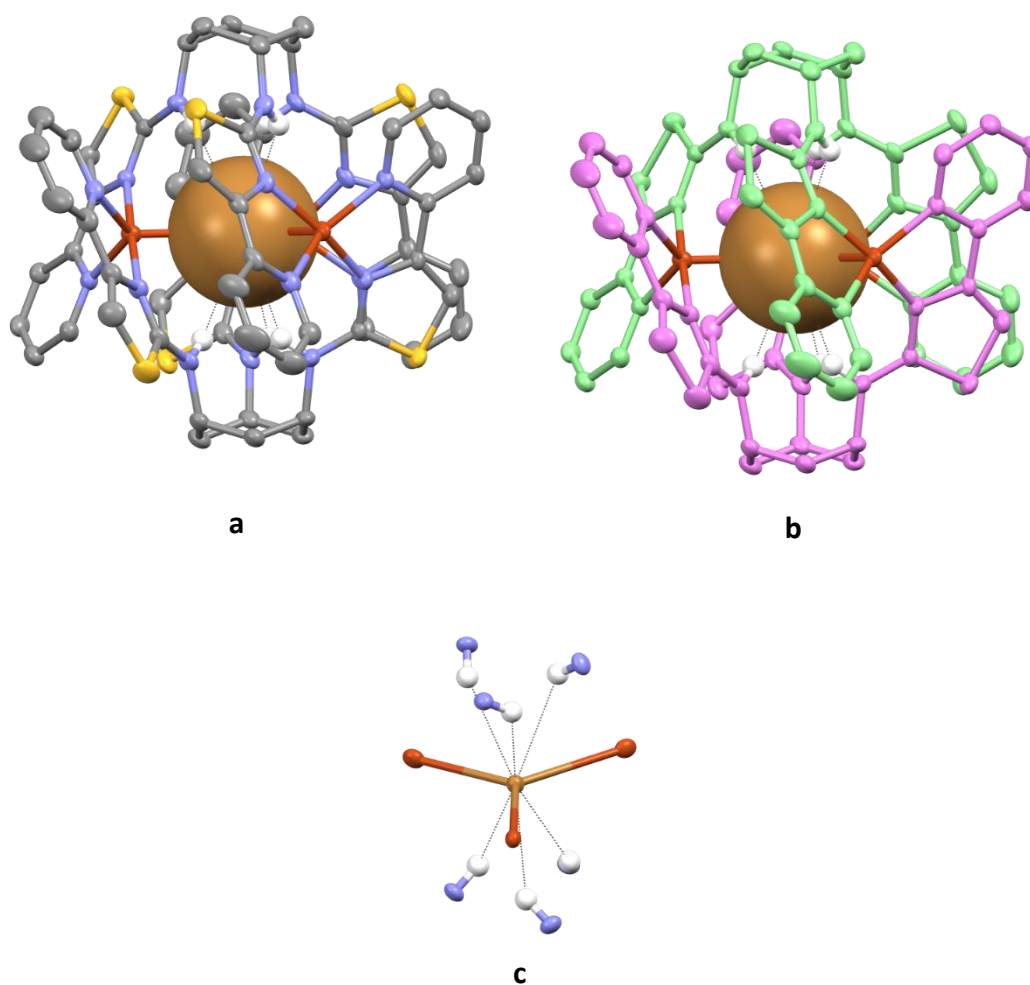


Figure 3.11. a) crystal structure of $[\mathbf{L}^3_2\text{Cu}_3(\text{Br})]^{5+}$; b) crystal structure with ligands coloured for clarity; c) co-ordination and hydrogen-bonding of the metals and ligand to the Br^- anion. Colour code: dark orange, Cu^{2+} ; brown, Br; red, O; blue, N; yellow, S; grey, C; white, H (apart from (b) where the ligands have been coloured for clarity). Non-acidic hydrogen atoms and tetrafluoroborate anions are omitted for clarity. Thermal ellipsoids shown at the 50% probability level.

Reaction of the ligand with 1.5 equivalents of copper(II) trifluoromethanesulfonate and half an equivalent of tetra-*N*-butylammonium bromide gave ESI-MS ions at m/z 2085 and 968 corresponding to $\{[L^3_2Cu_3(Br)](trif)_2\}^+$ and $\{[L^3_2Cu_3(Br)](trif)\}^{2+}$ (Figure 3.12).

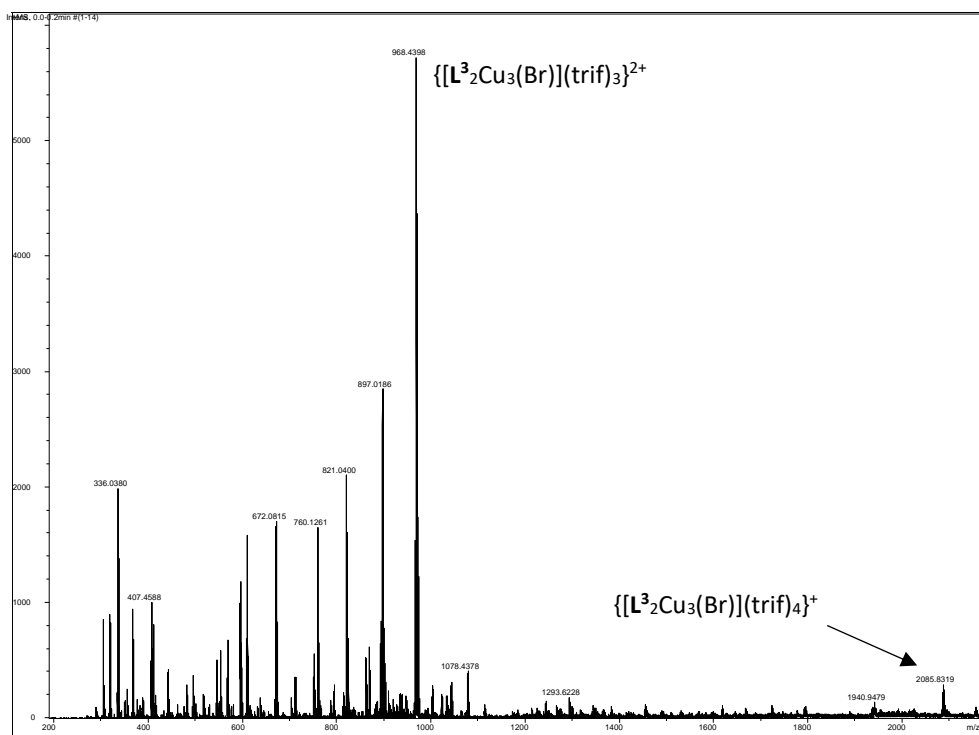
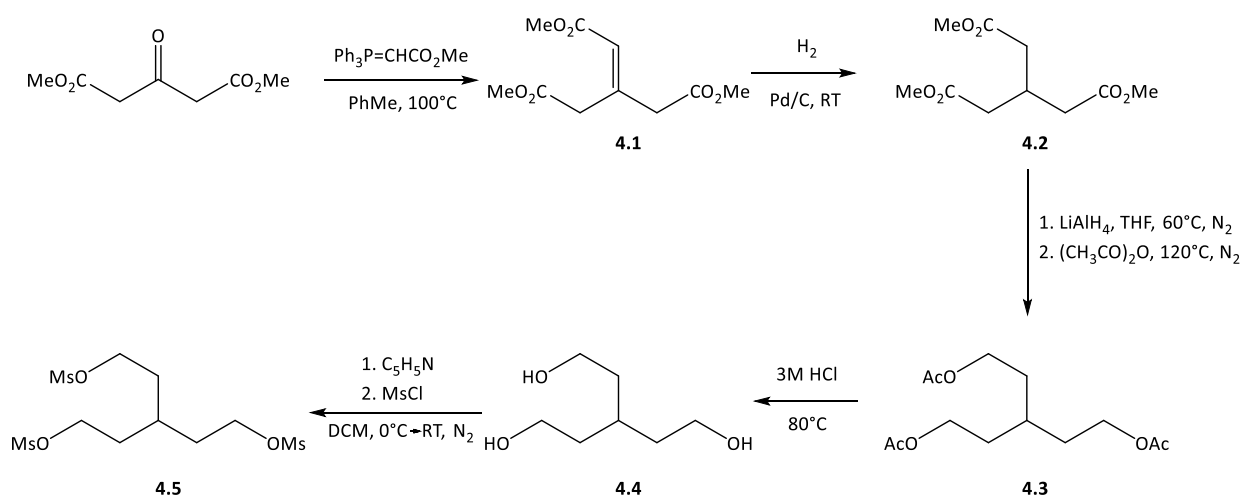


Figure 3.12. ESI-MS of $[L^3_2Cu_3(Br)](trif)_5$ showing ions at m/z 2085 and 968 corresponding to $\{[L^3_2Cu_3(Br)](trif)_4\}^+$ and $\{[L^3_2Cu_3(Br)](trif)_3\}^{2+}$ respectively.

3.3. Ligand L⁴

3.3.1. Synthesis

The tripodal ligand **L**⁴ is structurally identical to **L**¹, but instead of a central amine unit it instead incorporates a central, tertiary methine group. It was envisaged that the introduction of a R₃CH unit may positively influence the anion binding properties as it would allow interaction between the anion and the hydrogen atom as opposed to the unfavourable lone pair – anion interaction possible with complexes of **L**¹. It was predicted that **L**⁴ could be synthesised from the parent triamine, analogous to the synthesis of **L**¹, whereby *tris*-(2-aminoethyl)methane would be reacted with benzoyl isothiocyanate, followed by hydrolysis in hot sodium hydroxide solution and subsequent reaction with 2-(α -bromoacetyl)pyridine in ethanol.⁹⁷ In order to obtain the necessary triamine, the trimesylate precursor **4.5** had to be synthesised first (Scheme 3.3).¹¹¹



Scheme 3.3. Synthesis of $\text{HC}(\text{CH}_2\text{CH}_2\text{OMs})_3$ **4.5** from dimethyl-1,3-acetonedicarboxylate.¹¹¹

Initially, alkene **4.1** was produced by reaction of dimethyl-1,3-acetonedicarboxylate with carbomethoxymethylenetriphenylphosphorane in toluene followed purification by column chromatography. The pure product was confirmed by the presence of a singlet at 5.97 ppm in the ¹H

NMR spectrum indicative of a single alkene proton along with signals corresponding to the two methylene and three methyl-ester groups (Figure 3.13).

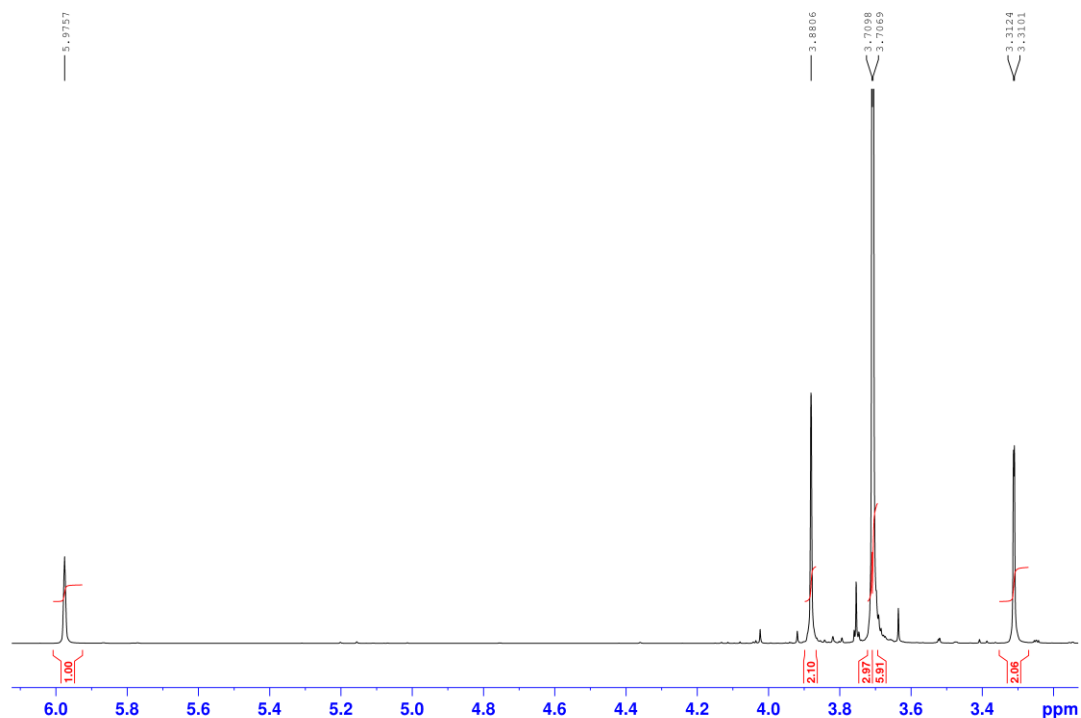


Figure 3.13. Aliphatic region of the ^1H NMR (CDCl_3) spectrum of **4.1**. N.B. the signal at 5.98 ppm corresponding to the alkene proton.

The triester **4.1** was then hydrogenated by stirring under a hydrogen atmosphere in the presence of a palladium catalyst, converting to the symmetric trimethyl ester **4.2**. The now-saturated central $\text{R}_3\text{-CH}$ group was clearly visible in the ^1H NMR spectrum (Figure 3.14), identifiable by its corresponding characteristic septet and confirmed pure by the absence of the unsaturated CH-group signal at 5.98 ppm in the ^1H NMR spectrum of **4.1**. The reaction gave a compound of sufficient purity to proceed to the next step without purification.

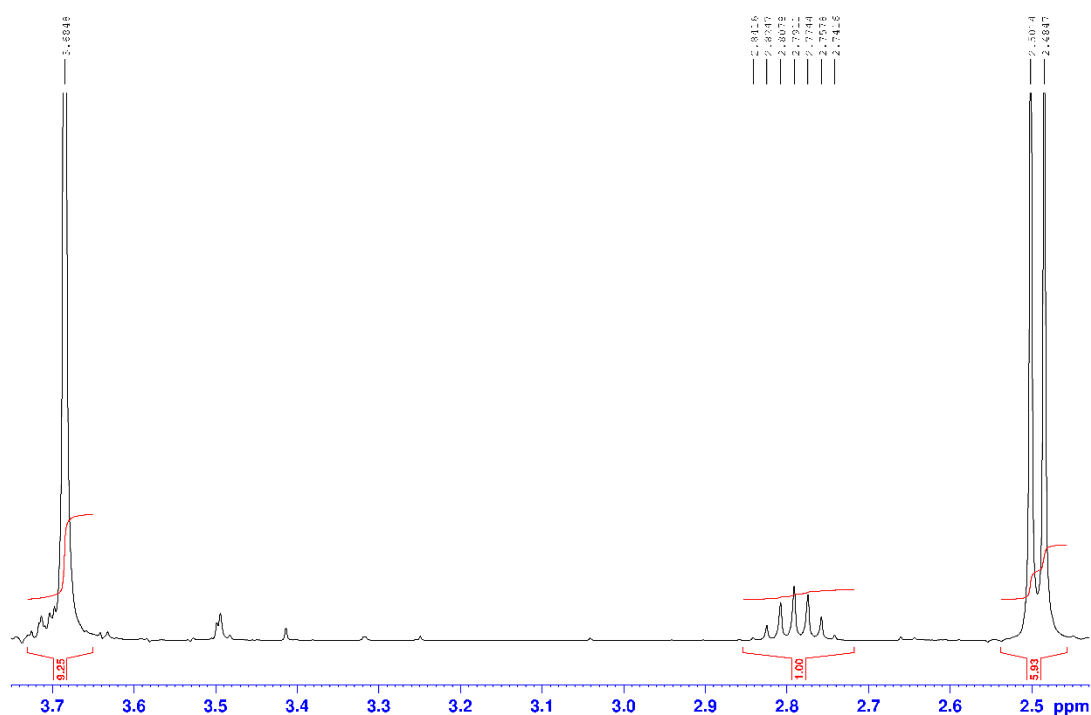


Figure 3.14. Aliphatic region of the ^1H NMR (CDCl_3) spectrum of **4.2** N.B. the septet at 2.79 and doublet at 2.49 ppm indicative of the $\text{HC}(\text{CH}_2\text{R})_3$ group.

This was converted to triacetate **4.3** by initial conversion to the triol with lithium aluminium hydride. Due to the solubility of the triol in aqueous media, it was directly converted to the triacetate by quenching with acetic acid, and subsequent acetylation with acetic anhydride at reflux. The presence of two triplets in the ^1H NMR spectrum was indicative of reduction of the carbonyl group. (Figure 3.15).

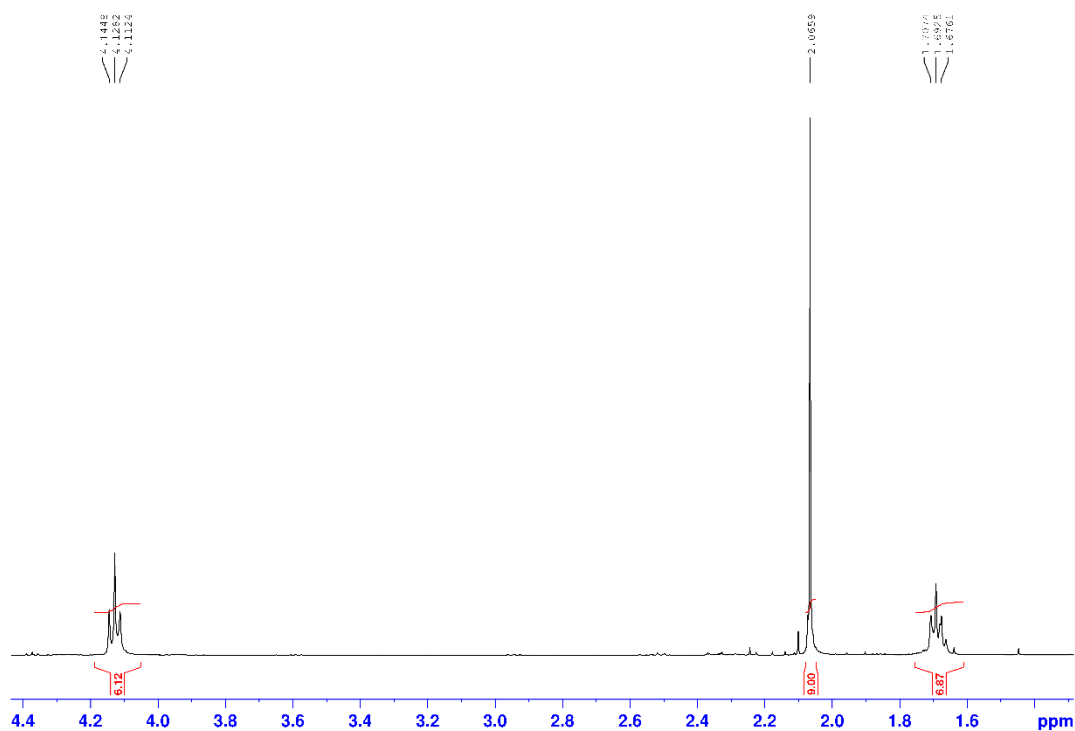


Figure 3.15. Aliphatic region of the ^1H NMR (CDCl_3) spectrum of **4.4** N.B. the triplets at 4.13 and 1.69 ppm corresponding to the $\text{HC}(\text{CH}_2\text{CH}_2\text{R})_3$ group; the $\underline{\text{H}}\text{C}(\text{CH}_2\text{CH}_2\text{R})_3$ signal coincides with the $\text{HC}(\underline{\text{C}}\text{H}_2\text{CH}_2\text{R})_3$ signal.

The literature method for conversion of the triacetate to the triol **4.4** required reaction with a large excess of ammonia under forcing conditions and then was compounded by high temperature distillation to remove the acetamide side-product;¹¹¹ however, a much simpler and milder method was developed by heating the triacetate at 80 °C in 3M hydrochloric acid. The excess acid, water and acetic acid were all removed by rotary evaporation, leaving the triol as a brown oil – characterised by the absence of the $-\text{COCH}_3$ singlet from the ^1H NMR and the absence of two signals from the ^{13}C NMR spectrum, one at 171 ppm corresponding to the ester carbonyl and one at 21 ppm corresponding to the methyl ester (Figure 6.57 c.f. Figure 6.60). Also present in the ^1H NMR spectrum were the three alcohol hydrogen atoms, identifiable by the distinctive broad singlet at 4.89 ppm (Figure 3.16).

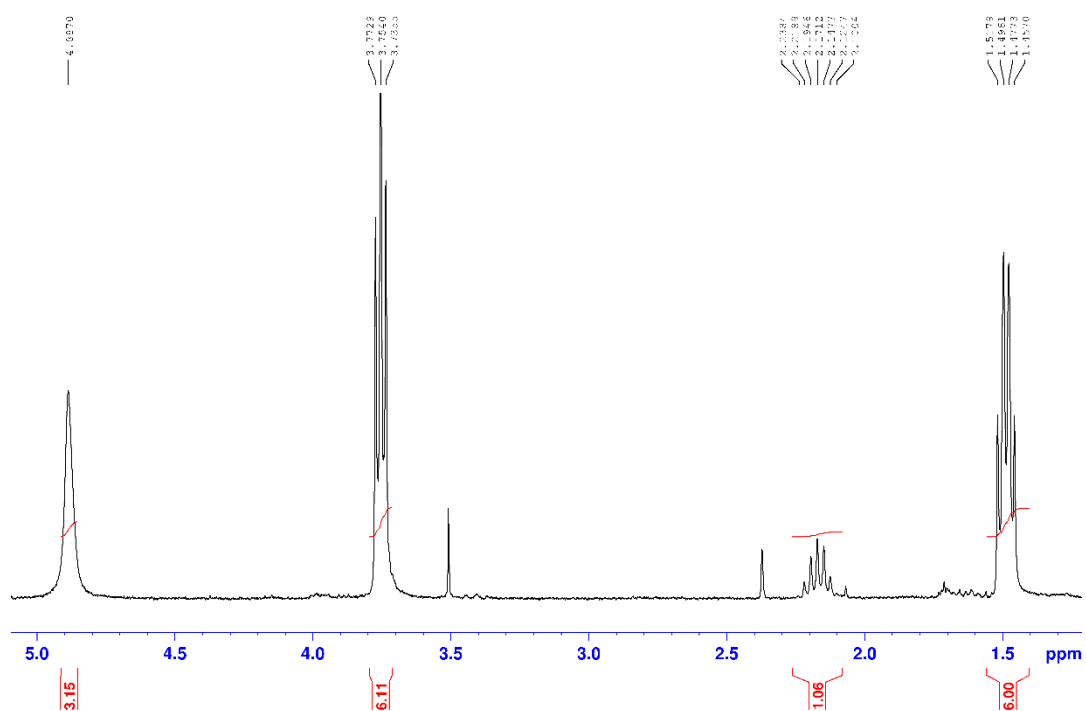


Figure 3.16. Aliphatic region of the ^1H NMR (CDCl_3) spectrum of **4.4**. N.B. the broad singlet at 4.89 ppm indicative of the three -OH protons.

For the next step it was important to ensure that the compound was anhydrous, so the triol was dried by using a toluene azeotrope removed by rotary evaporation and the process repeated several times. Once dry, the crude compound was reacted with methanesulfonyl chloride in the presence of pyridine in dry DCM under a nitrogen atmosphere. These resulting crude material required purification by column chromatography, but since TLC visualisation techniques proved to be ineffective, 20 mL fractions were collected and the solvent removed and analysed by ^1H NMR order to establish purity. The column was initially eluted with DCM, but after ~ 200 mL the solvent was changed to 1% MeOH in DCM after which time the vast majority of the product was eluted. The absence of the broad -OH singlet peak, as well as the addition of a singlet (integrating to 9 hydrogen atoms) corresponding to

the three mesylate groups in the ^1H NMR spectrum indicated successful synthesis of the product (Figure 3.17).

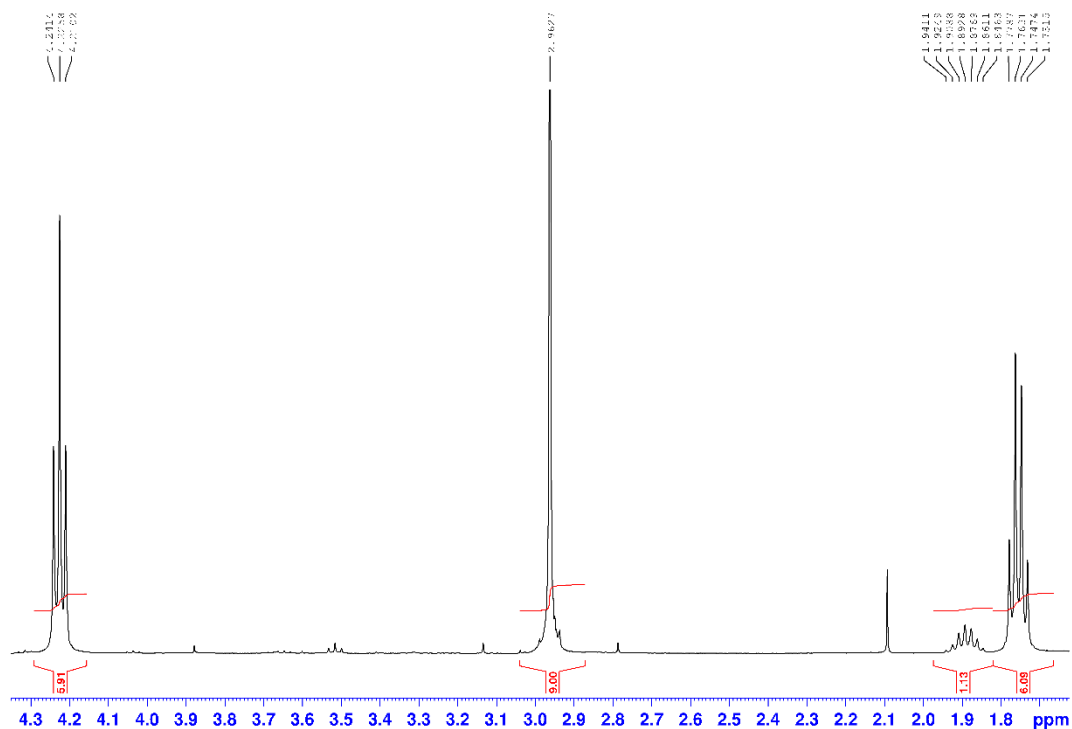
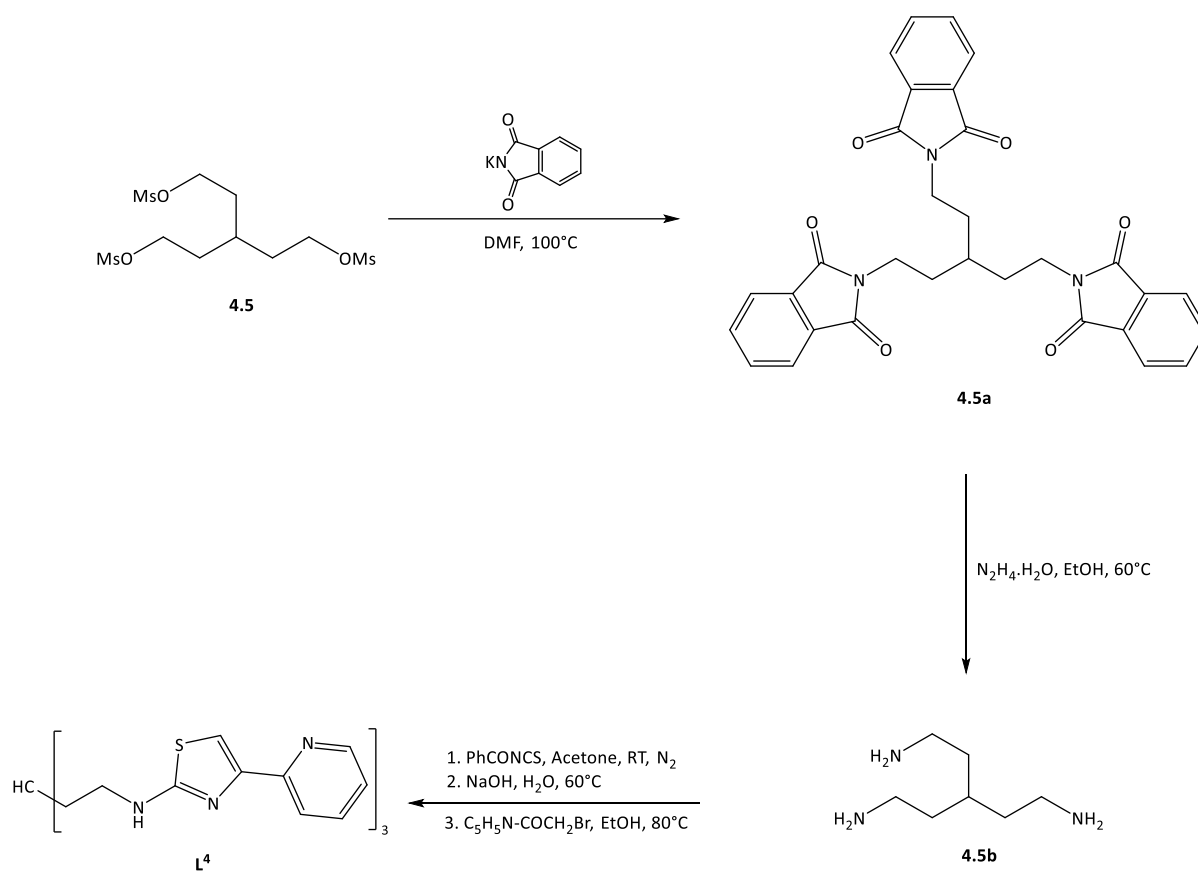


Figure 3.17. Aliphatic regions of the ^1H NMR (CDCl_3) spectrum of **4.5**. N.B. the strong singlet peak at 2.96 ppm indicative of three identical methanesulfonate groups.

From the mesylate **4.5**, the literature dictated the conversion of this to the triazide by reaction with sodium azide in anhydrous dimethylformamide.¹¹¹ However, this was undesirable due to the unstable nature of a small compound containing three azide groups. A preferable alternative was to convert this to the triamine **4.5a** using potassium phthalimide followed by hydrazine, and then subsequently follow the standard procedure to convert this to the final **L⁴** (Scheme 3.4).



*Scheme 3.4. Synthesis of ligand **L⁴** from trimesylate **4.5** via the phthalimide **4.5a** and triamine **4.5b**.*

Reaction of the trimesylate **4.5** with potassium phthalimide resulted in a pale-yellow solution. This was poured onto water which caused the product to precipitate **4.5a** as a fine white solid, which was isolated by filtration. The 1H NMR spectrum showed an absence of the methyl- signal at 2.96 ppm, and instead showed two doublets of doublets in the aromatic region corresponding to the three phthalimide groups (Figure 3.18).

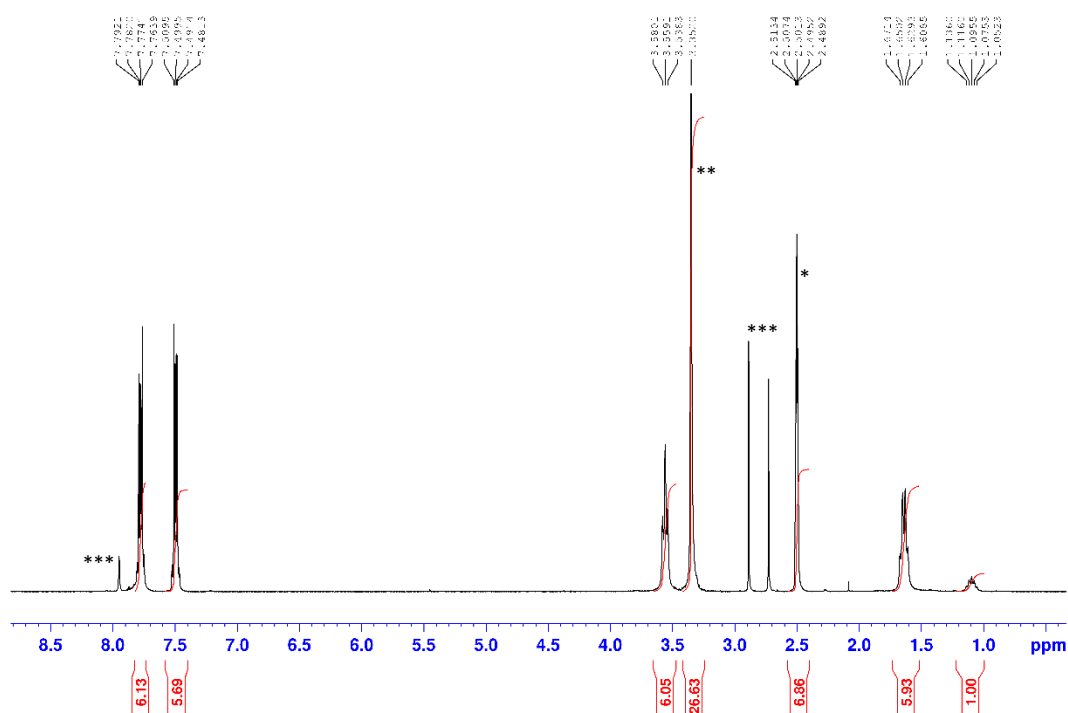


Figure 3.18. ^1H NMR ($(\text{CD}_3)_2\text{SO}$) spectrum of **4.5a**. N.B. pair of doublets of doublets in the aromatic region indicative of a phthalimide group. $^*(\text{CD}_3)(\text{CD}_2\text{H})\text{SO}$ impurity. $**\text{H}_2\text{O}$ impurity. $***$ DMF impurity.

Reduction of the *tris*-phthalimide **4.5a** using hydrazine resulted in the formation of a heavy, thick white precipitate. This was removed by gravity filtration and solvent removed from the filtrate to leave the triamine **4.5b** as a colourless oil, which showed signals indicative of three of the four environments (Figure 3.19). The amine signal is not clearly visible due to the labile amine protons undergoing fast exchange with water. The signals for the two $-\text{CH}_2-$ groups and the central $-\text{CH}$ group are shifted compared to the starting material and no aromatic signals are present indicating full conversion to the triamine **4.5a**.

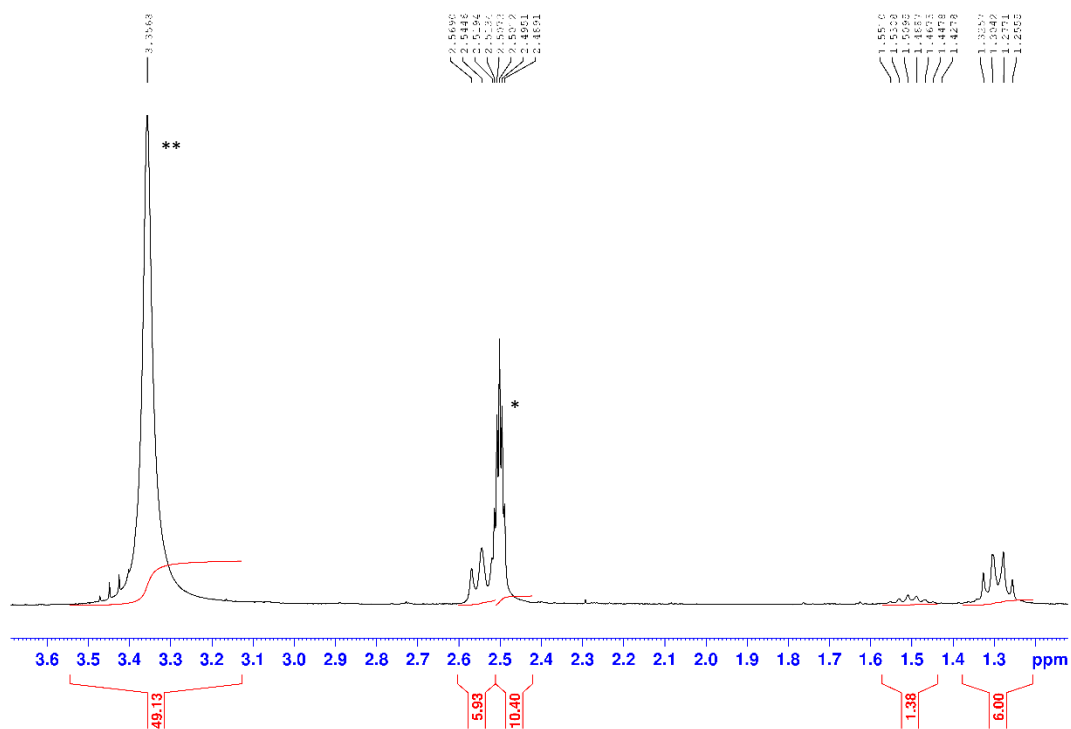
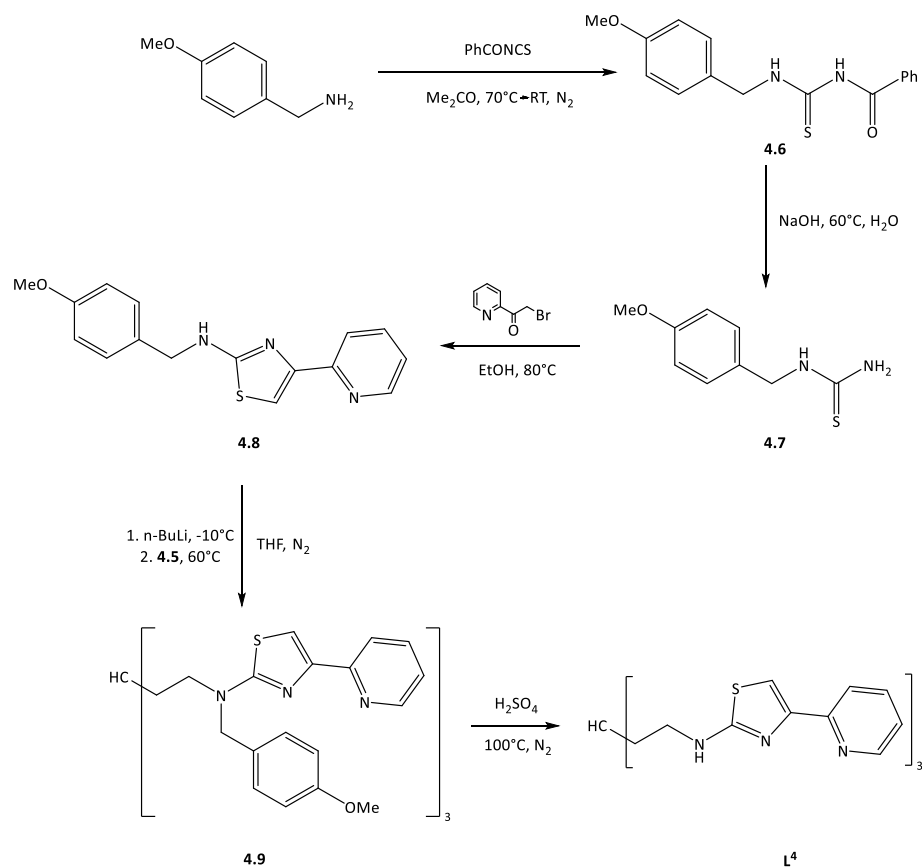


Figure 3.19. Aliphatic region of the ^1H NMR ($(\text{CD}_3)_2\text{SO}$) spectrum of **4.5b**. N.B. comparatively lower shifts for all three aliphatic signals. * $(\text{CD}_3)(\text{CD}_2\text{H})\text{SO}$ impurity. ** H_2O impurity.

Clearly the next step would involve conversion to the thiourea. However, the reaction of the triamine **4.5b** with benzoyl isothiocyanate gave an orange-red, viscous oil that was seemingly impossible to separate from the excess starting material. Recrystallisation techniques were unsuitable due to the difficulty of obtaining the *tris*-benzoylated product as a solid, with several solvents giving the attempted recrystallisation product as an impure oil. Column chromatography also failed to elute the product in sufficient purity; possibly in part due to hydrolysis of the product whilst on the column.

The failure to adequately purify the *tris*-benzoylated product to an acceptable standard rendered this synthesis route unsuitable. Therefore, a new method of synthesising this ligand was developed, using a simple amine protecting group consisting of a *para*-methoxybenzyl- group (Scheme 3.5):



Scheme 3.5. Synthesis of ligand L^4 from trimesylate **4.5** via the protected species **4.9**.

This was achieved by the initial reaction of *p*-methoxybenzylamine with benzoyl isothiocyanate (prepared in-situ) in dry acetone to produce the benzoylated thiourea species **4.6**. This was precipitated by pouring onto water, decanting and recrystallisation from isopropyl alcohol to give the product as slightly yellow needles. The ^1H NMR spectrum showed broad singlets at 10.95 and 9.03 indicative of the two -NH groups, one being shifted due to its location between both a carbonyl and a

thiocarbonyl group, as well as aromatic signals characteristic of both *para*-disubstituted phenyl- and *mono*-substituted phenyl- groups (Figure 3.20).

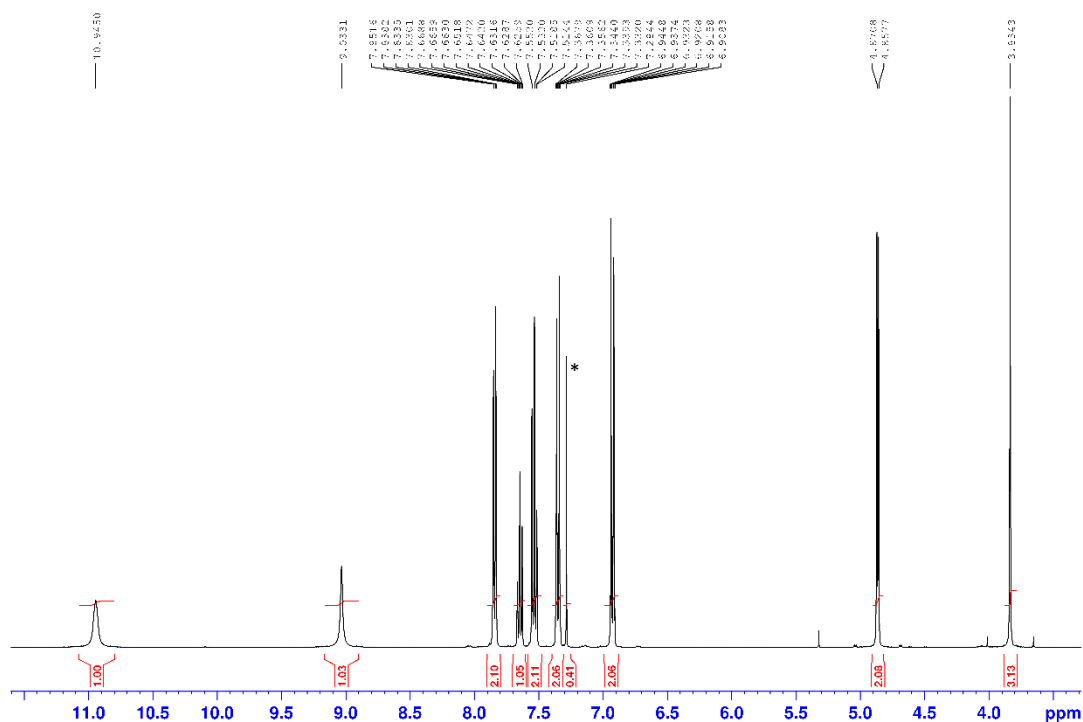


Figure 3.20. ^1H NMR spectrum of **4.6**. * CHCl_3 impurity.

This synthesis proceeded with the hydrolysis of the benzoylated thiourea **4.6** to the thiourea **4.7** in concentrated sodium hydroxide solution. Due to the insolubility of **4.6** in water, the solution never fully clarified due to the immediate precipitation of the thiourea **4.7** as a heavy white solid on reaction of the starting material with sodium hydroxide. After filtration and washing the thiourea was isolated as a crystalline white solid, the ^1H NMR spectrum of which showed the correct number of peaks (Figure 3.21). Due to the intra- and inter-molecular hydrogen-bonding properties of the thiourea the amine

peaks appear very broad, however the aromatic doublets for the *para*-disubstituted phenyl group and aliphatic peak for the methoxy- group are all prominent.

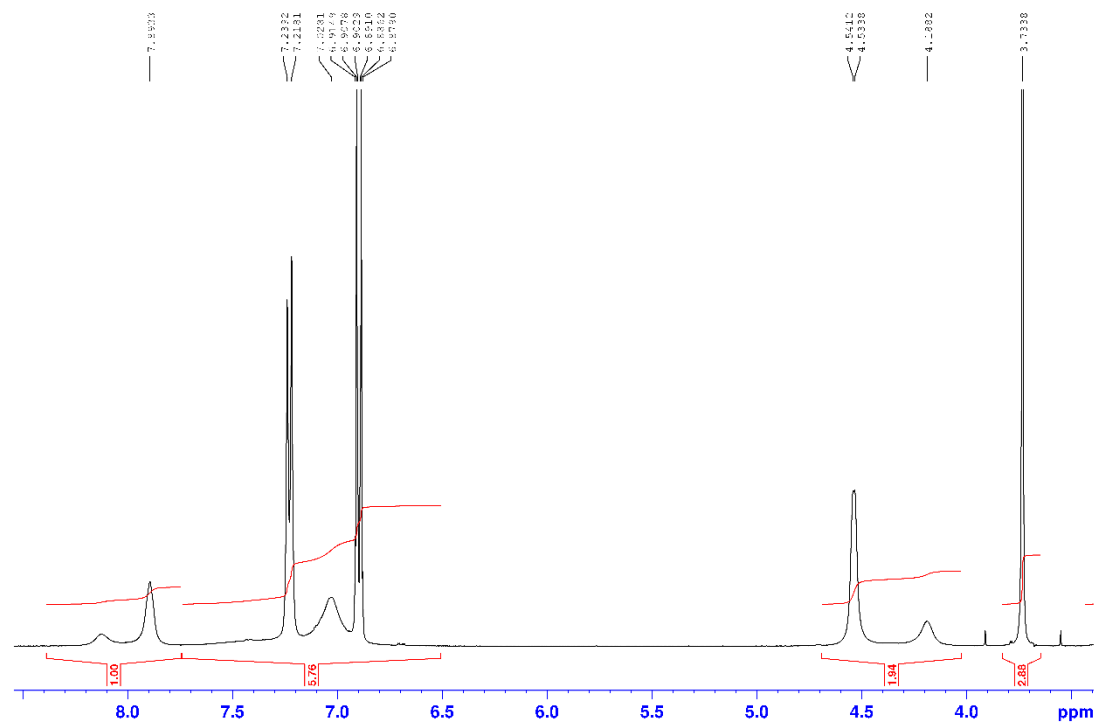


Figure 3.21. ^1H NMR spectrum of **4.7** with broad amine peaks due to hydrogen-bonding interactions.

The amine **4.7** was then converted to the protected ligand strand **4.8** using 2-(α -bromoacetyl)pyridine. The crude product was deprotonated by suspension in DCM and washing vigorously with sodium bicarbonate solution. Following column chromatography, the product was isolated as a pale yellow solid that showed peaks in the aromatic region characteristic of a *mono*-substituted pyridyl ring, one singlet indicative of a thiazole proton and two doublets corresponding to a *para*-disubstituted phenyl-group (Figure 3.22).

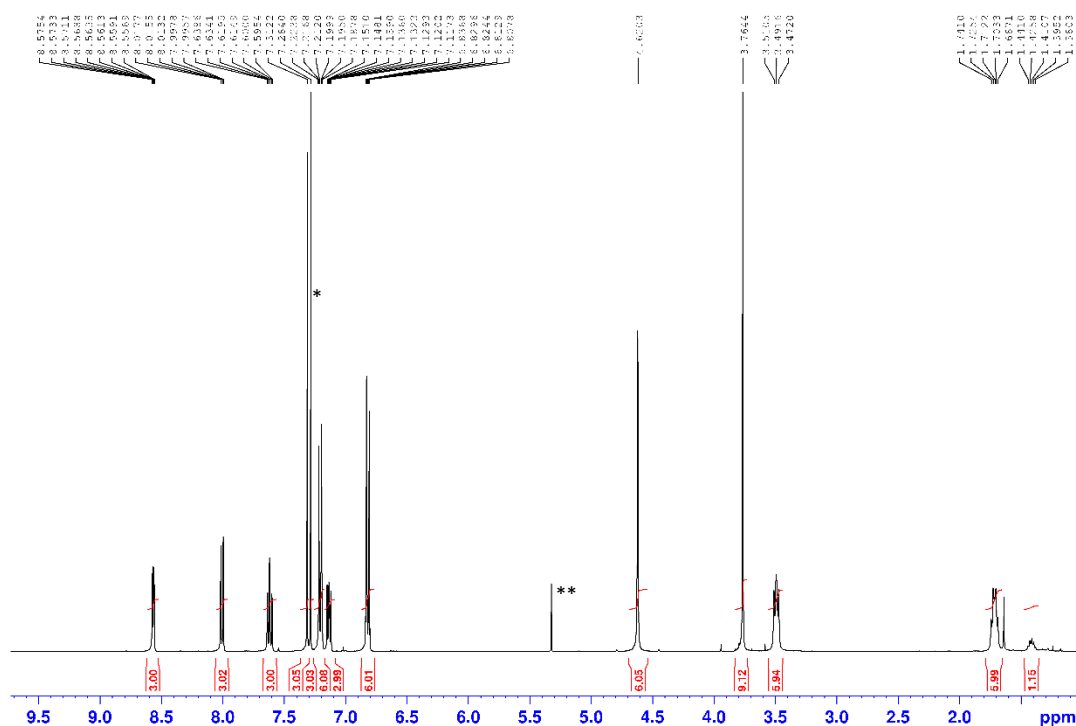
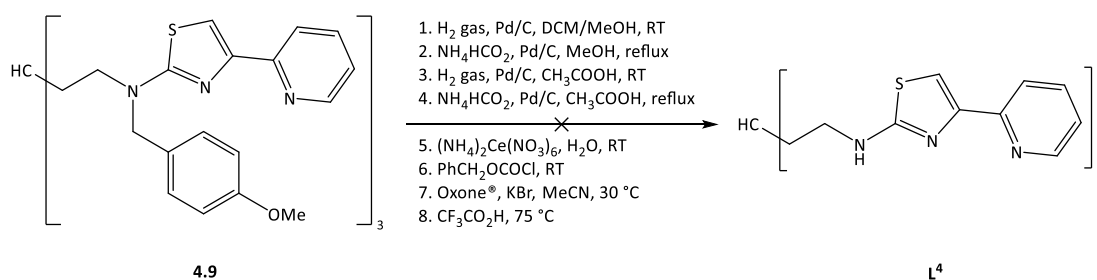


Figure 3.23. ^1H NMR spectrum of **4.9**, showing neither the mesylate CH_3 signal from **4.5** nor the amine singlet from **4.8**, indicative of complete reaction. * CHCl_3 impurity, ** CH_2Cl_2 impurity.

The protected ligand **4.9** was initially to be deprotected in a similar way to an amine-deprotection step in the synthesis of L^2 , using simple catalytic hydrogenation techniques. When this failed, other techniques were attempted (Scheme 3.6):^{112–117}



Scheme 3.6. Failed attempts to remove the benzyl-protecting group.^{112–117}

Ultimately, the protecting groups could only be removed by stirring compound **4.9** in concentrated sulfuric acid at 100 °C under a nitrogen atmosphere. The solid starting material immediately turned a dark magenta colour on the addition of the concentrated acid and after heating for four hours, was cooled and neutralised with a sodium hydroxide solution. After re-cooling and extracting the brown mixture into DCM, the ligand **L⁴** was obtained as a pale-yellow solid and used without further purification. The ¹H NMR spectrum was notably pure (barring some a small amount of grease in the aliphatic region) and the signals corresponding to the *p*-methoxybenzyl- protecting group were absent from both the ¹H NMR and ¹³C NMR spectrum (Figure 3.24 and Figure 3.25).

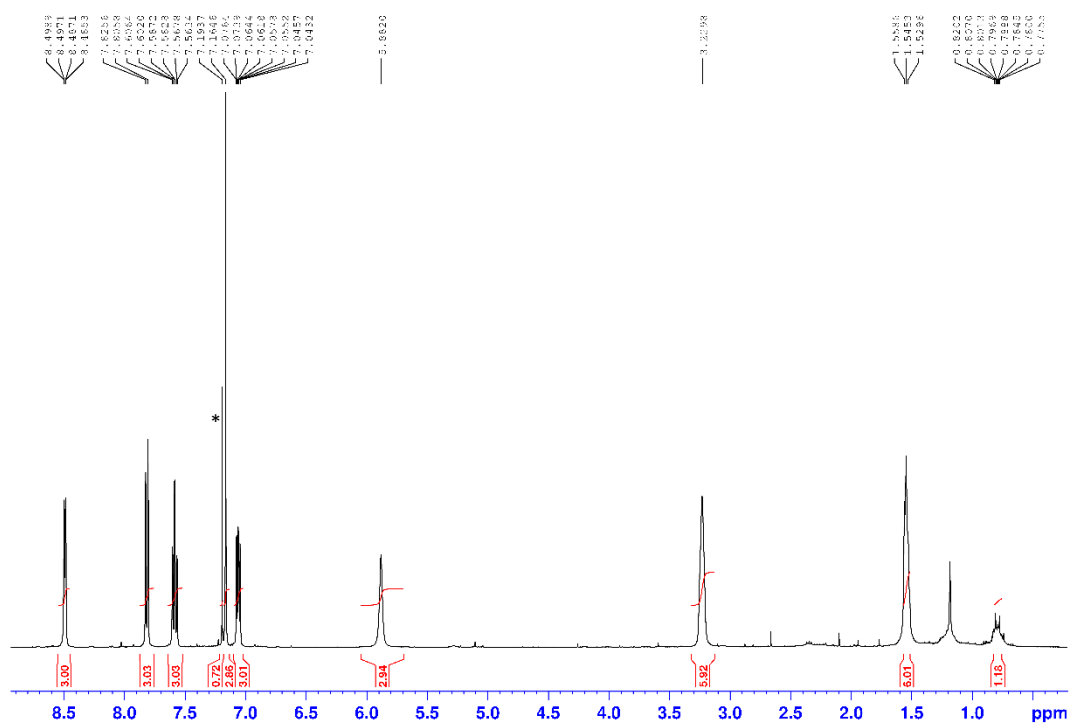


Figure 3.24. ¹H NMR spectrum of **L⁴**. The presence of the peak at 5.88 ppm corresponding to the three -NH groups, as well as the absence of the peaks corresponding to the three MeO-, -CH₂-Ph, and the four aromatic protons indicates that the protecting group has been successfully removed. *CHCl₃ impurity.

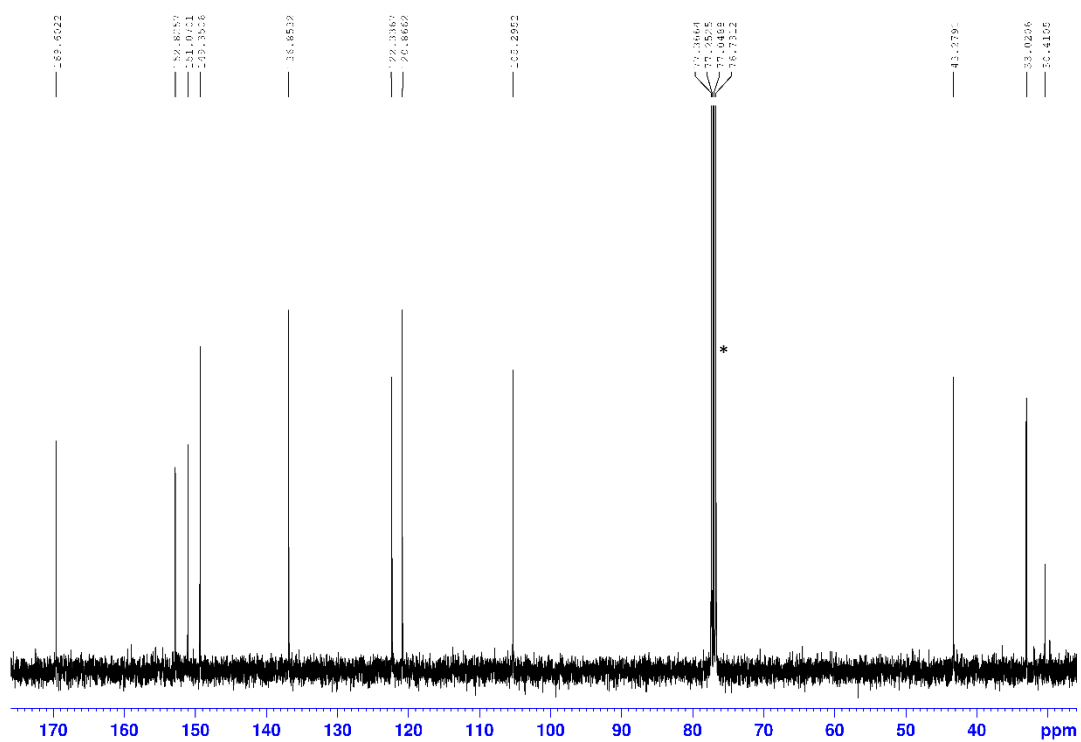
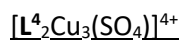


Figure 3.25. ^{13}C NMR spectrum of L^4 with eight aromatic signals and three aliphatic signals, indicating that the *para*-methoxybenzyl protecting group is no longer present.

3.3.2. Co-ordination chemistry



Ligand \mathbf{L}^4 was reacted with 1.5 equivalents of copper(II) perchlorate in a solution of acetonitrile and water resulting in a dark purple solution. To this was added an aqueous solution of tetra-*N*-butylammonium hydrogen sulfate, causing an immediate colour change to a pale-pink solution. Slow evaporation of this solution deposited pale-brown crystals which were analysed by X-ray crystallography. Analogously to complexes observed with similar ligands, this ligand forms a capsule from two ligand strands and three copper centres through N-Cu co-ordination interactions (i.e. $[\mathbf{L}^4_2\text{Cu}_3]^{6+}$), incorporating a tetrahedral anion within its central cavity; the first example of which is a sulfate anion (i.e. $[\mathbf{L}^4_2\text{Cu}_3(\text{SO}_4)]^{4+}$, Figure 3.26). This is encapsulated through bonds arising from three Cu...O co-ordination interactions (average Cu...O bond length 2.16 Å) and seven hydrogen-bonding interactions; three of which are located between one ligand strand and three of the oxygen atoms on the sulfate anion (average -NH...O bond length 2.36 Å). The remaining oxygen is bound to the opposite ligand strand through hydrogen-bonding to both the three -NH donor sites (average -NH...O bond length 2.19 Å) and the corresponding central -CH donor unit (average -CH...O bond length 2.33 Å, Figure 3.26c). As with all tetrahedral anion-encapsulating structures recorded with this ligand, the “lower” -CH domain is too far from the copper-bound oxygen atoms to be considered hydrogen-bonded (average -NH...O bond length 2.36 Å, -CH - O distance 3.10 Å).

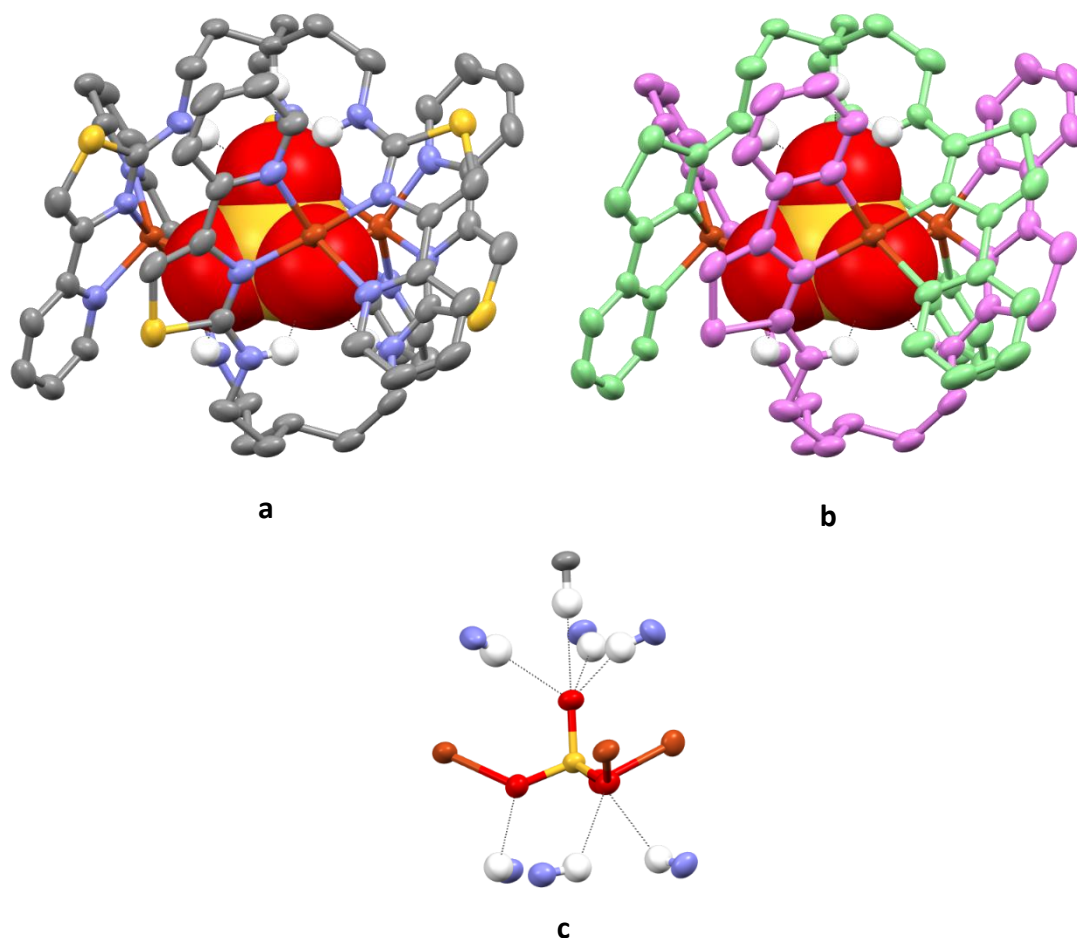


Figure 3.26. a) crystal structure of $[\text{L}^4_2\text{Cu}_3(\text{SO}_4)]^{4+}$; b) crystal structure with ligands coloured for clarity; c) co-ordination and hydrogen-bonding of the metals and ligand to the SO_4^{2-} anion. Colour code: dark orange, Cu^{2+} ; red, O; blue, N; yellow, S; grey, C; white, H (apart from (b) where the ligands have been coloured for clarity). Non-acidic hydrogen atoms and perchlorate anions are omitted for clarity.

Thermal ellipsoids shown at the 50% probability level.

The formation of the trinuclear assembly is also observed by ESI-MS; upon reaction of the ligand L^4 with 1.5 equivalents of copper(II) perchlorate gives ions at m/z 1940 and 919 corresponding to $\{[\text{L}^4_2\text{Cu}_3](\text{ClO}_4)_5\}^+$ and $\{[\text{L}^4_2\text{Cu}_3](\text{ClO}_4)_4\}^{2+}$ (Figure 3.27). Reaction of the complex with half an equivalent of tetra-*N*-butylammonium hydrogen sulfate gave ions at m/z 1836 and 868 corresponding to $\{[\text{L}^4_2\text{Cu}_3(\text{SO}_4)](\text{ClO}_4)_3\}^+$ and $\{[\text{L}^4_2\text{Cu}_3(\text{SO}_4)](\text{ClO}_4)_2\}^{2+}$ respectively (Figure 3.28).

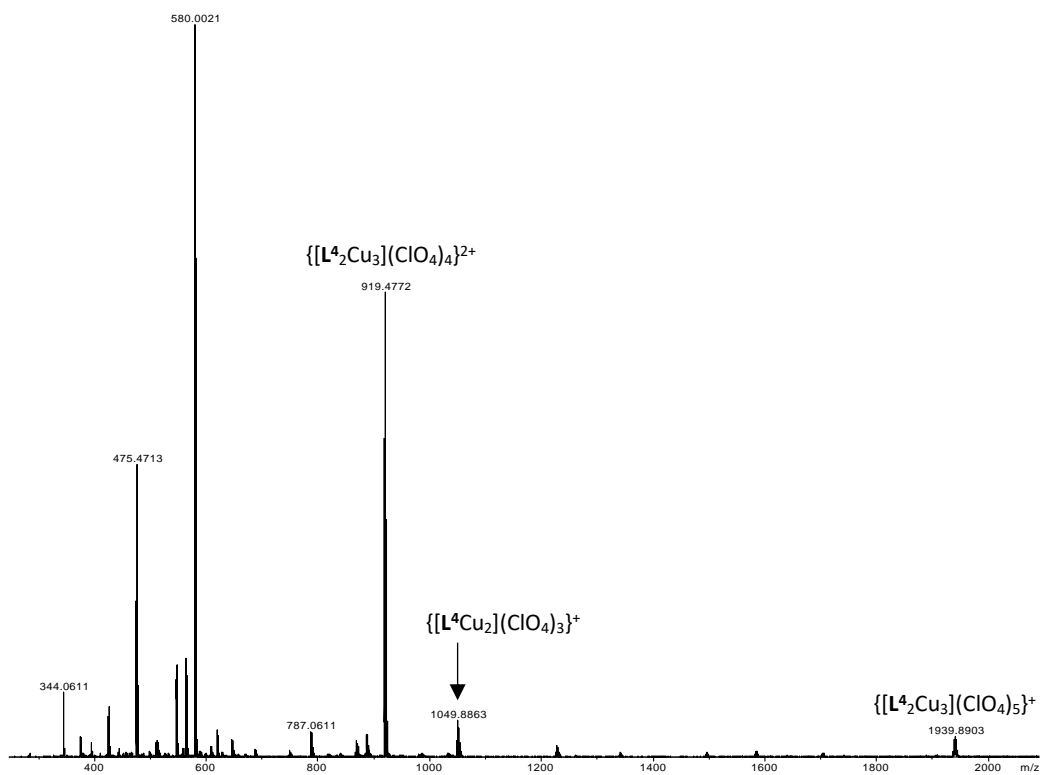


Figure 3.27. ESI-MS spectrum of $[L^4_2Cu_3](ClO_4)_6$.

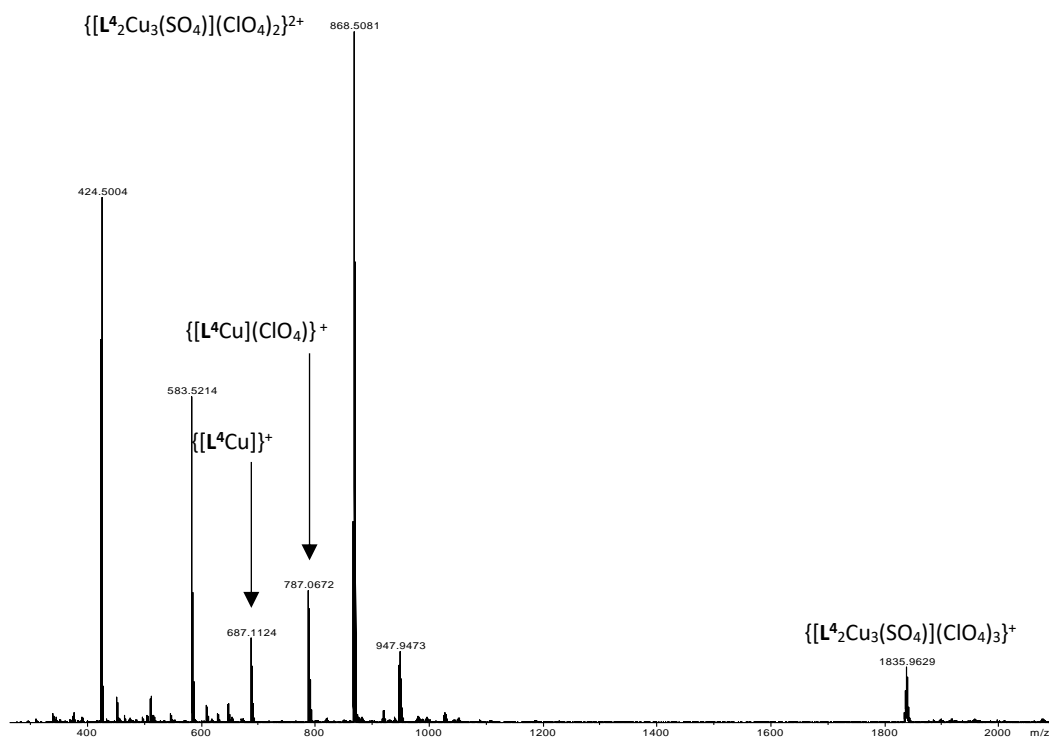


Figure 3.28. ESI-MS spectrum of $[L^4_2Cu_3(SO_4)](ClO_4)_4$.

Reaction of ligand L^4 with 1.5 equivalents of copper(II) trifluoromethanesulfonate in water/acetonitrile (1:1) gave a pale-brown solution (Figure 3.38a), the main UV-Vis-NIR spectrum peak being at a wavelength of 810 nm which is comparable to that obtained with the corresponding complex assembled from $L^{1,97}$ on addition of half an equivalent of tetra-*N*-butylammonium hydrogen sulfate the solution turned a pale pink colour (Figure 3.38g), giving new peaks at wavelengths of 920 and 520 nm (Figure 3.29).

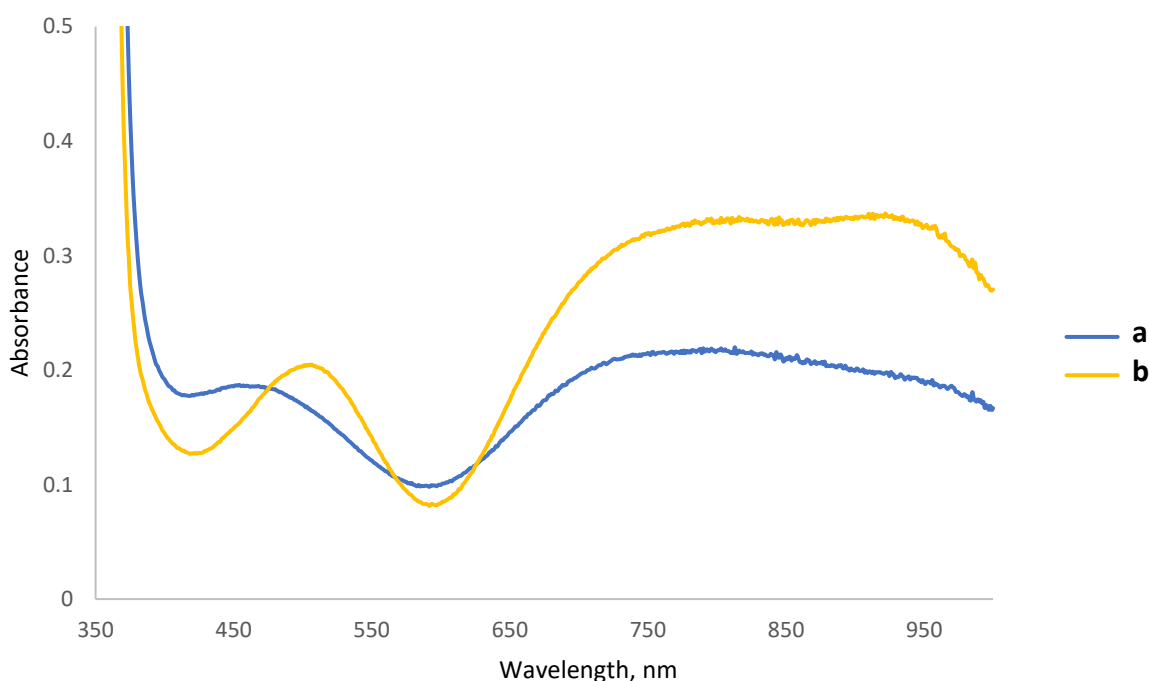
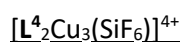


Figure 3.29. UV-Vis-NIR absorption spectra of solutions of a) $[L^4_2Cu_3](trif)_6$; b) $[L^4_2Cu_3](trif)_6$ plus the addition of one equivalent of tetra-*N*-butylammonium sulfate. Concentration of $[L^4_2Cu_3](trif)_6 = 0.8$ mM (1:1 acetonitrile in water).



Ligand L^4 forms complexes capable of encapsulating octahedral anions as well as tetrahedral anions. Addition of half an equivalent of ammonium hexafluorosilicate to a solution containing ligand L^4 with copper(II) perchlorate gave a pale-pink solution which, after being left to evaporate, deposited violet crystals which were confirmed by single-crystal X-ray crystal diffraction to follow the expected motif

demonstrated previously with this ligand (i.e. $[\text{L}^4_2\text{Cu}_3]^{6+}$); however, incorporated within the central cavity is an octahedral SiF_6^{2-} anion (i.e. $[\text{L}^4_2\text{Cu}_3(\text{SiF}_6)]^{4+}$, Figure 3.30). This is held in place through six $\text{Cu}\cdots\text{F}$ co-ordination interactions (average $\text{Cu}\cdots\text{F}$ bond length 2.57 Å), complemented by six $-\text{NH}\cdots\text{F}$ hydrogen-bonding interactions (average $-\text{NH}\cdots\text{F}$ bond length 2.28 Å); however, unlike the structure observed with the sulfate anion, the central $-\text{CH}$ group of both ligands are too far from the anion to be considered to have hydrogen-bonding interactions (average $-\text{CH} - \text{F}$ length 2.91 Å).

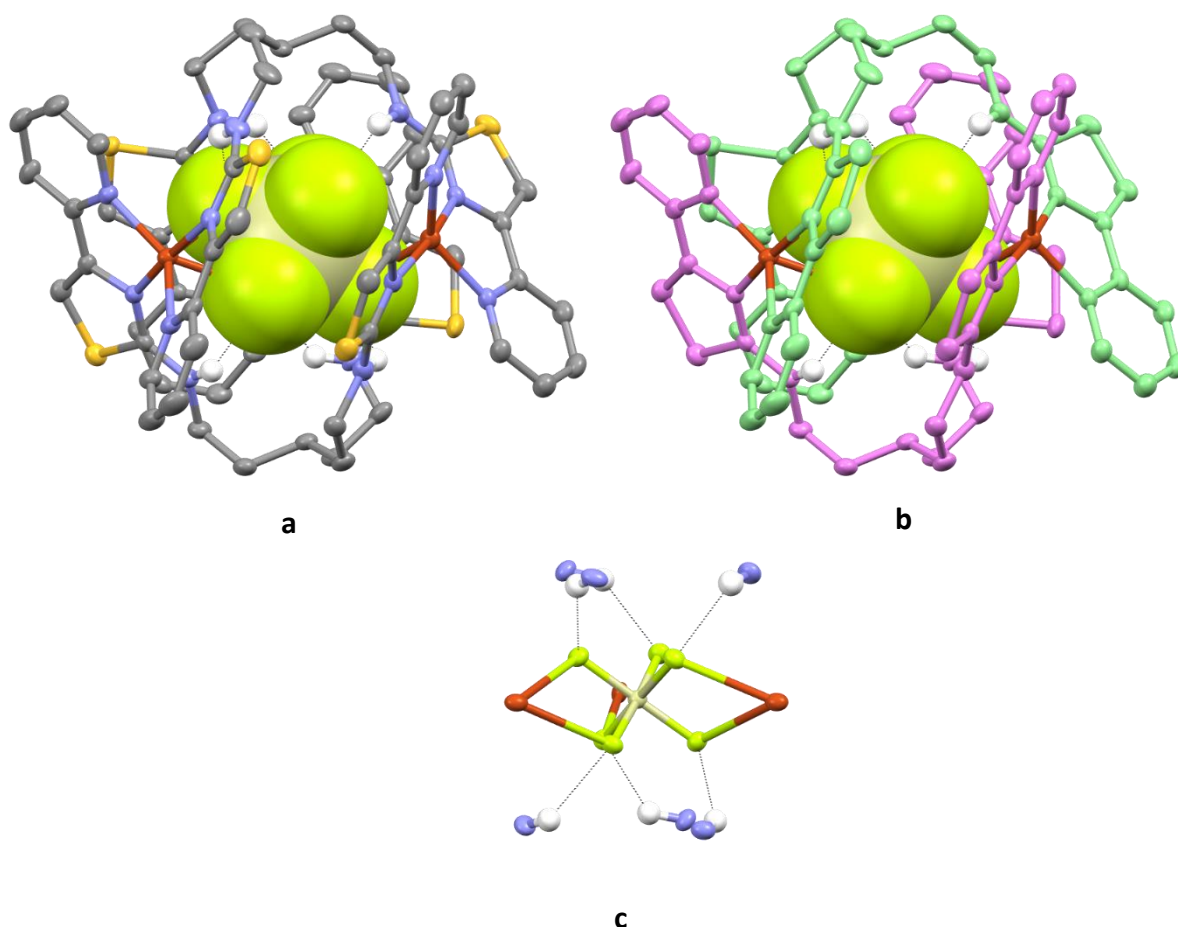


Figure 3.30. a) crystal structure of $[\text{L}^4_2\text{Cu}_3(\text{SiF}_6)]^{4+}$; b) crystal structure with ligands coloured for clarity; c) co-ordination and hydrogen-bonding of the metals and ligand to the SiF_6^{2-} anion. Colour code: dark orange, Cu^{2+} ; beige, Si; lime, F; red, O; blue, N; yellow, S; grey, C; white, H (apart from (b) where the ligands have been coloured for clarity). Non-acidic hydrogen atoms and perchlorate anions are omitted for clarity. Thermal ellipsoids shown at the 50% probability level.

Reaction of ligand L^4 with 1.5 equivalents of copper(II) trifluoromethanesulfonate in water/acetonitrile (1:1) gave the same pale-brown solution; on addition of half an equivalent of ammonium hexafluorosilicate the solution turned pink-purple (Figure 3.38h), giving a large peak in the UV-Vis-NIR spectrum at a wavelength of 505 nm (Figure 3.31).

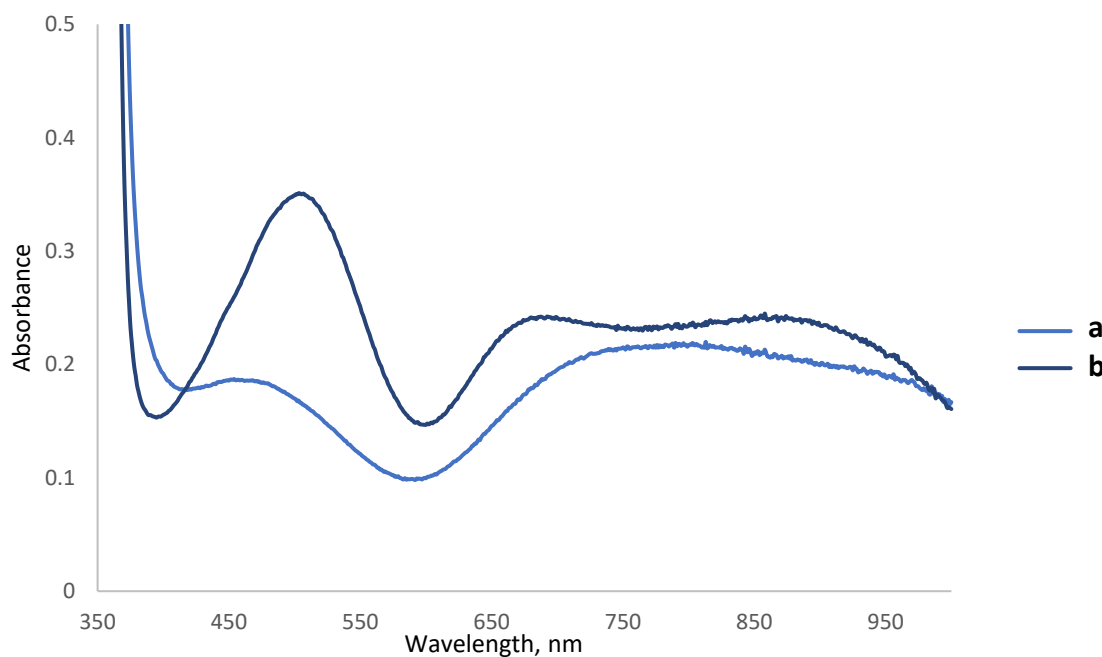


Figure 3.31. UV-Vis-NIR absorption spectra of solutions of a) $[L^4_2Cu_3](trif)_6$; b) $[L^4_2Cu_3](trif)_6$ plus the addition of one equivalent of ammonium hexafluorosilicate. Concentration of $[L^4_2Cu_3](trif)_6 = 0.8$ mM (1:1 acetonitrile in water).

$[L^4_2Cu_3(PO_4)]^{3+}$

Reaction of ligand L^4 with 1.5 equivalents of copper(II) perchlorate with half an equivalent of tetra-*N*-butylammonium dihydrogen phosphate, gave an immediate colour change to a lime-green colour, a colour which is characteristic of phosphate encapsulation and has been observed with analogous complexes assembled using L^1 (e.g. $[L^1_2Cu_3(PO_4)]^{3+}$). Slow evaporation of this solution deposited emerald-green crystals which were analysed by single-crystal X-ray crystal diffraction and confirmed to follow the usual self-assembly process, where two ligands and three metals form a capsule (i.e.

$[\text{L}^4_2\text{Cu}_3]^{6+}$), with the tetrahedral phosphate anion incorporated within the central cavity (i.e. $[\text{L}^4_2\text{Cu}_3(\text{PO}_4)]^{3+}$, Figure 3.32). In an identical manner to the L^4 sulfate complex previously described, the phosphate anion is held in place through three $\text{Cu}\cdots\text{O}$ bonding interactions (average $\text{Cu}\cdots\text{O}$ bond length 1.96 Å) and seven hydrogen-bonding interactions; three between the copper-bound oxygen atoms and the -NH donor domains on the corresponding ligand strand (average $\text{-NH}\cdots\text{O}$ bond length 2.21 Å) and four on the other oxygen atom; three of which are between the oxygen atom and the remaining three -NH donor units (average $\text{-NH}\cdots\text{O}$ bond length 2.02 Å) and one to the central methine -CH donor (average $\text{Cu}\cdots\text{O}$ bond length 2.30 Å, Figure 3.32c).

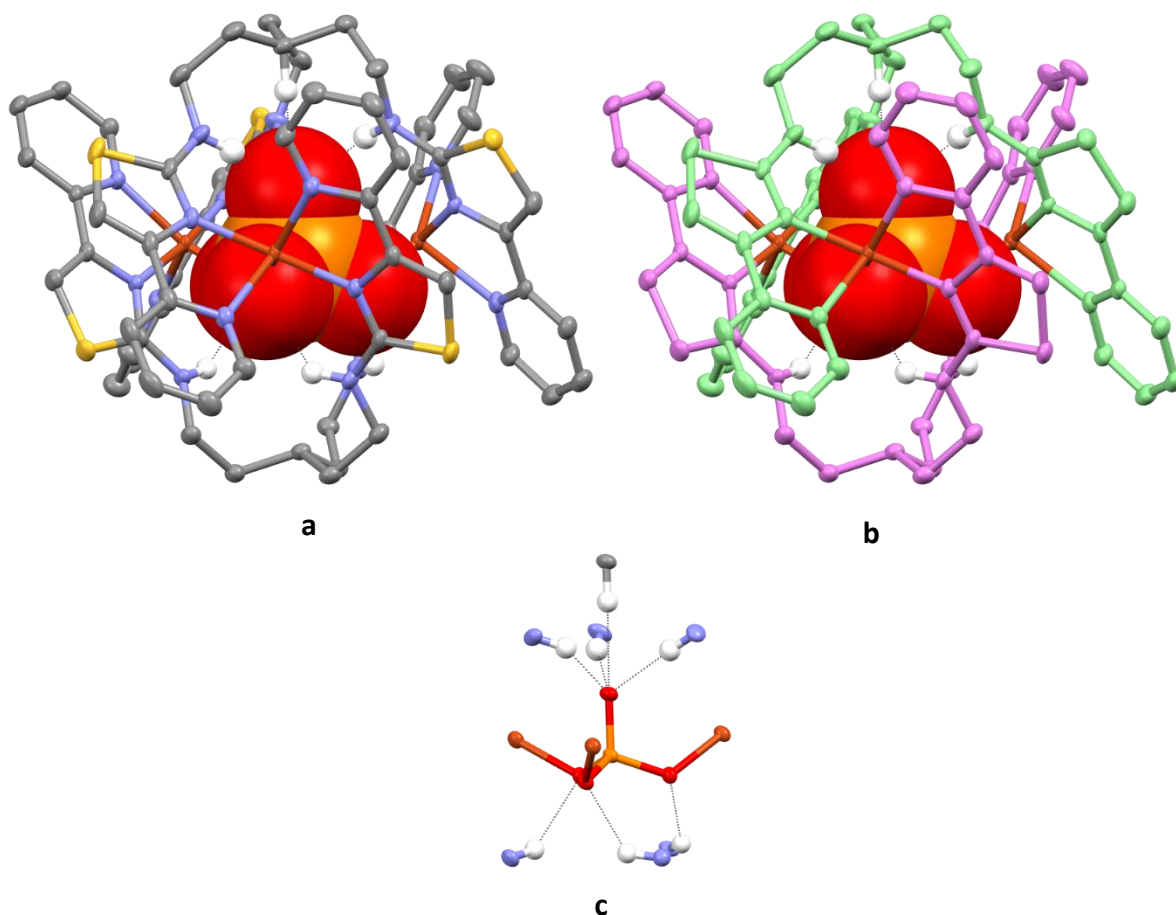


Figure 3.32. a) crystal structure of $[\text{L}^4_2\text{Cu}_3(\text{PO}_4)]^{3+}$; b) crystal structure with ligands coloured for clarity; c) co-ordination and hydrogen-bonding of the metals and ligand to the PO_4^{3-} anion. Colour code: dark orange, Cu^{2+} ; orange, P; red, O; blue, N; yellow, S; grey, C; white, H (apart from (b) where the ligands have been coloured for clarity). Non-acidic hydrogen atoms and perchlorate anions are omitted for clarity. Thermal ellipsoids shown at the 50% probability level.

Similarly to the complex with the sulfate anion, reaction of the complex with half an equivalent of tetra-*N*-butylammonium dihydrogen phosphate gave ESI-MS ions at m/z 1736 and 817 corresponding to $\{[L^4_2Cu_3(PO_4)](ClO_4)_2\}^+$ and $\{[L^4_2Cu_3(PO_4)](ClO_4)\}^{2+}$ (Figure 3.33).

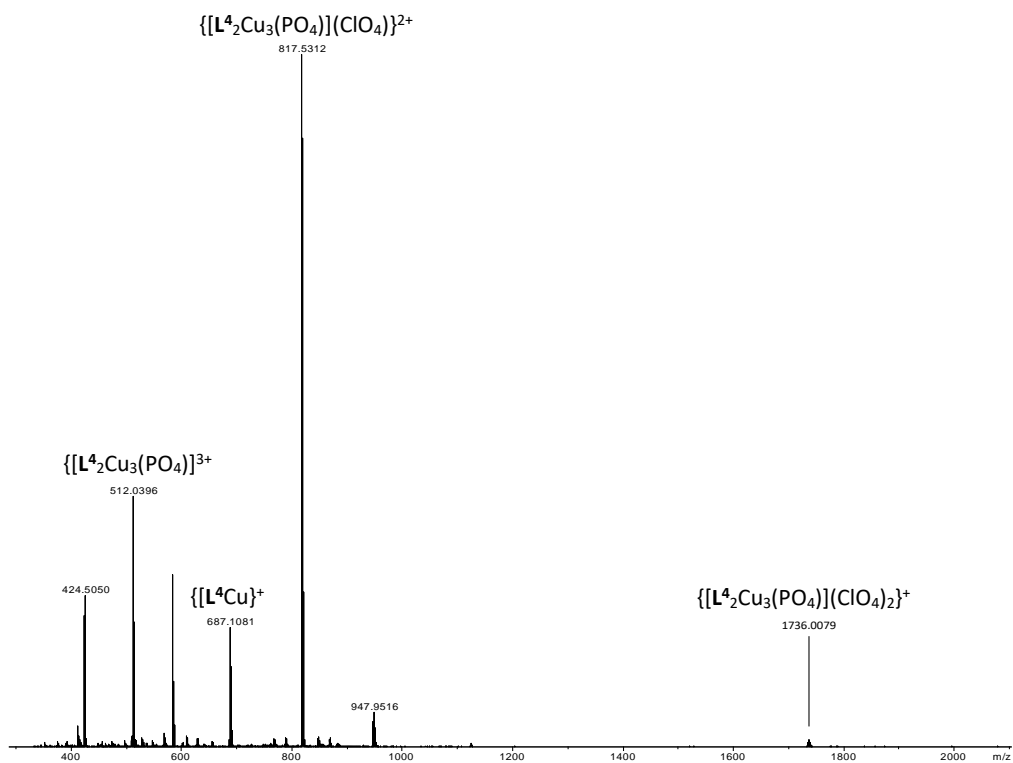


Figure 3.33. ESI-MS spectrum of $[L^4_2Cu_3(PO_4)](ClO_4)_3$.

Addition of half an equivalent of tetra-*N*-butylammonium dihydrogen phosphate to pale-brown solution of ligand L^4 with 1.5 equivalents of copper(II) trifluoromethanesulfonate in water/acetonitrile (1:1) resulted in an immediate colour change to the characteristic lime-green observed with other phosphate-encapsulating complexes (Figure 3.38c), with a peak in its UV-Vis-NIR spectrum at a wavelength of 755 nm (Figure 3.34).

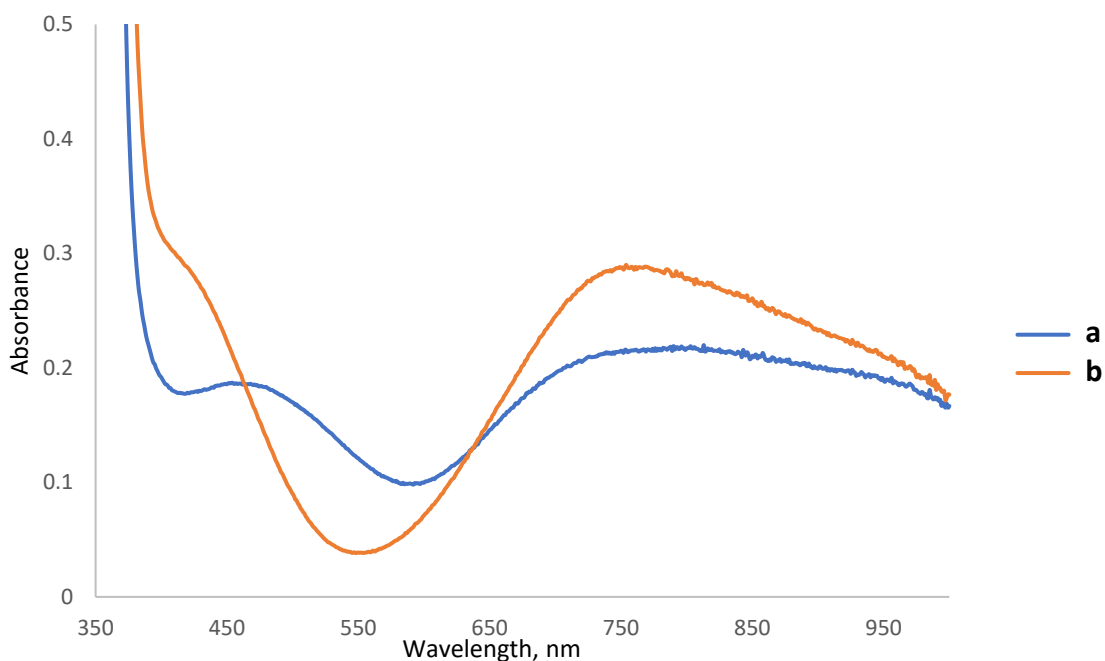


Figure 3.34. UV-Vis-NIR absorption spectra of solutions of a) $[\text{L}^4_2\text{Cu}_3](\text{trif})_6$; b) $[\text{L}^4_2\text{Cu}_3](\text{trif})_6$ plus the addition of one equivalent of tetra-N-butylammonium dihydrogen phosphate. Concentration of $[\text{L}^4_2\text{Cu}_3](\text{trif})_6 = 0.8 \text{ mM}$ (1:1 acetonitrile in water).

$[\text{L}^4_2\text{Cu}_3(\text{AsO}_4)]^{3+}$

Upon reaction with disodium arsenate, an almost identical lime-green solution to that containing the phosphate-encapsulating complex was observed. Emerald-green crystals were deposited on slow evaporation of this solution which were analysed by single-crystal X-ray diffraction. The complex observed is structurally identical to that observed with the phosphate anion, having the exact same structure and bonding properties (the co-ordination bond lengths increase slightly due to the larger size of the arsenate anion; average $\text{Cu}\cdots\text{O}$ bond length 1.98 \AA , average $\text{CuO}\cdots\text{HN}$ - bond length 2.20 \AA , average $-\text{NH}\cdots\text{O}$ bond length 2.04 \AA , $-\text{CH}\cdots\text{O}$ bond length 2.24 \AA ; Figure 3.35).

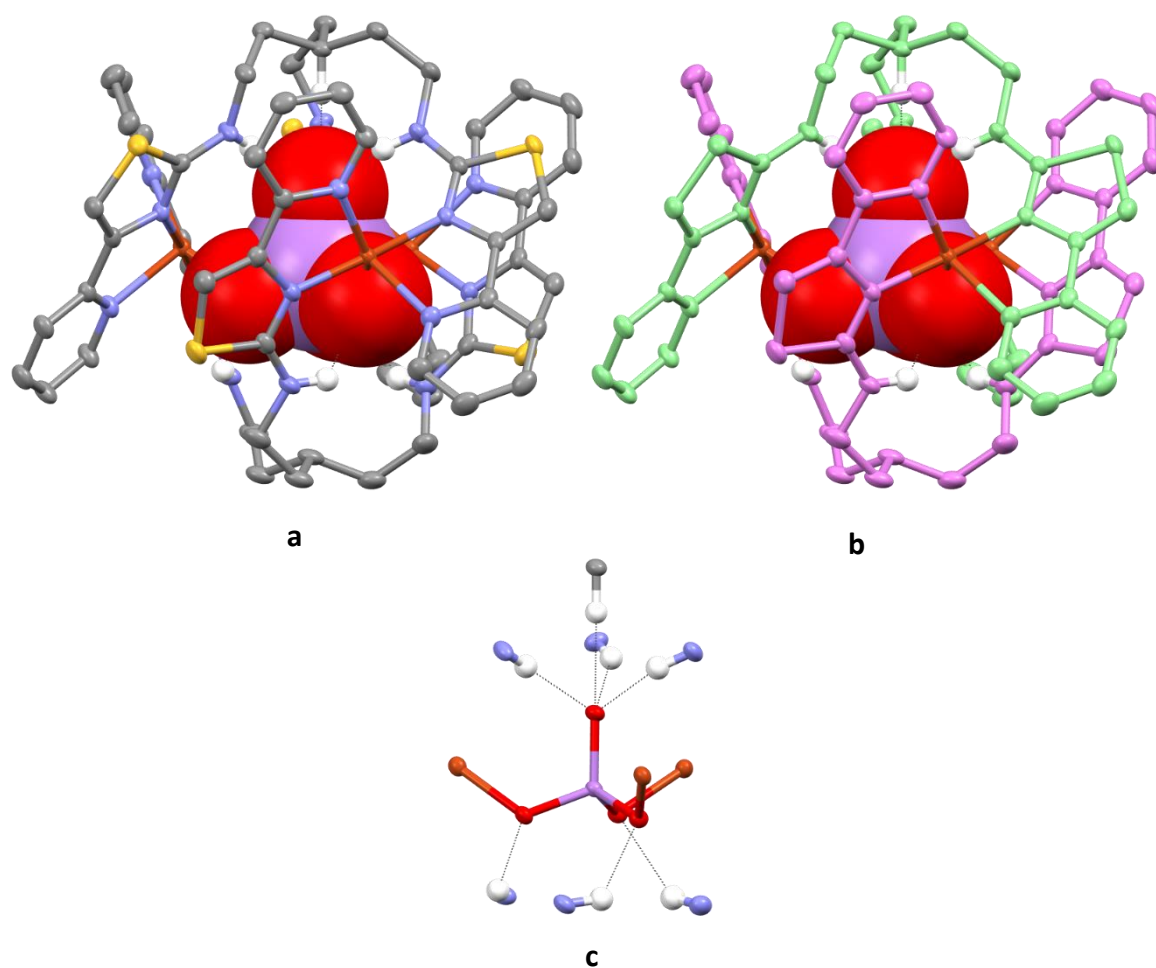


Figure 3.35. a) crystal structure of $[\text{L}^4_2\text{Cu}_3(\text{AsO}_4)]^{3+}$; b) crystal structure with ligands coloured for clarity; c) co-ordination and hydrogen-bonding of the metals and ligand to the AsO_4^{3-} anion. Colour code: dark orange, Cu^{2+} ; violet, As; red, O; blue, N; yellow, S; grey, C; white, H (apart from (b) where the ligands have been coloured for clarity). Non-acidic hydrogen atoms and perchlorate anions are omitted for clarity. Thermal ellipsoids shown at the 50% probability level.

Analogously to the phosphate-containing complex, ESI-MS of the complex when reacted with half an equivalent of disodium hydrogen arsenate gave ions at m/z 1780 and 839 corresponding to $\{[\text{L}^4_2\text{Cu}_3(\text{AsO}_4)](\text{ClO}_4)_2\}^+$ and $\{[\text{L}^4_2\text{Cu}_3(\text{AsO}_4)](\text{ClO}_4)\}^{2+}$ (Figure 3.36).

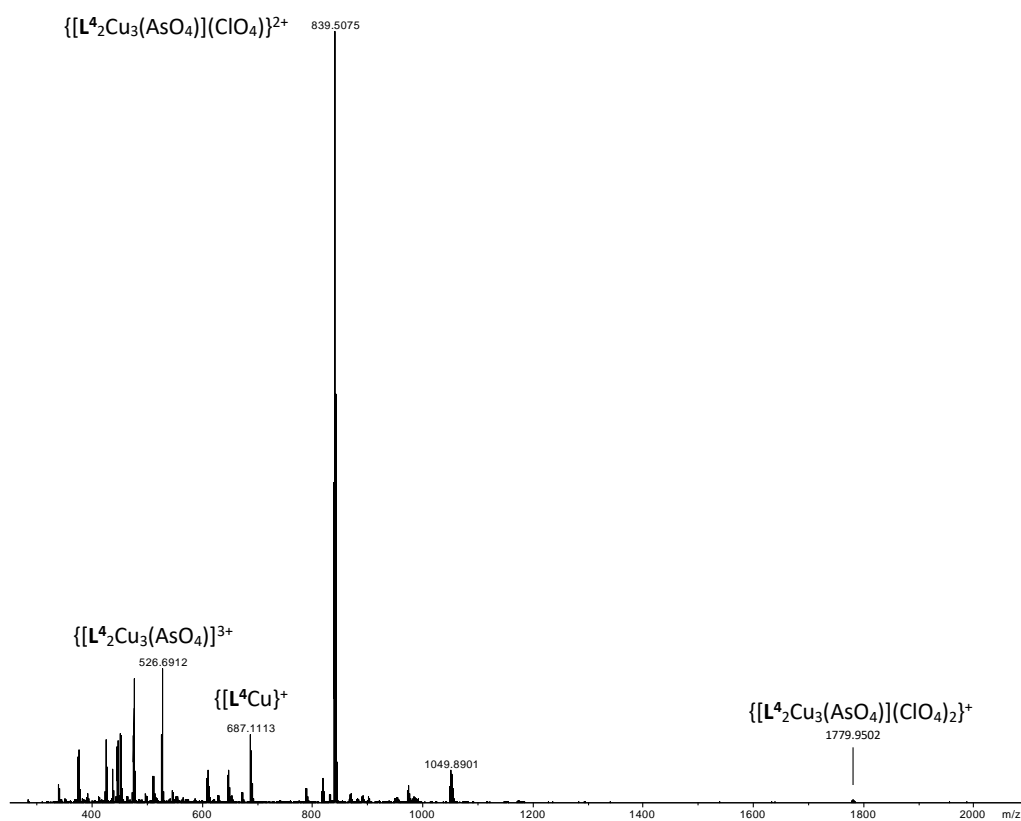


Figure 3.36. ESI-MS spectrum of $[L^4_2Cu_3(AsO_4)](ClO_4)_3$.

Addition of half an equivalent of disodium hydrogen arsenate to another solution of ligand L^4 with 1.5 equivalents of copper(II) trifluoromethanesulfonate in water/acetonitrile (1:1) resulted in the same lime-green colour change observed as when phosphate was added (Figure 3.38b), with a very similar UV-Vis-NIR spectrum; giving a peak at a wavelength of 745 nm (Figure 3.37).

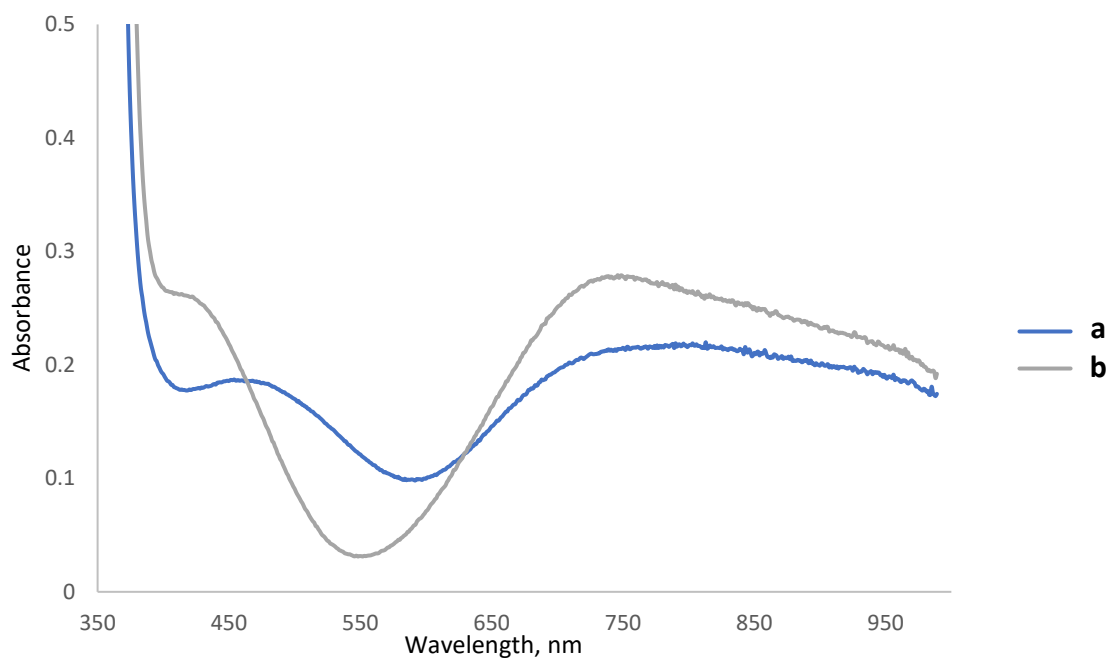


Figure 3.37. UV-Vis-NIR absorption spectra of solutions of a) $[\text{L}^4_2\text{Cu}_3](\text{trif})_6$; b) $[\text{L}^4_2\text{Cu}_3](\text{trif})_6$ plus the addition of one equivalent of disodium arsenate. Concentration of $[\text{L}^4_2\text{Cu}_3](\text{trif})_6 = 0.8 \text{ mM}$ (1:1 acetonitrile in water).

3.3.3. Selectivity experiments

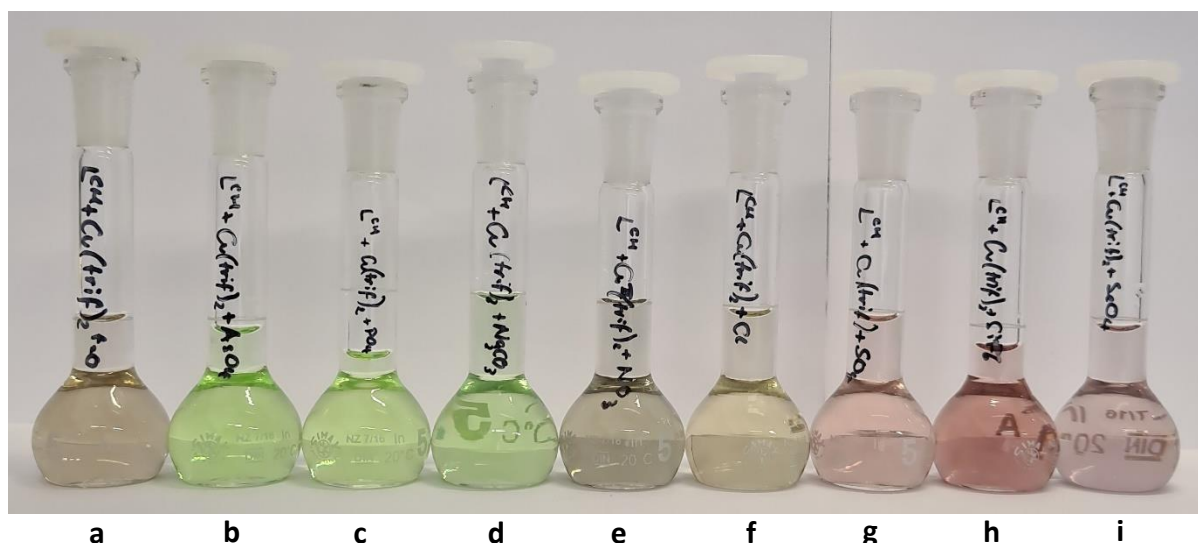


Figure 3.38. Range of colours observed with complexes of L^4 and $Cu(trif)_2$: a) $[L^4_2Cu_3]^{6+}$; b) $[L^4_2Cu_3]^{6+} + AsO_4^{3-}$; c) $[L^4_2Cu_3]^{6+} + PO_4^{3-}$; d) $[L^4_2Cu_3]^{6+} + CO_3^{2-}$; e) $[L^4_2Cu_3]^{6+} + NO_3^-$; f) $[L^4_2Cu_3]^{6+} + Cl^-$; g) $[L^4_2Cu_3]^{6+} + SO_4^{2-}$; h) $[L^4_2Cu_3]^{6+} + SiF_6^{2-}$; i) $[L^4_2Cu_3]^{6+} + SeO_4^{2-}$. Complexes assembled in a 1:1 MeCN/ H_2O solution with one equivalent of the corresponding anion as either their sodium, ammonium or tetra-*N*-alkylammonium salts at a concentration of 0.88 mM.

UV-Vis-NIR experiments

A variety of L^4 complexes in solution were analysed by UV-Vis-NIR spectroscopy, by dissolving ligand L^4 and 1.5 equivalents of copper(II) trifluoromethanesulfonate in a solution of acetonitrile/water (1:1) and adding half an equivalent of each anion as either their ammonium, tetra-*N*-alkylammonium or sodium salts, giving solutions of a variety of colours (Figure 3.38). Analysis of these solutions by UV-Vis-NIR spectroscopy showed that the solutions containing arsenate, phosphate and carbonate anions gave very similar spectra (Figure 3.39), as did those containing hexafluorosilicate, selenate and sulfate (Figure 3.40). However, addition of chloride anions seemed to have only a very slight effect on the spectrum in comparison to the trace containing purely the “empty” cage (i.e. $[L^4_2Cu_3]^{6+}$) and the nitrate anion seemed to have no effect at all (Figure 3.41).

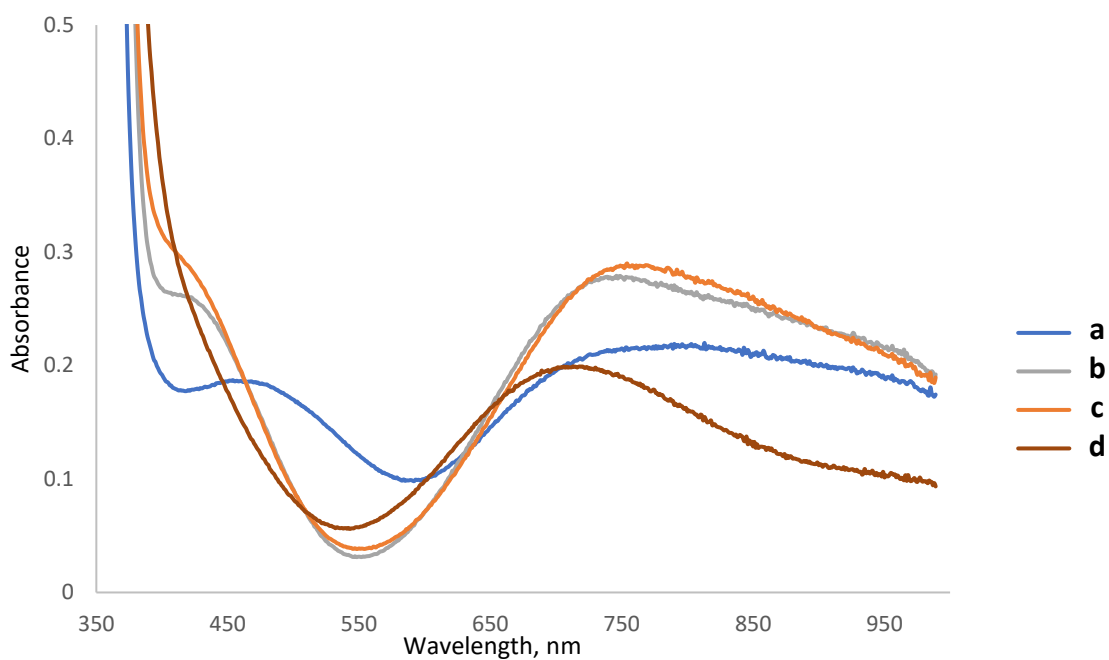


Figure 3.39. UV-Vis-NIR absorption spectra of solutions of a) $[\mathbf{L}^4_2\text{Cu}_3](\text{trif})_6$; b) $[\mathbf{L}^4_2\text{Cu}_3](\text{trif})_6 + \text{AsO}_4^{3-}$; c) $[\mathbf{L}^4_2\text{Cu}_3](\text{trif})_6 + \text{H}_2\text{PO}_4^-$; d) $[\mathbf{L}^4_2\text{Cu}_3](\text{trif})_6 + \text{CO}_3^{2-}$. Anions added as either their sodium, ammonium or tetra-N-alkylammonium salts as one equivalent with respect to complex. Concentration of $[\mathbf{L}^4_2\text{Cu}_3](\text{trif})_6 = 0.8 \text{ mM}$ (1:1 acetonitrile in water).

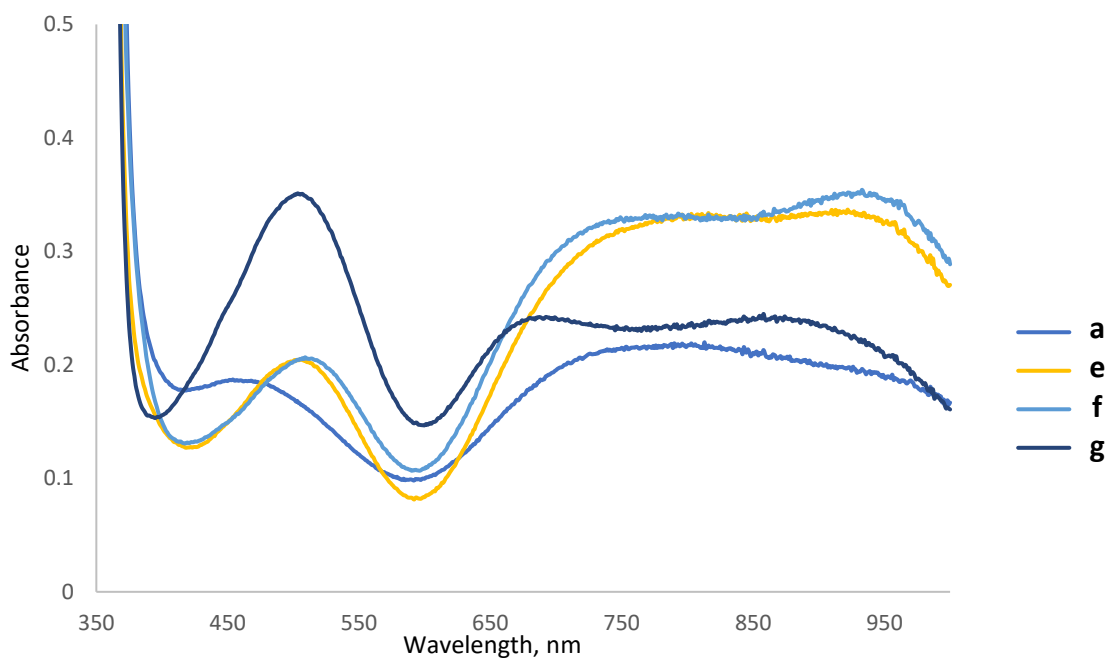


Figure 3.40. UV-Vis-NIR absorption spectra of solutions of a) $[\text{L}^4_2\text{Cu}_3](\text{trif})_6$; e) $[\text{L}^4_2\text{Cu}_3](\text{trif})_6 + \text{HSO}_4^-$; f) $[\text{L}^4_2\text{Cu}_3](\text{trif})_6 + \text{SeO}_4^{2-}$; g) $[\text{L}^4_2\text{Cu}_3](\text{trif})_6 + \text{SiF}_6^{2-}$. Anions added as either their sodium, ammonium or tetra-N-alkylammonium salts as one equivalent with respect to complex. Concentration of $[\text{L}^4_2\text{Cu}_3](\text{trif})_6 = 0.8 \text{ mM}$ (1:1 acetonitrile in water).

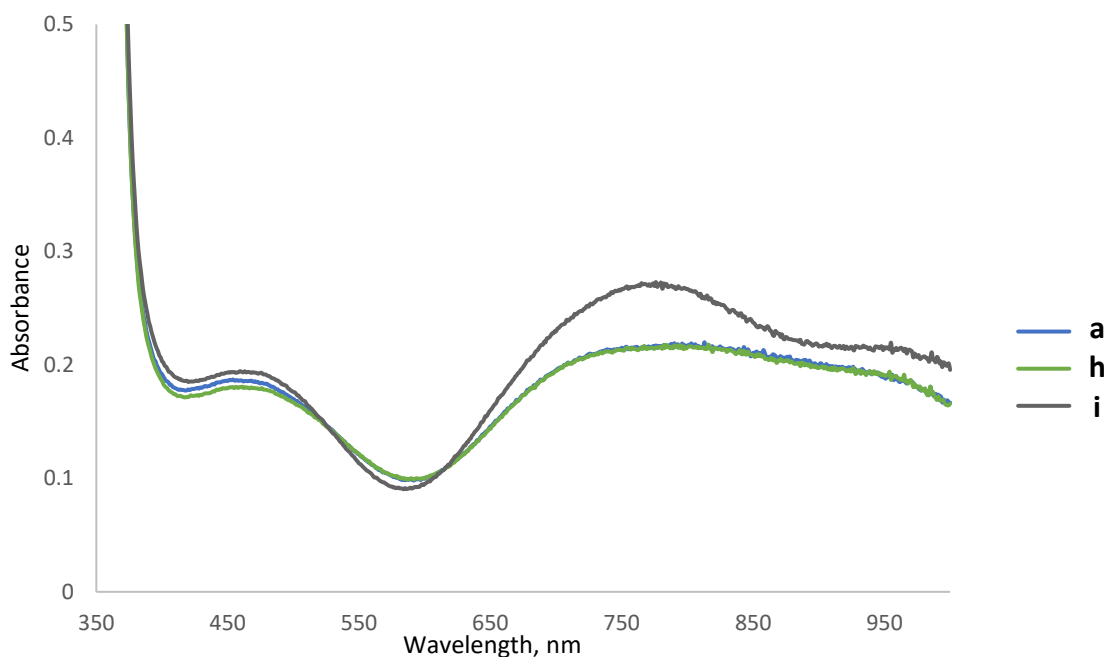


Figure 3.41. UV-Vis-NIR absorption spectra of solutions of a) $[\text{L}^4_2\text{Cu}_3](\text{trif})_6$; h) $[\text{L}^4_2\text{Cu}_3](\text{trif})_6 + \text{NO}_3^-$; i) $[\text{L}^4_2\text{Cu}_3](\text{trif})_6 + \text{Cl}^-$. Anions added as either their sodium, ammonium or tetra-N-alkylammonium salts as one equivalent with respect to complex. Concentration of $[\text{L}^4_2\text{Cu}_3](\text{trif})_6 = 0.8 \text{ mM}$ (1:1 acetonitrile in water).

To investigate the selective nature of the anion extraction properties of the complex, further UV-Vis-NIR studies were conducted by using various salts of phosphate and sulfate anions; this was carried out by adding one salt to a solution of the complex, recording the spectra, adding another salt and re-recording the spectra after thorough mixing. Reaction of the complex with sulfate and phosphate as their monosodium salts, the UV-Vis-NIR spectrum indicates neither $[\text{L}^4_2\text{Cu}_3](\text{PO}_4)]^{3+}$ or $[\text{L}^4_2\text{Cu}_3](\text{SO}_4)]^{4+}$ is the sole product (Figure 3.42) and this is likely due to the presence of both the phosphate- and sulfate-encapsulating complexes.

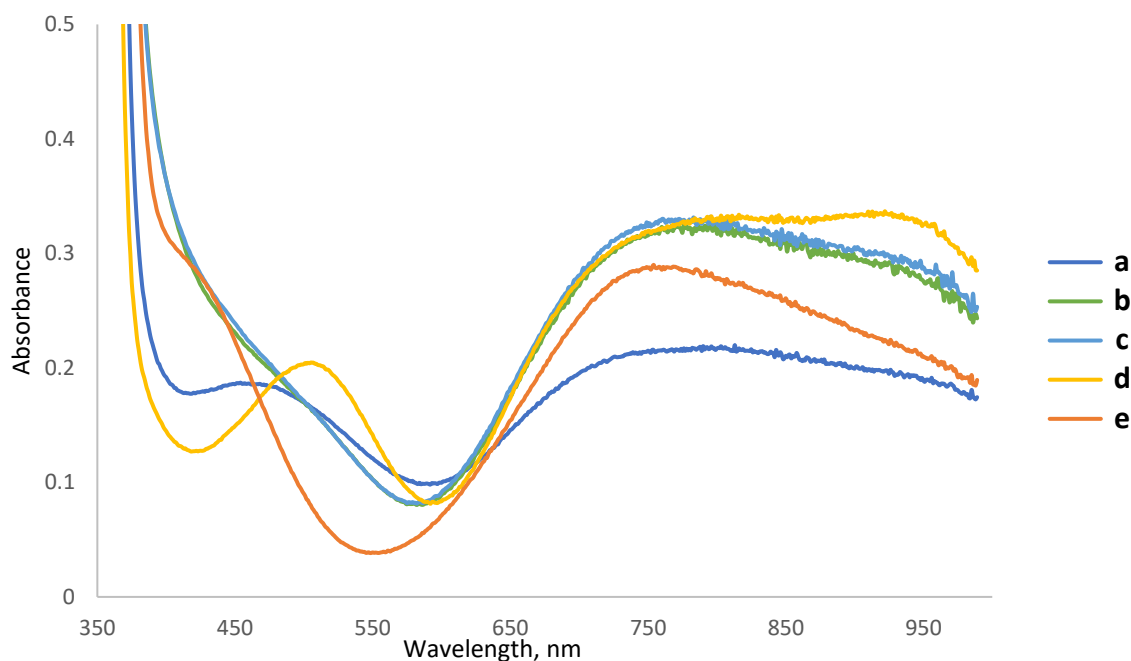


Figure 3.42. UV-Vis-NIR absorption spectra of solutions of a) $[L^4_2Cu_3](trif)_6$; b) $[L^4_2Cu_3](trif)_6 + NaH_2PO_4$ followed by $NaHSO_4$; c) $[L^4_2Cu_3](trif)_6 + NaHSO_4$ followed by NaH_2PO_4 ; d) $[L^4_2Cu_3(SO_4)](trif)_4$; e) $[L^4_2Cu_3(PO_4)](trif)_3$ in 1:1 acetonitrile in water. Anions added as one equivalent with respect to complex. Concentration of $[L^4_2Cu_3](trif)_6 = 0.8$ mM.

However, when the disodium salts of sulfate and phosphate are used, the UV-Vis-NIR spectrum indicates that $[L^4_2Cu_3](PO_4)^{3+}$ is the only complex present, indicating that a higher pH (where SO_4^{2-} and HPO_4^{2-} would predominate) the cavity is selective to phosphate (Figure 3.43).

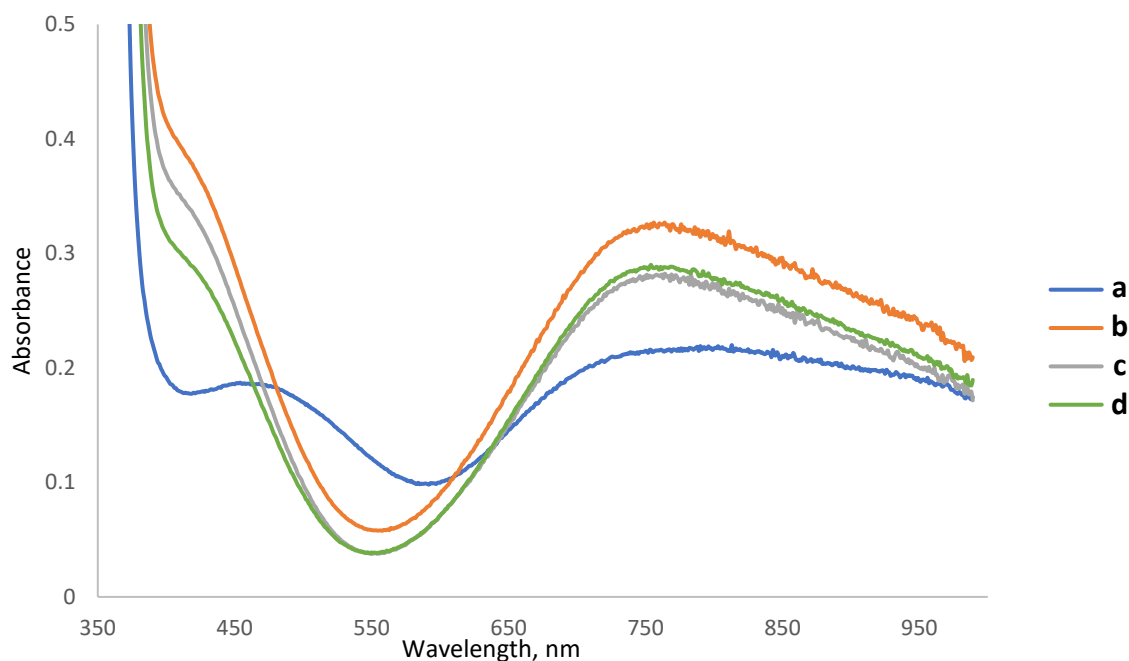


Figure 3.43. UV-Vis-NIR absorption spectra of solutions of a) $[\text{L}^4_2\text{Cu}_3](\text{trif})_6$; b) $[\text{L}^4_2\text{Cu}_3](\text{trif})_6 + \text{Na}_2\text{HPO}_4$ followed by Na_2SO_4 ; c) $[\text{L}^4_2\text{Cu}_3](\text{trif})_6 + \text{Na}_2\text{SO}_4$ followed by Na_2HPO_4 ; d) $[\text{L}^4_2\text{Cu}_3(\text{PO}_4)](\text{trif})_3$ in 1:1 acetonitrile in water. Anions added as one equivalent with respect to complex. Concentration of $[\text{L}^4_2\text{Cu}_3](\text{trif})_6 = 0.8 \text{ mM}$.

Ion chromatography experiments

The selectivity of the complex was also examined by ion chromatography, whereby aqueous solutions with known concentrations of four anions at various pH levels would be treated with the complex and the remaining solution analysed for the anion content. At lower pH, where HSO_4^- and H_2PO_4^- were used removal of the resultant precipitate and analysis of the remaining solution showed the complex extracted both sulfate and phosphate anions, with a slight selectivity toward phosphate anions (Figure 3.44). However, at a higher pH where the doubly-deprotonated anions (SO_4^{2-} and HPO_4^{2-}) would be more predominant, the complex is almost entirely selective to phosphate anions, removing 75% of the available phosphate in favour of the other anions (Figure 3.45). In both of these experiments, neither nitrate nor chloride are affected.

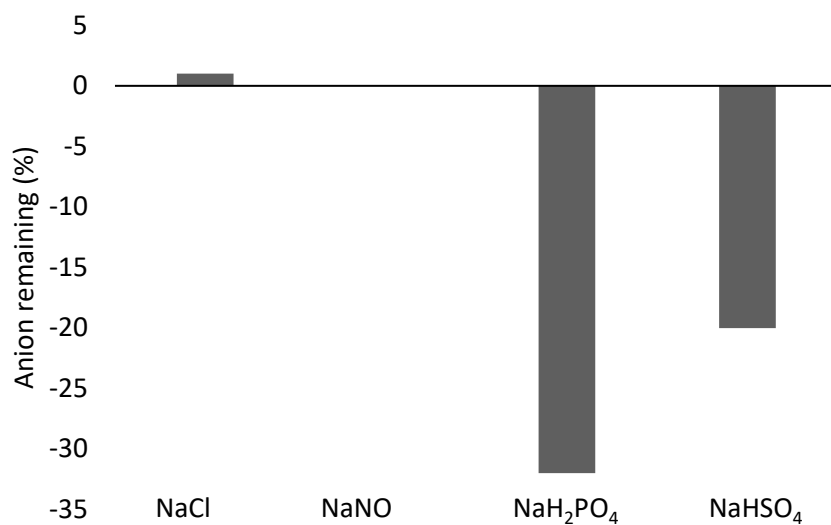


Figure 3.44. Percentage removal of NaCl, NaNO₃, NaH₂PO₄ and NaHSO₄ anions upon precipitation with [L⁴₂Cu₃](trif)₆. The contribution from the background concentration of the anions (~10%) has been removed.

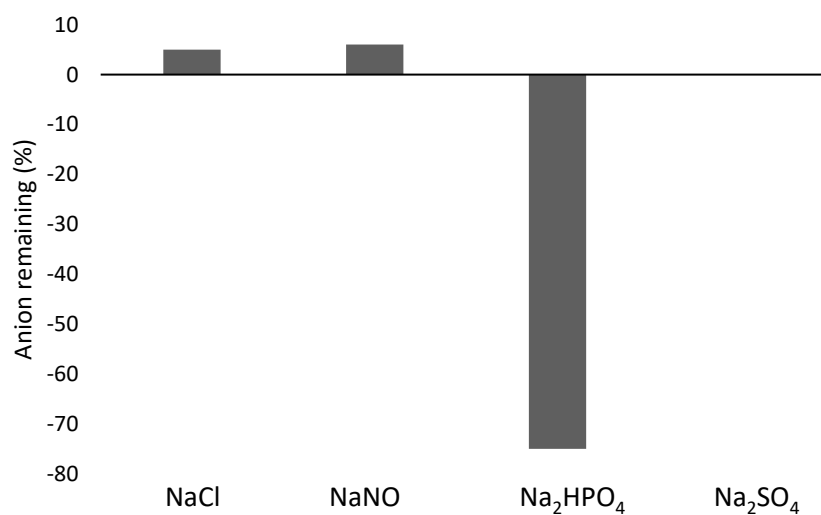


Figure 3.45. Percentage removal of NaCl, NaNO₃, Na₂HPO₄ and Na₂SO₄ anions upon precipitation with [L⁴₂Cu₃](trif)₆. The contribution from the background concentration of the anions (~10%) has been removed.

The difference in selectivity observed in both the UV-Vis-NIR and precipitation experiments can be rationalised by the acidity of the monoanion. In these complexes once encapsulation has occurred the anions are fully deprotonated regardless of their original protonated state (*c.f.* reaction of $[\mathbf{L}^4_2\text{Cu}_3]^{6+}$ with Bu_4NHSO_4 giving $[\mathbf{L}^4_2\text{Cu}_3(\text{SO}_4)]^{4+}$). The monoanionic HSO_4^- ($pK_a = 1.81$) is significantly more acidic than H_2PO_4^- ($pK_a = 7.21$) and as a result HSO_4^- is more readily deprotonated and will occupy the cavity in preference to dihydrogen phosphate. This issue does not arise with the dianionic SO_4^{2-} and the cavity is selective to the phosphate (due to the difference in anionic charge) demonstrating that the selectivity of anion encapsulation can be controlled by pH (for a solution of Na_2SO_4 and Na_2HPO_4 $pH = 8.85$ whereas NaHSO_4 and NaH_2PO_4 $pH = 2.81$). Whilst the previously reported complex with ligand \mathbf{L}^1 (e.g. $[\mathbf{L}^1_2\text{Cu}_3]^{6+}$) is selective to phosphate it does precipitate a substantial amount of sulfate from a competitive mixture of anions; whereas the complex formed from ligand \mathbf{L}^4 (e.g. $[\mathbf{L}^4_2\text{Cu}_3]^{6+}$) is totally selective to phosphate at high pH . This demonstrates that subtle differences in the ligand chain can further increase the selectivity and remove phosphate in the presence of other common anions.

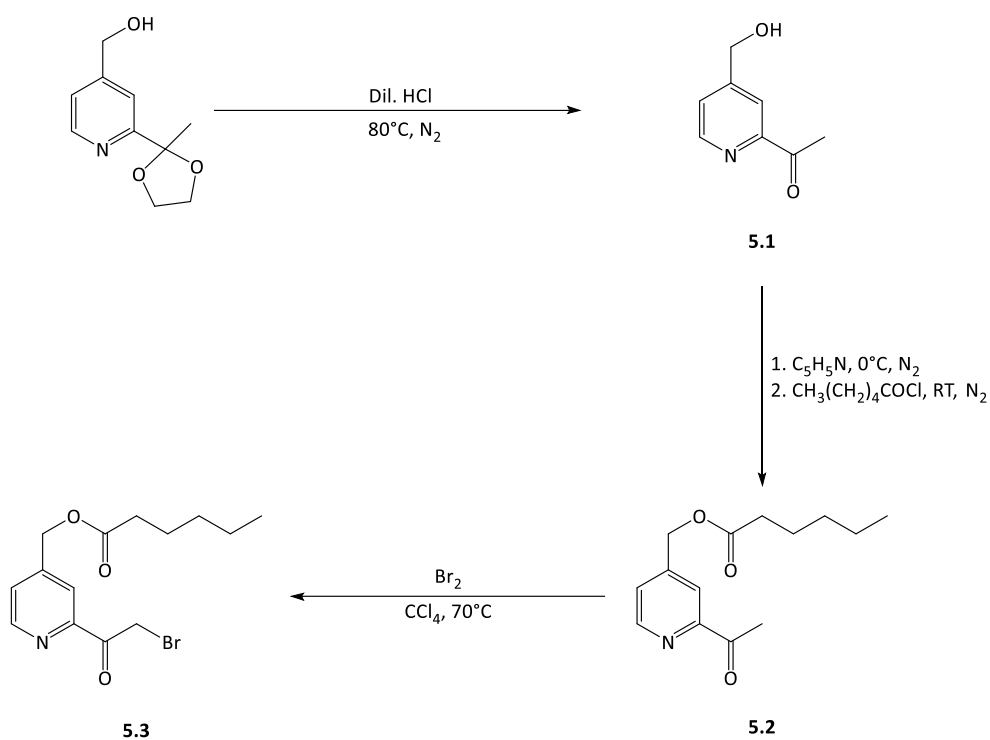
4. Lipophilic Receptors to Extract Aqueous Anions into Organic Media

In order to improve the practicality and efficiency of the anion extraction properties of these ligands, it was theorised that increasing the solubility of the ligand (and therefore the complexes) in organic solvents would allow the extraction of anions from aqueous media through liquid-liquid extraction.¹⁰⁸ Liquid-liquid extraction is advantageous over precipitation methods due to their ability to be used as a continuous process, whereas the latter process is batch-based. However, difficulty in extracting these anions into organic media arise from the hydrophilicity of the phosphate anion, especially in comparison to the less hydrophilic anions (e.g. halides, nitrate etc). Therefore, the ability to selectively extract phosphate anions into solvents immiscible with aqueous media is challenging but important if resource recovery is to be an achievable goal.

4.1.1. Synthesis

Synthesis of intermediate 5.3

To achieve this, ligands **L⁵** and **L⁶** were synthesised using thioureas **1.2** and **3.2** respectively resulting in the same ligand spacer unit and co-ordination domains as their parent ligands but incorporated within the ligand strands are an aliphatic chain group at the 4- position on each of the three pyridyl-groups of the ligand. 2-(α -Bromoacetyl)pyridine derivative **5.3** was reacted with the already prepared thioureas while including these aliphatic strands. This was synthesised from a keto-protected 4-(hydroxymethyl)-2-acetylpyridine (Scheme 4.1).^{118,119}



Scheme 4.1. Synthesis of brominated 2-acetylpyridine derivative 5.3 from (2-(2-methyl-1,3-dioxolan-2-yl)pyridin-4-yl)methanol.^{118,119}

Initially, the protecting group was removed from the 4-(hydroxymethyl)acetylpyridine starting material by refluxing in 3 M hydrochloric acid overnight, after which analysis by TLC showed the absence of the starting material. The solution was neutralised and extracted into DCM; removal of solvent left the crude product as a slightly orange oil. Analysis by ^1H NMR spectroscopy showed the product was suitably pure to use in the next step without further purification (Figure 4.1).

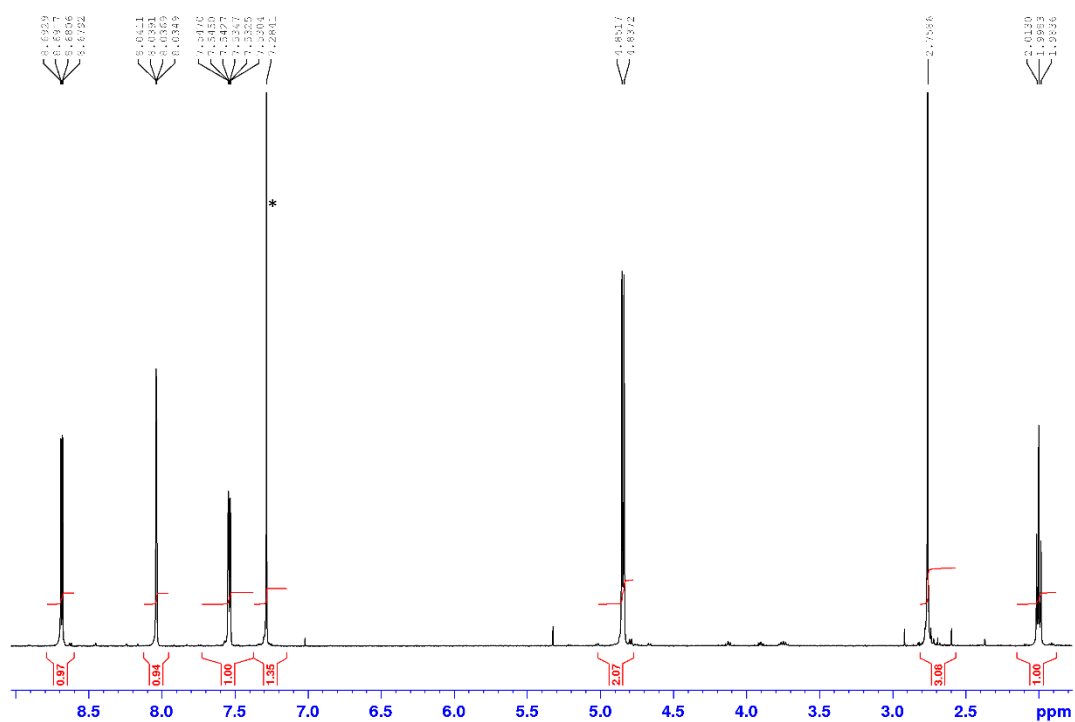


Figure 4.1. ^1H NMR (CDCl_3) spectrum of **5.1**. N.B. aromatic signals indicative of a disubstituted pyridyl- ring. Aliphatic doublet at 4.84 ppm shifted highly due to its proximity to a hydroxyl group.

* CHCl_3 impurity.

The reaction of alcohol **5.1** with hexanoyl chloride required the starting material to be as anhydrous as possible; this was done by the addition of toluene and removal of solvents by rotary evaporation to azeotropically remove water and repeated until the starting material was sufficiently dry. This was then reacted with hexanoyl chloride in the presence of pyridine and stirred at room temperature until analysis by TLC showed absence of the starting material. After neutralisation and extraction into DCM, the crude product was purified by column chromatography and analysed by ^1H NMR spectroscopy; the presence of a set of signals in the aliphatic region corresponding to the hexanoyl substituent confirmed the successful synthesis of **5.2** (Figure 4.2).

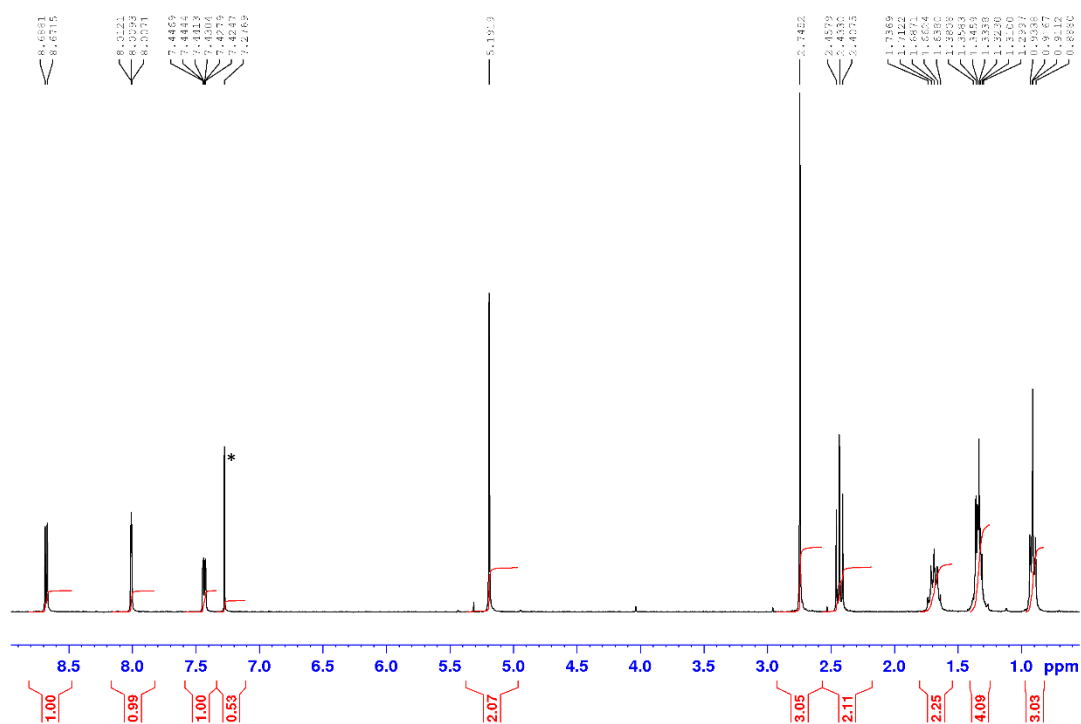


Figure 4.2. ^1H NMR (CDCl_3) spectrum of **5.2**. N.B. four new aliphatic signals corresponding to the hexanoyl linkage; two $-\text{CH}_2-$ groups are coincident at 1.34 ppm. $^*\text{CHCl}_3$ impurity.

Finally, conversion of the hexanoyl- derivative **5.2** to the brominated species **5.3** was done by the dropwise addition of bromine, diluted in carbon tetrachloride, to the acetylpyridine- derivative **5.2** starting material and followed by TLC analysis. This reaction produced a mixture of mono- and di-brominated acetylpyridine products which were separated by column chromatography after neutralisation and extraction of the reaction mixture. The pure product was analysed by ^1H NMR spectroscopy, which shows a shift of the signal corresponding to the ketone-adjacent methyl-group protons from 2.75 to 4.87 ppm (Figure 4.3). This reaction used carbon tetrachloride, which was undesirable due to its ozone-depleting properties and difficulties in procurement; however, the reaction in different solvents produced products of insufficient quality or yield. Specifically, the reaction in acetic acid gave almost entirely the dibrominated species (even with careful stoichiometry

control) and when performed in chloroform, almost none of the desired product was recovered. Use of a dioxane-bromine complex did produce the singly-brominated product but the yields were highly variable, and whilst the use of carbon tetrachloride is undesirable, this solvent gives the highest and most reliable yields.

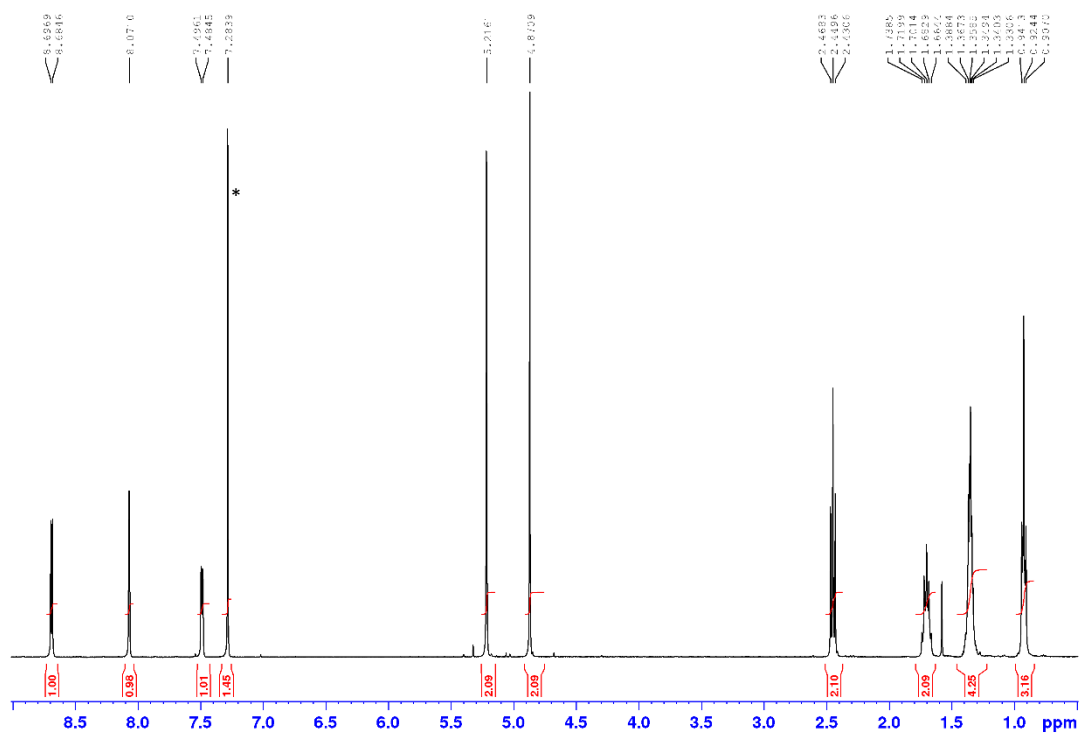
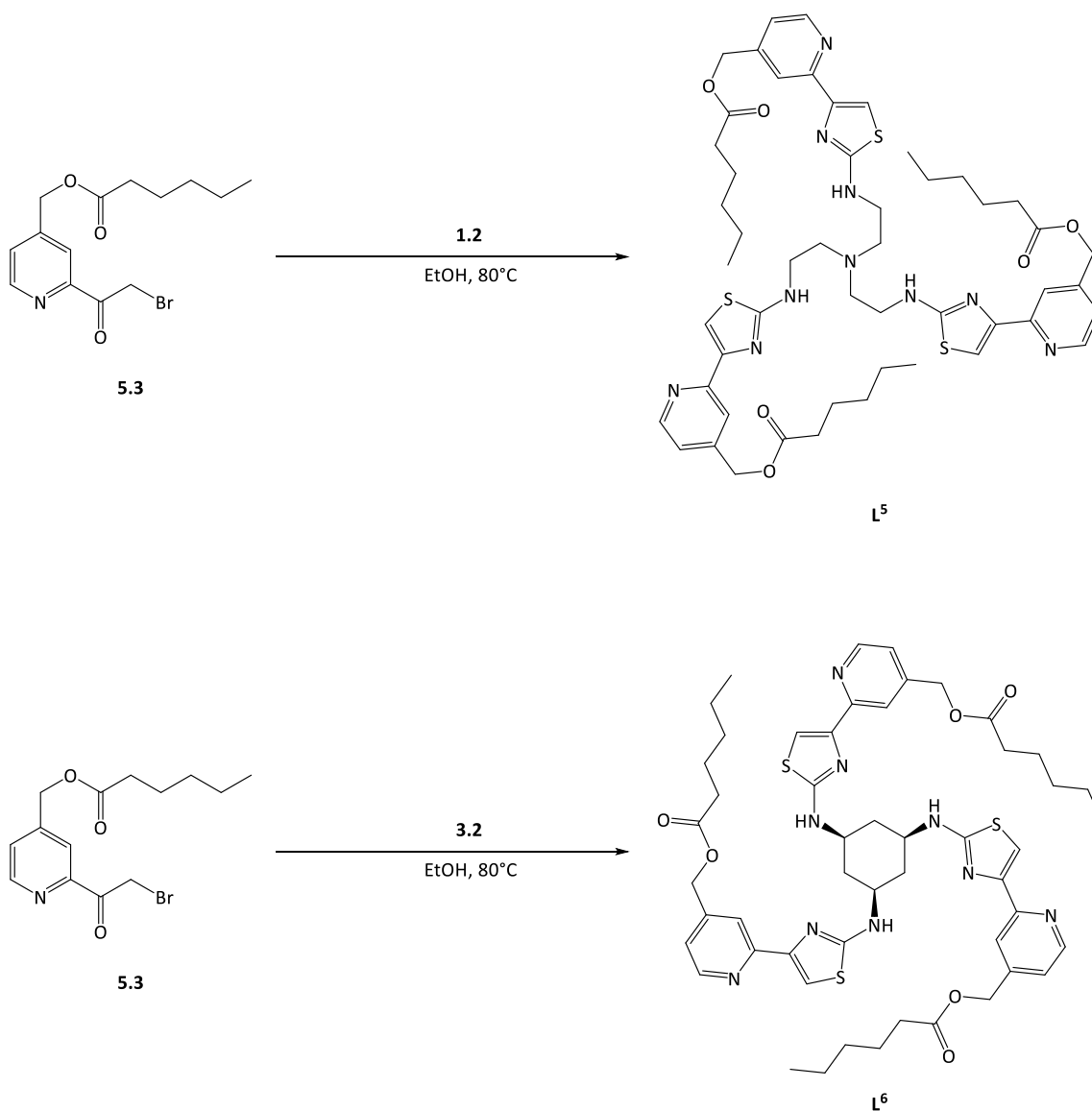


Figure 4.3. ^1H NMR (CDCl_3) spectrum of **5.3**. N.B. shifted ketone singlet signal (4.87 ppm) which integrates to two hydrogen atoms indicative of a $-\text{COCH}_2\text{Br}$ unit. $^*\text{CHCl}_3$ impurity.

Synthesis of ligand L⁵

With this precursor made, the ligands L⁵ and L⁶ could be made from their respective thioureas (Scheme 4.2). These ligands would incorporate the hexanoyl- group added in the previous reactions but would otherwise be identical to ligands L¹ and L³.



Scheme 4.2. Synthesis of ligands L⁵ and L⁶ from brominated acetylpyridine- species 5.3 and respective thioureas.

Ligand **L⁵** was synthesised from thiourea **1.2** by refluxing in ethanol overnight, neutralising the crude product after removal of the solvent and extraction into dichloromethane; this crude mixture required column chromatography to separate the pure product **L⁶** as a pink-orange oil. Analysis by ¹H NMR spectroscopy showed a singlet signal at 7.28 ppm corresponding to the lone thiazole proton environment, as well as the aliphatic region indicative of both the central ethyl- linkage and the aliphatic hexanoyl- groups, indicating the successful synthesis of the final ligand **L⁵** (Figure 4.4).

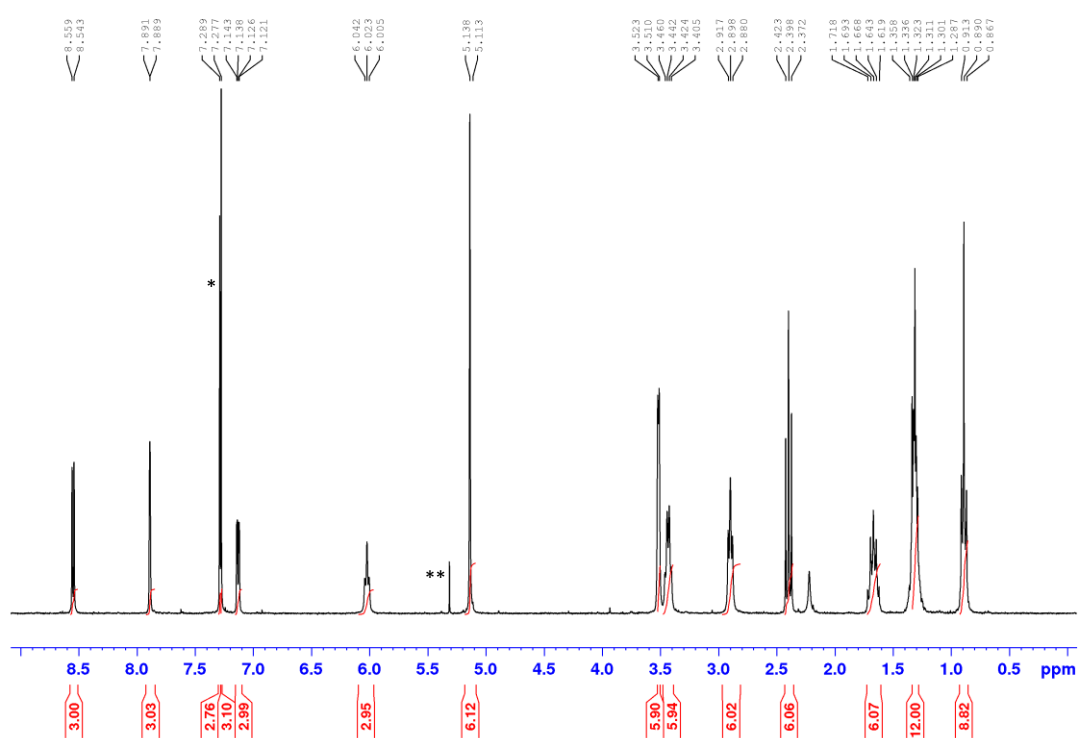


Figure 4.4. ¹H NMR (CDCl₃) spectrum of ligand **L⁵**. N.B. eight aliphatic signals, four aromatic signals and one -NH triplet signal at 6.02 ppm indicative of successful ligand synthesis. *CHCl₃ impurity.

**CH₂Cl₂ impurity.

4.2. Co-ordination chemistry

As both ligands contain the same basic tripodal *tris*-bidentate domains as their parent ligands L^1 and L^3 (whose co-ordination chemistry has been extensively investigated) it was reasonable to assume that both L^5 and L^6 would form the trimetallic cryptate assembly and these would encapsulate anions within the cavity. Reaction of either L^5 and L^6 with copper(II) trifluoromethanesulfonate in a 3% methanol in DCM solution gave dark-yellow and pale-yellow solutions respectively. The organic solubility and self-assembly were confirmed by ESI-MS analysis; these showed signals corresponding to the expected trinuclear species (e.g. m/z 2958 and 1402 corresponding to $\{[L^5_2Cu_3](trif)_5\}^+$ and $\{[L^5_2Cu_3](trif)_4\}^{2+}$ respectively), indicating that the ligand forms the expected capsule in organic media.

A solution of DCM containing the complex was then partitioned with an equal volume of water containing one equivalent of monosodium phosphate, resulting in a gradual colour change (over roughly 15 minutes) of the organic phase to the lime-green colour visually identical to that obtained with solutions of $[L^1_2Cu_3(PO_4)]^{3+}$ and $[L^4_2Cu_3(PO_4)]^{3+}$ (Figure 4.6) and indicative of phosphate encapsulation. Analysis of the organic phases by ESI-MS showed signals at m/z 2606 and 1228 for $\{[L^5_2Cu_3(PO_4)](trif)_2\}^+$ and $\{[L^5_2Cu_3(PO_4)](trif)\}^{2+}$ respectively and the solution with L^6 showed signals at 2572 and 1211 corresponding to $\{[L^6_2Cu_3(PO_4)](trif)_2\}^+$ and $\{[L^6_2Cu_3(PO_4)](trif)\}^{2+}$ respectively, indicating successful encapsulation of a phosphate anion in both cases, indicating that phosphate anions are transferred to the organic phase *via* this assembly.

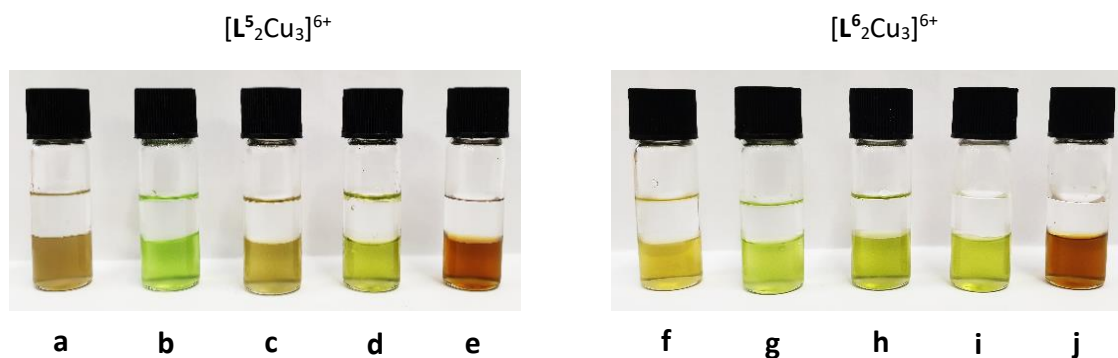


Figure 4.6. Extraction experiments of a DCM solution of a) - e) $[\text{L}^5_2\text{Cu}_3]^{6+}$, f) - j) $[\text{L}^6_2\text{Cu}_3]^{6+}$. Organic solutions partitioned with: a) and f) ultrapure water; aqueous solutions containing b) and g) one equivalent of Na_2HPO_4 , c) and h) one equivalent of each of NaCl , NaNO_3 , NaHSO_4 and NaH_2PO_4 , d) and i) one equivalent of each of NaCl , NaNO_3 , Na_2SO_4 and Na_2HPO_4 and e) and j) one equivalent of each of NaF , NaCl , NaBr and NaI .

UV-Vis-NIR experiments

The solutions containing phosphate and sulfate were analysed by UV-Vis-NIR spectroscopy and traces compared to those obtained with $[\text{L}^5_2\text{Cu}_3](\text{trif})_6$ and $[\text{L}^6_2\text{Cu}_3](\text{trif})_6$ (Figure 4.7 - Figure 4.10). The capsules containing the triflate anion from the copper(II) metal salt displayed peaks at 500 and 790 nm for $[\text{L}^5_2\text{Cu}_3](\text{trif})_6$ and a single peak at around 710 nm for the solution of $[\text{L}^6_2\text{Cu}_3](\text{trif})_6$. Reaction of $[\text{L}^5_2\text{Cu}_3](\text{trif})_6$ with half an equivalent of tetra-*N*-butylammonium hydrogen phosphate gave an immediate colour change to lime green (Figure 4.6b), which gave single peak in the UV-Vis-NIR spectra at 740 nm corresponding to $[\text{L}^5_2\text{Cu}_3(\text{PO}_4)](\text{trif})_3$ (Figure 4.7). However, on reaction with half an equivalent of tetra-*N*-butylammonium hydrogen sulfate, three maxima were observed in the spectrum for $[\text{L}^5_2\text{Cu}_3](\text{trif})_6$ at 500, 785 and 940 nm (Figure 4.8).

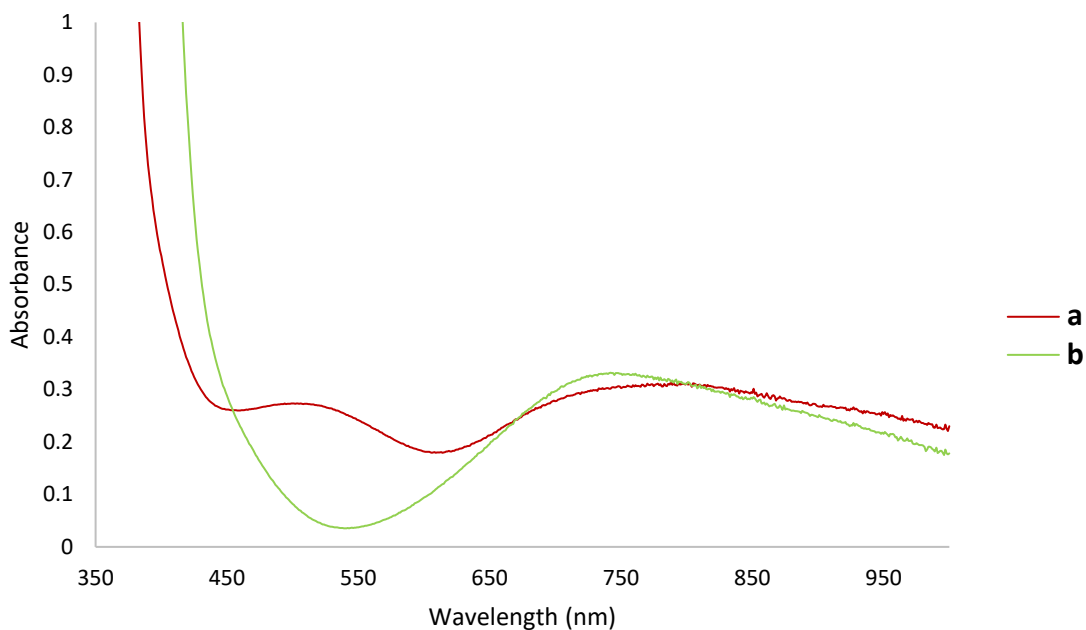


Figure 4.7. UV-Vis-NIR absorption spectra of a) $[L^5_2Cu_3]^{6+}$; b) $[L^5_2Cu_3]^{6+}$ plus half an equivalent of tetra-N-butylammonium dihydrogen phosphate. Concentration of complex = 0.8 mM (3% MeOH in DCM).

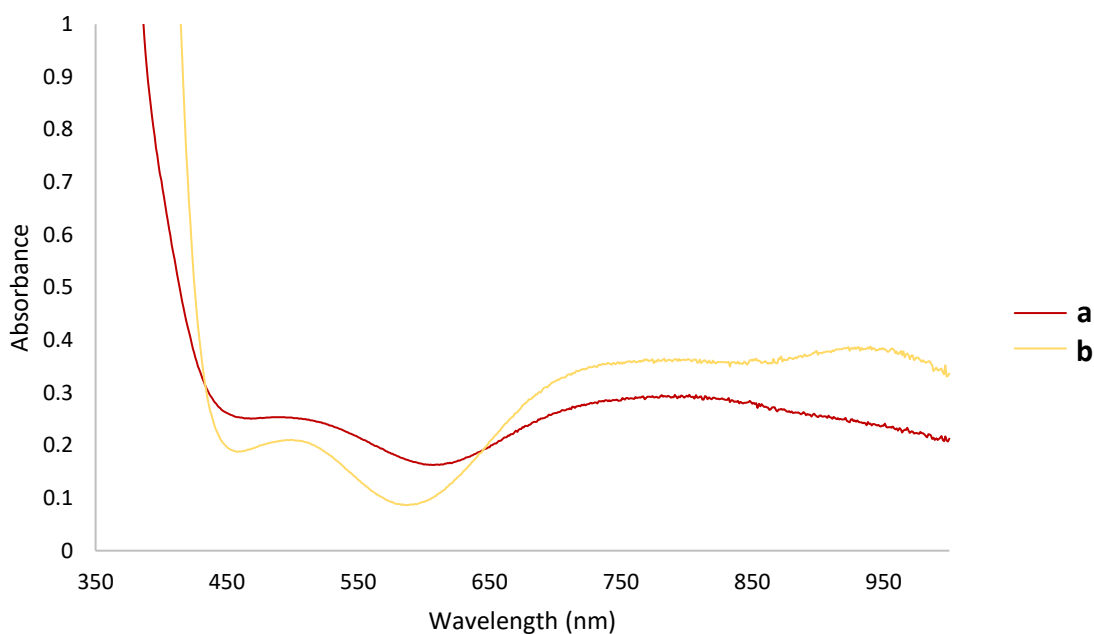


Figure 4.8. UV-Vis-NIR absorption spectra of a) $[L^5_2Cu_3]^{6+}$; b) $[L^5_2Cu_3]^{6+}$ plus half an equivalent of tetra-N-butylammonium hydrogen sulfate. Concentration of complex = 0.8 mM (3% MeOH in DCM).

Analogously to the previous experiment, reaction of $[\text{L}^6_2\text{Cu}_3](\text{trif})_6$ with half an equivalent of tetra-*N*-butylammonium hydrogen phosphate gave an immediate colour change to yellow-green (Figure 4.6g), which gave single peak in the UV-Vis-NIR spectra at 735 nm corresponding to $[\text{L}^6_2\text{Cu}_3(\text{PO}_4)](\text{trif})_3$ (Figure 4.9), and the same complex gave a single peak at 745 nm corresponding to $[\text{L}^6_2\text{Cu}_3(\text{SO}_4)](\text{trif})_4$ (Figure 4.10).

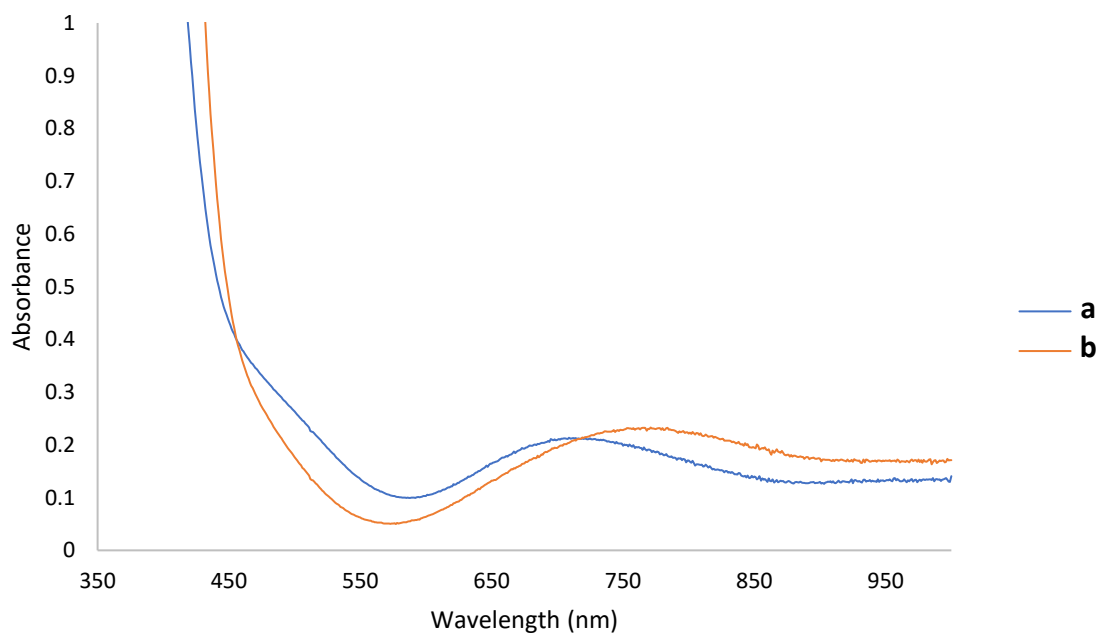


Figure 4.9. UV-Vis-NIR absorption spectra of a) $[\text{L}^6_2\text{Cu}_3]^{6+}$; b) $[\text{L}^6_2\text{Cu}_3]^{6+}$ plus half an equivalent of tetra-*N*-butylammonium dihydrogen phosphate. Concentration of complex = 0.8 mM (3% MeOH in DCM).

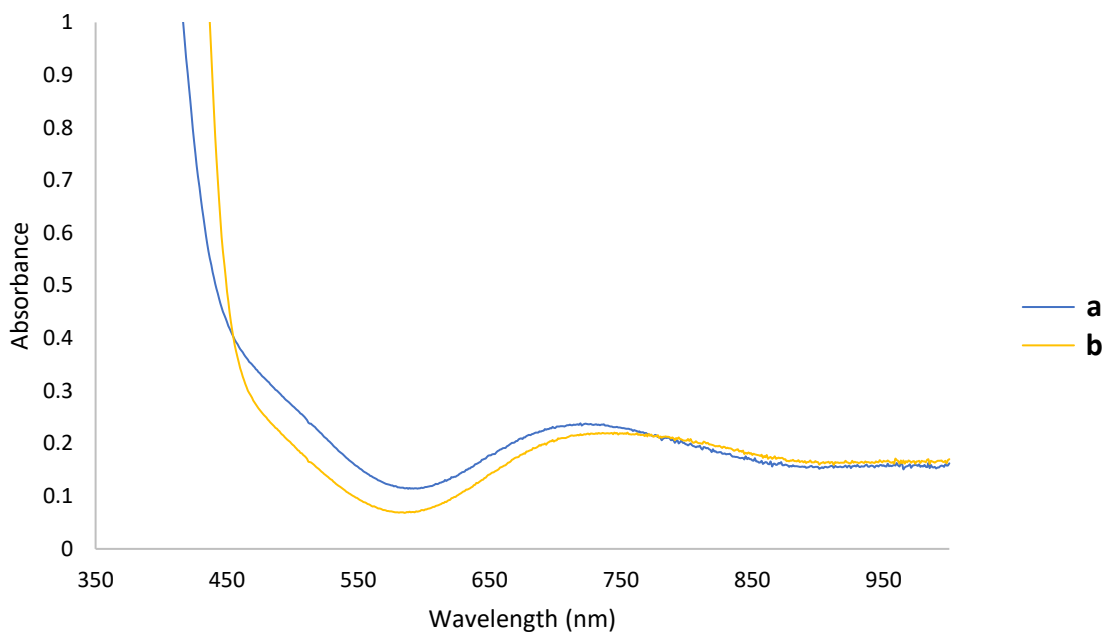


Figure 4.10. UV-Vis-NIR absorption spectra of a) $[\text{L}^6_2\text{Cu}_3]^{6+}$; b) $[\text{L}^6_2\text{Cu}_3]^{6+}$ plus half an equivalent of tetra-N-butylammonium hydrogen sulfate. Concentration of complex = 0.8 mM (3% MeOH in DCM).

Ion chromatography experiments

In order to quantitatively examine the phosphate extraction properties of these complexes, ion chromatography experiments were performed in which aqueous mixtures of the phosphate anion, at a known concentration, were treated with an organic solution containing one stoichiometric equivalent of each complex. These biphasic systems were stirred for 18 hours, during which time a noticeable colour change occurred, and 2 mL of the aqueous layer was removed. This was diluted to 5 mL and the solution analysed by ion chromatography; comparison of this data with that of the original solution allowed the magnitude of phosphate extraction to be measured (Table 4.1).

Excess of host	$[\text{L}^5_2\text{Cu}_3]^{6+}$	$[\text{L}^6_2\text{Cu}_3]^{6+}$
0%	82%	76%
10%	89%	80%
20%	94%	86%

Table 4.1. Percentage of phosphate anion extracted from aqueous solutions of Na_2HPO_4 after exposure to organic media containing each complex for 18 hours. Complexes assembled using copper(II) trifluoromethanesulfonate. Initial concentration of $\text{Na}_2\text{HPO}_4 = 0.66 \text{ mM}$.

When one stoichiometric equivalent of complex is used, the majority of phosphate is removed from the aqueous phase, with $[\text{L}^5_2\text{Cu}_3]^{6+}$ being slightly more effective than $[\text{L}^6_2\text{Cu}_3]^{6+}$ (82% vs 76% removal respectively). A 20% excess of complex raised these extraction figures to 94% and 86% extraction of phosphate for $[\text{L}^5_2\text{Cu}_3]^{6+}$ and $[\text{L}^6_2\text{Cu}_3]^{6+}$ respectively. It is important to note that the phosphate encapsulation releases three of the monoanionic triflate counterions from the complex depending on what copper(II) salt was used initially (e.g. $[\text{L}^5_2\text{Cu}_3](\text{trif})_6$ forms $[\text{L}^5_2\text{Cu}_3(\text{PO}_4)](\text{trif})_3$ plus three equivalents of triflate anion). However, a variety of copper(II) salts can be used to form these assemblies and a relatively benign anion (e.g. acetate, chloride) could be used in the exchange process.

Similar ion chromatography experiments were carried out in which aqueous mixtures of various common anions, at known concentrations, were treated with an organic solution containing a stoichiometric equivalent of each complex. The selectivity of extraction would then be measured between various anions at a certain pH by using the monosodium salts of each anion. Analogous to the previous method, these aqueous layers were examined by ion chromatography after being treated with a stoichiometric amount of each complex in organic media (Table 4.2).

Complex	NaCl	NaNO ₃	NaHSO ₄	NaH ₂ PO ₄
[L ⁵ ₂ Cu ₃] ⁶⁺	-8%*	-3%*	54%	28%
[L ⁶ ₂ Cu ₃] ⁶⁺	32%	0%	39%	38%

Table 4.2. Percentage of each anion extracted in aqueous solutions of NaCl, NaNO₃, NaHSO₄ and NaH₂PO₄ after exposure to organic media containing each complex for 18 hours. Initial concentration of each anion = 0.66 mM. pH = 2.79.

When exposed to the organic media containing [L⁵₂Cu₃]⁶⁺, sulfate anions are selectively extracted, with phosphates also being extracted to a certain extent. The experiment using [L⁶₂Cu₃]⁶⁺ saw no selectivity between sulfate and phosphate, extracting both roughly equally, but neither complex extracted nitrate. Some chloride was extracted by the second assembly but this could be a simple counteranion exchange rather than encapsulation by the complex (e.g. [L⁶₂Cu₃(SO₄)Cl]³⁺).

This experiment was repeated using the disodium salts of phosphate and sulfate for both complexes, the selectivity for phosphate increases drastically (Table 4.3).

Complex	NaCl	NaNO ₃	Na ₂ SO ₄	Na ₂ HPO ₄
[L ⁵ ₂ Cu ₃] ⁶⁺	-8%*	-1%*	16%	58%
[L ⁶ ₂ Cu ₃] ⁶⁺	4%	0%	5%	64%

Table 4.3. Percentage of each anion extracted in aqueous solutions of NaCl, NaNO₃, Na₂SO₄ and Na₂HPO₄ after exposure to organic media containing each complex for 18 hours. Initial concentration of each anion = 0.66 mM. pH = 8.85.

At this pH, both systems demonstrate a vastly increased selectivity for phosphate anions. With the [L⁵₂Cu₃]⁶⁺ complex, a small amount of sulfate is still extracted but the complex sequesters almost four times as much phosphate. As in the first experiment, chloride and nitrate are not extracted, which is

to be expected for this species due to its selectivity towards tetrahedral oxo-anions. The magnitude of selectivity with $[\mathbf{L}^6_2\text{Cu}_3]^{6+}$ is even greater, displaying an almost 13-fold preference to phosphate anions over sulfates; indeed, the sulfate extraction has decreased from 39% in the first experiment to only 5%, and chloride extraction expresses a similar reduction in removal.

The difference in selectivity between the mono- and dibasic phosphate and sulfate can be rationalised by the acidity of the monoanion. In these systems once encapsulation has occurred the anions are fully deprotonated, regardless of their original protonated state (*c.f.* reaction of $[\mathbf{L}^3_2\text{Cu}_3]^{6+}$ with Bu_4NHSO_4 giving $[\mathbf{L}^3_2\text{Cu}_3(\text{SO}_4)]^{4+}$). The monoanionic HSO_4^- ($pK_a = 1.81$) is significantly more acidic than H_2PO_4^- ($pK_a = 7.21$) and as a result HSO_4^- is more readily deprotonated and will therefore occupy the cavity in preference to dihydrogen phosphate. This issue does not arise with the dianionic SO_4^{2-} and the cavity is selective to the phosphate (due to the difference in anionic charge) demonstrating that the selectivity of anion encapsulation, and extraction into organic solutions, can be controlled by *pH*.

As a result, the initial issues surrounding phosphate extraction into organic media have been addressed through the adaptation of ligands \mathbf{L}^1 and \mathbf{L}^3 into \mathbf{L}^5 and \mathbf{L}^6 respectively, enabling the assembly of highly-selective phosphate encapsulating species in organic systems. Additionally, these complexes remain selective to phosphate anions in the presence of common contaminant anions that are not only less hydrophilic than phosphate but are also likely found in higher concentrations than phosphate in polluted water.

5. Conclusions

The research and development of anion receptors, whilst still juvenile, is becoming increasingly prevalent in modern-day chemistry due to their obvious industrial, biological and ecological applications. Self-assembled anion receptors are particularly attractive due to their relative ease of synthesis and pre-programmable nature of their component parts, which allows these to be used in a variety of applications.

For example, copper(II) complexes of ligand L^1 actively remove phosphate from aqueous media, the selectivity and potency of which has led to ground-breaking chemosensitivity studies through analysis of analogous transition metal complexes (i.e. those formed when assembled with Zn^{2+} and Mn^{2+}). Crystallographic evidence has shown that not only can this ligand adopt multiple motifs of coordination dependent on transition metal and anion (e.g. $[(L^1)_2M_3]^{6+}$, $[(L^1)_4M_8]^{16+}$ and $[(L^1)M_2]^{4+}$ have all been observed in the solid-state), but that a wide variety of anions can be encapsulated. This evidence led to the discovery that anionic phosphate esters (such as disodium phenylphosphate) can be bound or hydrolysed by these complexes depending on the metal used, and led to cytotoxicity studies which showed extraordinary *in vitro* selectivity and potency toward certain cancer cell lines compared to commercially available chemotherapy agents.

The substitution of the central amine bridging group in L^1 for various other aliphatic and alicyclic groups has led to the development of three new ligands, $L^2 - L^4$. Various studies on complexes using these ligands show that, with the exception of L^2 , these all adopt the same motif as analogous complexes using L^1 (i.e. $[(L)_2Cu_3]^{6+}$). Whilst colour changes indicative of complex formation are observed in most cases on the combining of complex and anion, solid-state structures of each ligand

were only observed when using certain anions, which may be an avenue for further research. Ion chromatography studies of L^4 complexes demonstrate selectivity toward phosphates in the presence of other common anions, variable with pH .

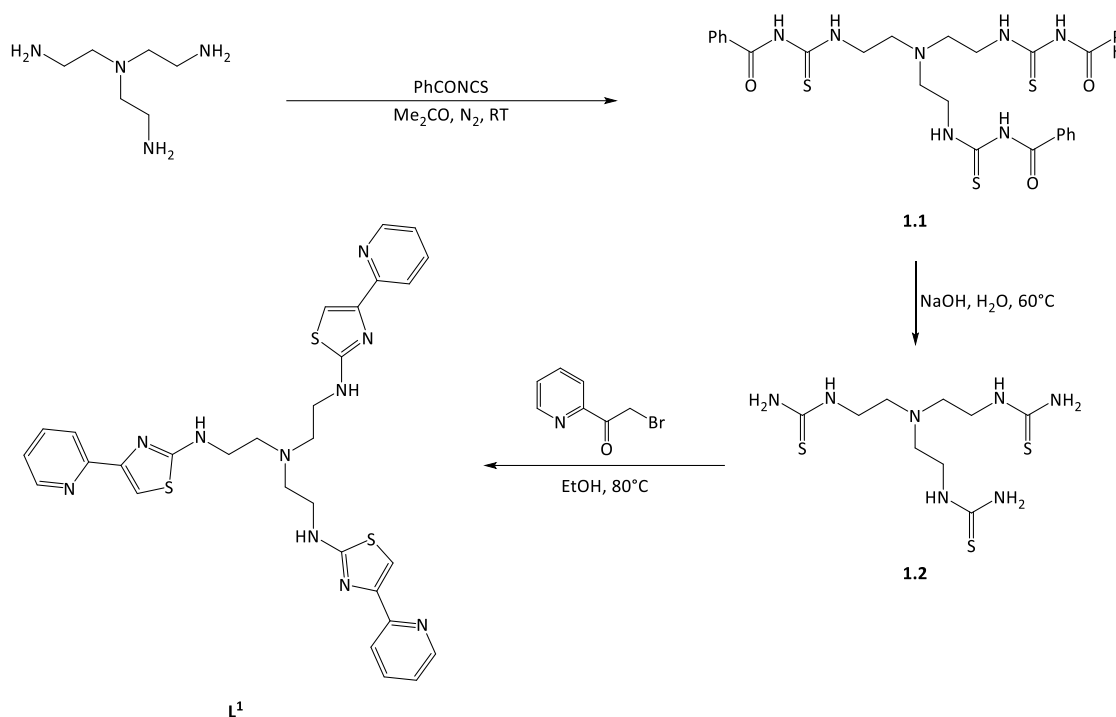
The addition of aliphatic ester groups onto ligands L^1 and L^3 have resulted in two more new ligands, L^5 and L^6 respectively. These have allowed the extraction of highly hydrophilic anions from aqueous to organic media owing to the increased solubility of the capsules in organic solvent. Ion chromatography studies indicate that both of these complexes are capable of extracting sulfate and phosphate and, depending on pH , demonstrate differing selectivities toward each anion, the potencies of which parallel those observed with their “parent” ligand complexes. Indeed, a modest 20% excess of complexes using L^5 and L^6 is sufficient to remove 94% and 86% of aqueous phosphate respectively.

6. Experimental

Unless otherwise stated, all solvents and materials were purchased from either Sigma Aldrich, Fisher Scientific or Fluorochem and were used without further purification. ^1H , ^{13}C , DEPT-90 and DEPT-135 NMR data was recorded on either a Bruker Fourier 300 MHz, Bruker Avance III (AVIII) 400 MHz or a Bruker Avance Neo 600 MHz NMR spectrometer. Mass spectra were obtained on an Agilent 6210 TOF MS with electrospray ionisation operating in positive ion mode and single crystal studies were recorded on a Bruker D8 Venture with Dual μS Microfocus Sources using Mo or Cu radiation at 150 (2) K. Single crystal X-ray diffraction data was collected at 150(2) K on a Bruker D8 Venture diffractometer equipped with a graphite monochromated $\text{Mo}(\text{K}\alpha)$ radiation source and a cold stream of N_2 gas. Solutions were generated by conventional heavy atom Patterson or direct methods and refined by full-matrix least squares on all F^2 data, using SHELXS-97, SHELXL and Olex2 software respectively.^{2,3} Absorption corrections were applied based on multiple and symmetry-equivalent measurements using SADABS.⁴ Almost all the structures contained some form of disorder with solvent molecules and/or counter anions (generally substitutional or rotation disorder). In these cases, the atoms were modelled using the *PART* instruction in the least squares refinement and refined over two positions. The anisotropic displacement parameters were treated with *SIMU*, *DELU* and in some cases *ISOR* where needed. Due to the diffuse nature of the electron density map the hydrogen atoms were not added to disordered solvent molecules. The structure $[\text{L}^1_2\text{Zn}_3\text{SO}_4](\text{BF}_4)_{3.5}$ contained extensively disordered tetrafluoroborate counter anions, one of which refined poorly and was modelled with 50% occupancy. The compounds 1,1,1-*tris*(aminomethyl)ethane trihydrochloride, *cis*, *cis*-1,3,5-triaminocyclohexane and [2-(2-Methyl-1,3-dioxolan-2-yl)-4-pyridinyl]methanol were produced by literature methods.^{106,109,110,118,119}

6.1. Chapter 2

6.1.1. Synthesis of ligand **L**¹



Scheme 6.1. Synthesis of ligand **L**¹.

The ligand **L**¹ (*N*¹-(4-(pyridin-2-yl)thiazol-2-yl)-*N*²,*N*²-bis(2-((4-(pyridin-2-yl)thiazol-2-yl)amino)ethyl)ethane-1,2-diamine) was prepared as described previously, however procedures for the synthesis of the benzoylated thioamide **1.1** and the thioamide **1.2** were slightly modified.^{97,99}

To a solution of *tris*(2-aminoethyl)amine (1.0 g, 6.84 mmol) in acetone (50 mL) under an atmosphere of nitrogen was added benzoyl isothiocyanate (3.7 g, 22.6 mmol) at such a rate to cause the reaction to gently reflux. After the addition, the reaction was stirred at ambient temperature overnight during which time a colourless precipitate formed. The precipitate was isolated by filtration and washed with acetone (3 × 5 mL) to afford the product as a white solid. Yield = 2.05 g (47 %). ¹H NMR [400 MHz,

(CD₃)₂SO]: δ (ppm) = 11.20 (s, 3H, -NH), 11.0 (t, 3H, $J = 4.8$, -CH₂NH), 7.81 (d, 6H, $J = 7.2$, Ph), 7.56 (t, 3H, $J = 7.4$, Ph), 7.38 (t, 6H, $J = 7.6$, Ph), 3.75 (q, 6H, $J = 5.7$, -CH₂CH₂NH), 2.89 (t, 6H, $J = 6.0$ Hz, -CH₂CH₂NH). ¹³C NMR [100 MHz, (CD₃)₂SO]: δ (ppm) = 180.5 (C=S), 168.2 (C=O), 133.1 (CH), 132.7 (C), 128.9 (CH), 128.6 (CH), 51.9 (CH₂), 42.6 (CH₂). ESI-MS m/z 636 [M + H]⁺, HR ESI-MS found 636.1882 C₃₀H₃₃N₇S₃O₃ requires 636.1880 (error 0.46 ppm).

Synthesis of **1.2**. To a solution of **1.1** (1.3 g, 2.05 mmol) in water (20 mL), sodium hydroxide (820 mg, 20.5 mmol) added. The reaction was then heated to 60 °C and after 48 hrs the temperature was incrementally decreased allowing the solution to slowly cool to room temperature (avoiding formation on an oil) resulting in the formation of a colourless precipitate. Isolation by filtration and washing with ice cold water (2 × 1 mL) gave the product as a colourless solid. Yield = 503 mg (76 %). ¹H NMR [400 MHz, (CD₃)₂SO]: δ (ppm) = 7.55 (br s, 3H, -NH), 7.08 (br s, 6H, -NH₂), 3.44 (br s, 6H, -CH₂CH₂NH), 2.58 (br s, 6H, -CH₂CH₂NH). ¹³C NMR [100 MHz, (CD₃)₂SO]: δ (ppm) = 183.5 (C=S), 52.9 (CH₂), 42.3 (CH₂). ESI-MS m/z 324 [M + H]⁺, HR ESI-MS found 324.1089 C₉H₂₁N₇S₃ requires 324.1093 (error 1.03 ppm).

Ligand **L**¹ was synthesised from **1.2** as previously reported (yield = 68%).⁹⁷

6.1.2. Complex synthesis

Synthesis of [L¹Zn](ClO₄)₂. To a solution of Zn(ClO₄)₂·6H₂O (10 mg, 0.027 mmol) in Me₂CO (1 ml) was added a suspension of ligand **L**¹ (12 mg, 0.019 mmol) in Me₂CO and the reaction sonicated until a clear solution had formed. To this was added water (~1 ml) and the solution slowly allowed to evaporate, during which time pale yellow crystals were formed which were isolated by filtration and dried (yield = 9 mg, 53%*). The [L¹Mn](ClO₄)₂ complex was prepared in an analogous fashion using Mn(ClO₄)₂·6H₂O

and MeCN giving yellow crystals (yield = 10 mg, 60%*). *percentage yield based on the moles of ligand used. C, 39.03; H, 3.44; N, 15.04%; $C_{30}H_{30}N_{10}S_3ZnCl_2O_8 \cdot 2H_2O$ requires C, 38.87; H, 3.7; N, 15.11%.

Synthesis of $[L^1_2Zn_3(SO_4)](ClO_4)_4$. To a solution of $Zn(ClO_4)_2 \cdot 6H_2O$ (10 mg, 0.027 mmol) in MeCN (1 ml) was added a suspension of ligand L^1 (12 mg, 0.019 mmol) in MeCN and the reaction sonicated until a clear solution had formed. To this was added water (~1 ml) containing Bu_4NHSO_4 (3.1 mg, 0.009 mmol) and the solution slowly allowed to evaporate during which time colourless crystals were formed which were isolated by filtration and dried (yield = 11 mg, 60%). The $[L^1_2Mn_3(SO_4)](ClO_4)_4$ complex was prepared in an analogous fashion using $Mn(ClO_4)_2 \cdot 6H_2O$ giving yellow crystals (yield = 9 mg, 50%). Found: C, 36.33; H, 3.28; N, 14.02%; $C_{60}H_{60}N_{20}S_7Zn_3O_{20}Cl_4 \cdot 3H_2O$ requires C, 36.08; H, 3.33; N, 14.02%.

Synthesis of $[L^1_2Cu_3(O_3POPh)](ClO_4)_4$. To a solution of $Cu(ClO_4)_2 \cdot 6H_2O$ (10 mg, 0.027 mmol) in MeCN (1 ml) was added a suspension of ligand L^1 (12 mg, 0.019 mmol) in MeCN and the reaction sonicated until a clear solution had formed. To this was added water (~1 ml) containing Na_2O_3POPh (2.3 mg, 0.009 mmol) and the solution slowly allowed to evaporate giving green crystals which were isolated by filtration and dried (yield = 9 mg, 47 %).

Synthesis of $[L^1_2Zn_3(PO_4)](ClO_4)_3$. To a solution of $Zn(ClO_4)_2 \cdot 6H_2O$ (10 mg, 0.027 mmol) in MeCN (1 ml) was added a suspension of ligand L^1 (12 mg, 0.019 mmol) in acetone and the reaction sonicated until a clear solution had formed. To this was added water (~1 ml) containing Na_2O_3POPh (2.3 mg, 0.009 mmol) and the solution slowly allowed to evaporate giving yellow crystals which were isolated by filtration and dried (yield = 10 mg, 54 %). The $[L^1_2Mn_3(PO_4)](ClO_4)_3$ complex was prepared in an analogous fashion using $Mn(ClO_4)_2 \cdot 6H_2O$ and a few drops of MeOH to aid dissolution, giving yellow crystals (yield = 9 mg, 50%). $[L^1_2Cu_3(PO_4)](BF_4)_3$. Found: C, 40.86; H, 3.6; N, 15.13%; $C_{60}H_{60}N_{20}S_6Zn_3PO_4B_3F_{12} \cdot C_3H_6O$ requires C, 40.61; H, 3.57; N, 15.04%.

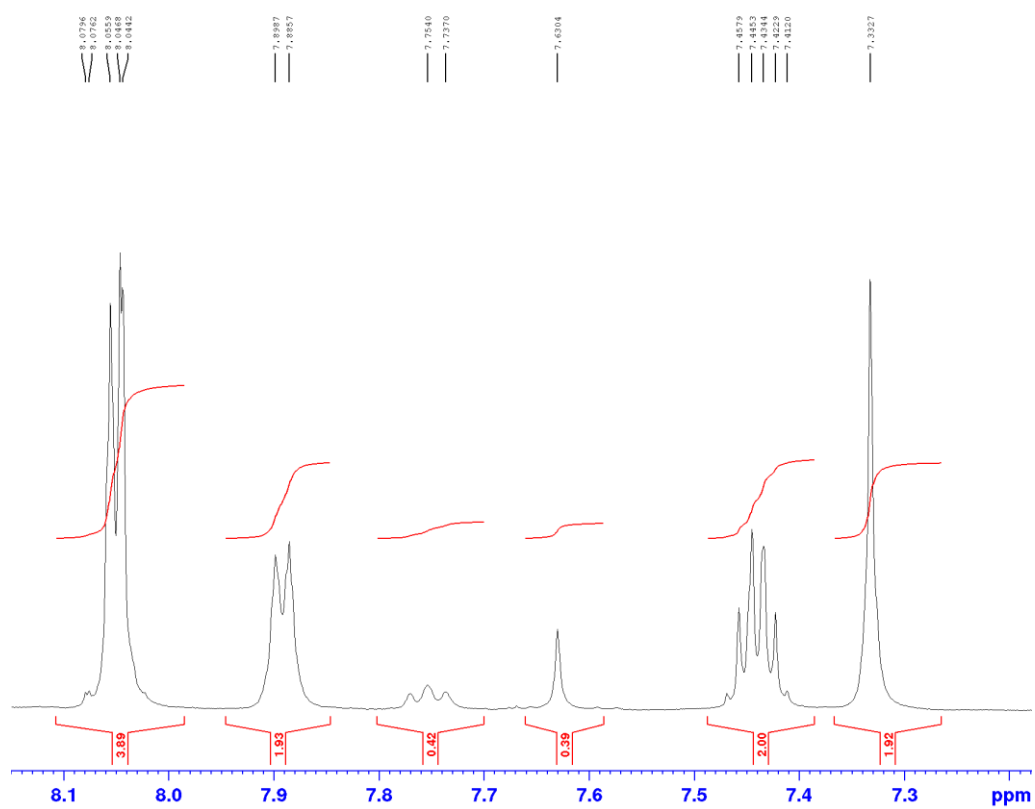


Figure 6.1. ^1H NMR (10% CD_3OD in CD_3CN) spectra of the aromatic region for $[\text{L}^1_2\text{Zn}_3(\text{PO}_4)](\text{OTf})_3$.

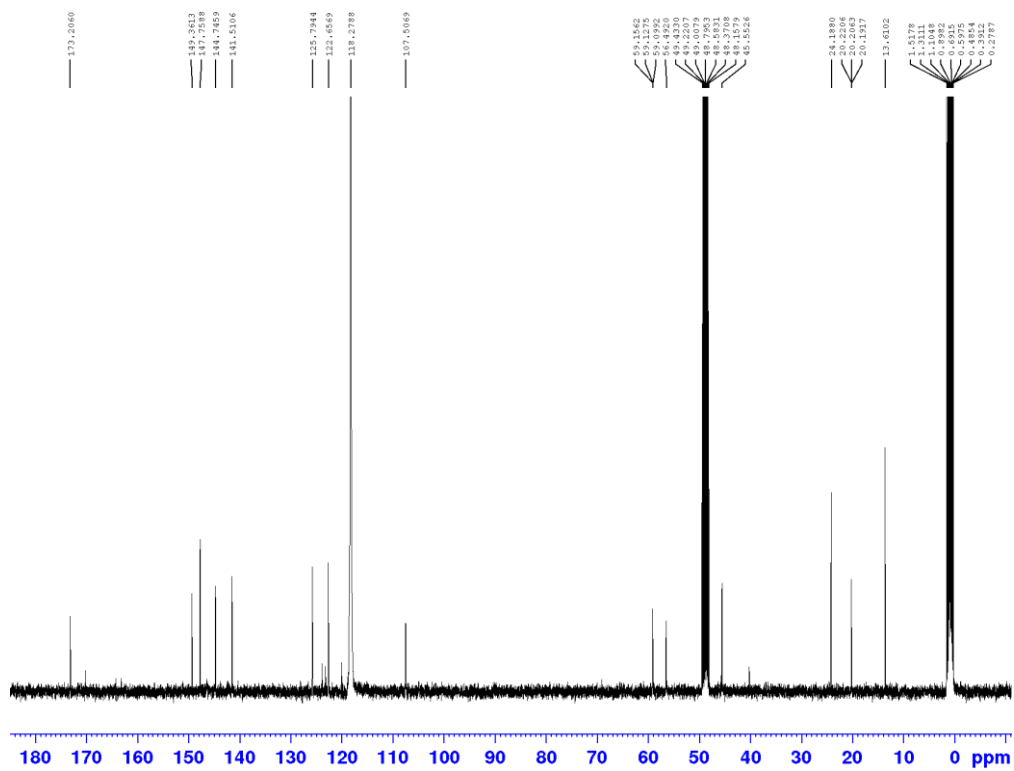


Figure 6.2. ^{13}C NMR (10% CD_3OD in CD_3CN) spectra of $[\text{L}^1_2\text{Zn}_3(\text{PO}_4)](\text{OTf})_3$.

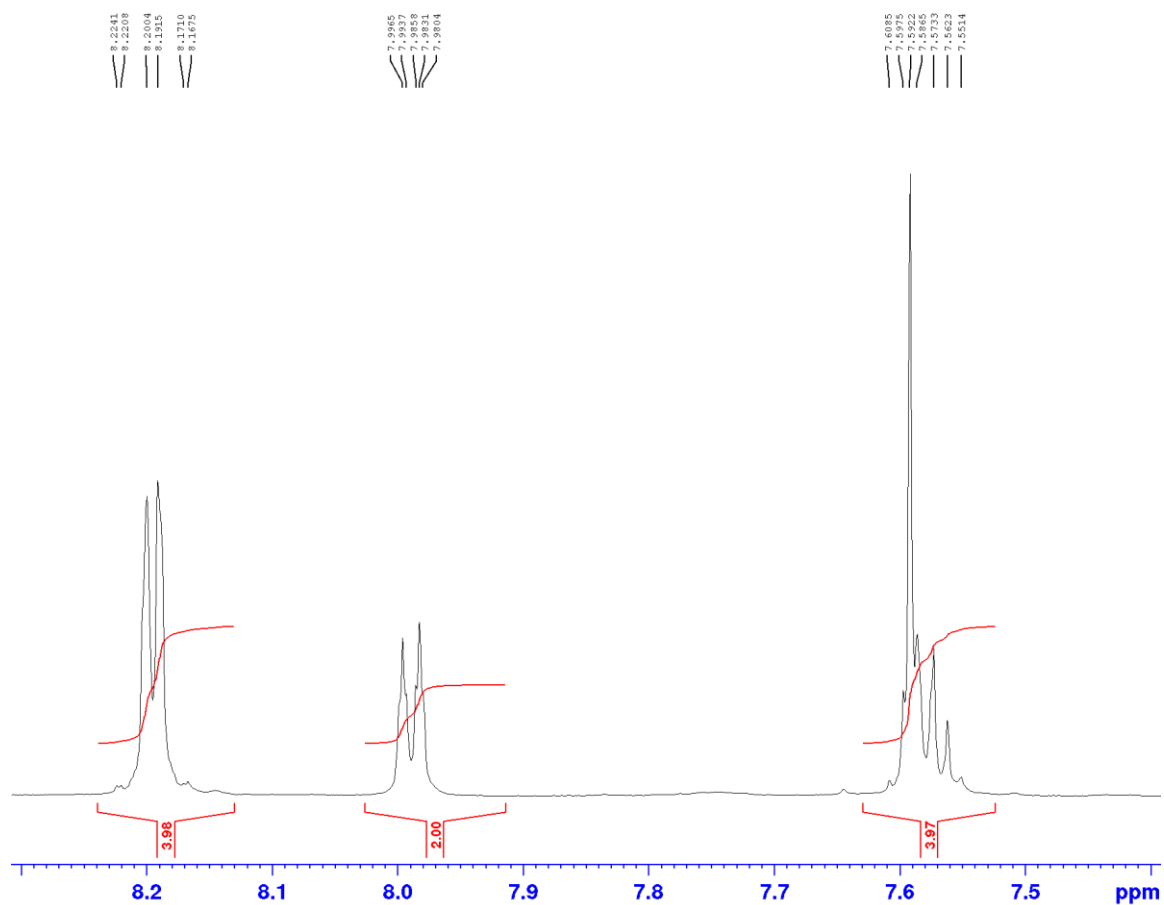


Figure 6.3. ^1H NMR (10% CD_3OD in CD_3CN) spectra of the aromatic region for $[\text{L}^1_2\text{Zn}_3(\text{SO}_4)](\text{OTf})_4$.

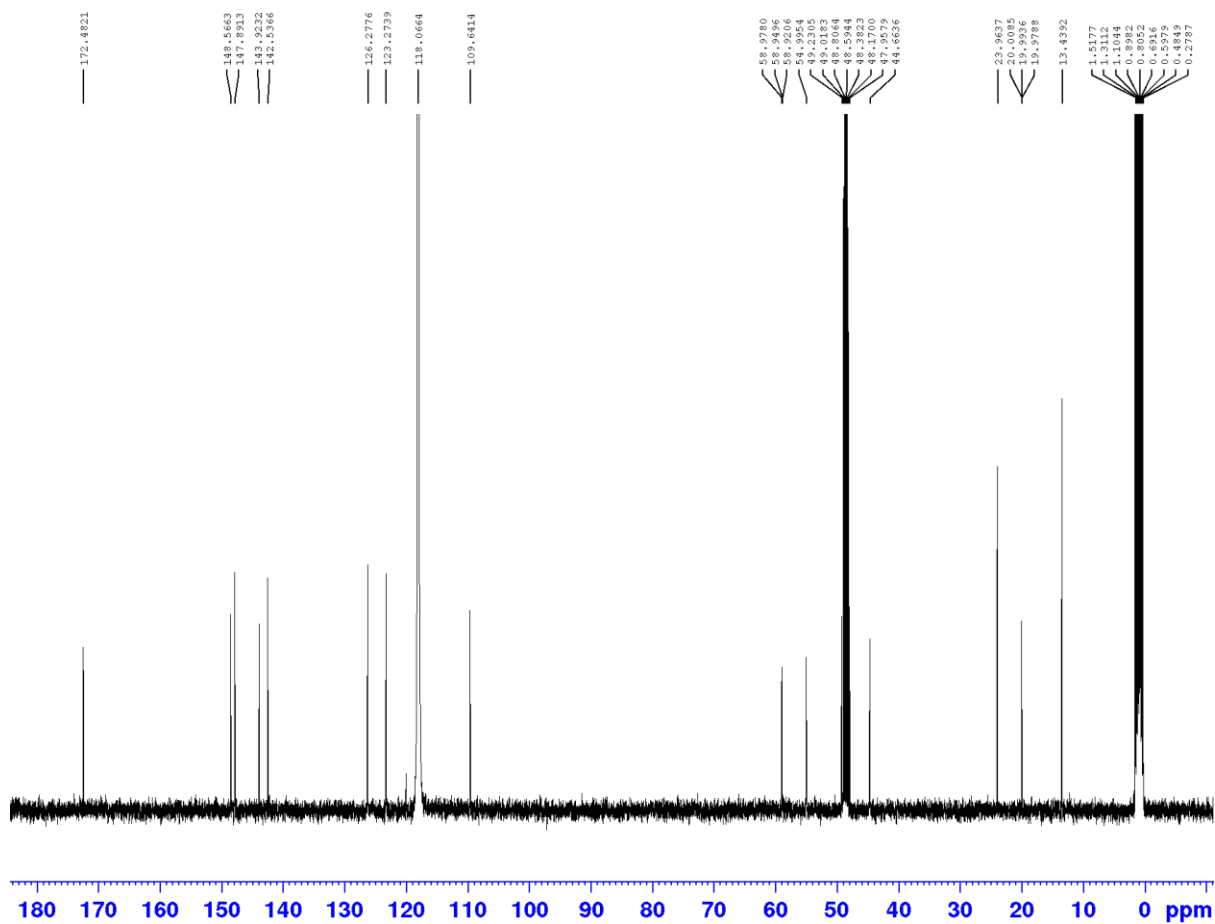


Figure 6.4. ^{13}C NMR (10% CD_3OD in CD_3CN) spectra for $[\text{L}^1_2\text{Zn}_3(\text{SO}_4)](\text{OTf})_4$.

6.1.3. Crystallography of L¹ complexes

Compound	[L ¹ ₂ Cu ₃ (PhOPO ₃)](BF ₄) ₄ ·2 MeCN·3H ₂ O	[L ¹ Zn](ClO ₄) ₂ ·Me ₂ CO	[L ¹ ₂ Zn ₃ (PO ₄)](ClO ₄) ₃ ·2MeCN	[L ¹ ₂ Zn ₃ (SO ₄)] (BF ₄) _{3.5} ·MeCN
Formula	C ₇₀ H ₆₅ B ₄ Cu ₃ F ₁₆ N ₂₂ O ₇ PS ₆	C ₃₃ H ₃₆ Cl ₂ N ₁₀ O _{9.50} S ₃ Zn	C ₆₄ H ₆₆ Cl ₃ N ₂₂ O ₁₆ PS ₆ Zn ₃	C ₆₂ H ₆₀ B _{3.5} F ₁₄ N ₂₁ O ₄ S ₇ Zn ₃
<i>M</i>	2087.72	957.17	1925.17	1887.82
Crystal system	Triclinic	Triclinic	Monoclinic	Monoclinic
Space group	P -1	P -1	P 21/c	C 1 2/c 1
<i>a</i> (Å)	13.6338(10)	12.1349(5)	19.6676(8)	36.775(7)
<i>b</i> (Å)	14.3519(10)	13.5143(6)	22.0889(8)	20.777(4)
<i>c</i> (Å)	23.1506(18)	14.0968(6)	17.9988(8)	27.448(5)
α (°)	76.225(3)	70.316(2)	90	90
β (°)	83.869(3)	65.002(2)	98.433(2)	115.095(9)
γ (°)	85.279(3)	80.535(2)	90	90
<i>V</i> (Å ³)	4366.9(6)	1972.14(15)	7734.8(5)	18993(6)
<i>Z</i>	2	2	4	8
ρ_{calc} (Mg cm ⁻³)	1.5876	1.612	1.653	1.3203
<i>F</i> (000)	2118.8058	984	3936	7669.9894
Crystal dimensions (mm)	0.18, 0.11, 0.03	0.22, 0.20, 0.09	0.12, 0.07, 0.07	0.18, 0.15, 0.10
Reflections measured	55621	30907	80079	121061

Range	$2.04 \leq \theta \leq 28.32^\circ$	$2.48 \leq \theta \leq 33.10^\circ$	$2.34 \leq \theta \leq 32.13^\circ$	$2.29 \leq \theta \leq 27.43^\circ$
<i>hkl</i> range indecis	$-18 \leq h \leq 18, -19 \leq k \leq 19, -30 \leq l \leq 30$	$-18 \leq h \leq 18, -20 \leq k \leq 19, -21 \leq l \leq 20$	$-28 \leq h \leq 28, -32 \leq k \leq 32, -22 \leq l \leq 26$	$-49 \leq h \leq 48, -27 \leq k \leq 27, -36 \leq l \leq 36$
N° independent reflections	21484	14937	25665	23507
Reflections with $I > 2\sigma(I)$	14358	10352	17419	15289
R _{int}	0.0771	0.0445	0.0636	0.0592
Final R ₁ values	0.0725	0.0499	0.0479	0.0653
Final wR(F ²) values	0.1969	0.1159	0.1011	0.1851
Final R ₁ values (all data)	0.1124	0.0839	0.0857	0.1050
Final wR(F ²) values (all data)	0.2326	0.1344	0.1155	0.2298
GOF	1.0879	1.020	1.015	1.1131
Refined parameters	1209	553	1057	1111
Restraints	81	24	42	82

Largest peak and hole (e Å ⁻³)	1.5905, -1.5497	0.983, -0.920	1.147, -0.751	2.2859, -0.9214
CCDC number	2005186	2005132	2005189	2005221

Table 6.1. X-ray crystallographic data for $[\text{L}^1\text{Cu}_3(\text{PhOPO}_3)]^{4+}$, $[\text{L}^1\text{Zn}]^{2+}$, $[\text{L}^1_2\text{Zn}_3(\text{PO}_4)]^{3+}$ and $[\text{L}^1_2\text{Zn}_3(\text{SO}_4)]^{4+}$.

Compound	$[\text{L}^1\text{Mn}](\text{ClO}_4)_2 \cdot \text{MeCN} \cdot \text{H}_2\text{O}$	$[\text{L}^1_2\text{Mn}_3(\text{PO}_4)](\text{ClO}_4)_3 \cdot \text{MeCN} \cdot 2\text{MeOH}$	$[\text{L}^1_2\text{Mn}_3(\text{SO}_4)](\text{ClO}_4)_4 \cdot 3\text{H}_2\text{O} \cdot 2\text{MeCN}$
Formula	$\text{C}_{32}\text{H}_{39}\text{Cl}_2\text{MnN}_{11}\text{O}_{11}\text{S}_3$	$\text{C}_{65.804}\text{H}_{75}\text{Cl}_3\text{Mn}_3\text{N}_{21}\text{O}_{21}$ PS_6	$\text{C}_{63.636}\text{H}_{67}\text{Cl}_4\text{Mn}_3\text{N}_{21.818}$ $\text{O}_{26.085}\text{S}_7$
<i>M</i>	975.78	1990.65	2085.91
Crystal system	Monoclinic	Triclinic	Orthorhombic
Space group	P 1 21/c 1	P -1	P b c a
<i>a</i> (Å)	25.3201(10)	13.769(3)	26.4653(7)
<i>b</i> (Å)	17.9313(7)	15.509(3)	23.3289(5)
<i>c</i> (Å)	19.1082(6)	20.200(4)	28.1102(6)
α (°)	90	91.564(8)	90
β (°)	109.6360(10)	104.592(9)	90
γ (°)	90	96.722(11)	90
<i>V</i> (Å ³)	8171.0(5)	4138.4(13)	17355.4(7)
<i>Z</i>	8	2	8
ρ_{calc} (Mg cm ⁻³)	1.5863	1.5974	1.5965
<i>F</i> (000)	4033.8382	2049.1485	8545.5634

Crystal dimensions (mm)	0.20, 0.18, 0.05	0.16, 0.12, 0.12	0.23, 0.21, 0.18
Reflections measured	67342	64143	164752
Range	$2.05 \leq \theta \leq 30.55^\circ$	$2.32 \leq \theta \leq 33.01^\circ$	$2.27 \leq \theta \leq 33.13^\circ$
<i>hkl</i> range indices	$-27 \leq h \leq 36, -25 \leq k \leq 21, -27 \leq l \leq 27$	$-21 \leq h \leq 21, -23 \leq k \leq 23, -30 \leq l \leq 28$	$-39 \leq h \leq 40, -35 \leq k \leq 32, -43 \leq l \leq 40$
N° independent reflections	24905	30920	32977
Reflections with $I > 2\sigma(I)$	16699	21994	23821
R_{int}	0.0494	0.0453	0.0487
Final R_1 values	0.0580	0.0500	0.0544
Final $wR(F^2)$ values	0.1363	0.1219	0.1328
Final R_1 values (all data)	0.0973	0.0797	0.0839
Final $wR(F^2)$ values (all data)	0.1606	0.1464	0.1535
GOF	1.0879	1.0740	1.0833
Refined parameters	1140	1109	1258
Restraints	15	28	24

Largest peak and hole (e Å ⁻³)	1.1456, -1.0796	1.3806, -1.6085	1.5168, -1.2101
CCDC number	2005133	2005190	2005222

Table 6.2. X-ray crystallographic data for [L¹Mn]²⁺, [L¹₂Mn₃(PO₄)]³⁺ and [L¹₂Mn₃(SO₄)]⁴⁺.

6.1.4. Mass spectrometry studies

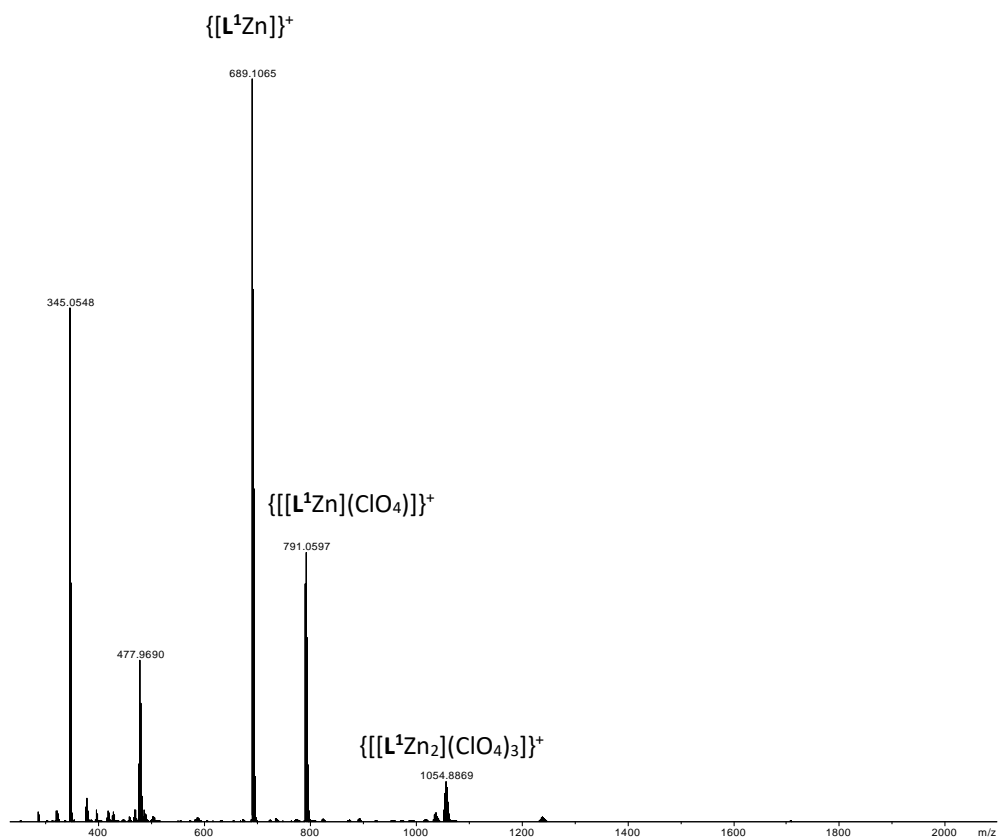


Figure 6.5. ESI-MS of $[L^1Zn](ClO_4)_2$.

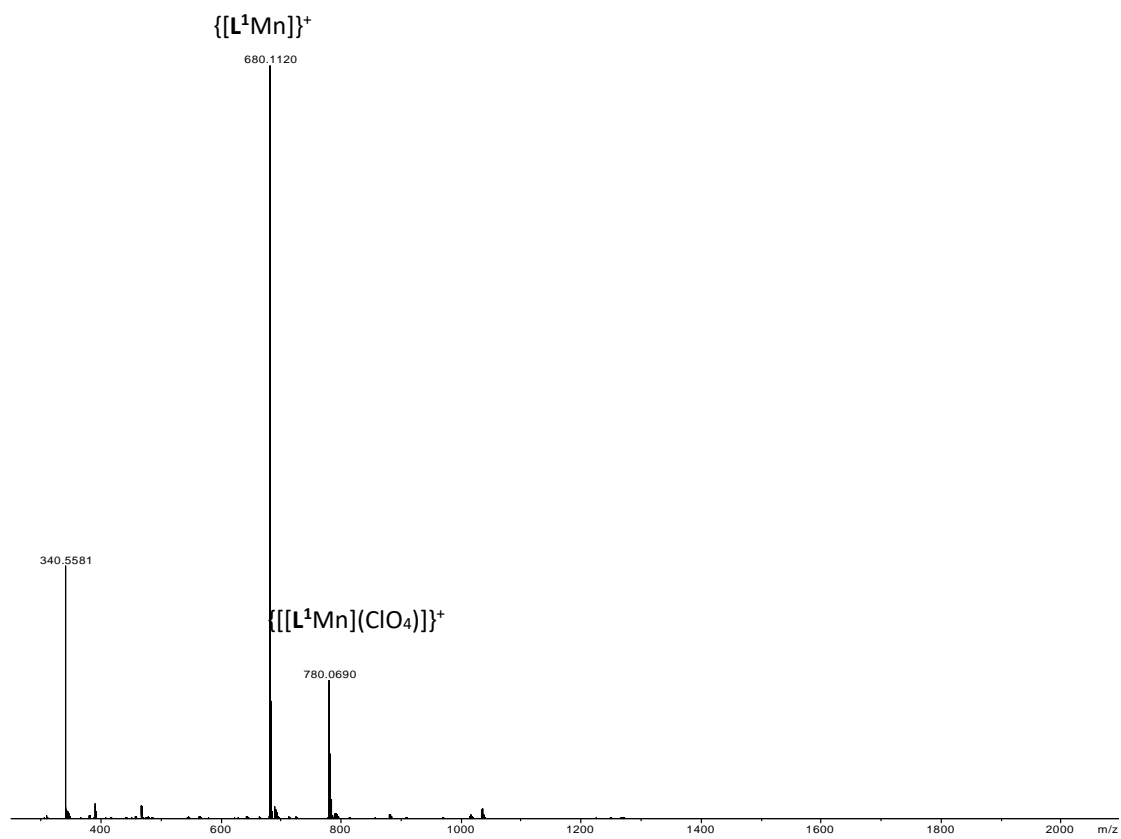


Figure 6.6. ESI-MS of $[L^1Mn](ClO_4)_2$.

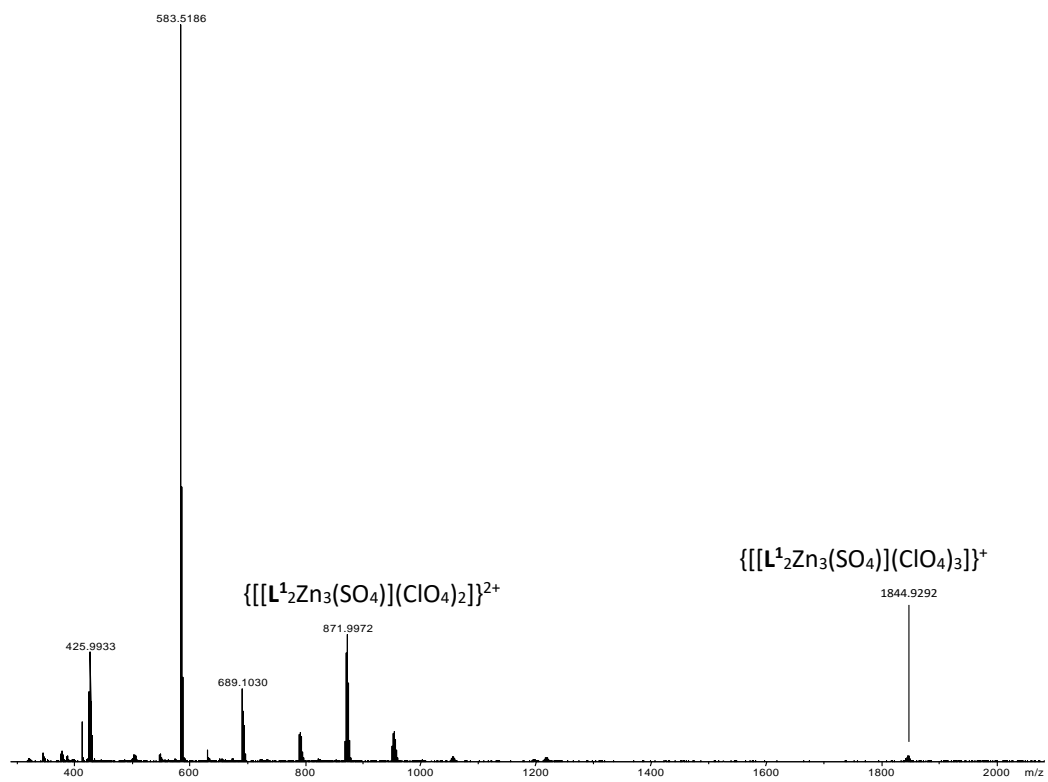


Figure 6.7. ESI-MS of $[L^1_2Zn_3(SO_4)](ClO_4)_4$.

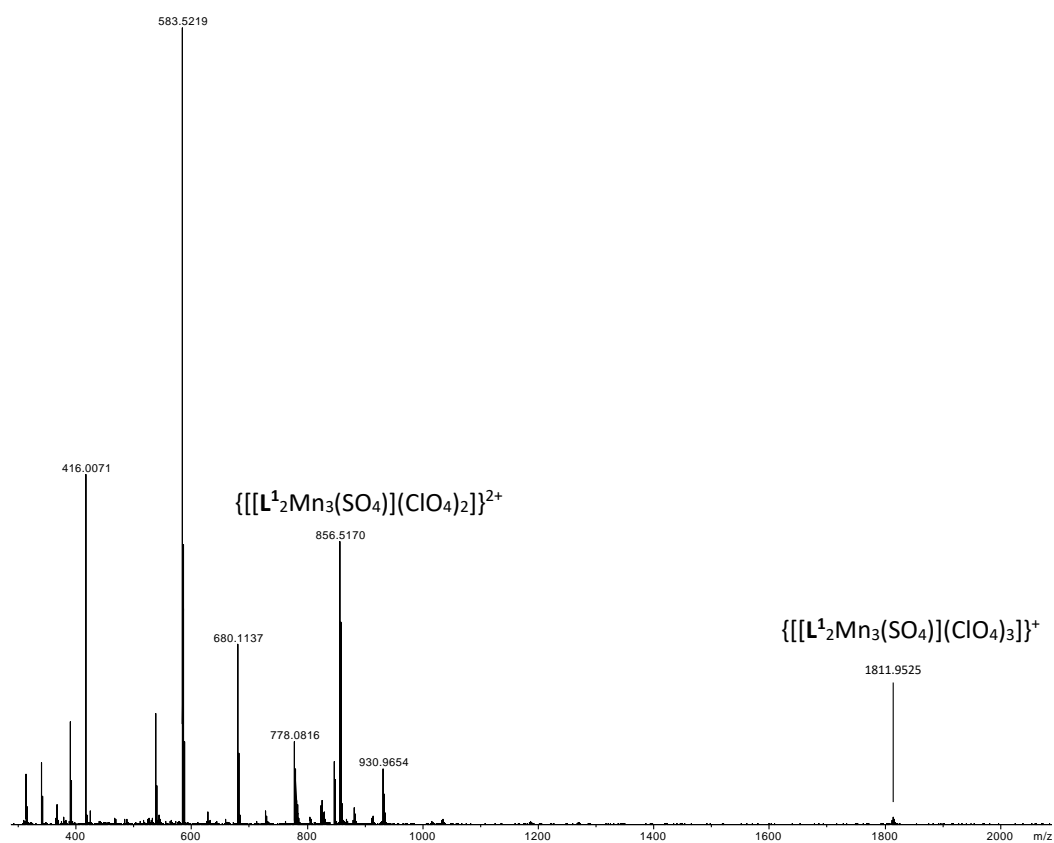


Figure 6.8. ESI-MS of $[L^1_2Mn_3(SO_4)](ClO_4)_4$.

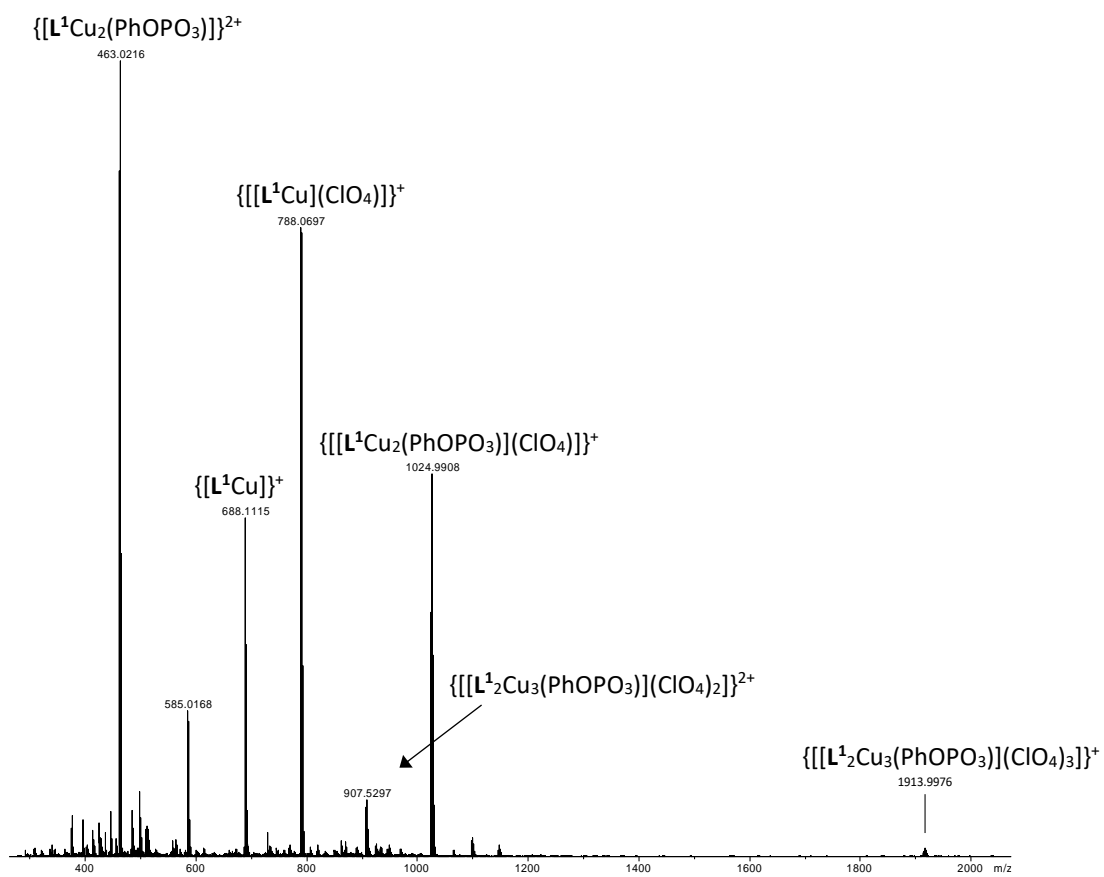


Figure 6.9. ESI-MS of $[L^1_2Cu_3(PhOPO_3)](ClO_4)_4$.

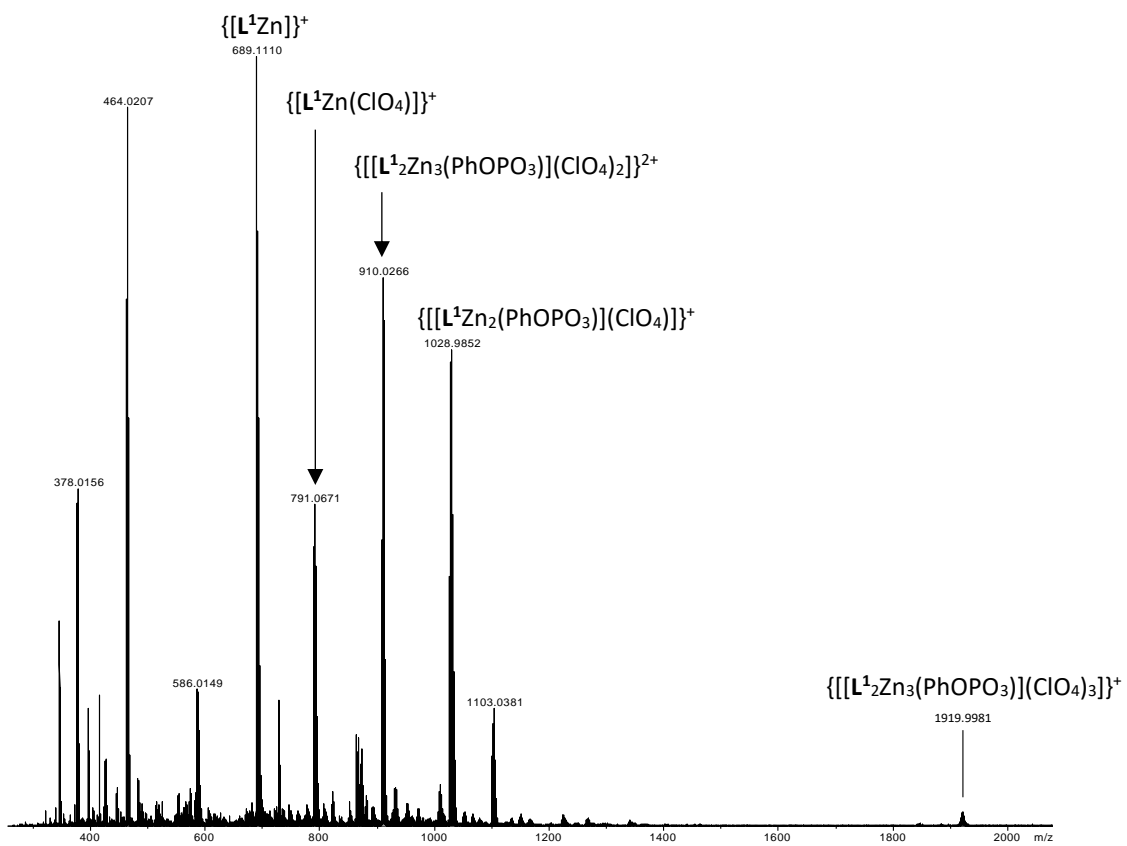


Figure 6.10. ESI-MS of $[L^1_2Zn_3(PhOPO_3)](ClO_4)_4$.

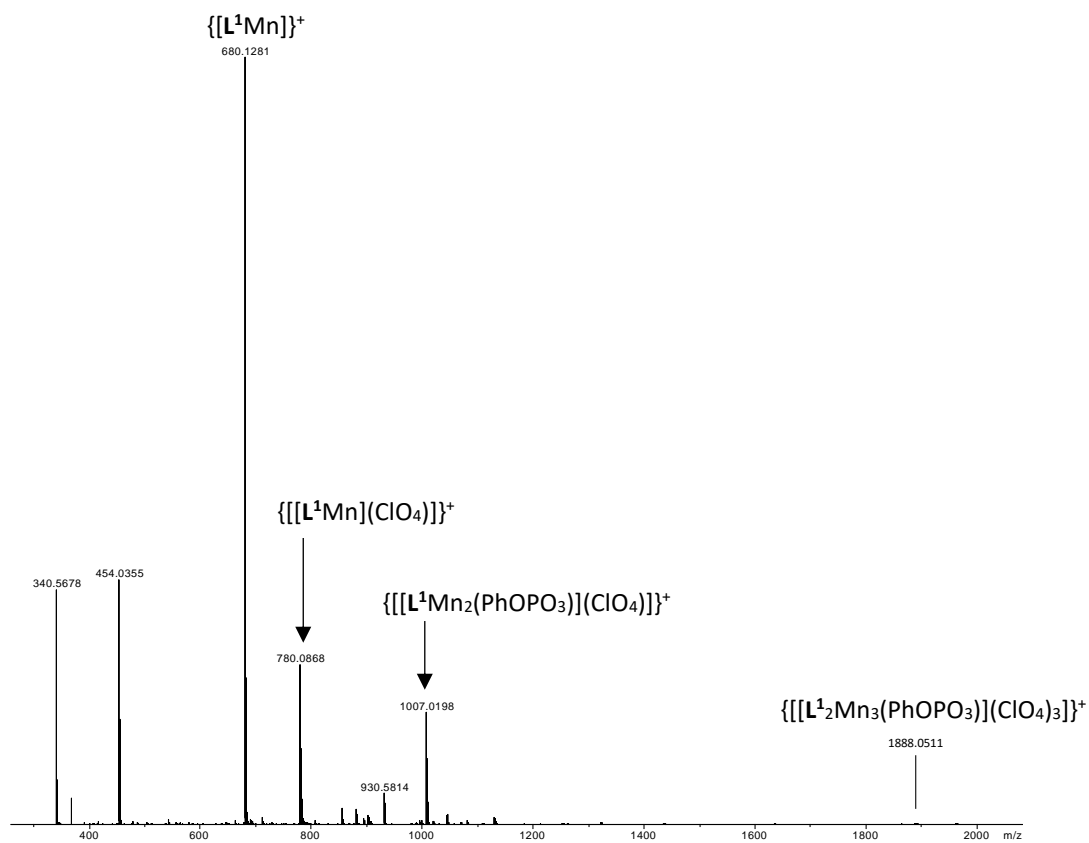


Figure 6.11. ESI-MS of $[L^1_2Mn_3(PhOPO_3)](ClO_4)_4$.

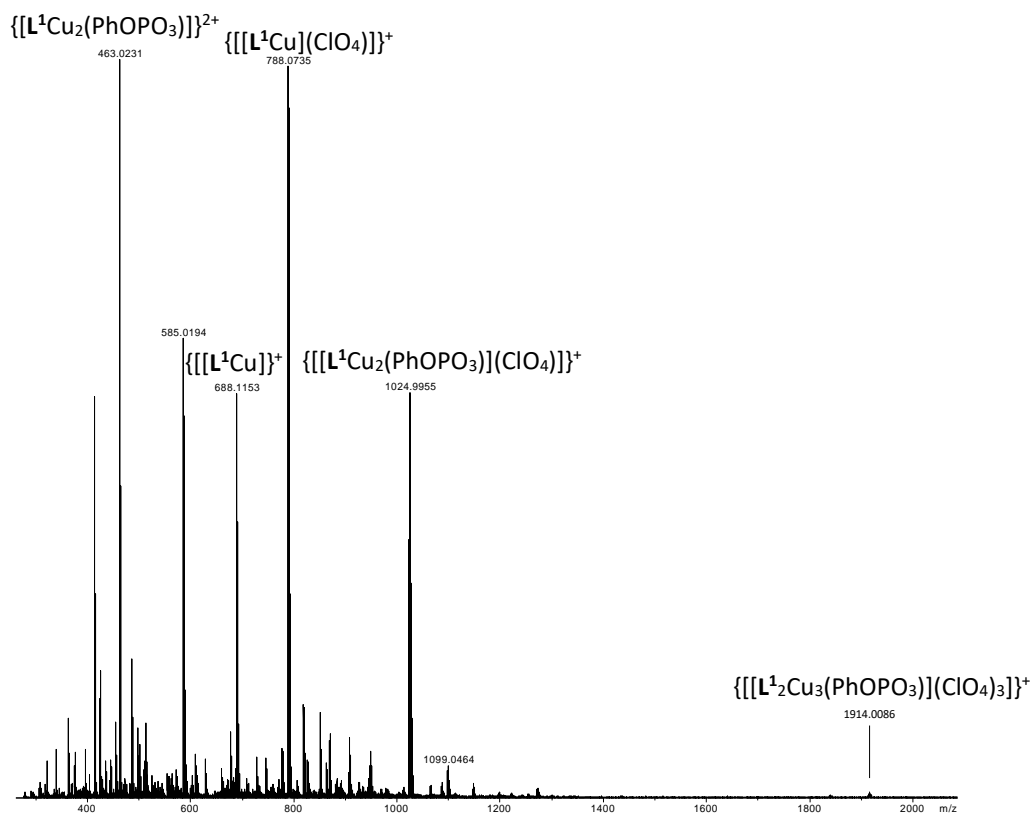


Figure 6.12. ESI-MS of $[L^1_2Cu_3(PhOPO_3)](ClO_4)_4$ after being heated at 80 °C for 1 hour.

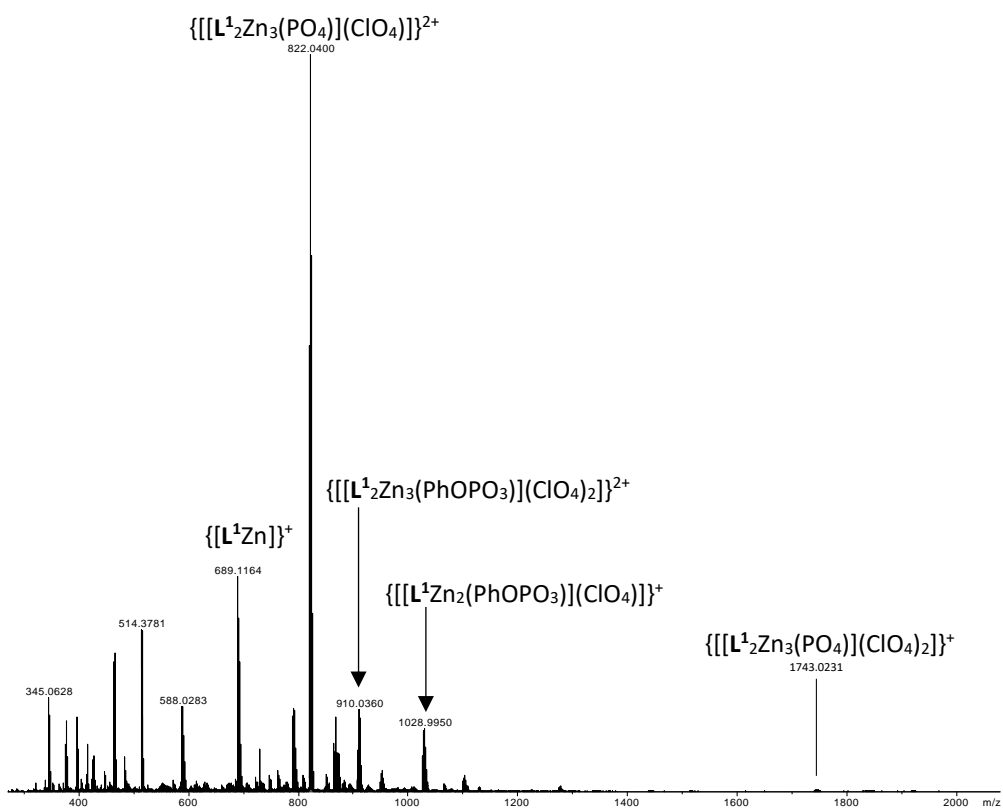


Figure 6.13. ESI-MS of $[L^1_2Zn_3(PhOPO_3)](ClO_4)_4$ after being heated at 80 °C for 1 hour.

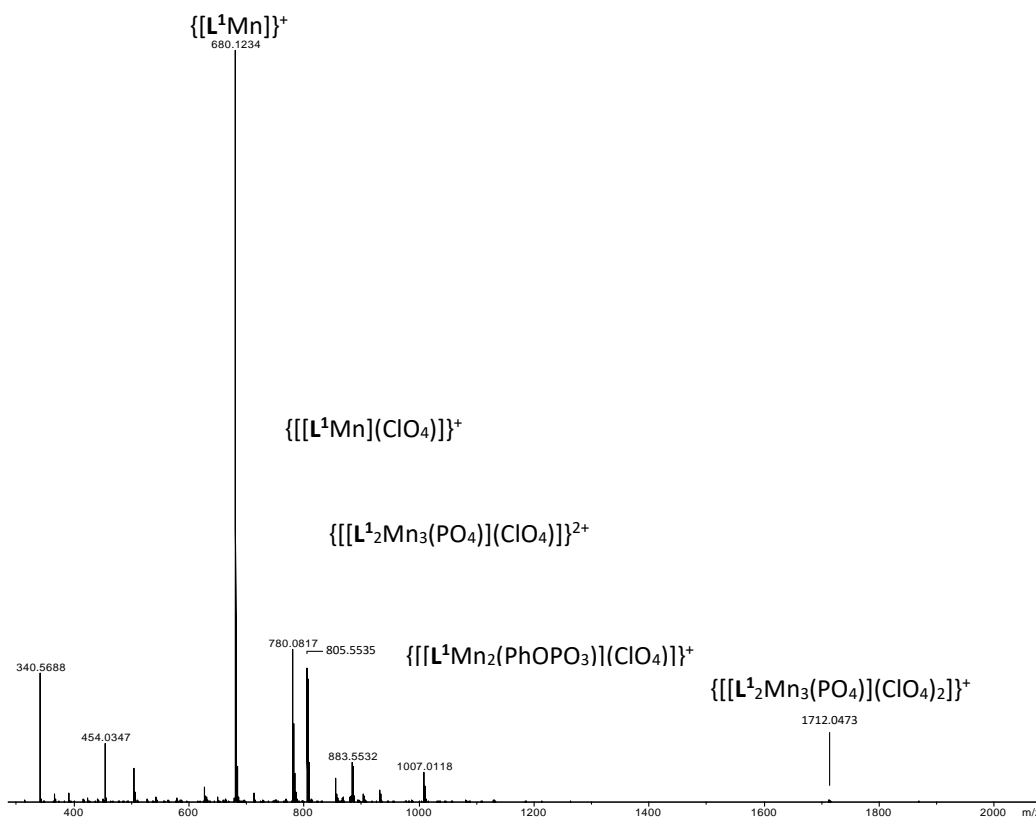


Figure 6.14. ESI-MS of $[L^1_2Mn_3(PhOPO_3)](ClO_4)_4$ after being heated at $80\text{ }^\circ\text{C}$ for 1 hour.

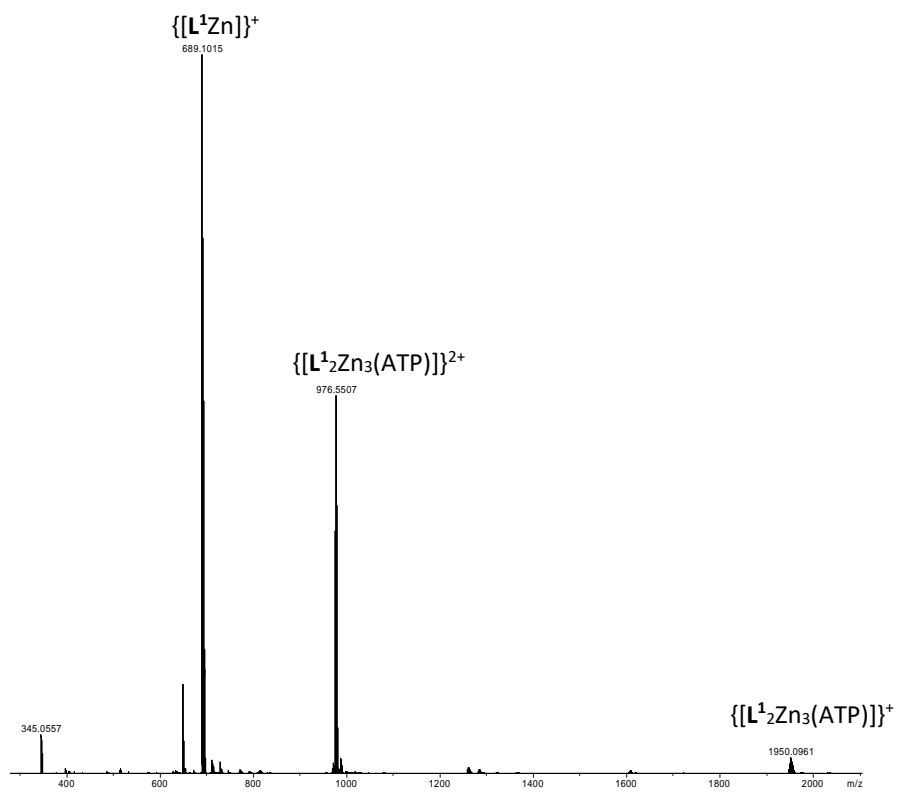


Figure 6.15. ESI-MS of $[L^1_2Zn_3(ATP)(CH_3CO_2)_2]$.

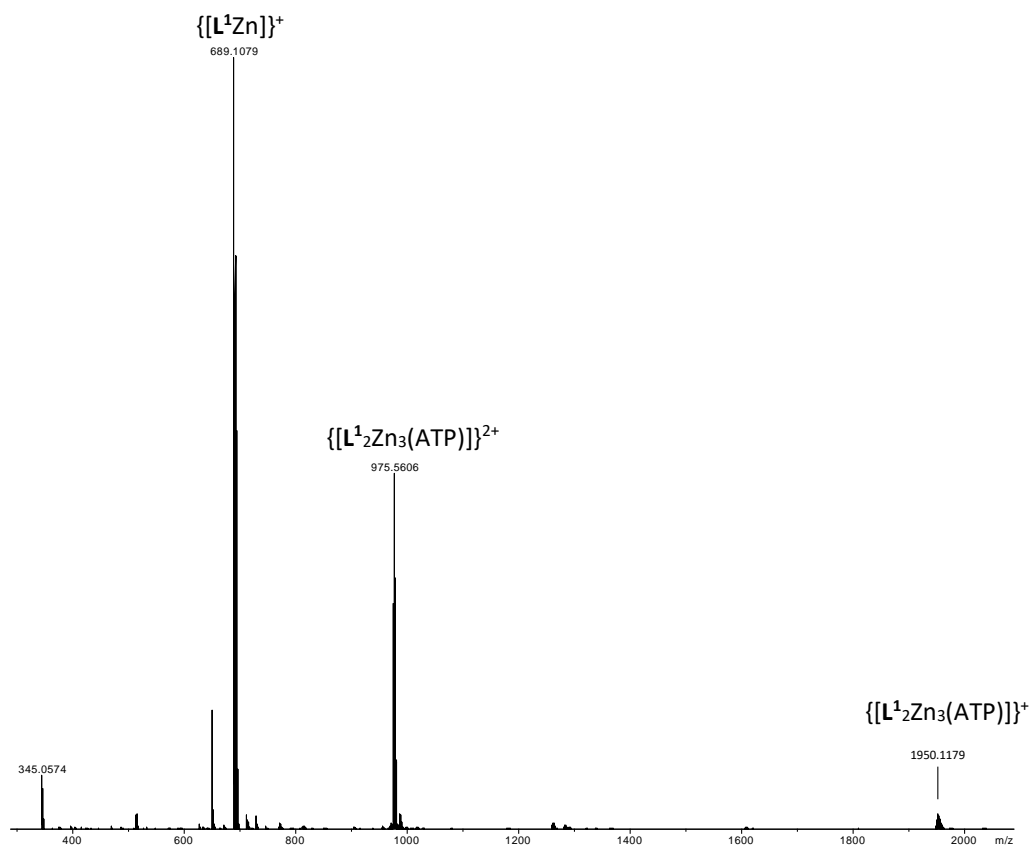


Figure 6.16. ESI-MS of $[L^1_2Zn_3(ATP)(CH_3CO_2)_2]$ after heating at 37 °C for 60 hours.

6.1.5. NMR studies

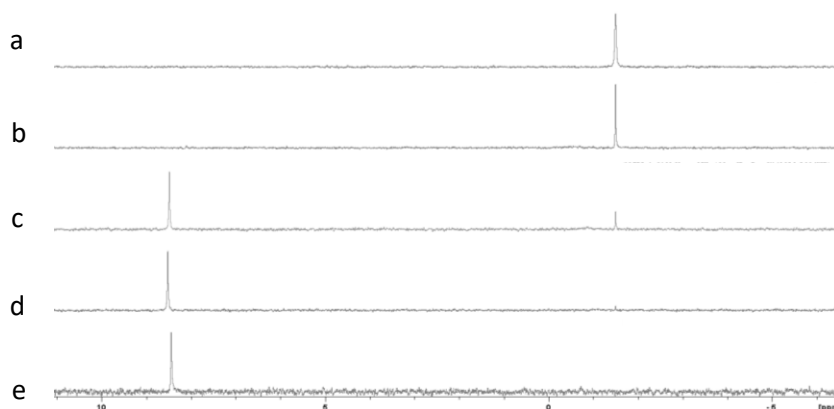


Figure 6.17. ^{31}P NMR spectrum (600 μL HEPES 60 mmol (@ pH 7.4) and 200 μL d_6 -DMSO) of a) $\text{PhOPO}_3\text{Na}_2$, 44hrs incubated @ 37 $^\circ\text{C}$, b) $[\text{L}^1_2\text{Zn}_3]^{6+} + \text{PhOPO}_3\text{Na}_2$, $T = 0$, c) $[\text{L}^1_2\text{Zn}_3]^{6+} + \text{PhOPO}_3\text{Na}_2$, $T = 19$ hrs incubated @ 37 $^\circ\text{C}$, d) $[\text{L}^1_2\text{Zn}_3]^{6+} + \text{PhOPO}_3\text{Na}_2$, $T = 44$ hrs incubated @ 37 $^\circ\text{C}$, e) $[\text{L}^1_2\text{Zn}_3]^{6+} + \text{Bu}_4\text{NH}_2\text{PO}_4$. The NMR solutions were prepared by dissolving L^1 and $\text{Zn}(\text{C}_2\text{H}_3\text{O}_2)_2$ (in a ratio of 1:1.5) in d_6 -DMSO (200 μL). The relevant anion (0.5 equiv w.r.t ligand) was dissolved in HEPES (600 μL , @ pH 7.4) and these solutions were then combined. Heating of the sample was carried out by incubating the sample @ 37 $^\circ\text{C}$.

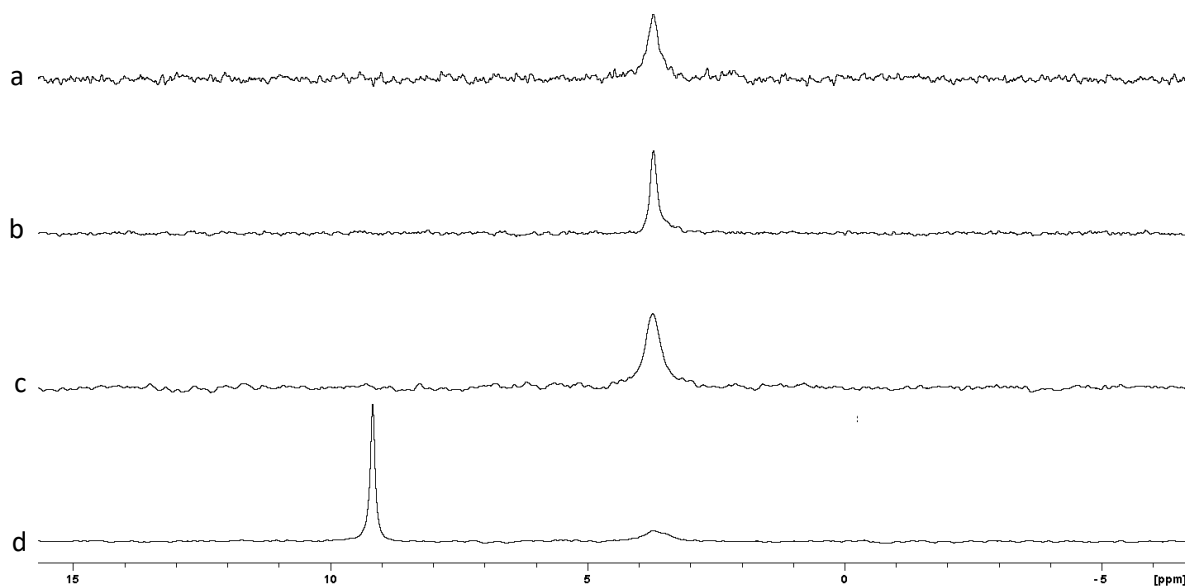


Figure 6.18. ^{31}P NMR spectrum (10% D_2O in CD_3CN) of a) $[\text{L}^1_2\text{Zn}_3]^{6+} + \text{Bu}_4\text{NH}_2\text{PO}_4$, b) $[\text{L}^1_2\text{Zn}_3]^{6+} + \text{PhOPO}_3\text{Na}_2$, $T = 0$, c) $[\text{L}^1_2\text{Zn}_3]^{6+} + \text{PhOPO}_3\text{Na}_2$, $T = 1$ hr incubated @ 80°C , d) phenol. The NMR solutions were prepared by dissolving L^1 and $\text{Zn}(\text{C}_2\text{H}_3\text{O}_2)_2$ (in a ratio of 1:1.5) in CD_3CN ($600\ \mu\text{L}$). The relevant anion (0.5 equiv w.r.t ligand) was dissolved in D_2O ($60\ \mu\text{L}$) and these solutions were then combined. Heating of the sample was carried out @ 80°C in a water bath for the specified amount of time.

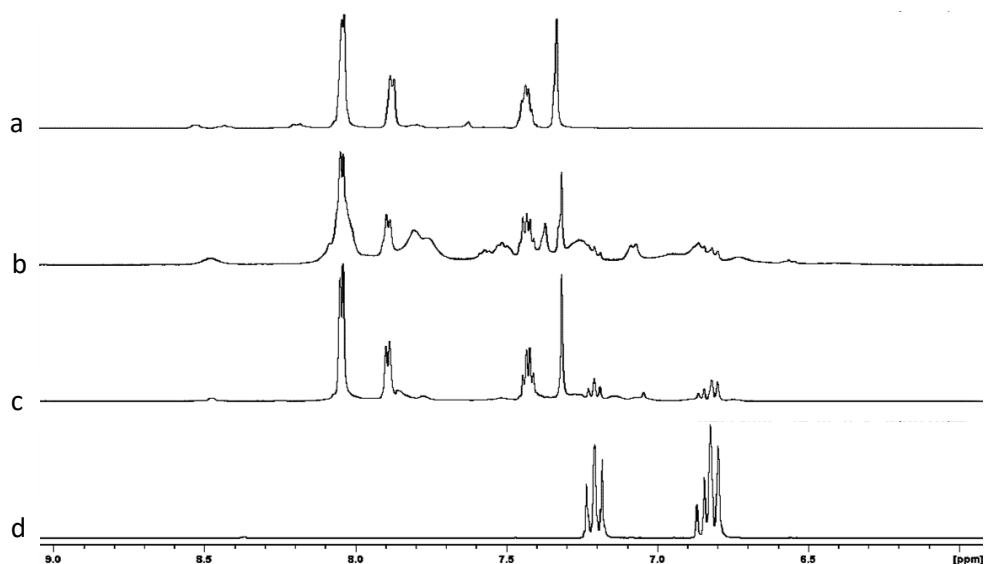


Figure 6.19. ^1H NMR spectra (600 μL HEPES (@ pH 7.4) and 200 μL d_6 -DMSO) of a) $[\text{L}^1_2\text{Zn}_3]^{6+}$ + peptide- OPO_3^{2-} (HMRSAMS*GLHLVKRR) $t = 0$, b) $[\text{L}^1_2\text{Zn}_3]^{6+}$ + peptide- OPO_3^{2-} $t = 48$ hrs @ 37 $^\circ\text{C}$, c) $[\text{L}^1_2\text{Zn}_3]^{6+}$ + peptide- OPO_3^{2-} $t = 48$ hrs @ 37 $^\circ\text{C}$ and then 2 hrs 80 $^\circ\text{C}$, d) $[\text{L}^1_2\text{Zn}_3]^{6+}$ + peptide- OPO_3^{2-} + $\text{Bu}_4\text{NH}_2\text{PO}_4$ with the shift at ~ 9 ppm corresponding to $[\text{L}^1_2\text{Zn}_3(\text{PO}_4)]^{3+}$. The NMR solutions were prepared by dissolving L^1 and $\text{Zn}(\text{C}_2\text{H}_3\text{O}_2)_2$ (in a ratio of 1:1.5) in d_6 -DMSO (200 μL). The peptide- OPO_3^{2-} (0.5 equiv w.r.t ligand) was dissolved in HEPES (600 μL , 60 mmol @ pH 7.4) and these solutions were then combined. Heating of the sample was carried out by incubating the sample @ 37 $^\circ\text{C}$ and a further 2 hrs @ 80 $^\circ\text{C}$ in a water bath.

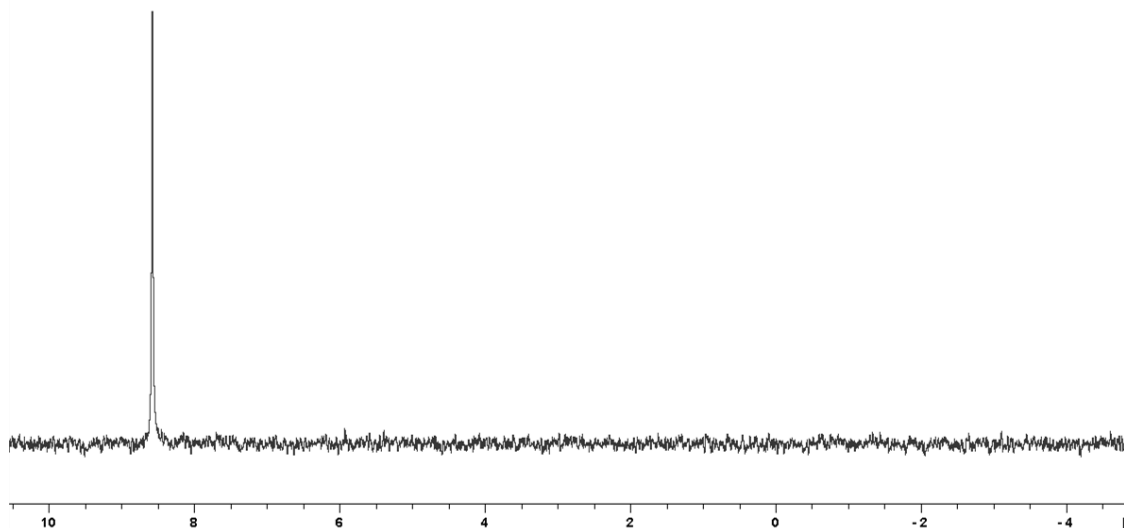


Figure 6.20. ^{31}P NMR spectra (600 μL HEPES (60 mmol @ pH 7.4) and 200 μL d_6 -DMSO) of $[\text{L}^1_2\text{Zn}_3]^{6+}$ showing the signal at ~ 9 ppm corresponding to $[\text{L}^1_2\text{Zn}_3(\text{PO}_4)]^{3+}$ demonstrating no competition from HEPES as no observed signal at ~ 0 ppm corresponding to free phosphate. Solution contains an approximately 10-fold excess of HEPES.

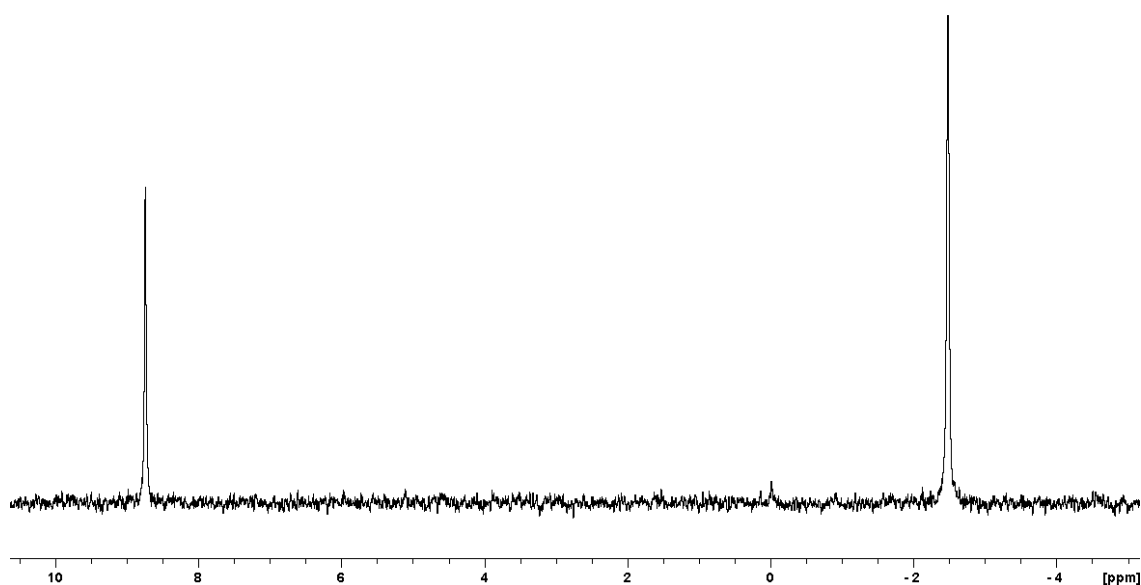


Figure 6.21. ^{31}P NMR spectra (600 μL HEPES (60 mmol @ pH 7.4) and 200 μL d_6 -DMSO) of $[\text{L}^1_2\text{Zn}_3(\text{PO}_4)]^{3+}$ plus one equivalent of $\text{Na}_2\text{O}_2\text{POPh}$ showing the signal at ~ 9 ppm corresponding to $[\text{L}^1_2\text{Zn}_3(\text{PO}_4)]^{3+}$ and -2.5 ppm corresponding to $\text{Na}_2\text{O}_2\text{POPh}$. No change in either the ratio of $[\text{L}^1_2\text{Zn}_3(\text{PO}_4)]^{3+}$ to $\text{Na}_2\text{O}_2\text{POPh}$ and no signal at ~ 0 ppm (corresponding to free PO_4^{3-}) was observed, indicating lack of catalytic activity.

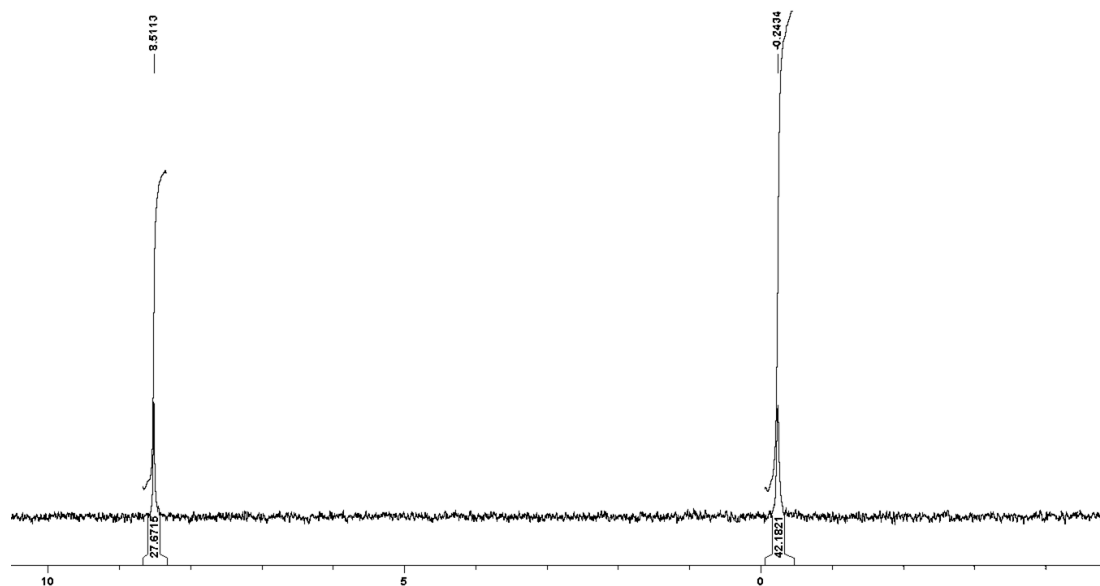


Figure 6.22. ^{31}P NMR spectra (600 μL HEPES (60 mmol @ pH 7.4) and 200 μL d_6 -DMSO) of $[\text{L}^1_2\text{Zn}_3(\text{SO}_4)]^{4+}$ plus one equivalent of NaH_2PO_4 showing the signal at ~ 9 ppm corresponding to $[\text{L}^1_2\text{Zn}_3(\text{PO}_4)]^{3+}$ and ~ 0 ppm corresponding to unbound NaH_2PO_4 . This indicates that a proportion, but not all, of the sulfate has been displaced but the presence of “free” NaH_2PO_4 demonstrates that $[\text{L}^1_2\text{Zn}_3(\text{SO}_4)]^{4+}$ still persists as the major species ($\sim 66\%$).

6.1.6. -UV-Vis-NIR studies

UV-Vis-NIR studies were carried out on a Cary 60 UV-Vis-NIR spectrophotometer with Thermo cyclor attachment and the wavelength range of 800 – 250 nm was scanned every hour for 43 hours whilst the solution was heated at a constant temperature of 37 °C. Progress of hydrolysis of 4-nitrophenyl phosphate to 4-nitrophenol was measured by monitoring the increase in absorption at the wavelength of 400 nm (typical for 4-nitrophenol). HEPES buffer was prepared at pH 7.4.

For $[[L^1_2Cu_3](C_2H_3O_2)_6]$, $[[L^1_2Zn_3](C_2H_3O_2)_6]$ and $[[L^1_2Mn_3](C_2H_3O_2)_6]$:

Solutions were prepared by dissolving the ligand L^1 (3.1 mg, 0.005 mmol) and the relevant metal salt (1.5 equiv w.r.t. ligand) in DMSO (5 mL). 4-nitrophenyl phosphate (18.6 mg, 0.050 mmol) was dissolved in HEPES buffer (~10 mL, 60 mmol) These solutions were then combined and made up volumetrically to 50 mL with HEPES buffer.

For $[[L^1_2Cu_3(PO_4)](C_2H_3O_2)_3]$, $[[L^1_2Zn_3(PO_4)](C_2H_3O_2)_3]$ and $[[L^1_2Mn_3(PO_4)](C_2H_3O_2)_3]$:

Solutions were prepared by dissolving the ligand L^1 (3.1 mg, 0.005 mmol) and the relevant metal salt (1.5 equiv w.r.t. ligand) in DMSO (5 mL). Tetra-*N*-butylammonium phosphate (0.84 mg, 0.0025 mmol) was dissolved in HEPES buffer (~1 mL, 60 mmol) and these solutions were combined. The 4-nitrophenyl phosphate (18.6 mg, 0.050 mmol) was dissolved separately in HEPES buffer (~10 mL) before being combined with the solution containing the complex and making up volumetrically to 50 mL with HEPES buffer.

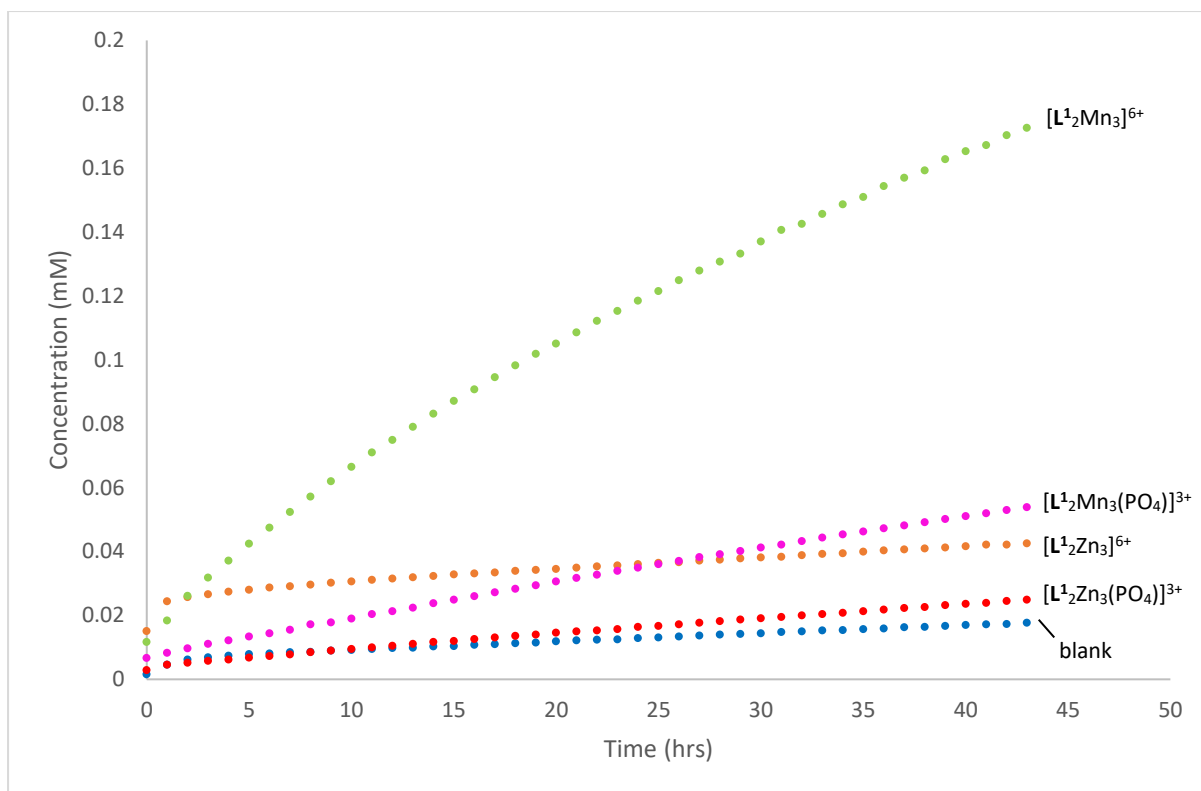


Figure 6.23. Concentration of 4-nitrophenol (mM) verses time in the presence of different complexes.

Compound	Concentration of 4-nitrophenol (mM) after 24 hours at 37 °C
blank	0.0129
$[L^{1_2}Zn_3](CH_3CO_2)_6$	0.0361
$[L^{1_2}Mn_3](CH_3CO_2)_6$	0.1185
$[L^{1_2}Zn_3(PO_4)](CH_3CO_2)_3$	0.0164
$[L^{1_2}Mn_3(PO_4)](CH_3CO_2)_3$	0.0350

Table 6.3. Concentration of 4-nitrophenol (mM) at 24 hr at 37 °C.

Calibration standards:

Calibration of 4-nitrophenol was carried out by observing the 400 nm wavelength of a series of standards over the range of 0.01, 0.025, 0.05, 0.075, 0.1, 0.15, 0.175, 0.200, 0.225 and 0.250 mM in a solution of 10% DMSO in HEPES-buffered water (concentration of HEPES = 60 mM).

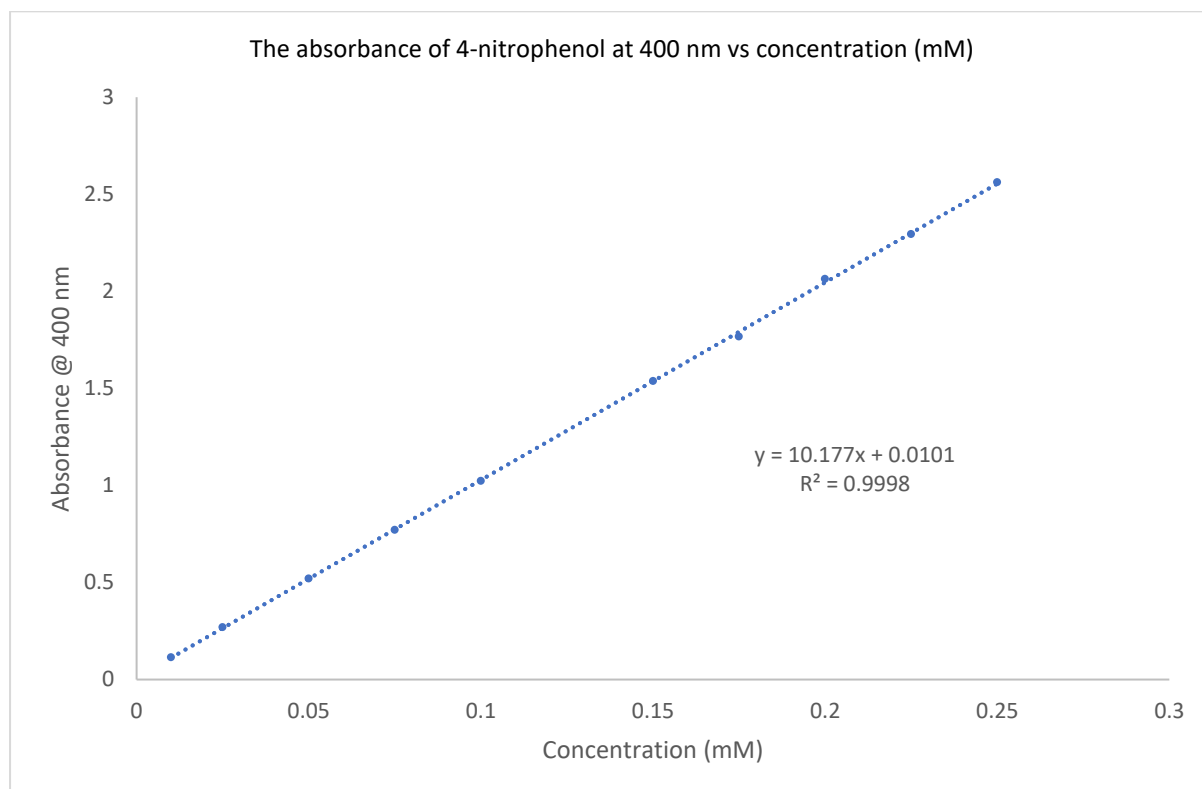


Figure 6.24. Calibration curve of 4-nitrophenol (10% DMSO in 60 mM HEPES-buffered H₂O).

6.1.7. Cell studies

All cell lines were purchased from and maintained as monolayers as described by the American Type Culture Collection with the exception of the p53^{+/+} and p53^{-/-} isogenic clones of HCT116 human colorectal adenocarcinoma cells which were a kind gift from Professor Bert Vogelstein¹²⁰. GBM1 cells were established from a primary GBM tumour by Heiko Wurdak and colleagues. Non-cancerous adult brain neural progenitor (NP1) cells were derived from a patient undergoing surgery to treat epilepsy.^{121,122} Cell culture and growth media for NP1 and GBM1 cells were as described.^{121,122} The response of cells following a continuous 96-h exposure to test compounds and platينات was determined using the MTT assay. Potency was recorded as the IC₅₀ and the selectivity index (SI) was defined as the ratio of IC₅₀ values for non-cancer to cancer cell lines with values >1 representing selectivity for cancer cells as opposed to non-cancer cells.¹²³

Chemosensitivity studies results

The effect of anions on the potency and selectivity of all test compounds evaluated is presented in Figure 6.25 - Figure 6.28. The inclusion of anions either increased, decreased or had no effect on both potency (Figure 6.25) and the selectivity (Figure 6.26) of [L¹₂Cu₃]⁶⁺ and [L¹₂Zn₃]⁶⁺. Enhanced or reduced effects on potency and selectivity relative to [L¹₂Cu₃]⁶⁺ and [L¹₂Zn₃]⁶⁺ was strongly cell line dependent (Figure 6.27). Particularly marked enhancement of both potency and selectivity (relative to ARPE-19) was observed for PSN1 and HCT116 p53^{+/+} cells treated with Cu²⁺ and Zn²⁺ ligands plus sulfate and phenyl phosphate anions. In contrast, the potency of the Cu²⁺ ligand plus the phenyl phosphate anion against BxPC3 cells is significantly reduced resulting in a reduction in selectivity compared to ARPE-19 cells. Different effects on non-cancer cell lines were also observed with only marginal effects of anion inclusion observed for the Cu²⁺ ligand (against both ARPE-19 and MCF10A cells) whereas for the Zn²⁺

ligand, its activity in the presence of all the anions tested was significantly reduced resulting in a relative loss of selectivity (Figure 6.27). The mechanistic reasons for these differential effects require further investigation but it suggests that the activity and selectivity of complexes can be tailored to individual cell lines, presumably via modulation of specific kinase inhibition activity and cell line dependent susceptibility to subsequent effects on the kinome. The ligand (L^1) and the mononuclear complex ($[L^1M]^{2+}$) are cytotoxic to cells in vitro but these species lack the selectivity exhibited by $[L^1_2M_3]^{6+}$ (Figure 6.28).

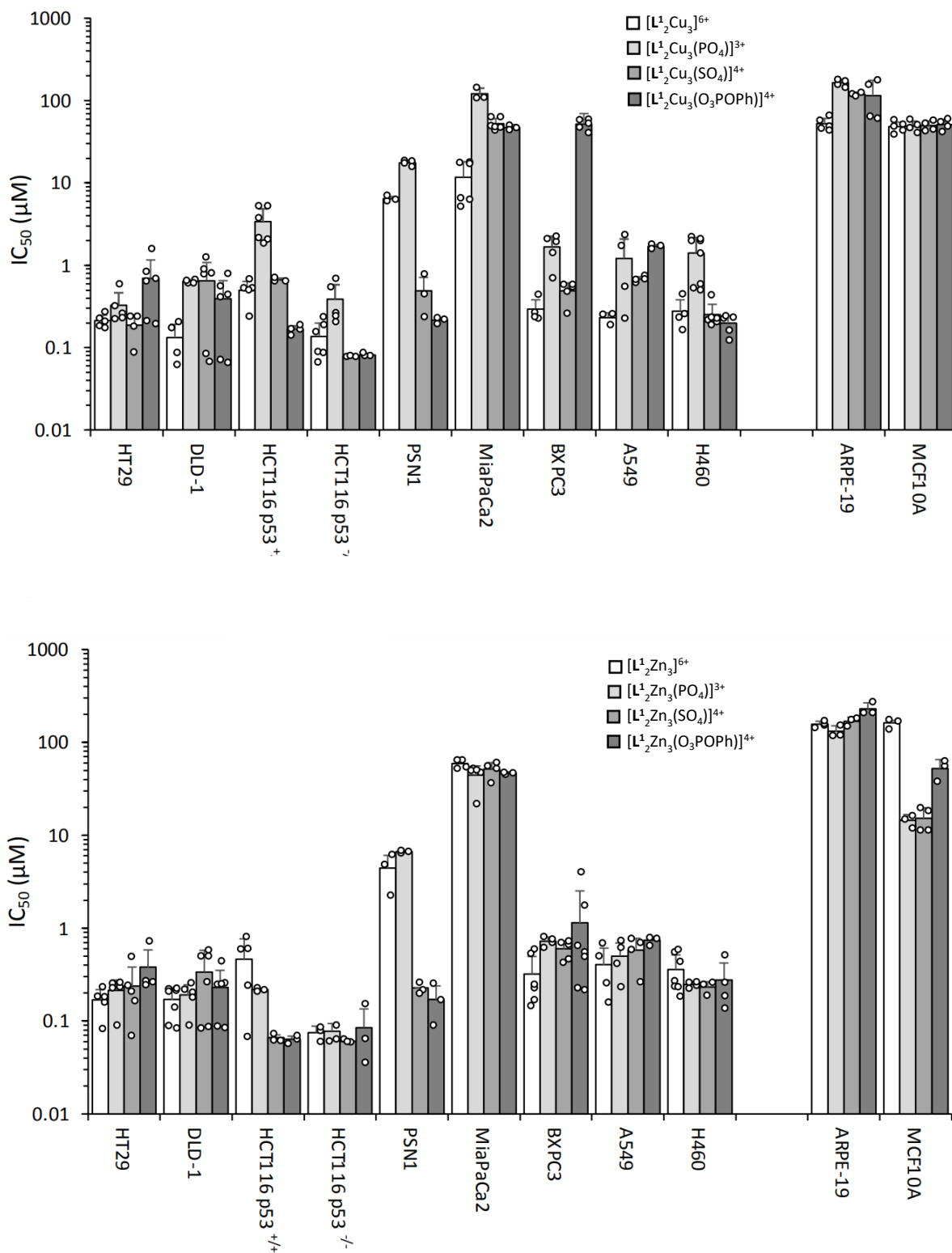


Figure 6.25. The effect of anions of the potency of $[L^1_2Cu_3]^{6+}$ and $[L^1_2Zn_3]^{6+}$. The results represent the mean IC_{50} values \pm standard deviation for at least three independent experiments.

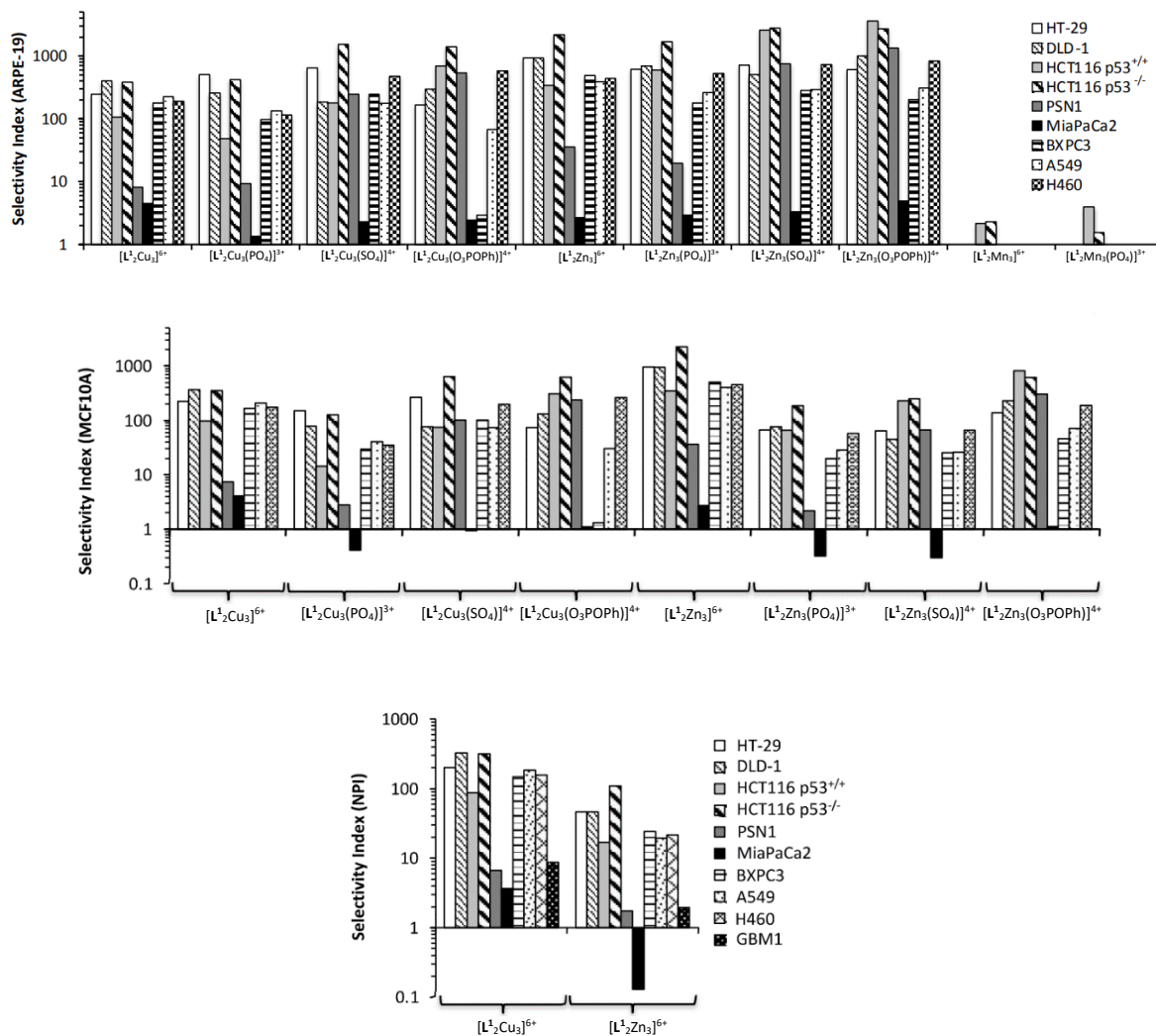


Figure 6.26. The effect of anions on the selectivity of $[L^1_2Cu_3]^{6+}$ and $[L^1_2Zn_3]^{6+}$. All values presented here were determined from the mean IC_{50} values in Figure 6.25 for each of the non-cancer cell lines (ARPE-19, MCF10A and NP1) used in this study. As mean IC_{50} values are used to calculate SI, no error bars are presented. The experimental error is accounted for in Figure 6.25.

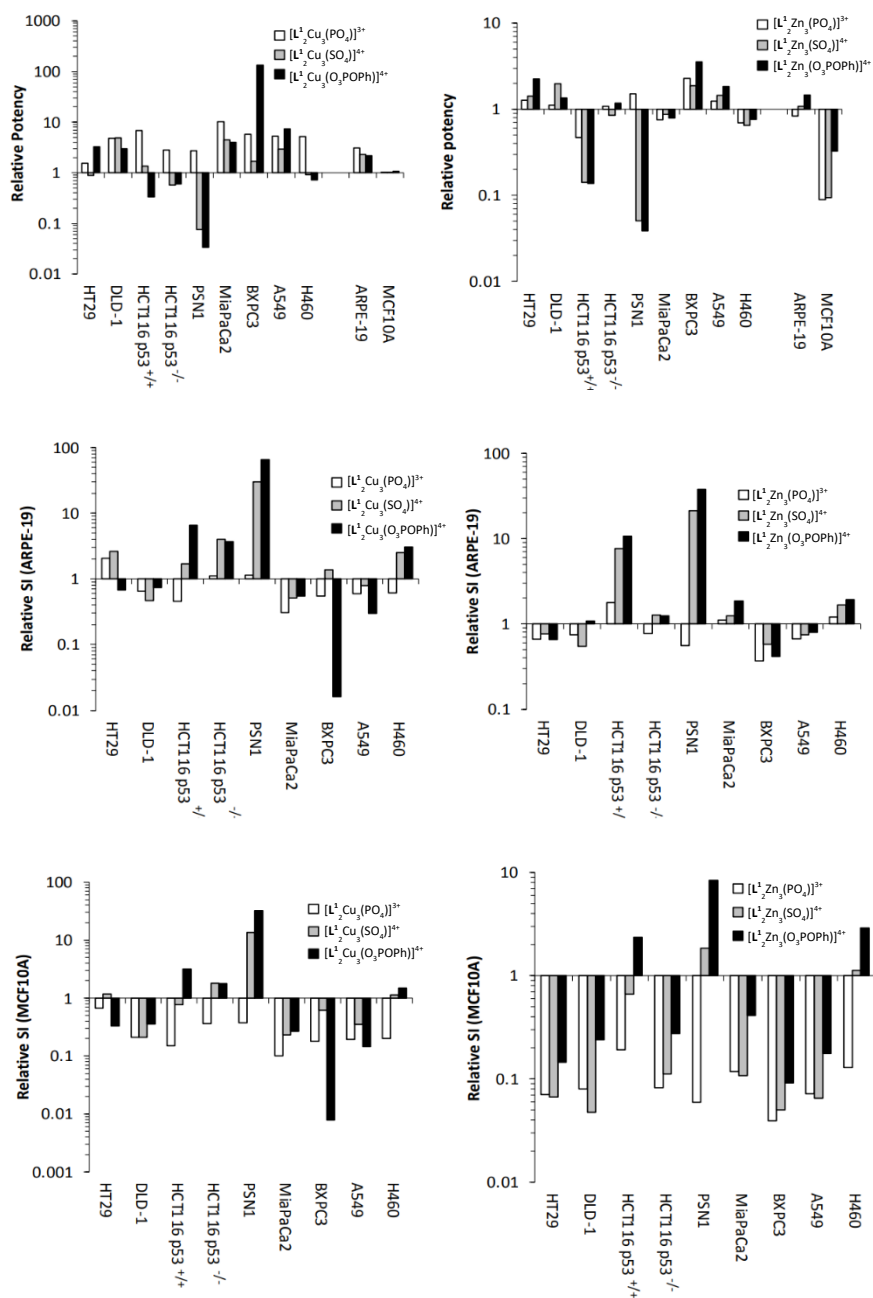


Figure 6.27. The effect of anions on the potency and selectivity relative to $[L^1_2Cu_3]^{6+}$ and $[L^1_2Zn_3]^{6+}$.

Relative potency was determined by dividing the IC_{50} of test compounds plus respective anions divided by IC_{50} values for $[L^1_2Cu_3]^{6+}$ and $[L^1_2Zn_3]^{6+}$. Values > 1 represent an increase in potency and conversely, values < 1 represent a reduction in potency. Relative selectivity index (SI) values were determined by dividing the SI value for test compounds plus respective anions divided by SI values for $[L^1_2Cu_3]^{6+}$ and $[L^1_2Zn_3]^{6+}$. Values > 1 represent an increase in selectivity and conversely, values < 1 represent a reduction in selectivity.

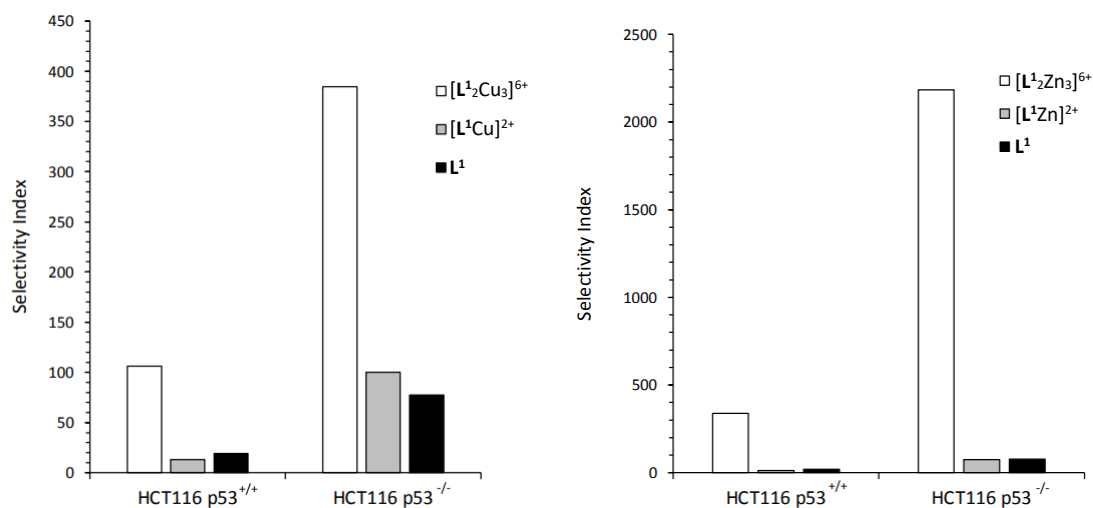


Figure 6.28. Comparative selectivity of $[L^1_2M_3]^{6+}$ to $[L^1M]^{2+}$ and L^1 . The selectivity index (SI) values were determined by dividing the mean IC_{50} of each test compound against ARPE-19 cells by the mean IC_{50} for HCT116 p53^{+/+} and p53^{-/-} cells. The results demonstrate that whilst $[L^1M]^{2+}$ and L^1 are cytotoxic to cells, selectivity for cancer cells is property confined primarily to the $[L^1_2M_3]^{6+}$ complexes. $[L^1M]^{2+}$ refers to an experiment where stoichiometric amounts of ligand and metal ions are used (as opposed to $2L^1$ plus $3M^{2+}$) thereby forcing the formation of $[L^1M]^{2+}$. In all likelihood, in the presence of tetrahedral oxoanions, this would result in forming $[L^1_2M_3(EO_4)]^{3/4+}$ (where $E = P$ or S) and free ligand.

Inhibition of kinase activity

The effect of $[\text{L}^1_2\text{Cu}_3]^{6+}$ and $[\text{L}^1_2\text{Zn}_3]^{6+}$ on the activity of 140 human recombinant kinases is presented in Figure 6.29. Both compounds are multi-kinase inhibitors and visually, there are clear differences between the kinases that are inhibited by $[\text{L}^1_2\text{Cu}_3]^{6+}$ and $[\text{L}^1_2\text{Zn}_3]^{6+}$ with more $[\text{L}^1_2\text{Cu}_3]^{6+}$ inhibiting more kinases than $[\text{L}^1_2\text{Zn}_3]^{6+}$. The differences that exist indicate that a different spectrum of inhibitory activity exists with evidence of selectivity. Of interest are the results demonstrating that the activity of some kinases is enhanced following drug treatment, particularly Src where significant stimulation of kinase activity was observed in these cell free assays.

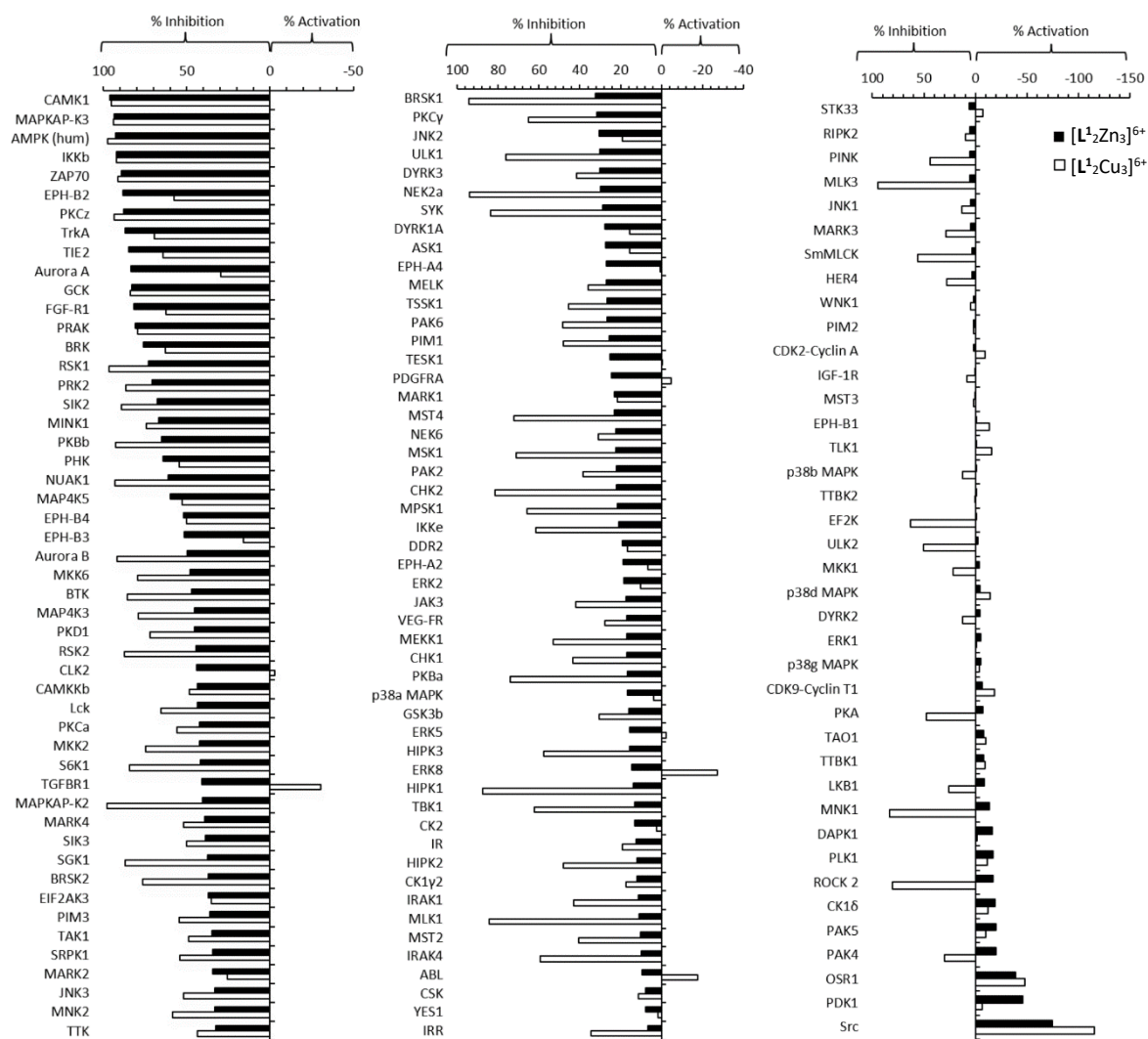


Figure 6.29. The effect of $[L^1_2Zn_3]^{6+}$ and $[L^1_2Cu_3]^{6+}$ on the activity of recombinant human kinases. The compounds were submitted to the MRC Protein Phosphorylation and Ubiquitination Unit International Centre for Kinase Profiling (University of Dundee) and tested at a concentration of $10 \mu M$ against 140 human kinases (Premier Screen).

Phosphatase assay results

The effects of $[L^1_2Zn_3]^{6+}$ concentration and duration of $[L^1_2Zn_3]^{6+}$ exposure on dephosphorylation of recombinant AMPK (pT172 AMPK α 1 and pS108 AMPK β 1) are presented in Figure 6.30. For analysis of effects on pT172 AMPK α 1, purified human α 1 β 2 γ 1 AMPK kinase was used. For analysis of effects on pS108 of AMPK β 1, purified human α 2 β 1 γ 1 AMPK kinase was used. Where total levels of the AMPK subunit decreased in response to incubation with $[L^1_2Zn_3]^{6+}$, we hypothesise that this could be due to either some precipitation of the kinase by the $[L^1_2Zn_3]^{6+}$ complex or a consequence of dephosphorylation of the kinase by $[L^1_2Zn_3]^{6+}$ resulting in its destabilisation and increased susceptibility to degradation. Dependency on ATP for dephosphorylation and the impact of AMP were also studied and are presented in Figure 6.31. Effects of $[L^1_2Zn_3]^{6+}$ on p-T172 appeared to be dependent on the presence of ATP or AMP although observed effects were quite modest (Figure 6.31). AMP binding to the regulatory γ AMPK subunit is known to help protect pT172 from physiological phosphatases.¹⁰³ In an AMPK kinase activity assay (Promega), however, increasing AMP concentration (0-160 μ M) had no adverse effect on the percentage inhibition of AMPK kinase activity by $[L^1_2Zn_3]^{6+}$ (Figure 6.31).

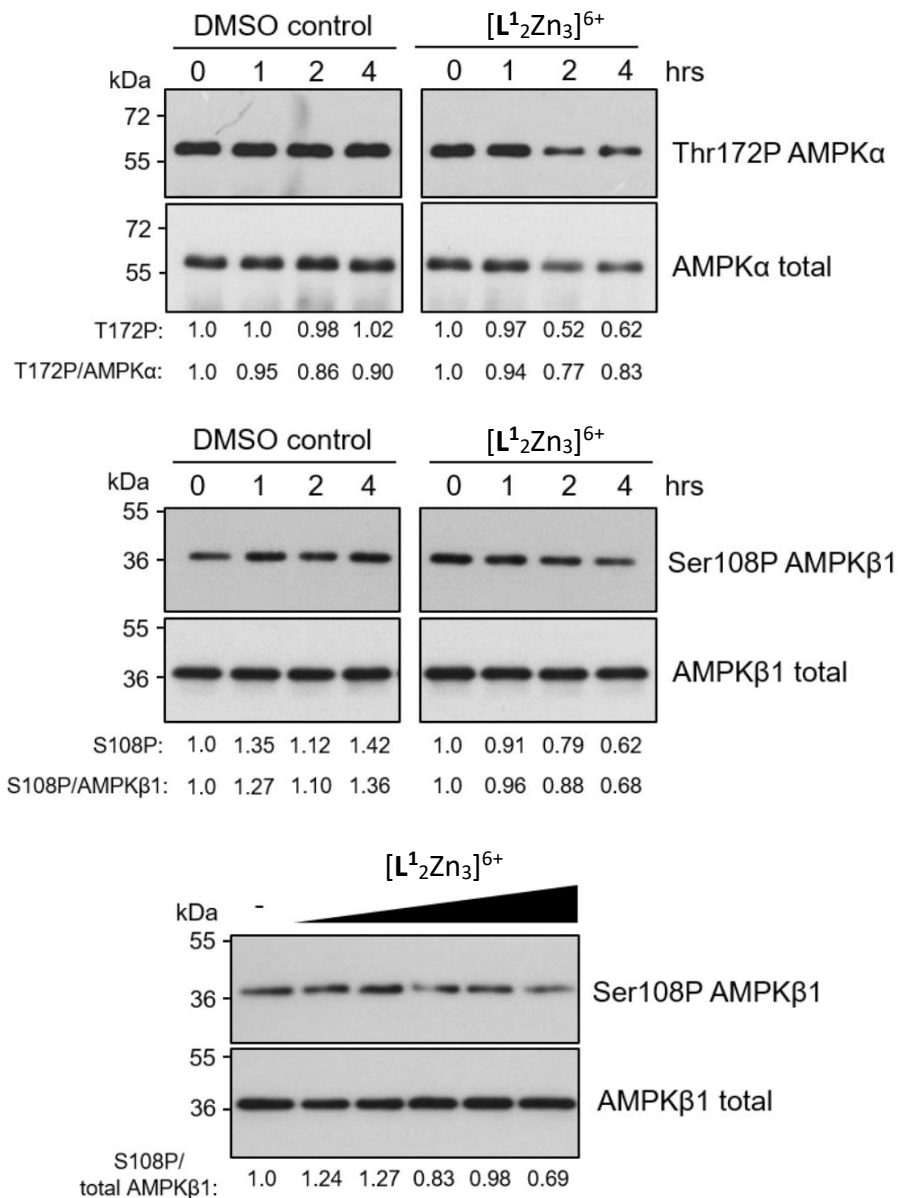


Figure 6.30. Effects of [L¹₂Zn₃]⁶⁺ on phospho-T172 levels of recombinant AMPKα1 and phospho-S108 levels of recombinant AMPKβ1. a) and b) time course of 50 μM [L¹₂Zn₃]⁶⁺ co-incubation with recombinant AMPK enzyme (α1β2γ1 for (a) and α2β1γ1 for (b)) and effects on phosphorylation levels of T172 of AMPKα1 (a) and S108 of AMPKβ1 (b). Densitometric quantification of levels of phosphorylated AMPK subunit and relative to total levels of the subunit are indicated; all quantification relative to t = 0; c) effect of increasing concentrations of [L¹₂Zn₃]⁶⁺ (0-50 μM, 2-fold dilution series) on phospho-S108 AMPK β1 relative to total AMPK β1. Similar results were obtained in a minimum of n = 2 independent experiments.

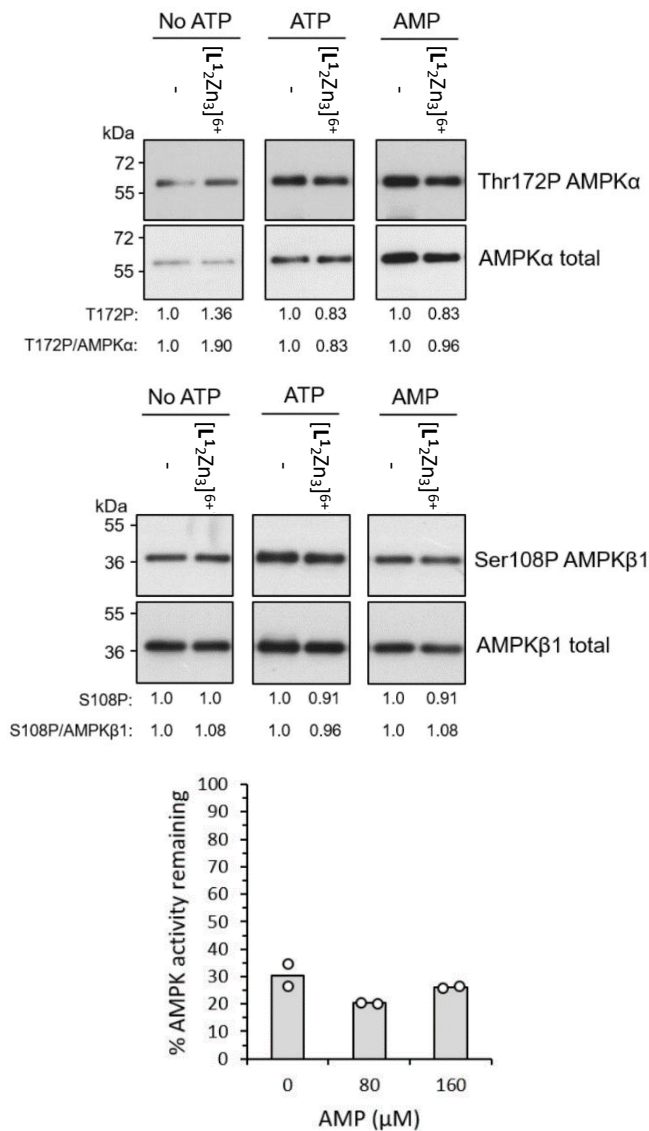
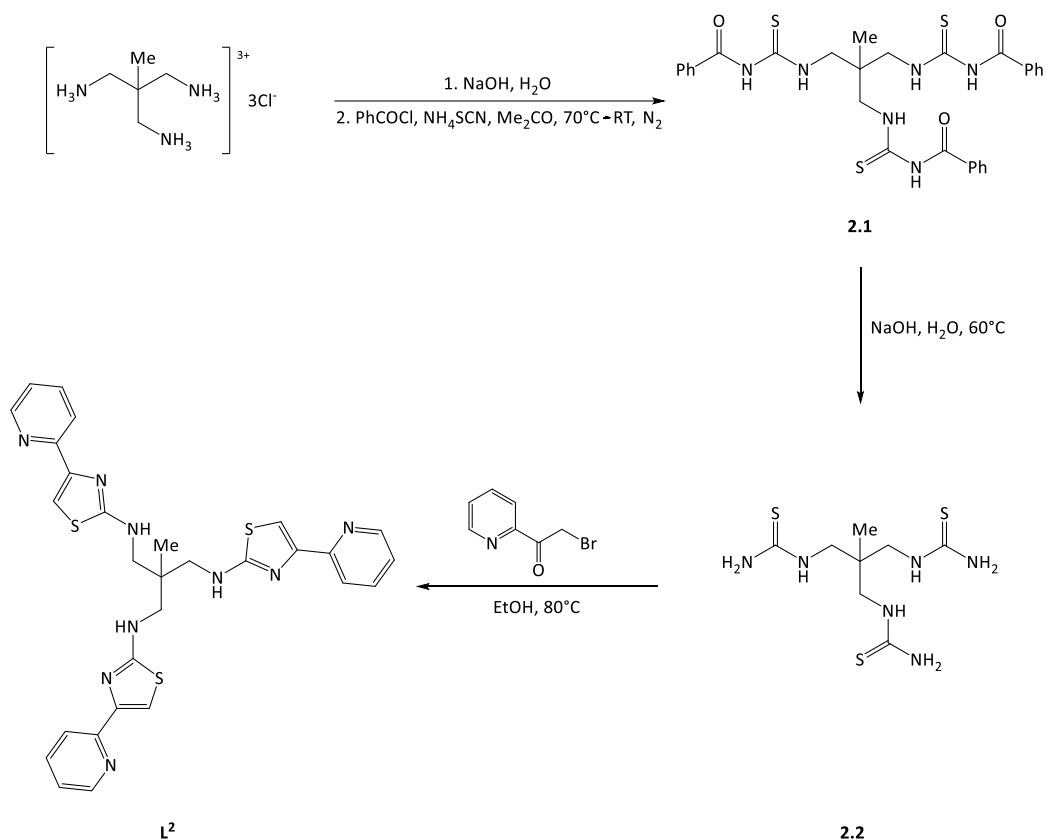


Figure 6.31. Influence of AMP and ATP on the effects of $[L^1_2Zn_3]^{6+}$ on phosphorylation levels of recombinant AMPK and on AMPK kinase activity. a) and b) Effects of no ATP, 50 μ M ATP or 50 μ M AMP on the effects of 50 μ M $[L^1_2Zn_3]^{6+}$ on phospho-T172 AMPK α 1 of α 1 β 2 γ 1 AMPK kinase (a) and phospho-S108 of AMPK β 1 of α 2 β 1 γ 1 AMPK kinase (b). Densitometric quantification of levels of phosphorylated AMPK subunit and relative to total levels of the subunit are indicated; all quantification relative to solvent control. For a) and b), similar results were obtained in a minimum of $n=2$ independent experiments. c) effect of increasing concentrations of AMP (0, 80, 160 μ M) on AMPK kinase inhibition by $[L^1_2Zn_3]^{6+}$. % AMPK activity is relative to activity in the vehicle control \pm AMP (0, 80 or 160 μ M AMP). $N = 2$ independent experiments, with corresponding data points as indicated.

6.2. Chapter 3

6.2.1. Synthesis of ligand L^2



Scheme 6.2. Synthesis of ligand L^2 .

Synthesis of **2.1**. To a solution of 1,1,1-tris(aminomethyl)ethane trihydrochloride¹⁰⁶ (1.78 g, 7.86 mmol) dissolved in minimal water (~5 mL), sodium hydroxide (0.94 g, 23.50 mmol) was added and solution stirred for 10 minutes. The water was then removed by rotary evaporation using ethanol to azeotropically remove any remaining water. Separately, to a solution of ammonium thiocyanate (2.39 g, 31.44 mmol) in dry acetone (50 mL), benzoyl chloride (4.42 g, 31.44 mmol) was added dropwise and slowly at such a rate as to cause a gentle reflux, causing a white precipitate to form. This solution was refluxed for 15 minutes during which time the colourless solution turned yellow. To this was added the dried triamine suspended in dry acetone (5 mL) slowly and dropwise, at such a rate as to cause a

gentle reflux. This mixture was stirred at 55 °C for 24 hours, cooled and poured onto water (100 mL) which precipitated the crude product as an immiscible viscous orange oil. To this was added dichloromethane (50 mL) and solution sonicated and stirred until all the oil dissolved. The organic layer was removed and the aqueous layer extracted further with DCM (2 × 50 mL). The organic layers were combined, dried over anhydrous magnesium sulfate and the solvent removed by rotary evaporation. The crude product was recrystallised from ethanol to afford the product as a slightly yellow solid (2.15 g, 45%). ¹H NMR [300 MHz, CDCl₃]: δ (ppm) = 11.13 (t, 3H, *J* = 6.1, -CSNH), 9.08 (s, 3H, PhCO-NH), 7.75 (m, 6H, Ph), 7.60 (t, 3H, *J* = 7.4, Ph), 7.44 (t, 6H, *J* = 8.0, Ph), 4.07 (d, 6H, *J* = 6.3 Hz, -CH₂-), 1.29 (s, 3H, -CH₃). ¹³C NMR [100 MHz, CDCl₃]: δ (ppm) = 181.4 (C=S), 166.6 (C=O), 133.4 (CH), 131.7 (C), 129.0 (CH), 127.5 (CH), 51.1 (CH₂), 42.0 (C), 20.5 (CH₃). ESI-MS *m/z* 607.1615 [M + H]⁺, observed neutral mass 606.1542, C₂₉H₃₀N₆O₃S₃ requires 606.1542 (error 0.19 ppm).

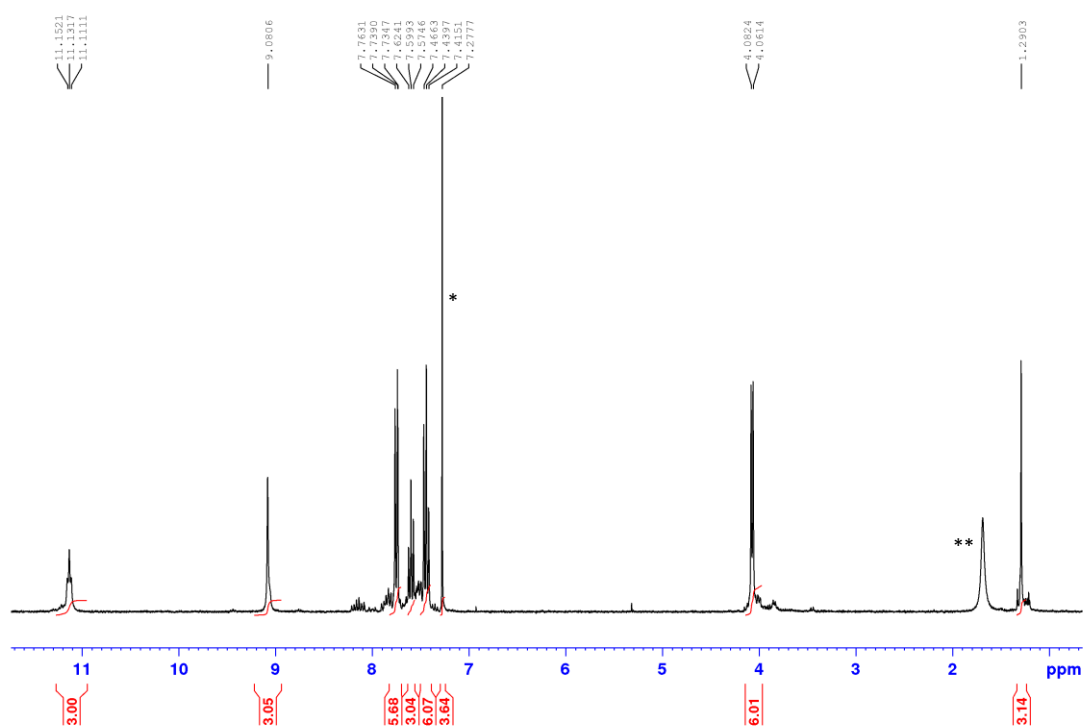


Figure 6.32. ¹H NMR Spectrum of **2.1** [300 MHz, CDCl₃]. *CHCl₃ impurity. **H₂O impurity.

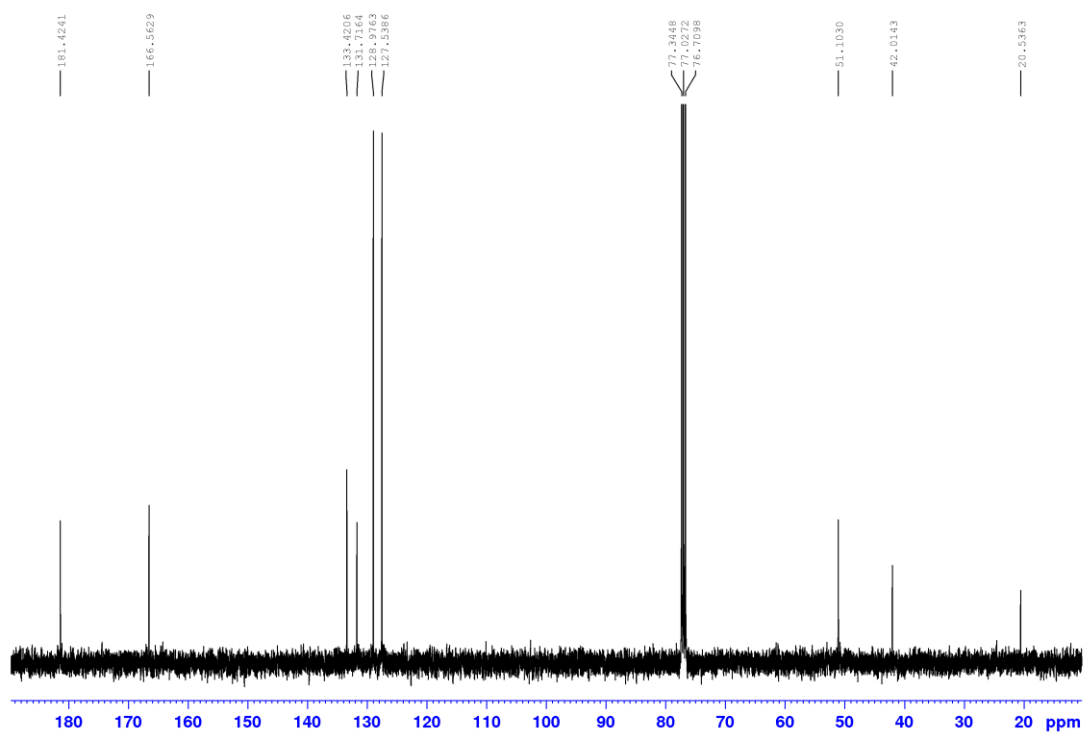


Figure 6.33. ^{13}C NMR Spectrum of **2.1** [100 MHz, CDCl_3].

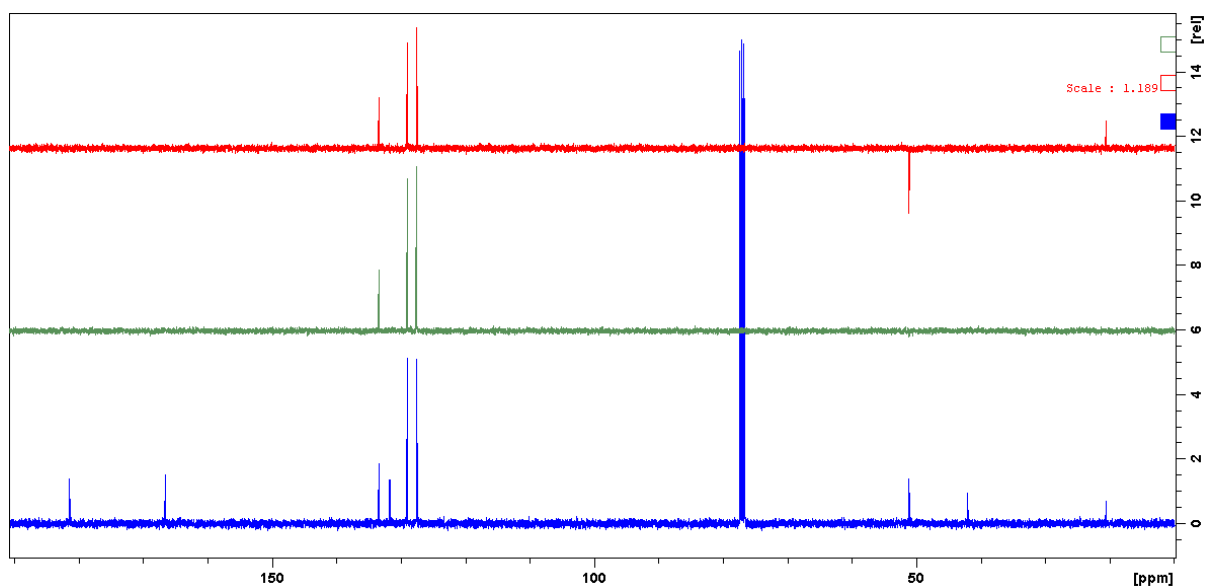


Figure 6.34. ^{13}C NMR Spectrum of **2.1** (blue) with the corresponding DEPT-135 (red) and DEPT-90 (green) NMR spectra [100 MHz, CDCl_3].

Synthesis of **2.2**. To a stirred suspension of benzoylated thiourea **2.1** (1.00 g, 1.65 mmol) in water (20 mL), sodium hydroxide (660 mg, 16.50 mmol) was added. The solution was heated to 60 °C and stirred for 18 hours, during which time the solution clarified. The solution was cooled to ambient temperature during which time a heavy white precipitate formed. The solid was isolated by vacuum filtration and washed with water (3 × 5 mL) to afford the product as a white solid (115 mg, 24%). ¹H NMR [400 MHz, (CD₃)₂SO]: δ (ppm) = 7.70 (br s, 3H, -NH), 7.14 (br s, 6H, -NH₂), 0.81 (s, 3H, CH₃). ¹³C NMR [100 MHz, (CD₃)₂SO]: δ (ppm) = 184.1 (C=S), 48.6 (CH₂), 41.6 (C), 19.2 (CH₃). ESI-MS *m/z* 295.0833 [M + H]⁺, observed neutral mass 294.0759, C₈H₁₈N₆S₃ requires 294.0755 (error 1.29 ppm).

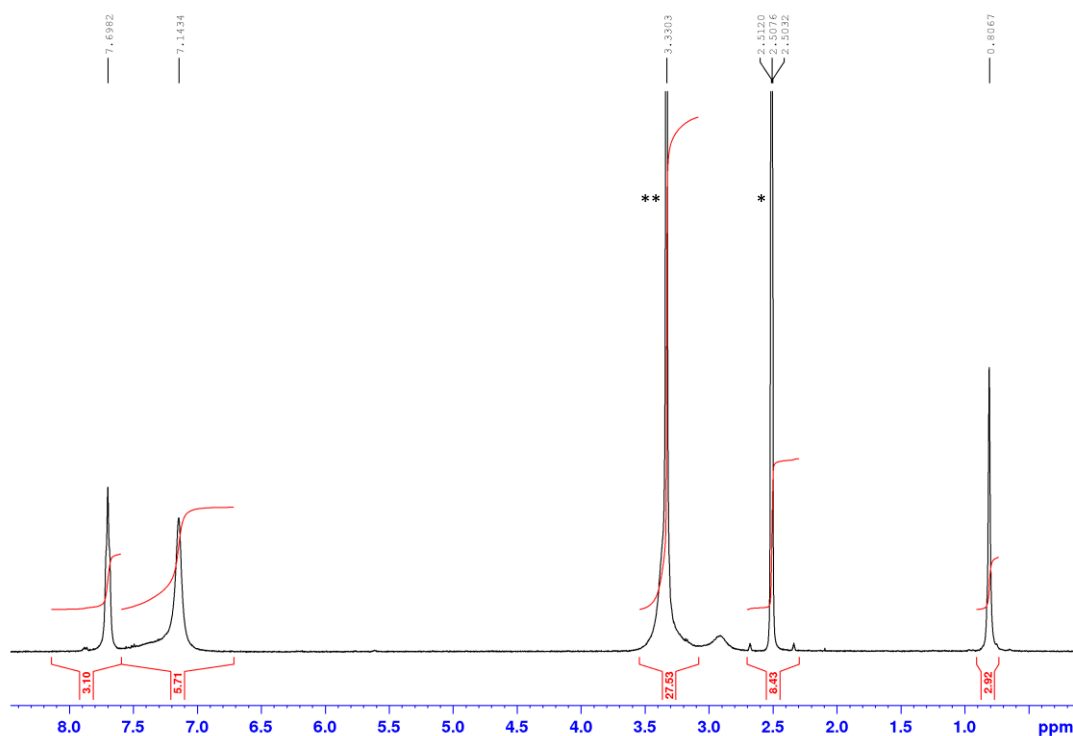


Figure 6.35. ¹H NMR Spectrum of **2.2** [400 MHz, (CD₃)₂SO]. *(CD₃)(CD₂H)SO impurity. **H₂O impurity.

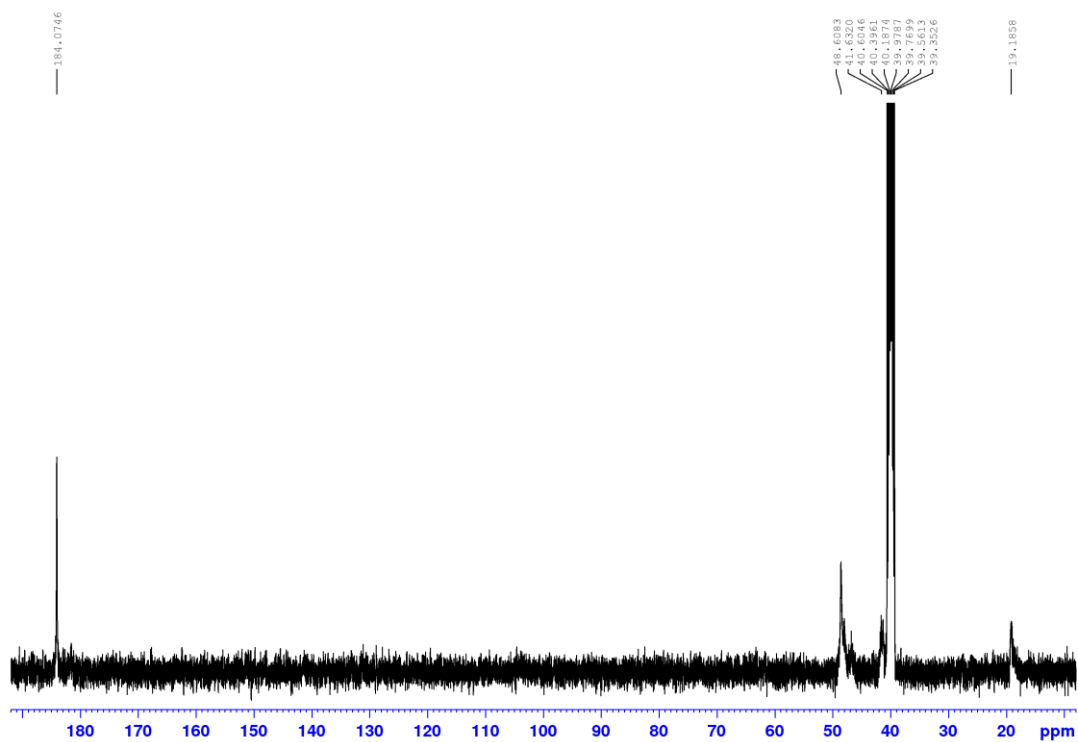


Figure 6.36. ^{13}C NMR Spectrum of **2.2** [100 MHz, $(\text{CD}_3)_2\text{SO}$].

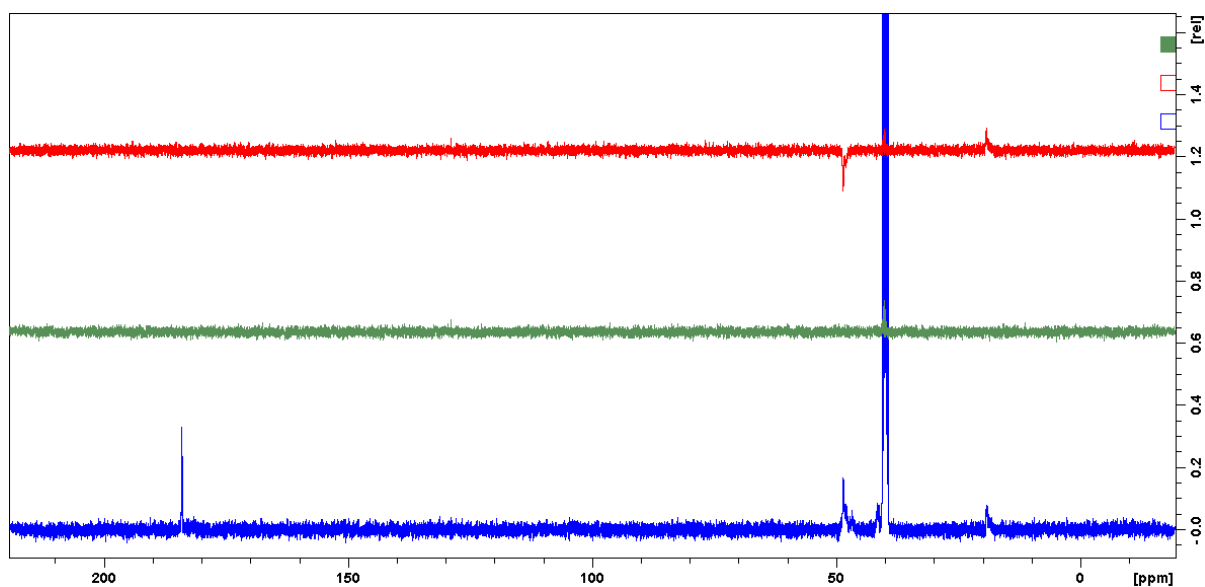


Figure 6.37. ^{13}C NMR Spectrum of **2.2** (blue) with the corresponding DEPT-135 (red) and DEPT-90 (green)

Synthesis of 2-methyl-*N*¹,*N*³-bis(4-(pyridin-2-yl)thiazol-2-yl)-2-(((4-(pyridin-2-yl)thiazol-2-yl)amino)-methyl)propane-1,3-diamine (ligand **L**²). To a solution of α -bromo-2-acetylpyridine (224 mg, 1.12 mmol) in ethanol (15 mL), thiourea **2.2** (100 mg, 0.34 mmol) was added, causing the colourless solution to turn yellow on stirring. The solution was heated to 80 °C and stirred for 24 hours, during which time a brown-yellow precipitate formed. After cooling to ambient temperature, the solution was vacuum filtered and solid washed with ethanol (2 \times 5 mL) to leave the ligand **L**² as its yellow trihydrobromide salt. This was deprotonated by stirring in concentrated ammonia (5 mL) for 4 hours, during which time the brown-yellow powder turned green-grey. The solid was isolated by vacuum filtration and washed with water (3 \times 5 mL) to leave the pure ligand as a grey powder (97 mg, 48%). ¹H NMR [400 MHz, (CD₃)₂SO]: δ (ppm) = 8.60 (ddd, 3H, *J* = 4.8, 1.7, 0.8, Py), 8.04, (t, 3H, *J* = 6.4, -NH), 7.94 (d, 3H, *J* = 7.9, Py), 7.82 (td, 3H, *J* = 7.6, 1.8, Py), 7.31 (s, 3H, tz), 7.29 (ddd, 3H, *J* = 7.4, 4.8, 1.1, Py), 3.43 (d, 6H, *J* = 6.2 Hz, -CH₂-), 1.05 (s, 3H, -CH₃). ¹³C NMR [100 MHz, (CD₃)₂SO]: δ (ppm) = 169.9 (C), 152.8 (C), 150.2 (C), 149.7 (CH), 137.5 (CH), 122.8 (CH), 120.8 (CH), 105.5 (CH), 49.4 (CH₂), 42.6 (C), 19.9 (CH₃). ESI-MS *m/z* 598.1619 [M + H]⁺, observed neutral mass 597.1548, C₂₉H₂₇N₉S₃ requires 597.1552 (error 0.67 ppm).

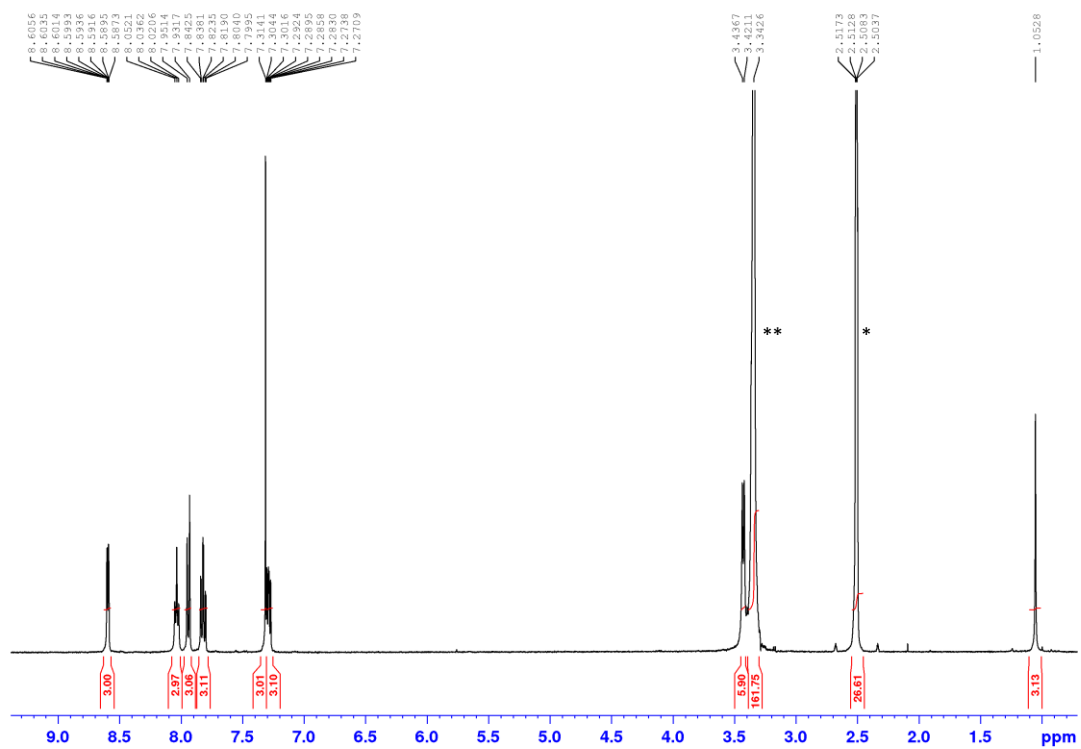


Figure 6.38. ^1H NMR Spectrum of L^2 [400 MHz, $(\text{CD}_3)_2\text{SO}$]. * $(\text{CD}_3)(\text{CD}_2\text{H})\text{SO}$ impurity. ** H_2O impurity.

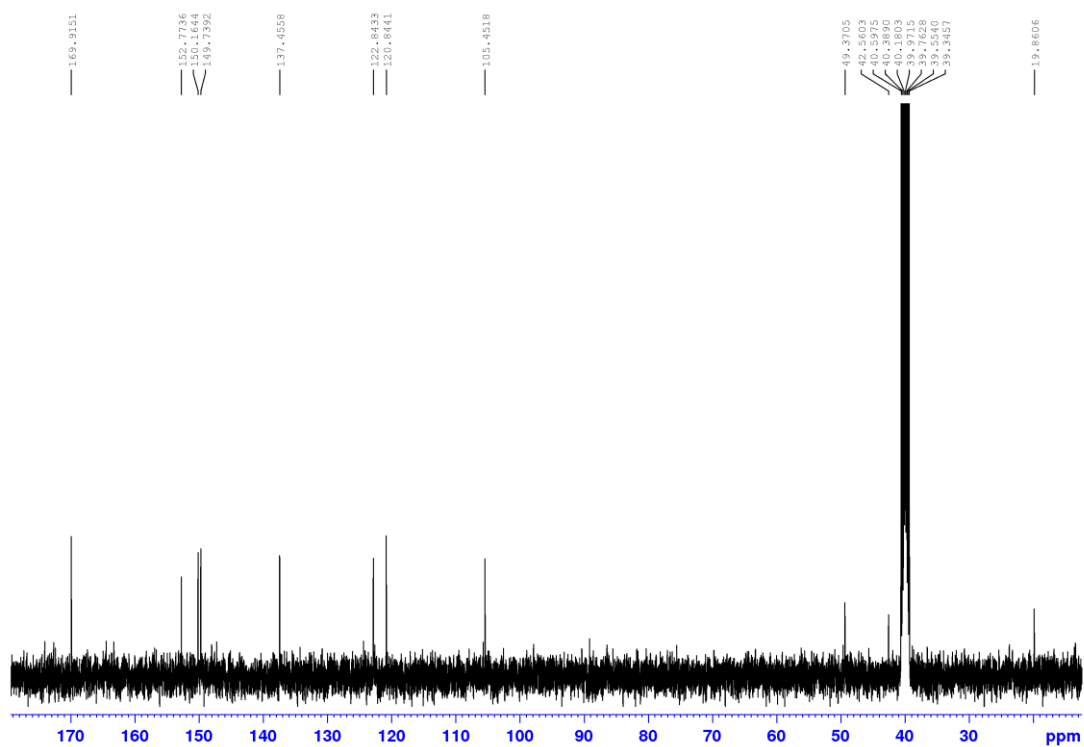


Figure 6.39. ^{13}C NMR Spectrum of L^2 [100 MHz, $(\text{CD}_3)_2\text{SO}$].

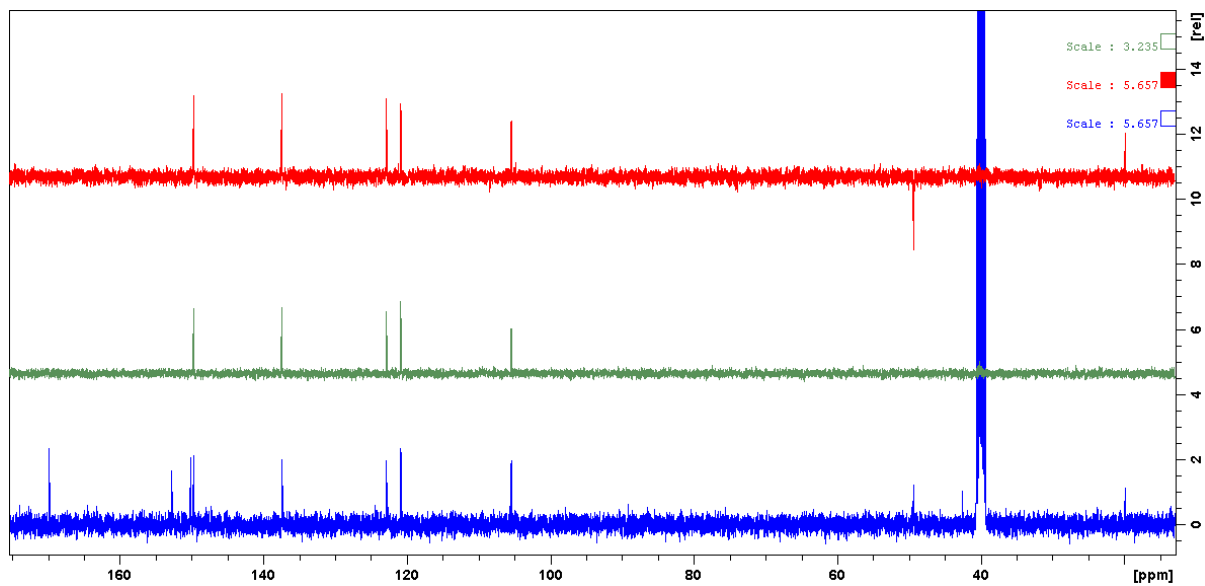
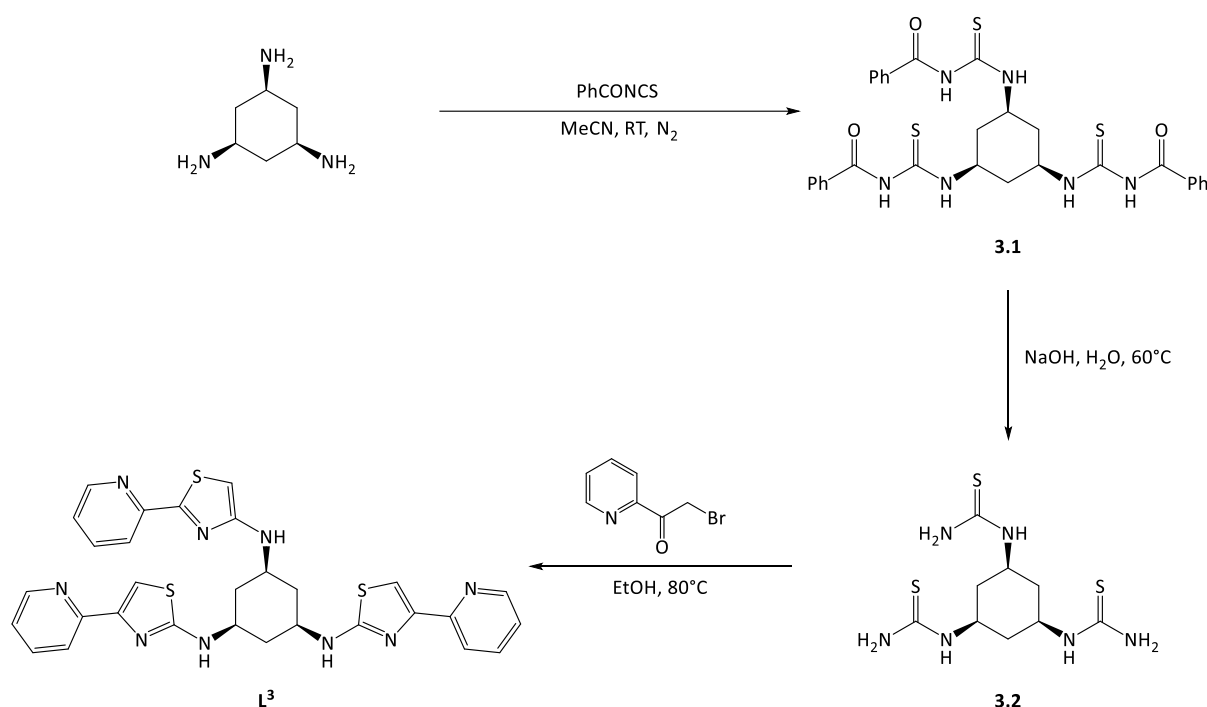


Figure 6.40. ^{13}C NMR Spectrum of L^2 (blue) with the corresponding DEPT-135 (red) and DEPT-90 (green) NMR spectra [100 MHz, $(\text{CD}_3)_2\text{SO}$].

6.2.2. Synthesis of ligand **L**³



Scheme 6.3. Synthesis of ligand **L**³.

Synthesis of **3.1**. To a solution of *cis*, *cis*-1,3,5-triaminocyclohexane^{109,110} (520 mg, 4.05 mmol) in acetonitrile (25 mL) was added benzoyl isothiocyanate (2.17 g, 13.30 mmol) dropwise under an atmosphere of nitrogen, causing a pale yellow precipitate to form. The solution was stirred for 24 hours and product isolated by vacuum filtration. This was washed with acetonitrile (2 × 5 mL) to afford the product as a pale-yellow solid (1.88 g, 75%). ¹H NMR [400 MHz, (CD₃)₂SO]: δ (ppm) = 11.34 (s, 3H, PhCO-NH), 10.86 (d, 3H, *J* = 7.6, cy-NH), 7.83 (d, 6H, *J* = 7.5, Ph), 7.56 (t, 3H, *J* = 7.4, Ph), 7.42 (t, 6H, *J* = 7.6, Ph), 4.35 (m, 3H, cy-CH), 2.44 (br m, coincident with residual solvent peak, 3H, cy-CH), 1.59 (m, 3H, cy-CH). ¹³C NMR [100 MHz, (CD₃)₂SO]: δ (ppm) = 179.9 (C=S), 168.8 (C=O), 133.5 (CH), 132.6 (C), 129.0 (CH), 128.9 (CH), 50.8 (CH), 35.0 (CH₂). ESI-MS *m/z* 619.1612 [M + H]⁺, observed neutral mass 618.1536, C₂₉H₃₀N₆O₃S₃ requires 618.1542 (error 0.86 ppm).

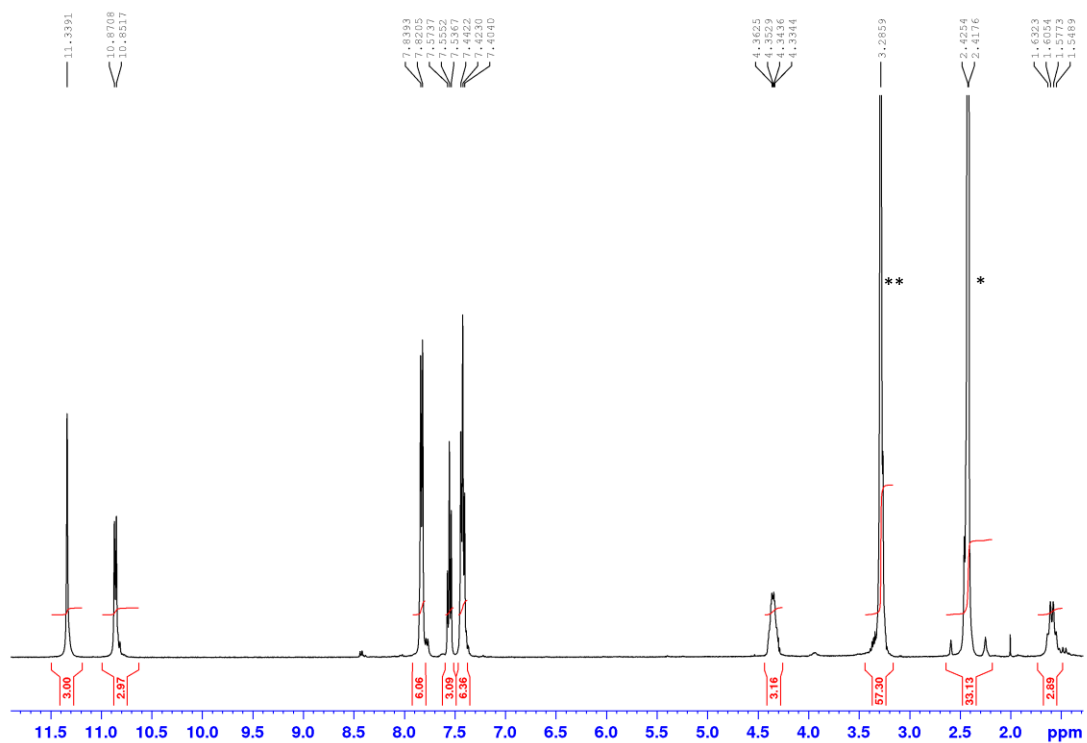


Figure 6.41. ^1H NMR Spectrum of **3.1** [400 MHz, $(\text{CD}_3)_2\text{SO}$]. * $(\text{CD}_3)(\text{CD}_2\text{H})\text{SO}$ impurity. ** H_2O impurity.

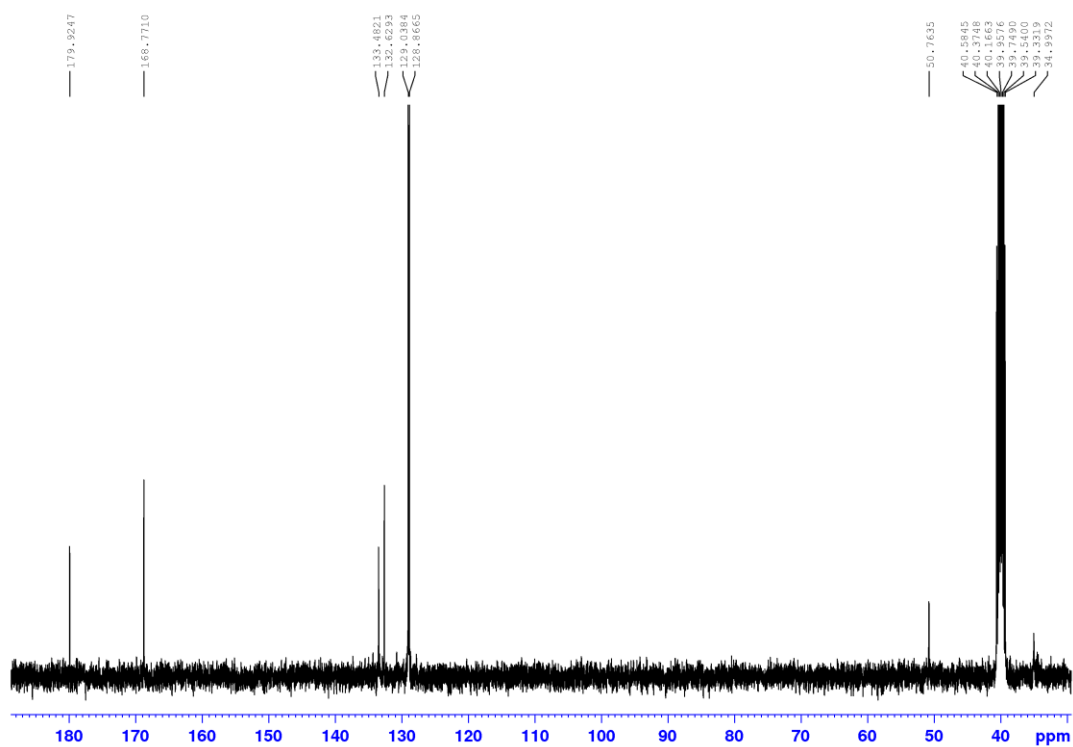


Figure 6.42. ^{13}C NMR Spectrum of **3.1** [100 MHz, $(\text{CD}_3)_2\text{SO}$].

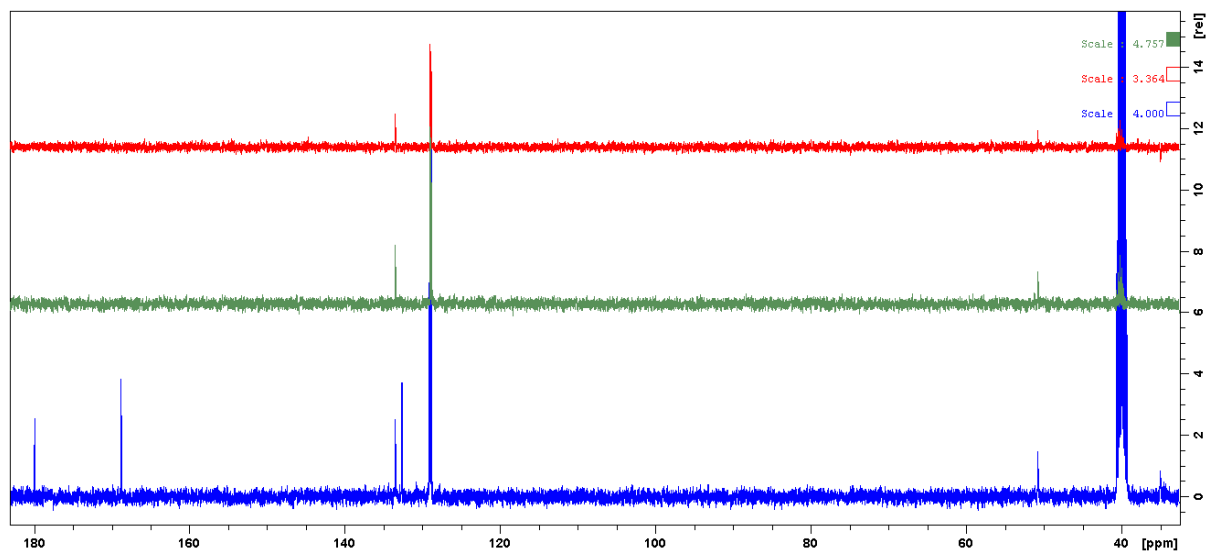
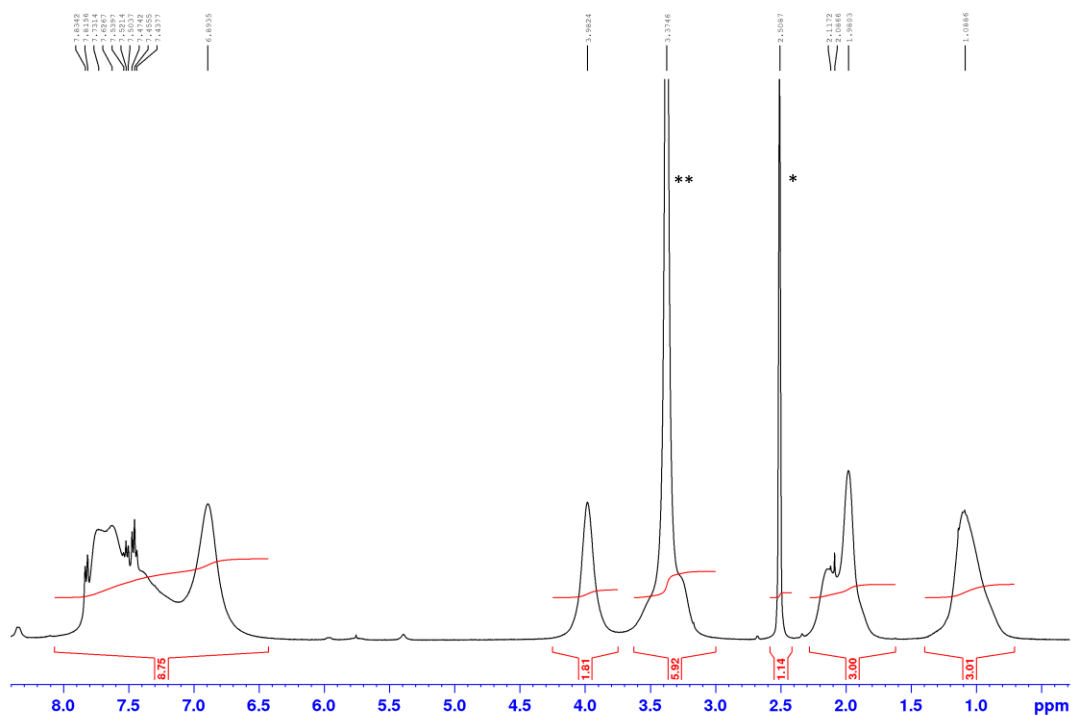


Figure 6.43. ^{13}C NMR Spectrum of **3.1** (blue) with the corresponding DEPT-135 (red) and DEPT-90 (green) NMR spectra [100 MHz, $(\text{CD}_3)_2\text{SO}$].

Synthesis of **3.2**. To a stirred suspension of **3.1** (1.88 g, 3.04 mmol) in water (30 mL) sodium hydroxide (1.22 g, 30.50 mmol) was added. The solution was stirred at 60 °C for 18 hours during which time the solution clarified. The reaction was allowed to cool to ambient temperature, resulting in the formation of a white precipitate, which was isolated by vacuum filtration and washed with water to leave the pure product as a white solid (635 mg, 68%). ¹H NMR [600 MHz, (CD₃)₂SO]: δ (ppm) = 7.90 – 6.70 (br m, 9H, -NH and -NH₂), 3.98 (br s, 3H, cy-CH), 2.30– 1.70 (br m, 3H, cy-CH), 1.09 (br s, 3H, cy-CH). ESI-MS *m/z* 307.0842 [M + H]⁺, observed neutral mass 306.0761, C₉H₁₈N₆S₃ requires 306.0755 (error -1.94 ppm).



was stirred at 80 °C for 24 hours, during which time the solution clarified and a bright yellow precipitate formed. After cooling to ambient temperature, the solution was vacuum filtered and the solid washed with ethanol (2 × 5 mL) to afford the ligand **L**³ as the yellow trihydrobromide salt. The salt was deprotonated by stirring in concentrated ammonia (5 mL) for 4 hours, during which time the bright yellow powder turned pale brown, the solid was isolated by vacuum filtration and washed with water (3 × 5 mL) to afford the pure ligand as a pale yellow-brown solid (322 mg, 81%). ¹H NMR [600 MHz, (CD₃)₂SO]: δ (ppm) = 7.90 – 6.70 (br m, 9H, -NH and -NH₂), 3.98 (br s, 3H, cy-CH), 2.30 – 1.70 (br m, 3H, cy-CH), 1.09 (br s, 3H, cy-CH). ¹³C NMR [150 MHz, (CD₃)₂SO]: δ (ppm) = 167.5 (C), 152.0 (C), 149.6 (C), 148.8 (CH), 137.5 (CH), 122.5 (CH), 120.4 (CH), 105.3 (CH), 50.4 (CH), 37.7 (CH₂). ESI-MS *m/z* 305.5858 [M + 2H]²⁺, observed neutral mass 609.1573, C₃₀H₂₇N₉S₃ requires 609.1552 (error -3.55 ppm).

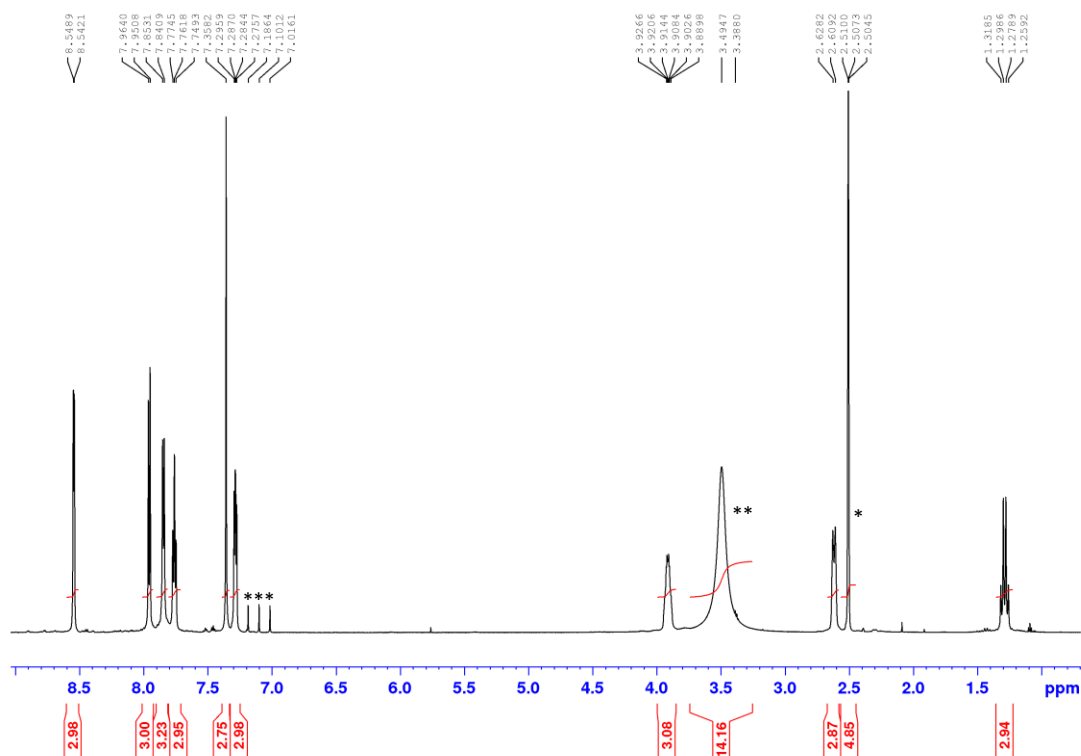


Figure 6.45. ¹H NMR Spectrum of **L**³ [600 MHz, (CD₃)₂SO]. *(CD₃)(CD₂H)SO impurity. **H₂O impurity.

*** NH₄⁺ impurity.

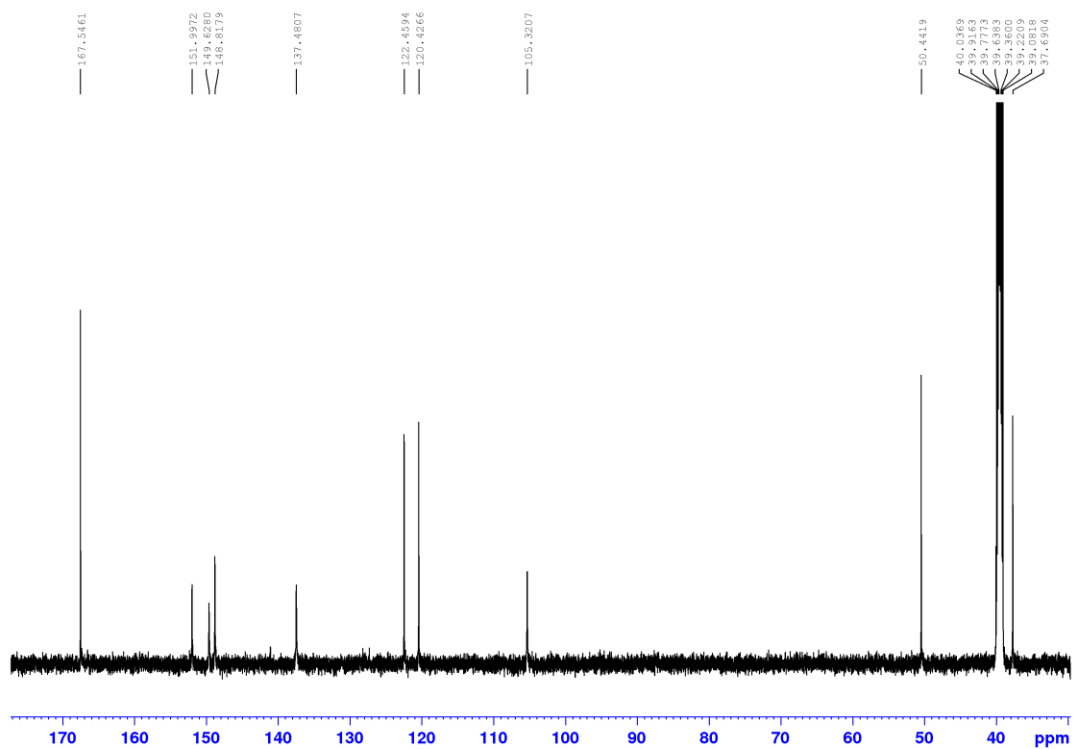


Figure 6.46. ^{13}C NMR Spectrum of L^3 [150 MHz, $(\text{CD}_3)_2\text{SO}$].

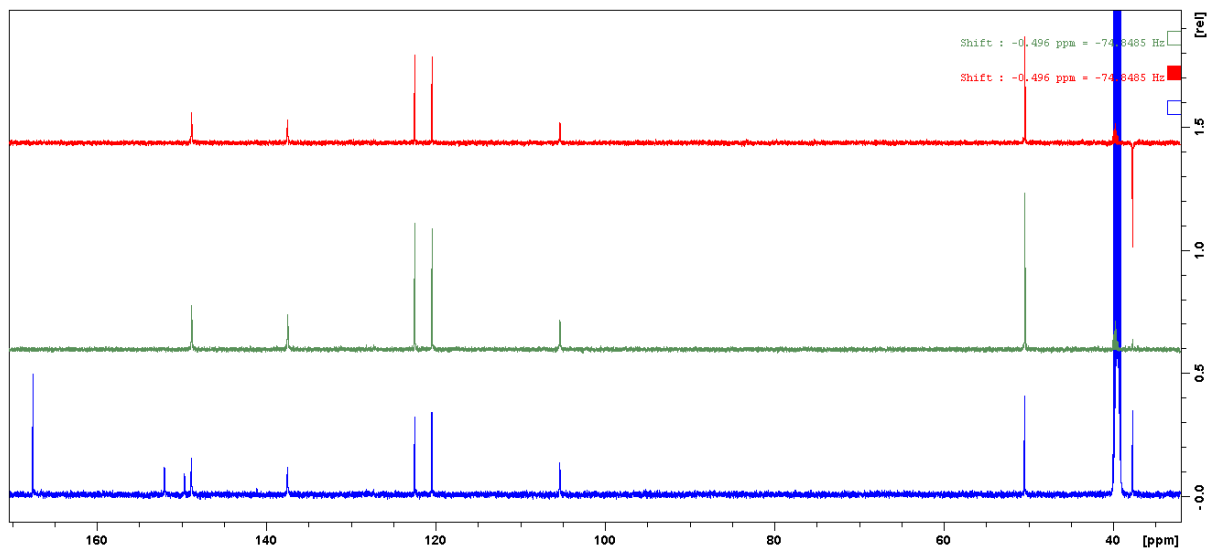


Figure 6.47. ^{13}C NMR Spectrum of L^3 (blue) with the corresponding DEPT-135 (red) and DEPT-90 (green) NMR spectra [150 MHz, $(\text{CD}_3)_2\text{SO}$].

6.2.3. Crystallography of L^3 complexes

Compound	$[L^3_2Cu_3(SO_4)](ClO_4)_4$	$[L^3_2Cu_3Br](BF_4)_5$
Formula	$C_{67.12}H_{66}Cl_4Cu_3N_{23}O_{29.75}S_7$	$C_{60}H_{54}B_{4.538}BrCu_3F_{18.153}N_{18}O_3S_6$
M	2227.75	1932.16
Crystal system	Monoclinic	Triclinic
Space group	$C2/c$	$C2/c$
a (Å)	30.9946(8)	30.483(7)
b (Å)	26.3900(7)	25.801(6)
c (Å)	25.3578(6)	23.930(6)
α (°)	90	90
β (°)	120.8910(10)	120.638(9)
γ (°)	90	90
V (Å ³)	17799.1(8)	16193(7)
Z	8	8
ρ_{calc} (Mg cm ⁻³)	1.663	1.5849
$F(000)$	9078	7760.4587
Crystal dimensions (mm)	0.15, 0.02, 0.02	0.20, 0.22, 0.29
Reflections measured	100877	94378
Range	$2.36 \leq \theta \leq 72.20^\circ$	$2.38 \leq \theta \leq 29.97^\circ$
hkl range indices	$-38 \leq h \leq 38, -32 \leq k \leq 32, -31 \leq l \leq 34$	$-43 \leq h \leq 43, -28 \leq k \leq 36, -34 \leq l \leq 34$

N° independent reflections	17510	24716
Reflections with $I > 2\sigma(I)$	14250	15392
R_{int}	0.0616	0.0681
Final R_1 values	0.0536	0.0720
Final $wR(F^2)$ values	0.1425	0.1864
Final R_1 values (all data)	0.0679	0.1237
Final $wR(F^2)$ values (all data)	0.1528	0.2193
GOF	1.018	1.0676
Refined parameters	1321	1091
Restraints	163	80
Largest peak and hole ($e \text{ \AA}^{-3}$)	1.632, -1.042	3.4034, -1.4582
CCDC number	1941880	1941879

Table 6.4. X-ray crystallographic data for $[\text{L}^3_2\text{Cu}_3(\text{SO}_4)]^{4+}$ and $[\text{L}^3_2\text{Cu}_3(\text{Br})]^{5+}$.

6.2.4. Mass spectrometry studies of L^3 complexes

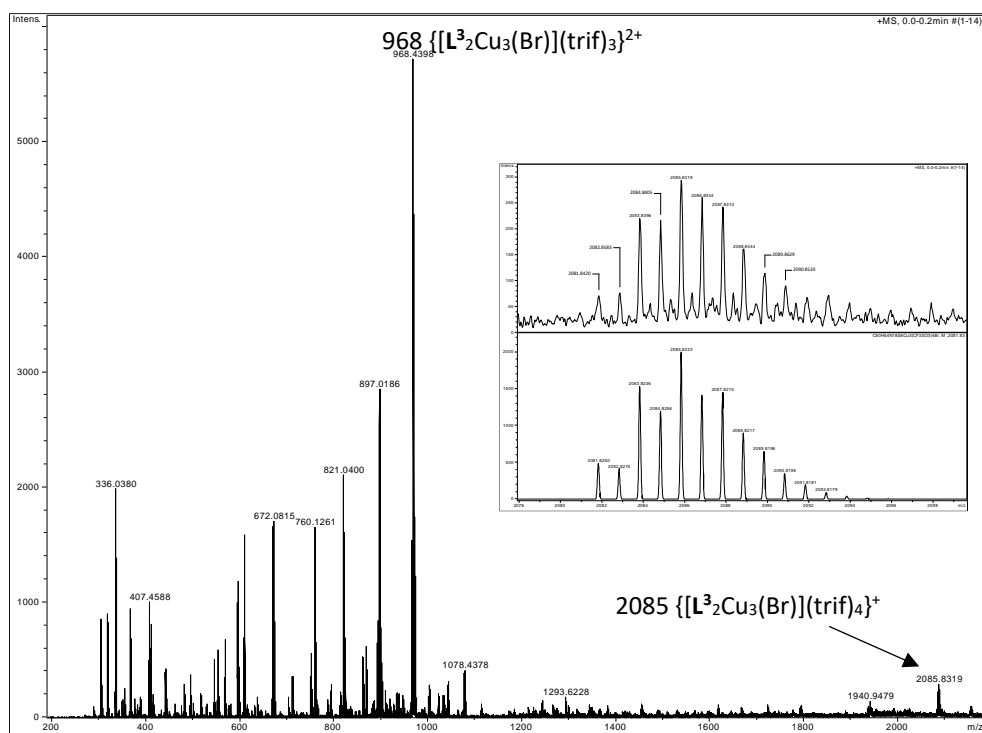


Figure 6.48. ESI-MS of $[L^3_2Cu_3(Br)](trif)_5$ showing ions at m/z 2085 and 968 corresponding to $[L^3_2Cu_3(Br)](trif)_4^+$ and $[L^3_2Cu_3(Br)](trif)_3^{2+}$ for each ligand respectively. The isotope pattern for the ion at m/z 2085 is shown inset (top observed and bottom calculated).

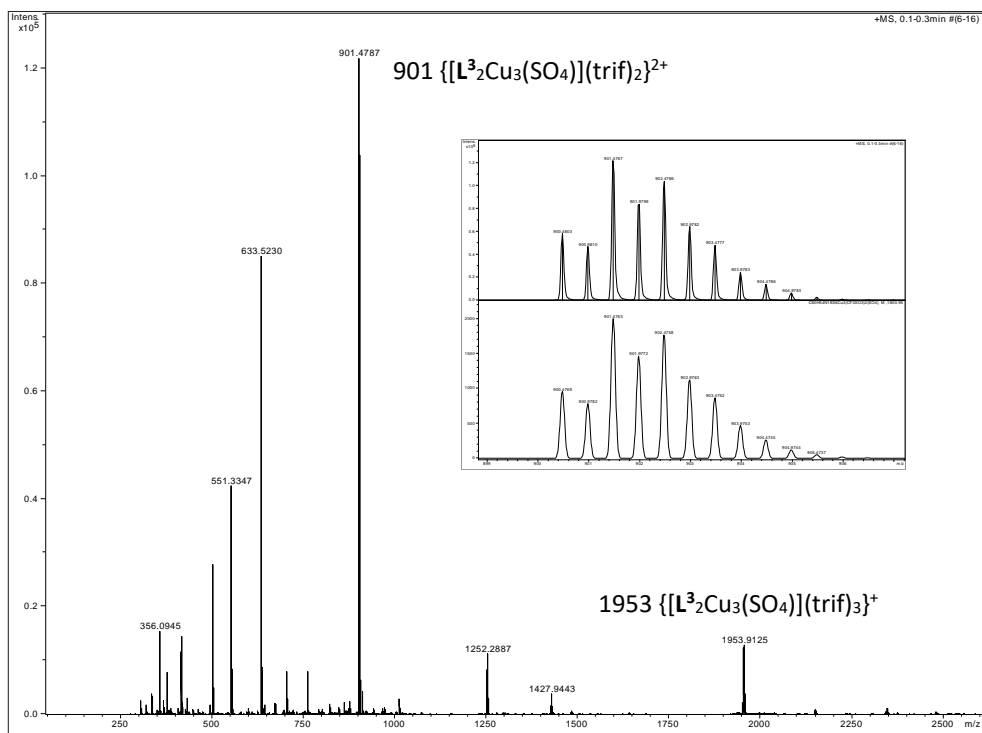
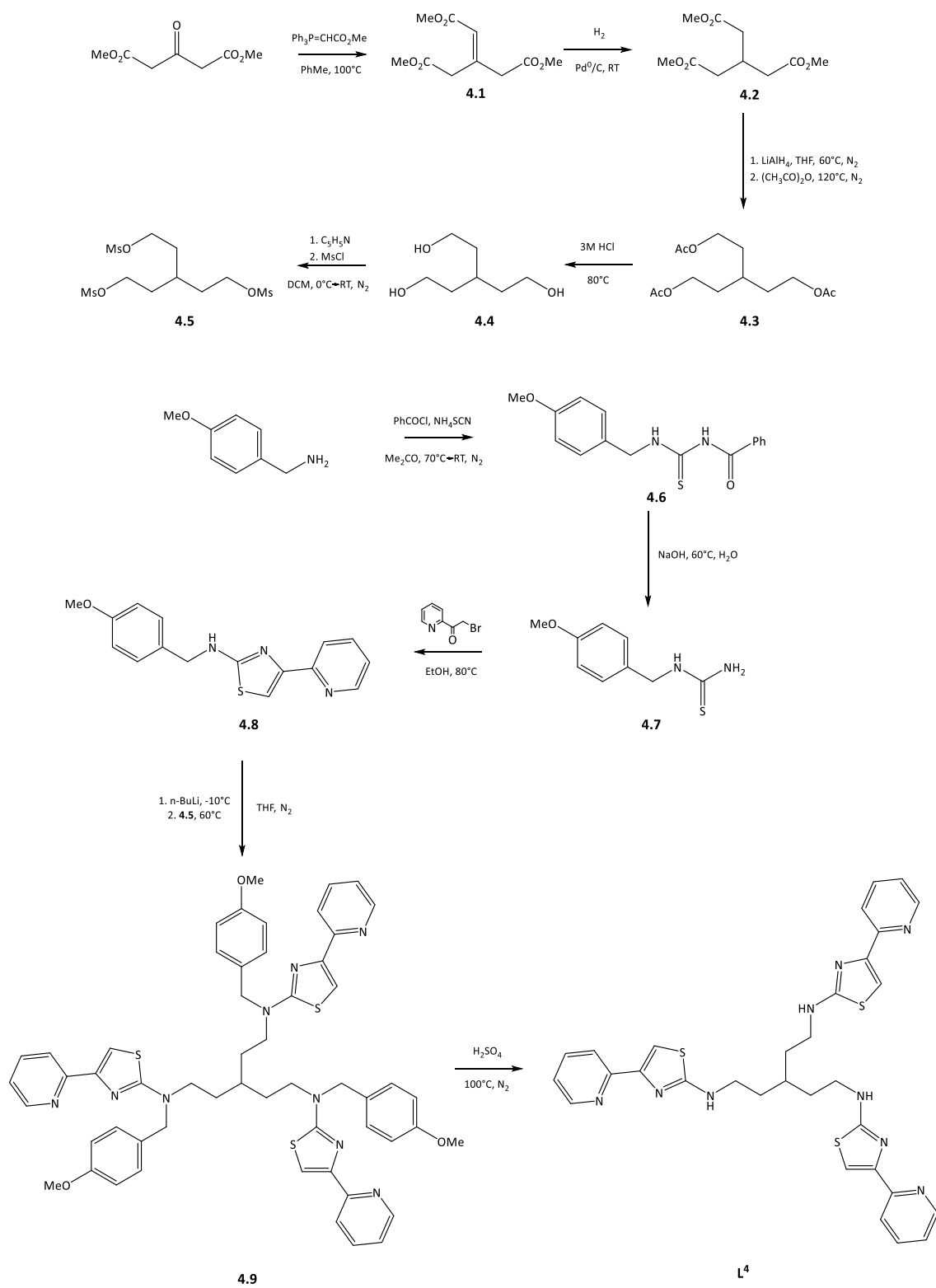


Figure 6.49. ESI-MS of $[L^3Cu_3(SO_4)](trif)_4$ showing ions at m/z 1954 and 901 corresponding to $\{[L^3]_2Cu_3(SO_4)\}(trif)_3^+$ and $\{[L^3]_2Cu_3(SO_4)\}(trif)_2^{2+}$ for each ligand respectively. The isotope pattern for the ion at m/z 901 is shown inset (top observed and bottom calculated).

6.2.5. Synthesis of ligand **L⁴**



Scheme 6.4. Synthesis of ligand **L⁴**.

Synthesis of **4.1**. To a suspension of carbomethoxymethylenetriphenylphosphorane (16.68 g, 49.89 mmol) in toluene (70 mL), dimethyl-1,3-acetonedicarboxylate (8.69 g, 49.89 mmol) was added. The solution was stirred at 100 °C for 16 hours under an atmosphere of nitrogen, during which time the colourless solution turned yellow and clarified. The solution was allowed to cool and concentrated *in vacuo*, after which the resulting orange oily residue was triturated with ethyl acetate and petroleum ether 40–60 °C (1:1, 3 × 100 mL). The washes were combined and solvent removed by rotary evaporation to leave the crude product as an orange oil. The product was purified by flash column chromatography (ethyl acetate, SiO₂, KMnO₄ stain to visualise spots) to afford the product as a yellow oil (9.91 g, 86%). ¹H NMR [400 MHz, CDCl₃]: δ (ppm) = 5.98 (s, 1H, -C=CH), 3.88 (s, 2H, -CH₂), 3.71 (s, 3H, -C=CHCOCH₃), 3.71 (s, 6H, -CH₃), 3.31 (d, 2H, *J* = 0.9 Hz, -CH₂). ¹³C NMR [100 MHz, CDCl₃]: δ (ppm) = 170.5 (C=O), 170.1 (C=O), 166.0 (C=O), 146.1 (C=CH), 122.3 (C=CH), 52.2 (CH₃), 52.1 (CH₃), 51.4 (CH₃), 43.7 (CH₂), 36.5 (CH₂). ESI-MS *m/z* 253.0687 [M + Na]⁺, observed neutral mass 230.0796, C₁₀H₁₄O₆ requires 230.0790 (error 2.30 ppm).

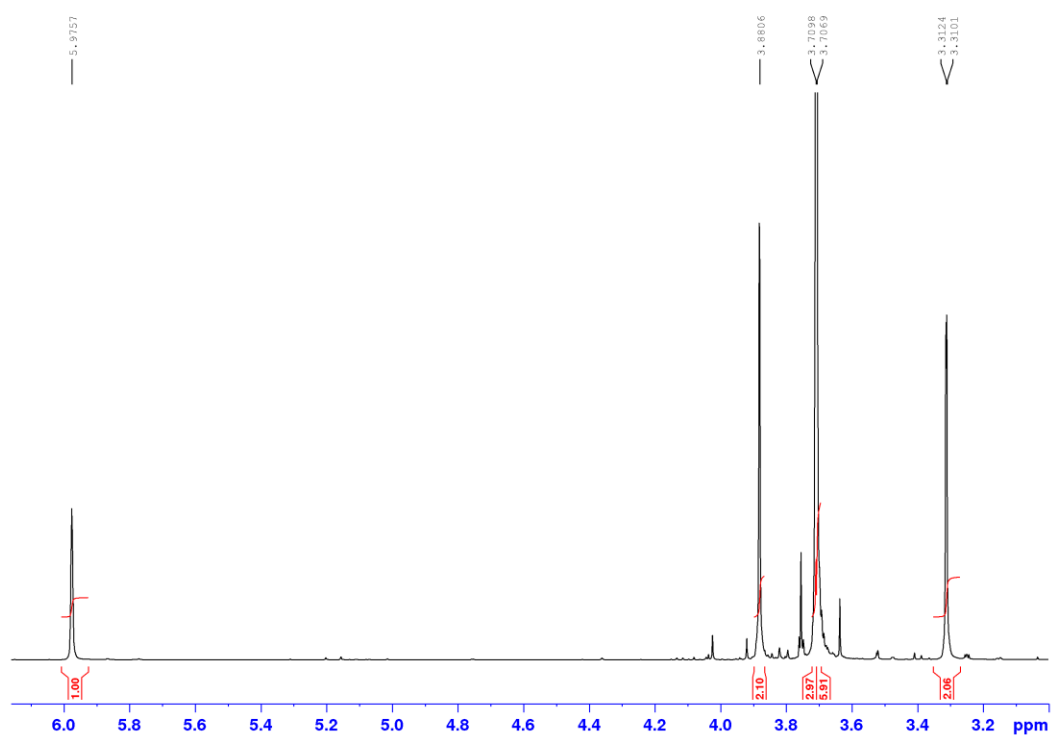


Figure 6.50. ¹H NMR Spectrum of **4.1** [400 MHz, CDCl₃].

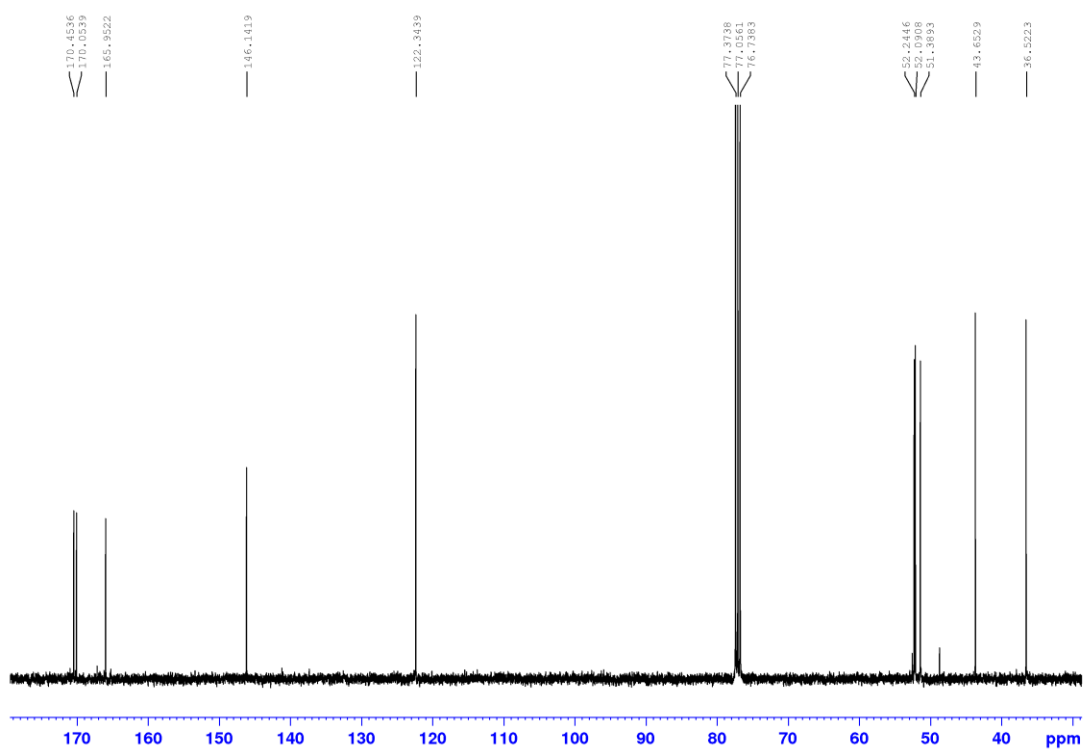


Figure 6.51. ^{13}C NMR Spectrum of **4.1** [100 MHz, CDCl_3].

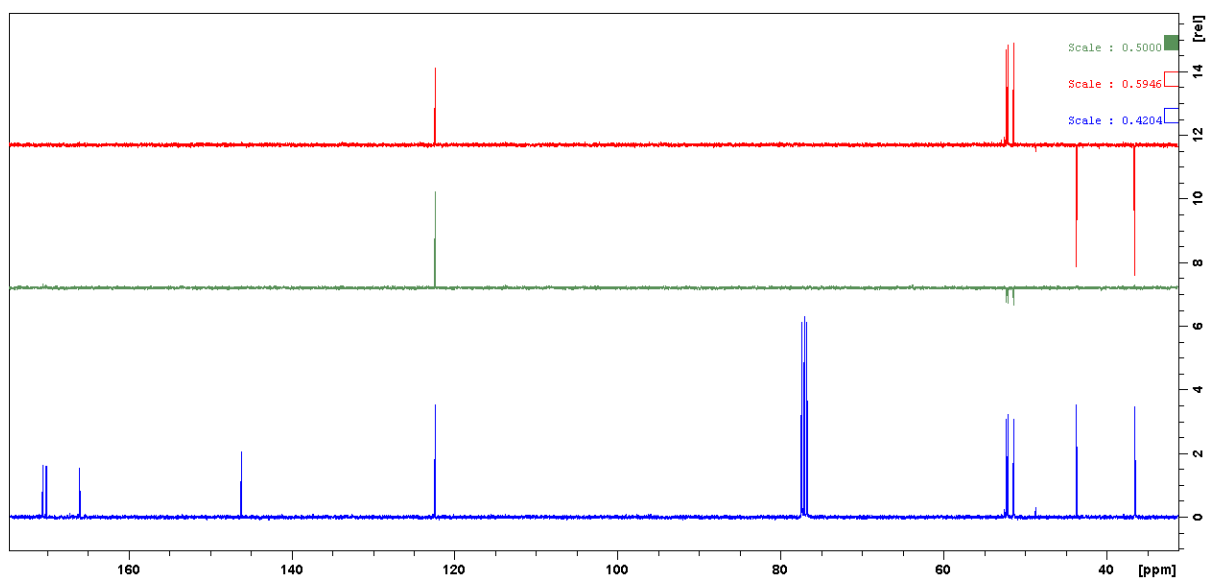


Figure 6.52. ^{13}C NMR Spectrum of **4.1** (blue) with the corresponding DEPT-135 (red) and DEPT-90 (green) NMR spectra [100 MHz, CDCl_3].

Synthesis of **4.2**. A solution of **4.1** (12.41 g, 53.90 mmol) and palladium on activated carbon (10% loading, 1.20 g) in methanol (40 mL) was stirred at room temperature under a hydrogen atmosphere for 18 hours. The solution was purged with nitrogen, filtered and the solid washed with methanol. The filtrates were combined and solvent removed by rotary evaporation to leave the product as a slightly yellow oil (11.96g, 96%). This was used without further purification. ^1H NMR [400 MHz, CDCl_3]: δ (ppm) = 3.68 (s, 9H, $-\text{CH}_3$), 2.79 (sept, 1H, $J = 6.7$, $-\text{CH}$), 2.49 (d, 6H, $J = 6.7$ Hz, $-\text{CH}_2$). ^{13}C NMR [100 MHz, CDCl_3]: δ (ppm) = 172.3 (C=O), 51.7 (CH_3), 37.5 (CH_2), 28.7 (CH). ESI-MS m/z 233.1024 [$\text{M} + \text{H}$] $^+$, observed neutral mass 232.0950, $\text{C}_{10}\text{H}_{16}\text{O}_6$ requires 232.0947 (error 1.46 ppm).

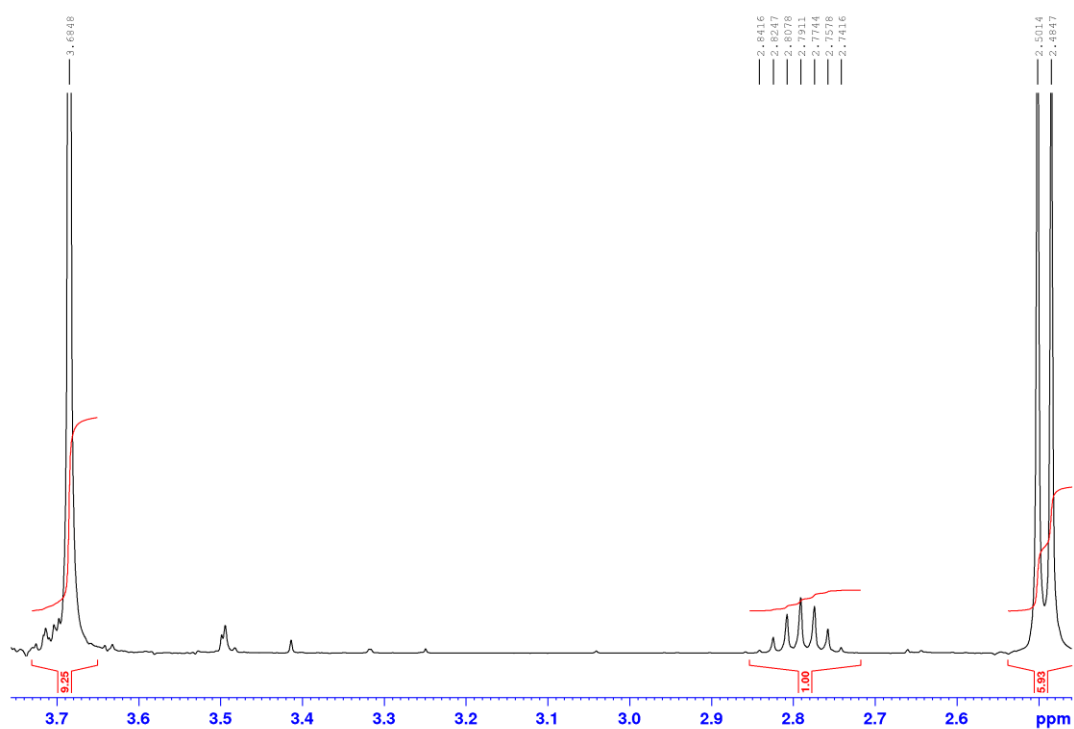


Figure 6.53. Aliphatic region of the ^1H NMR Spectrum of **4.2** [400 MHz, CDCl_3].

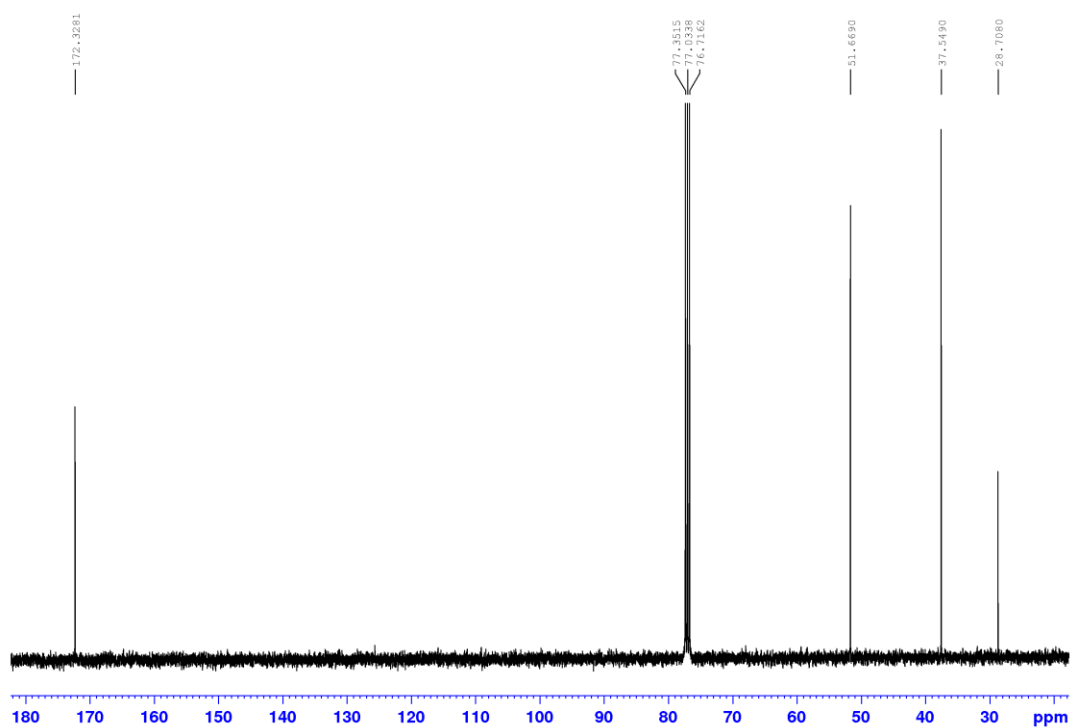


Figure 6.54. ^{13}C NMR Spectrum of **4.2** [100 MHz, CDCl_3].

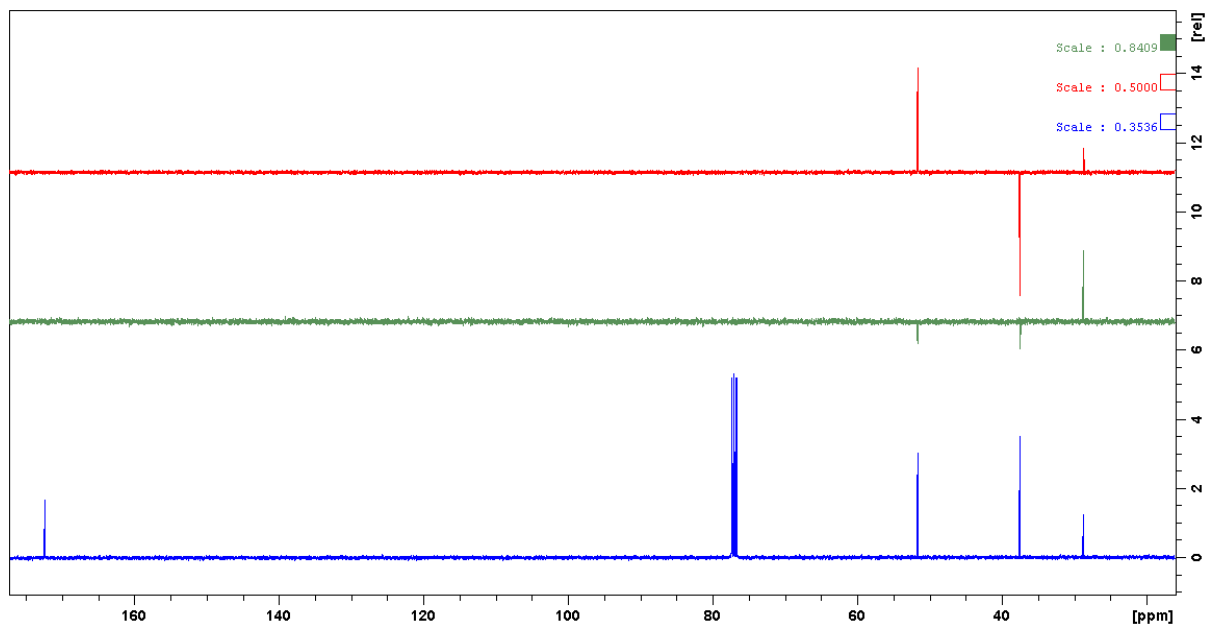


Figure 6.55. ^{13}C NMR Spectrum of **4.2** (blue) with the corresponding DEPT-135 (red) and DEPT-90 (green) NMR spectra [100 MHz, CDCl_3].

Synthesis of **4.3**. To a stirred suspension of lithium aluminium hydride (2.94 g, 77.47 mmol) in anhydrous THF (70 mL) at room temperature, **4.2** (6.00 g, 25.84 mmol) was added dropwise under an atmosphere of nitrogen, causing vigorous effervescence to occur and a yellow-grey, cloudy solution to form. The solution was stirred for 16 hours and the reaction quenched by the dropwise addition of acetic acid (40 mL), followed by acetic anhydride (20 mL). The mixture was concentrated *in vacuo*, further acetic anhydride (100 mL) was added and the solution refluxed for 16 hours. This was then cooled, filtered under vacuum and the solid washed with ethyl acetate, and the combined solvents removed by rotary evaporation. The residue was suspended in saturated aqueous potassium carbonate solution (50 mL) and extracted with ethyl acetate (3 × 100 mL). The organic layers were combined, dried over anhydrous magnesium sulfate and solvent removed by rotary evaporation to afford the product as a brown oil (6.92 g, 98%). ¹H NMR [400 MHz, CDCl₃]: δ (ppm) = 4.13 (t, 6H, *J* = 6.2 Hz, -CH₂), 2.07 (s, 9H, -CH₃), 1.73-1.65 (m, 7H, -CH & -CH₂). ¹³C NMR [100 MHz, CDCl₃]: δ (ppm) = 171.1 (C=O), 62.2 (CH₂), 32.2 (CH₂), 29.3 (CH), 21.0 (CH₃). ESI-MS *m/z* 275.4960 [M + H]⁺, observed neutral mass 274.1420, C₁₃H₂₂O₆ requires 274.1416 (error 1.18 ppm).

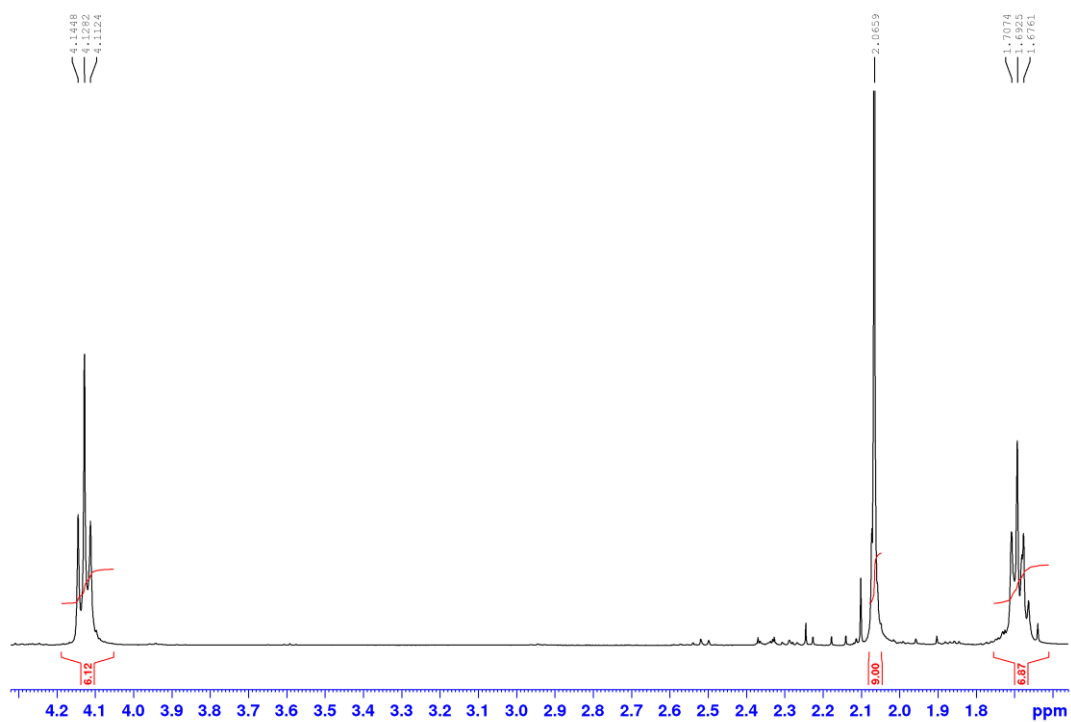


Figure 6.56. Aliphatic region of the ^1H NMR Spectrum of **4.3** [400 MHz, CDCl_3].

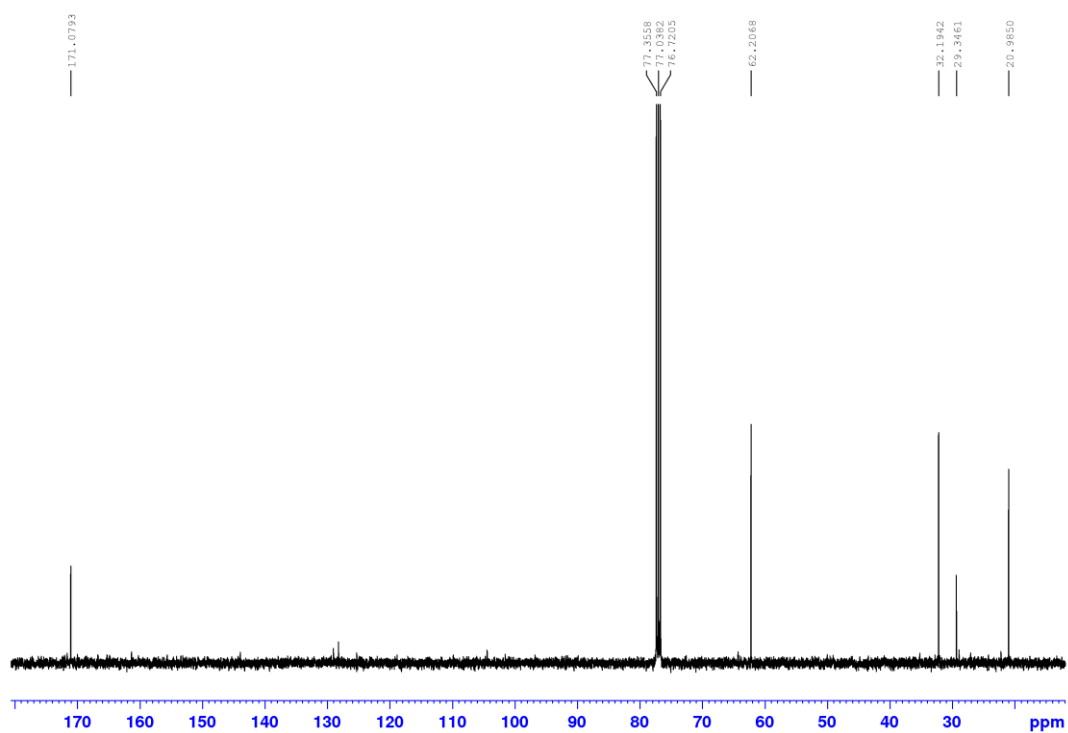


Figure 6.57. ^{13}C NMR Spectrum of **4.3** [400 MHz, CDCl_3].

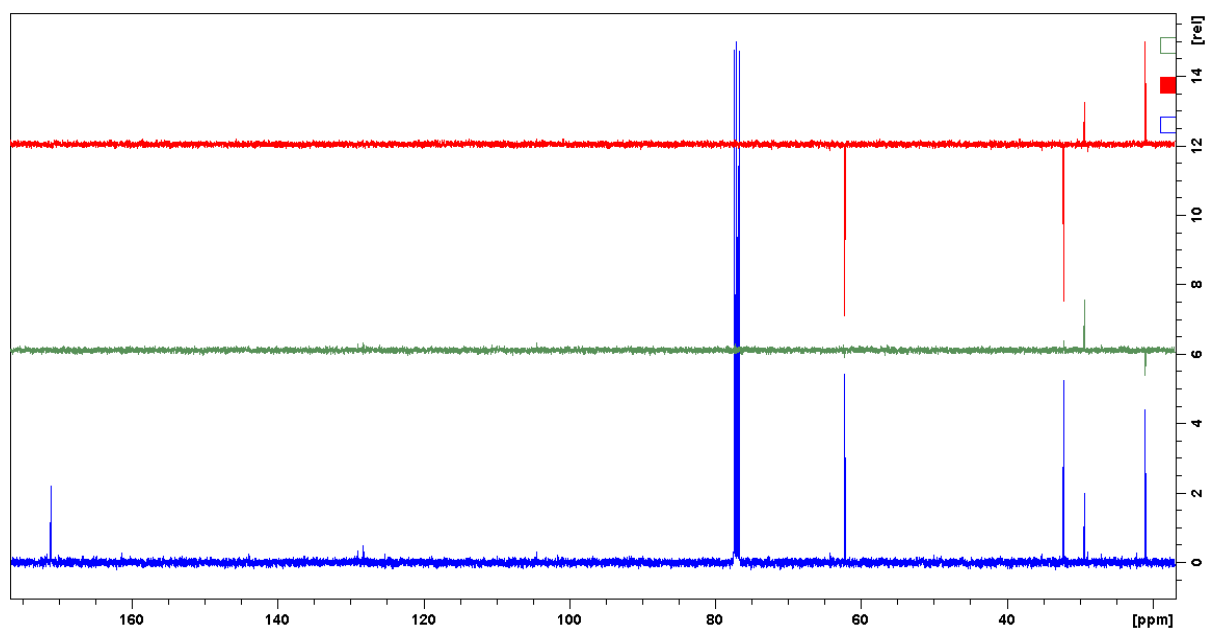


Figure 6.58. ^{13}C NMR Spectrum of **4.3** (blue) with the corresponding DEPT-135 (red) and DEPT-90 (green) NMR spectra [100 MHz, CDCl_3].

Synthesis of **4.4**. A solution of **4.3** (4.75 g, 17.32 mmol) in 3 M hydrochloric acid (30 mL) was stirred at 70 °C for 48 hours. The reaction was allowed to cool and the water and acid were carefully removed by rotary evaporation, using toluene to azeotropically remove any remaining water, affording the product as a brown oil (2.40 g, 94%). This was used without further purification. ^1H NMR [300 MHz, CDCl_3]: δ (ppm) = 4.89 (br s, 3H, -OH), 3.75 (t, 6H, $J = 5.6$, - CH_2), 2.17 (sept, 1H, $J = 7.0$, -CH), 1.49 (dt, 6H, $J = 5.6, 6.5$ Hz, - CH_2). ^{13}C NMR [100 MHz, CDCl_3]: δ (ppm) = 57.7 (CH_2), 33.8 (CH_2), 21.9 (CH). ESI-MS m/z 171.0994 [$\text{M} + \text{Na}$] $^+$, observed neutral mass 148.1099, $\text{C}_7\text{H}_{16}\text{O}_3$ requires 148.1099 (error 0.02 ppm).

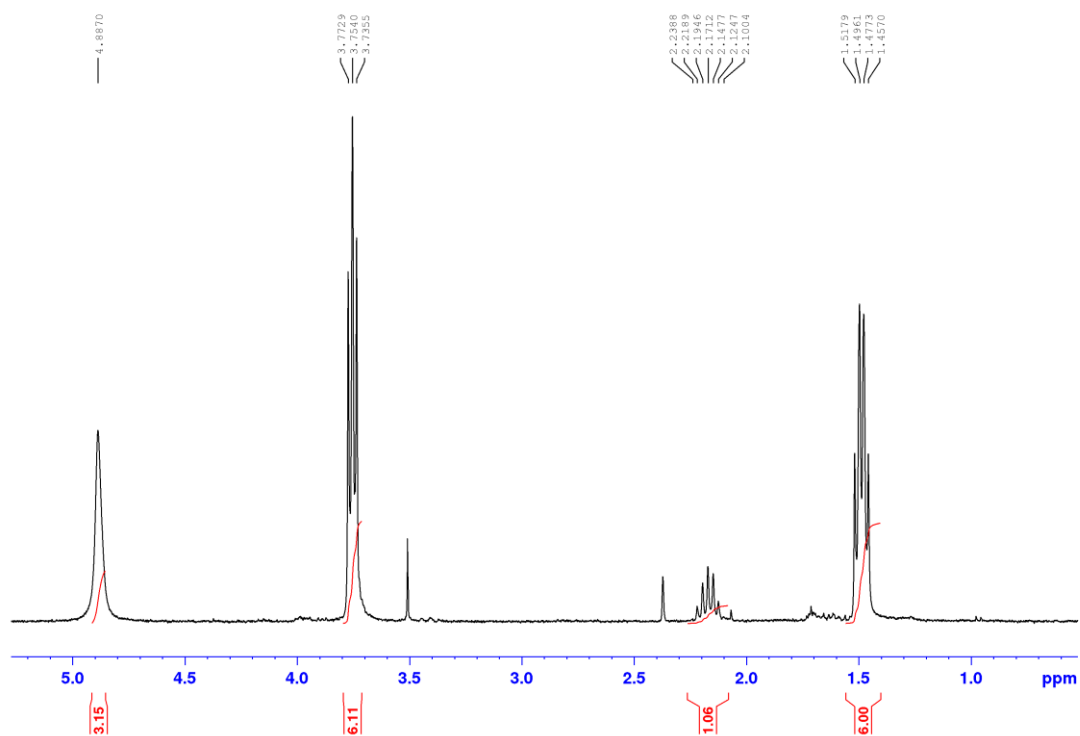


Figure 6.59. Aliphatic region of the ^1H NMR Spectrum of **4.4** [300 MHz, CDCl_3].

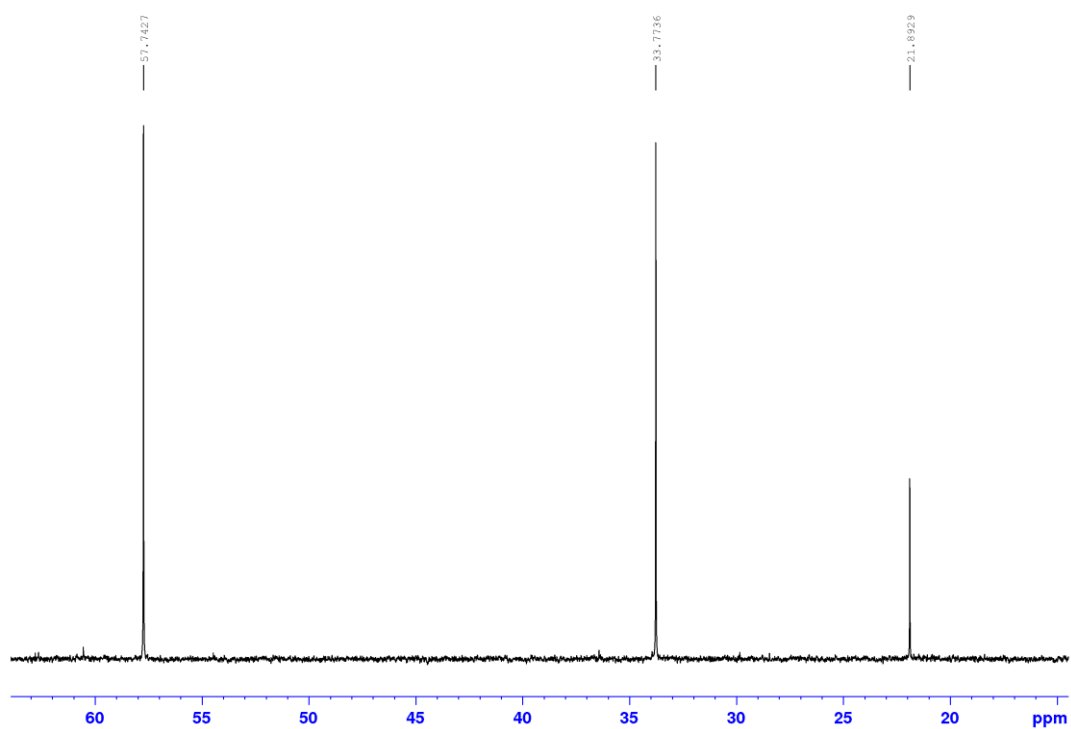


Figure 6.60. Aliphatic region of the ^{13}C NMR Spectrum of **4.4** [100 MHz, CDCl_3].

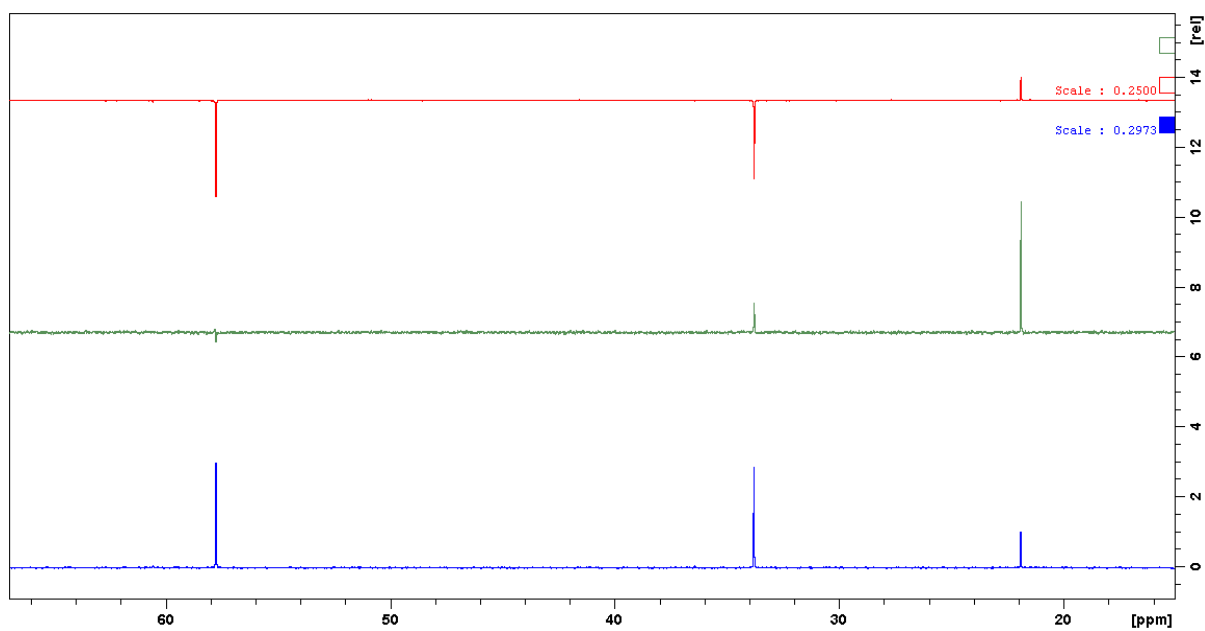


Figure 6.61. Aliphatic region of the ^{13}C NMR Spectrum of **4.4** (blue) with the corresponding DEPT-135 (red) and DEPT-90 (green) NMR spectra [100 MHz, CDCl_3].

Synthesis of **4.5**. To an ice-cooled solution of **4.4** (2.56 g, 17.27 mmol) in anhydrous DCM (100 mL), methanesulfonyl chloride (9.92 g, 86.60 mmol) was added dropwise under an atmosphere of nitrogen, followed by pyridine (5.47 g, 69.15 mmol). The solution was stirred at room temperature for 48 hours, during which the immiscible brown oily starting material dissolved, and the colour changed to an orange-brown. The reaction was diluted with DCM (100 mL) and washed with 5 M HCl (2 × 50 mL). The organic layers were combined, dried over anhydrous magnesium sulfate and solvent removed by rotary evaporation to leave the crude product as a brown oil. The product was purified by column chromatography (Al₂O₃, DCM – 1% MeOH in DCM; *N.B.* small fractions were collected ~ 20 mL and NMR used to assess the purity) to give the pure mesylated product as a slightly yellow oil that crystallised on cooling (3.65 g, 55%). ¹H NMR [400 MHz, CDCl₃]: δ (ppm) = 4.23 (t, 6H, *J* = 6.2, -CH₂-CH₂O), 2.96 (s, 9H, -CH₃), 1.89 (sept, 1H, *J* = 6.4, -CH), 1.75 (q, 6H, *J* = 6.3 Hz, -CH₂CH₂O). ¹³C NMR [100 MHz, CDCl₃]: δ (ppm) = 67.1 (CH₂), 37.5 (CH₃), 32.7 (CH₂), 28.0 (CH). ESI-MS *m/z* 405.0307 [M + Na]⁺, observed neutral mass 382.0417, C₁₀H₂₂O₃S₃ requires 382.0417 (error 2.46 ppm).

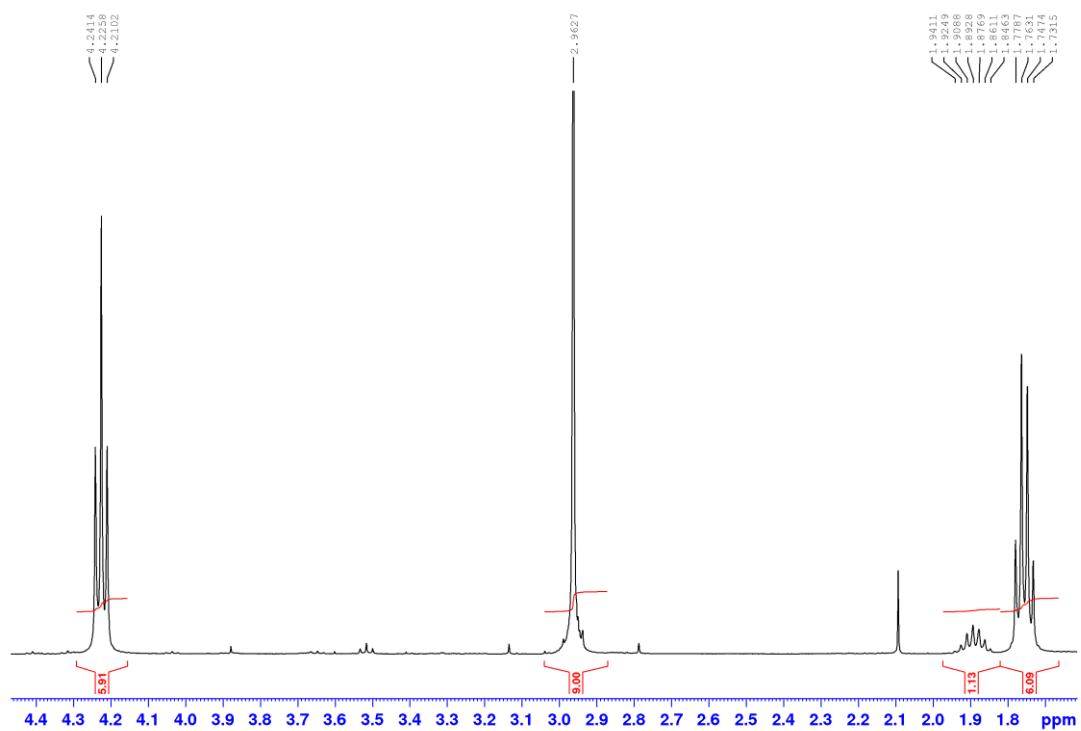


Figure 6.62. Aliphatic region of the ^1H NMR Spectrum of **4.5** [400 MHz, CDCl_3].

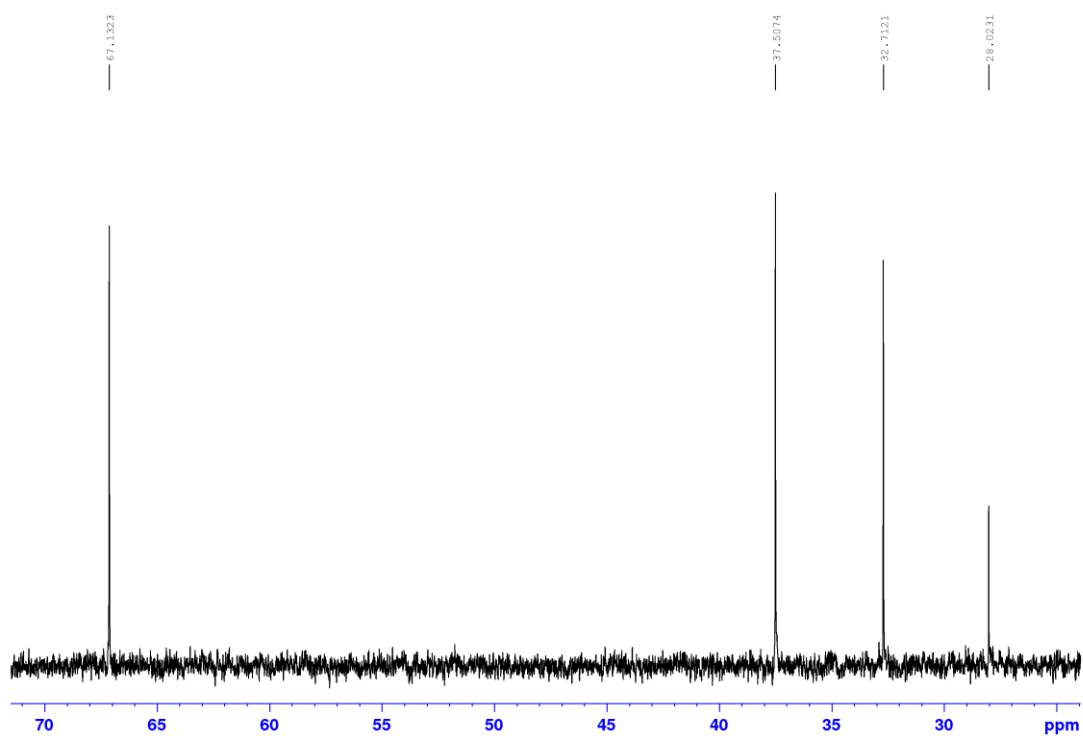


Figure 6.63. Aliphatic region of the ^{13}C NMR Spectrum of **4.5** [100 MHz, CDCl_3].

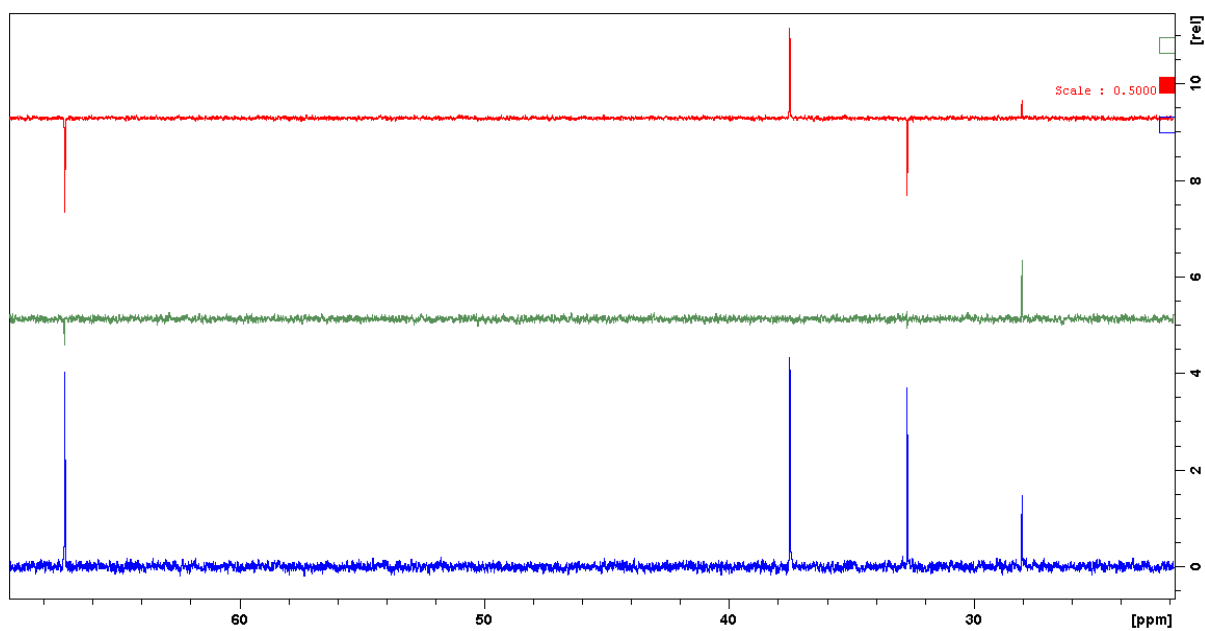


Figure 6.64. Aliphatic region of the ^{13}C NMR Spectrum of **4.5** (blue) with the corresponding DEPT-135 (red) and DEPT-90 (green) NMR spectra [100 MHz, CDCl_3].

Synthesis of **4.6**. To a solution of ammonium thiocyanate (3.80 g, 49.92 mmol) in dry acetone (50 mL), benzoyl chloride (6.44 g, 45.81 mmol) was added slowly, causing a white precipitate to form. This solution was refluxed for 10 minutes, during which time the solution turned a pale yellow colour. 4-Methoxybenzylamine (5.71 g, 41.62 mmol) was slowly added under an atmosphere of nitrogen at such a rate as to cause a gentle reflux. The reaction was stirred for 1 hour at room temperature after which the solution was slowly poured onto water (150 mL) while stirring, causing the product to form as a heavy yellow precipitate. The solid was isolated by vacuum filtration and washed with water (3 × 5 mL), allowed to dry and recrystallised from isopropyl alcohol. The crystals were isolated by vacuum filtration and washed with cold isopropyl alcohol to afford the product as pale yellow needles (6.92 g, 55%). ¹H NMR [400 MHz, CDCl₃]: δ (ppm) = 10.95 (br s, 1H, -NH), 9.03 (br s, 1H, -CH₂NH), 7.84 (m, 2H, C₆H₅), 7.65 (tt, 1H, *J* = 7.4, 1.7, C₆H₅), 7.53 (t, 2H, *J* = 7.4, C₆H₅), 7.35 (m, 2H, -CH₂Ph-*H*), 6.93 (m, 2H, CH₂Ph-*H*), 4.86 (d, 2H, 5.2 Hz, CH₂), 3.83 (s, 3H, CH₃). ¹³C NMR [100 MHz, CDCl₃]: δ (ppm) = 179.7 (C=S), 166.7 (C=O), 159.4 (C), 133.6 (CH), 131.7 (C), 129.4 (CH), 129.2 (CH), 128.2 (C), 127.4 (CH), 114.3 (CH), 55.3 (CH₃), 49.4 (CH₂). ESI-MS *m/z* 301.1008 [M + H]⁺, observed neutral mass 300.0935, C₁₆H₁₆N₂O₂S requires 300.0932 (error 1.00 ppm).

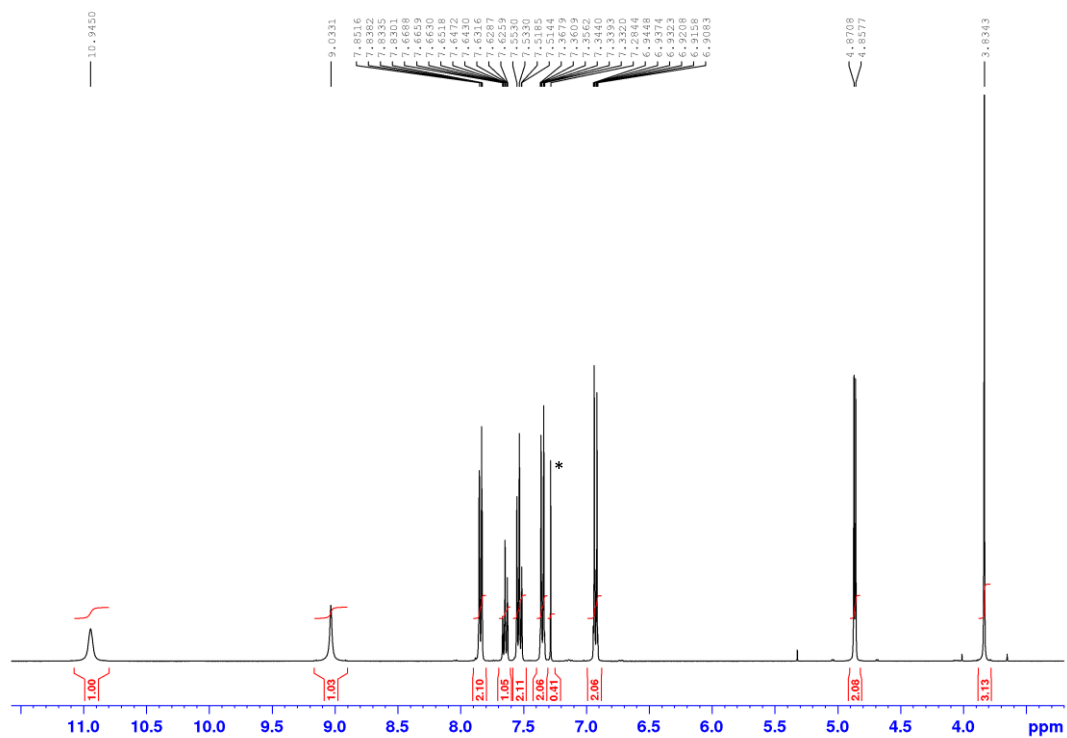


Figure 6.65. ^1H NMR Spectrum of **4.6** [400 MHz, CDCl_3]. * CHCl_3 impurity.

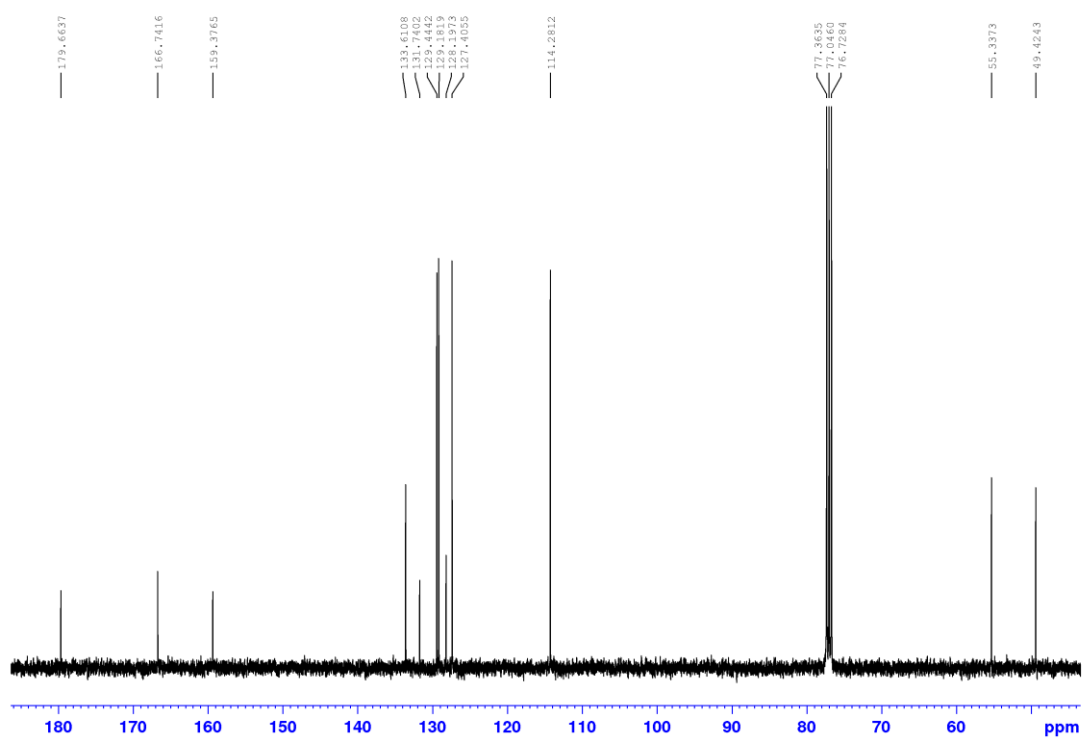


Figure 6.66. ^{13}C NMR Spectrum of **4.6** [100 MHz, CDCl_3].

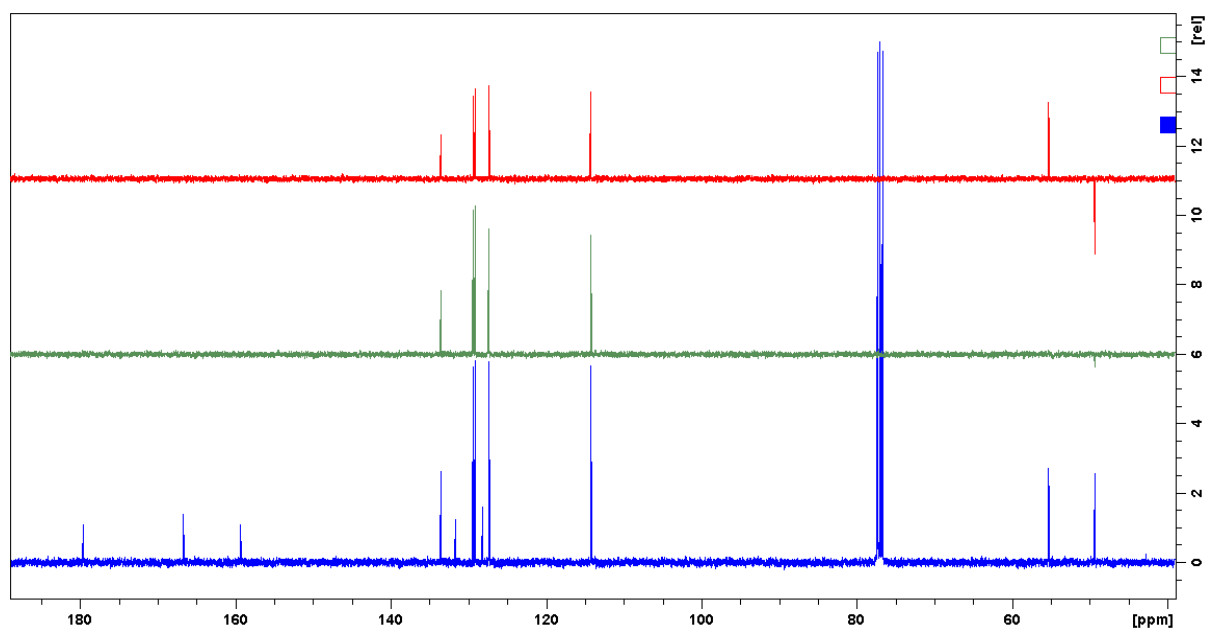


Figure 6.67. ^{13}C NMR Spectrum of **4.6** (blue) with the corresponding DEPT-135 (red) and DEPT-90 (green) NMR spectra [100 MHz, CDCl_3].

Synthesis of **4.7**. To a suspension of **4.6** (3.82 g, 12.73 mmol) in water (30 mL), sodium hydroxide (1.91 g, 47.75 mmol) was added. The reaction was stirred at 60 °C for 1 hour, during which time the solution clarified and product precipitated as a heavy white solid. The precipitate was isolated by vacuum filtration and washed with water (2 × 5 mL) to afford the product as a white crystalline solid (2.27 g, 91%). ¹H NMR [400 MHz, (CD₃)₂SO]: δ (ppm) = 8.21–7.78 (br m, 1H, -NH), 7.73–6.63 (m, 6H, -C₆H₄ and -NH₂), 4.60–4.11 (br m, 2H, CH₂), 3.73 (s, 3H, OCH₃). ¹³C NMR [100 MHz, (CD₃)₂SO]: δ (ppm) = 183.6 (C=S), 158.8 (C), 131.6 (C), 129.3 (CH), 114.1 (CH), 55.5 (CH₃), 47.4 (CH₂). ESI-MS *m/z* 197.0742 [M + H]⁺, observed neutral mass 196.0670, C₉H₁₂N₂SO requires 196.0670 (error 0.16 ppm).

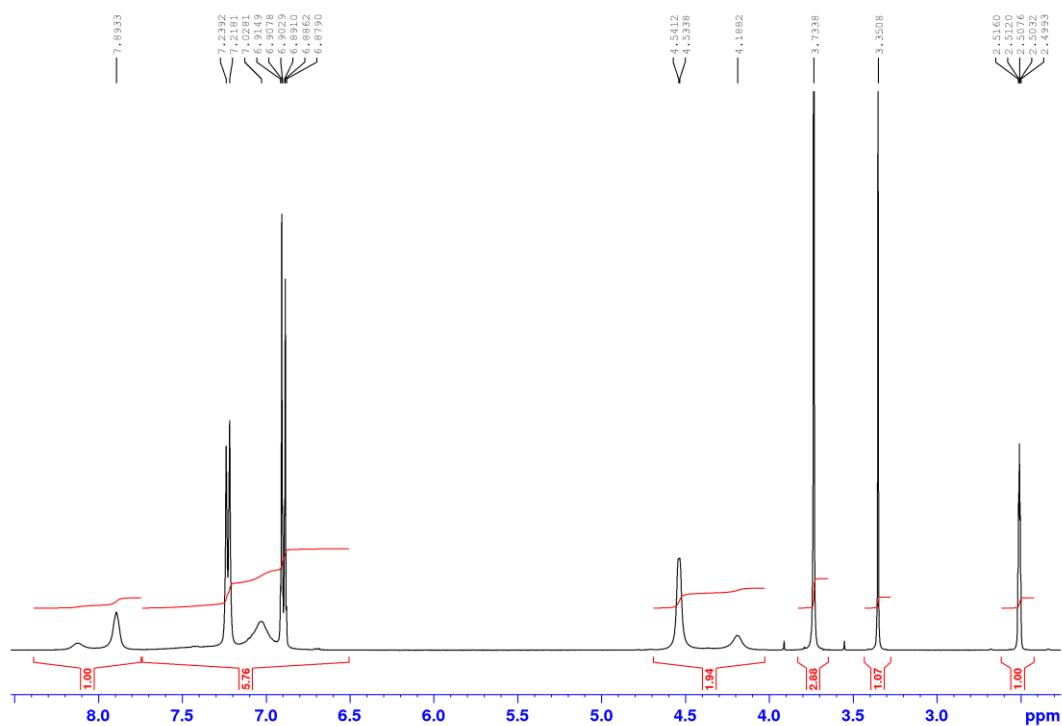


Figure 6.68. ¹H NMR Spectrum of **4.7** [400 MHz, (CD₃)₂SO].

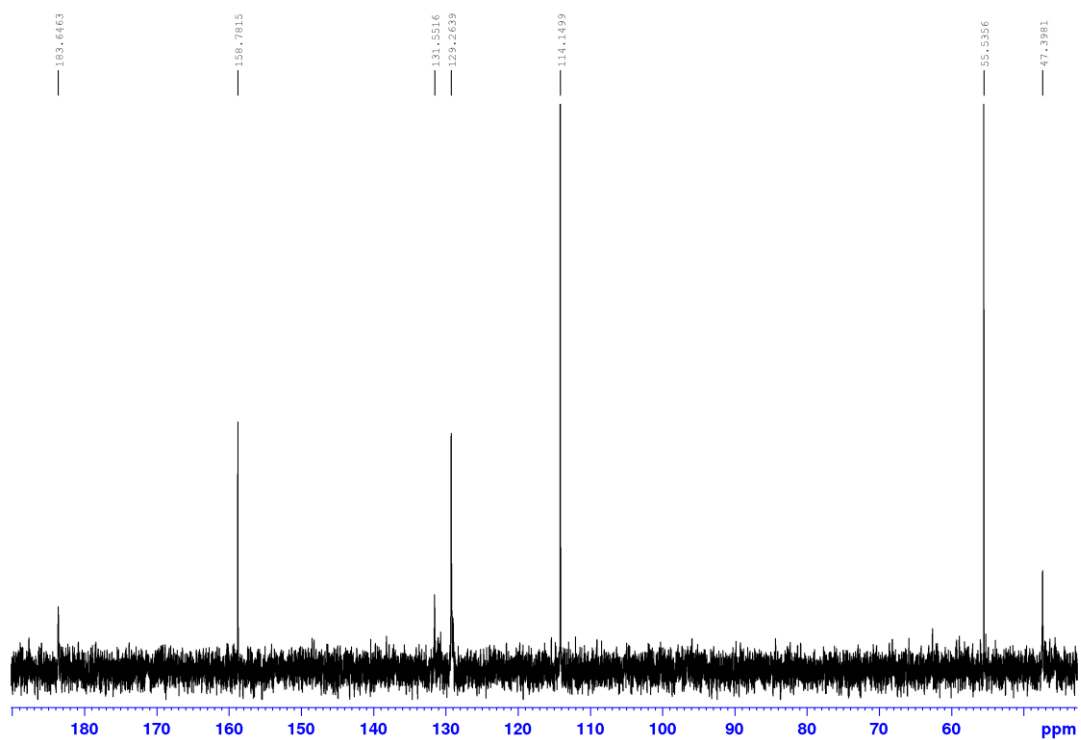


Figure 6.69. ^{13}C NMR Spectrum of **4.7** [100 MHz, $(\text{CD}_3)_2\text{SO}$].

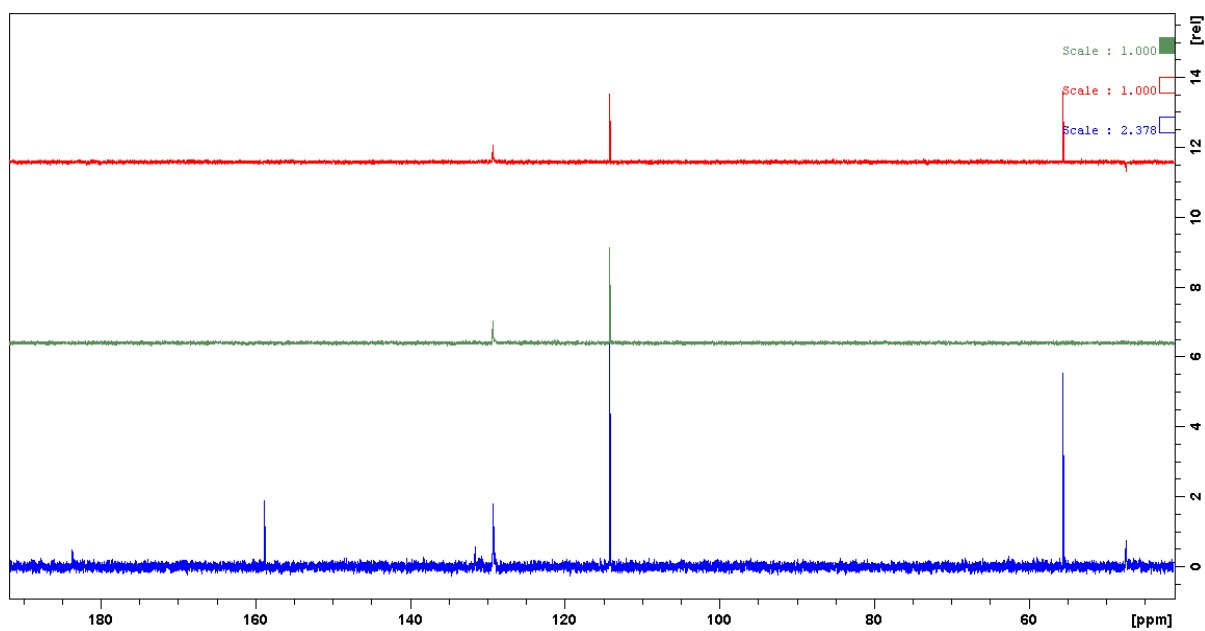


Figure 6.70. ^{13}C NMR Spectrum of **4.7** (blue) with the corresponding DEPT-135 (red) and DEPT-90 (green) NMR spectra [100 MHz, $(\text{CD}_3)_2\text{SO}$].

Synthesis of **4.8**. To a solution of **4.7** (1.40 g, 7.14 mmol) in ethanol (25 mL), α -bromo-2-acetylpyridine (1.71 g, 8.55 mmol) was added. The solution was stirred at 80 °C for 16 hours, during which time the solution turned yellow-brown and clarified. The reaction was allowed to cool and concentrated *in vacuo* to leave a light brown residue, which was suspended in DCM (70 mL) and washed with saturated aqueous sodium bicarbonate (30 mL), causing a colour change in the organic layer from yellow-brown to light orange. The organic layer was collected, dried over anhydrous magnesium sulfate, filtered and solvent removed by rotary evaporation to afford the crude product as a slightly yellow-orange oil. The product was purified by column chromatography (1% MeOH in DCM, Al₂O₃) to afford the pure product as a beige solid (1.70 g, 80%). ¹H NMR [400 MHz, CDCl₃]: δ (ppm) = 8.51 (ddd, 1H, *J* = 4.8, 1.7, 0.8, Py), 7.86 (dt, 1H, *J* = 8.0, 1.0, Py), 7.63 (td, 1H, *J* = 7.6, 1.8, Py), 7.26 (m, 2H, -CH₂Ph), 7.22 (s, 1H, tz), 7.10 (ddd, 1H, *J* = 7.5, 4.8, 1.2, Py), 6.82 (m, 2H, -CH₂Ph), 5.44 (s, 1H, -NH), 4.39 (d, 2H, *J* = 5.4 Hz, -CH₂), 3.74 (s, 3H, -CH₃). ¹³C NMR [100 MHz, CDCl₃]: δ (ppm) = 169.4 (C), 159.2 (C), 152.9 (C), 151.2 (CH), 149.4 (C), 136.8 (CH), 129.6 (CH), 129.0 (CH), 122.3 (CH), 120.8 (CH), 114.1 (CH), 105.5 (CH), 55.3 (CH₃), 49.3 (CH₂). ESI-MS *m/z* 298.1007 [M + H]⁺, observed neutral mass 297.0934, C₁₆H₁₅N₃SO requires 297.0936 (error 0.67 ppm).

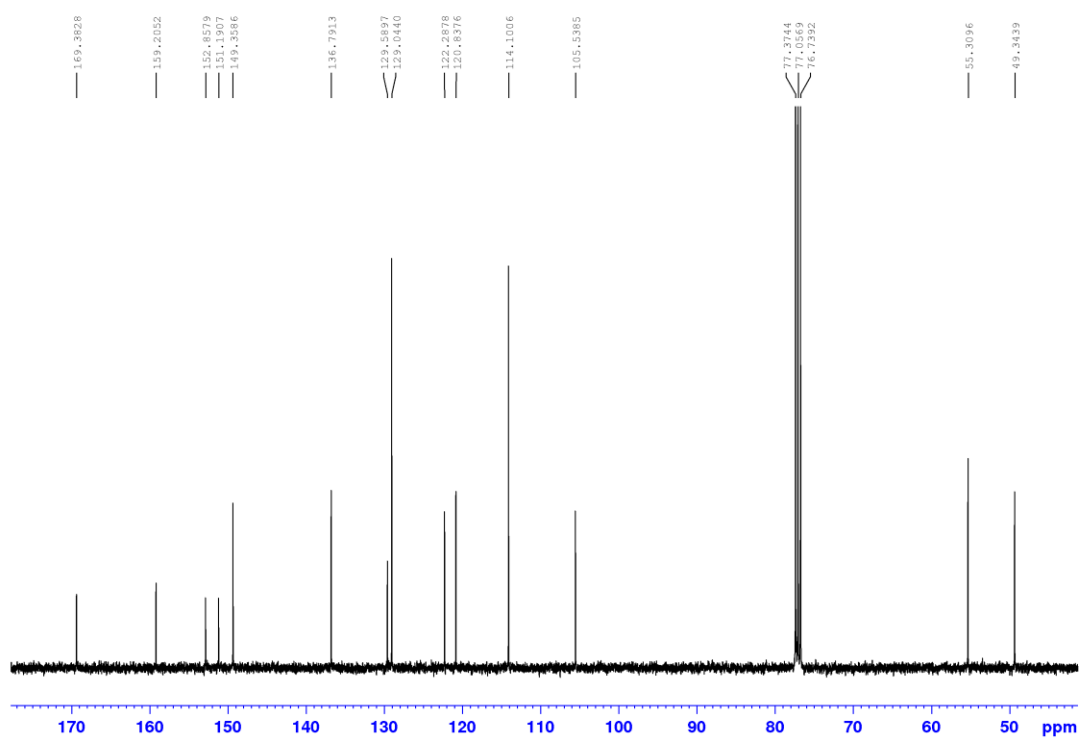


Figure 6.72. ^{13}C NMR Spectrum of **4.8** [100 MHz, CDCl_3].

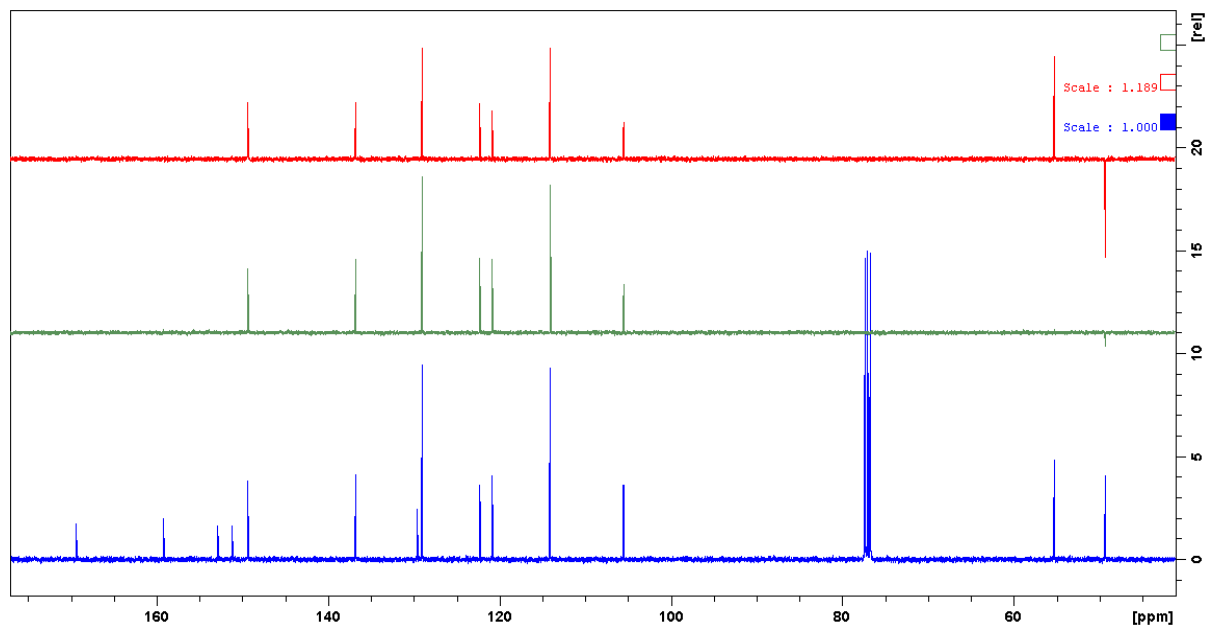


Figure 6.73. ^{13}C NMR Spectrum of **4.8** (blue) with the corresponding DEPT-135 (red) and DEPT-90 (green) NMR spectra [100 MHz, CDCl_3].

Synthesis of **4.9**. To an ice-cooled solution of **4.8** (816 mg, 2.75 mmol) in anhydrous THF (30 mL) under an atmosphere of nitrogen, n-Butyllithium (1.6 M in hexanes, 1.71 mL) was added dropwise causing the solution to turn yellow. The reaction was stirred for 30 minutes, after which **5.5** [300 mg, 0.78 mmol) was slowly added. This was then stirred for 1 hour and then heated to reflux and stirred for 18 hours, by which time TLC (1% MeOH in DCM, Al₂O₃) showed the absence of starting material. The solution was quenched by the dropwise addition of methanol and solvent removed by rotary evaporation. The residue was suspended in water (20 mL) and extracted into DCM (3 × 50 mL). The organic layers were combined, dried over anhydrous magnesium sulfate, and solvent removed by rotary evaporation. The product was purified by column chromatography (1% MeOH in DCM, Al₂O₃) to afford the product as a slightly yellow solid (520 mg, 68%). ¹H NMR [400 MHz, CDCl₃]: δ (ppm) = 8.57 (ddd, 3H, *J* = 4.8, 1.7, 0.8, Py), 8.01 (dt, 3H, *J* = 8.0, 0.9, Py), 7.62 (td, 3H, *J* = 7.6, 1.8, Py), 7.31 (s, 3H, tz), 7.21 (m, 6H, -CH₂Ph), 7.13 (ddd, 3H, *J* = 7.5, 4.8, 1.2, Py), 6.82 (m, 6H, -CH₂Ph), 4.62 (s, 6H, -CH₂Ph), 3.76 (s, 9H, CH₃), 3.49 (t, 6H, *J* = 7.6, -CH₂CH₂N), 1.72 (m, 6H, -CH₂CH₂N), 1.41 (sept, 1H, *J* = 6.2 Hz, -CH). ¹³C NMR [100 MHz, CDCl₃]: δ (ppm) = 170.1 (C), 159.1 (C), 153.1 (C), 151.5 (C), 149.2 (CH), 136.8 (CH), 129.0 (CH), 128.9 (C), 122.2 (CH), 121.1 (CH), 114.0 (CH), 104.8 (CH), 55.2 (CH₃), 54.0 (CH₂), 48.4 (CH₂), 31.4 (CH), 30.4 (CH₂). ESI-MS *m/z* 986.3664 [M + H]⁺, observed neutral mass 985.3590 C₅₅H₅₅N₉S₃O₃ requires 985.3590 (error 0.00 ppm).

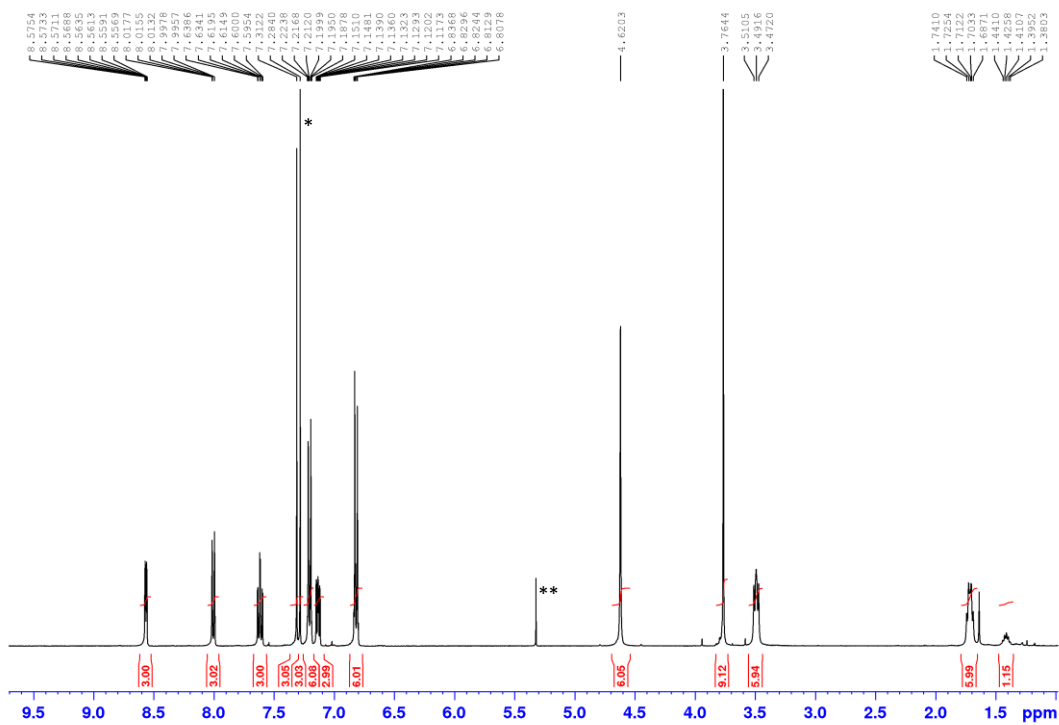


Figure 6.74. ^1H NMR Spectrum of **4.9** [400 MHz, CDCl_3]. * CHCl_3 impurity. ** CH_2Cl_2 impurity.

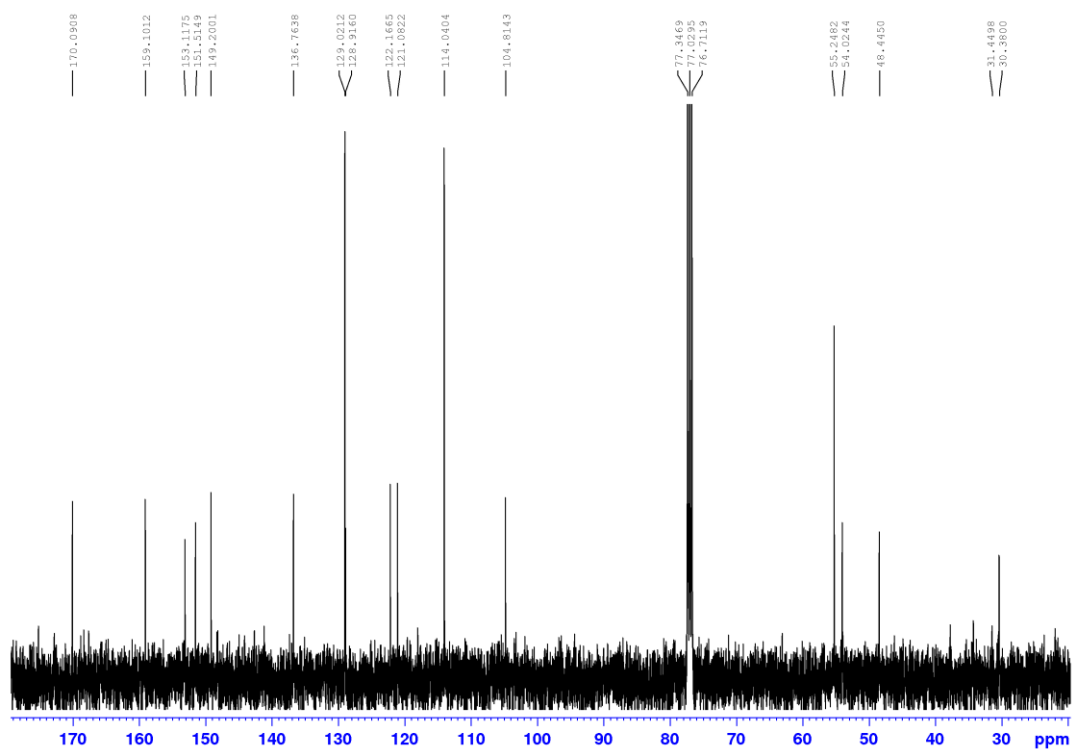


Figure 6.75. ^{13}C NMR Spectrum of **4.9** [100 MHz, CDCl_3].

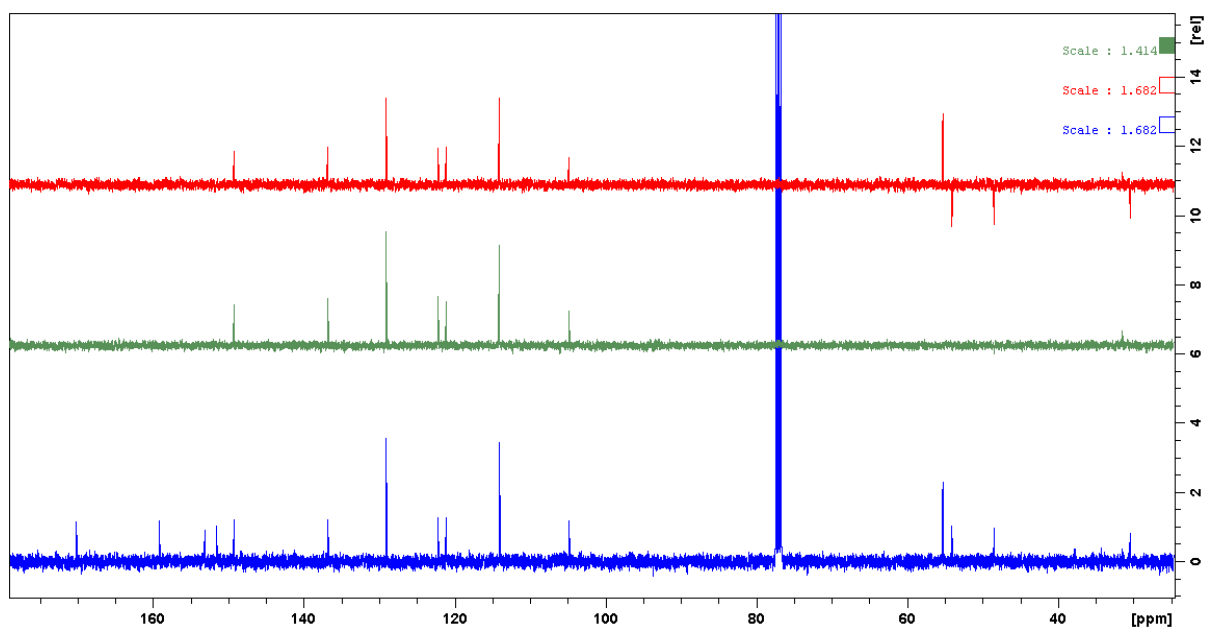


Figure 6.76. ^{13}C NMR Spectrum of **4.9** (blue) with the corresponding DEPT-135 (red) and DEPT-90 (green) NMR spectra [100 MHz, CDCl_3].

Synthesis of N^1,N^5 -bis(4-(pyridin-2-yl)thiazol-2-yl)-3-(2-((4-(pyridin-2-yl)thiazol-2-yl)amino)ethyl)-pentane-1,5-diamine (ligand L^4). To a flask charged with the methoxybenzyl-protected ligand **4.9** (520 mg, 0.53 mmol) was added sulfuric acid (8 mL) under an atmosphere of nitrogen, which caused an immediate colour change to dark magenta. The solution was heated to 100 °C for 4 hours, cooled to ambient temperature and poured onto water (20 mL), which caused a black precipitate to form and yellow solution. This was made strongly basic by the addition of concentrated sodium hydroxide (pH ~ 14), which caused a highly exothermic reaction and the solution to turn brown. After cooling to ambient temperature the product was extracted with DCM (3 × 50 mL), the organic layers were combined, dried over anhydrous magnesium sulfate, filtered and solvent removed by rotary evaporation to afford the product as a pale orange solid (170 mg, 51%). ^1H NMR [400 MHz, CDCl_3]: δ (ppm) = 8.49 (dd, 3H, $J = 4.7, 0.7$, Py), 7.82 (d, 3H, $J = 7.9$, Py), 7.59 (td, 3H, $J = 7.7, 1.8$, Py), 7.16 (s, 3H, tz), 7.06 (ddd, 3H, $J = 7.4, 4.8, 1.0$, Py), 5.88 (br s, 3H, -NH), 3.23 (br s, 6H, $-\text{CH}_2\text{CH}_2\text{NH}$), 1.55 (t, 6H, $J = 5.32$ Hz, $-\text{CH}_2\text{CH}_2\text{NH}$), 0.85–0.75 (m, 1H, -CH). ^{13}C NMR [100 MHz, CDCl_3]: δ (ppm) = 169.6 (C), 152.8 (C), 151.1 (C), 149.4 (CH), 136.9 (CH), 122.3 (CH), 120.9 (CH), 105.3 (CH), 43.3 (CH_2), 33.0 (CH_2), 30.4 (CH). ESI-MS m/z 626.1935 $[\text{M} + \text{H}]^+$, observed neutral mass 625.1863, $\text{C}_{31}\text{H}_{31}\text{N}_9\text{S}_3$ requires 625.1865 (error 0.32 ppm).

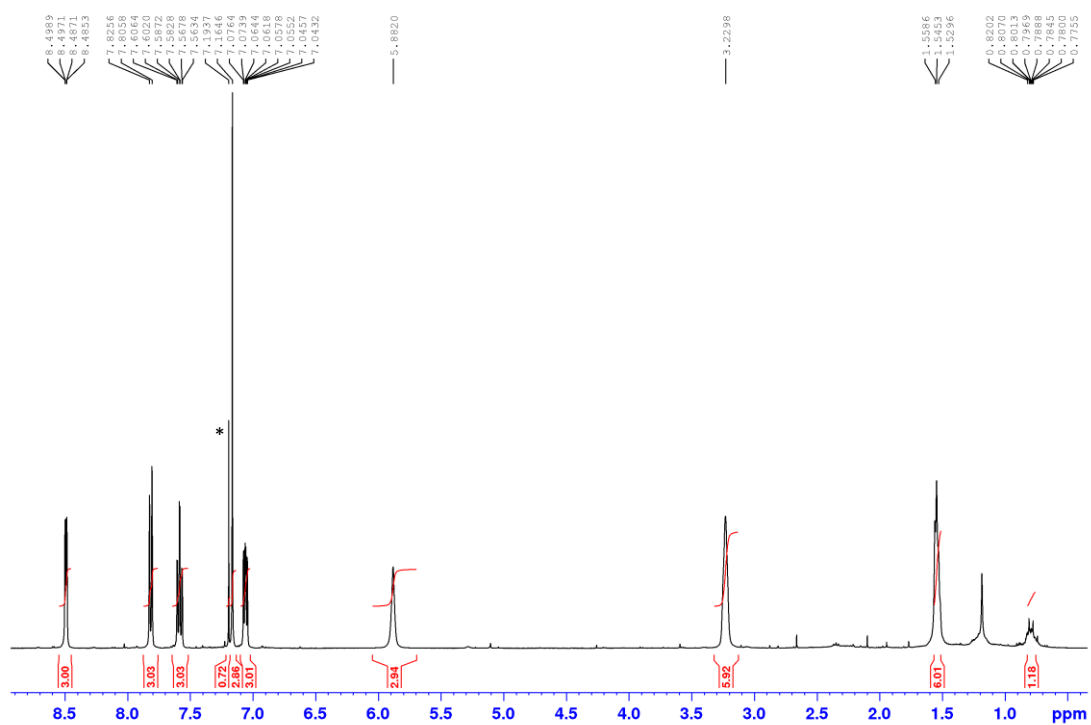


Figure 6.77. ^1H NMR Spectrum of L^4 [400 MHz, CDCl_3]. * CHCl_3 impurity.

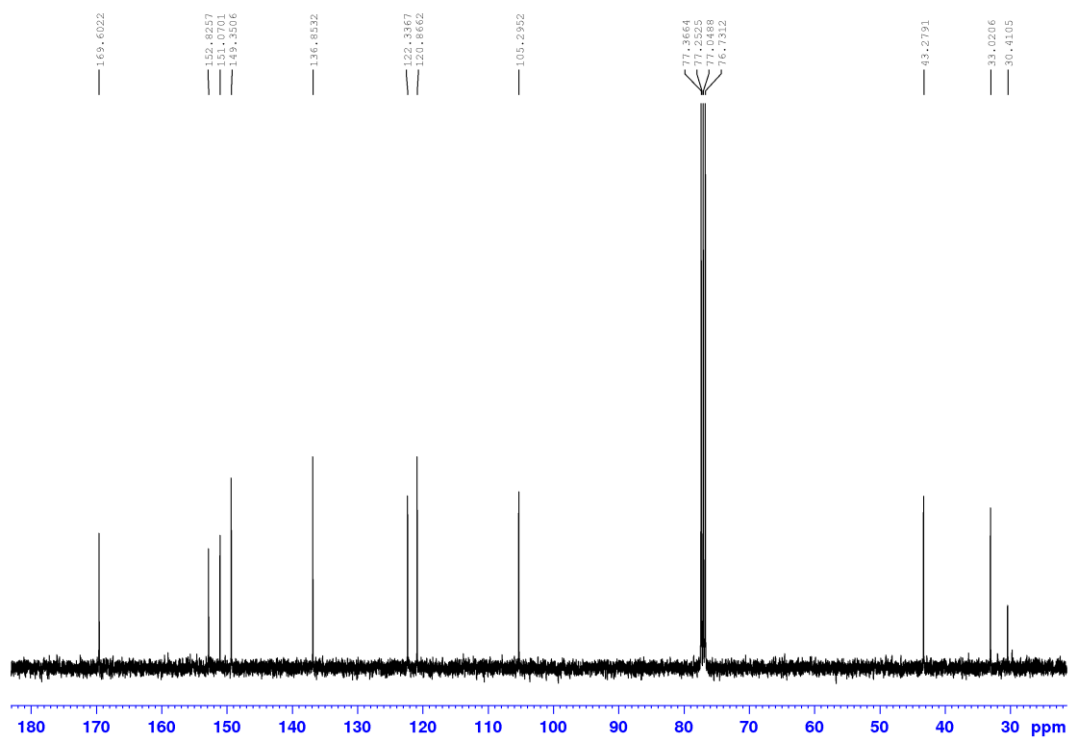


Figure 6.78. ^{13}C NMR Spectrum of L^4 [100 MHz, CDCl_3].

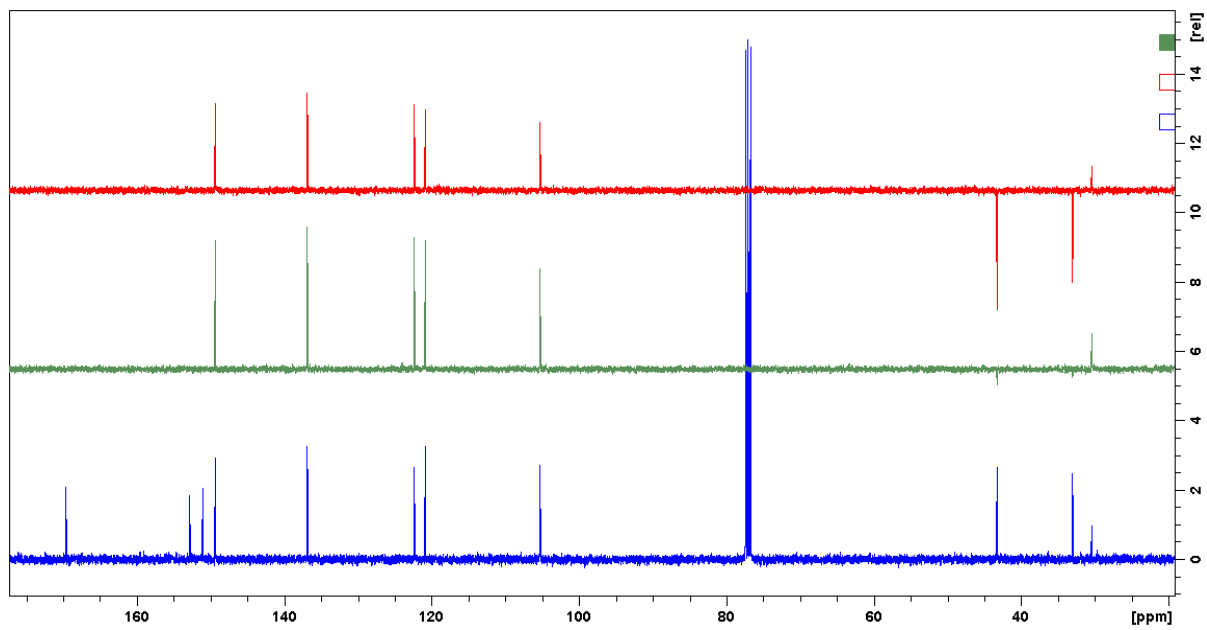


Figure 6.79. ^{13}C NMR Spectrum of L^4 (blue) with the corresponding DEPT-135 (red) and DEPT-90 (green) NMR spectra [100 MHz, CDCl_3].

6.2.6. Crystallography data of L^4 complexes

Compound	$[(L^4)_2Cu_3(PO_4)](ClO_4)_3 \cdot 4MeCN$	$[(L^4)_2Cu_3(AsO_4)](ClO_4)_3 \cdot 3MeCN \cdot H_2O$	$[(L^4)_2Cu_3(SiF_6)](ClO_4)_4 \cdot 5MeCN \cdot H_2O$	$[(L^4)_2Cu_3(SO_4)](ClO_4)_4 \cdot 2MeCN$
Formula	$C_{70}H_{71}Cl_3Cu_3N_{22}O_{16}PS_6$	$C_{62}H_{62}AsCl_3Cu_3N_{21}O_{17}S_6$	$C_{72}H_{64}Cl_4Cu_3F_6N_{23}O_{17}S_6Si$	$C_{66}H_{62}Cl_4Cu_3N_{20}O_{22.865}S_7$
<i>M</i>	1996.78	2011.71	2190.37	2058.10
Crystal system	Triclinic	Orthorhombic	Monoclinic	Monoclinic
Space group	P -1	Pbca	P 1 21/n 1	P 1 21/c 1
a (Å)	14.935(2)	25.8038(9)	15.3230(4)	25.5738(11)
b (Å)	16.0718(19)	20.6206(5)	23.4319(6)	23.6118(12)
c (Å)	19.904(3)	31.1484(8)	26.2964(9)	15.0517(8)
α (°)	79.368(7)	90	90	90
β (°)	81.128(8)	90	105.2930(10)	103.115(2)
γ (°)	63.116(7)	90	90	90
<i>V</i> (Å ³)	4174.3(11)	16573.7(8)	9107.3(5)	8851.8(8)
<i>Z</i>	2	8	4	4
ρ_{calc} (Mg cm ⁻³)	1.589	1.6123	1.5974	1.5442
<i>F</i> (000)	2044	8197.1359	4459.6870	4203.3139
Crystal dimensions (mm)	0.18, 0.15, 0.09	0.25, 0.15, 0.10	0.21, 0.20, 0.15	0.16, 0.12, 0.11
Reflections measured	67587	132610	115468	97388
Range	$2.056 \leq \theta \leq 25.242^\circ$	$1.97 \leq \theta \leq 30.51^\circ$	$1.63 \leq \theta \leq 31.51^\circ$	$1.91 \leq \theta \leq 28.34^\circ$
<i>hkl</i> range indices	$-21 \leq h \leq 21, -22 \leq k \leq 22,$ $-23 \leq l \leq 28$	$-36 \leq h \leq 36, -28 \leq k \leq 29,$ $-44 \leq l \leq 35$	$-22 \leq h \leq 22, -34 \leq k \leq 28,$ $-38 \leq l \leq 38$	$-34 \leq h \leq 33, -31 \leq k \leq 31,$ $-16 \leq l \leq 20$
N° independent reflections	25171	25289	30284	13688
Reflections with <i>I</i> > 2σ(<i>I</i>)	19083	17538	21257	21899
<i>R</i> _{int}	0.0712	0.0769	0.0412	0.0767
Final <i>R</i> ₁ values	0.0522	0.0569	0.0532	0.0844
Final <i>wR</i> (<i>F</i> ²) values	0.1303	0.1172	0.1358	0.2384
Final <i>R</i> ₁ values (all data)	0.0731	0.0937	0.0853	0.1348

Final $wR(F^2)$ values (all data)	0.1454	0.1325	0.1639	0.2853
GOF	1.036	1.0480	1.0981	1.1196
Refined parameters	1112	1140	1279	1146
Restraints	60	103	169	54
Largest peak and hole ($e \text{ \AA}^{-3}$)	1.268, -1.263	1.8507, -1.2160	1.6011, -1.0707	2.0477, -0.9504
CCDC Number				

Table 6.5. X-ray crystallographic data for $[\text{L}^4\text{Mn}]^{2+}$, $[\text{L}^4_2\text{Mn}_3(\text{PO}_4)]^{3+}$ and $[\text{L}^4_2\text{Mn}_3(\text{SO}_4)]^{4+}$.

All the structures contained substitutionally disordered solvent molecules and, in some cases, rotationally disordered counter anions. In these cases, the atoms were modelled using the part instruction and refined over two positions. The anisotropic displacement parameters were treated with *SIMU*, *DELU* and in some cases *ISOR* where needed.

6.2.7. Mass spectrometry studies of L^4 complexes

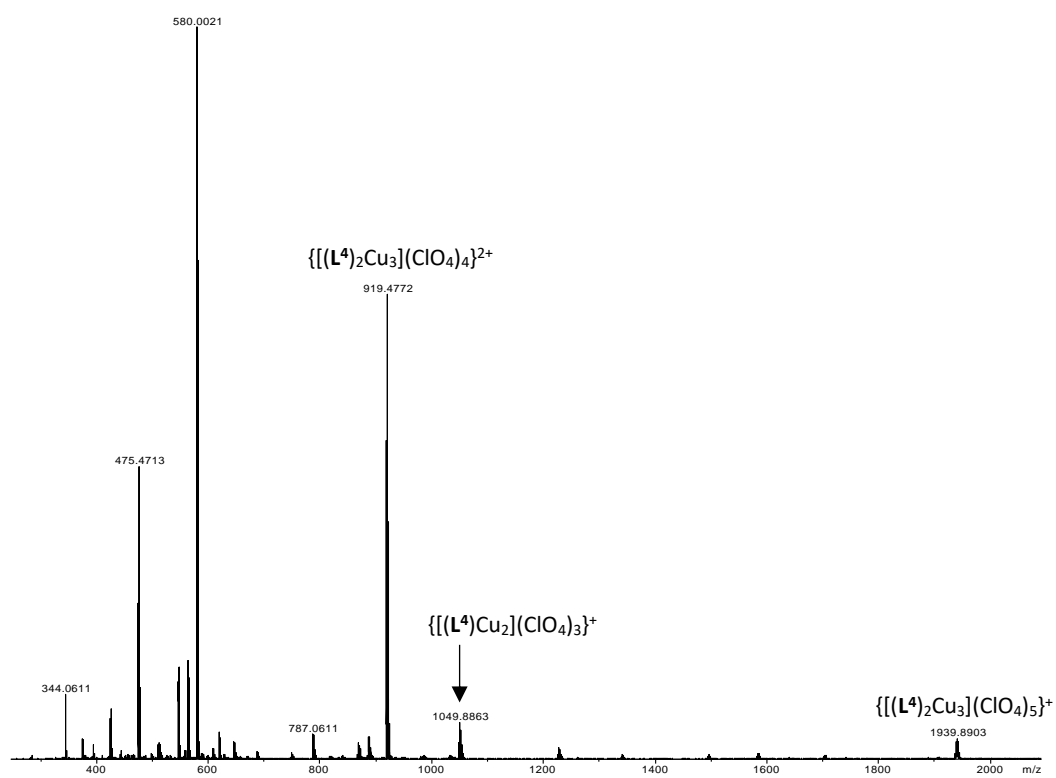


Figure 6.80. ESI-MS spectrum of $[L^4_2Cu_3](ClO_4)_6$.

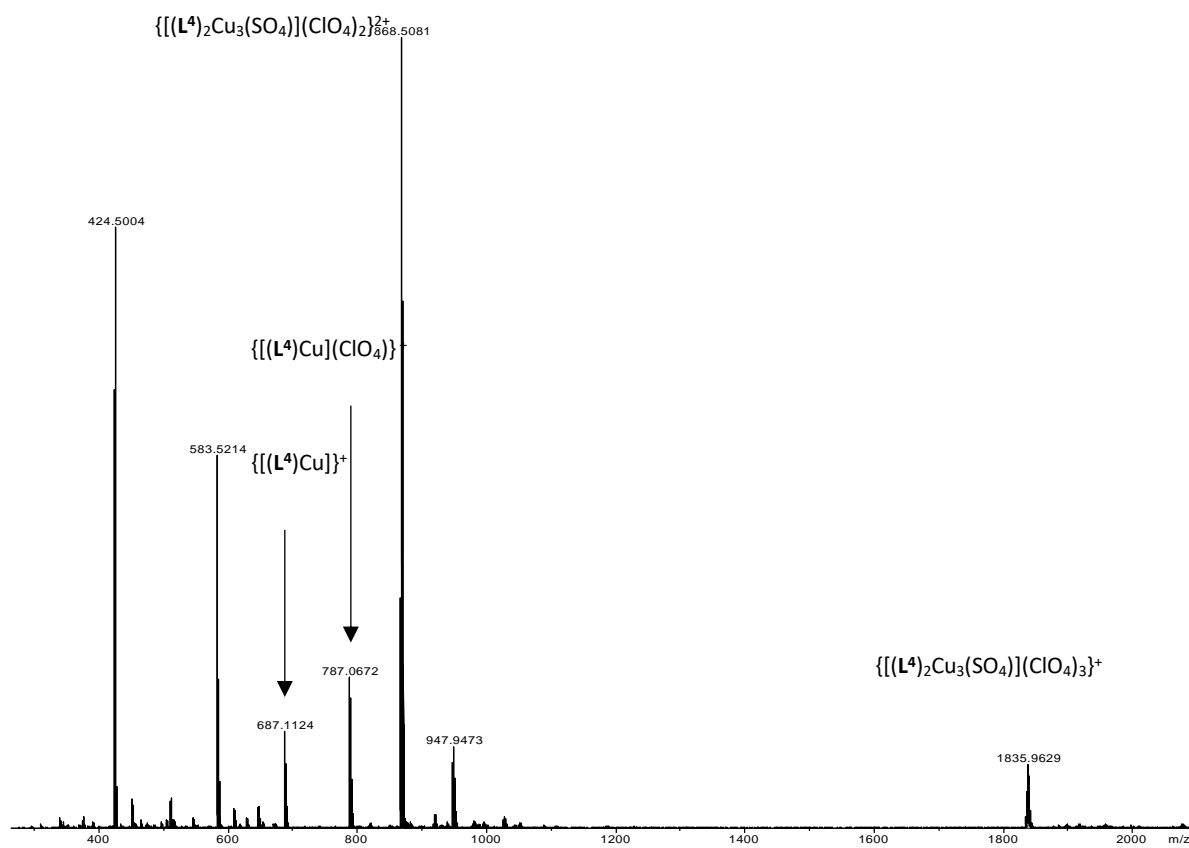


Figure 6.81. ESI-MS spectrum of $[(L^4)_2Cu_3(SO_4)](ClO_4)_4$.

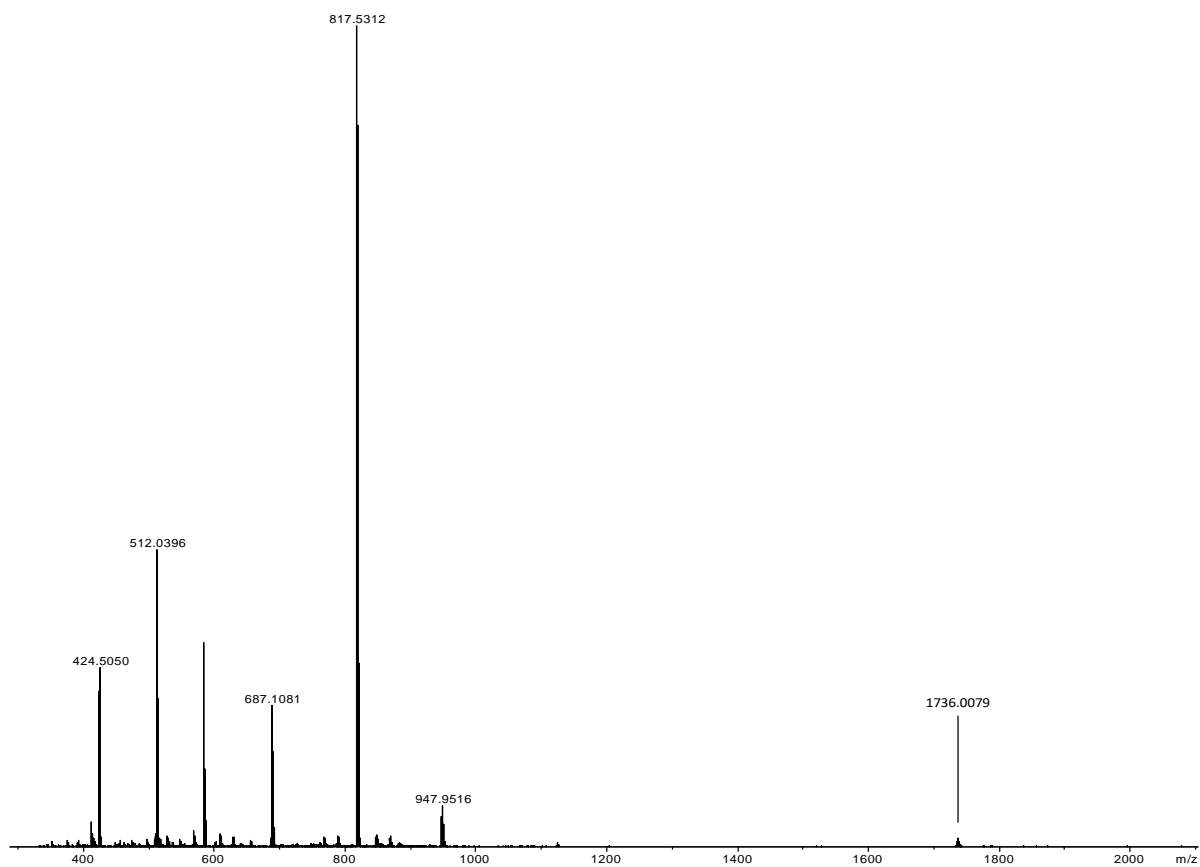


Figure 6.82. ESI-MS spectrum of $[(L^4)_2Cu_3(PO_4)](ClO_4)_3$.

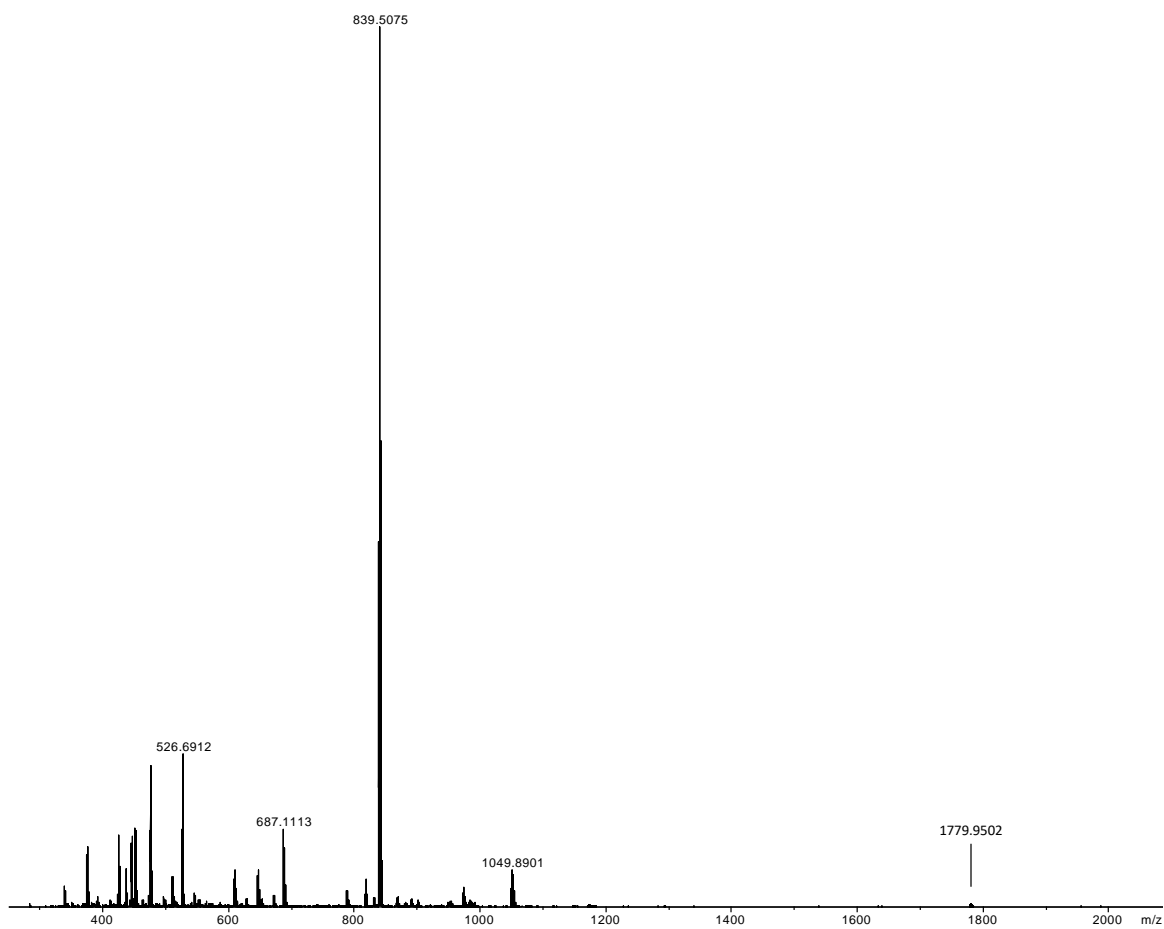


Figure 6.83. ESI-MS spectrum of $[(L^4)_2Cu_3(AsO_4)](ClO_4)_3$.

6.2.8. UV-Vis-NIR studies of L^4 complexes

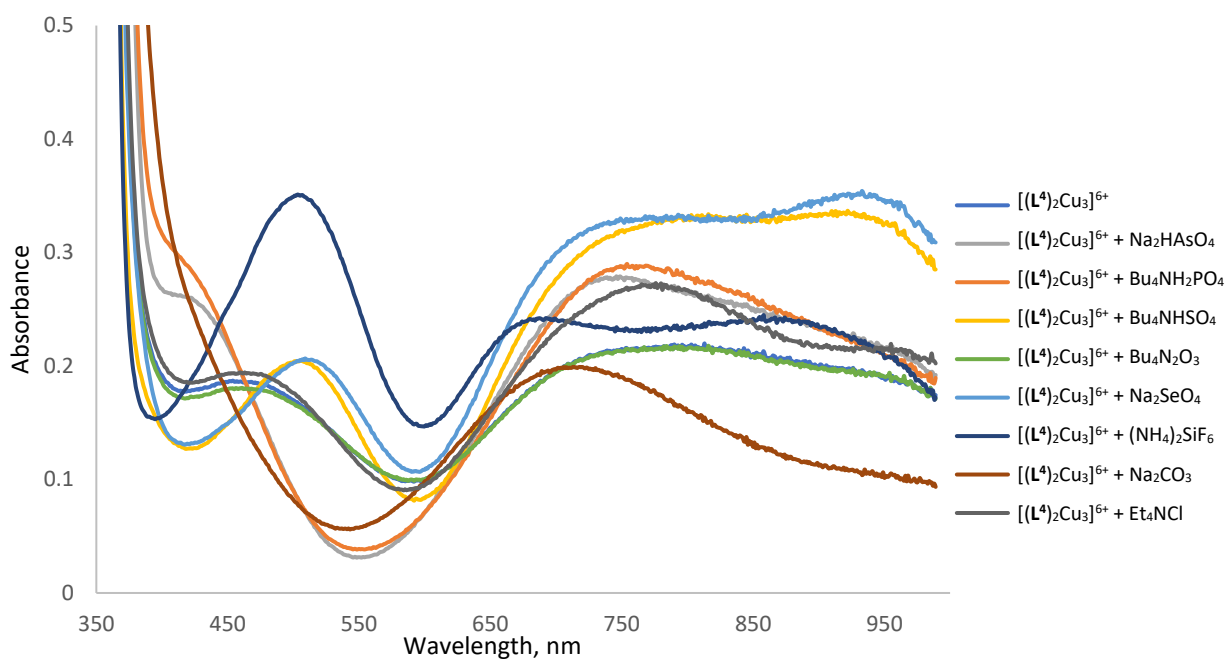


Figure 6.84. UV-Vis-NIR absorption spectra of a solution of $[(L^4)_2Cu_3](trif)_6$ in 1:1 MeCN in H_2O plus the addition of one equivalent of various anions (as either their ammonium, sodium, tetra-N-ethyl- or tetra-N-butyl-ammonium salts). $[(L^4)_2Cu_3](trif)_6 = 0.8$ mM.

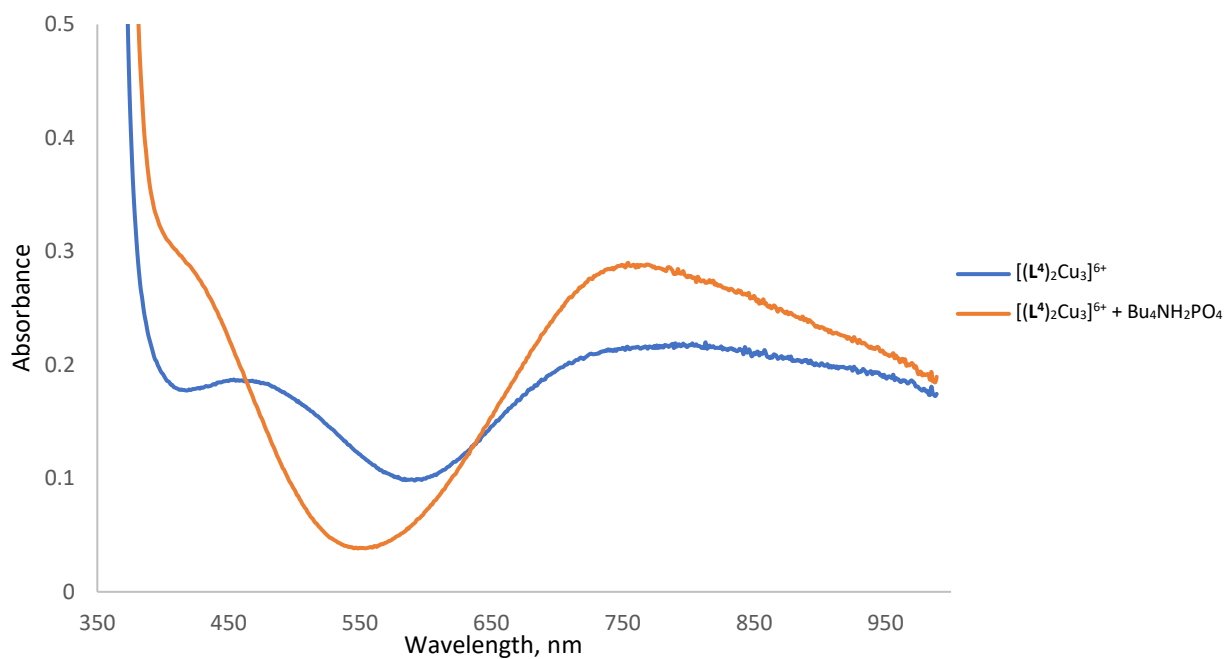


Figure 6.85. UV-Vis-NIR absorption spectra of a solution of $[(L^4)_2Cu_3](trif)_6$ in 1:1 MeCN in H_2O plus the addition of one equivalent of tetra-N-butyl-ammonium dihydrogen phosphate. $[(L^4)_2Cu_3](trif)_6 = 0.8$ mM.

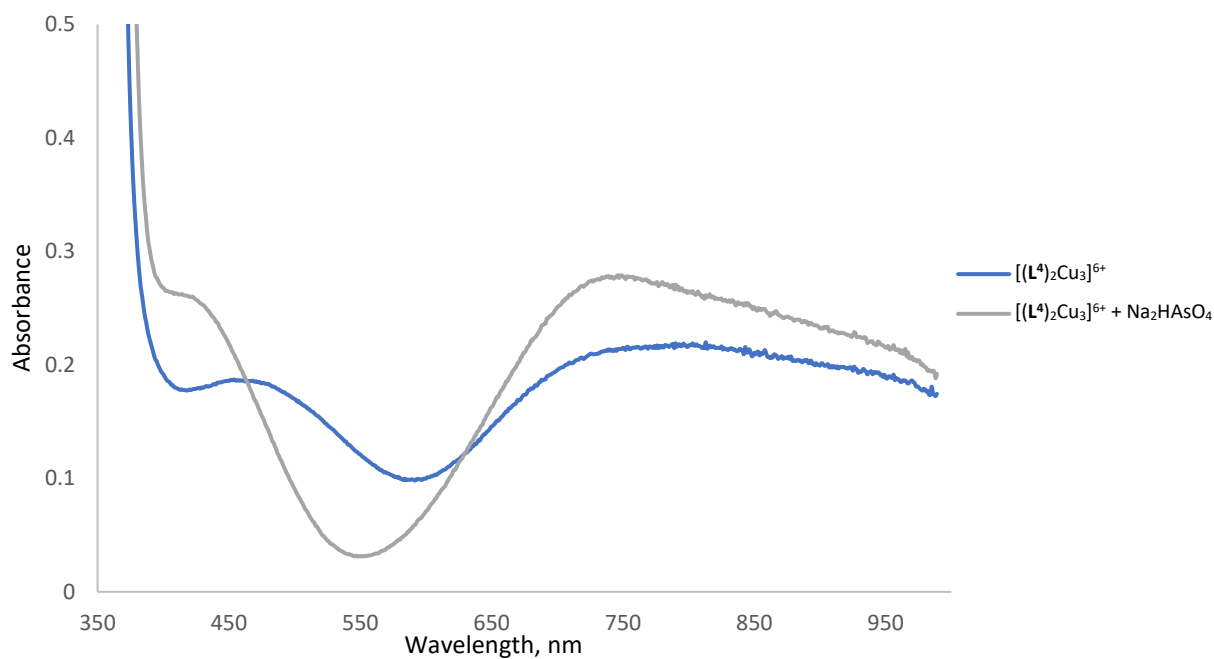


Figure 6.86. UV-Vis-NIR absorption spectra of a solution of $[(L^4)_2Cu_3](trif)_6$ in 1:1 MeCN in H_2O plus the addition of one equivalent of disodium arsenate. $[(L^4)_2Cu_3](trif)_6 = 0.8$ mM.

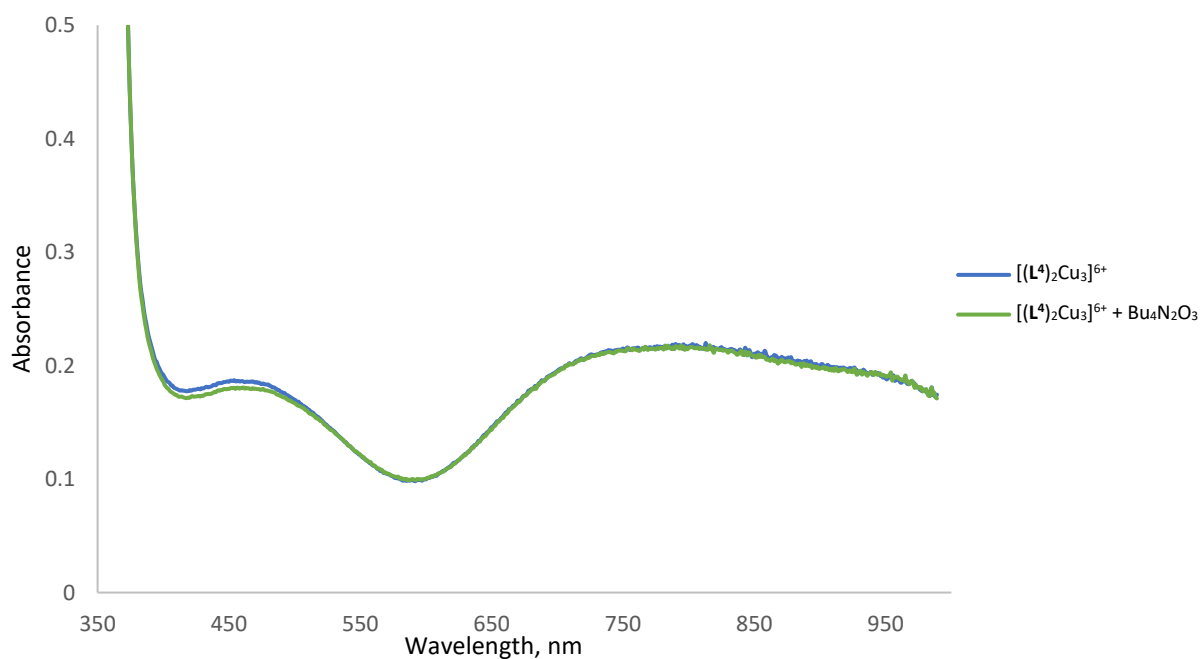


Figure 6.87. UV-Vis-NIR absorption spectra of a solution of $[(L^4)_2Cu_3](trif)_6$ in 1:1 MeCN in H_2O plus the addition of one equivalent of tetra-N-butylammonium nitrate. $[(L^4)_2Cu_3](trif)_6 = 0.8$ mM.

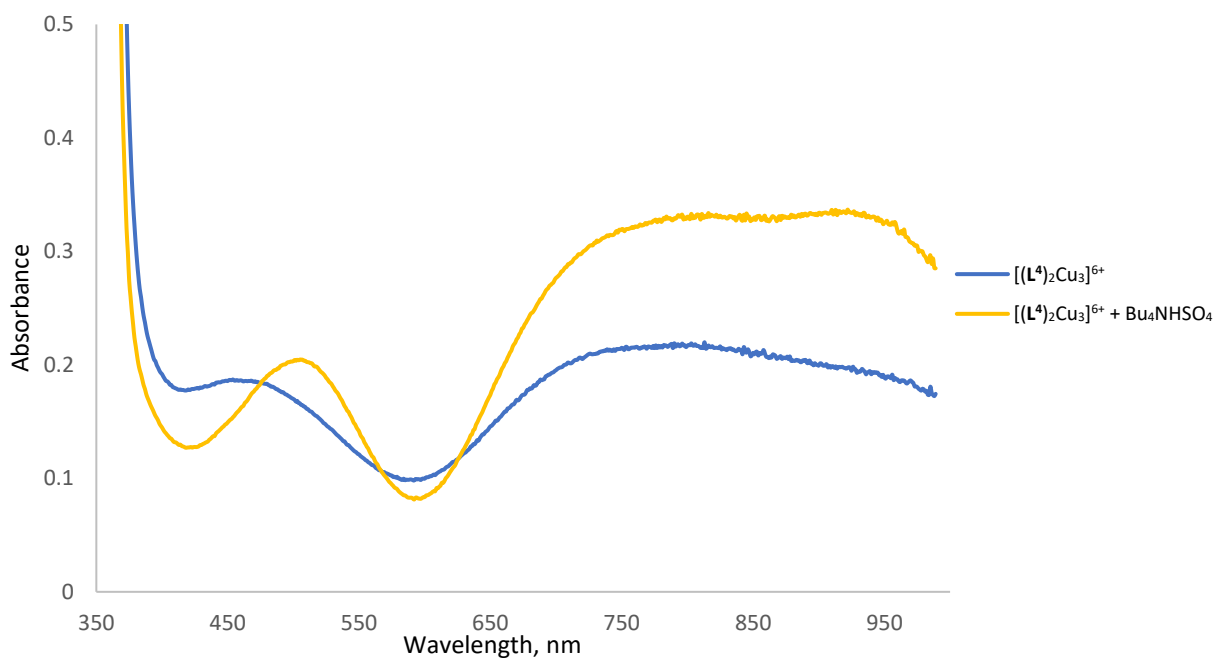


Figure 6.88. UV-Vis-NIR absorption spectra of a solution of $[(L^4)_2Cu_3](trif)_6$ in 1:1 MeCN in H_2O plus the addition of one equivalent of tetra-N-butylammonium hydrogen sulfate. $[(L^4)_2Cu_3](trif)_6 = 0.8$ mM.

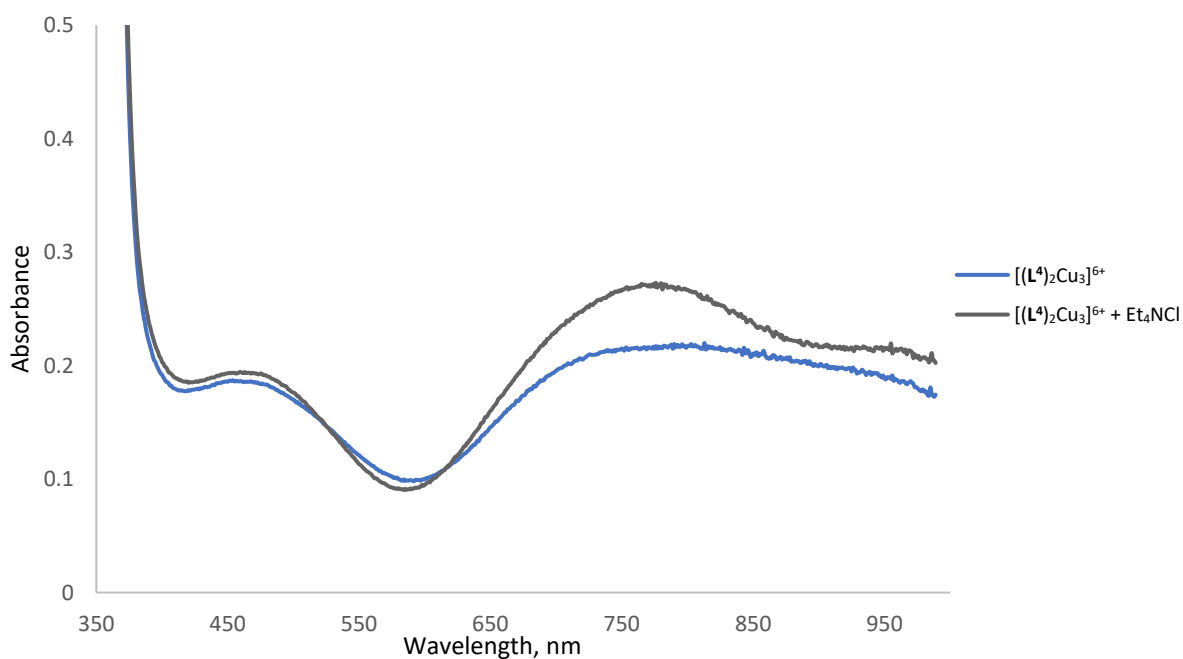


Figure 6.89. UV-Vis-NIR absorption spectra of a solution of $[(L^4)_2Cu_3](trif)_6$ in 1:1 MeCN in H_2O plus the addition of one equivalent of tetra-N-ethylammonium chloride. $[(L^4)_2Cu_3](trif)_6 = 0.8$ mM.

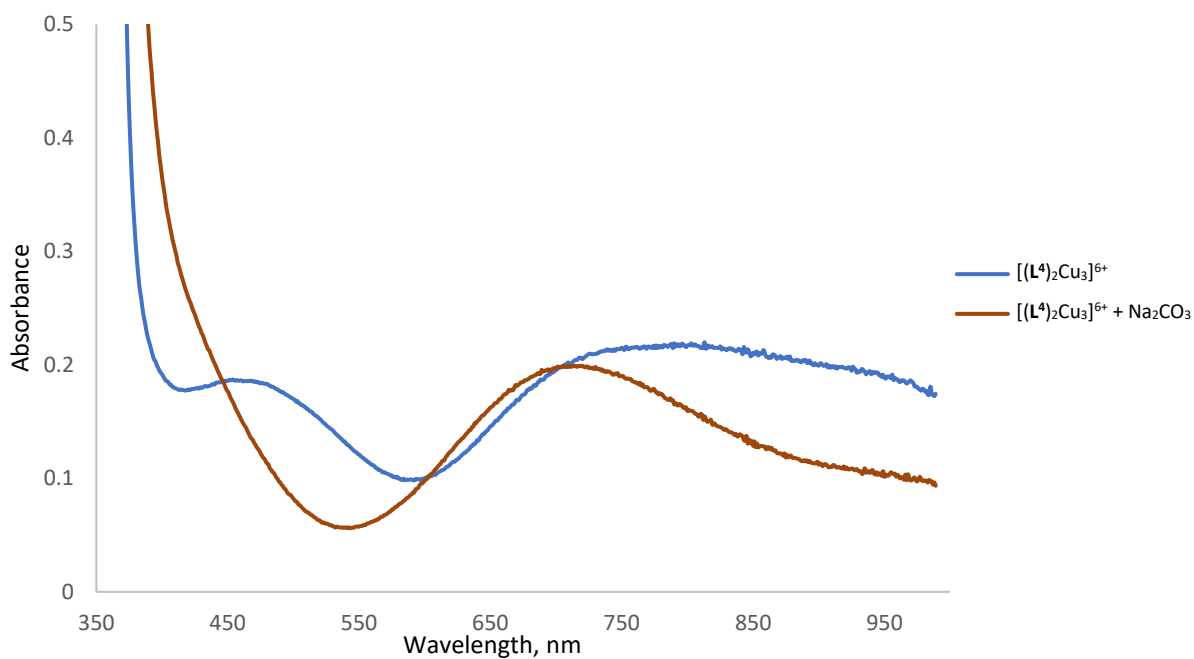


Figure 6.90. UV-Vis-NIR absorption spectra of a solution of $[(L^4)_2Cu_3](trif)_6$ in 1:1 MeCN in H_2O plus the addition of one equivalent of disodium carbonate. $[(L^4)_2Cu_3](trif)_6 = 0.8$ mM.

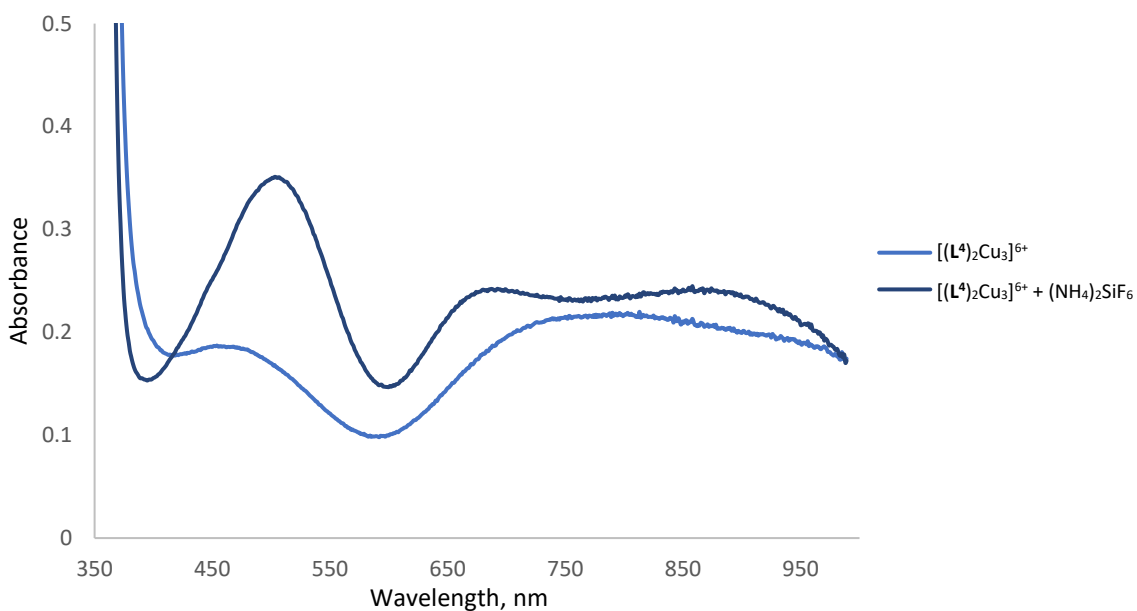


Figure 6.91. UV-Vis-NIR absorption spectra of a solution of $[(L^4)_2Cu_3](trif)_6$ in 1:1 MeCN in H_2O plus the addition of one equivalent of ammonium hexafluorosilicate. $[(L^4)_2Cu_3](trif)_6 = 0.8$ mM.

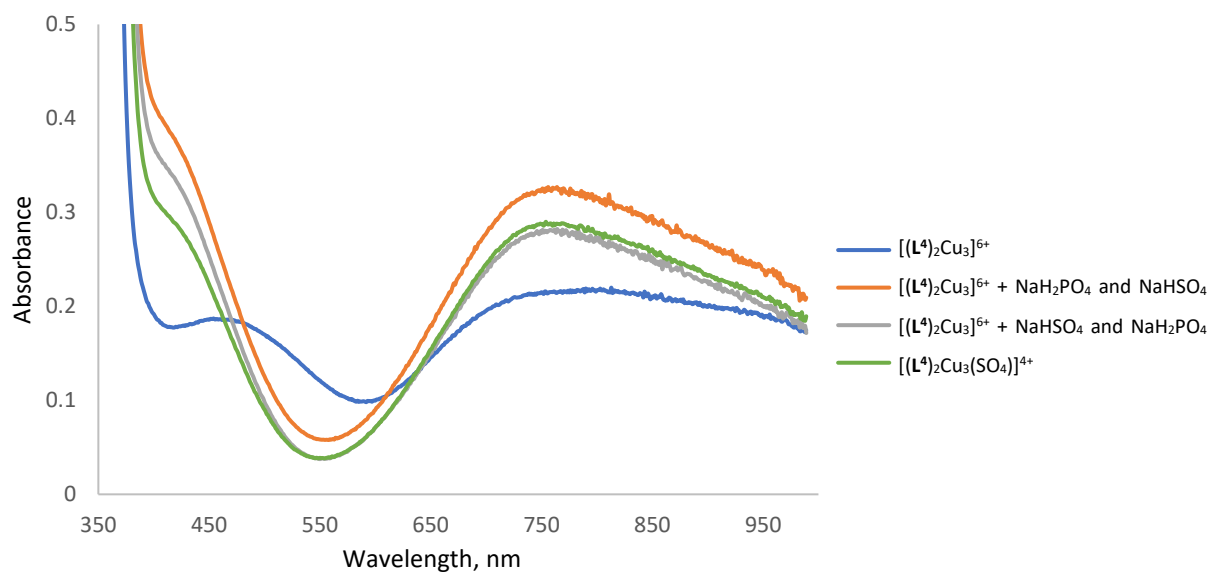


Figure 6.92. UV-Vis-NIR absorption spectra of a solution of $[(L^4)_2Cu_3](trif)_6$ and $[(L^4)_2Cu_3(SO_4)](trif)_4$ in 1:3 MeCN in H_2O . To $[(L^4)_2Cu_3](trif)_6$ was added one equivalent of monosodium sulfate and monosodium dihydrogenphosphate, in the order shown, and then the addition reversed.

$[(L^4)_2Cu_3](trif)_6$ 0.8 mM.

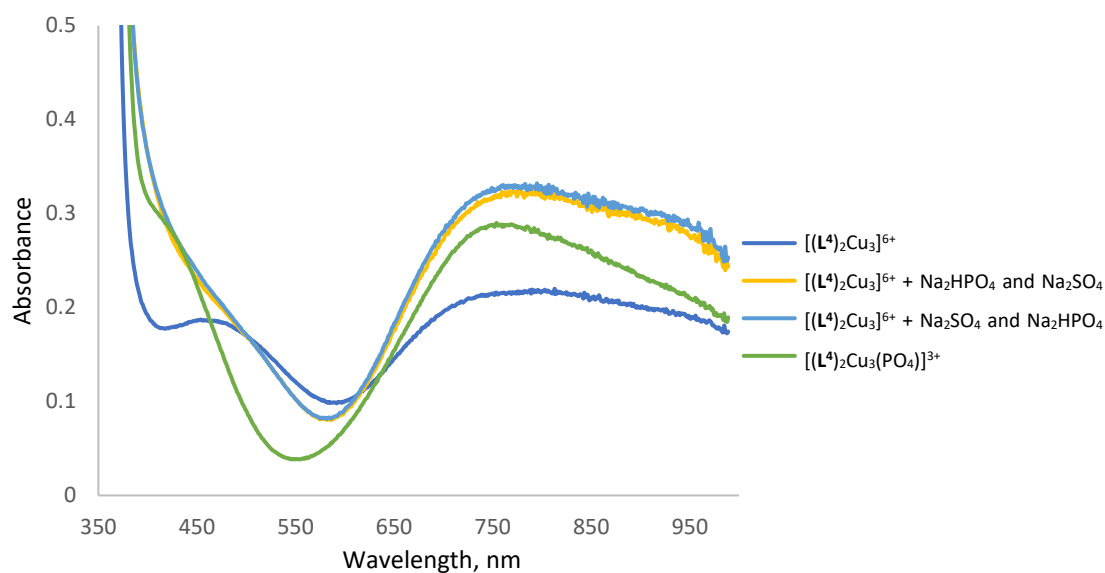


Figure 6.93. UV-Vis-NIR absorption spectra of a solution of $[(L^4)_2Cu_3](trif)_6$ and $[(L^4)_2Cu_3(PO_4)](trif)_3$ in 1:3 MeCN in H_2O . To $[(L^4)_2Cu_3](trif)_6$ was added one equivalent of disodium sulfate and disodium hydrogenphosphate, in the order shown, and then the addition reversed. $[(L^4)_2Cu_3](trif)_6$ 0.8 mM.

6.2.9. Ion chromatography studies of L⁴ complexes

Conditions and instrumentation:

IC		
Instrument	Metrohm 850 IC system	
Column	Metrohm A Supp 5 column (150 mm x 4.0 mm)	
Oven (°C)	30°C	
Pump	Mobile Phase A	3.2 mM Sodium Carbonate / 1.0 mM Sodium Bicarbonate
	Mobile Phase B	N.A.
	Flow (mls/min)	0.70
	Isocratic/Gradient	Isocratic
	Runtime (mins)	20
Injector	Volume (μl)	10
Suppressor	Regenerant Solution	0.1 M Oxalic acid / 0.1 M Sulfuric acid in 10% acetone
Detector	Conductance / PAD	Conductance

Table 6.6. Conditions for ion chromatography analysis of L⁴ complexes.

Experiment IC-1 and IC-2 (calibration curves):

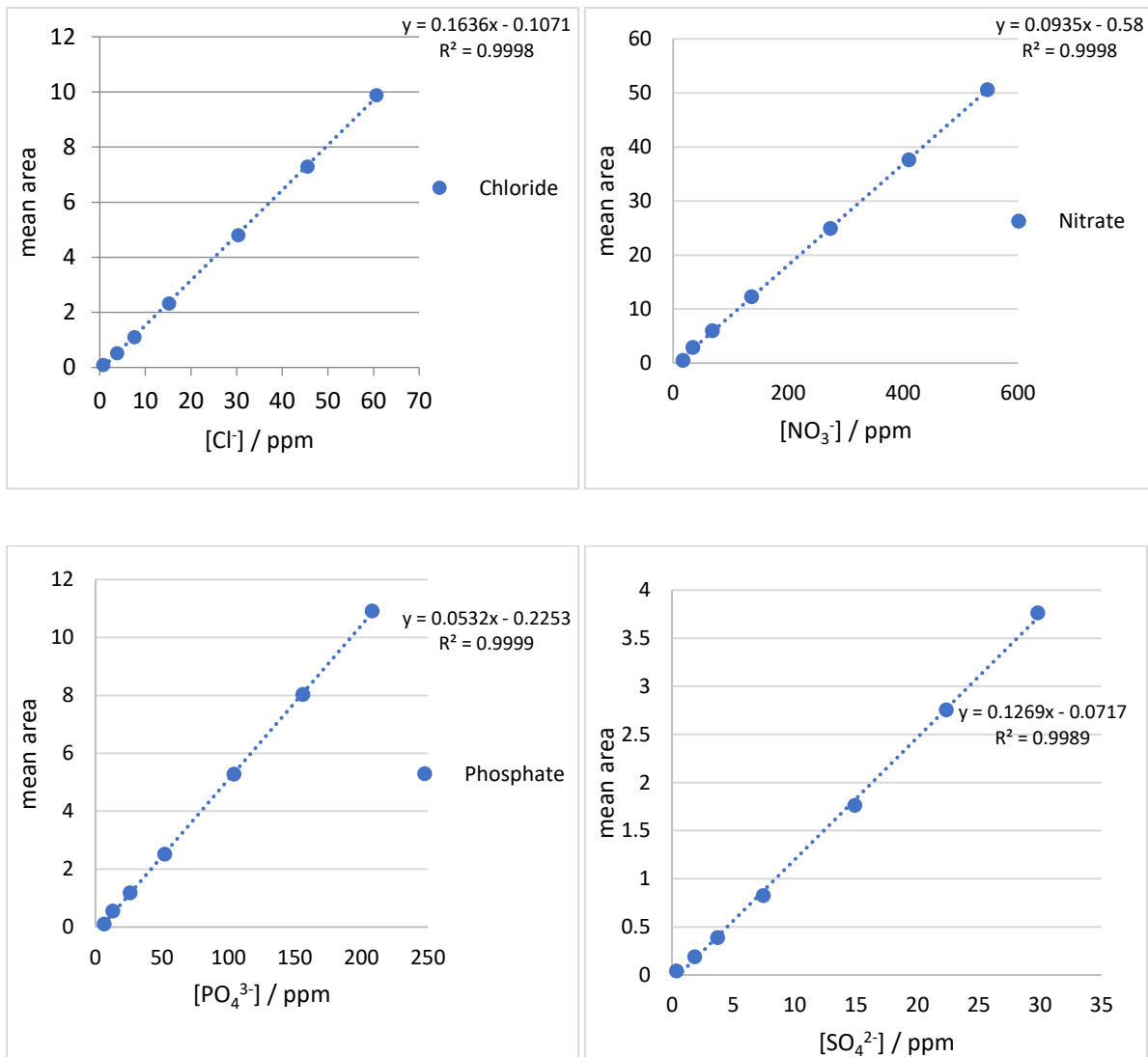


Figure 6.94. Calibration curve (ppm) for chloride, nitrate, phosphate and sulphate anions.

Experimental details of experiments IC-1 and IC-2

For the disodium salt experiment **IC-1**, $\text{Na}_2\text{SO}_4 \cdot 10\text{H}_2\text{O}$ (33.46 mg, 0.104 mmol), $\text{Na}_2\text{HPO}_4 \cdot 2\text{H}_2\text{O}$ (18.49 mg, 0.104 mmol), NaNO_3 (8.83 mg, 0.104 mmol) and NaCl (6.07 mg, 0.104 mmol) as dissolved in water (UP, 50 mL) and via pipette 10 ml of this solution was added to a vial. To this was then added a solution of acetone (2 mL) containing L^4 (26 mg, 0.042 mmol) and $\text{Cu}(\text{trif})_2$ (22.6 mg, 0.062 mmol) which gave a lime green solution and a small amount of fine green powder. Acetone was then carefully added (1~2 mL) until the solid dissolved and it was then allowed to slowly evaporate over several days during which time a light green crystalline precipitate formed. The sample was then filtered and directly measured by ion chromatography. The mono-sodium experiment **IC-2** was done in an analogous fashion using $\text{NaHSO}_4 \cdot \text{H}_2\text{O}$ (14.48 mg, 0.104 mmol) and $\text{NaH}_2\text{PO}_4 \cdot \text{H}_2\text{O}$ (14.33 mg, 0.104 mmol) instead of $\text{Na}_2\text{SO}_4 \cdot 10\text{H}_2\text{O}$ and $\text{Na}_2\text{HPO}_4 \cdot 2\text{H}_2\text{O}$.

Experiment IC-1 and IC-2 chromatography results:

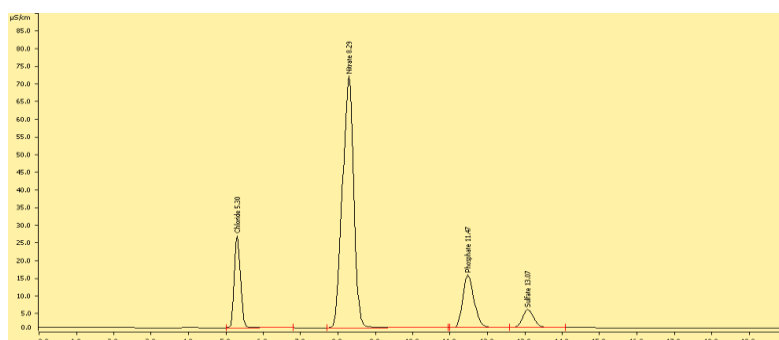


Figure 6.95. Ion Chromatography chromatograms: 0.5 mM standard.

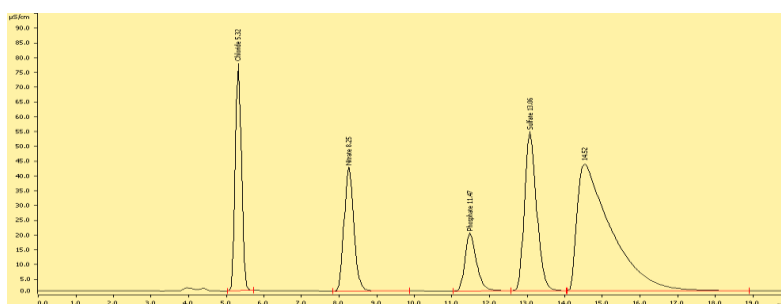


Figure 6.96. Experiment IC-1 Ion Chromatography chromatograms: NaCl, NaNO₃, NaH₂PO₄ and NaHSO₄ (0.0208 mmols of each) after exposure to [(L⁴)₂Cu₃](trif)₆ (0.0208 mols). The response at ~15 mins is due to CF₃SO₃⁻ anions.

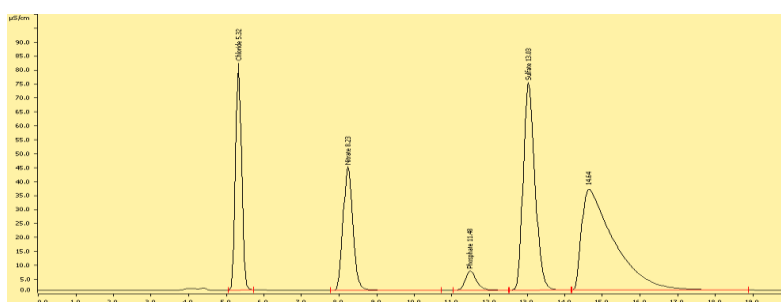


Figure 6.97. Experiment IC-2 Ion Chromatography chromatograms: NaCl, NaNO₃, Na₂HPO₄ and Na₂SO₄ (0.0208 mmols of each) after exposure to [(L⁴)₂Cu₃](trif)₆ (0.0208 mols). The response at ~15 mins is due to CF₃SO₃⁻ anions.

Sample	Cl ⁻	NO ₃ ⁻	PO ₄ ³⁻	SO ₄ ²⁻
NaHSO ₄ and NaH ₂ PO ₄ / area	14.342	12.616	6.991	20.051
ppm sample	88.3	141.1	135.6	158.6
Expected (ppm)	73.5	129	199	199
% Change	120	108	68	80
Background (ppm)	13.9	11.5	>1	12.3
Correction (ppm)	74.4	129.6	135.6	146.3
% Change	101%	100%	68%	74%

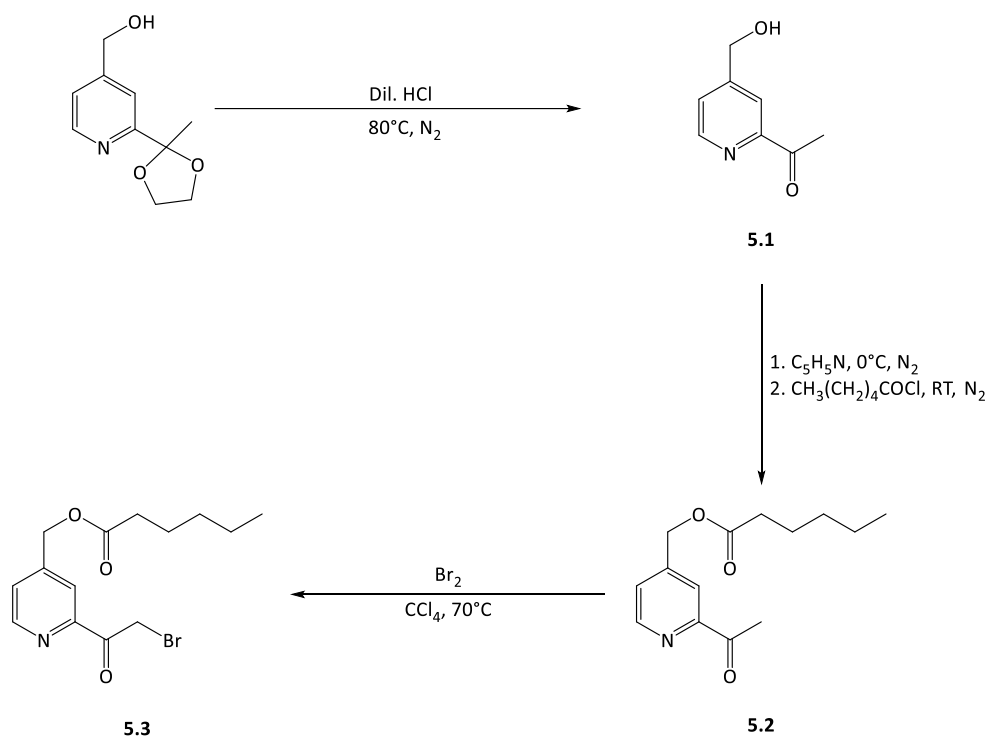
Table 6.7. Monosodium experiment **IC-1** Ion Chromatography results.

Sample	Cl ⁻	NO ₃ ⁻	PO ₄ ³⁻	SO ₄ ²⁻
Na ₂ SO ₄ and Na ₂ HPO ₄ / area	14.75	13.332	2.387	26.885
ppm sample	90.8	148.8	49.1	212.4
Expected (ppm)	73.5	129	199	199
% Change	120.0	113.0	25.0	105.0
Background (ppm)	13.9	11.5	>1	12.3
Correction (ppm)	76.9	137.3	49.1	200.1
% Change	105%	106%	25.0%	100%

Table 6.8. Disodium experiment **IC-2** Ion Chromatography results.

6.3. Chapter 4

6.3.1. Synthesis of intermediate 5.3



Scheme 6.5. Synthesis of brominated 2-acetylpyridine derivative 5.3.

Synthesis of **5.1**. [2-(2-methyl-1,3-dioxolan-2-yl)pyridin-4-yl]methanol (1.86 g, 9.54 mmol)^{118,119} was stirred for 12 hours in 3 M HCl (20 mL) at 60 °C. The reaction was cooled and the pH adjusted to alkaline with solid sodium bicarbonate. This mixture was then extracted into 2% methanol in dichloromethane (4 × 100 mL), the organic layer was dried over anhydrous magnesium sulfate and solvent removed under reduced pressure, affording the product as a yellow oil (1.20 g, 83%). This was used without further purification. ¹H NMR [400 MHz, CDCl₃]: δ (ppm) = 8.67 (dd, 1H, *J* = 5.0, 0.6, py), 8.04 (dd, 1H, *J* = 1.7, 0.8, py), 7.54 (m, 1H, py), 4.84 (d, 2H, *J* = 5.8, CH₂-OH), 2.76 (s, 3H, COCH₃), 2.00 (t, 1H, *J* = 5.9 Hz, -OH). ¹³C NMR [100 MHz, CDCl₃]: δ (ppm) = 200.3 (C, COCH₃), 153.6 (C), 151.2 (C), 149.2 (CH), 124.4

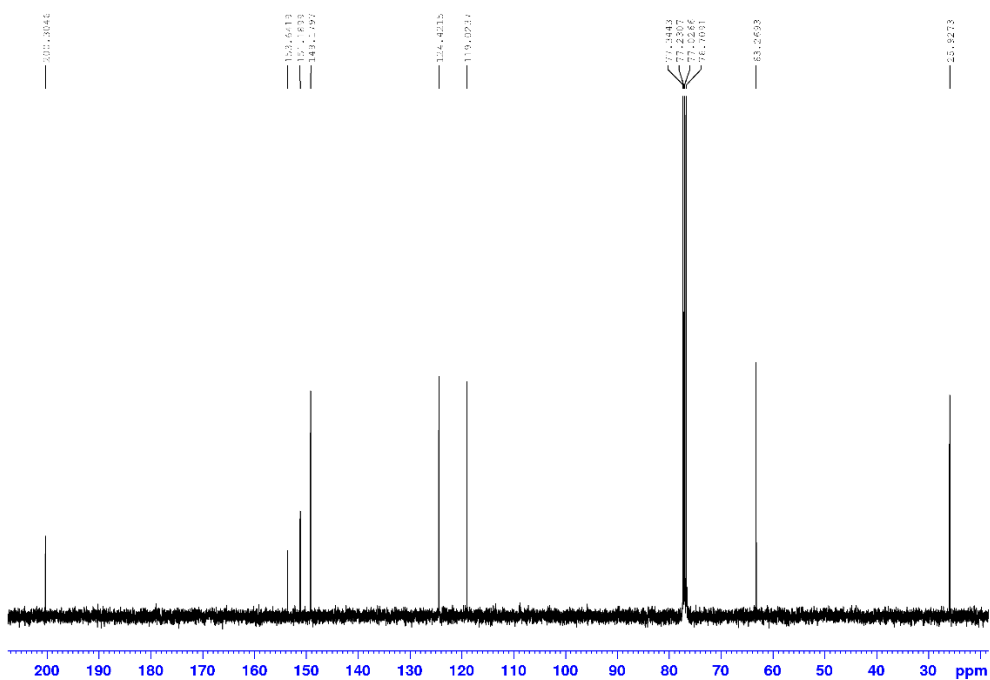


Figure 6.99. ^{13}C NMR Spectrum of **5.1** [100 MHz, CDCl_3].

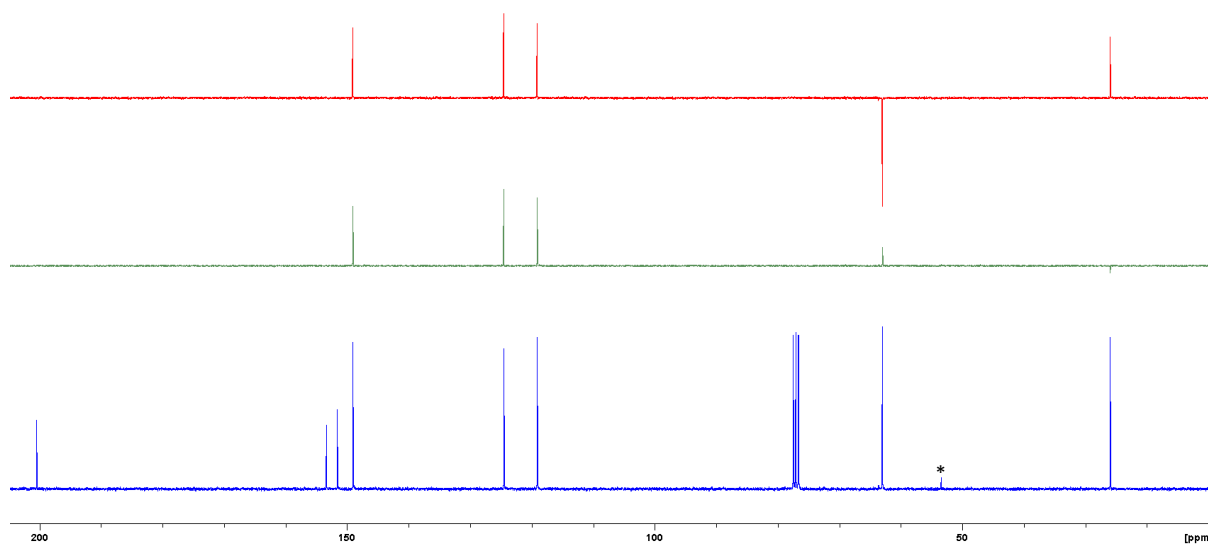


Figure 6.100. ^{13}C NMR Spectrum of **5.1** (blue) with the corresponding DEPT-135 (red) and DEPT-90 (green) NMR spectra [100 MHz, CDCl_3]. * CH_2Cl_2 impurity.

Synthesis of **5.2**. To a solution of **5.1** (600 mg, 3.97 mmol) and pyridine (0.38 mL, 4.77 mmol) in anhydrous dichloromethane (20 mL) was added dropwise hexanoyl chloride (0.67 mL, 4.77 mmol)

under an atmosphere of nitrogen. The reaction was stirred at room temperature for 2 hours, until analysis via TLC (SiO₂, 1% MeOH in DCM) showed no starting material remained. The mixture was diluted with DCM (20 mL) and washed with saturated aqueous sodium bicarbonate (15 mL). The organic portion was dried over anhydrous magnesium sulfate and the solvent removed under reduced pressure, providing the crude product as a slightly pink oil. The product was purified by column chromatography (SiO₂, 1% methanol in dichloromethane), affording the product as a colourless oil (820 mg, 83%). ¹H NMR [300 MHz, CDCl₃]: δ (ppm) = 8.68 (d, 1H, *J* = 5.0, py), 8.01 (dd, 1H, *J* = 1.5, 0.8, py), 7.44 (dd, 1H, *J* = 5.0, 0.8, py), 5.19 (s, 2H, pyCH₂-), 2.75 (s, 3H, -COCH₃), 2.43 (t, 2H, *J* = 7.7, -COCH₂-), 1.68 (pent, 2H, *J* = 7.4, -COCH₂CH₂-), 1.33 (m, overlap, 4H, -COCH₂CH₂CH₂CH₂- and -COCH₂CH₂CH₂CH₂-), 0.91 (t, 3H, *J* = 6.8 Hz, -CH₂CH₃). ¹³C NMR [100 MHz, CDCl₃]: δ (ppm) = 199.9 (PyCOCH₃), 173.3 (-CH₂CO₂CH₂-), 153.8 (C), 149.3 (CH), 146.5 (C), 125.1 (CH), 119.7 (CH), 63.8 (CH₂), 34.1 (CH₂), 31.3 (CH₂), 25.9 (-COCH₃), 24.6 (CH₂), 22.3 (CH₂), 13.9 (-CH₂CH₃). ESI-MS *m/z* 250.1439 [M + H]⁺, observed neutral mass 249.1367, C₁₄H₁₉NO₃ requires 249.1365 (error 0.84 ppm).

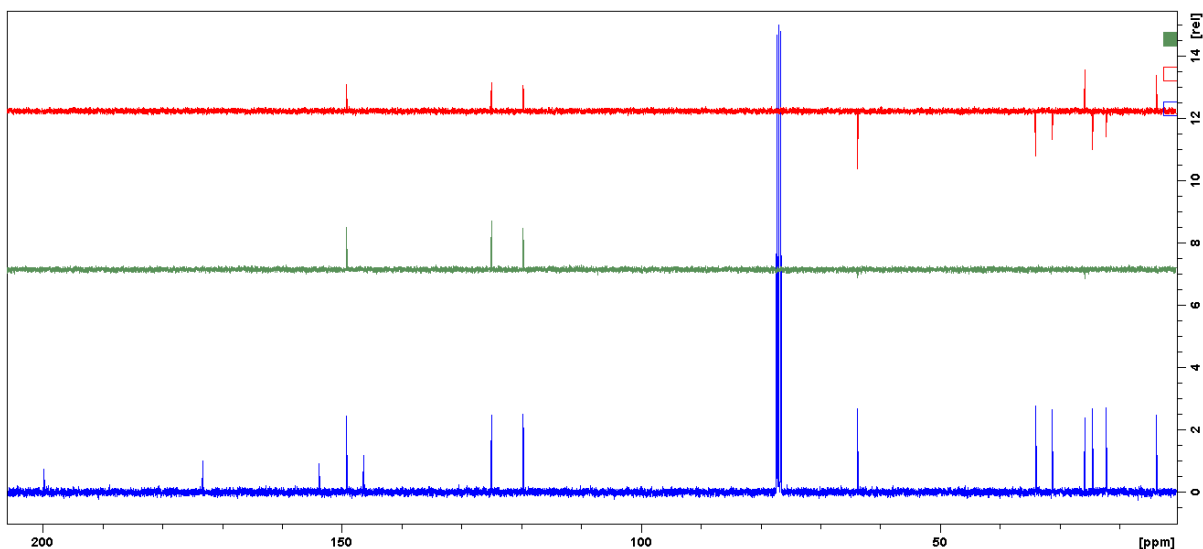


Figure 6.103. ^{13}C NMR Spectrum of **5.2** (blue) with the corresponding DEPT-135 (red) and DEPT-90 (green) NMR spectra [100 MHz, CDCl_3].

Synthesis of **5.3**. A solution of bromine (462 mg, 2.89 mmol) in carbon tetrachloride (1 mL) was added dropwise to a solution of **5.2** (600 mg, 2.41 mmol) in carbon tetrachloride (20 mL) at 70 °C. The reaction was monitored by TLC (SiO_2 , 1% MeOH in DCM) and the bromine solution added slowly until all the starting material had been consumed, during which time a yellow precipitate formed. The mixture was allowed to cool, diluted with dichloromethane (30 mL) and washed with saturated aqueous sodium bicarbonate (20 mL). The organic layer was dried over anhydrous magnesium sulfate and the solvent evaporated under reduced pressure to give the crude material as a slightly yellow oil. The product was purified by column chromatography (SiO_2 , 1% MeOH in DCM) to afford the product as a colourless oil (505 mg, 64%). ^1H NMR [400 MHz, CDCl_3]: δ (ppm) = 8.69 (d, 1H, $J = 5.0$, Py), 8.07 (d, 1H, $J = 0.6$, Py), 7.49 (dt, 1H, $J = 4.8, 0.7$, Py), 5.22 (s, 2H, PyCH_2 -), 4.87 (s, 2H, $-\text{PyCOCH}_2$ -), 2.45 (t, 2H, $J = 7.6$, $-\text{COCH}_2$ -), 1.70 (pent, 2H, $J = 7.4$, $-\text{COCH}_2\text{CH}_2$ -), 1.35 (m, overlap, 4H, $-\text{COCH}_2\text{CH}_2\text{CH}_2\text{CH}_2$ - and $-\text{COCH}_2\text{CH}_2\text{CH}_2\text{CH}_2$ -), 0.92 (t, 3H, $J = 7.0$ Hz, $-\text{CH}_2\text{CH}_3$). ^{13}C NMR [100 MHz, CDCl_3]: δ (ppm) = 192.3 (C, PyCOCH_2 -), 173.3 (C, $\text{CH}_2\text{CO}_2\text{CH}_2$ -), 151.7 (C), 149.4 (CH), 146.9 (C), 125.8 (CH), 120.7 (CH), 63.7 (CH_2),

34.0 (CH₂), 32.3 (CH₂), 31.3, (CH₂) 24.6 (CH₂), 22.3 (CH₂), 13.9 (CH₃). ESI-MS *m/z* 328.0547 [M + H]⁺,
 observed neutral mass 327.0475, C₁₄H₁₈NO₃Br requires 327.0470 (error 1.48 ppm).

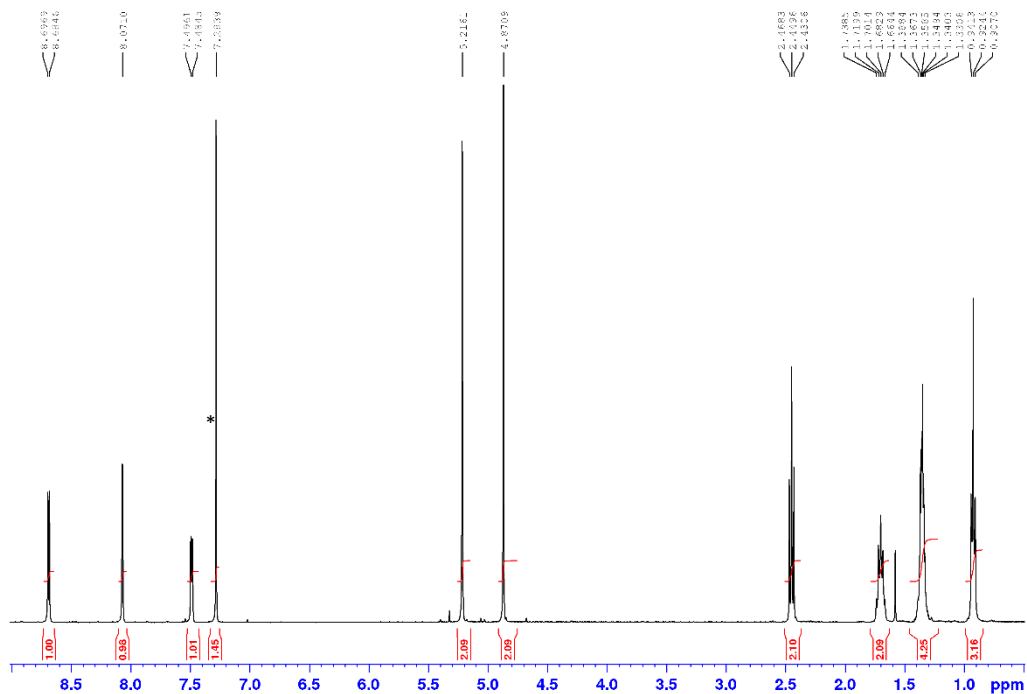


Figure 6.104. ¹H NMR Spectrum of **5.3** [400 MHz, CDCl₃]. *CHCl₃ impurity.

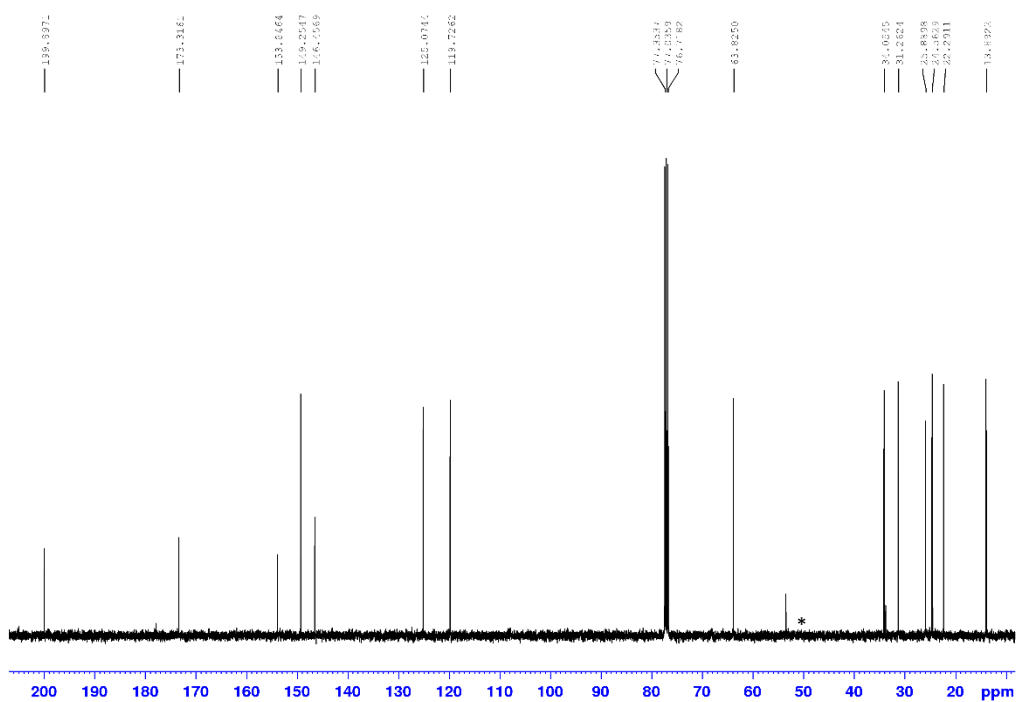


Figure 6.105. ^{13}C NMR Spectrum of **5.3** [100 MHz, CDCl_3]. * CH_2Cl_2 impurity.

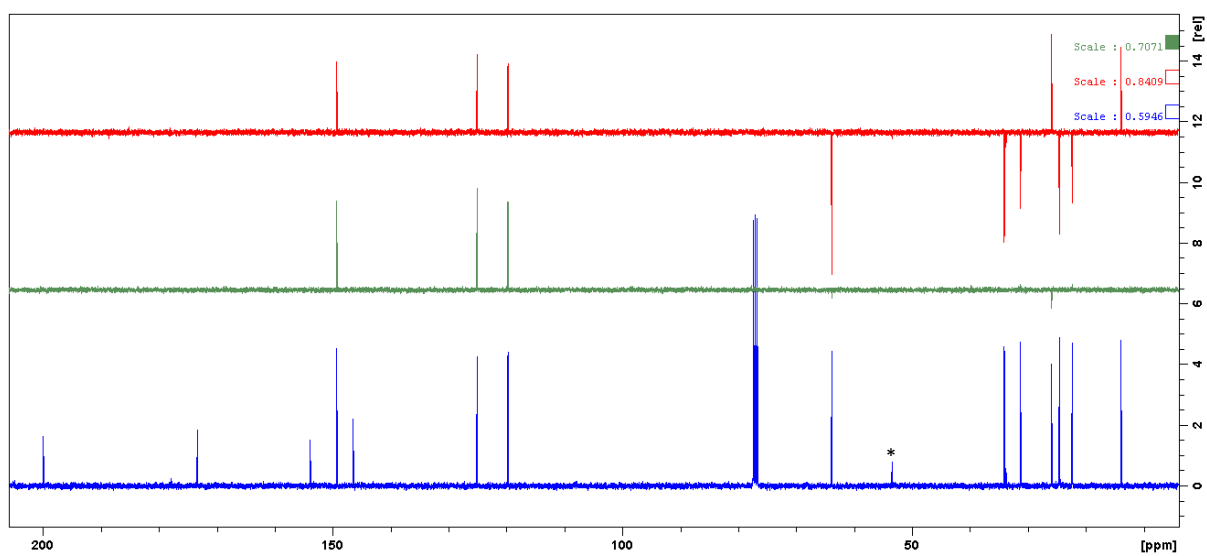
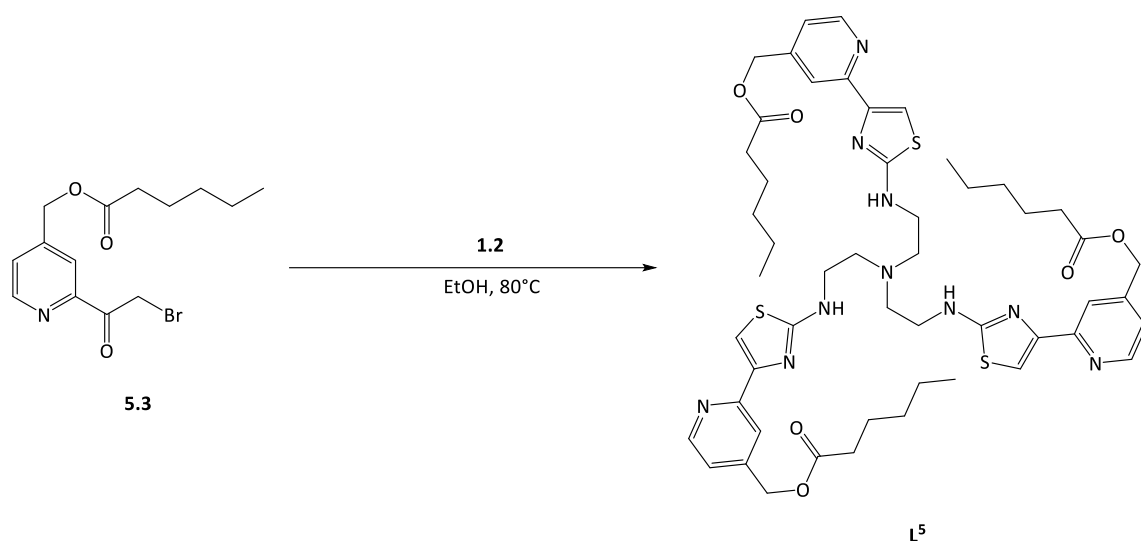


Figure 6.106. ^{13}C NMR Spectrum of **5.3** (blue) with the corresponding DEPT-135 (red) and DEPT-90 (green) NMR spectra [100 MHz, CDCl_3]. * CH_2Cl_2 impurity.

6.3.2. Synthesis of ligand L^5



Scheme 6.6. Synthesis of ligand L^5 .

Synthesis of (((nitriлотris(ethane-2,1-diyl))tris(azanediy))tris(thiazole-2,4-diyl))tris(pyridine-2,4-diyl))-tris(methylene) trihexanoate (ligand L^5). To a solution of **5.3** [300 mg, 0.915 mmol) in ethanol (20 mL), *tris*-thiourea **1.2** (90 mg, 0.278 mmol) was added. The reaction was then heated to 80 °C for 12 h, during which time all the solid dissolved and the solution turned yellow. The solution was allowed to cool and the solvent removed under reduced pressure. The resultant oil was dissolved in dichloromethane (30 mL) and washed with saturated aqueous sodium bicarbonate (15 mL). The organic portion was dried over anhydrous magnesium sulfate and the solvent removed under reduced pressure to give the crude product as a brown/yellow oil. The product was purified by column chromatography (SiO_2 , 10% MeOH in DCM) to afford L^5 as a light brown oil (155mg, 55%). 1H NMR [300 MHz, $CDCl_3$]: δ (ppm) = 8.55 (d, 3H, J = 5.0, py), 7.89 (s, 3H, py), 7.26 (s, 3H, tz) 7.13 (dd, 3H, J = 4.9, 0.7, py), 5.90 (s, 3H, NH), 5.14 (s, 6H, $pyCH_2$ -), 3.44 (q, 6H, J = 5.3, NCH_2CH_2NH -), 2.90 (t, 6H, J = 5.6, NCH_2CH_2NH -), 2.40 (t, 6H, J = 7.6, $-COCH_2$ -), 1.67 (quint, 6H, J = 7.3, $-COCH_2CH_2$ -), 1.31 (m, overlap, 12H, $-COCH_2CH_2CH_2CH_2$ - and $-COCH_2CH_2CH_2CH_2$ -), 0.89 (t, 9H, J = 6.5 Hz, $-CH_2CH_3$). ^{13}C NMR [100 MHz, $CDCl_3$]: δ (ppm) = 173.4 (C, $-CO_2$ -), 169.5 (C), 153.0 (C), 150.6 (C), 149.6 (CH), 145.9 (C), 120.4 (CH),

119.1 (CH), 106.0 (CH), 64.3 (CH₂), 53.0 (CH₂) 43.3 (CH₂), 34.1 (CH₂), 31.3 (CH₂), 24.6 (CH₂), 22.3 (CH₂), 13.9 (CH₃, -CH₂CH₃). ESI-MS m/z 1011.4416 [M + H]⁺, observed neutral mass 1010.4341, C₅₁H₆₆N₁₀S₃O₆ requires 1010.4329 (error 1.24 ppm).

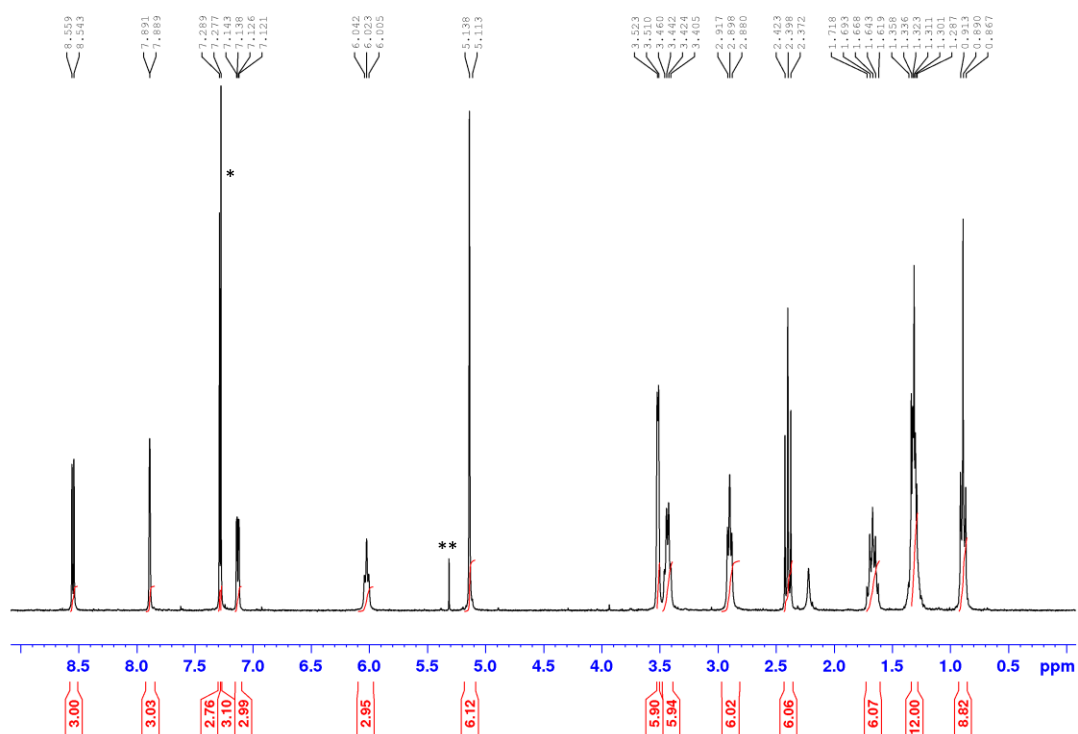


Figure 6.107. ¹H NMR Spectrum of L⁵ [300 MHz, CDCl₃]. *CHCl₃ impurity. **CH₂Cl₂ impurity.

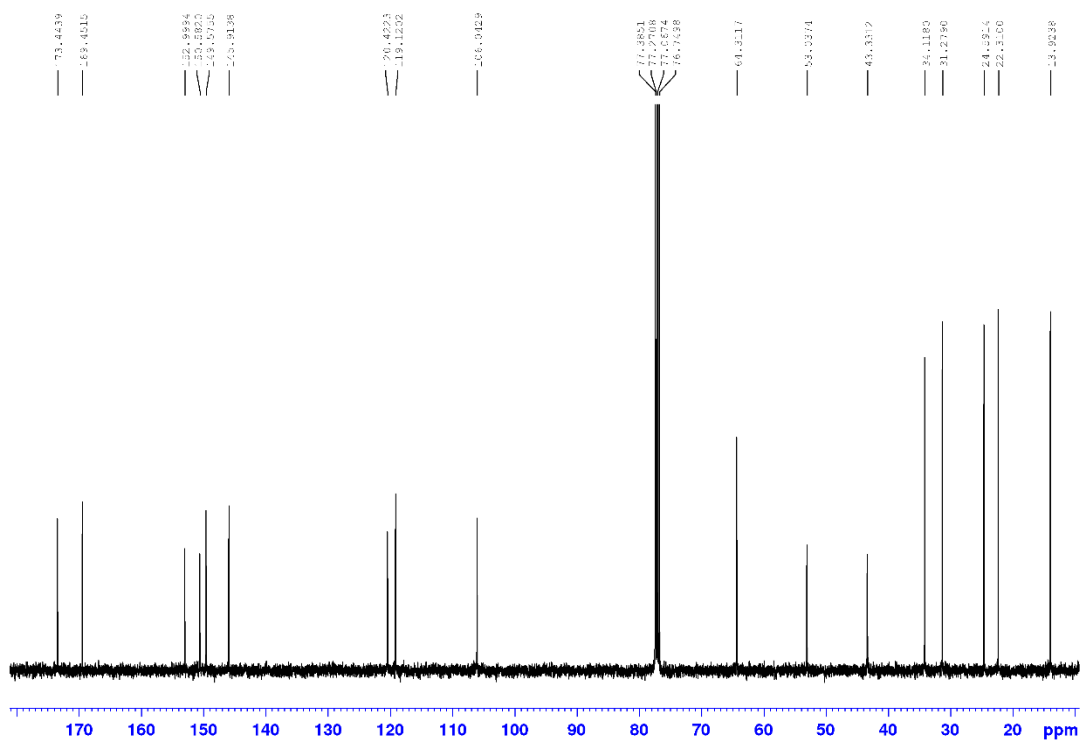


Figure 6.108. ^{13}C NMR Spectrum of L^5 [100 MHz, CDCl_3].

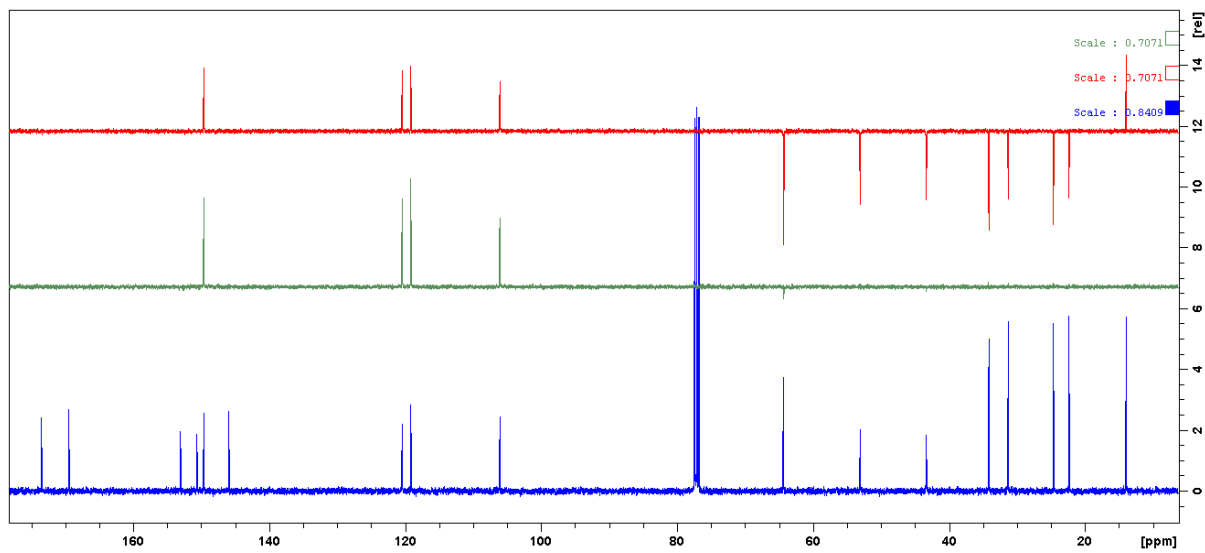
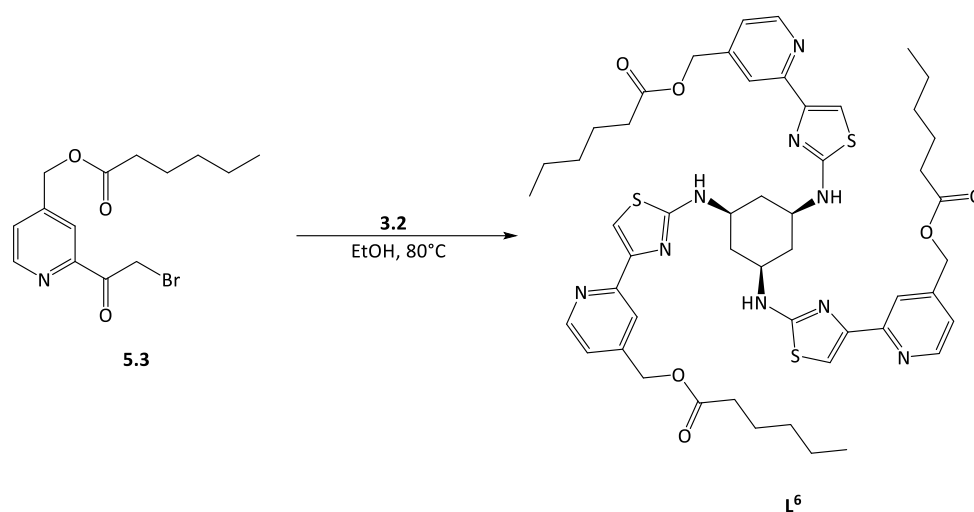


Figure 6.109. ^{13}C NMR Spectrum of L^5 (blue) with the corresponding DEPT-135 (red) and DEPT-90 (green) NMR spectra [100 MHz, CDCl_3].

6.3.3. Synthesis of ligand **L**⁶



Scheme 6.7. Synthesis of ligand **L**⁶.

Synthesis of (((((1*s*,3*s*,5*s*)-cyclohexane-1,3,5-triyl)tris(azanediyl))tris(thiazole-2,4-diyl))tris(pyridine-2,4-diyl))tris(methylene) trihexanoate (ligand **L**⁶). To a solution of **5.3** (373 mg, 1.13 mmol) in ethanol (20 mL), **3.2** (105 mg, 0.343 mmol) was added. The reaction was heated to 80 °C for 12 hours, during which time all the solid dissolved and the solution turned yellow. The solution was then allowed to cool and solvent removed under reduced pressure. The resultant oil was dissolved in dichloromethane (40 mL) and washed with saturated aqueous sodium bicarbonate (20 mL). The organic portion was dried over anhydrous magnesium sulfate and solvent removed under reduced pressure to give the crude product as a yellow solid. The product was purified by column chromatography (SiO₂, 10% MeOH in DCM) to afford the pure product as a dark yellow solid (220 mg, 64%). ¹H NMR [400 MHz, CDCl₃]: δ (ppm) = 8.47 (d, 3H, *J* = 5.0, py), 7.80 (s, 3H, py), 7.25 (s, 3H, tz), 7.06 (dd, 3H, *J* = 5.0, 1.1, py), 5.61 (d, 3H, *J* = 7.4, NH), 5.07 (s, 6H, py-CH₂-), 3.65 (m, 3H, cy-CH), 2.64 (d, 3H, *J* = 11.4, cy-CH), 2.32 (t, 6H, *J* = 7.5, COCH₂), 1.58 (quint, 6H, COCH₂CH₂-), 1.21 (m, overlap, 12H, -COCH₂CH₂CH₂CH₂- and -COCH₂CH₂CH₂CH₂-), 1.00 (q, 3H, *J* = 11.8, cy-CH), 0.79 (t, 9H, *J* = 6.9 Hz, -CH₂CH₃). ¹³C NMR [100 MHz, CDCl₃]: δ (ppm) = 173.49 (C, -CO₂-), 168.04 (C), 153.0 (C), 150.8 (C), 149.7 (CH), 146.1 (C), 120.4 (CH), 119.1 (CH), 106.1 (CH), 64.3 (CH₂), 51.5 (CH), 38.5 (CH₂), 34.1 (CH₂), 31.3 (CH₂), 24.6 (CH₂), 22.3 (CH₂),

13.9 (CH₃). ESI-MS m/z 1016.3954 [M + Na]⁺, observed neutral mass 993.4063, C₅₁H₆₃N₉S₃O₆ requires 993.4063 (error 0.04 ppm).

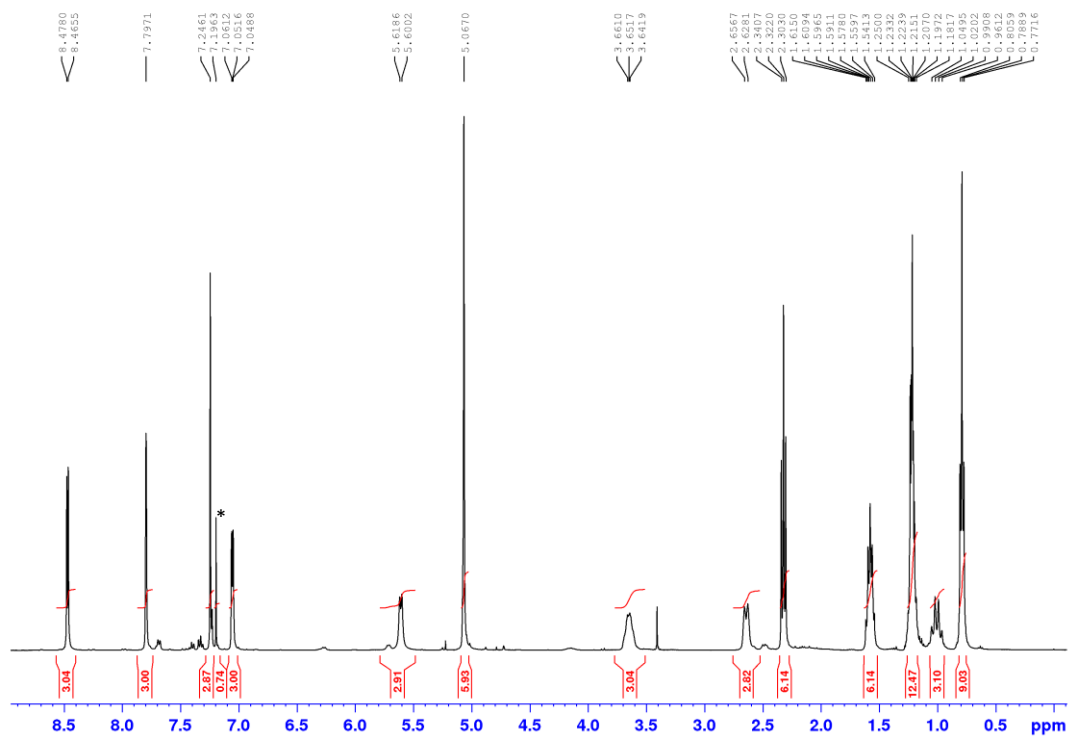


Figure 6.110. ¹H NMR Spectrum of L⁶ [400 MHz, CDCl₃]. *CHCl₃ impurity.

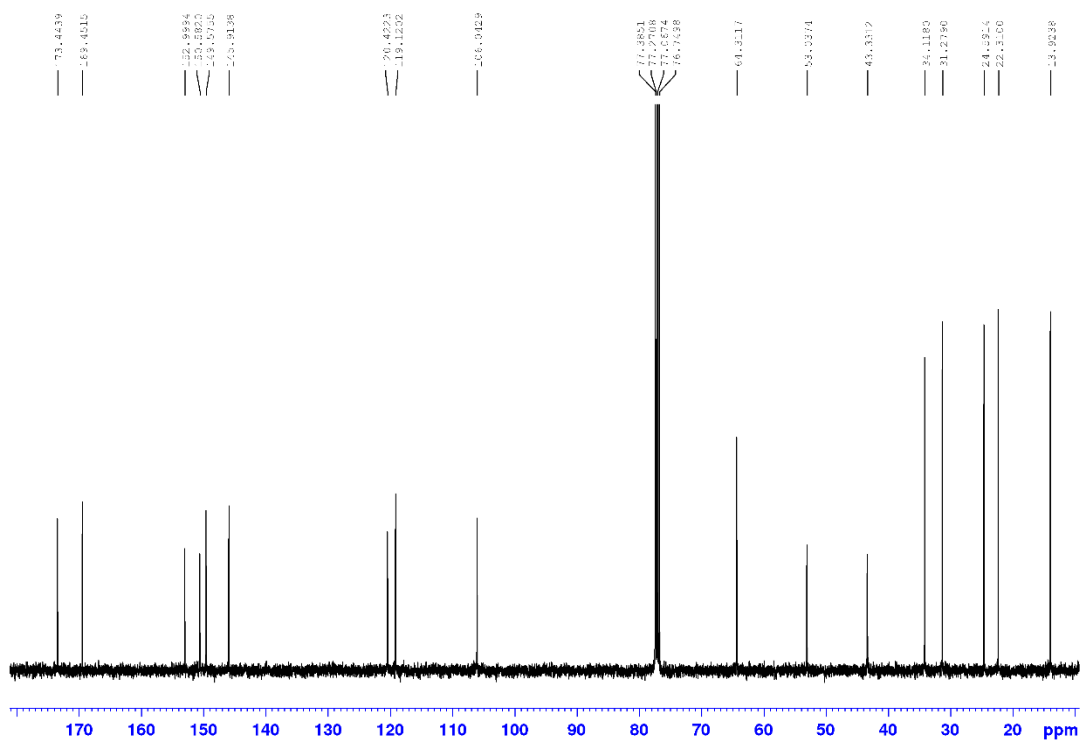


Figure 6.111. ^{13}C NMR Spectrum of L^6 [100 MHz, CDCl_3].

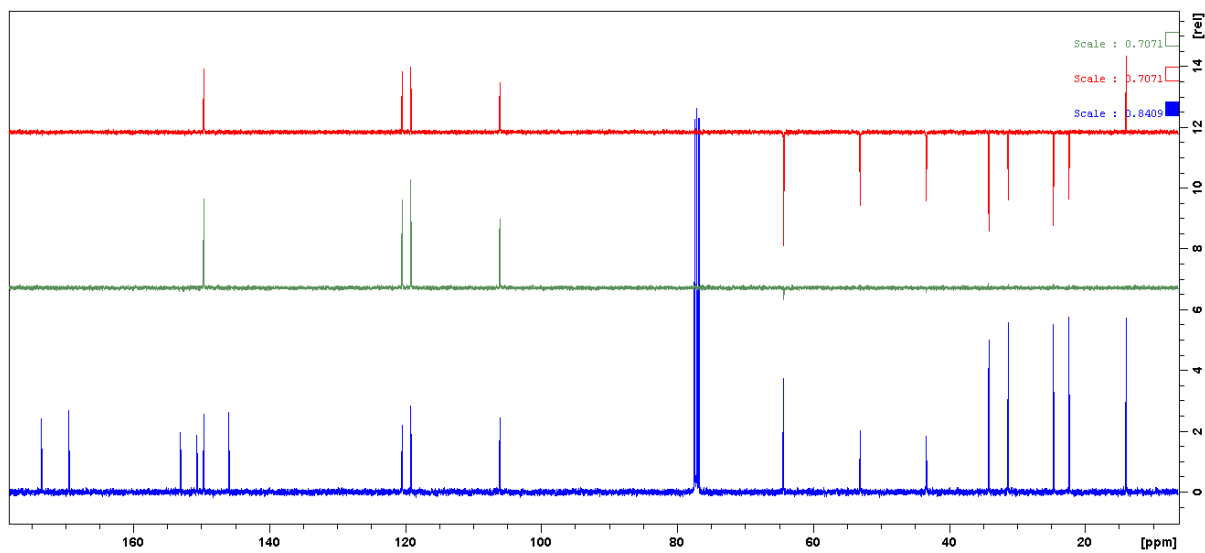


Figure 6.112. ^{13}C NMR Spectrum of L^6 (blue) with the corresponding DEPT-135 (red) and DEPT-90 (green) NMR spectra [100 MHz, CDCl_3].

6.3.4. Mass spectrometry studies of L^5 and L^6 complexes

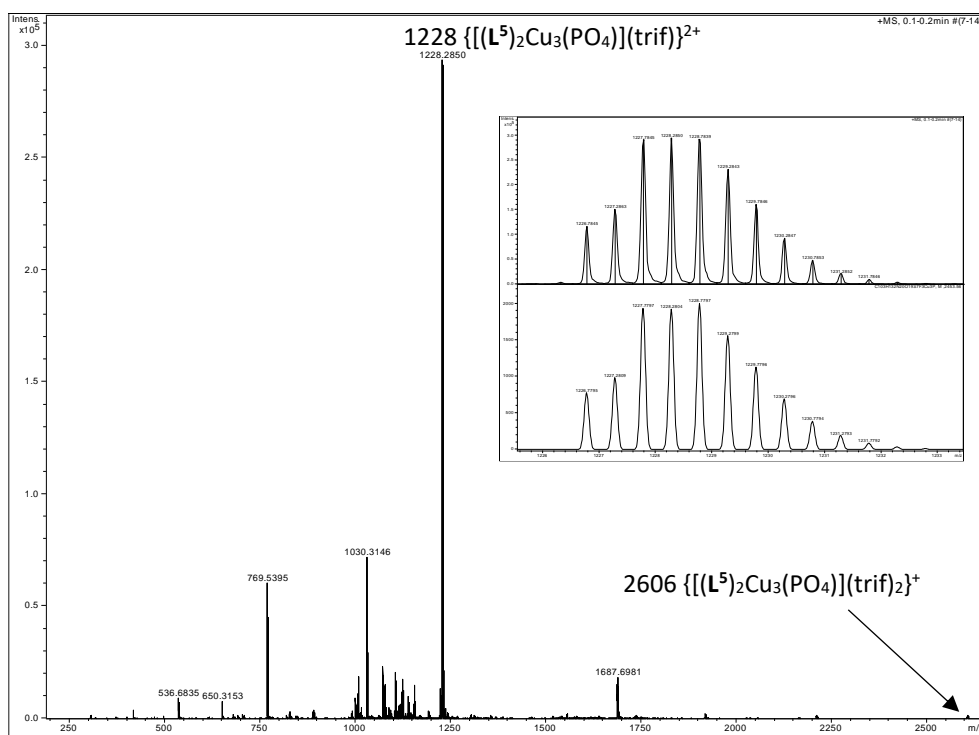


Figure 6.113. ESI-MS of $[(L^5)_2Cu_3(PO_4)](trif)_3$ showing ions at m/z 2606 and 1228 corresponding to $\{[(L^5)_2Cu_3(PO_4)](trif)_2\}^+$ and $\{[(L^5)_2Cu_3(PO_4)](trif)\}^{2+}$ respectively. The isotope pattern for the ion at m/z 1228 is shown inset (top observed and bottom calculated). The ion at m/z 2606 is small but reproducible.

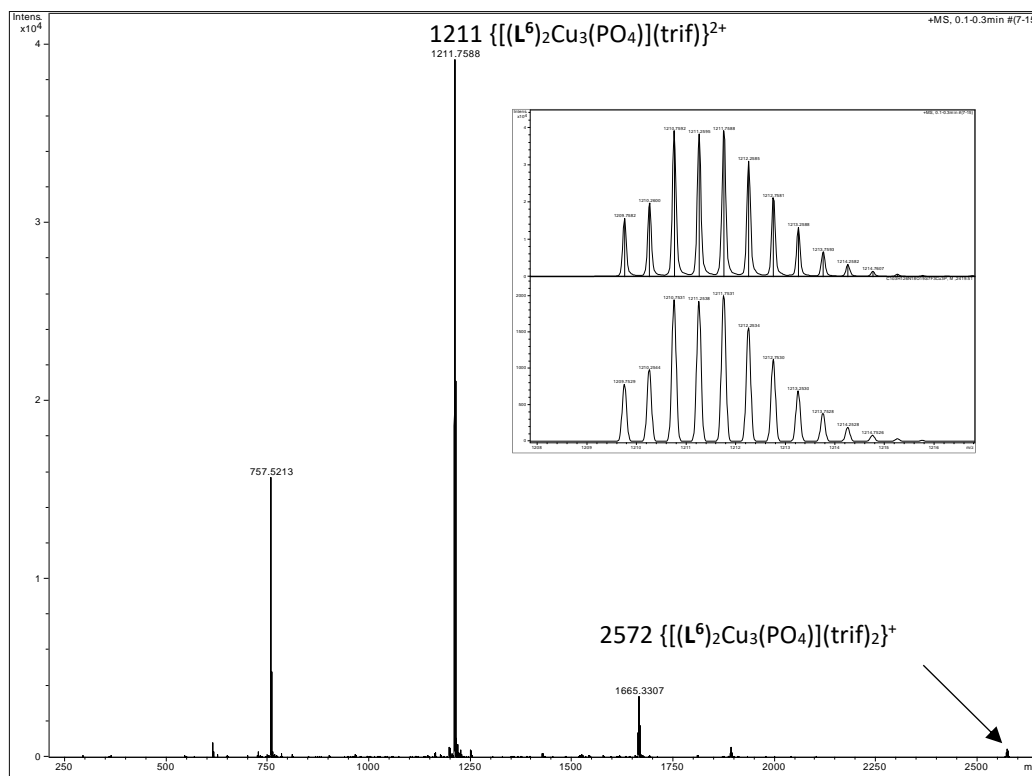


Figure 6.114. ESI-MS of $[(L^6)_2Cu_3(PO_4)](trif)_3$ showing ions at m/z 2572 and 1221 corresponding to $\{[(L^6)_2Cu_3(PO_4)](trif)_2\}^+$ and $\{[(L^6)_2Cu_3(PO_4)](trif)\}^{2+}$ respectively. The isotope pattern for the ion at m/z 1222 is shown inset (top observed and bottom calculated). The ion at m/z 2572 is small but reproducible.

6.3.5. UV-Vis-NIR studies of L^5 and L^6 complexes

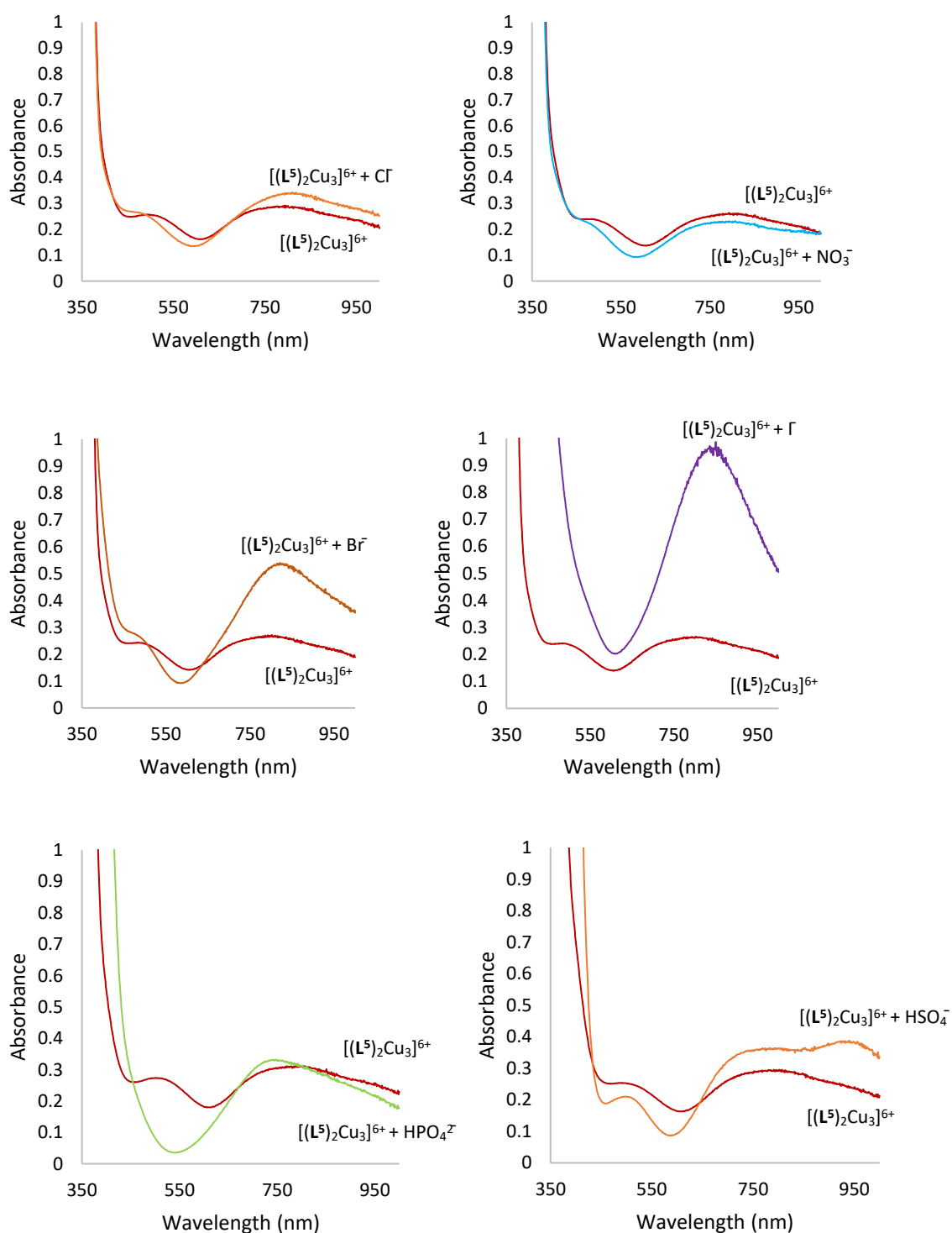


Figure 6.115. UV-Vis-NIR absorption spectra of a solution of $[(L^5)_2Cu_3](trif)_6$ in 3% MeOH in DCM plus the addition of one equivalent of various anions (as either their tetra-N-ethyl- or tetra-N-butyl-ammonium salts). Concentration of $[(L^5)_2Cu_3](trif)_6 = 0.8$ mM.

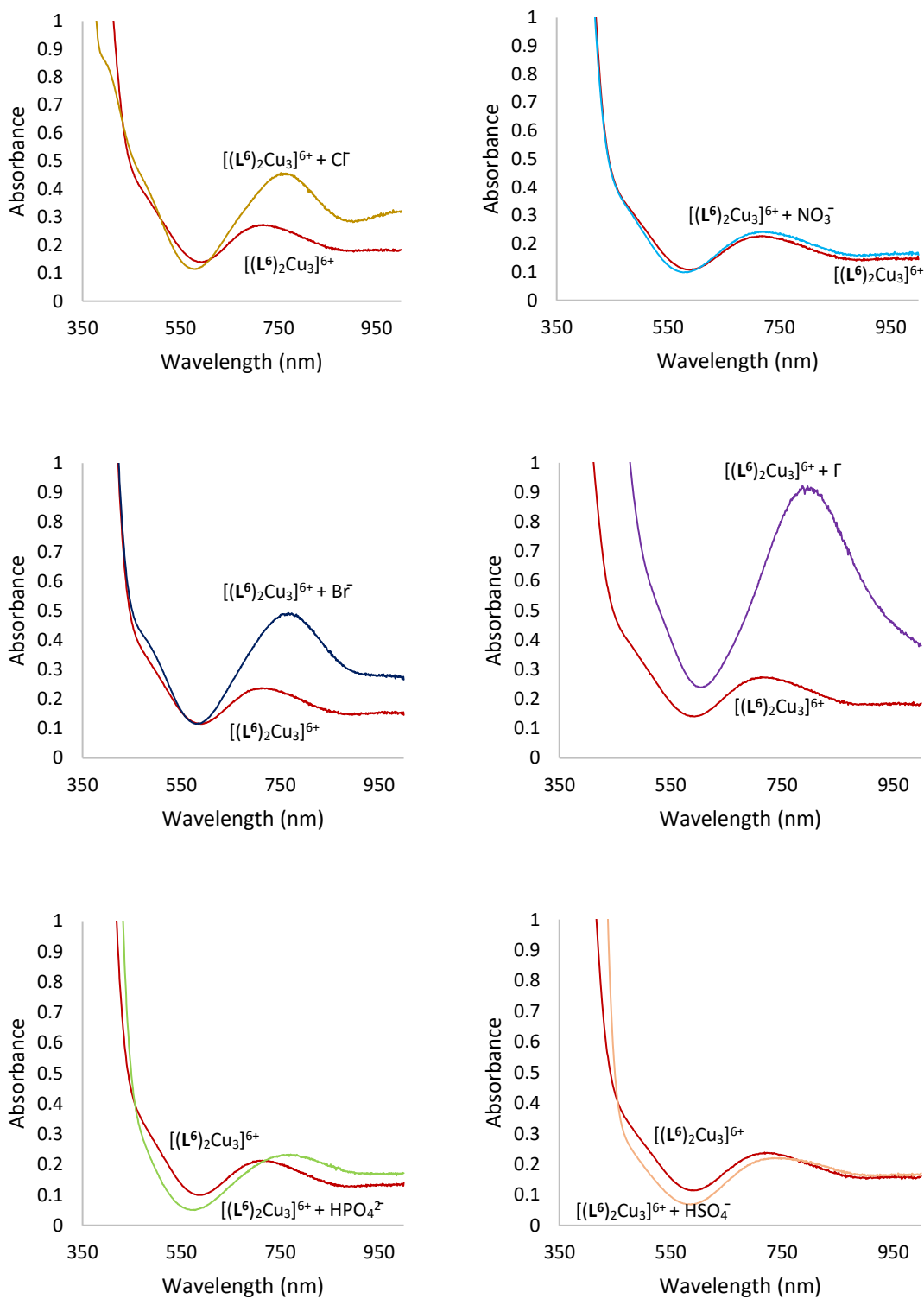


Figure 6.116. UV-Vis-NIR absorption spectra of a solution of $[(L^6)_2Cu_3](trif)_6$ in 3% MeOH in DCM plus the addition of one equivalent of various anions (as either their tetra-N-ethyl- or tetra-N-butyl-ammonium salts). Concentration of $[(L^6)_2Cu_3](trif)_6 = 0.8$ mM.

6.3.6. Ion chromatography studies of L⁵ and L⁶ complexes

Calibration standards of the concentrations 0.2, 0.4, 0.6, 0.8 and 1.0 mM were prepared by the standard dilution of a 20 mM stock of each mixed salt solution used. These are detailed below:

Calibration for Experiment IC-3. Competitive extraction of common anions (NaCl, NaNO₃, NaHSO₄ and NaH₂PO₄). NaHSO₄·H₂O (138.0 mg, 1.0 mmol), NaH₂PO₄ (120.0 mg, 1.0 mmol), NaCl (58.5 mg, 1.0 mmol) and NaNO₃ (85.0 mg, 1.0 mmol) in ultrapure H₂O (50 mL, 18.2 MΩ-cm).

Calibration for Experiment IC-4. Competitive extraction of common anions (NaCl, NaNO₃, Na₂SO₄ and Na₂HPO₄) and total phosphate concentration experiments. Na₂SO₄·10H₂O (322.2 mg, 1.0 mmol), Na₂HPO₄·2H₂O (178.0 mg, 1.0 mmol), NaCl (58.5 mg, 1.0 mmol) and NaNO₃ (85.0 mg, 1.0 mmol) in ultrapure H₂O (50 mL, 18.2 MΩ-cm).

Experiment IC-3. In a typical experiment; To a solution of L⁵ (10 mg, 0.010 mmol) and Cu(trif)₂ (5.37 mg, 0.015 mmol) in 3% MeOH in DCM (3 mL) and ultrapure H₂O (2 mL, 18.2 MΩ-cm) was added 1 mL of a mixed salts solution consisting of NaHSO₄·H₂O (68.3 mg, 0.495 mmol), NaH₂PO₄ (59.4 mg, 0.495 mmol), NaCl (29.0 mg, 0.495 mmol) and NaNO₃ (42.1 mg, 0.495 mmol) in ultrapure H₂O (100 mL, 18.2 MΩ-cm) and this was set to stir at RT for 18 hours. After this time, 2 mL of the aqueous layer was taken and adjusted volumetrically to 5 mL with ultrapure H₂O for analysis by IC (theoretical maximum concentration of each anion 0.66mM). The remaining experiments were carried out in an identical manner but using different mixed salts solutions and the details of these are below.

Experiment IC-4 was carried out in an identical manner to experiment **IC-3**. $\text{Na}_2\text{SO}_4 \cdot 10\text{H}_2\text{O}$ (159.4 mg, 0.495 mmol), $\text{Na}_2\text{HPO}_4 \cdot 2\text{H}_2\text{O}$ (88.1 mg, 0.495 mmol), NaCl (29.0 mg, 0.495 mmol) and NaNO_3 (42.1 mg, 0.495 mmol) in ultrapure H_2O (100 mL, 18.2 M Ω -cm).

Experiment IC-5, measurement of total phosphate extraction. In a typical experiment; To a solution of L^5 (10 mg, 0.010 mmol) and $\text{Cu}(\text{trif})_2$ (5.37 mg, 0.015 mmol) in 3% MeOH in DCM (3 mL) was added 1 mL of a solution containing $\text{Na}_2\text{HPO}_4 \cdot 2\text{H}_2\text{O}$ (88.1 mg, 0.5 mmol) in ultrapure H_2O (100 mL), ultrapure H_2O (2 mL, 18.2 M Ω -cm) and this was set to stir at RT for 18 hours. 2 mL of the aqueous layer was then taken and adjusted volumetrically to 5 mL with ultrapure H_2O for analysis by IC (theoretical maximum concentration of phosphate = 0.66mM).

Further experiments (experiments **IC-6 – IC-10**) were carried out in an identical manner but using differing amounts of L^5 and L^6 and the resulting change in the stoichiometric amount of $\text{Cu}(\text{trif})_2$ to form the complex and the details of these are tabulated below.

Experiment no.	Ligand (L)	Mass of L (mg)	Mass of $\text{Cu}(\text{Trif})_2$ (mg)
IC-6	L^5	11.0	5.91
IC-7	L^5	12.0	6.44
IC-8	L^6	10.0	5.38
IC-9	L^6	11.0	5.92
IC-10	L^6	12.0	6.46

Table 6.9. The masses of ligand and stoichiometric amounts of $\text{Cu}(\text{trif})_2$ used in experiments **IC-6 –**

IC-10.

Conditions and instrumentation:

IC		
Instrument	Metrohm 850 IC system	
Column	Metrohm A Supp 5 column (150 mm x 4.0 mm)	
Oven (°C)	30°C	
Pump	Mobile Phase A	3.2 mM Sodium Carbonate / 1.0 mM Sodium Bicarbonate
	Mobile Phase B	N.A.
	Flow (mls/min)	0.70
	Isocratic/Gradient	Isocratic
	Runtime (mins)	20
Injector	Volume (µl)	10
Suppressor	Regenerant Solution	0.1 M Oxalic acid / 0.1 M Sulfuric acid in 10% acetone
Detector	Conductance / PAD	Conductance

Table 6.10. Conditions for ion chromatography analysis of L^5 and L^6 complexes.

Experiment IC-3 (calibration curves):

[Cl ⁻] / mM	Peak area
0.2	1.071
0.4	2.118
0.6	3.237
0.8	4.359
1	5.457

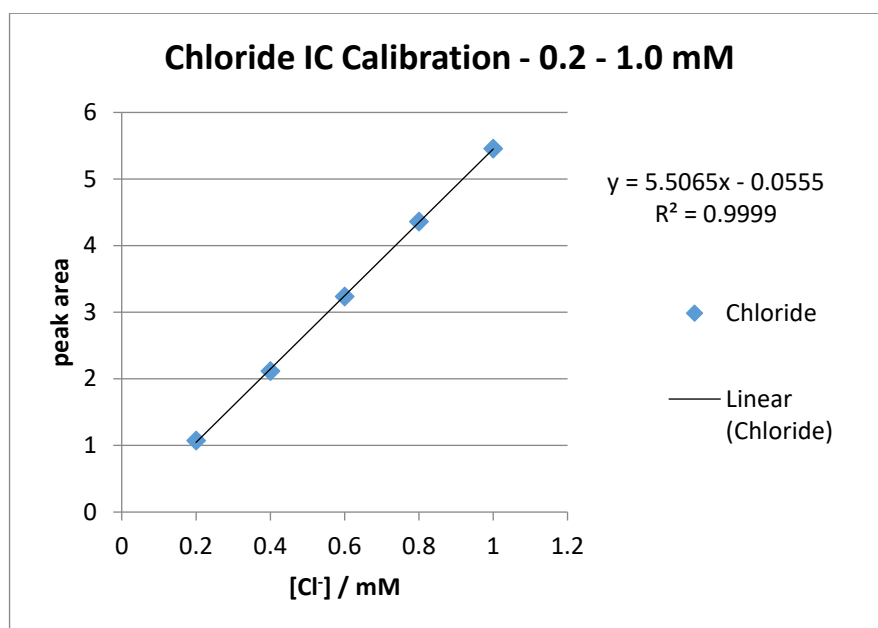


Figure 6.117. IC calibration curve of 0.2 – 1.0 mM solutions of NaCl for experiment IC-3.

[NO ₃ ⁻] / mM	Peak area
0.2	1.034
0.4	2.046
0.6	3.143
0.8	4.236
1	5.296

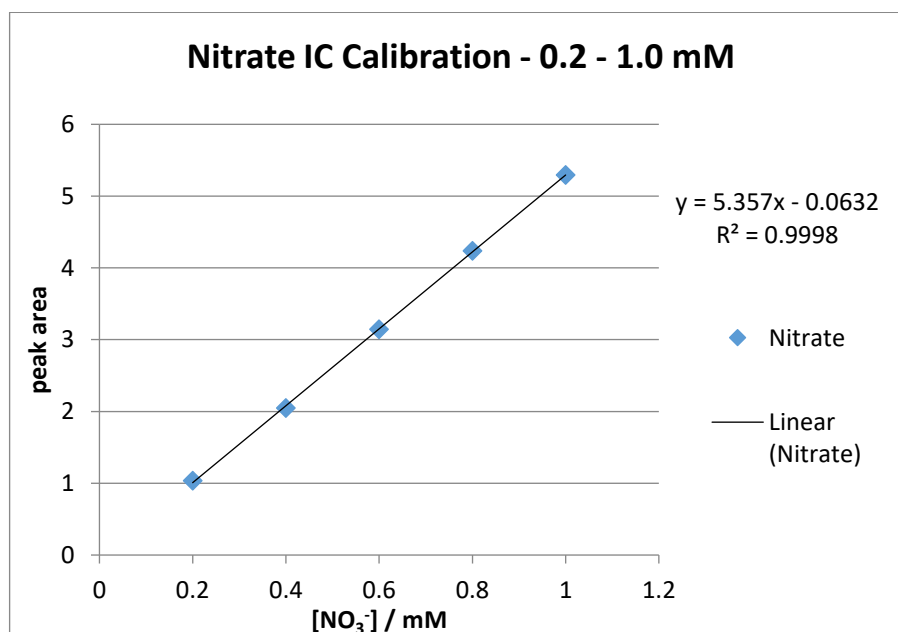


Figure 6.118. IC calibration curve of 0.2 – 1.0 mM solutions of NaNO₃ for experiment IC-3.

[PO ₄ ³⁻] / mM	Peak area
0.2	0.849
0.4	1.723
0.6	2.676
0.8	3.624
1	4.569

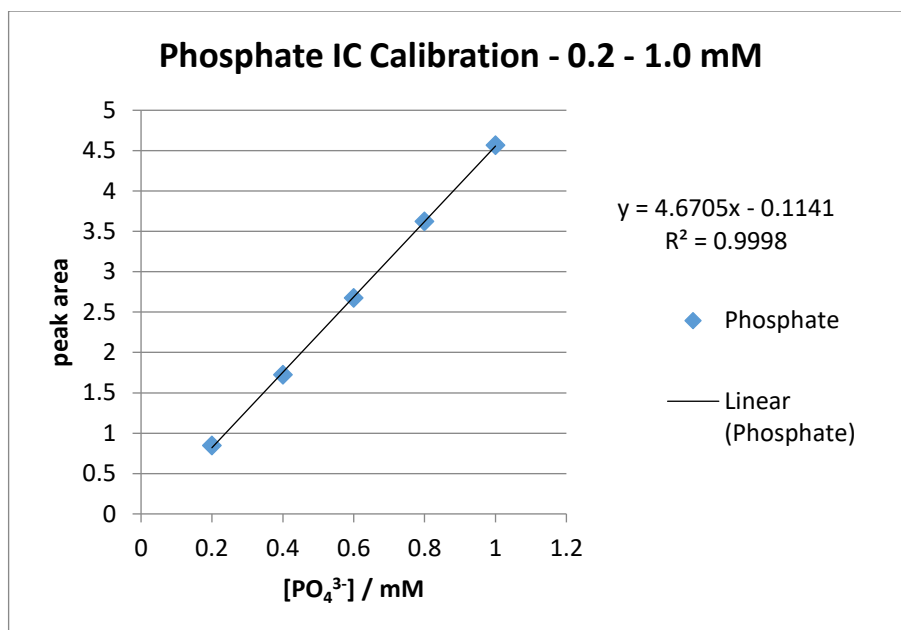


Figure 6.119. IC calibration curve of 0.2 – 1.0 mM solutions of NaH₂PO₄ for experiment IC-3.

[SO ₄ ²⁻] / mM	Peak area
0.2	2.184
0.4	4.35
0.6	6.645
0.8	8.93
1	11.161

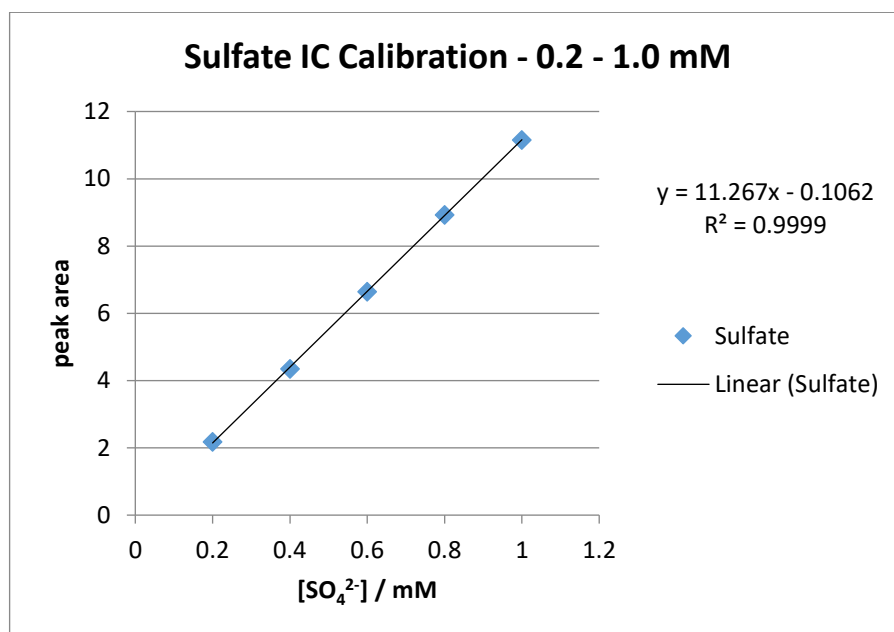


Figure 6.120. IC calibration curve of 0.2 – 1.0 mM solutions of NaHSO₄·H₂O for experiment IC-3.

Experiment IC-4 (calibration curves):

[Cl ⁻] / mM	Peak area
0.2	1.07
0.4	2.122
0.6	3.232
0.8	4.332
1	5.436

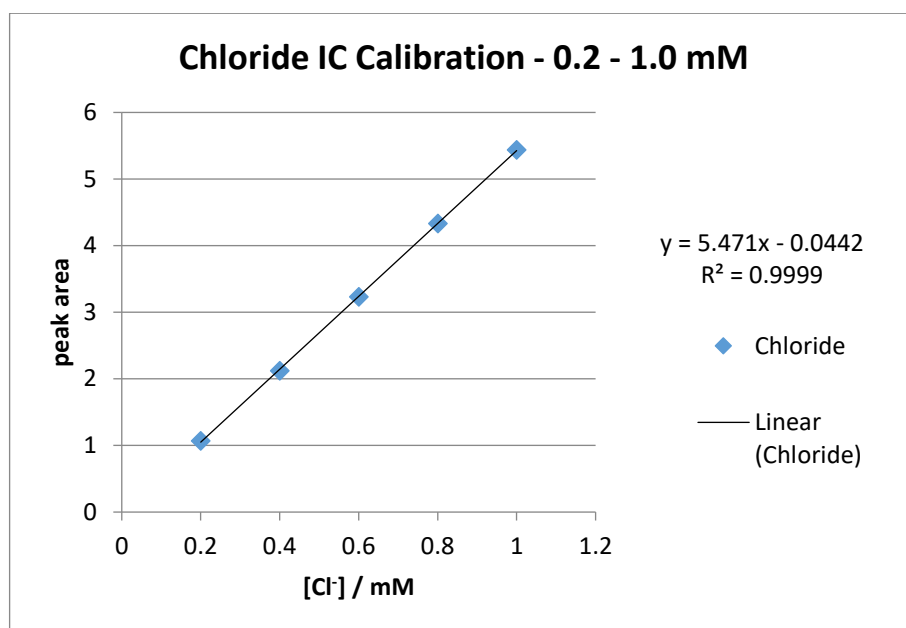


Figure 6.121. IC calibration curve of 0.2 – 1.0 mM solutions of NaCl for experiment IC-4.

[NO ₃ ⁻] / mM	Peak area
0.2	1.033
0.4	2.05
0.6	3.138
0.8	4.208
1	5.282

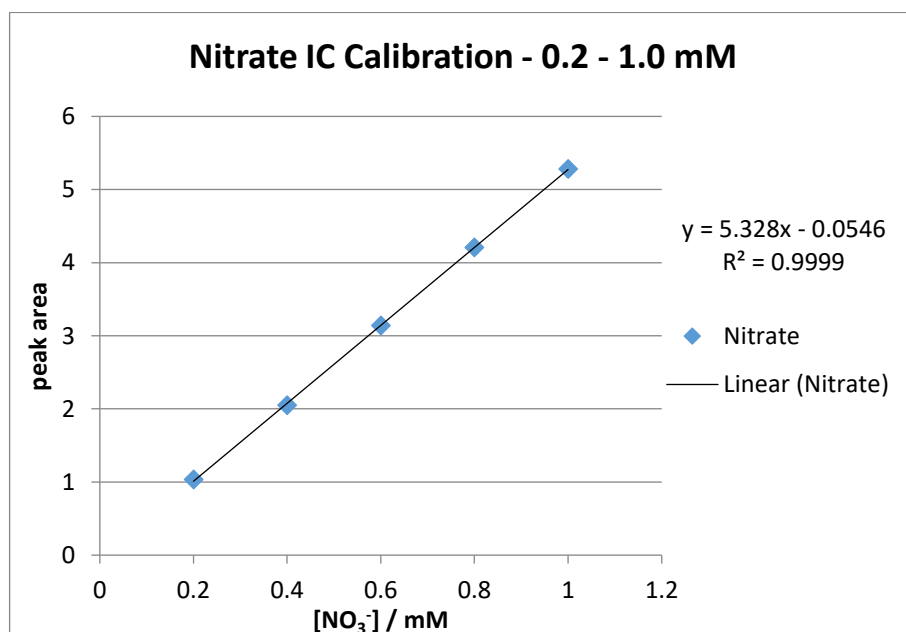


Figure 6.122. IC calibration curve of 0.2 – 1.0 mM solutions of NaNO₃ for experiment IC-4.

[PO ₄ ³⁻] / mM	Peak area
0.2	0.855
0.4	1.727
0.6	2.658
0.8	3.603
1	4.545

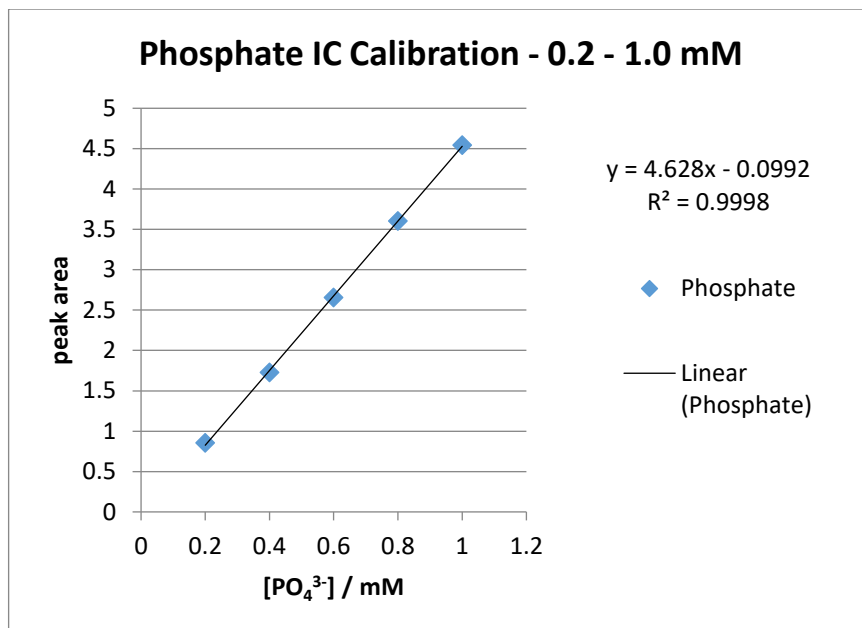


Figure 6.123. IC calibration curve of 0.2 – 1.0 mM solutions of Na₂HPO₄·2H₂O for experiment IC-4.

[SO ₄ ²⁻] / mM	Peak area
0.2	2.189
0.4	4.337
0.6	6.598
0.8	8.891
1	11.091

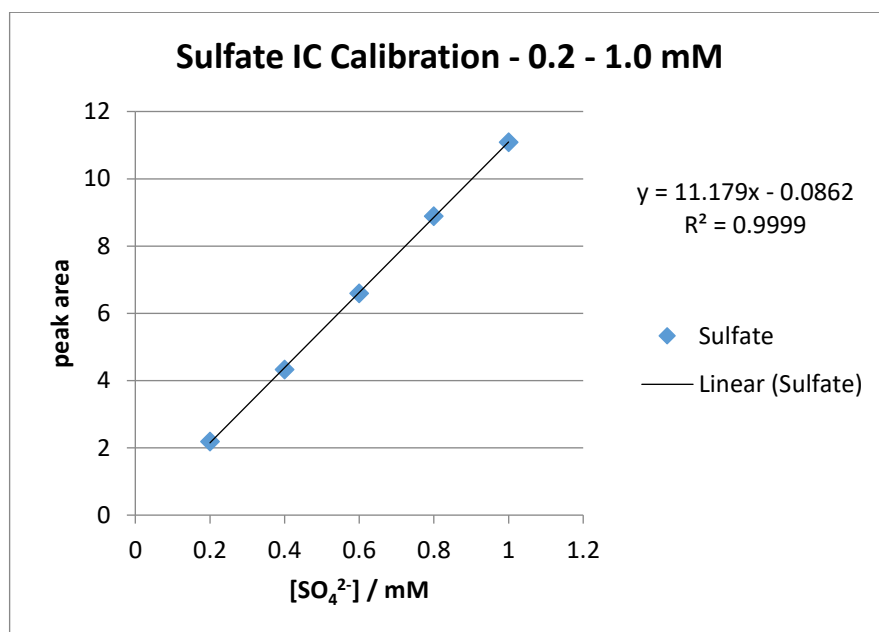


Figure 6.124. IC calibration curve of 0.2 – 1.0 mM solutions of Na₂SO₄·10H₂O for experiment IC-4.

Experiment IC-5 – IC-8 (calibration curves):

[Na ₂ HPO ₄] / mM	Peak area
0.2	0.88
0.4	1.84
0.6	2.84
0.8	3.874
1	4.875

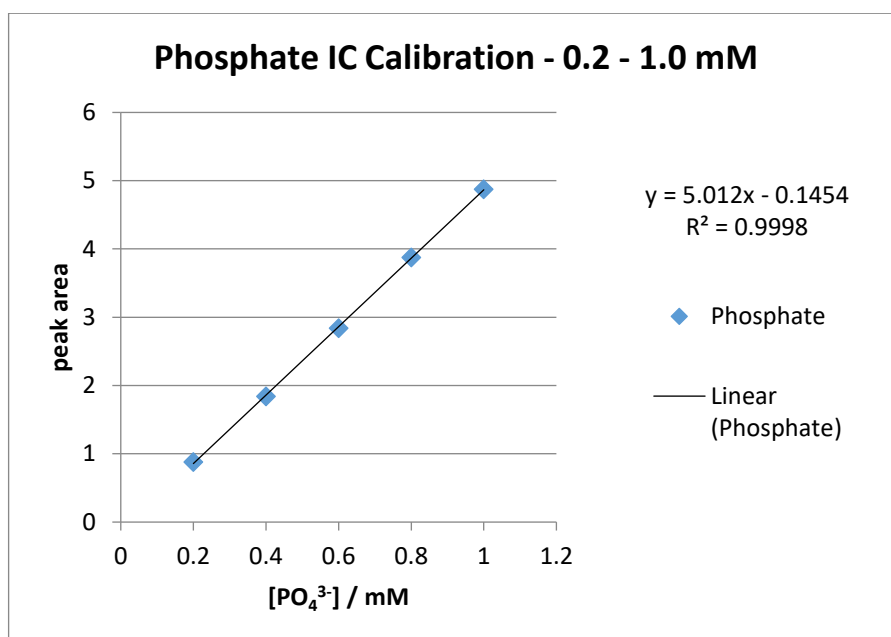


Figure 6.125. IC calibration curve of 0.2 – 1.0 mM solutions of Na₂HPO₄·2H₂O for experiment IC-5 –

IC-8.

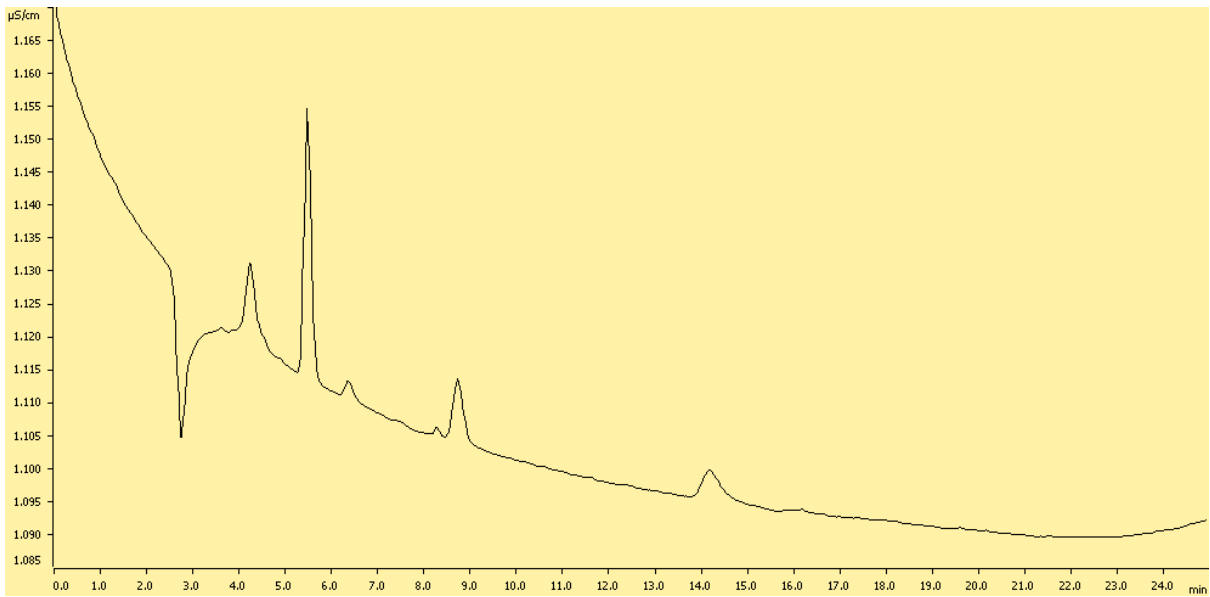


Figure 6.126. An IC plot of the background signals present in the ultrapure water used for experiments IC-3 – IC-10.

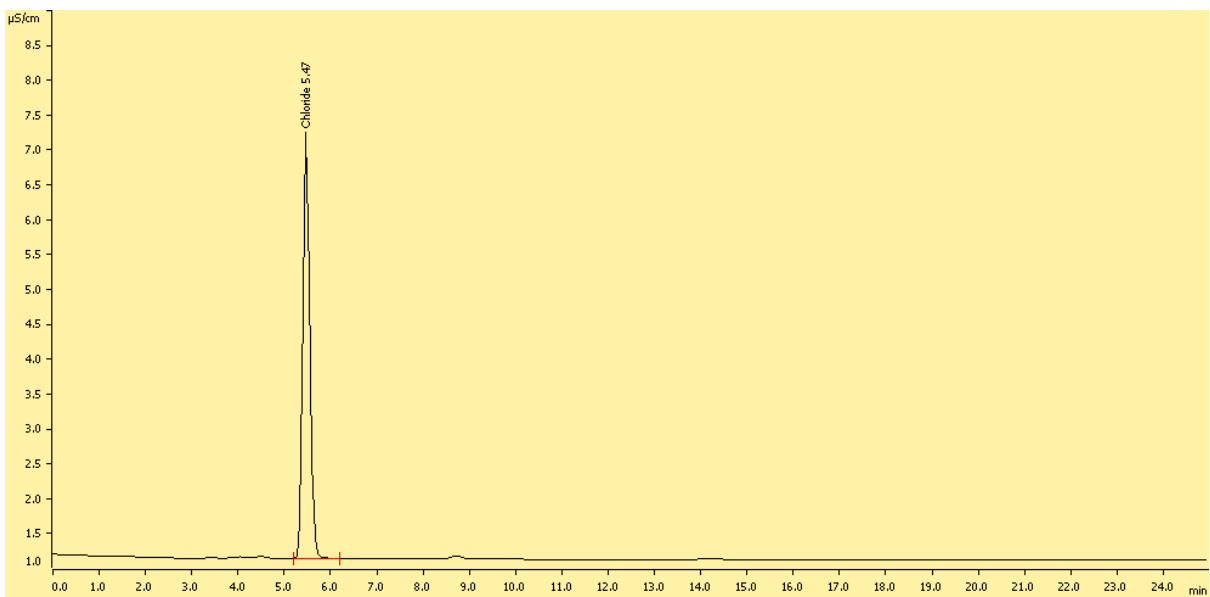


Figure 6.127. An IC plot showing the individual peak for Cl^- ions at 0.6 mM concentration at 5.47 minutes.

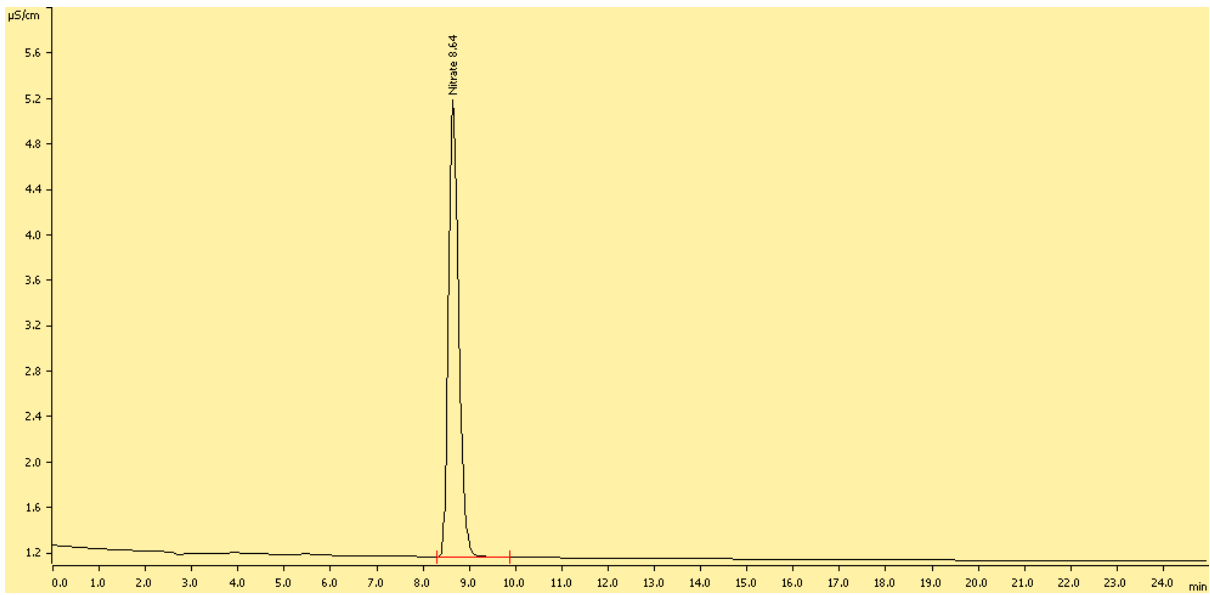


Figure 6.128. An IC plot showing the individual peak for NO_3^- ions at 0.6 mM concentration at 8.64 minutes.

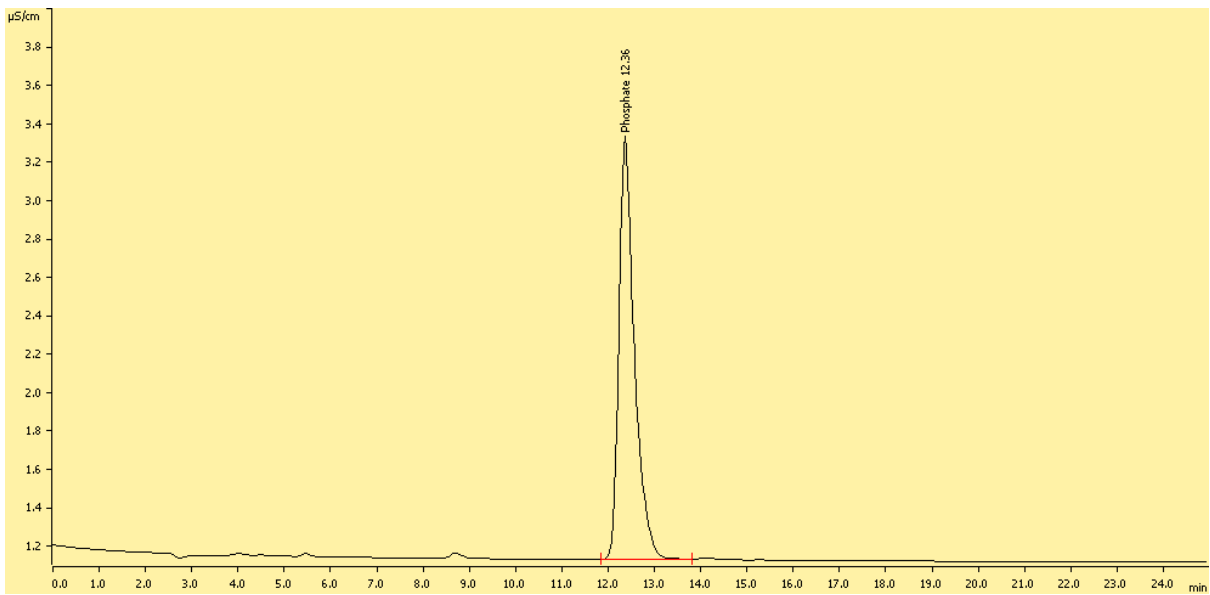


Figure 6.129. An IC plot showing the individual peak for PO_4^{3-} ions at 0.6 mM concentration at 12.36 minutes.

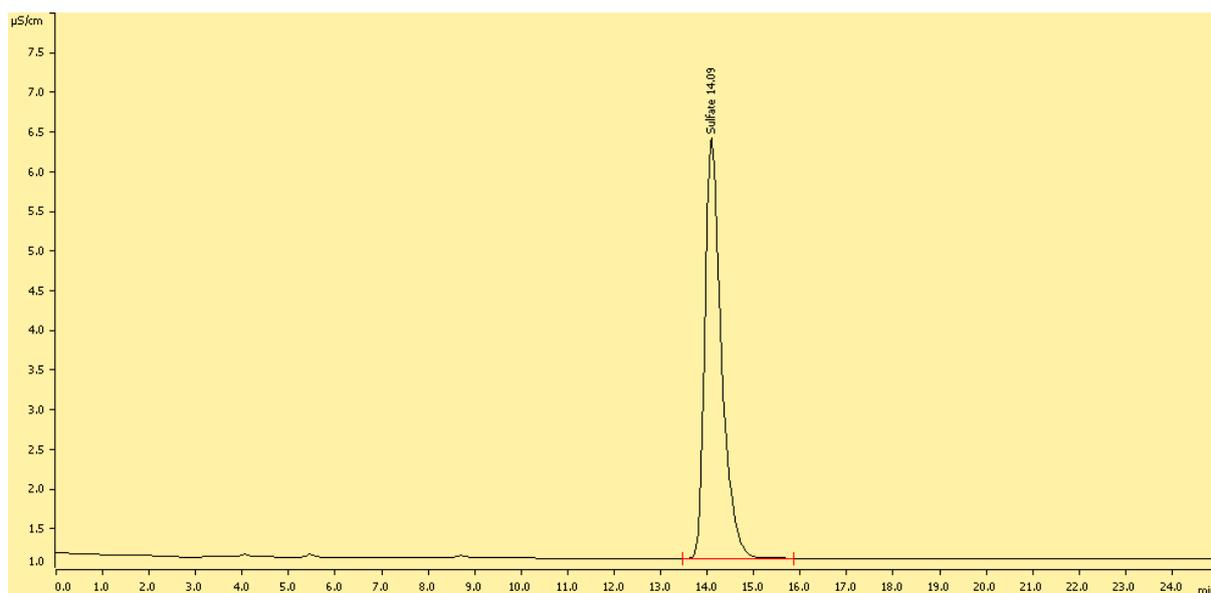


Figure 6.130. An IC plot showing the individual peak for SO_4^{2-} ions at 0.6 mM concentration at 14.09 minutes.

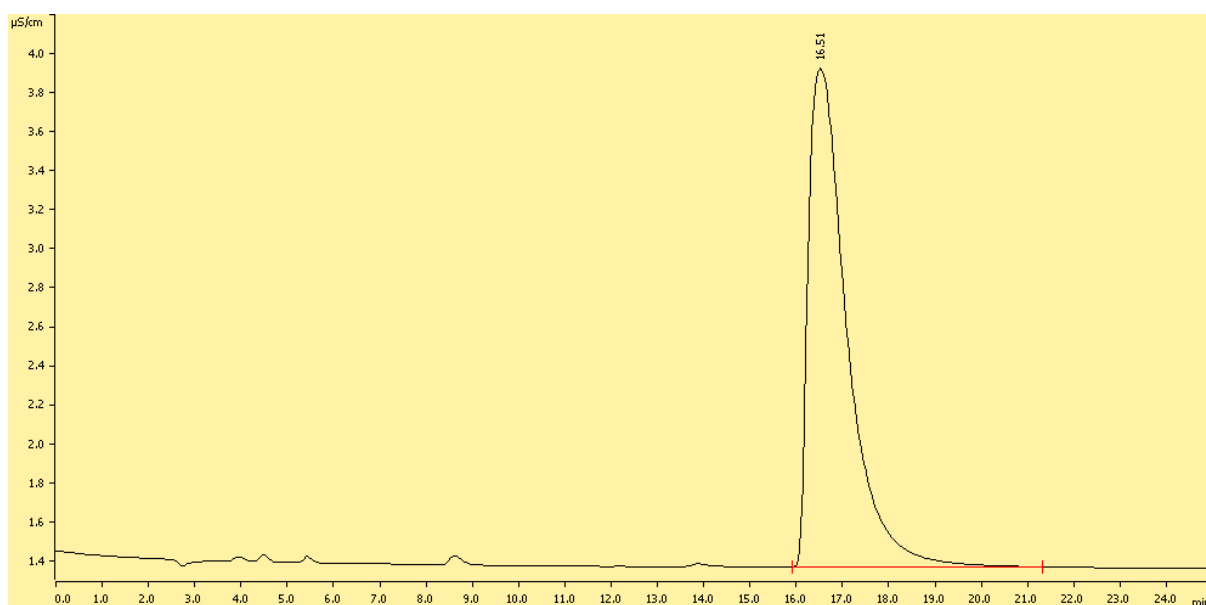


Figure 6.131. An IC plot showing the individual peak for triflate ions at 0.6 mM concentration at 16.51 minutes.

Experiment IC-3 (monosodium salts):

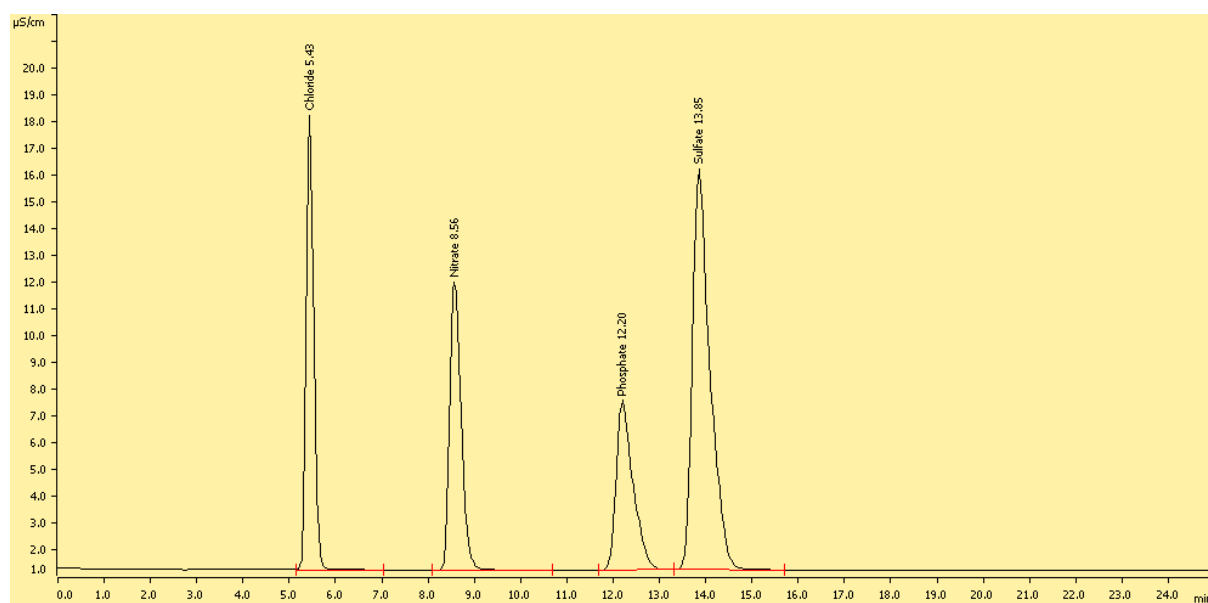


Figure 6.132. The IC chromatogram showing the four individual peaks of the mono-sodium salts at 0.6 mM concentration with the peaks at 5.43, 8.56, 12.20 and 13.85 minutes corresponding to Cl^- , NO_3^- , PO_4^{3-} and SO_4^{2-} ions respectively.

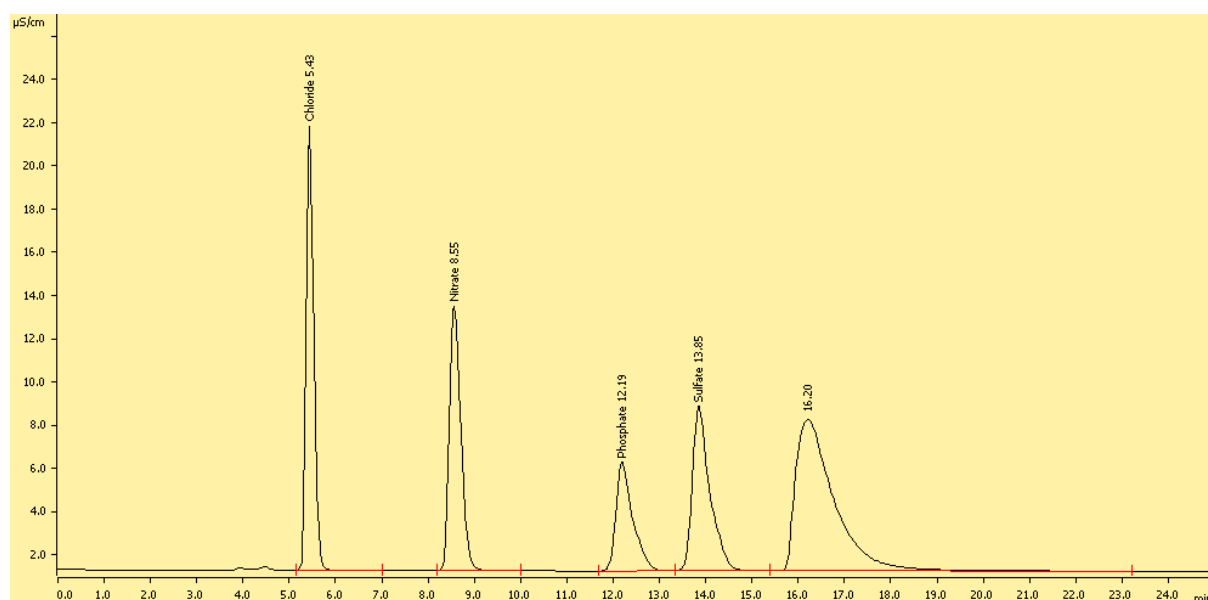


Figure 6.133. The IC chromatogram of experiment IC-3 after treatment with the $[(\text{L}^5)_2\text{Cu}_3](\text{trif})_6$ complex showing the amounts of Cl^- , NO_3^- , PO_4^{3-} and SO_4^{2-} ions present. The peak at 16.20 minutes corresponds to triflate anions.

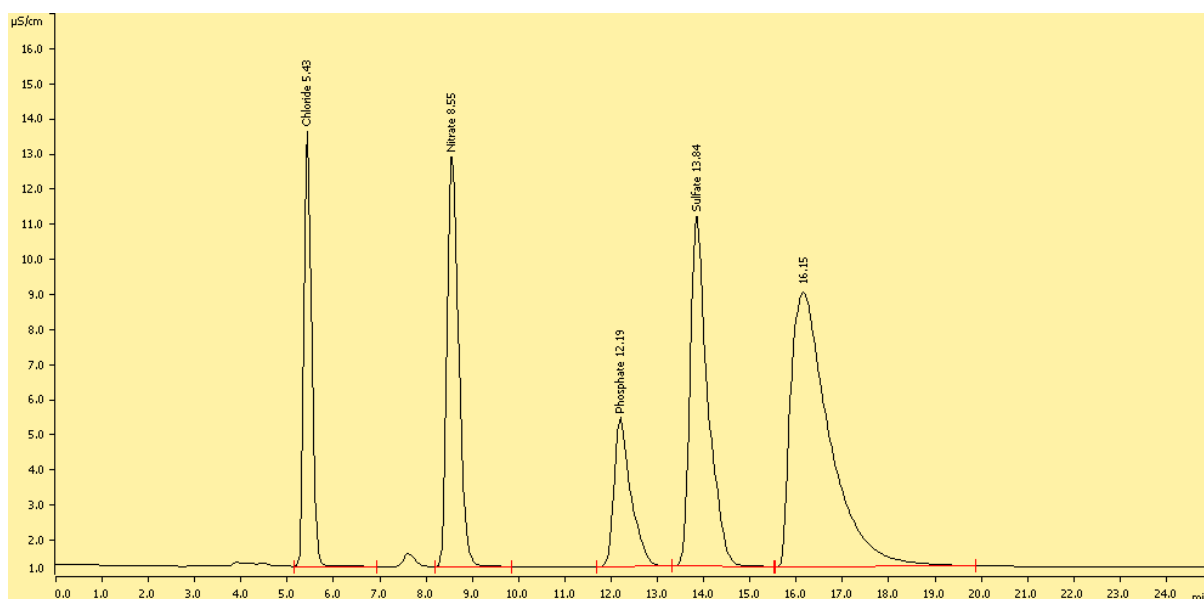


Figure 6.134. The IC chromatogram of experiment IC-3 after treatment with the $[(L^6)_2Cu_3](trif)_6$ complex showing the amounts of Cl^- , NO_3^- , PO_4^{3-} and SO_4^{2-} ions present. The peak at 16.15 minutes corresponds to the triflate anions.

Salt	Amount of salt present remaining after treatment with $[(L^5)_2Cu_3](trif)_6$ (mM)	Amount of salt present remaining after treatment with $[(L^6)_2Cu_3](trif)_6$ (mM)
Cl^-	0.73 (110%)	0.45 (68%)
NO_3^-	0.69 (105%)	0.65 (99%)
PO_4^{3-}	0.48 (73%)	0.41 (62%)
SO_4^{2-}	0.31 (47%)	0.40 (61%)

Table 6.11. Amount of Cl^- , NO_3^- , PO_4^{3-} and SO_4^{2-} ions present in the aqueous solution after treatment with the $[(L^5)_2Cu_3](trif)_6$ and the $[(L^6)_2Cu_3](trif)_6$ complexes. Initial theoretical maximum concentration of each anion = 0.66 mM.

Experiment IC-4 (disodium salts):

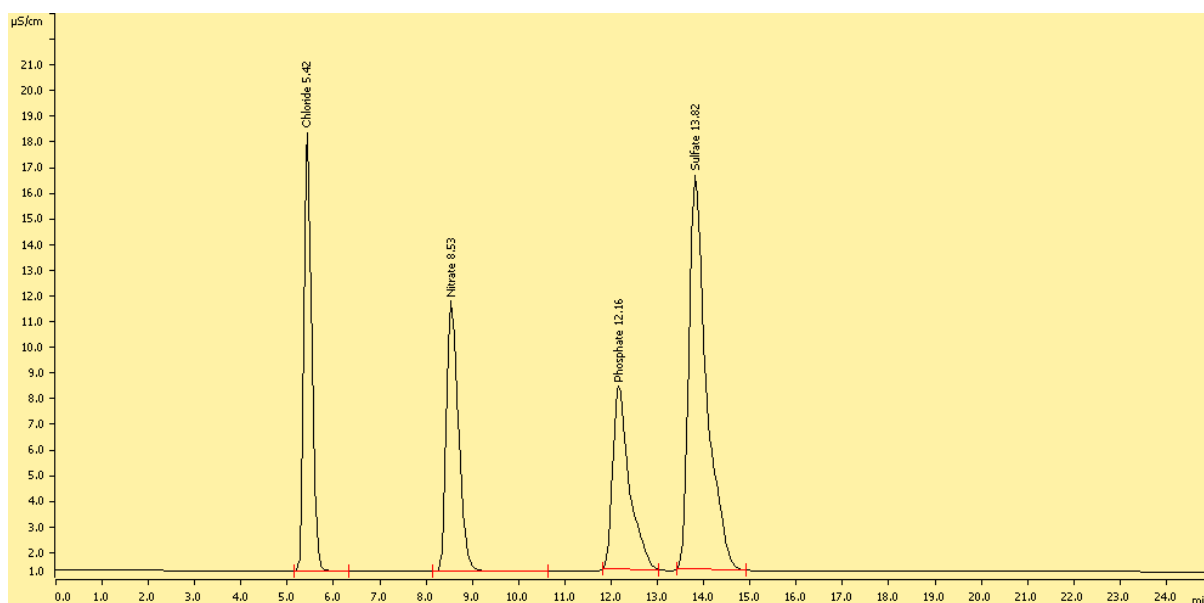


Figure 6.135. The IC chromatogram plot showing the four individual peaks of the di-sodium salts at 0.6 mM concentration with the peaks at 5.42, 8.53, 12.16 and 13.82 minutes corresponding to Cl^- , NO_3^- , PO_4^{3-} and SO_4^{2-} ions respectively.

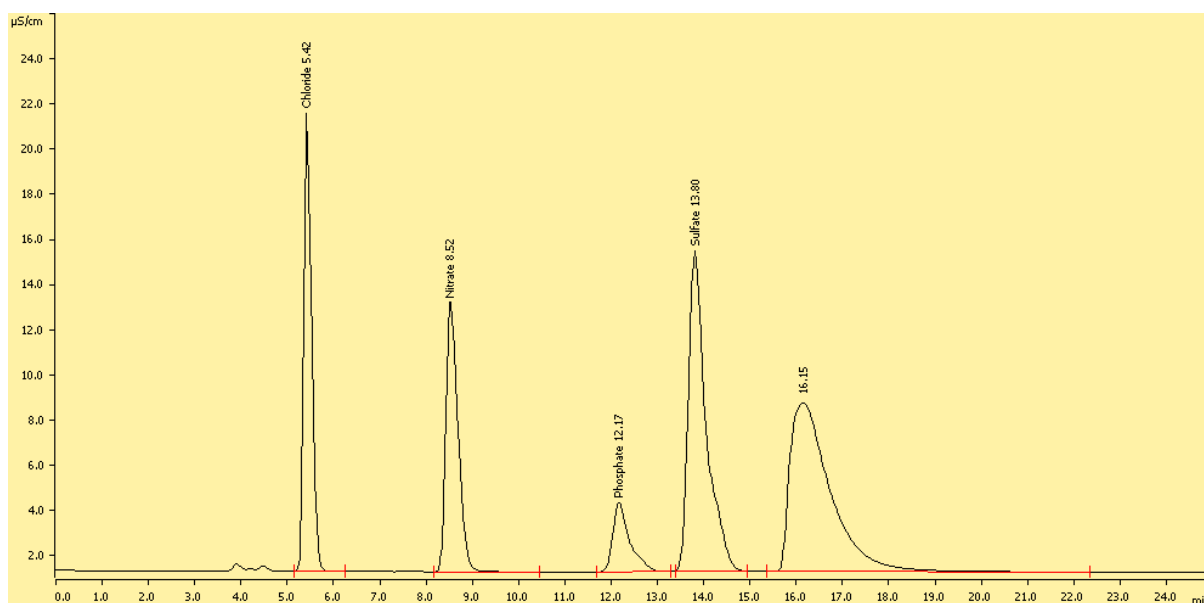


Figure 6.136. The IC chromatogram of experiment IC-4 after treatment with the $[(\text{L}^5)_2\text{Cu}_3](\text{trif})_6$ complex showing the decrease in amounts of Cl^- , NO_3^- , PO_4^{3-} and SO_4^{2-} ions present. The peak at 16.15 minutes corresponds to triflate anions.

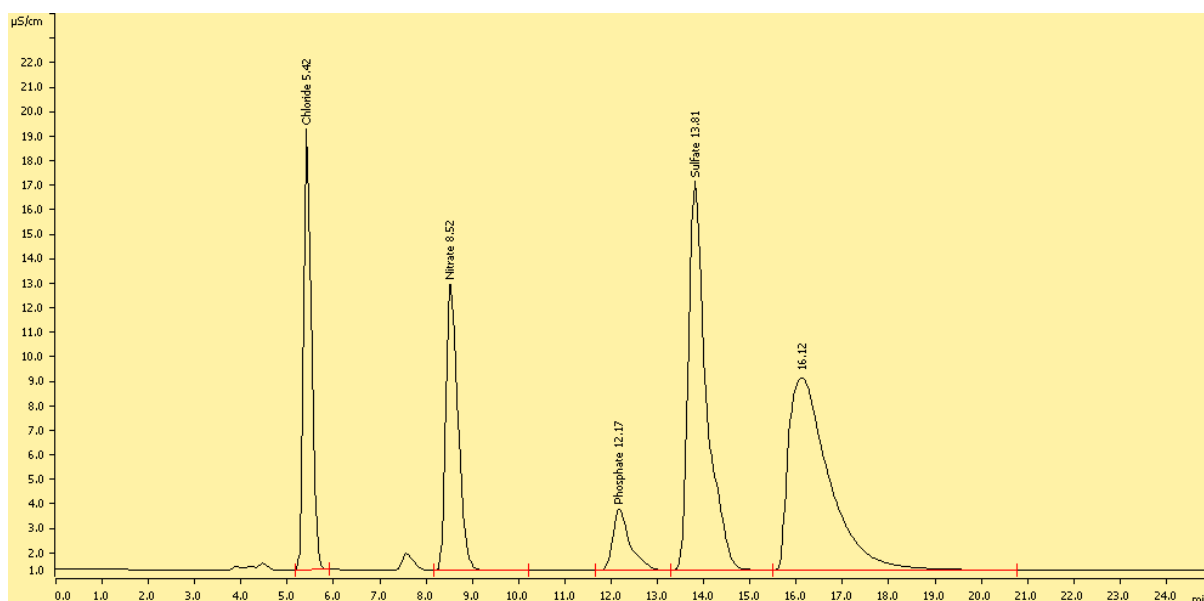


Figure 6.137. The IC chromatogram of experiment IC-4 after treatment with the $[(L^6)_2Cu_3](trif)_6$ complex showing the decrease in amounts of Cl^- , NO_3^- , PO_4^{3-} and SO_4^{2-} ions present. The peak at 16.12 minutes corresponds to triflate anions.

Salt	Amount of salt present remaining after treatment with $[(L^5)_2Cu_3](trif)_6$ (mM)	Amount of salt present remaining after treatment with $[(L^6)_2Cu_3](trif)_6$ (mM)
Cl^-	0.71 (107%)	0.64 (97%)
NO_3^-	0.67 (101%)	0.66 (100%)
PO_4^{3-}	0.27 (41%)	0.24 (36%)
SO_4^{2-}	0.56 (85%)	0.63 (95%)

Table 6.12. Amount of Cl^- , NO_3^- , PO_4^{3-} and SO_4^{2-} ions present in the aqueous solution after treatment with the $[(L^5)_2Cu_3](trif)_6$ and the $[(L^6)_2Cu_3](trif)_6$ complexes. Initial theoretical maximum concentration of each anion = 0.66 mM.

Experiments IC-5 – IC-7:

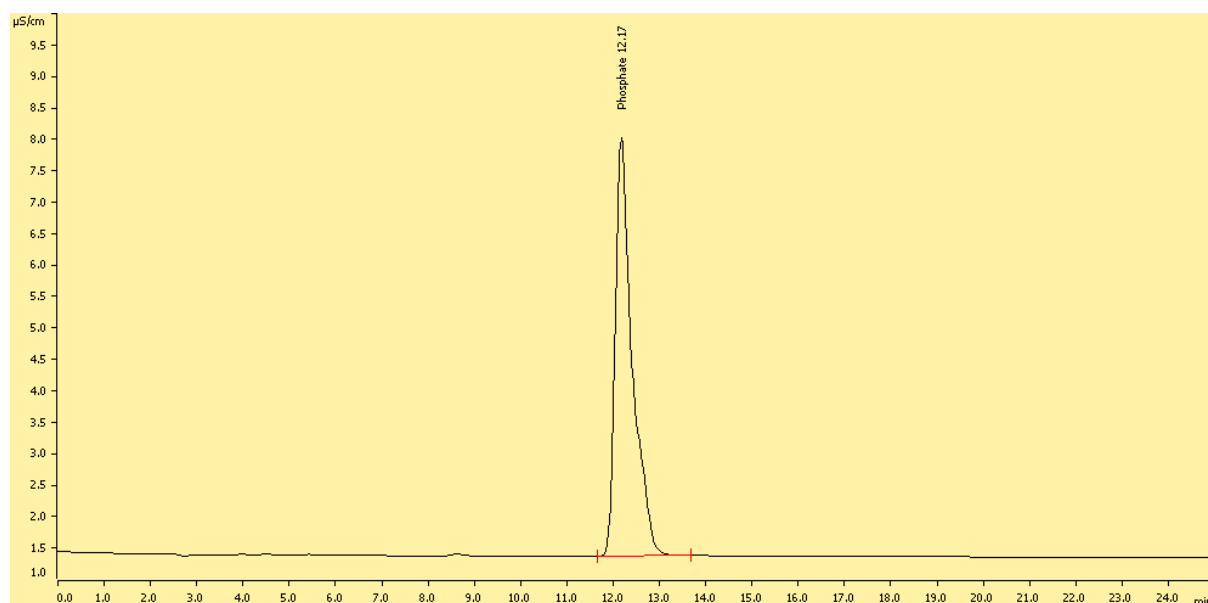


Figure 6.138. An IC plot showing the individual peak for PO_4^{3-} ions at 0.66 mM concentration at 12.17 minutes.

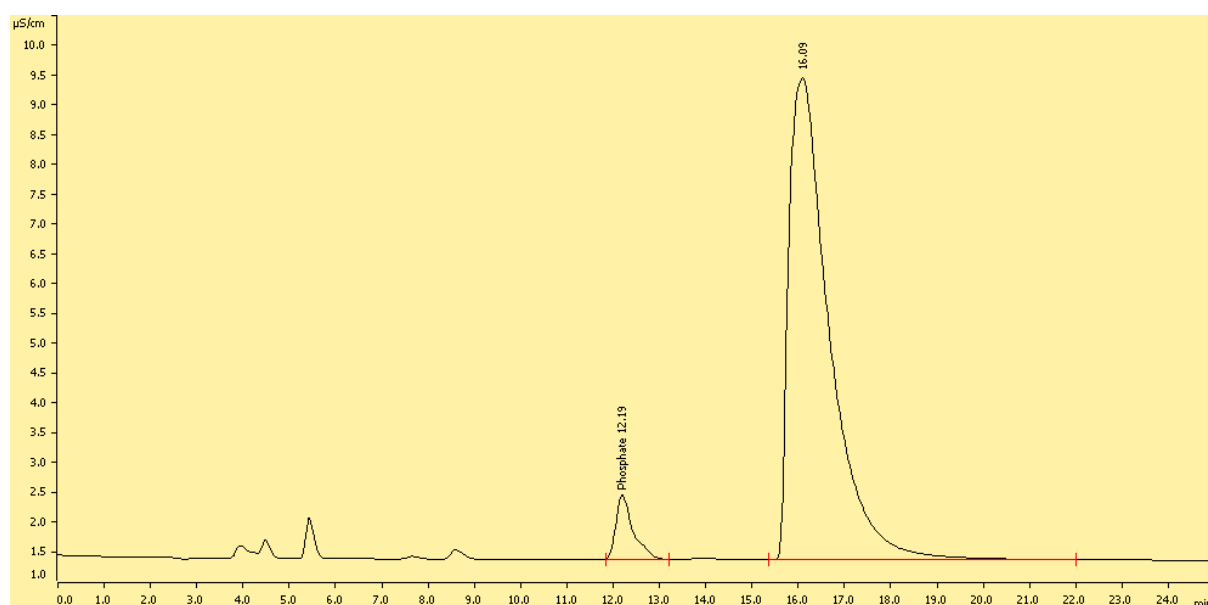


Figure 6.139. The IC chromatogram for experiment IC-5 showing the total amount of PO_4^{3-} ions left in the aqueous solution after treatment with the $[(\text{L}^5)_2\text{Cu}_3](\text{trif})_6$ complex. The peak at 16.09 minutes corresponds to triflate anions.

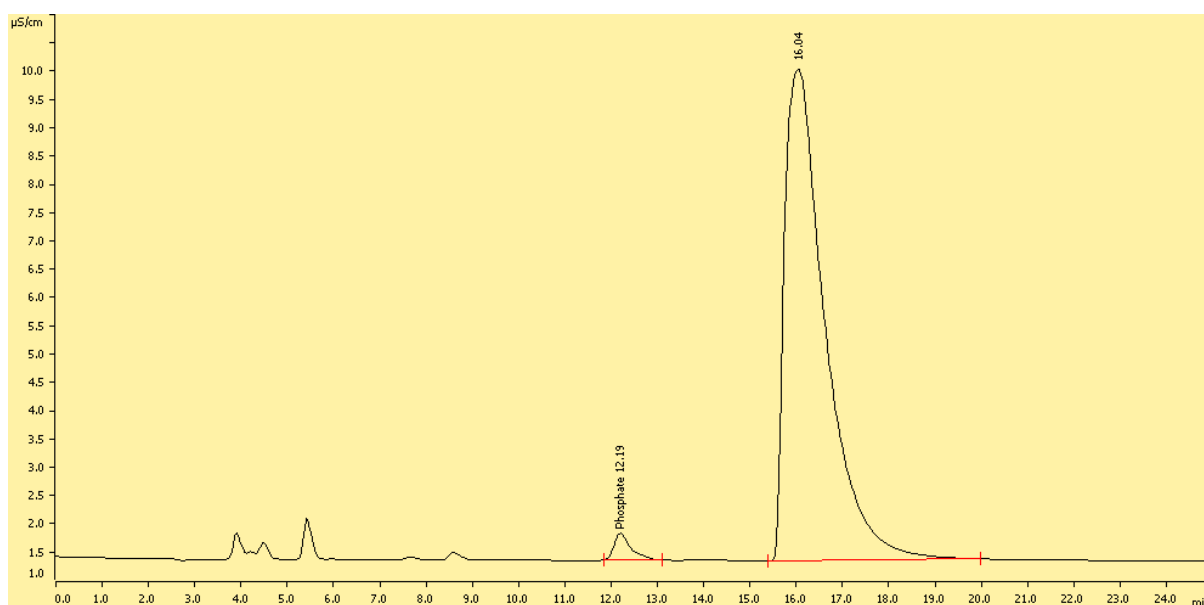


Figure 6.140. The IC chromatogram for experiment IC-6 showing the total amount of PO_4^{3-} ions left in the aqueous solution after treatment with the $[(\text{L}^5)_2\text{Cu}_3](\text{trif})_6$ complex where the complex was formed from the corresponding masses of ligand and $\text{Cu}(\text{trif})_2$ in Table 3. The peak at 16.04 minutes corresponds to triflate anions.

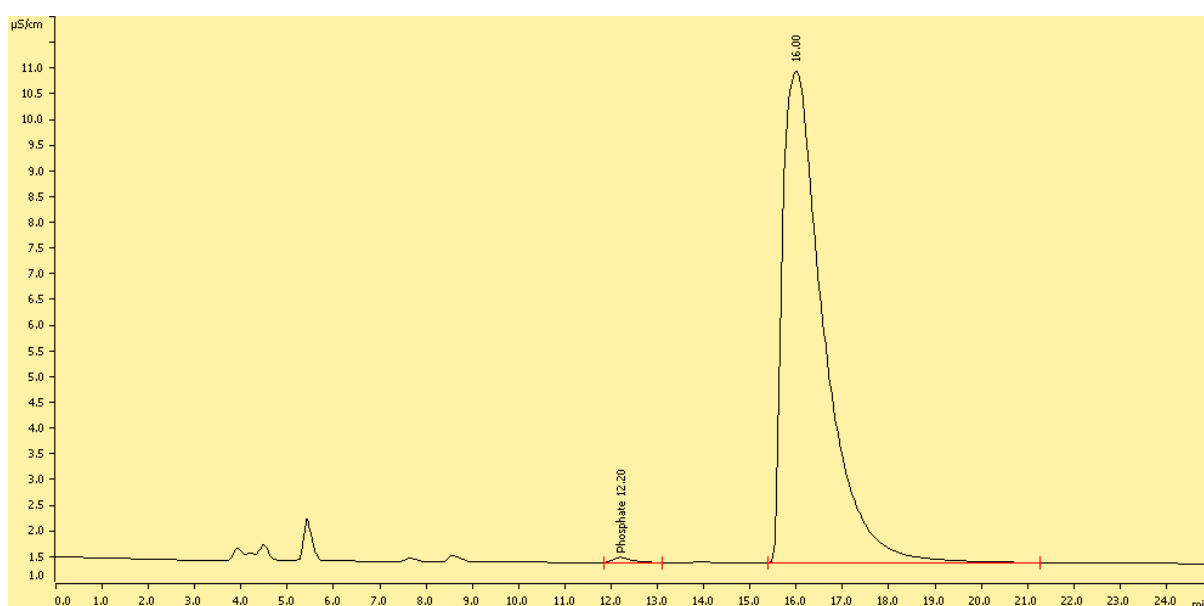


Figure 6.141. The IC chromatogram for experiment IC-7 showing the total amount of PO_4^{3-} ions left in the aqueous solution after treatment with the $[(\text{L}^5)_2\text{Cu}_3](\text{trif})_6$ complex where the complex was

formed from the corresponding masses of ligand and $\text{Cu}(\text{trif})_2$ in Table 3. The peak at 16.00 minutes corresponds to triflate anions.

Experiment no.	Amount of PO_4^{3-} ions present (mM) after treatment with the corresponding stoichiometric amount of $[(\text{L}^5)_2\text{Cu}_3](\text{trif})_6$ detailed in Table 3
IC-5	0.122 (18%)
IC-6	0.07 (11%)
IC-7	0.038 (6%)

Table 6.13. Decrease in the amount of PO_4^{3-} ions present in the aqueous solution as the ratio of the $[(\text{L}^5)_2\text{Cu}_3](\text{trif})_6$ complex present increases (initial concentration of $\text{PO}_4^{3-} = 0.66 \text{ mM}$).

Experiments IC-8 – IC-10:

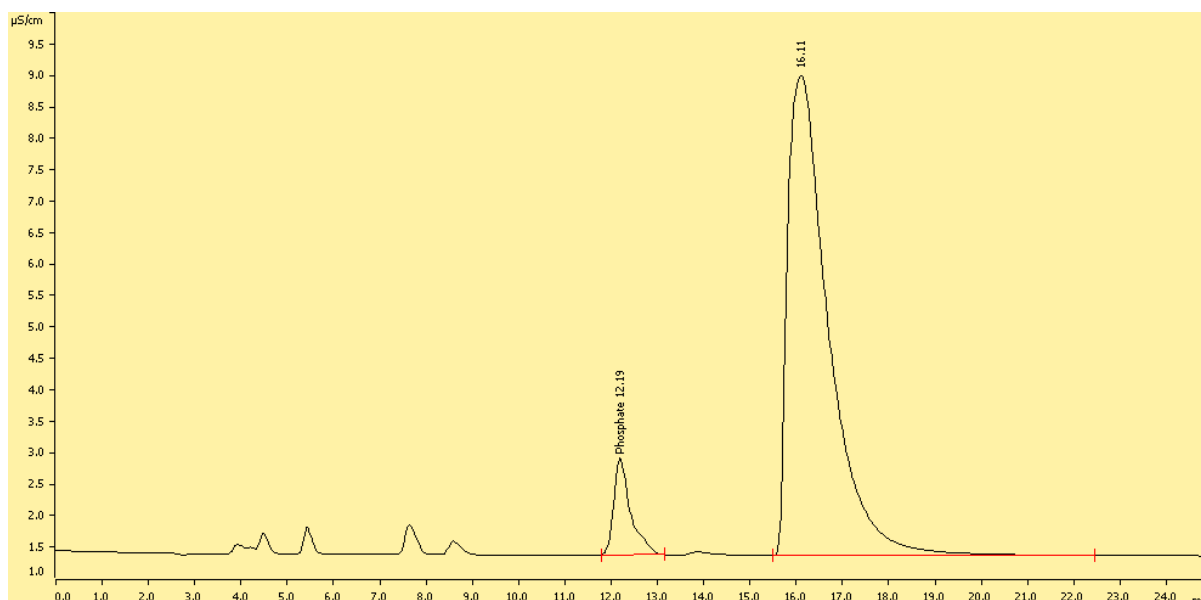


Figure 6.142. The IC chromatogram for experiment IC-8 showing the total amount of PO_4^{3-} ions left in the aqueous solution after treatment with the $[(\text{L}^6)_2\text{Cu}_3](\text{trif})_6$ complex where the complex was

formed from the corresponding masses of ligand and $\text{Cu}(\text{trif})_2$ in Table 3. The peak at 16.11 minutes corresponds to triflate anions.

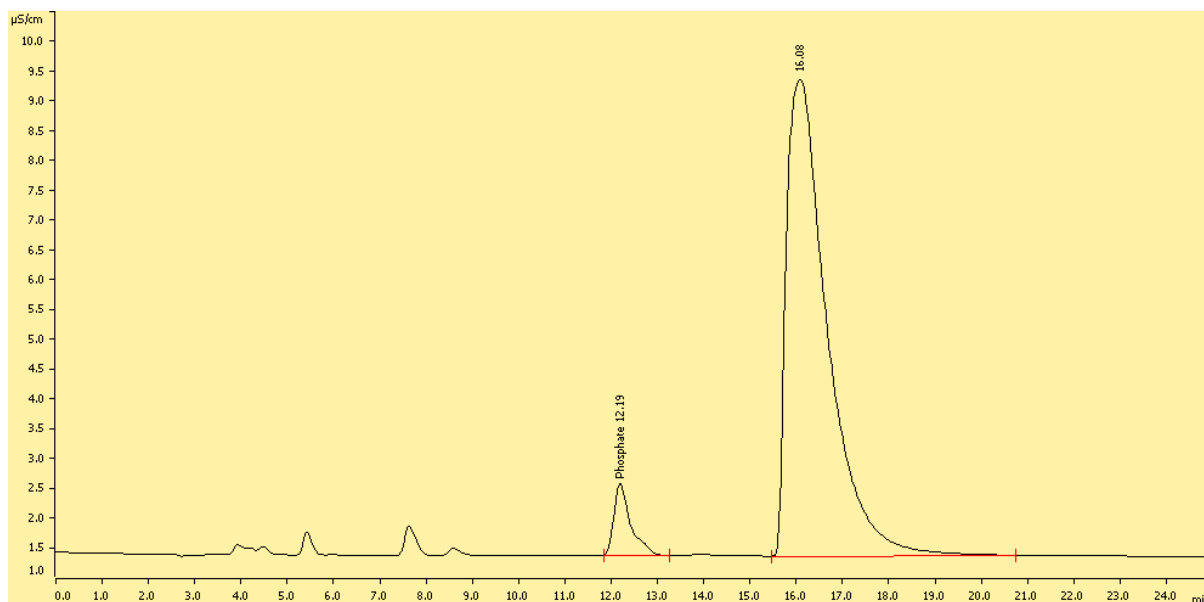


Figure 6.143. The IC chromatogram for experiment IC-9 showing the total amount of PO_4^{3-} ions left in the aqueous solution after treatment with the $[(\text{L}^6)_2\text{Cu}_3](\text{trif})_6$ complex where the complex was formed from the corresponding masses of ligand and $\text{Cu}(\text{trif})_2$ in Table 3. The peak at 16.08 minutes corresponds to triflate anions.

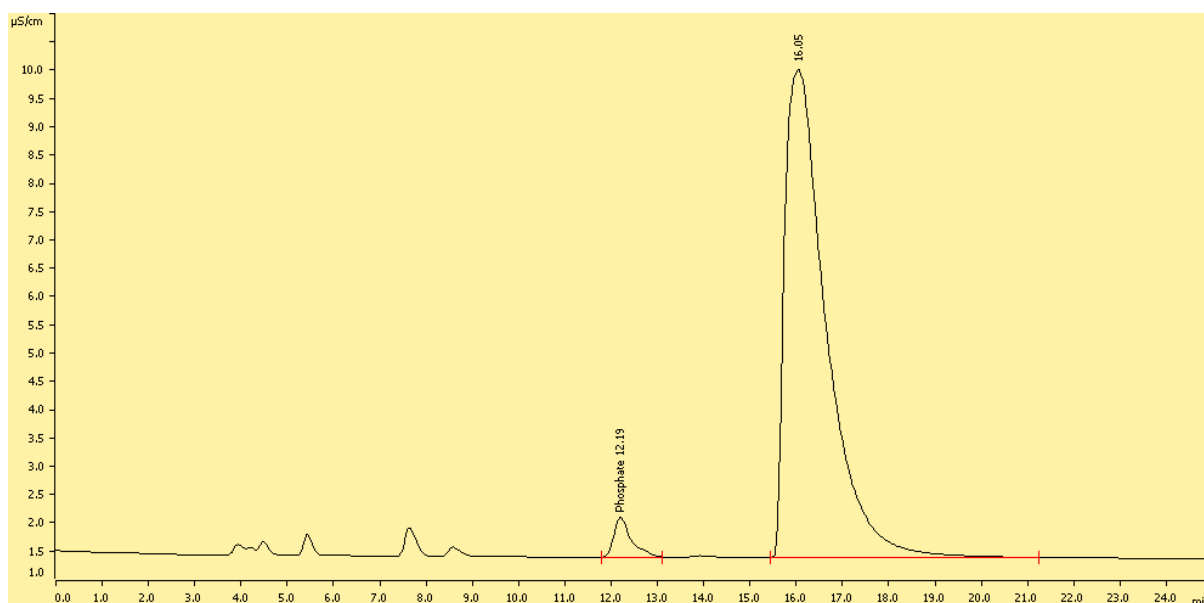


Figure 6.144. The IC chromatogram for experiment **IC-10** showing the total amount of PO_4^{3-} ions left in the aqueous solution after treatment with the $[(L^6)_2Cu_3](trif)_6$ complex where the complex was formed from the corresponding masses of ligand and $Cu(trif)_2$ in Table 3. The peak at 16.05 minutes corresponds to triflate anions.

Experiment no.	Amount of PO_4^{3-} ions present (mM) after treatment with the corresponding stoichiometric amount of $[(L^6)_2Cu_3](trif)_6$ detailed in Table 3
IC-8	0.159 (24%)
IC-9	0.133 (20%)
IC-10	0.090 (14%)

Table 6.14. Decrease in the amount of PO_4^{3-} ions present in the aqueous solution as the amount of the $[(L^6)_2Cu_3](trif)_6$ complex present increases (initial concentration of $PO_4^{3-} = 0.66$ mM).

7. References

- 1 J.-M. Lehn, *Angew. Chemie Int. Ed. English*, 1988, **27**, 89–112.
- 2 J.-M. Lehn, *Angew. Chemie Int. Ed. English*, 1990, **29**, 1304–1319.
- 3 J.-M. Lehn, *Science*, 1993, **260**, 1762–1763.
- 4 J.-M. Lehn, in *Supramolecular Chemistry: Concepts and Perspectives*, 1995, pp. 1–9.
- 5 S. B. T. Nguyen, D. L. Gin, J. T. Hupp and X. Zhang, *Proc. Natl. Acad. Sci. U. S. A.*, 2001, **98**, 11849–11850.
- 6 X. Zhao, F. Pan, H. Xu, M. Yaseen, H. Shan, C. A. E. Hauser, S. Zhang and J. R. Lu, *Chem. Soc. Rev.*, 2010, **39**, 3480–3498.
- 7 R. V. Uljijn and A. M. Smith, *Chem. Soc. Rev.*, 2008, **37**, 664–675.
- 8 H. Kuhn and J. Waser, *Angew. Chemie Int. Ed. English*, 1981, **20**, 500–520.
- 9 E. Pungor, *Anal. Chem.*, 1967, **39**, 28–45.
- 10 W. S. Wadsworth, *Org. React.*, 1977, 73–253.
- 11 R. B. King, *Acc. Chem. Res.*, 1970, **3**, 417–427.
- 12 R. J. Phipps, G. L. Hamilton and F. D. Toste, *Nat. Chem.*, 2012, **4**, 603–614.
- 13 F. J. Millero, *Annu. Rev. Earth Planet. Sci.*, 1974, **2**, 101–150.
- 14 M. Mohapatra, S. Anand, B. K. Mishra, D. E. Giles and P. Singh, *J. Environ. Manage.*, 2009, **91**, 67–77.
- 15 L. L. Diosady, J. O. Alberti, S. Fitzgerald and M. G. Venkatesh Mannar, *Food Nutr. Bull.*, 1999, **20**, 208–214.
- 16 Z.-H. Wang, S.-X. Li and S. Malhi, *J. Sci. Food Agric.*, 2007, **88**, 7–23.
- 17 D. Cordell, J. O. Drangert and S. White, *Glob. Environ. Chang.*, 2009, **19**, 292–305.
- 18 J. A. Foley, N. Ramankutty, K. A. Brauman, E. S. Cassidy, J. S. Gerber, M. Johnston, N. D. Mueller, C. O’Connell, D. K. Ray, P. C. West, C. Balzer, E. M. Bennett, S. R. Carpenter, J. Hill, C. Monfreda, S. Polasky, J. Rockström, J. Sheehan, S. Siebert, D. Tilman and D. P. M. Zaks, *Nature*, 2011, **478**, 337–342.
- 19 E. Bennet and J. Elser, *Nature*, 2011, **478**, 29–31.
- 20 D. Cordell and S. White, *Annu. Rev. Environ. Resour.*, 2014, **39**, 161–188.
- 21 J. Grantham, *Nature*, 2012, **491**, 303.
- 22 L. Guo, *Science*, 2007, **317**, 1166.
- 23 R. Stone, *Science*, 2011, **333**, 1210–1211.
- 24 S. Kilpimaa, H. Runtti, T. Kangas, U. Lassi and T. Kuokkanen, *J. Ind. Eng. Chem.*, 2015, **21**, 1354–1364.
- 25 A. M. Michalak, E. J. Anderson, D. Beletsky, S. Boland, N. S. Bosch, T. B. Bridgeman, J. D. Chaffin, K. Cho, R. Confesor, I. Daloglu, J. V. DePinto, M. A. Evans, G. L. Fahnenstiel, L. He, J. C. Ho, L.

- Jenkins, T. H. Johengen, K. C. Kuo, E. LaPorte, X. Liu, M. R. McWilliams, M. R. Moore, D. J. Posselt, R. P. Richards, D. Scavia, A. L. Steiner, E. Verhamme, D. M. Wright and M. A. Zagorski, *Proc. Natl. Acad. Sci. U. S. A.*, 2013, **110**, 6448–6452.
- 26 D. W. Schindler, R. E. Hecky and G. K. McCullough, *J. Great Lakes Res.*, 2012, **38**, 6–13.
- 27 K. D. Jöhnk, J. Huisman, J. Sharples, B. Sommeijer, P. M. Visser and J. M. Stroom, *Glob. Chang. Biol.*, 2008, **14**, 495–512.
- 28 T. Hunter, *Philos. Trans. R. Soc. B Biol. Sci.*, 2012, **367**, 2513–2516.
- 29 D. J. Matthews and M. E. Gerritsen, *Targeting Protein Kinases for Cancer Therapy*, 2010.
- 30 R. Wing, H. Drew, T. Takano, C. Broka, S. Tanaka, K. Itakura and R. E. Dickerson, *Nature*, 1980, **287**, 755–758.
- 31 A. E. Senior, S. Nadanaciva and J. Weber, *Biochim. Biophys. Acta - Bioenerg.*, 2002, **1553**, 188–211.
- 32 G. Manning, D. B. Whyte, R. Martinez, T. Hunter and S. Sudarsanam, *Science*, 2002, **298**, 1912–1934.
- 33 Y. Marcus, *J. Chem. Soc., Faraday Trans.*, 1993, **89**, 713–718.
- 34 Y. Marcus, *Biophys. Chem.*, 1994, **51**, 111–127.
- 35 W. Kunz, J. Henle and B. W. Ninham, *Curr. Opin. Colloid Interface Sci.*, 2004, **9**, 19–37.
- 36 A. E. Hargrove, S. Nieto, T. Zhang, J. L. Sessler and E. V. Anslyn, *Chem. Rev.*, 2011, **111**, 6603–6782.
- 37 B. A. Moyer, R. Custelcean, B. P. Hay, J. L. Sessler, K. Bowman-James, V. W. Day and S.-O. Kang, *Inorg. Chem.*, 2013, **52**, 3473–3490.
- 38 C. A. Seipp, N. J. Williams, M. K. Kidder and R. Custelcean, *Angew. Chemie - Int. Ed.*, 2017, **56**, 1042–1045.
- 39 N. J. Williams, C. A. Seipp, K. A. Garrabrant, R. Custelcean, E. Holguin, J. K. Keum, R. J. Ellis and B. A. Moyer, *Chem. Commun.*, 2018, **54**, 10048–10051.
- 40 J. S. Mendy, M. L. Pilate, T. Horne, V. W. Day and M. A. Hossain, *Chem. Commun.*, 2010, **46**, 6084–6086.
- 41 M. A. Saeed, D. R. Powell, F. R. Fronczek and M. A. Hossain, *Tetrahedron Lett.*, 2010, **51**, 4233–4236.
- 42 C. Caltagirone, P. A. Gale, J. R. Hiscock, S. J. Brooks, M. B. Hursthouse and M. E. Light, *Chem. Commun.*, 2008, 3007–3009.
- 43 P. A. Gale, J. R. Hiscock, C. Z. Jie, M. B. Hursthouse and M. E. Light, *Chem. Sci.*, 2010, **1**, 215–220.
- 44 T. Wang, Y. Bai, L. Ma and X. P. Yan, *Org. Biomol. Chem.*, 2008, **6**, 1751–1755.
- 45 L. M. Hancock, L. C. Gilday, S. Carvalho, P. J. Costa, V. Félix, C. J. Serpell, N. L. Kilah and P. D. Beer, *Chem. - A Eur. J.*, 2010, **16**, 13082–13094.
- 46 S. J. Moore, C. J. E. Haynes, J. González, J. L. Sutton, S. J. Brooks, M. E. Light, J. Herniman, G. J. Langley, V. Soto-Cerrato, R. Pérez-Tomás, I. Marques, P. J. Costa, V. Félix and P. A. Gale, *Chem. Sci.*, 2013, **4**, 103–117.

- 47 E. Masliah, M. Alford, R. DeTeresa, M. Mallory and L. Hansen, *Ann. Neurol.*, 1996, **40**, 759–766.
- 48 E. Foran and D. Trotti, *Antioxidants Redox Signal.*, 2009, **11**, 1587–1602.
- 49 P. F. Behrens, P. Franz, B. Woodman, K. S. Lindenberg and G. B. Landwehrmeyer, *Brain*, 2002, **125**, 1908–1922.
- 50 J. S. Clark, D. H. Vandorpe, M. N. Chernova, J. F. Heneghan, A. K. Stewart and S. L. Alper, *J. Physiol.*, 2008, **586**, 1291–1306.
- 51 D. W. Yoon, D. E. Gross, V. M. Lynch, J. L. Sessler, B. P. Hay and C. H. Lee, *Angew. Chemie - Int. Ed.*, 2008, **47**, 5038–5042.
- 52 M. A. Hossain, M. A. Saeed, F. R. Fronczek, B. M. Wong, K. R. Dey, J. S. Mendy and D. Gibson, *Cryst. Growth Des.*, 2010, **10**, 1478–1481.
- 53 M. A. Saeed, F. R. Fronczek, M. J. Huang and M. Alamgir Hossain, *Chem. Commun.*, 2010, **46**, 404–406.
- 54 Y. Haketa and H. Maeda, *Chem. - A Eur. J.*, 2011, **17**, 1485–1492.
- 55 B. Portis, A. Mirchi, M. H. Hasan, M. E. Khansari, C. R. Johnson, J. Leszczynski, R. Tandon and M. Alamgir Hossain, *ChemistrySelect*, 2020, **5**, 1401–1409.
- 56 J. L. Sessler, S. Camiolo and P. A. Gale, *Coord. Chem. Rev.*, 2003, **240**, 17–55.
- 57 L. C. Gilday and P. D. Beer, *Chem. - A Eur. J.*, 2014, **20**, 8379–8385.
- 58 M. C. T. Fyfe, P. T. Glink, S. Menzer, J. F. Stoddart, A. J. P. White and D. J. Williams, *Angew. Chemie (International Ed. English)*, 1997, **36**, 2068–2070.
- 59 P. A. Gale, J. R. Hiscock, S. J. Moore, C. Caltagirone, M. B. Hursthouse and M. E. Light, *Chem. - An Asian J.*, 2010, **5**, 555–561.
- 60 R. Custelcean, L. H. Delmau, B. A. Moyer, J. L. Sessler, W. S. Cho, D. Gross, G. W. Bates, S. J. Brooks, M. E. Light and P. A. Gale, *Angew. Chemie - Int. Ed.*, 2005, **44**, 2537–2542.
- 61 H. G. Jeon, H. B. Jang, P. Kang, Y. R. Choi, J. Kim, J. H. Lee, M. G. Choi and K. S. Jeong, *Org. Lett.*, 2016, **18**, 4404–4407.
- 62 J. Zhao, D. Yang, Y. Zhao, X. J. Yang, Y. Y. Wang and B. Wu, *Angew. Chemie - Int. Ed.*, 2014, **53**, 6632–6636.
- 63 P. Yang, J. Wang, C. Jia, X. J. Yang and B. Wu, *European J. Org. Chem.*, 2013, 3446–3454.
- 64 B. Wu, F. Cui, Y. Lei, S. Li, N. De Sousa Amadeu, C. Janiak, Y. J. Lin, L. H. Weng, Y. Y. Wang and X. J. Yang, *Angew. Chemie - Int. Ed.*, 2013, **52**, 5096–5100.
- 65 D. Yang, J. Zhao, Y. Zhao, Y. Lei, L. Cao, X. J. Yang, M. Davi, N. De Sousa Amadeu, C. Janiak, Z. Zhang, Y. Y. Wang and B. Wu, *Angew. Chemie - Int. Ed.*, 2015, **54**, 8658–8661.
- 66 B. Wu, S. Li, Y. Lei, H. Hu, N. D. S. Amadeu, C. Janiak, J. S. Mathieson, D. L. Long, L. Cronin and X. J. Yang, *Chem. - A Eur. J.*, 2015, **21**, 2588–2593.
- 67 M. A. Saeed, J. J. Thompson, F. R. Fronczek and M. A. Hossain, *CrystEngComm*, 2010, **12**, 674–676.
- 68 I. Ravikumar, P. S. Lakshminarayanan, M. Arunachalam, E. Suresh and P. Ghosh, *J. Chem. Soc. Dalt. Trans.*, 2009, 4160–4168.

- 69 B. Wu, C. Jia, X. Wang, S. Li, X. Huang and X. J. Yang, *Org. Lett.*, 2012, **14**, 684–687.
- 70 M. J. Kim, H. W. Lee, D. Moon and K. S. Jeong, *Org. Lett.*, 2012, **14**, 5042–5045.
- 71 H. Maeda, Y. Bando, K. Shimomura, I. Yamada, M. Naito, K. Nobusawa, H. Tsumatori and T. Kawai, *J. Am. Chem. Soc.*, 2011, **133**, 9266–9269.
- 72 C. Jia, B. Wu, S. Li, X. Huang, Q. Zhao, Q. S. Li and X. J. Yang, *Angew. Chemie - Int. Ed.*, 2011, **50**, 486–490.
- 73 S. J. Coles, J. G. Frey, P. A. Gale, M. B. Hursthouse, M. E. Light, K. Navakhun and G. L. Thomas, *Chem. Commun.*, 2003, 568–569.
- 74 M. Arunachalam and P. Ghosh, *Chem. Commun.*, 2009, 5389–5391.
- 75 S. Li, C. Jia, B. Wu, Q. Luo, X. Huang, Z. Yang, Q. S. Li and X. J. Yang, *Angew. Chemie - Int. Ed.*, 2011, **50**, 5721–5724.
- 76 J. O. Yu, C. Scott Browning and D. H. Farrar, *Chem. Commun.*, 2008, 1020–1022.
- 77 I. Ravikumar, P. S. Lakshminarayanan and P. Ghosh, *Inorganica Chim. Acta*, 2010, **363**, 2886–2895.
- 78 P. S. Lakshminarayanan, I. Ravikumar, E. Suresh and P. Ghosh, *Chem. Commun.*, 2007, 5214–5216.
- 79 T. K. Ghosh, R. Ghosh, S. Chakraborty, P. Saha, S. Sarkar and P. Ghosh, *J. Water Process Eng.*, 2020, **37**, 101364.
- 80 C. R. Bondy, P. A. Gale and S. J. Loeb, *J. Am. Chem. Soc.*, 2004, **126**, 5030–5031.
- 81 F. Cui, S. Li, C. Jia, J. S. Mathieson, L. Cronin, X. J. Yang and B. Wu, *Inorg. Chem.*, 2012, **51**, 179–187.
- 82 L. P. Zhou and Q. F. Sun, *Chem. Commun.*, 2015, **51**, 16767–16770.
- 83 H. T. Chifotides, I. D. Giles and K. R. Dunbar, *J. Am. Chem. Soc.*, 2013, **135**, 3039–3055.
- 84 L. Xu, D. Zhang, T. K. Ronson and J. R. Nitschke, *Angew. Chemie - Int. Ed.*, 2020, **59**, 7435–7438.
- 85 C. R. K. Glasson, J. K. Clegg, J. C. McMurtrie, G. V. Meehan, L. F. Lindoy, C. A. Motti, B. Moubaraki, K. S. Murray and J. D. Cashion, *Chem. Sci.*, 2011, **2**, 540–543.
- 86 C. R. K. Glasson, G. V. Meehan, J. K. Clegg, L. F. Lindoy, P. Turner, M. B. Duriska and R. Willis, *Chem. Commun.*, 2008, 1190–1192.
- 87 J. S. Fleming, K. L. V. Mann, C. A. Carraz, E. Psillakis, J. C. Jeffery, J. A. McCleverty and M. D. Ward, *Angew. Chemie - Int. Ed.*, 1998, **37**, 1279–1281.
- 88 R. L. Paul, Z. R. Bell, J. C. Jeffery, J. A. McCleverty and M. D. Ward, *Proc. Natl. Acad. Sci. U. S. A.*, 2002, **99**, 4883–4888.
- 89 V. S. Bryantsev and B. P. Hay, *J. Am. Chem. Soc.*, 2006, **128**, 2035–2042.
- 90 B. P. Hay, A. A. Oliferenko, J. Uddin, C. Zhang and T. K. Firman, *J. Am. Chem. Soc.*, 2005, **127**, 17043–17053.
- 91 R. Custelcean, J. Bosano, P. V. Bonnesen, V. Kertesz and B. P. Hay, *Angew. Chemie - Int. Ed.*, 2009, **48**, 4025–4029.
- 92 R. Custelcean, P. V. Bonnesen, N. C. Duncan, X. Zhang, L. A. Watson, G. Van Berkel, W. B. Parson

- and B. P. Hay, *J. Am. Chem. Soc.*, 2012, **134**, 8525–8534.
- 93 O. V. Dolomanov, A. J. Blake, N. R. Champness, M. Schröder and C. Wilson, *Chem. Commun.*, 2003, **3**, 682–683.
- 94 R. Vilar, D. M. P. Mingos, A. J. P. White and D. J. Williams, *Angew. Chemie - Int. Ed.*, 1998, **37**, 1258–1261.
- 95 R. A. Faulkner, L. P. Harding, J. Higginson, C. R. Rice and C. Slater, *Angew. Chemie - Int. Ed.*, 2014, **53**, 13540–13543.
- 96 R. A. Faulkner, N. J. Patmore, C. R. Rice and C. Slater, *Chem. Commun.*, 2018, **54**, 9159–9162.
- 97 C. R. Rice, C. Slater, R. A. Faulkner and R. L. Allan, *Angew. Chemie*, 2018, **130**, 13255–13259.
- 98 C. J. Clemett, R. A. Faulkner, G. Midgley, C. Slater and C. R. Rice, *Polyhedron*, 2020, **182**, 114483.
- 99 S. J. Allison, J. Bryk, C. J. Clemett, R. A. Faulkner, M. Ginger, H. B. S. Griffiths, J. Harmer, P. Jane Owen-Lynch, E. Pinder, H. Wurdak, R. M. Phillips and C. R. Rice, *Nat. Commun.*, 2022, **12**, 3898.
- 100 P. Cohen, *Nat. Rev. Drug Discov.*, 2002, **1**, 309–315.
- 101 T. Hunter, *Cell*, 1995, **80**, 225–236.
- 102 J. Zhao, *Pharmacol. Ther.*, 2016, **160**, 145–158.
- 103 D. G. Hardie, F. A. Ross and S. A. Hawley, *Nat. Rev. Mol. Cell Biol.*, 2012, **13**, 251–262.
- 104 T. Hunter, *Cell*, 1987, **49**, 1–4.
- 105 S. M. Thomas and J. S. Brugge, *Annu. Rev. Cell Dev. Biol.*, 1997, **13**, 513–609.
- 106 C. J. Qin, L. James, J. D. Chartres, L. J. Alcock, K. J. Davis, A. C. Willis, A. M. Sargeson, P. V. Bernhardt and S. F. Ralph, *Inorg. Chem.*, 2011, **50**, 9131–9140.
- 107 R. L. Frank and P. V. Smith, *Org. Synth.*, 1948, **28**, 89–91.
- 108 R. Andrews, S. Begum, C. J. Clemett, R. A. Faulkner, M. L. Ginger, J. Harmer, M. Molinari, G. M. B. Parkes, Z. M. H. Qureshi, C. R. Rice, M. D. Ward, H. M. Williams and P. B. Wilson, *Angew. Chemie*, 2020, **132**, 20660–20664.
- 109 T. Bowen, R. P. Planalp and M. W. Brechbiel, *Bioorganic Med. Chem. Lett.*, 1996, **6**, 807–810.
- 110 D. Ben-Ishai and A. Berger, *J. Org. Chem.*, 1952, **17**, 1564–1570.
- 111 Int. Pat., WO2012041862, 2012, 26–27.
- 112 A. L. Williams, S. R. Dandepally and S. V. Kotturi, *Mol. Divers.*, 2010, **14**, 697–707.
- 113 S. Ram and L. D. Spicer, *Tetrahedron Lett.*, 1987, **18**, 515–516.
- 114 J. Yoshimura, M. Yamaura, T. Suzuki and H. Hashimoto, *Chem. Lett.*, 1983, 1001–1002.
- 115 S. D. Bull, S. G. Davies, C. Fenton, A. W. Mulvaney, R. Shyam Prasad and A. D. Smith, *J. Chem. Soc. Perkin Trans. 1*, 2000, 3765–3774.
- 116 J. V. B. Kanth, C. K. Reddy and M. Periasamy, *Synth. Commun.*, 1994, **24**, 313–319.
- 117 K. Moriyama, Y. Nakamura and H. Togo, *Org. Lett.*, 2014, **16**, 3812–3815.
- 118 C. Mikel and P. G. Potvin, *Polyhedron*, 2002, **21**, 49–54.

- 119 A. Jacques, S. Cerfontaine and B. Elias, *J. Org. Chem.*, 2015, **80**, 11143–11148.
- 120 W. E. Stamm, L. Duncan, J. Schaeffer, C. Langenaur, N. Agabian, M. Romantschuk, D. H. Bamford, D. E. Bradley, M. Kagayama, L. A. McTaggart, R. C. Rigby, D. T. Uehling, K. Mizutani, E. Balish, R. P. Becker, J. F. Hinman, L. Reed, R. C. B. Slack, B. F. Martin, B. I. Eisenstein, F. C. Minion and J. D. Goguen, *Science*, 1998, **282**, 1497–1501.
- 121 H. Wurdak, S. Zhu, A. Romero, M. Lorgner, J. Watson, C. Yuan Chiang, J. Zhang, V. S. Natu, L. L. Lairson, J. R. Walker, C. M. Trussell, G. R. Harsh, H. Vogel, B. Felding-Habermann, A. P. Orth, L. J. Miraglia, D. R. Rines, S. L. Skirboll and P. G. Schultz, *Cell Stem Cell*, 2010, **6**, 37–47.
- 122 E. S. Polson, V. B. Kuchler, C. Abbosh, E. M. Ross, R. K. Mathew, H. A. Beard, B. Da Silva, A. N. Holding, S. Ballereau, E. Chuntharpursat-Bon, J. Williams, H. B. Griffiths, H. Shao, A. Patel, A. J. Davies, A. Droop, P. Chumas, S. C. Short, M. Lorgner, J. E. Gestwicki, L. D. Roberts, R. S. Bon, S. J. Allison, S. Zhu, F. Markowitz and H. Wurdak, *Sci. Transl. Med.*, 2018, **10**, eaar2718.
- 123 S. J. Allison, D. Cooke, F. S. Davidson, P. I. P. Elliott, R. A. Faulkner, H. B. S. Griffiths, O. J. Harper, O. Hussain, P. J. Owen-Lynch, R. M. Phillips, C. R. Rice, S. L. Shepherd and R. T. Wheelhouse, *Angew. Chemie - Int. Ed.*, 2018, **57**, 9799–9804.